Triannual Report 2002 — 2004

Research Group "Scanning Probe Methods"

University of Hamburg
Microstructure Advanced
Research Center Hamburg
and Institute of Applied Physics

Jungiusstraße 11
D-20355 Hamburg, Germany

Contact:
Prof. Dr. Roland Wiesendanger
Tel. (++49) 40-42838-5244 (direct)
(++49) 40-42838-3203/-7045 (secretary)
FAX (++49) 40-42838-6188
e-mail wiesendanger@physnet.uni-hamburg.de
WWW www.nanoscience.de

Contents

Chapter 1

Preface

This is the fourth triannual report of the research group "Scanning Probe Methods" at the Institute of Applied Physics and "Microstructure Advanced Research Center Hamburg (MARCH)" of the University of Hamburg. MARCH was officially opened in February 1996 and was established as a joint effort of the Federal Government (the "Bund") and the State of Hamburg. Six experimental research groups are involved in MARCH covering the following topics: nanostructure physics, semiconductor physics, scanning probe methods, surface and interface physics, magnetism and low temperature physics, and growth of semiconductor heterostructures and nanostructures. Almost 150 scientists are working at MARCH.

In 1997, one year after the opening of MARCH, a DFG-Sonderforschungsbereich (SFB 508) on "Quantum materials" was established (chairperson: Prof. Dr. Detlef Heitmann, MARCH) which involves research groups from MARCH, from the I. Institute of Theoretical Physics, from HASYLAB/DESY, and from the Institute of Physical Chemistry. The SFB 508 deals with quantum phenomena in nanostructured III-V-semiconductors which are manifested in energy-quantization, tunnel-effects, as well as Coulomb, exchange, and correlation effects. The three primary research areas include "lateral nanostrucures", "hybrid structures", and "clusters".

Currently, we are initiating a second DFG-Sonderforschungsbereich (SFB 668) on "Magnetism from the single atom to the nanostructure" which is focussed on fundamental studies of magnetic properties of nanostructures in contact with a substrate, including spin structures in thermal equilibrium as well as transport and dynamic properties. This new SFB involves research groups from MARCH, from the I. Institute of Theoretical Physics, from the Institute of Experimental Physics, from the research center GKSS, and from the Institute of Experimental and Applied Physics of the University of Kiel.

Since 1998 MARCH is hosting a coordination site of the German "Center of Competence in Nano-scale Analysis" (CCN) funded by the Federal Ministry for Education and Research (BMBF). This Center of Competence is organized as a transregional network of research groups at universities, at research centers, and in industry and promotes technology transfer, activities leading to new start-up companies, and public information services in the area of nanoscience and nanotechnology. In 2003, the CCN coordination site at Hamburg has been refocussed towards a more regional perspective and has been named "HanseNanoTec". It provides a valuable support of the infrastructure at MARCH, e.g. for secretary services, public relation services, technology transfer, and preparation of research proposals.

A very important event in 2004 was the opening of a renewed building (Jungiusstrasse 9A), the historical "Otto-Stern-building", for the HanseNanoTec and for the steadiliy increasing research activities of our group. This major event was celebrated with an International Symposium entitled "Atom manipulation, single spins, and atomic forces: Novel perspectives in the nanoscience era". Similar to the MARCH building, the "Otto-Stern building" now offers several special labs with separate foundations and acoustic shielding for highest resolution scanned probe spectroscopy experiments.

Another important event in 2004 was the decision of the Free and Hanseatic City of Hamburg to establish a new Interdisciplinary Nanoscience Center Hamburg (INCH). The declared long-term goal of this new center is to gain fundamental insight into nanoscience-related problems through more intense research in areas bordering the traditional disciplines. In particular, this new center should bridge the gap between the activities in physical-based ("dry") nanotechnology and biochemical-based ("wet") nanotechnology. An International Symposium on "Nanobiomedicine" held in July 2004 at the University Hospital Eppendorf (UKE) has highlighted the current status and future challenges of this exciting research field.

In this triannual report the scientific achievements of the research group "Scanning Probe Methods" are summarized covering the following topics: magnetic nanostructures, semiconductor quantum structures and hybrid systems, insulators, molecular systems, and instrumental developments. The research activities of our group in the time period 2002 - 2004 resulted in 75 scientific publications (among them 2 in "Science" and 14 "Physical Review Letters") and 300 presentations at conferences, colloquia or seminars (including 100 invited talks at international meetings). Several prizes and awards were given to members of our group in the past three years, including the Prof. Dr. Jürgen Geiger Prize 2002 (Dr. André Kubetzka), the Philip Morris Forschungspreis 2003 (Prof. Dr. Roland Wiesendanger and Dr. Matthias Bode), the Walter Schottky Prize 2004 (PD Dr. Markus Morgenstern), the German Nanoscience Prize 2004 (Dr. Oswald Pietzsch), the Research Award of the Hamburg Foundation of Science, Development, and Culture 2004 (Dr. Kirsten von Bergmann), and the Hertha

Sponer Prize 2005 (Dr. Elena Vedmedenko). Furthermore, Dr. Markus Morgenstern received a Heisenberg-stipend from the German Science Foundation (DFG) and finally a call from the RWTH Aachen to become Full Professor (C4) in 2004. He is already the fourth member of our group who has been offered a professorship.

This research report provides a good opportunity to thank all funding agencies including the DFG, the BMBF, the EU, the Stifterverband für die Deutsche Wissenschaft, as well as several industrial companies for their financial support of our research activities. In particular we would like to thank the Ministry of Science and Health (BWG) of the Free and Hanseatic City of Hamburg and the University of Hamburg for their continuous strong support of our activities in nanoscience and nanotechnology. I would also like to take the opportunity to thank all the past and present members of the research group "Scanning Probe Methods" for their strong devotion to establish MARCH as an internationally recognized Center of Excellence. Finally, we gratefully acknowledge the excellent support by our central mechanical and electronic workshops, as well as by our secretaries and administration staff.

Hamburg, January 2005

Prof. Dr. Roland Wiesendanger

(Managing Director of the Institute of Applied Physics,
Coordinator of the Center of Competence HanseNanoTec, and
Scientific Coordinator of the Interdisciplinary Nanoscience Center Hamburg)

Chapter 2

Staff Members

Head

Prof. Dr. Roland Wiesendanger

Secretary

Ute Brenger
Renate Schulze

Public Relations Office

Dipl.-Chem. Heiko Fuchs
Dr. Shenja Langkat (until December 2004)
Dipl.-Jour. Dipl.-Phys. Klaus Schoepe (until July 2004)

Technical Support

Dipl.-Ing. Michael Langer
PTA Norbert Dix

Senior Scientists

Dr. Makoto Ashino
Dr. Kirsten von Bergmann
Dr. habil. Matthias Bode
PD Dr. Mathias Getzlaff (until December 2002)
Dr. Martin Janson (until December 2004)
Dr. Katsushi Hashimoto
Dr. Daniel Haude
Dr. Germar Hoffmann
Dr. André Kubetzka

Dr. Giuseppe Maruccio
Dr. Tomohiro Matsui
Dr. Christian Meyer
PD Dr. Markus Morgenstern (until July 2004)
Dr. Oswald Pietzsch
Dr. Robert Ravlić
Dr. Tobias Richter
Dr. Alexander Schwarz
Dr. Elena Vedmedenko
Dr. Jens Wiebe
Dr. Michaela Zeyer-Düsterer

Ph. D. Students

Timo Behnke (until December 2004)
Luis Berbil-Bautista
Torben Hänke
Volker Hagen (until June 2003)
Johannes Isenbart (until June 2002)
Uwe Kaiser
Jan Klijn (until September 2003)
Stefan Krause
Stefan Kuck
Marcus Liebmann (until March 2003)
Theophilos Maltezopoulos (until March 2004)
Felix Marczinowski
Focko Meier
Lilli Sacharow
Martin von Sprekelsen
André Wachowiak (until May 2003)

Diploma Students

Oliver Lemcke (until May 2004)
Knud Lämmle
Torge Mashoff (until July 2004)
Nico Plock (until April 2004)
René Schmidt
Niklas Stein
Jan Wienhausen

Guest Researchers

Dr. Julian Chen, IBM Yorktown Heights, USA
Dr. Jaques Dumont, Facultés Universitaires Notre-Dame de la Paix, Numur, Belgium (March - December 2003)
Prof. Dr. Ulrich Gradmann, Clausthal-Zellerfeld, Germany (October 2003)
Dr. Elena Konenkova, Ioffe-Institute, Russian Academy of Sciences, St. Petersburg, Russia (July 2003 - June 2004)
Prof. Dr. Bang-Gui Liu, Institute of Physics, Chinese Academy of Science, Beijing, China (January 2003)
Dr. Ichiro Shiraki, Dept. of Physics, University of Tokyo, Japan (February 2002)

Chapter 3

Research Activities 2002-2004

3.1 Overview

R. Wiesendanger

Our research activities are concentrated on nanometer-scale probe methods. In particular, emphasis is put on the investigation of the fundamental relationship between nanostructure and nanophysical properties. Scanning probe methods are ideally suited for such investigations because they provide high spatial resolution combined with spectroscopical capabilities. By choosing an appropriate type of interaction between probe tip and sample, almost any kind of nanophysical property can be studied by scanning probe methods. We apply scanning probe methods (SPM) to various classes of materials, including metals, semiconductors, insulators, superconductors, magnetic materials, as well as organic thin films and molecular materials.

To be able to make significant contributions to this rapidly developing field, a major part of our activities is devoted to new developments or further improvements on SPM instrumentation, including the development of new positioning devices with nanometer-scale accuracy, the development of new types of sensors, or the development of dedicated SPM instruments which can operate under extreme conditions (e.g. UHV, low temperatures and high magnetic fields). Special emphasis is also put on the development of new experimental methods based on the local probe geometry, which usually requires adjustments of the hardware and software for SPM data acquisition. These developments are often made in close collaboration with European companies specialized in SPM instrumentation.

In the following, a brief summary of the highlights of our research activities in the time period of 2002 - 2004 is provided. For further information, please do not hesitate to contact us. We will be glad to provide reprints of publications on specific topics.

3.2 Magnetic nanostructures

3.2.1 Spin-polarized scanning tunneling microscopy (SP-STM) and spectroscopy (SP-STS) studies

In recent years great progress has been achieved in the preparation of self-organized and lithographically manufactured magnetic nanostructures [1]. The structural properties of these nanostructures could routinely be investigated by high-resolution real-space imaging techniques like scanning electron microscopy (SEM) and scanning tunneling microscopy (STM) down to the atomic scale. In contrast, a detailed understanding of nanomagnetic properties has been hindered by the fact that experimental data have been obtained by methods which average over a fraction of the sample surface being much larger than the atomic length scale. So far, the limit of spatial resolution of the most advanced magnetic imaging techniques like magnetic force microscopy (MFM) and SEM with polarization analysis (SEMPA) has been on the order of several tens of nanometers (nm). Therefore, it has been proposed very early to make the tip of the STM sensitive to the spin of the tunneling electrons by illuminating GaAs tips with circularly polarized light or by using ferromagnetic tips. Although spin-polarized electron tunneling in planar junctions is an established experimental technique it turned out that the realization of this idea is difficult. Spin-polarized tunneling using an STM has first been observed by Wiesendanger and co-workers in the early 1990s. In this experiment, CrO_2 thin film tips with a high degree of spin polarization were successfully used to detect periodic alternations of the measured monatomic step heights in constant-current images. The deviations of the measured step height values from the topographic monatomic step height could directly be related with the effective spin polarization of the tunnel junction. A significant drawback of this experimental approach was the superposition of topographic and magnetic structure information. As we have shown in the previous triannual report of our research group we could overcome this problem by combining SP-STM with spectroscopic techniques.

This allowed the successful separation of topographic, electronic and magnetic information thereby achieving magnetic domain and domain wall images of even micromagnetically complicated magnetic surfaces with subnanometer spatial resolution. Nevertheless, spin-polarized scanning tunneling microscopy (SP-STM) performed in the constant-current mode is still the method of choice to resolve complex surface spin-structures, as, e.g., collinear or non-collinear antiferromagnetic structures, on the atomic scale.

3.2.2 Magnetism of clean and Fe–covered Cr(001)

M. Bode, R. Ravlić, M. Kleiber, A. Kubetzka, and R. Wiesendanger

Introduction

Since the discovery of novel magnetic effects such as giant magnetoresistance [1,2] and interlayer exchange coupling [3] and their rapid application in data storage devices the magnetism of Cr has attracted considerable interest. Bulk Cr exhibits a transversal spin-density wave (SDW) below the Néel transition temperature $T_{\mathrm{N}} = 311\,\mathrm{K}$ and a longitudinal SDW below the spin-flip temperature $T_{\mathrm{SF}} = 121\,\mathrm{K}$. In particular, (001) terminated interfaces have been used in Fe/Cr multilayers [4]. The magnetic properties of the Cr(001) surface have been studied theoretically and experimentally. Early experimental results were rather confusing since angle- and energy-resolved photoemission indicated that the Cr surface states are exchange split [5] but no net magnetization was found by spin-resolved photoemission [6]. This apparent inconsistency was explained by Blügel *et al.* [7] who calculated that the magnetic moments of any atomically flat terrace couple parallel but—as a result of the antiferromagnetism of Cr—adjacent terraces are magnetized antiparallel. Since this model implies a close link between the surface topology and the magnetic structure the magnetic state of Cr(001) was called "topological antiferromagnetism". It was confirmed experimentally by the SP-STM study of Wiesendanger et al. in 1990.

Here we review the magnetic structure of the clean Cr(001) surface, the influence of screw and step dislocations, which are regularly found even in single crystalline samples, and on the magnetic behavior of Fe islands and films on Cr(001).

Experimental setup

The experiments were performed in an ultra-high vacuum (UHV) system with two separate chambers: a preparation chamber for the tip and sample treatment and an analysis chamber for sample surface characterization by means of low-energy–electron-diffraction (LEED) and Auger–electron-spectroscopy (AES). Furthermore, a satellite of the analysis chamber contains a combined atomic force and scanning tunneling microscope (AFM/STM) which has a maximum scan range of $6\,\mu\mathrm{m} \times 6\,\mu\mathrm{m}$ and which is operated at room temperature (RT). The base pressure in both chambers is in the low 10^{-11} torr range. The Cr(001) single crystal was cleaned by prolonged cycles of Ar^+-ion etching at elevated temperatures ($T \leq 1100\,\mathrm{K}$) and subsequent annealing for 20–30 min at $T = 1150\,\mathrm{K}$. Compared to earlier results the amount of residual impurities could be reduced significantly by using an Ar^+-ion gun with a mass filter (Wien filter). Eventually, the Cr(001) surface contains less than 2% of carbon (C). All other elements, as, e.g., O, S and N, are below the AES sensitivity limit of $\leq 1\%$. The cleanliness of the surface is corroborated by the existence of a d_{z^2}-like surface state close to the Fermi level E_{F} which showed up as a distinct peak in scanning tunneling

spectroscopy (STS) measurements [8, 9] and which is characteristic for clean bcc(001) surfaces [10].

We used polycrystalline W tips which were electrochemically etched *ex situ* and cleaned *in vacuo* by a high-temperature flash at $T \geq 2200\,\mathrm{K}$. Spin-resolved studies were carried out by using *in situ* prepared Fe-coated W tips. Details of the tip preparation procedure are described in Ref. [11]. We know from previous experiments, which partly have been performed in an external magnetic field, that Fe-coated W tips are preferentially magnetized perpendicular to the tip axis [11, 12], i.e., parallel to the sample's surface plane. The tunneling spectra were measured by adding a modulation voltage $U_{\mathrm{mod}} = 15\,\mathrm{mV_{rms}}$ to the applied sample bias U and recording the $\mathrm{d}I/\mathrm{d}U$ signal by lock-in technique.

All "topographic" STM images shown below were measured in the constant-current mode of operation. The STM data have been plane-fitted on atomically flat terraces to correct for the tilt of the sample. In order to enhance the contrast we mixed the tip height z and its derivative with respect to the fast scan direction x, $\mathrm{d}z/\mathrm{d}x$. This image processing suggests to the spectator a topography which is illuminated by an invisible light source from the left.

The clean Cr(001) substrate

The constant-current STM image in Fig 3.1(a) shows the topography of a Cr(001) surface. Ten smooth terraces are visible descending from the lower right to the upper left edge. The section in the lower panel of Fig 3.1(a) drawn along the line in the image shows that adjacent terraces are separated by monatomic, straight step edges of 1.45 Å height. A distinct peak close to the Fermi level E_{F} [inset of Fig. 3.1(a)] shows up in scanning tunnelling spectroscopy (STS) measurements of the Cr(001) surface [8, 9]. This peak was identified as the spectroscopic signature of a d_{z^2}-like surface state which is characteristic for clean bcc(001) surfaces [10]. The cleanliness of the Cr substrate was also corroborated by LEED and AES. The above mentioned d_{z^2}-like surface state is the minority spin-part of an exchange split d-band. It possesses a high spin polarization and is therefore well-suited for the spin-polarized scanning tunnelling spectroscopy (SP-STS) carried out by using a magnetic tip. In this case the tunneling current that flows between the electronically homogeneous Cr(001) sample surface and the tip depends on their relative magnetization directions [13]:

$$I_{\mathrm{sp}}(\vec{r}, U_0) = I_0[1 + P_{\mathrm{s}} P_{\mathrm{t}} \cdot \cos(\vec{M}_{\mathrm{s}}, \vec{M}_{\mathrm{t}})] \;, \tag{3.1}$$

where $I_0 = I_0(\vec{r}, U_0)$ is the non–spin-polarized part of the tunnelling current, $\vec{M}_{\mathrm{t}}$ and $\vec{M}_{\mathrm{s}}$ are the magnetization vectors of the tip and the sample, respectively, $P_{\mathrm{t}} = P_{\mathrm{t}}(E_{\mathrm{F}})$ is the spin polarization of the tip at E_{F}, and $P_{\mathrm{s}} = P_{\mathrm{s}}(E_{\mathrm{F}} + eU_0)$ is the spin polarization of the sample at the energy $E_{\mathrm{F}} + eU_0$.

As mentioned above the magnetic moments of any atomically flat terrace couple parallel but—as a result of the antiferromagnetism of Cr—adjacent terraces are magnetized antiparallel. Since this model implies a close link between the surface topology

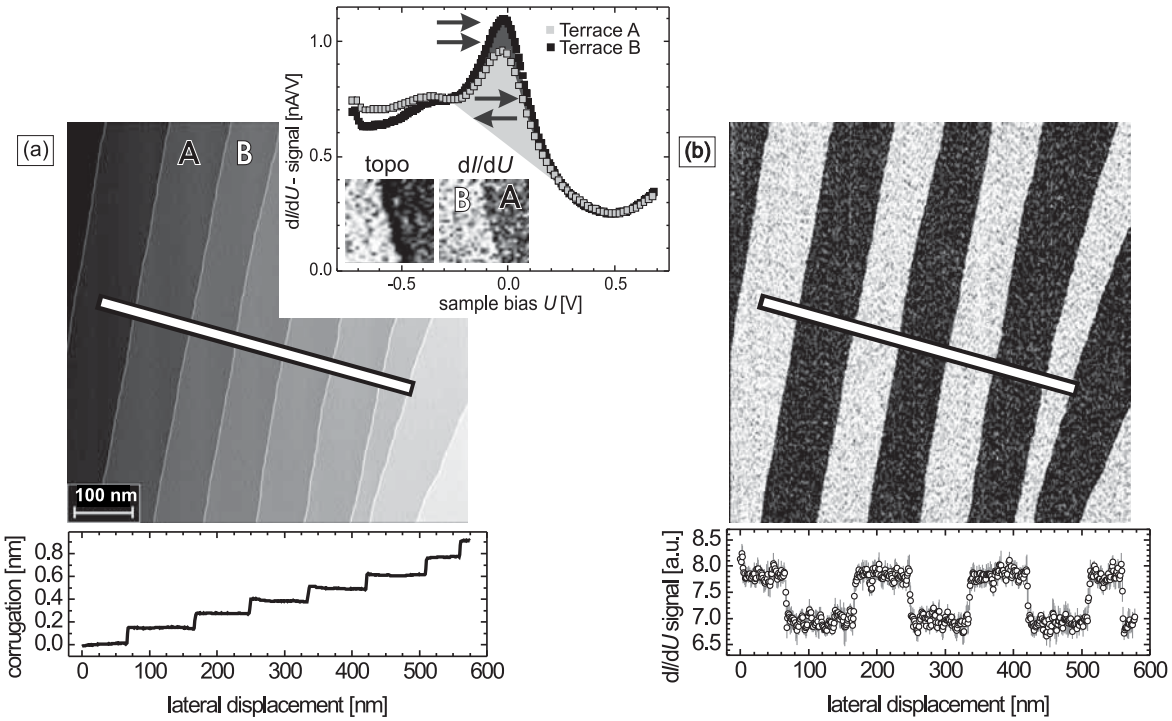

Figure 3.1: **(a)** Topography and **(b)** map of the $\mathrm{d}I/\mathrm{d}U$ signal of the clean Cr(001) surface as measured with a Fe coated W tip in the constant-current mode. The averaged cross section in the lower panels were drawn along the lines in the images. Neighbored terraces are always separated by a monatomic step of 1.45 Å height. The inset in **(a)** shows tunneling spectra recorded above adjacent terraces A and B being magnetized in opposite directions. As a result of different relative orientation between tip and sample magnetization the surface state peak exhibits a distinct intensity variation. The measurement parameters were $U = -150\,\mathrm{mV}$ and $I = 0.7\,\mathrm{nA}$.

and the magnetic structure the magnetic state of Cr(001) was called "topological antiferromagnetism" [7]. The inset in Fig 3.1(a) shows experimental tunneling spectra which have been measured with a Fe coated W tip over two neighbored terraces A and B indicated in Fig 3.1(a). As a result of different relative orientations between the magnetization of the tip and the sample we observe different peak intensities [cf. Eq. 3.1]. This intensity variation may be used for mapping the $\mathrm{d}I/\mathrm{d}U$ signal in the constant-current mode at a suitable bias voltage U simultaneously with the topographic image. For example, Fig 3.1(b) shows a $\mathrm{d}I/\mathrm{d}U$ map which has been measured simultaneously with the topographic data of Fig 3.1(a) at $U - 150\,\mathrm{mV}$. Obviously, the $\mathrm{d}I/\mathrm{d}U$ signal abruptly alternates between two discrete levels when crossing a monatomic step edge separating adjacent Cr(001) terraces thereby confirming the model of "topological antiferromagnetism" [7]. Typically, the magnetic variation of the $\mathrm{d}I/\mathrm{d}U$ signal amounts to 10-12%.

Step and screw dislocations

To our experience structural defects are regularly found even on well-prepared Cr(001) surfaces. These defects may be complex, but they can always be reduced to a superposition of the two elementary defects, i.e., screw and step dislocations as schematically represented in Fig. 3.2(a) and (b), respectively. Both, screw as well as step dislocations, are defined by the so-called Burgers-vector $\vec{b}$ which describes the line along which one half of the crystal is displaced. The Burgers-vector $\vec{b}$ of a screw dislocation is pointing parallel to the dislocation line $\overline{\mathrm{BC}}$. If the top plane of Fig. 3.2(a) is imaged an additional, semi-infinite step edge appears on the surface at point C. The Burgers-vector $\vec{b}$ of a step dislocation is perpendicular to the dislocation line $\overline{\mathrm{BC}}$. Effectively, an additional semi-infinite plane (as indicated by the grey line) is inserted into the crystal. If the dislocation line $\overline{\mathrm{BC}}$ is located sufficiently close to the imaged surface [top plane of Fig. 3.2(b)] the resulting mechanical strain cannot relax and the surface buckles by half of the cubic lattice constant. As we will see in the following, both dislocations make the magnetic structure more complicated.

Figure 3.3(a) shows the topography of a surface area of the Cr(001) single crystal with two screw dislocations which are marked by arrows. Each screw dislocation leads to the formation of a semi-infinite step edge which starts at the respective point of interception of the dislocation line with the Cr(001) surface plane. The two step edges propagate into opposite directions. Our results indicate that step edges which are caused by screw dislocations are oriented almost parallel towards other step edges. Thereby, the crossing of different step edges is avoided.

Obviously, the resulting terrace-and-step structure of Fig. 3.3(a) cannot exhibit a perfect topological antiferromagnetic order as shown in Fig. 3.1. Between the two screw dislocations a domain wall is formed. We have determined the domain wall width by drawing line sections along the lines (i) and (ii) in Fig. 3.3(b). The result is plotted

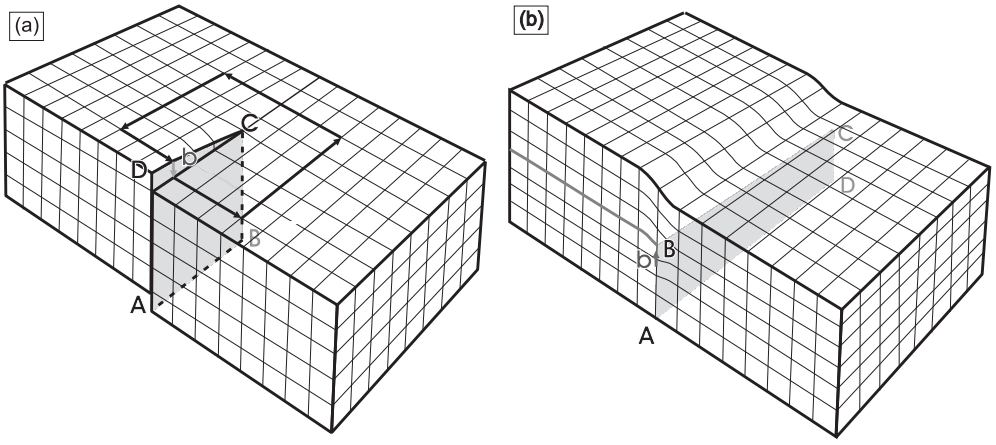

Figure 3.2: Schematic representation of **(a)** a screw and **(b)** a step dislocation.

in Fig. 3.3(c). A quantitative analysis can be performed on the basis of continuum micromagnetic theory [25]. We have fitted the measured data with a standard domain wall profile

$$y(x) = y_0 + y_{\mathrm{sp}} \cdot \cos(\arccos[\tanh((x - x_0)/(w/2))] + \phi)\,, \tag{3.2}$$

where $y(x)$ is the $\mathrm{d}I/\mathrm{d}U$ signal measured at position x, x_0 is the position of the domain wall, w the domain wall width, y_0 and y_{sp} are the non–spin-polarized and spin-polarized part of the $\mathrm{d}I/\mathrm{d}U$ signal. ϕ is the angle between the tip and sample magnetization. The best fits for domain wall profiles were achieved with $\phi = 30\,^\circ$ leading to a width of $w_{\mathrm{i}} = 145 \pm 4\,\mathrm{nm}$ and $w_{\mathrm{ii}} = 109 \pm 3\,\mathrm{nm}$. The width of wall (i) is in good agreement with former results which showed a domain wall width of 120-170 nm [8, 9]. As we will see below the width of the wall (ii) is reduced because of its close proximity to the screw dislocation.

We have experimentally studied the dependence of the domain wall width on the distance from the screw dislocation at the location of the Cr(001) surface which is shown in Fig. 3.4(a). Approximately 100 nm from the next step edge a single screw dislocation can be recognized in the upper left corner of the image. The magnetic $\mathrm{d}I/\mathrm{d}U$ map of Fig. 3.4(b) reveals that this screw dislocation is the starting point of a domain wall which propagates towards the upper side of the image. Starting at the tail of the arrow (zero lateral displacement) we have drawn eight circular line sections counterclockwise around the screw dislocation at different radii r_{avg} from 75 nm down to 7.5 nm. The data are plotted in Fig. 3.4(c). In order to improve the signal-to-noise ratio the data have been averaged between r_{min} and r_{max}. Again, the domain wall profiles were fitted with Eq. 3.2. The results are shown as grey lines in [Fig. 3.4(c)]. Except for the smallest average radius ($r_{\mathrm{avg}} = 7.5 \pm 2.5\,\mathrm{nm}$) we find an excellent agreement with the experimental data. At an average radius $r_{\mathrm{avg}} = 75\,\mathrm{nm}$

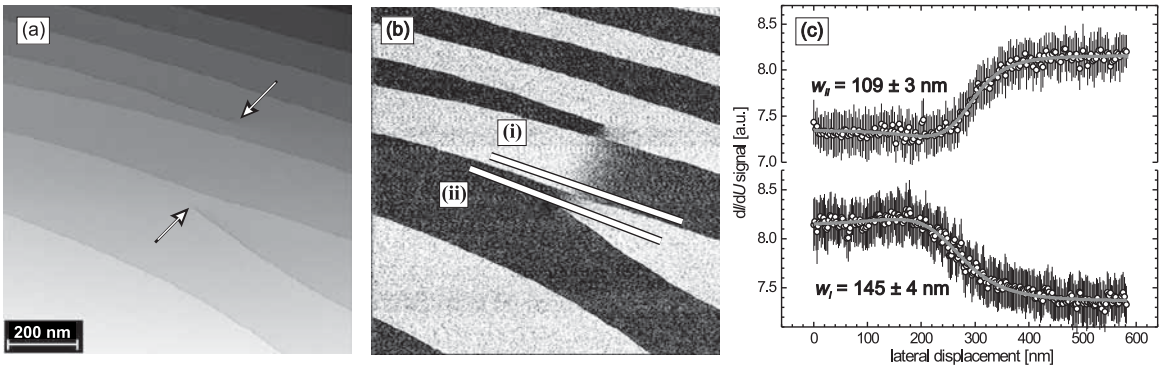

Figure 3.3: **(a)** Topography and **(b)** magnetic $\mathrm{d}I/\mathrm{d}U$ signal of a Cr(001) surface with two screw dislocations (measurement parameters: $U = -150\,\mathrm{mV}$ and $I = 0.7\,\mathrm{nA}$). The magnetic frustration leads to the formation of a domain wall between the dislocations. **(c)** Line sections drawn across the domain wall on two adjacent terraces along the lines in (b). The fits of the domain wall profiles result in wall widths of 145 nm and 110 nm.

the domain wall width is $w_1 = 125 \pm 3\,\mathrm{nm}$ being in close agreement with the intrinsic domain wall width of Cr(001) as determined far away from screw dislocations. This may not be surprising as the circumference amounts to 471 nm which is much larger than the intrinsic domain wall width. However, as soon as r_{avg} is reduced below 60 nm a significant reduction of the domain wall width can be observed although the circumference still exceeds the intrinsic domain wall width.

We have simulated the spin structure which is formed around a screw dislocation by

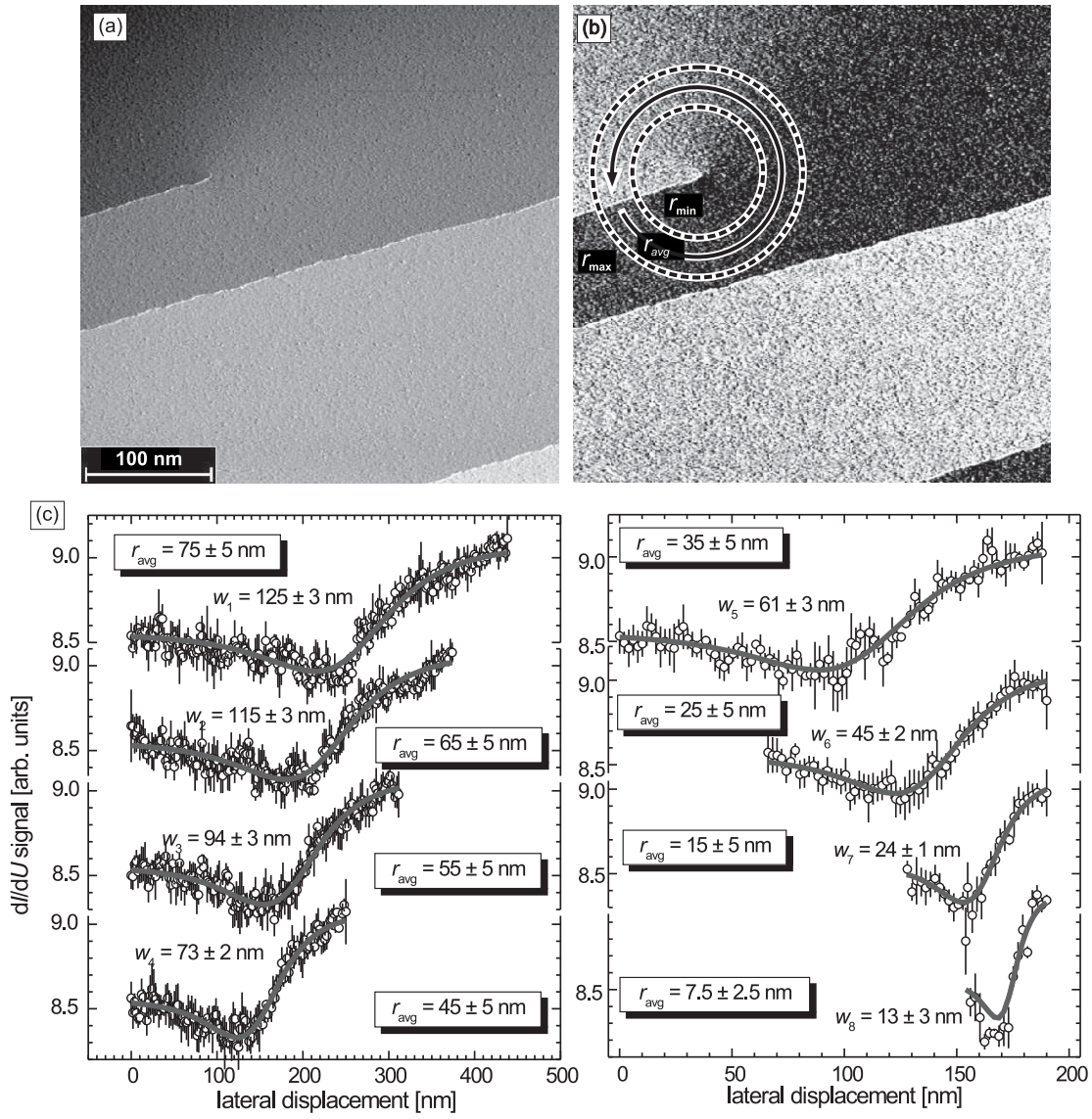

Figure 3.4: **(a)** Topography and **(b)** magnetic $\mathrm{d}I/\mathrm{d}U$ signal of a Cr(001) surface with a single screw dislocation (measurement parameters: $U = -43\,\mathrm{mV}$ and $I = 0.22\,\mathrm{nA}$). The magnetic frustration leads to the formation of a domain wall. **(c)** Circular sections drawn at different radii around the center of the screw dislocation.

performing micromagnetic calculations [14]. The magnetic frustration of a screw dislocation was mimicked by a negative exchange coupling along the line $\overline{\mathrm{AB}}$ in Fig. 3.5(a) while keeping the exchange coupling positive elsewhere. The sample has lateral dimensions of 1000 nm × 750 nm and a height of 2 nm. It was discretized into cells of 1 nm × 1 nm × 2 nm. According to the relationship $w = 2\sqrt{A/k}$ the domain wall width

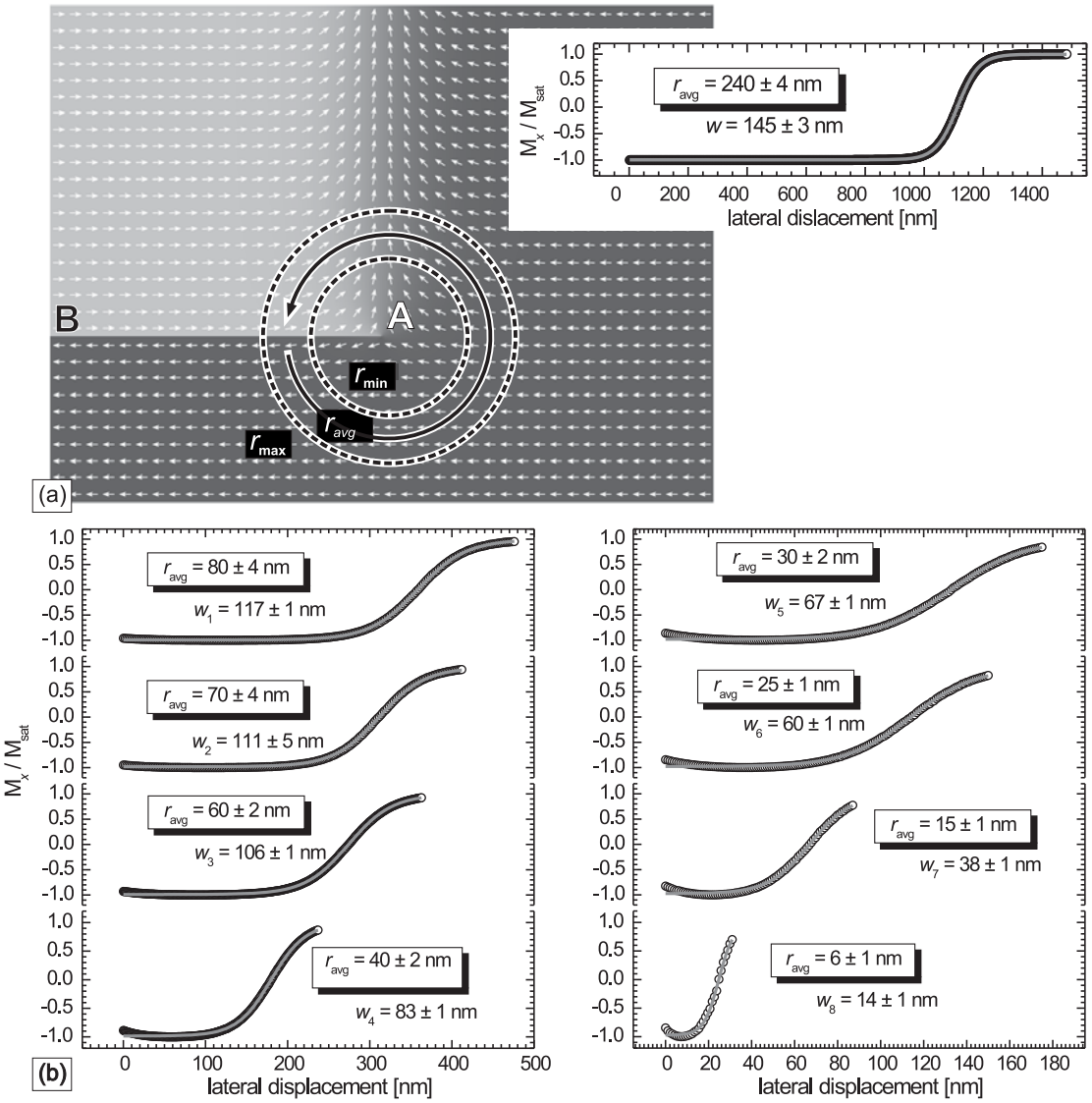

Figure 3.5: **(a)** Calculated spin structure [14] of a screw dislocation (1000 nm × 750 nm). The inset shows a circular section around the screw dislocation of the x-component of the magnetization measured at an average radius $r_{\mathrm{avg}} = 240$ nm. This and larger radii result in domain wall widths w being consistent with an infinite domain wall. **(b)** Circular sections of the calculated spin-structure (∘) drawn at different radii around the center of the screw dislocation. Each circular section was fitted with Eq. 3.2 (grey line).

w is one-to-one determined by the ratio A/k, where A is the so-called exchange stiffness and k is the effective anisotropy energy density. On the basis of the measured Cr domain wall width $w_{\mathrm{Cr}} = 150\,\mathrm{nm}$ we can deduce that $A_{\mathrm{Cr}}/k_{\mathrm{Cr}} = 5.625 \times 10^{-15}\,\mathrm{m}^2$. For instance, we may assume that $A_{\mathrm{Cr}} = 1 \times 10^{-11}\,\mathrm{J/m}$ and $k_{\mathrm{Cr}} = 1.77 \times 10^{3}\,\mathrm{J/m}^3$. Since the magnetic moments of adjacent atoms in antiferromagnets compensate each other Cr produces no stray field. Therefore, it is not necessary to consider any demagnetizing field.

The inset of Fig. 3.5(a) reveals that the chosen material parameters lead to a domain wall width that is consistent with an infinite wall as long as a circular line section with a sufficiently large average radius ($r_{\mathrm{avg}} > 240\,\mathrm{nm}$) is drawn around the screw dislocation. In some respects the spin structure around the screw dislocation shown in Fig. 3.5(a) resembles the magnetic configuration as found in small ferromagnetic islands, e.g., circular dots of permalloy with sub-micrometer size [15, 16] or small Fe islands on W(110) [17] which will be discussed in Sec. 3.2.4. There exist, however, two differences between the spin frustration in an antiferromagnet around a screw dislocation and the spin structure of a ferromagnetic vortex which are of great importance for the resulting spin structure: (i) In contrast to the ferromagnetic vortex where the magnetization continuously rotates by 360° around the vortex core and —as no other direction is left— must go out-of-plane in the vortex core center, the intersection of the screw dislocation with the Cr(001) surface causes a spin frustration which may be compensated by a rotation of magnetization either through the out-of-plane or through the in-plane direction being perpendicular to the magnetization direction far away from the screw dislocation. In other words, a perpendicular component is possible but not necessary. We believe that in the case of Cr(001) the surface anisotropy prefers an in-plane orientation. (ii) In contrast to a ferromagnetic vortex core for which the size and shape is governed by only two material parameters, i.e., the exchange stiffness and the saturation magnetization, the latter plays no role in an antiferromagnet and is to be replaced by the effective anisotropy.

In analogy to the previously presented experimental results [cf. Fig. 3.4(b)], eight circular line sections which were drawn at different average radii r_{avg} around the simulated screw dislocation (point A) are shown in Fig. 3.5(b). In order to quantify the domain wall width each circular section was fitted with Eq. 3.2 (grey line). Experimental and theoretical results are summarized in Fig. 3.6. The excellent agreement between experimental and micromagnetically simulated data confirms that the shape of the spin structure around the screw dislocation in a layered antiferromagnet is determined by the exchange stiffness A and the effective anisotropy k. The small deviation at $20\,\mathrm{nm} \leq r_{\mathrm{avg}} \leq 50\,\mathrm{nm}$ may be caused by the elastic deformation of the crystal lattice around the screw dislocation which has not been considered in the simulations.

The second distortion of the crystal structure we want to discuss is a step dislocation. The constant current "topography" image in Fig. 3.7(a) exhibits eleven almost parallel step edges running from the upper left to the lower right corner. These step edges are crossed by another almost perpendicularly running step edge. We relate the

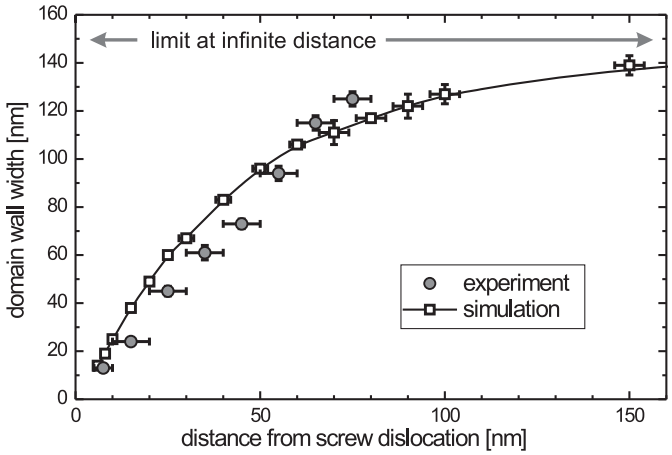

Figure 3.6: Plot of the experimentally determined and micromagnetically simulated domain wall width in a layered antiferromagnet in dependence on the distance from a screw dislocation. The interconnecting line between the data points serves as a guide for the eye only.

latter step edge to a relaxed step dislocation. As a result of these crossing steps a double step exists at the point of intersection with kinks in either step edge. A comparison between a normal step and the relaxed step dislocation reveals an identical step height of 1.47 ± 0.03 Å being consistent with the Cr lattice constant. As evidenced by the magnetic $\mathrm{d}I/\mathrm{d}U$ map in Fig. 3.7(b) every step edge—irrespective of its origin—leads to a reversal of the surface magnetization, i.e., the topological antiferromagnetic order is maintained.

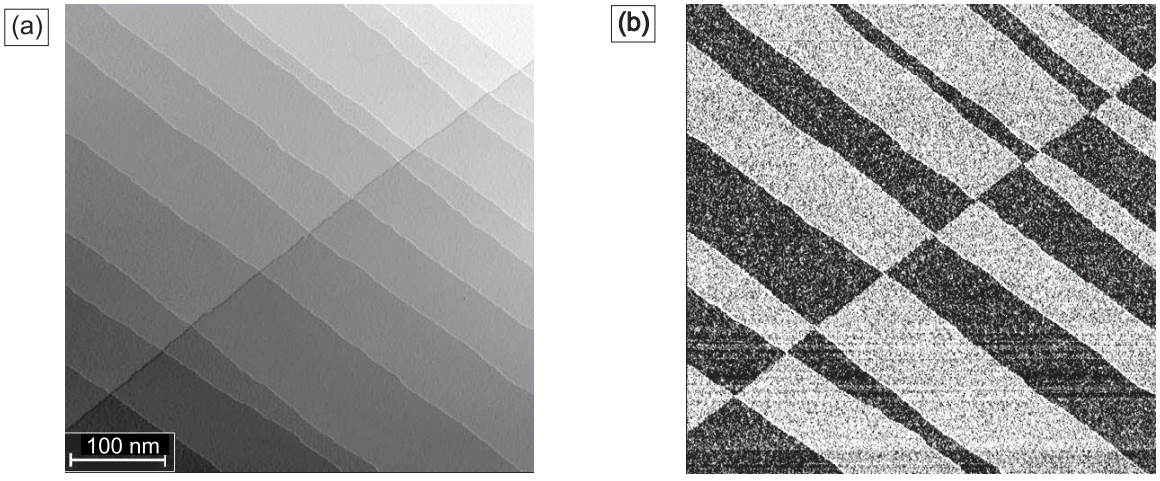

Figure 3.7: **(a)** Topography and **(b)** map of the magnetic $\mathrm{d}I/\mathrm{d}U$ signal of a Cr(001) surface with a step dislocation (measurement parameters: $U = -130\,\mathrm{mV}$ and $I = 0.5\,\mathrm{nA}$). The topological antiferromagnetic order of the surface is not distorted by the step dislocation.

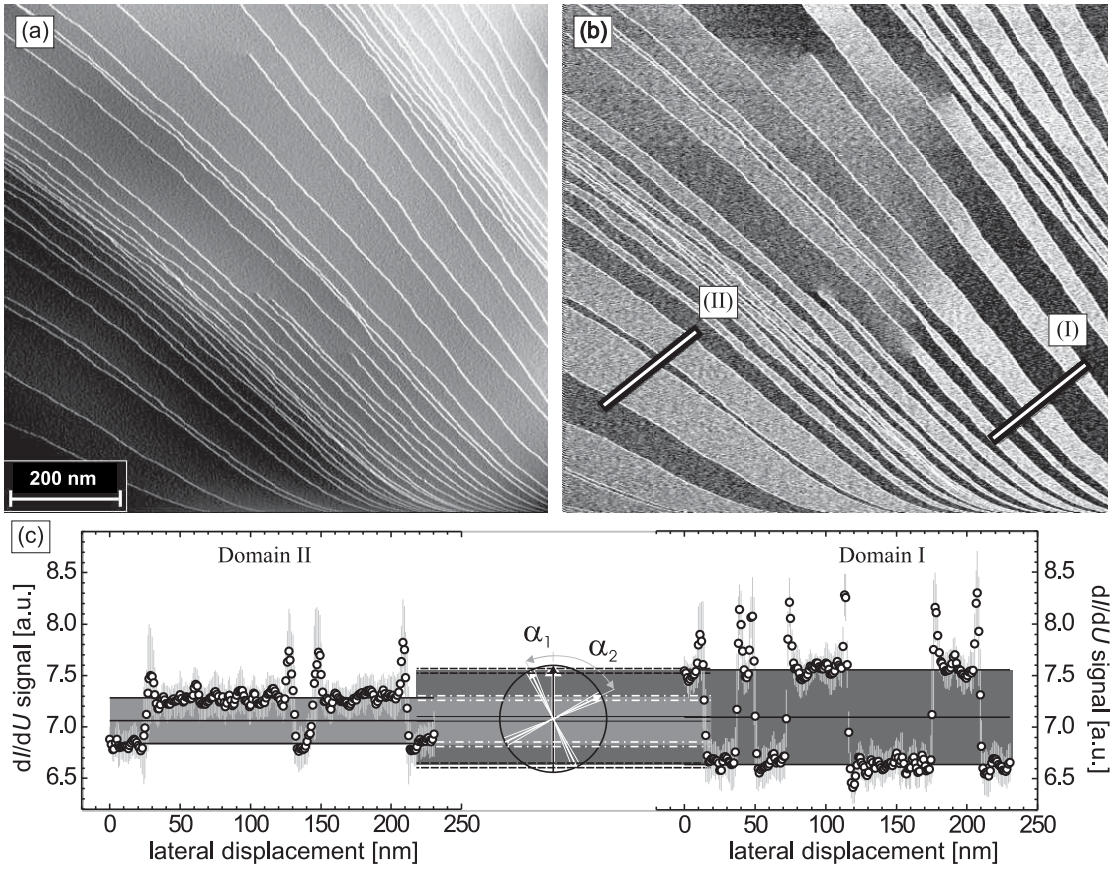

Figure 3.8: Large scale images of the **(a)** topography and **(b)** magnetic $\mathrm{d}I/\mathrm{d}U$ signal of a Cr(001) surface with multiple screw dislocations (measurement parameters: $U = -130\,\mathrm{mV}$ and $I = 0.5\,\mathrm{nA}$). In (b) the magnetic contrast is much stronger on the right (I) than on the left side (II) of the image. The variation of the contrast is caused by two domains which are rotated by 90 ° towards each other and which are equivalent on Cr(001) with its fourfold symmetry. **(c)** An analysis of the line sections measured along the lines indicated in (b) allows a determination of the azimuth of the tip magnetization direction.

Domain issues

As bcc Cr has a fourfold symmetry two degenerate domains of the topological antiferromagnetic order with an orientation perpendicular to each other are possible. Since SP-STM is sensitive to the projection of the surface magnetization onto the tip magnetization [cf. Eq. 3.1] such a domain formation would generally lead to two different dark/bright intensities. Only the unlikely case that the tip magnetization is rotated by 45° with respect to *both* domains would result in the same signal strength. In some rare cases we have also found evidence for the existence of degenerate domains on clean Cr(001). For example, the constant current image of Fig. 3.8(a) shows the topography of a particular location of the Cr single crystal with numerous steps and screw dislocations. Two different contrast levels can be distinguished in the left and

right side of the $\mathrm{d}I/\mathrm{d}U$ map [Fig. 3.8(b)]. We have analyzed the signal strength in both regions by drawing two line sections. The result is plotted in Fig. 3.8(c). In fact, the respective amplitudes in domains I and II, $A_{\mathrm{I}} = 0.91$ a.u. (arb. units) and $A_{\mathrm{II}} = 0.44$ a.u., differ significantly. On the basis of Eq. 3.1 we can calculate the relative orientation between the tip magnetization and the magnetization of the two domains which is given by the relations:

$$\tan \alpha_1 = \frac{A_{\mathrm{II}}}{A_{\mathrm{I}}} \tag{3.3}$$

and

$$\alpha_1 + \alpha_2 = 90\,^\circ\,. \tag{3.4}$$

We obtained $\alpha_1 = 25.8 \pm 4.5\,^\circ$ and $\alpha_2 = 64.2 \pm 4.6\,^\circ$. The result is schematically represented in the middle part of Fig. 3.8(c) with the tip as a black upright arrow and the orientation of the sample domains as white arrows and error margins.

Growth of Fe on Cr(001)

The magnetic coupling between a Cr substrate and an Fe overlayer is of considerable interest since multilayer systems consisting of these two materials exhibit an exciting variety of magnetic properties, such as exchange coupling [18], giant magnetoresistance [2] and oscillatory interlayer coupling [19]. As theoretical and experimental investigations showed, the magnetic properties of the multilayer system does not only depend on the Cr film thickness but also correlate with the intrinsic magnetic structure of Cr and structural properties of the Fe/Cr interface, as, e.g., the occurrence of intermixing.

Figure 3.9 shows Fe coverage-dependent constant-current images representing the topography of Fe/Cr(001) in the coverage range between 0.05 ML and 3.2 ML. Four different growth regimes can be distinguished: In the first regime up to $\theta \leq 0.35$ ML we observe the nucleation of isotropic monolayer islands preferentially in the middle of Cr(001) terraces and a roughening of the step edges. In the second growth regime with $0.4 \leq \theta \leq 1.48$ ML we find an almost perfect layer-by layer growth: After the coalescence of the islands and—though a few small holes remain visible—the completion of first layer, islands of the second Fe layer nucleate and grow in size. Neither on the coalesced first layer nor inside the holes we could detect any hint of an ordered Fe/Cr alloy formation. At $\theta = 1.27$ ML numerous second layer islands can be recognized. The island edges are preferentially oriented along the [100] and [010] direction. Between $\theta = 1.27$ ML and $\theta = 1.48$ ML the islands of the second layer start to coalesce. As we will show below the surface of the second Fe layer is much smoother than the first which is a first indication of a thickness-dependent intermixing between Fe and the Cr(001) substrate.

The third growth regime starts between $\theta = 1.48$ ML and $\theta = 1.91$ ML. It is characterized by the simultaneous growth of third layer islands and the progressive filling of the holes in the second layer. Again, we found that the surface RMS roughness depends

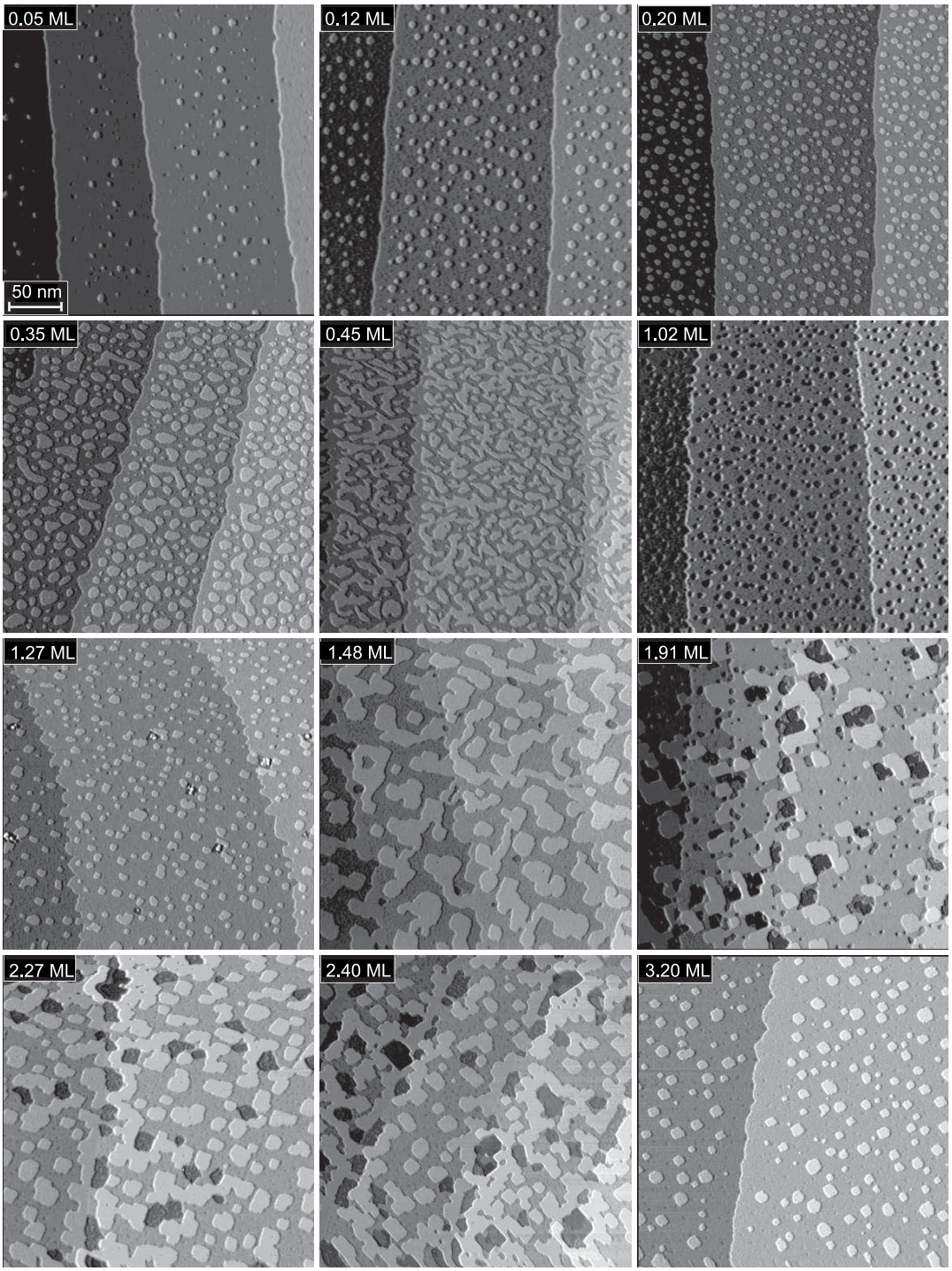

Figure 3.9: Overview of the growth of Fe on Cr(001). The STM constant-current topographs (image size: $250 \times 250\,\mathrm{nm}^2$) show the topography of Fe/Cr(001) at total nominal coverages between 0.05 ML up to 3.2 ML.

on the local coverage θ_{loc} which—to our interpretation—points to different degrees of intermixing. Fig. 3.10 shows constant-current images of Fe/Cr(001) in the nominal total coverage range between $\theta = 1.02\,\mathrm{ML}$ and $\theta = 2.4\,\mathrm{ML}$ at higher magnification.

Magnetic properties of Fe on Cr(001)

We have performed magnetically sensitive SP-STS measurements by using Fe coated W tips. Fig. 3.11 shows typical SP-STS spectra of 0.2 ML Fe/Cr(001) with a topography similar to the respective coverage in Fig. 3.9. As indicated by different surface state intensities on adjacent atomically flat terraces the topological antiferromagnetic order of the Cr(001) substrate is maintained in spite of the deposition of Fe onto the sample surface: At E_{F} the left terrace (empty circles) exhibits a lower $\mathrm{d}I/\mathrm{d}U$ signal than the right one (empty squares). The intensities of the $\mathrm{d}I/\mathrm{d}U$ signal at the surface state peak position as measured above Fe islands (filled circles and squares) are always opposite with respect to those of the underlying Cr(001) terraces indicating an antiferromagnetic coupling.

Based on this knowledge of the spin-resolved electronic structure of the Cr(001) substrate and Fe monolayer islands the spatial variation of the magnetization direction

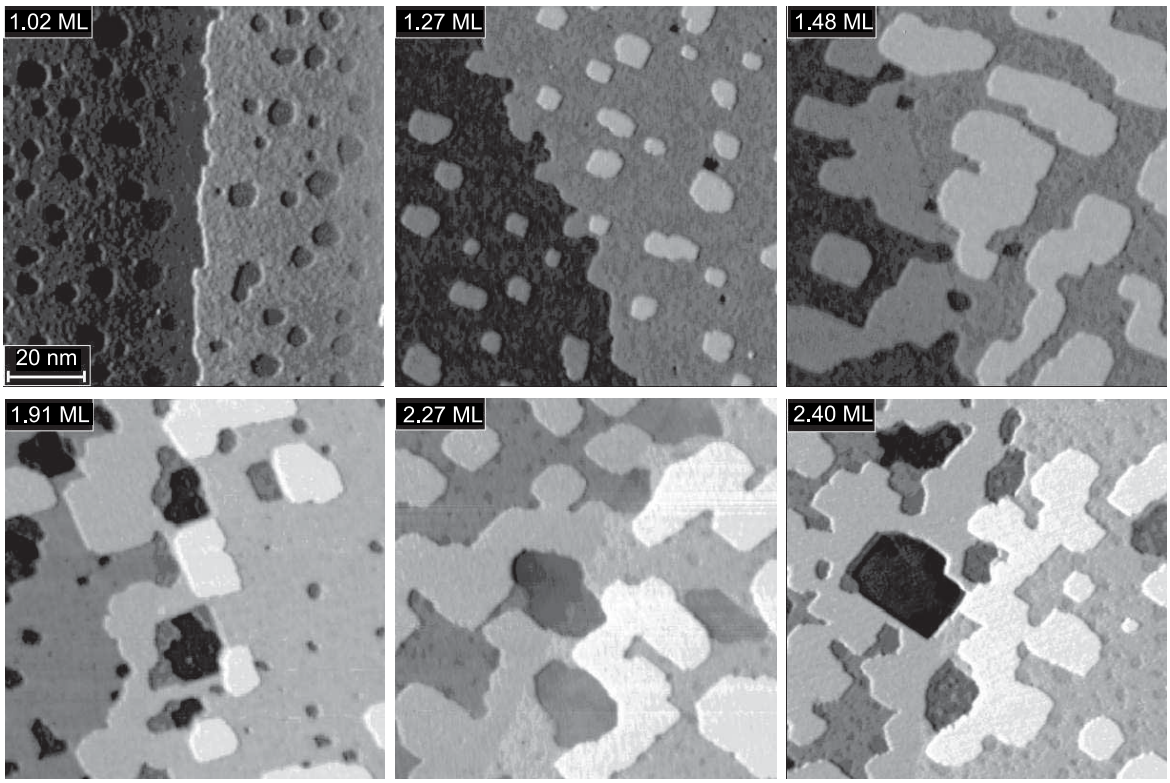

Figure 3.10: Topographic STM images of Fe/Cr(001) at coverages in the range of $1.02 \leq \Theta \leq 2.4\,\mathrm{ML}$. The image size is $100 \times 100\,\mathrm{nm}^2$.

can be revealed by mapping the spin-resolved $\mathrm{d}I/\mathrm{d}U$ signal simultaneously with the sample topography. Fig. 3.12 shows a series of topographic images (left) and spin-resolved $\mathrm{d}I/\mathrm{d}U$ maps (right) at different Fe coverages on Cr(001). Up to a total Fe coverage $\theta = 0.2\,\mathrm{ML}$ the well-known alternating contrast from adjacent Cr(001) terraces indicates that the topological antiferromagnetic order of the substrate is maintained. Additionally, a clear contrast between islands on different terraces can be recognized: Dark islands are found on bright terraces and *vice versa*. The magnetic contrast amounts up to 10-12%, the same value as found on clean Cr(001). A minute increase of the total Fe coverage, however, leads to a dramatic reduction of the magnetic signal strength. Already at $\theta = 0.22\,\mathrm{ML}$ the contrast between adjacent Cr(001) terraces becomes weaker and the island contrast almost disappears. This trend continues until at $\theta > 0.4\,\mathrm{ML}$ the magnetic contrast of the substrate and the islands completely vanishes. Although we repeatedly tried to achieve magnetic contrast at Fe coverages $0.4\,\mathrm{ML} < \theta < 3\,\mathrm{ML}$ this was never observed.

Only for $\theta > 3\,\mathrm{ML}$ a weak magnetic contrast reappears. Fig. 3.13 shows the topography (a) and the magnetic $\mathrm{d}I/\mathrm{d}U$ signal (b) of a 3.2 ML Fe film on Cr(001). A magnetic contrast is found in the $\mathrm{d}I/\mathrm{d}U$ signal of the closed third layer. Similar to the topological antiferromagnetic order of the uncovered Cr(001) substrate the contrast changes between adjacent terraces. However, this general rule is violated occasionally as can be seen at the left and the right side of Fig. 3.13(b): We would like to emphasize that the observed contrast was always much lower than for submonolayer films and

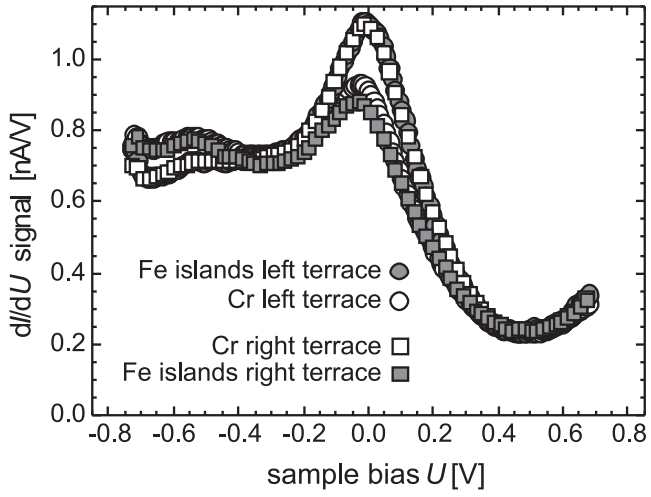

Figure 3.11: Spin-resolved tunneling spectra of $\theta \leq 0.2\,\mathrm{ML}$ Fe/Cr(001) as measured with a Fe coated W tip. At the surface state peak position close to E_F ($U = 0\,\mathrm{V}$) the left Cr terrace (○) exhibits a lower $\mathrm{d}I/\mathrm{d}U$ signal than the right one (□). The Fe island peaks (●, ■) behave always oppositely with respect to those of the underlying Cr(001) terraces indicating an antiferromagnetic coupling between Cr and Fe.

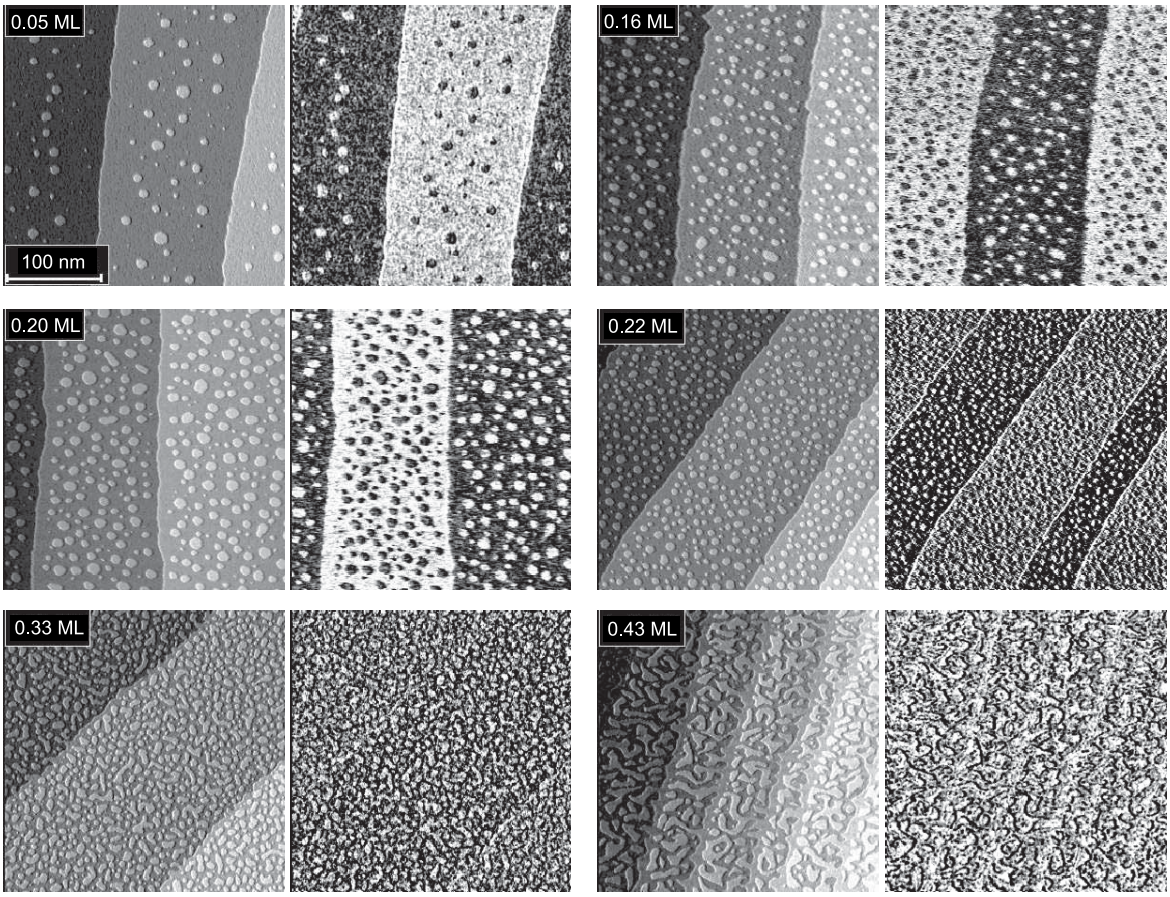

Figure 3.12: Fe coverage-dependent series of images ($250 \times 250\,\mathrm{nm}^2$) showing the topography (left) and the simultaneously recorded spin-resolved $\mathrm{d}I/\mathrm{d}U$ map (right). An AFM coupling of the first Fe layer to the Cr surface is found at $\theta \leq 0.2\,\mathrm{ML}$. An increase of the Fe coverage leads to a gradual equalization of the $\mathrm{d}I/\mathrm{d}U$ signal of all Fe islands and of the Cr(001) terraces. At $\theta \geq 0.33\,\mathrm{ML}$ an almost homogeneous $\mathrm{d}I/\mathrm{d}U$ signal is detected over the whole sample surface. This figure is continued on the next page.

for the uncovered Cr(001) substrate and never exceeded 1-2%.

Two aspects of the experimental results presented are puzzling, i.e., the absence of magnetic $\mathrm{d}I/\mathrm{d}U$ contrast in the coverage range $0.4\,\mathrm{ML} < \theta < 3\,\mathrm{ML}$ and the reappearance of a very small magnetic contrast at $\theta > 3\,\mathrm{ML}$. To our opinion the former is caused by intermixing between the Fe overlayer and the Cr substrate. It is well-known that the Néel temperature T_N of $\mathrm{Fe}_x/\mathrm{Cr}_{1-x}$ alloys strongly depends on the Fe content x [20]: An admixture of only 2% Fe in Cr decreases T_N by 50 K. We speculate that with increasing Fe deposition the surface-near substrate region accumulates Fe until it becomes paramagnetic at $\theta > 0.4\,\mathrm{ML}$ because $T_\mathrm{N} < 290\,\mathrm{K}$.

At $\theta \geq 3\,\mathrm{ML}$ the Curie temperature T_C exceeds the sample temperature of 300 K and the Fe film becomes ferromagnetic [21]. Now, the ferromagnetic intralayer Fe–

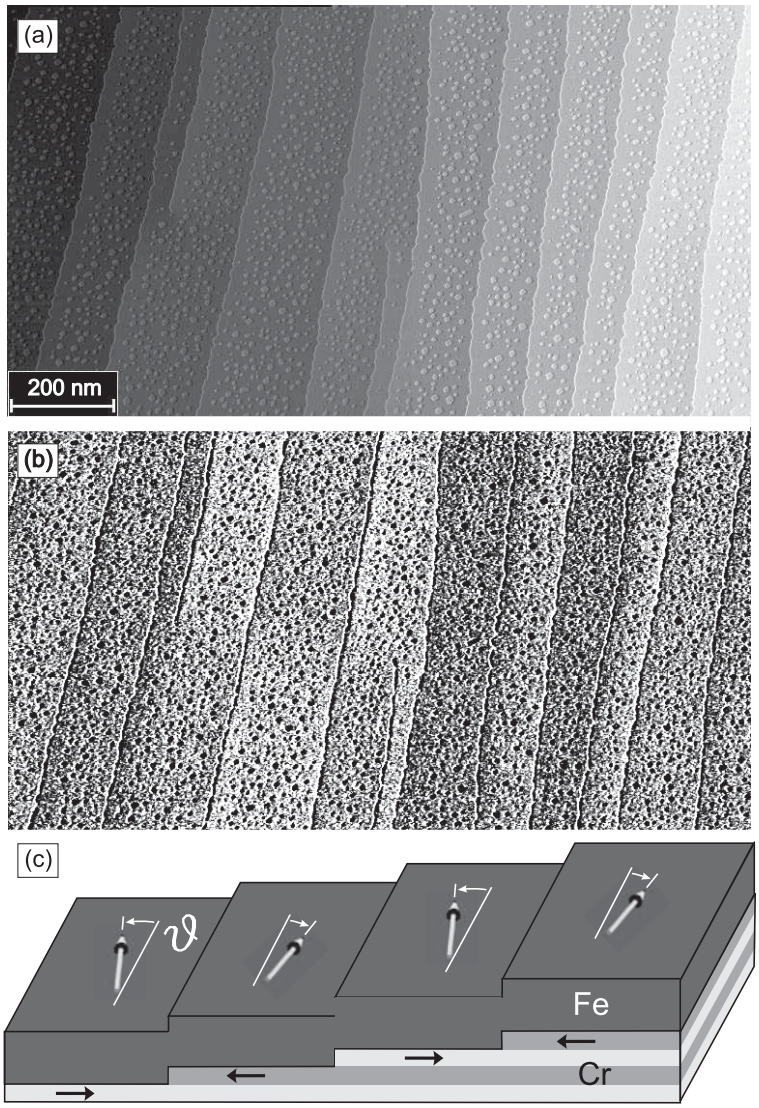

Figure 3.13: **(a)** Topography and **(b)** spin-resolved $\mathrm{d}I/\mathrm{d}U$ map of 3.2 ML Fe/Cr(001). In the central region of (b) a weak magnetic contrast between adjacent terraces can be recognized. **(c)** This contrast can be explained by a small remaining antiferromagnetic component in the coupling term which describes the exchange between the substrate and the overlayer. This leads to a canting of the Fe magnetization in a direction antiparallel to the magnetization direction of the underlying Cr(001) substrate.

Fe interaction, $-J_0 \sum_{ij} \vec{S}_{\mathrm{Fe},i} \cdot \vec{S}_{\mathrm{Fe},j}$, competes with the interfacial Fe–Cr interaction, $J_1 \sum_{ij} \vec{S}_{\mathrm{Cr},i} \cdot \vec{S}_{\mathrm{Fe},j}$ and on average leads to a 90°-coupling [22]. The Fe moments are, however, not perfectly normal with respect to the Cr moments since the Fe–Cr coupling energy $E_1 \approx J_1 \vartheta W/a$ with W being the terrace width and a the lattice constant can be lowered by twisting the Fe moments within the film plane by an angle ϑ into the direction antiparallel to the underlying Cr terrace [23]. Of coarse, on adjacent terraces

the twisting occurs into opposite directions. This situation is schematically represented in Fig. 3.13(c). Under the assumption that the resulting ϑ-degree domain wall ranges over the full terrace width W the wall energy is given by $E_0 = J_0 \vartheta^2 d_{\mathrm{Fe}}/W$, where d is the Fe film thickness [23]. Since the actual terrace width exceeds 100 nm while the exchange length of bulk Fe only amounts to $L = 21\,\mathrm{nm}$ we can replace W by L. By minimization of the total energy Escorcia-Aparicio *et al.* [23] found $\vartheta \approx J_1 W^2/(2J_0 ad)$. With $J_0/k_{\mathrm{B}} = 375\,\mathrm{K}$ and $J_1/k_{\mathrm{B}} = -40\,\mathrm{K}$ [24] we get $\vartheta = 18°$. On clean Cr(001)—a material with comparable electronic properties—a 180° wall causes a $\mathrm{d}I/\mathrm{d}U$ signal variation of 10%. Since the contrast scales with the projection of the sample onto the tip magnetization we shall expect a contrast of 3% for a 2ϑ (36°) domain wall. This result is in fair agreement with the magnetic contrast strength of the $\mathrm{d}I/\mathrm{d}U$ signal of 2% observed in Fig. 3.13(b). A closer comparison between Figs. 3.13(a) and (b) reveals that the contrast changes do not always coincide with surface step edges. This may be caused by surface and interface step edge positions that do not match but are slightly shifted with respect to each other leading to a lateral variation of the local Fe coverage. As a result we may observe a surface step edge that does not lead to a change of the magnetic contrast since the magnetization direction of the underlying (atomically flat) Cr substrate remains the same.

References

[1] G. Binasch, P. Grünberg, F. Saurenbach, and W. Zinn, Phys. Rev. B **39**, 4828 (1989).

[2] M. N. Baibich, J. M. Broto, A. Fert, F. N. V. Dau, F. Petroff, P. Eitenne, G. Creuzet, A. Friederich, and J. Chazelas, Phys. Rev. Lett. **61**, 2472 (1988).

[3] P. Grünberg, Prog. Surf. Sci. **18**, 1 (1985).

[4] H. Zabel, J. Phys.: Condens. Matter **11**, 9303 (1999).

[5] L. E. Klebanoff, S. W. Robey, G. Liu, and D. A. Shirley, Phys. Rev. B **30**, 1048 (1984).

[6] F. Meier, D. Pescia, and T. Schriber, Phys. Rev. Lett. **48**, 645 (1982).

[7] S. Blügel, D. Pescia, and P. H. Dederichs, Phys. Rev. B **39**, 1392 (1989).

[8] M. Kleiber, M. Bode, R. Ravlić, and R. Wiesendanger, Phys. Rev. Lett. **85**, 4606 (2000).

[9] M. Kleiber, M. Bode, R. Ravlić, N. Tezuka, and R. Wiesendanger, J. Magn. Magn. Mater. **240**, 64 (2002).

[10] J. A. Stroscio, D. T. Pierce, A. Davies, R. J. Celotta, and M. Weinert, Phys. Rev. Lett. **75**, 2960 (1995).

[11] M. Bode, O. Pietzsch, A. Kubetzka, and R. Wiesendanger, J. Electr. Spectr. Relat. Phenom. **114-116**, 1055 (2001a).

[12] M. Bode, O. Pietzsch, A. Kubetzka, S. Heinze, and R. Wiesendanger, Phys. Rev. Lett. **86**, 2142 (2001b).

[13] J. C. Slonczewski, Phys. Rev. B **39**, 6995 (1989).

[14] `We used the OOMMF program, release 1.2 alpha 2 (http://math.nist.gov/oommf/).`

[15] T. Shinjo, T. Okuno, R. Hassdorf, K. Shigeto, and T. Ono, Science **289**, 930 (2000).

[16] J. Raabe, R. Pulwey, R. Sattler, T. Schweinböck, J. Zweck, and D. Weiss, J. Appl. Phys. **88**, 4437 (2000).

[17] A. Wachowiak, J. Wiebe, M. Bode, O. Pietzsch, M. Morgenstern, and R. Wiesendanger, Science **298**, 577 (2002).

[18] Grünberg P, Schreiber R, Pang Y, Brodsky M B, and Sowers H, Phys. Rev. Lett. **59**, 2442 (1986).

[19] Parkin S S P, More N, and Roche K P, Phys. Rev. Lett. **64**, 2304 (1990).

[20] E. Fawcett, H. L.Alberts, V. Y. Galkin, D. R. Noakes, and J V Yakhmi, Rev. Mod. Phys. **66**, 25 (1994).

[21] W. Guo, L. P. Shi, and D. L. Lin, Phys. Rev. B **62**, 14259 (2000).

[22] J. C. Slonczewski, Phys. Rev. Lett. **67**, 3172 (1991).

[23] E. J. Escorcia-Aparicio, H. J. Choi, W. L. Ling, R. K. Kawakami, and Z Q Qiu, Phys. Rev. Lett. **81**, 2144 (1998).

[24] P. Bödeker, A. Hucht, A. Schreyer, J. Borchers, F. Güthoff, and H. Zabel, Phys. Rev. Lett. **81**, 914 (1998).

[25] A. Hubert and R. Schäfer, *Magnetic Domains*, Springer (1998).

3.2.3 Magnetism of Fe on W(001) studied by SP-STM

K. v. Bergmann, A. Kubetzka, O. Pietzsch, M. Bode, and R. Wiesendanger

Introduction

The system of Fe on W(001) has proven not to be straightforward concerning the magnetic properties. For higher coverage θ, the magnetic properties are also accessible by other methods than SP-STM, but the situation is different in the low coverage regime. Experimental studies with various techniques have been performed but no conclusive results have been obtained for many years. Structural properties have been investigated previously and it was consistently found that there is three-dimensional island growth for higher coverage at elevated temperature [1, 2], a transition region with a (9×1) reconstruction due to strain relief when the local coverage is $\geq 5\,\mathrm{ML}$ [1,3], and pseudomorphic growth for $\theta \leq 4\,\mathrm{ML}$ [4]. In the high coverage regime, i.e., the three-dimensional island growth, magnetic investigations showed uniformly magnetized areas with lateral dimensions $> 50\,\mathrm{nm}$ and an easy axis along $\langle 100 \rangle$ [1, 2]. Conflicting reports have been published about the magnetic properties in the pseudomorphic regime. Especially concerning the direction of the easy axis, measurements with spatially averaging methods have led to contrary interpretations. While in early magneto-optical Kerr effect (MOKE) measurements, an easy axis along $\langle 110 \rangle$ was found for $1 - 3\,\mathrm{ML}$ Fe on W(001) [5], spin-polarized electron diffraction experiments suggested an easy axis along $\langle 100 \rangle$ [6]. Recent MOKE data, however, support the former results, i.e., a magnetic easy axis along $\langle 110 \rangle$ up to a coverage of about 6 ML [3]. No magnetic signal was found for the monolayer, which was interpreted as a non-magnetic or antiferromagnetic state [3, 7, 8]. The antiferromagnetic ground state was also predicted by density functional theory calculations [9].

To overcome these discrepancies for the pseudomorphic structures and identify the state of the monolayer, SP-STM is employed to review the system of Fe on W(001) with the main focus on magnetism in the pseudomorphic growth regime [4, 10]. The strength of SP-STM, i.e., the combination of high spatial resolution and magnetic sensitivity, is essential to gain a deeper insight into the magnetic properties of this system. It is expected that when the coverage is reduced and the lateral structures become smaller, a morphology- or layer-induced change in anisotropy may lead to magnetic structures in the 10 nm regime. When there is a coexistence of layers with different anisotropy, the appropriate method to study this system is SP-STM, since it has been shown that magnetic structures down to the atomic scale can be resolved laterally [11, 13].

Experimental

The experiments were performed in a multi-chamber ultra high vacuum system with a base pressure in the low 10^{-11} mbar range. The tungsten crystal is cleaned by cycles

of annealing in oxygen atmosphere and flashing to high temperature. Annealing of the substrate is possible during or after deposition of Fe, which is evaporated from a rod. For the spin-resolved measurements presented in this section the tips are coated with Fe to show a magnetic sensitivity to magnetism in the sample surface plane. STM measurements are performed in a cryogenic STM [14] with sample and tip held at $T \approx 13\,\mathrm{K}$. A magnetic field of up to $\vec{B} = \pm 2.5\,\mathrm{T}$ can be applied perpendicular to the sample surface.

Growth

Figure 3.14 shows an overview of the growth mode in the low coverage regime. Depending on the amount of deposited iron and the annealing conditions different structures are observed. The first four monolayers grow pseudomorphic while uniaxial strain relief is observed for higher coverage.

No ordered growth mode is found for a coverage below 1 ML as shown in (a). Presumably, at $T < 600\,\mathrm{K}$, the Fe ad-atom mobility on the W substrate is too low to allow diffusion as previously shown for Co on W(001) [12]. When the coverage exceeds 1 ML, a closed monolayer with small 2^{nd} ML islands on top is formed as shown for a sample with a coverage of 1.1 ML in (b). This leads to the conclusion that the mobility of the Fe ad-atoms on the 1^{st} ML Fe is higher than on the W(001) substrate and that downward diffusion occurs until the completion of the first monolayer.

When the coverage is between 1 and 2 ML as in the following topography images (c)

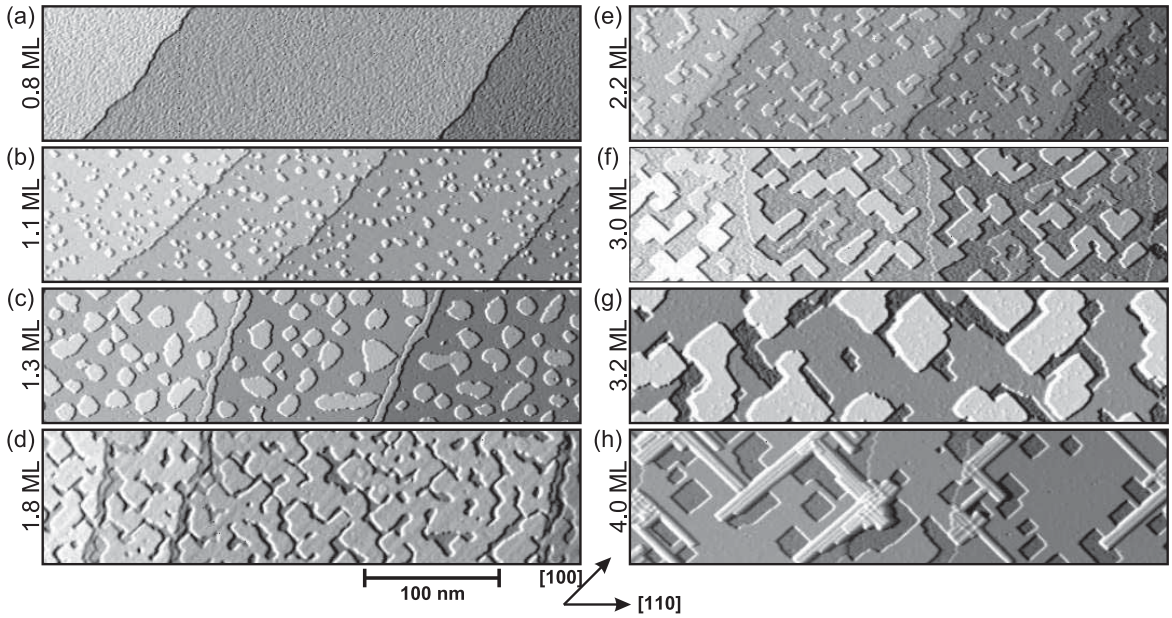

Figure 3.14: Growth study: (a)-(i) Topography of different samples of Fe on W(001) with the coverage as indicated in monolayers (ML).

and (d), the 2nd ML grows on top of the closed monolayer. Isolated islands are formed at lower coverage as observed in (c), while a meander-like morphology is observed as a result of the coalescence of the 2nd ML islands when the coverage is just below the completion of two monolayers and the substrate temperature during deposition is approximately 350 K (d).

For higher coverage two different growth modes are observed in the pseudomorphic growth regime. When depositing Fe at lower temperature ($T \approx 525\,\mathrm{K}$) small 3rd ML islands on top of a two monolayer thick wetting layer are formed as shown in (e). At this substrate temperature the inter-layer diffusion is hindered which results in the coexistence of exposed 2nd ML, 3rd ML, and 4th ML as shown in (g). When the substrate temperature is higher during Fe deposition ($T \approx 550\,\mathrm{K}$) islands of a local coverage of 4 ML are observed on the 2 ML thick wetting layer, while the formation of areas with a local coverage of 3 ML is unfavorable as observed in (f). In the topography images (e)-(h) it can be observed that the 4th as well as the 3rd ML forms edges which preferentially run along $\langle 100 \rangle$ directions.

As shown previously [1, 3] a (9×1) reconstruction is observed when the local coverage exceeds 5 ML as shown in Fig. 3.14(h). Lines running along the $\langle 100 \rangle$ directions indicate reconstructed areas.

Magnetism: Theory

Previous experiments showed an in-plane anisotropy in the pseudomorphic regime. Accordingly, magnetically sensitive SP-STM measurements were performed with Fe-coated W tips. In this way the spin polarization of the tip P_t in conjunction with the spin polarization of the sample P_s leads to a spin-polarized tunnel current I_SP at the tip position $\vec{r}$ which can be described by

$$I_\mathrm{SP}(\vec{r}, U_0) = I_0 \left[1 + P_\mathrm{s} \cdot P_\mathrm{t} \cdot \cos(\vec{M}_\mathrm{s}, \vec{M}_\mathrm{t}) \right] \tag{3.5}$$

where $\vec{M}_\mathrm{s}$ is the sample and $\vec{M}_\mathrm{t}$ the tip magnetization and α the angle between them. Considering the crystal surface symmetry a fourfold in-plane anisotropy is expected. In this case the absolute value of the angle α can be extracted from the experimental data. First, the amplitude A of the $\mathrm{d}I/\mathrm{d}U$ signals of oppositely magnetized domains is calculated and then the angle α is obtained as follows:

$$A_{\mathcal{A}-\mathcal{D}} = \frac{\mathrm{d}I}{\mathrm{d}U}_{\mathcal{A}} - \frac{\mathrm{d}I}{\mathrm{d}U}_{\mathcal{D}}, \quad A_{\mathcal{B}-\mathcal{C}} = \frac{\mathrm{d}I}{\mathrm{d}U}_{\mathcal{B}} - \frac{\mathrm{d}I}{\mathrm{d}U}_{\mathcal{C}} \tag{3.6}$$

$$\tan\alpha = \frac{A_{\mathcal{A}-\mathcal{D}}}{A_{\mathcal{B}-\mathcal{C}}} \ . \tag{3.7}$$

It is important to note that the same contrast levels are observed experimentally for $+\alpha$ and $-\alpha$, the information about the sign is not accessible since the azimuthal angle of the tip magnetization with respect to the crystallographic directions is not known.

Magnetism: Fourth and third monolayer

Figure 3.15 shows a sample of 3.2 ML Fe on W(001) measured with an Fe-coated W tip. The topography (a) shows few patches of the two monolayer thick wetting layer, a nearly closed 3rd ML and islands of the 4th ML. The simultaneously measured $\mathrm{d}I/\mathrm{d}U$ map in (b) shows different contrast levels for the magnetic domains. For the 3rd ML three different signal strengths can be found and the middle is the average of the brighter and the darker one. On the basis of Eq. 3.5 they can be assigned to the directions of sample magnetization with respect to the tip magnetization. The result for the three equidistant contrast levels of the 3rd ML is sketched in Fig. 3.15(c). On the other hand, there are only two contrast levels for the 4th ML observed not only in this image, but in a large investigated area. Consideration of Eq. 3.5 leads to the conclusion that the two-stage contrast of the 4th ML can be interpreted as illustrated in Fig. 3.15(d). A direct comparison of the sketches for the two different layers in Fig. 3.15(c) and (d) shows that there is a rotation of the magnetic easy axis from the 4th ML to the 3rd ML by 45°. Since the azimuthal direction of the tip magnetization is not known, these SP-STM measurements cannot directly assign the magnetic easy axis to a crystallographic direction of the sample.

Magnetism: Fourth and second monolayer

Figure 3.16 shows a sample of 3.0 ML of Fe on W(001) deposited at higher temperature to allow inter-layer mass transport. Islands of a local coverage of 4 Fe layers are observed on top of the two monolayer thick wetting layer. The topography is shown in (a) and a corresponding $\mathrm{d}I/\mathrm{d}U$ map with spin-polarized contrast is presented in (b).

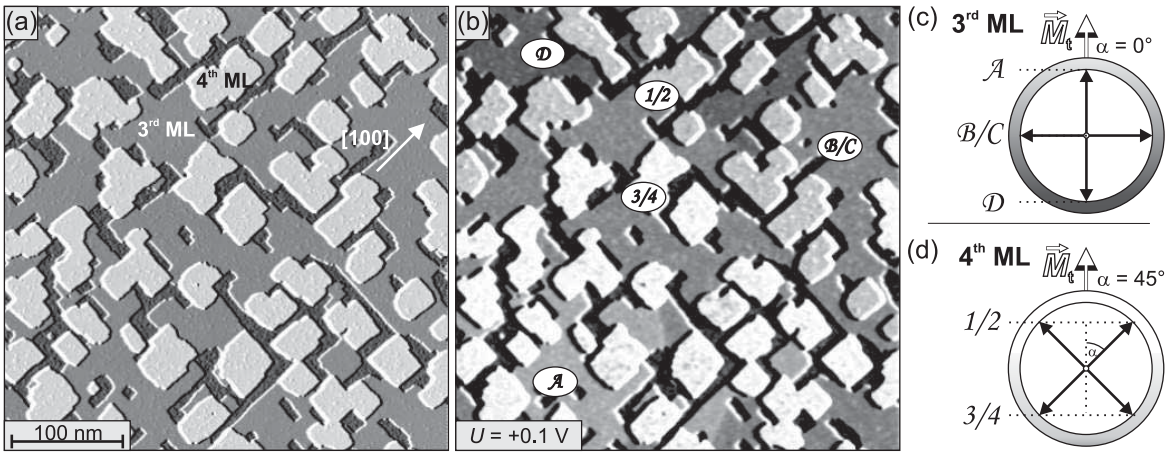

Figure 3.15: Sample of 3.2 ML of Fe on W(001) grown at $T \approx 525\,\mathrm{K}$ (see Fig. 3.14(g)) measured with an Fe-coated W tip. (a) topography and (b) corresponding $\mathrm{d}I/\mathrm{d}U$ map; (c),(d) sketches of the relationship between tip and sample magnetization for the 3rd and the 4th ML, respectively.

Two different signal strengths are observed for the 4$^{\text{th}}$ ML islands. As shown before (see Fig. 3.15(d)) this indicates an angle of $\alpha = 45°$ between the tip magnetization and two of the magnetic domains, denominated by *1/2*. The other two domains show a different contrast and are denominated with *3/4*. Full dI/dU spectroscopy was performed in the central area of this image. The spectra for the 4$^{\text{th}}$ ML islands with different signal strength are shown in (c). One prominent feature in the unoccupied states together with two less distinct featured are observed at $U = +0.46\,\text{V}$, $+0.24\,\text{V}$ and $+0.03\,\text{V}$, respectively. All of them show different intensities for the two different island types and are therefore spin-polarized. The asymmetry is shown at the bottom of the graph and changes sign from the most prominent peak to the two smaller features.

Magnetic contrast is also observed for the two monolayer thick wetting layer in the dI/dU map of Fig. 3.16(b). The three different contrast levels are characteristic of a collinear alignment of the tip magnetization with two of the four possible domains.

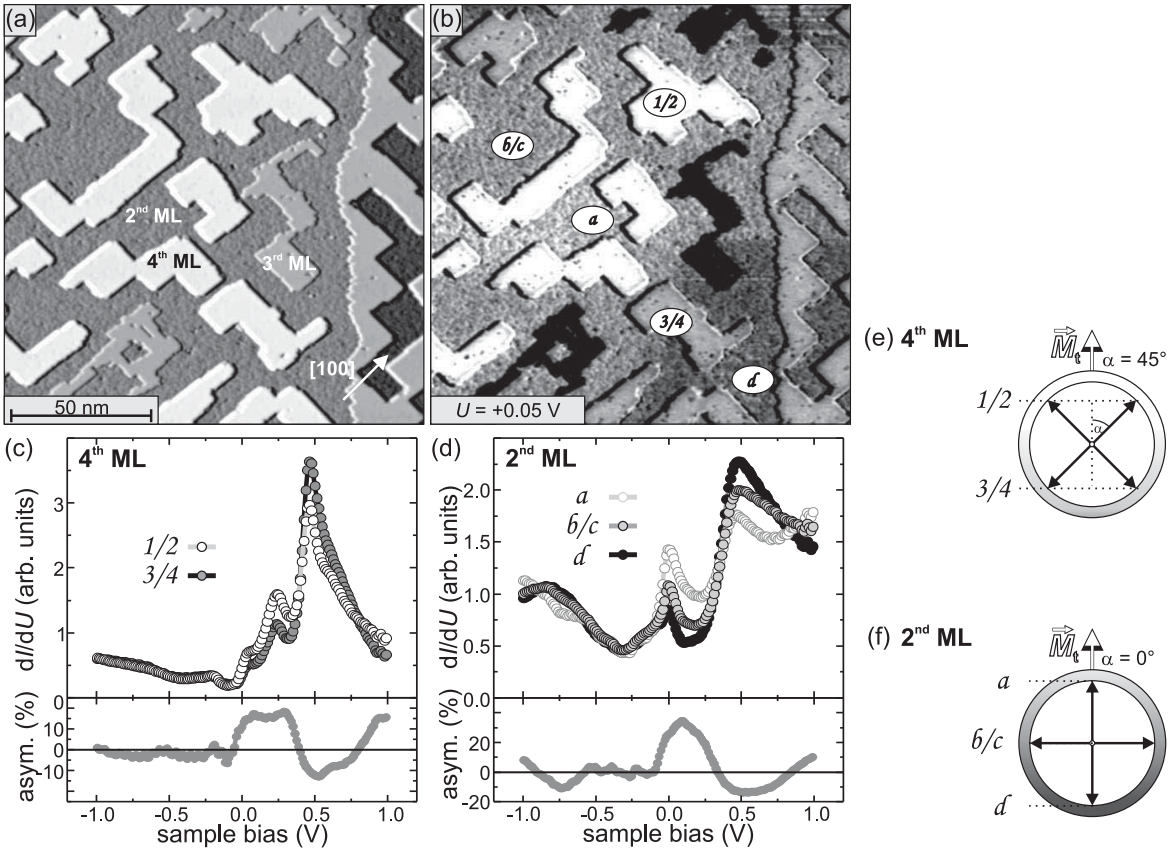

Figure 3.16: Sample of 3.0 ML of Fe on W(001) grown at $T \approx 550\,\text{K}$ (see Fig. 3.14(f)) measured with an Fe-coated W tip. (a) topography and (b) corresponding dI/dU map; spin-resolved dI/dU spectroscopy (stabilization parameters: $U = +1.0\,\text{V}$, $I = 1.0\,\text{nA}$) and asymmetry of the different domains of (c) the 2$^{\text{nd}}$ ML and (d) the 4$^{\text{th}}$ ML; (e),(f) sketches of the relationship between tip and sample magnetization for the two different layers as indicated.

The different areas are therefore denominated with *a*, *b*/*c* and *d*. The spin-resolved spectra for the 2nd ML are shown in (d). Two peaks with opposite spin polarization are observed at $U = +0.47\,\mathrm{V}$ and at the Fermi energy. The $\mathrm{d}I/\mathrm{d}U$ spectrum for domains *b*/*c* is the intermediate of the spectra of domains *a* and *d* and is thus equivalent to a non–spin-polarized spectrum of the 2nd ML Fe on W(001).

For both layers a large asymmetry is observed only at positive sample bias, whereas there is hardly any asymmetry at negative voltages. Since this was observed for all measurements with different tips this seems to be a property of the sample and not due to the tip.

In (e) and (f) the directions of the magnetization for the 4th and 2nd ML domains are sketched and it is obvious that the easy axes include an angle of 45° as was already observed for 4th and 3rd ML. This leads to the conclusion that 2nd and 3rd ML couple collinearly, while the magnetization of the 4th ML is rotated by 45°.

Magnetism: Second and first monolayer

Figure 3.17 shows an extended experiment to gain information about the magnetic properties of the monolayer. A sample of 1.3 ML Fe on W(001) is investigated (see Fig 3.14(g)) and the measurement is performed with an Fe-coated W tip. Fig. 3.17(a) shows a measurement in zero magnetic field $\vec{B} = 0\,\mathrm{T}$. The tip is sensitive to the magnetic in-plane component of the sample surface magnetism and all of the four degenerate domains of 2nd ML islands are observed and indicated with *a*, *b*, *c* and *d* in the $\mathrm{d}I/\mathrm{d}U$ map on the left. To the right the corresponding topography is presented. Atomic resolution of the 1st ML was not achieved but instead a uniform plane is observed. Then the magnetic field is increased to $\vec{B} = +2.5\,\mathrm{T}$ (b) and held at this value during the following measurement. This forces the magnetic moment of the Fe coating into the direction of $\vec{B}$, i.e. along the tip axis and thus introduces a sensitivity to a magnetic out-of-plane component. Also an angular momentum acts upon the 2nd ML islands, but since there remains some variation in the signal of the 2nd ML islands in the $\mathrm{d}I/\mathrm{d}U$ map (left panel) it can be concluded that at +2.5 T neither the tip nor the sample is fully aligned with the applied field. A close view to the topography of the 1st ML is shown to the right in (b). In an applied magnetic field of $\vec{B} = +2.5\,\mathrm{T}$ a periodic primitive cubic structure is observed on the 1st ML, while it was featureless without the magnetic field. It has been shown before that for antiferromagnetic structures the spin-polarized part dominates the topography image [13]. Therefore, we conclude that the observed cubic superstructure stems from the spin-polarized contribution to the tunnel current. The position of a line profile along $\langle 100 \rangle$ is indicated in (b) and it is shown below the topography image. The measured value of the diagonal of the magnetic unit cell is 0.68 nm and agrees well with twice of the lattice constant of the atomic unit cell ($2 \times a = 0.633\,\mathrm{nm}$). This suggests an antiferromagnetic checkerboard arrangement of the 1st ML, which results in a magnetic unit cell twice the size of the structural unit cell and rotated by 45°. In the next measurement step (c) the

direction of the magnetic field is inverted to $\vec{B} = -2.5\,\mathrm{T}$, which has also an effect on the direction of the Fe-coated W tip and the 2nd ML islands. Again in the $\mathrm{d}I/\mathrm{d}U$ map on the left a variation in the signal strength on the islands can be observed. Also the topography to the right shows the same structure as in (b). The measured value for the diagonal of the magnetic unit cell is 0.67 nm. In the following the adsorbate in the bottom right corner of the topography images of (b) and (c) is used as a position marker. A direct spatial comparison reveals, that the phase of the primitive cubic structure has shifted by half a period. Again the magnetic field was changed to $\vec{B} = +2.5\,\mathrm{T}$, i.e. to the starting polarity and the observed magnetic structure (not shown) was identical to that shown in (b).

Since the antiferromagnetic structure of the monolayer is unaffected by the external field, while at the same time the tip's magnetization is reversed following the direction of $\vec{B}$, an "inversion" of the constant-current image is observed for (c) compared to (b). This proves that the monolayer is in a c(2×2) antiferromagnetic state with perpendicular anisotropy, i.e. a checkerboard arrangement of opposite spins as sketched in (d).

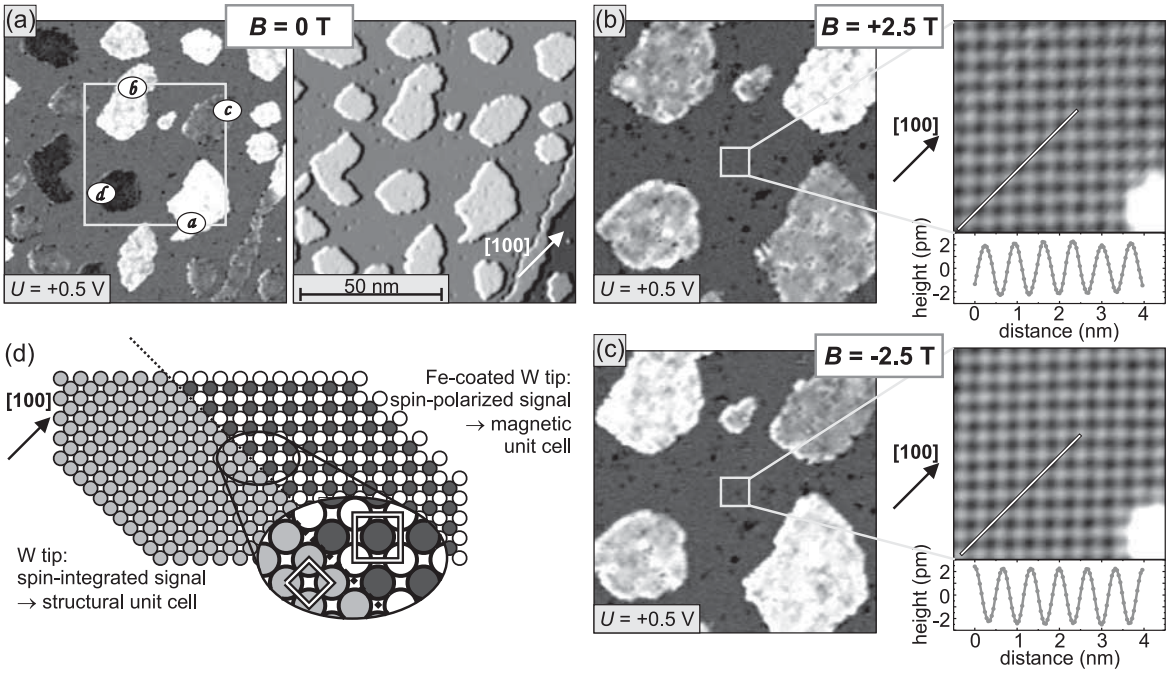

Figure 3.17: $\mathrm{d}I/\mathrm{d}U$ maps (left panel) and topography (right panel) of a sample of 1.3 ML of Fe on W(001) grown at $T \approx 350\,\mathrm{K}$ (see Fig. 3.14(g)) measured with an Fe-coated W tip. The positions of the line profiles are indicated in the respective (slightly Fourier-filtered) topography images. (a) without magnetic field $\vec{B}$; with magnetic field of (b) +2.5 T and (c) -2.5 T; (d) sketch of the structural unit cell in comparison to the magnetic unit cell.

Conclusions

The presented SP-STM measurements lead to a detailed understanding of the magnetic properties of iron on tungsten in the pseudomorphic regime. Measurements have been performed on samples with different coverage and morphology and it has been shown that for the 4^{th}, the 3^{rd} and the 2^{nd} ML the magnetization lies in the surface plane with four degenerate magnetization directions according to the substrate symmetry. A rotation of the easy axis by 45° from the 4^{th} to the 3^{rd} and 2^{nd} ML has been observed. The crystallographic direction of the easy axes cannot be determined by the SP-STM measurements presented here. Considerations of results of previous experiments [3, 5] lead to the conclusion that the 4^{th} ML has an easy axis along $\langle 100 \rangle$ and therefore the 3^{rd} and the 2^{nd} ML must be magnetized along $\langle 110 \rangle$ directions. It should be emphasized that the change in the magnetic direction is on a scale that is not easily accessible by an experimental method other than STM: for example if one crosses a 4^{th} ML island which is surrounded by the two monolayer thick wetting layer, the direction of magnetization rotates from $\langle 110 \rangle$ to $\langle 100 \rangle$ and back to $\langle 110 \rangle$ on a scale of about 10 nm. In contrast to the other methods applied to study this system, SP-STM has the required spatial resolution to reveal this change in magnetic anisotropy in the pseudomorphic regime.

The magnetic state of the monolayer Fe on W(001) has been an open question up to now. Density functional theory predicted an antiferromagnetic state [9]. Experimentally no magnetic signal was found for a coverage less than 1 ML [7] which was interpreted as a paramagnetic or antiferromagnetic state for the monolayer. The SP-STM measurements presented in this work prove for the first time that the monolayer is antiferromagnetically ordered with the spins orientated perpendicular to the surface plane.

References

[1] W. Wulfhekel, F. Zavaliche, R. Hertel, S. Bodea, G. Steierl, G. Liu, J. Kirschner, and H. P. Oepen, Phys. Rev. B **68**, 144416 (2003).

[2] A. Yamasaki, W. Wulfhekel, R. Hertel, S. Suga, and J. Kirschner, Phys. Rev. Lett. **91**, 127201 (2003).

[3] W. Wulfhekel, F. Zavaliche, F. Porrati, H. P. Oepen, and J. Kirschner, Europhys. Lett. **49**, 651 (2000).

[4] K. von Bergmann, M. Bode, and R. Wiesendanger, Phys. Rev. B **70**, 174455 (2004).

[5] G. A. Mulhollan, R. L. Fink, J. L. Erskine, and G. K. Walters, Phys. Rev. B **43**, 13645 (1991).

[6] T. L. Jones and D. Venus, Surf. Sci. **302**, 126 (1994).

[7] J. Chen and J. L. Erskine, Phys. Rev. Lett. **68**, 1212 (1992).

[8] H. J. Elmers and J. Hauschild, Surf. Sci. **320**, 134 (1994).

[9] R. Wu and A. J. Freeman, Phys. Rev. B **45**, 7532 (1992).

[10] A. Kubetzka, P. Ferriani, M. Bode, S. Heinze, G. Bihlmayer, K. von Bergmann, O. Pietzsch, S. Blügel, and R. Wiesendanger, submitted to Phys. Rev. Lett. (2004).

[11] R. Wiesendanger, I. V. Shvets, D. Bürgler, G. Tarrach, H.-J. Güntherodt, J. M. D. Coey, and S. Gräser, Science **255**, 583 (1992).

[12] W. Wulfhekel, T. Gutjahr-Löser, F. Zavaliche, D. Sander, and J. Kirschner, Phys. Rev. B **64**, 144422 (2001).

[13] S. Heinze, M. Bode, A. Kubetzka, O. Pietzsch, X. Nie, S. Blügel, and R. Wiesendanger, Science **288**, 1805 (2000).

[14] O. Pietzsch, A. Kubetzka, D. Haude, M. Bode, and R. Wiesendanger, Rev. Sci. Instr. **71**, 424 (2000b).

3.2.4 Magnetic structure of three–dimensional Fe(110) islands on W(110)

M. Bode, J. Wiebe, A. Wachowiak, M. Morgenstern, A. Kubetzka, O. Pietzsch, and R. Wiesendanger

Introduction

The detailed understanding of the magnetism of nanostructures is a major requirement for the future progress in magnetic data storage technology. Nevertheless, several basic questions are still unsettled due to the lack of appropriate experimental techniques. One of these questions is the spin-structure of a magnetic vortex core. Detailed theoretical predictions are available [1, 2] but they have never been proven experimentally. Only recently, the very existence of magnetic vortex cores could be verified experimentally by magnetic force microscopy (MFM) [14, 15]. However, MFM suffers from three problems: (i) the lateral resolution of MFM typically is limited to $\approx$ 50 nm being larger than the vortex core, (ii) the magnetic stray field of the tip easily interferes with the vortex as the tip–sample distance becomes too small, and (iii) the sensitivity is restricted to the out-of-plane component of the stray field. All three problems are avoided by using spin-polarized scanning tunneling microscopy (SP-STM). Firstly, SP-STM is capable to resolve magnetic domain walls [3] and superstructures [4] down to the atomic scale. Secondly, it has recently been shown that any dipolar stray field from the tunneling tip and thereby any dipolar interaction between tip and sample can be avoided by the use of antiferromagnetic probe tips. The magnetic moments of such tips cancel out each other [8] and hence, the net magnetization of the tip vanishes while the spin-polarization of the outermost tip atom responsible for the tunneling process is preserved. Thirdly, by varying the thickness of the antiferromagnetic deposit on the tip we are able to prepare tips with either in-plane or out-of-plane sensitivity. With this technique we study the vortex core that appears on iron (Fe) nanoislands.

Sample preparation

The measurements were performed with a low-temperature scanning tunneling microscope designed for high-resolution studies of surface magnetism [9]. During the measurements tip and sample had a temperature $T = 14 \pm 1$ K. A superconducting magnet supplies a magnetic field normal to the surface plane. By an appropriate variation of the chromium (Cr) film thickness on the tip we prepared antiferromagnetic tips with either in-plane or out-of-plane sensitivity: while thick Cr films were found to be sensitive to the in-plane component of the sample magnetization, relatively thin films (thickness $\Theta < 50$ ML) resulted in an out-of-plane sensitivity [8]. Nanoscale magnetic particles have been prepared under ultra-high vacuum conditions ($p \leq 1 \times 10^{-10}$ mbar) by means of self-organized growth of Fe on the (110) surface of a tungsten (W) single crystal. We thermally evaporated 8–10 monolayers (ML) Fe on a stepped W(110) sub-

strate held at room temperature. Subsequently, the sample was thermally annealed for 10 minutes at 800 ± 100 K. As shown in the rendered perspective STM topograph of Fig. 3.18, this preparation procedure leads to the formation of more or less elongated "islands" with lateral dimensions of 200–500 nm $\times$ 150–250 nm along the [001] and the $[1\bar{1}0]$ directions, respectively, and an average height of 8–9 nm. The areas between the islands are covered with a single pseudomorphic ML of Fe [10].

The magnetic ground state of Fe islands of that size is expected to be a vortex. At this particular size regime the lateral dimensions of the particles are too large to form a single-domain state because this would cost a relatively high stray field (or dipolar) energy. On the other hand, they are too small to form domains like in macroscopic pieces of magnetic material because the additional cost of domain wall energy cannot be compensated by the reduction of stray field energy. Instead, the magnetization continuously curls around the particle center. Thereby, the stray field energy is drastically reduced. Simultaneously, the continuous rotation reduces the energy which has to be paid for the non-parallel alignment of nearest-neighbor spins (exchange stiffness). However, the angle between adjacent spins becomes the larger the closer they are to the center of the particle. Therefore, as illustrated in the inset of Fig. 3.18 the magnetization in the vortex core was predicted to turn into the surface normal [1, 2].

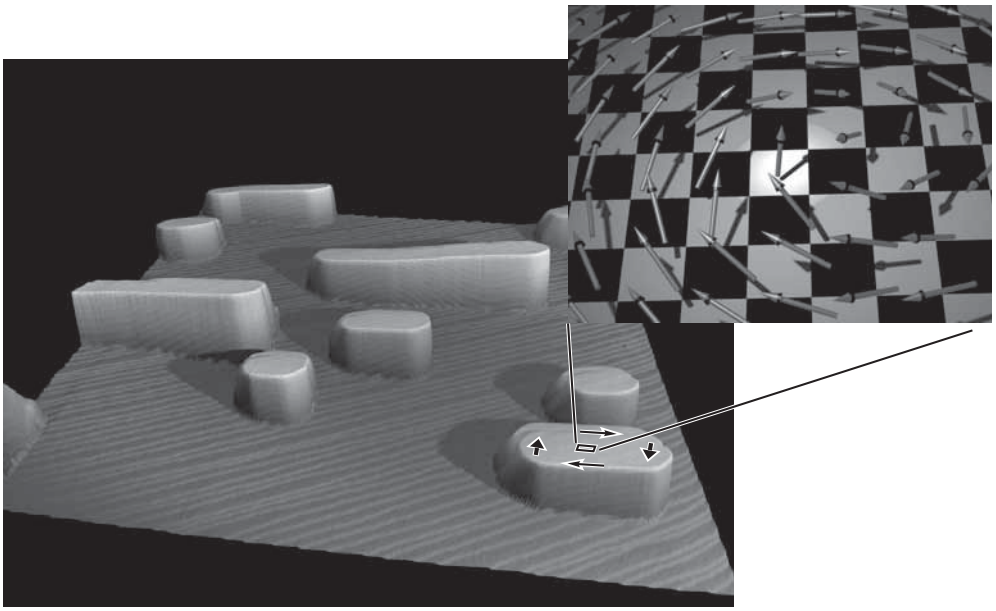

Figure 3.18: Rendered perspective STM image of Fe islands on W(110) which are expected to form a magnetic vortex structure. The image size is 1.5 μm $\times$ 1.5 μm. The islands which are elongated along the [001] direction have an average height of 8 nm. The inset shows a schematic representation of a vortex core. Far away from the vortex core the magnetization continuously curls around the center with the orientation in the surface plane. In the center of the core the magnetization is perpendicular to the plane.

Magnetic imaging

Figure 3.19(a) shows a constant-current topograph of a single Fe island. The lateral size of this particular Fe island is 400 nm along the [001] direction and 200 nm along the $[1\bar{1}0]$ direction. The quasi-hexagonal symmetry of the W(110) surface leads to tapered ends. Step edges of the underlying substrate are weakly visible as a diagonal height modulation caused by the different layer thickness of Fe and W. The dark spots appearing on the island surface are probably caused by a small amount of adsorbates. While the $\mathrm{d}I/\mathrm{d}U$ signal on top of such Fe islands is found to be spatially constant as long as measurements are performed with uncovered tungsten tips (not shown), a spatial pattern can be recognized in the $\mathrm{d}I/\mathrm{d}U$ map of Fig. 3.19(b) measured with a probe tip coated with more than 100 ML Cr. This variation is caused by spin-polarized tunneling between the magnetic sample and the polarized tip. Since this particular tip also showed a strong domain contrast on the pseudomorphic Fe ML [3], with the easy axis pointing in the $[1\bar{1}0]$ direction, we conclude that $\vec{M}_\mathrm{T}$ is parallel to the surface plane and approximately oriented along the $[1\bar{1}0]$ direction. Four different regions which will be referred to hereafter as domains can be distinguished in Fig. 3.19(b).

We have zoomed into the central region where the four "domains" touch and where the rotation of the magnetization into the surface normal is expected. Maps of the $\mathrm{d}I/\mathrm{d}U$ signal which have been measured with Cr coated tips that are sensitive to the in-plane and out-of-plane component of $\vec{M}_\mathrm{S}$ are shown in Fig. 3.20(a) and (b), respectively. The $\mathrm{d}I/\mathrm{d}U$ signal as measured along a circular path at a distance of 19 nm around the vortex core [circle in Fig. 3.20(a)] is plotted in Fig. 3.20(c). The cosine-like modulation

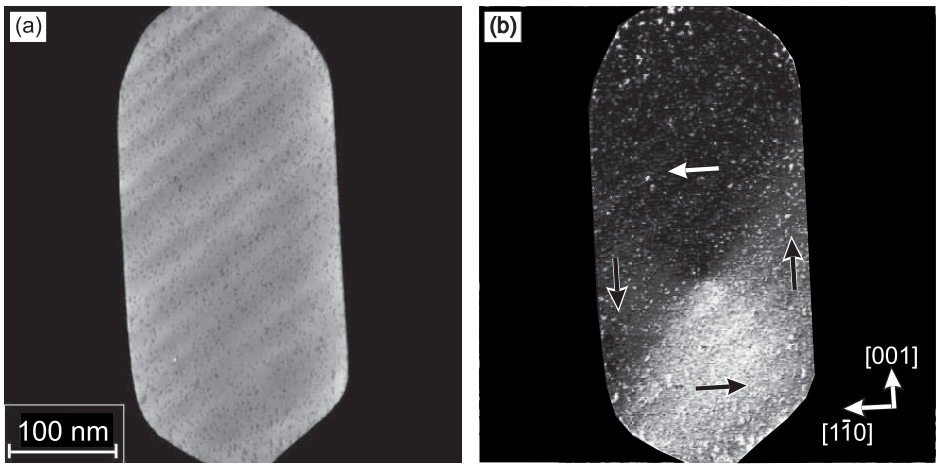

Figure 3.19: (**a**) Topography and (**B**) map of the $\mathrm{d}I/\mathrm{d}U$ signal of a single 8 nm high Fe island recorded with a Cr coated W tip. The vortex domain pattern can be recognized in (b). Arrows illustrate the orientation of the domains. Since the sign of the spin-polarization and the magnetization of the tip is unknown the sense of vortex rotation could also be reversed. The measurement parameters were $I = 0.5$ nA and $U_0 = +100$ mV. The crystallographic orientations were determined by low-energy electron diffraction.

indicates that the in-plane component of $\vec{M}_{\rm S}(\vec{r})$ continuously curls around the vortex core. Figure 3.20(b) which was measured with an out-of-plane sensitive tip on an identically prepared sample exhibits a bright spot approximately in the center of the island. Since $\vec{M}_{\rm T}$ of this tip is perpendicular to the surface plane, $\cos\theta = 0$ in Eq. 3.5 as long as the local sample magnetization $\vec{M}_{\rm S}(\vec{r})$ exhibits no out-of-plane component prohibiting the domain contrast as observed in Fig.3.20(a). Consequently, the $\mathrm{d}I/\mathrm{d}U$ map of Fig. 3.20(b) unambiguously confirms that the local magnetization $\vec{M}_{\rm S}(\vec{r})$ in the vortex core is tilted normal to the surface plane, as expected and schematically represented in Fig. 3.18(a).

Figure 3.20(d) shows $\mathrm{d}I/\mathrm{d}U$ line sections measured along the lines in (a) and (b) across the vortex core. One sees that the vortex core laterally extends over a width of

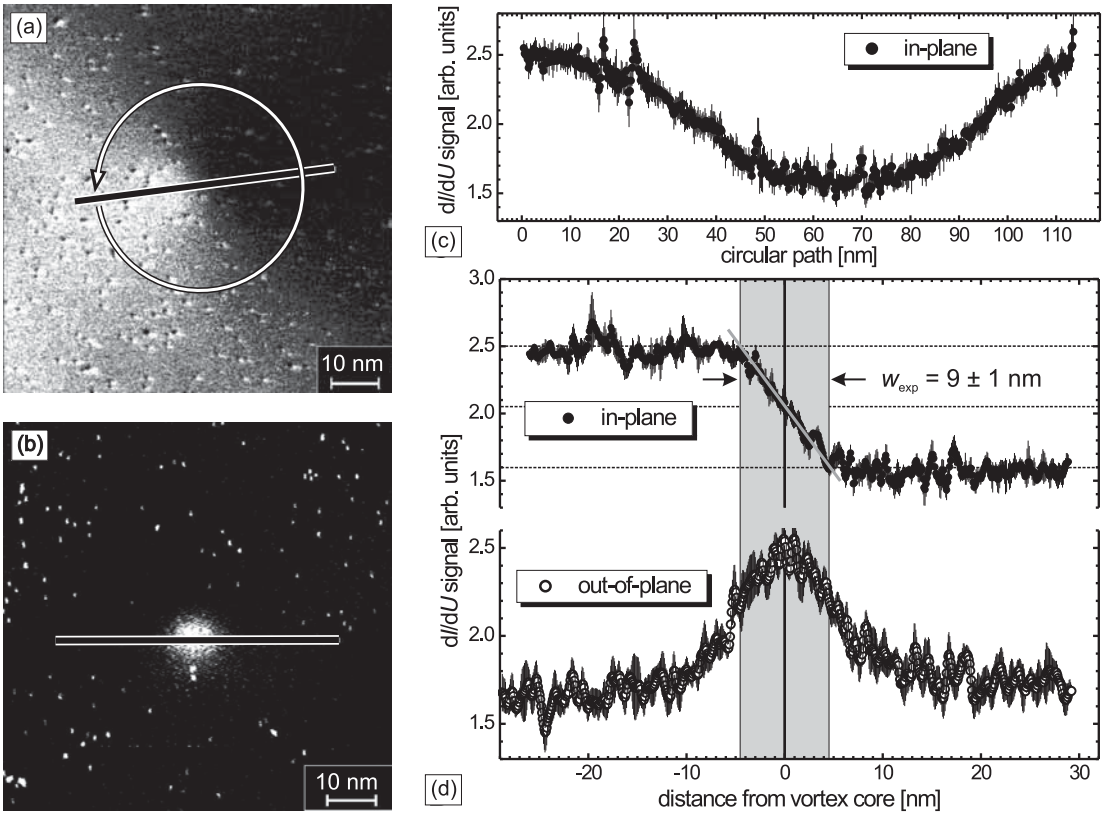

Figure 3.20: Magnetic $\mathrm{d}I/\mathrm{d}U$ maps as measured with an (**a**) in-plane and an (**a**) out-of-plane sensitive Cr tip. The curling in-plane magnetization around the vortex core is recognizable in (a) and the perpendicular magnetization of the vortex core is visible as a bright area in (b). (**c**) $\mathrm{d}I/\mathrm{d}U$ signal around the vortex core at a distance of 19 nm [circle in Fig. 3.20(a)]. (**d**) $\mathrm{d}I/\mathrm{d}U$ signal along the lines in (a) and (b). The line profiles can be fitted by a domain wall profile (grey lines) resulting in a consistent domain wall width of 8.4 ± 0.4 nm for both images. The measurement parameters were (a) $I = 0.6$ nA, $U_0 = -300$ mV and (b) $I = 1.0$ nA, $U_0 = -350$ mV.

about 10 nm. A quantitative result can be obtained by fitting the $\mathrm{d}I/\mathrm{d}U$ line sections by 180° Bloch wall profiles as calculated from continuum micromagnetic theory [2]. In spite of the fact that both measurements have been performed on *different* samples using *different* tips, both fits give an almost identical result for the experimentally determined wall width $w_{\mathrm{exp}} = 8.4 \pm 0.4$ nm. In continuum micromagnetic theory the corresponding width is usually expressed by $w_{\mathrm{theo}} = 2L = 2\sqrt{A/K}$, where L is the exchange length, A is the exchange stiffness and K is the anisotropy constant. Using the bulk exchange stiffness $A \approx 2 \times 10^{-11}$ J/m and for K the volume magnetocrystalline anisotropy $K_1 \approx 5 \times 10^4$ J/m^3 of Fe results in $w_{\mathrm{theo}} = 2L = 2\sqrt{A/K_1} \approx$ 40 nm being much larger than the observed value w_{exp}. The reason is that the stray field of the core region has been neglected so far. Since the magnetization in the center is completely aligned perpendicular to the surface plane, a strong local stray field exists. Its energy density is given by $K_{\mathrm{d}} = \mu_0 M_{\mathrm{sat}}^2/2$ with M_{sat} being the saturation magnetization. For the iron islands considered here we find $K_{\mathrm{d}} \approx 2 \times 10^6$ J/m^3 which is one order of magnitude larger than energies due to surface and bulk magnetocrystalline anisotropies [5,6]. Therefore, K is governed by K_{d}. This results in $w_{\mathrm{theo}} = 2\sqrt{A/K_{\mathrm{d}}} \approx 6.3$ nm, a value being much closer to the experimental value $w_{\mathrm{exp}} = 8.4 \pm 0.4$ nm. We conclude that the observed core size is determined by the interplay between the exchange stiffness and the stray field caused by the out-of-plane component of the magnetization in the vortex core and is not considerably influenced by magnetocrystalline anisotropies. Remaining discrepancies between experiment and theory are caused by the simplicity of the model which does not include the rotational symmetry of the problem as shown below.

Next we will discuss the shape of the vortex core in more detail. Figure 3.21(a) shows the $\mathrm{d}I/\mathrm{d}U$ map of a Fe island as measured with a mainly out-of-plane sensitive Cr coated probe tip at zero field. Again, the vortex core appears as a bright spot approximately in the center of the island. A weak variation of the $\mathrm{d}I/\mathrm{d}U$ signal between the upper and lower part of the island can be recognized. It is caused by a slight tilt of $\vec{M}_{\mathrm{T}}$ out of the surface normal resulting in a small in-plane contribution to the measured signal. In order to improve the signal-to-noise ratio the $\mathrm{d}I/\mathrm{d}U$ signal has been averaged on circles of a certain radius d_{VC} around the vortex core. Due to the circular symmetry [cp. Fig. 3.18(a)] this also removes any in-plane contribution to the measured signal and only the part of the $\mathrm{d}I/\mathrm{d}U$ signal that contains information on the perpendicular magnetization M_z remains. The resulting radial line section is shown as a grey line in Fig. 3.21(c). Again, a vortex core width of about 8–9 nm is found.

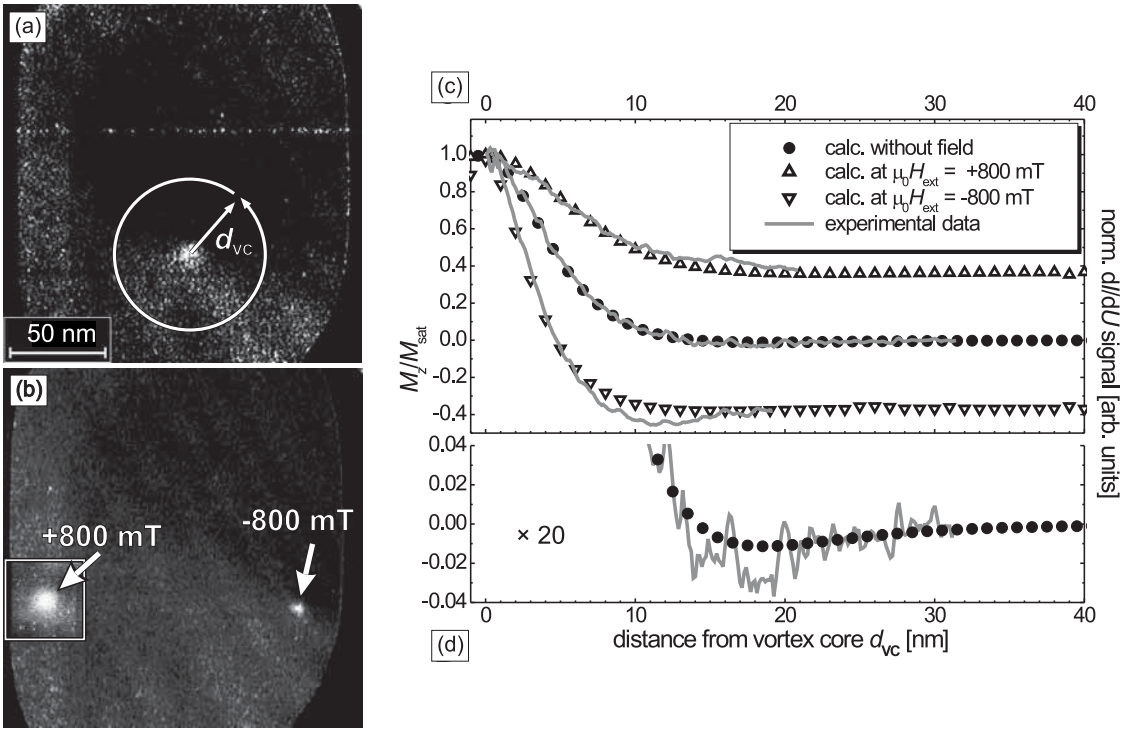

Figure 3.21: dI/dU maps measured with an out-of-plane sensitive Cr tip at (**a**) zero field and (**b**) a perpendicular field $\mu_0 H_{\rm ext} = -800$ mT. The inset shows the vortex core at the position it is found at $\mu_0 H_{\rm ext} = +800$ mT. The measurement parameters were $I = 0.5$ nA and $U = -0.3$ V. (**c**) Experimental (lines) and calculated (points) data of the perpendicular magnetization of the vortex core at different external magnetic fields. Note that the width of the core is changed by a factor of two between negative and positive field. (**d**) Magnified representation of the zero field data in (c). At a distance of ≈ 18 nm the data show a weak magnetization opposite to the magnetization in the vortex core. This result is confirmed by the calculation.

The experimental results are compared with micromagnetic simulations [1] using Fe bulk parameters for A, K, and $M_{\rm sat}$. The resulting calculated distance dependence of the normalized perpendicular magnetization $M_z/M_{\rm sat}$ is also shown in Fig. 3.21(c) (•). An almost perfect agreement between the measurement and the simulation is found. Experimental and calculated data are plotted at an enhanced y-scale in Fig. 3.21(D). At $d_{\rm VC} \approx 18$ nm a weak component in the direction opposite to the central area appears in the calculated data [2, 15]. It is also found experimentally. As already

[1]The simulations were performed using the OOMMF program, release 1.2 alpha 2 (http://math.nist.gov/oommf/). The lateral size of a typical island as shown in Fig. 3.19(A) was subdivided in a two-dimensional grid with a cell-size of = 1 nm^2. Additionally, the averaged island height of 8 nm was taken into account. For the exchange stiffness A, the magneto-crystalline anisotropy K, and the saturation magnetization $M_{\rm sat}$ we used material properties of bulk Fe. Since the height of the Fe islands of about 8 nm is only 2.5–3 times larger than $\sqrt{A/K_{\rm d}}$, the magnetization was assumed to be independent of the z-coordinate [2, 6].

mentioned in Ref. [2] this reversed component is caused by partial flux closure of the magnetic stray field of the vortex core. Note that, although this effect only amounts to 1 % of M_{sat}, it is recognizable in the experimental data.

Finally, we investigated the influence of an external field on the vortex core. Figure 3.21(B) shows $\mathrm{d}I/\mathrm{d}U$ maps of the same island as described before but now with a perpendicular field $\mu_0 H_{\mathrm{ext}} = -800$ mT applied. Obviously, the vortex core is pushed away from the center of the island towards its right rim. This lateral movement is most likely caused by a non-perfect alignment of the externally applied field with the island's surface normal. The application of a positive field ($\mu_0 H_{\mathrm{ext}} = +800$ mT) causes the vortex core to move in the opposite direction, i.e. towards the left rim of the Fe island. More important, averaged radial sections of the experimental $\mathrm{d}I/\mathrm{d}U$ data reveal that the vortex becomes narrower (broader) as the external field is negative (positive). Qualitatively, the field-dependence of the width of the vortex core can easily be understood: The energy which has to be paid for the perpendicular magnetization direction in the vortex core increases for an antiparallel and decreases for a parallel orientation. Indeed, the data of the calculated normalized perpendicular magnetization M_z/M_{sat} at positive ($\triangle$) and negative ($\triangledown$) external fields indicate that the magnetization of the whole island, which was in-plane except for the vortex core at zero field, is tilted into the field direction. Again, the core width and shape as derived from the simulated data is in rather good agreement with the experimental results [2].

By an appropriate variation of the total Fe coverage and the annealing time and temperature, we could tune the average island height h between 3-9 nm while keeping the lateral dimensions approximately constant. The left column of Fig. 3.22 shows the topography of Fe islands on W(110). The mean island height h varies between 3.5 nm and 8.5 nm. Note, that the lateral dimensions of the islands—irrespective of their height—is almost equal, i.e., about 250 nm × 500 nm along the $[1\bar{1}0]$ and the [001] direction, respectively. The islands shown in Fig. 3.22(a) exhibit an average height of approximately 3.5 nm (see line section). In the second panel of Fig. 3.22(a) the different magnetization states of islands can be distinguished by means of different $\mathrm{d}I/\mathrm{d}U$ intensities. Since no significant variation was found we conclude that these Fe islands are single domain as schematically represented in the right panel of Fig. 3.22(a). Evidently, there exists a close correlation between the magnetization direction of individual Fe islands and the surrounding Fe ML: dark (bright) Fe islands are always surrounded by a dark (bright) ML. Since the easy axis of the Fe ML on W(110) is $[1\bar{1}0]$ [7] we assume that the islands in Fig 3.22(a) are also magnetized along $[1\bar{1}0]$. With increasing thickness the magnetic pattern of the Fe islands becomes more and more complex. At $h = 4.5$ nm [Fig. 3.22(b)] we find a two domain state. The island in Fig. 3.22(c) exhibits a height $h = 7.5$ nm. The corresponding spin-resolved $\mathrm{d}I/\mathrm{d}U$ map

[2] The small deviation between experimental and simulated data at $d_{\mathrm{vc}} = 10$–15 nm is caused by the lateral movement of the vortex core as observed experimentally [Fig. 3.21(B)] but which has not been considered in the simulations (no in-plane component of H_{ext}). At the rim of the Fe island the magnetization tilts further into the direction of H_{ext} than in the island center.

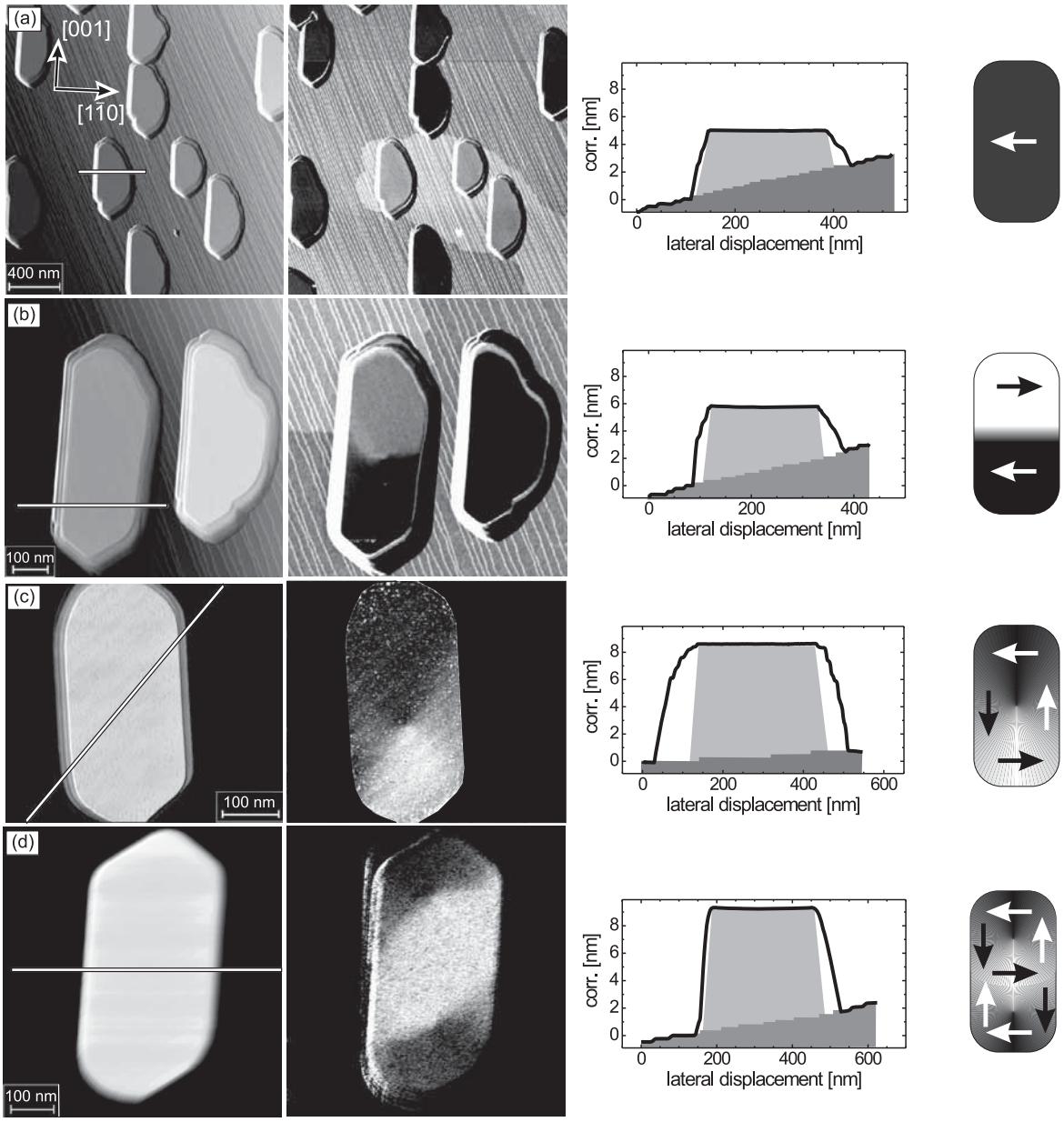

Figure 3.22: Topographic images (1st column), spin-resolved $\mathrm{d}I/\mathrm{d}U$ maps (2nd column), and topographic line sections (3rd column) of Fe islands on W(110) with different mean island heights h: (a) $h = 3.5\,\mathrm{nm}$, (b) $h = 4.5\,\mathrm{nm}$, (c) $h = 7.5\,\mathrm{nm}$, and (d) $h = 8.5\,\mathrm{nm}$. The data were obtained at $T = 14 \pm 1\,\mathrm{K}$. The resulting island domain configurations are schematically represented in the 4th column, $I = 0.5$ nA, $U = -400$ mV (1st and 2nd row), $U = 100$ mV (3rd row), $U = -350$ mV (4th row).

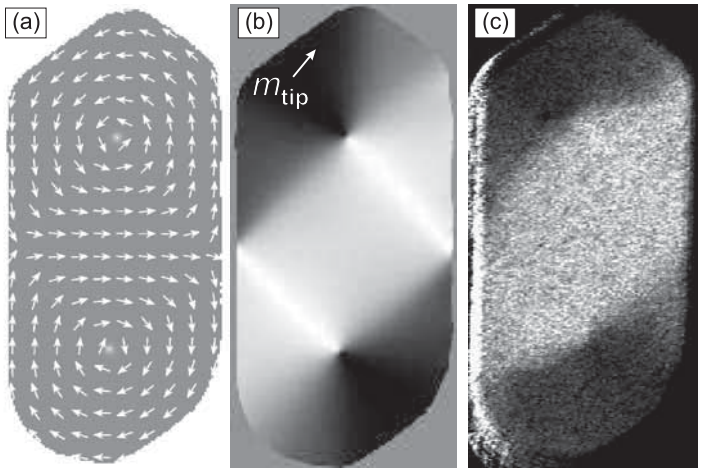

Figure 3.23: (a) Calculated magnetization pattern of this island. (b) Simulated SP-STS signal by projecting the sample magnetization from (b) onto the tip magnetization axis $\vec{m}_{\rm tip}$ (arrow). (c) Spin-resolved $\mathrm{d}I/\mathrm{d}U$ map of the island shown in Fig. 3.22(d).

shows the typical pattern of a single vortex state [13]. A diamond state is found on the even higher island shown in Fig. 3.22(d) ($h = 8.5\,\mathrm{nm}$) as proven by micromagnetic calculations (see below).

The magnetic properties of Fe/W(110) were intensively studied in the past [5,7,11]. For Fe films with a thickness d = 3-10 nm an in-plane easy axis along $[1\bar{1}0]$ was found. At a critical thickness of 7-8 nm the azimuth of the easy magnetization axis of *continuous* films rotates from the $[1\bar{1}0]$ direction into the [001] direction, i.e., the easy axis of bulk Fe. This behavior was mainly attributed to the Fe(110) surface anisotropy. [11] We approximate the anisotropy of the Fe islands by $K = K_{\rm b} - K_{\rm s}/h[\mathrm{nm}] = (48 - 450/h)\,\mathrm{kJ/m^3}$.

We have calculated the total energy densities of the islands by means of micromagnetic simulations employing the widely used OOMMF package [12]. The island shape and its average height was taken from the topographic images (left column of Fig. 3.22). We adopted bulk Fe parameters for the exchange stiffness and the saturation magnetization. The islands were discretized by cuboids with a lateral size of 2–3 nm. Since the islands are very thin the magnetization is assumed to be independent of z [2]. As illustrated in Fig. 3.23 for the island in the diamond state shown in Fig. 3.22(d) an excellent agreement between measured and calculated data is generally obtained. By projecting the calculated magnetization pattern [Fig. 3.23(a)] onto an appropriately chosen tip magnetization direction indicated by an arrow in Fig. 3.23(b) we reproduce the experimental data [Fig. 3.23(c)].

References

[1] E. Feldtkeller and H. Thomas, Phys. kondens. Materie **4**, 8 (1965).

[2] A. Hubert and R. Schäfer, *Magnetic Domains*, Springer (1998).

[3] M. Pratzer, H. J. Elmers, M. Bode, O. Pietzsch, A. Kubetzka, and R. Wiesendanger, Phys. Rev. Lett. **87**, 127201 (2001).

[4] S. Heinze, M. Bode, A. Kubetzka, O. Pietzsch, X. Nie, S. Blügel, and R. Wiesendanger, Science **288**, 1805 (2000).

[5] H. J. Elmers, T. Furubayashi, M. Albrecht, and U. Gradmann, J. Appl. Phys. **70**, 5764 (1991).

[6] U. Gradmann, J. Korecki, and G. Waller, Appl. Phys. A **39**, 101 (1986).

[7] H. J. Elmers, J. Hauschild, and U. Gradmann, Phys. Rev. B **54**, 15224 (1996).

[8] A. Kubetzka, M. Bode, O. Pietzsch, and R. Wiesendanger, Phys. Rev. Lett. **88**, 057201 (2002).

[9] O. Pietzsch, A. Kubetzka, D. Haude, M. Bode, and R. Wiesendanger, Rev. Sci. Instr. **71**, 424 (2000b).

[10] U. Gradmann, G. Liu, H. J. Elmers, and M. Przybylski, Hyp. Int. **57**, 1845 (1990).

[11] H. J. Elmers and U. Gradmann, Appl. Phys. A **51**, 255 (1990).

[12] We used the OOMMF program, release 1.2 alpha 2 (http://math.nist.gov/oommf/).

[13] A. Wachowiak, J. Wiebe, M. Bode, O. Pietzsch, M. Morgenstern, and R. Wiesendanger, Science **298**, 577 (2002).

[14] T. Shinjo, T. Okuno, R. Hassdorf, K. Shigeto, and T. Ono, Science **289**, 930 (2000).

[15] J. Raabe, R. Pulwey, R. Sattler, T. Schweinböck, J. Zweck, and D. Weiss, J. Appl. Phys. **88**, 4437 (2000).

3.2.5 Spectroscopic signature of stacking faults and dislocation lines on Co(0001)/W(110)

J. Wiebe, L. Sacharow, A. Wachowiak, G. Bihlmayer, S. Heinze, S. Blügel, M. Morgenstern, and R. Wiesendanger

Introduction

It has been shown recently by Vázques de Parga *et al.* [1] using scanning tunneling spectroscopy (STS) on Co/Cu(111) that the electronic structure of the Co(0001) surface depends sensitively on stacking. Nevertheless the spectroscopic results are contradictory to other STS measurements by Pietzsch *et al.* [2], Diekhöner *et al.* [3] and Okuno *et al.* [4]. One possible explanation for the discrepancy is an intermixing of Co and Cu which depends sensitively on the preparation process [5, 6]. A way to circumvent this effect is the use of a W(110) substrate which excludes any intermixing.

Apart from the question of the influence of stacking, there are also contradictory results concerning the surface related states of Co(0001) itself. Early angle resolved photoelectron spectroscopy (ARUPS) measurements claimed an *sp*-like surface state at −0.3 eV with respect to the Fermi energy [7, 8] which was later ascribed to a $d_{3z^2-r^2}$-like state [9]. Some of the recent STS experiments confirm the existence of this state by showing a peak at −0.31 eV or at a slightly different energy −0.43 eV [2–4]. In contrast Vázques de Parga *et al.* [1] found no spectroscopic features below E_F.

Here we present the first STS study of Co on W(110) [10]. We found a peak in STS at −0.3 eV similar to the one which was measured on the Co/Cu(111) system. This peak turned out to be sensitive to the stacking at the continuous film or island surface as well as to dislocation lines within the continuous films. First-principle electronic structure calculations helped to assign the peak to a surface *resonance* with minority-spin character being mainly $d_{3z^2-r^2}$-like. In contrast to previous results [3, 4], the corresponding states are located in a ring-like region *off* from the $\bar{\Gamma}$-point.

Growth of Co on W(110)

The growth of Co on W(110) has been investigated extensively although only few studies have been reported using STM [11–13]. Figs. 3.24 (a-c) show constant-current images of a 3 ML Co film grown on the W crystal with 10 nm terrace width. The film was annealed at increasing temperature as indicated in the images. In agreement with previous results we find two-dimensional growth below ≈ 500 K. Three-dimensional island growth is found for higher annealing temperatures as shown in Fig. 3.24 (b) and (c).

Figs. 3.24 (e-g) show constant-current images of a 10 ML Co film grown on the W crystal with 200 nm terrace width. The film was annealed at different temperatures

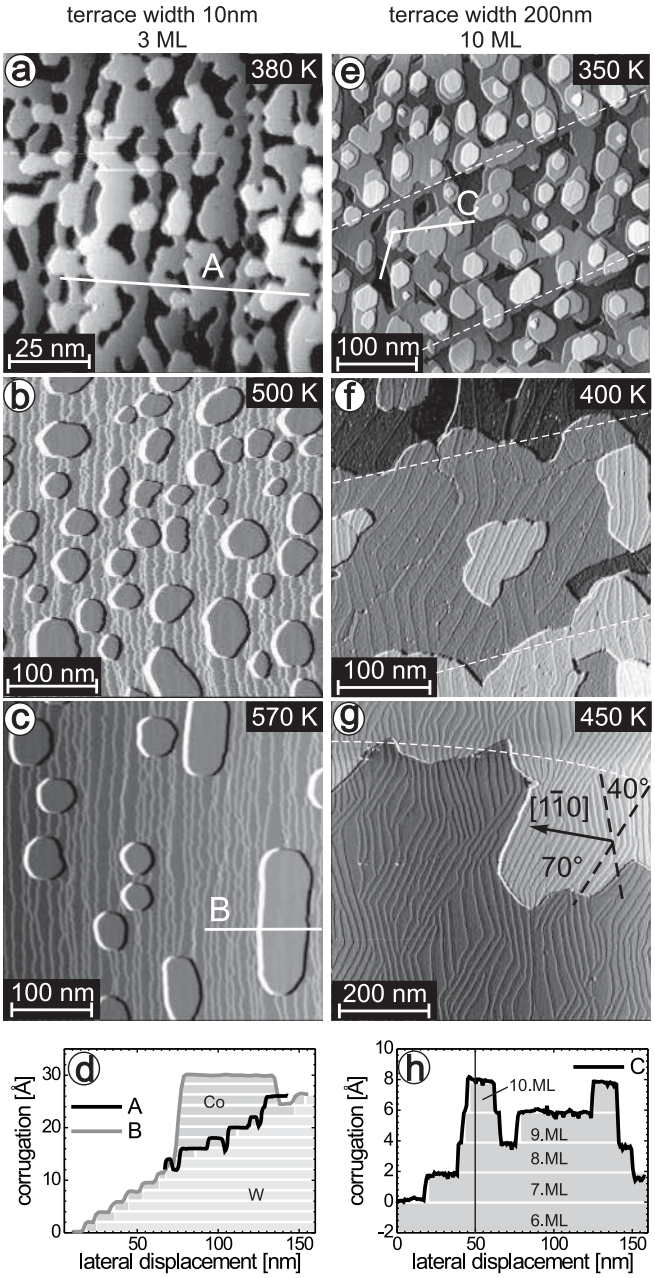

Figure 3.24: Growth of Co on W(110) at different annealing temperatures as indicated in the images. (a-c) Constant-current images of 3 ML Co on a W(110)-crystal with an average terrace width of 10 nm ((a,b) $I = 0.3$ nA, $V = -0.3$ V; (c) $I = 0.2$ nA, $V = -0.8$ V; $T = 300$ K). (d) Line sections along the lines A and B in (a) and (c), respectively. (e-g) Constant-current images of 10 ML Co on a W(110)-crystal with an average terrace width of 200 nm. The step edges of the W substrate run along the white dashed lines ((e) $I = 0.6$ nA, $V = -0.33$ V; (f) $I = 0.7$ nA, $V = -0.33$ V; (g) $I = 0.3$ nA, $V = 1$ V; $T = 6$ K). (h) Line section along the line C in (e). The assigned numbers of MLs have been deduced as described in the text. Note that the contrast of the dislocation lines in (e) is reduced with respect to (f) and (g) because of a smaller contrast per ML.

below the critical temperature for island growth as indicated. Again, quasi layer by layer growth is found in this temperature range. Obviously the roughness is reduced for increasing annealing temperature. The film annealed at 450 K shows a continuous layer where the observable Co steps follow the steps of the W substrate. To illustrate that, the step edges of the underlying W substrate have been identified by the faint height corrugation mentioned previously and are marked as white dashed lines in Figs. 3.24 (e-g). Note that the 10 pseudomorphic ML Co film contains only 8.5 closed-packed MLs if one takes into account the relaxation in the different layers.

As clearly visible in Fig. 3.24 (f) and (g) the Co terraces show a periodic zig-zag shaped height modulation consisting of stripes. The stripes run under an angle of $\pm(70^\circ \pm 5^\circ)$ to the $[1\bar{1}0]$-direction of the W(110) substrate which itself is known from LEED measurements. A closer look to this structure is presented in the constant-current image of Fig. 3.25 (a). It reveals that the stripes consist of two protrusions with different height as more clearly visible in the line section of Fig. 3.25 (b). The closest distance between shallower and higher stripes is 5 ± 1 nm and thus is approximately one third of the period of the whole structure of 15 ± 2 nm. Close inspection of Fig. 3.24 (e) reveals that the stripes are also present after annealing at 350 K. However they appear more irregular and with a lower density than in the film annealed at higher temperatures. Since the last annealing step at 450 K has no measurable effect on the stripe density we conclude that the stripe arrangement of Fig. 3.24 (g) is already close to equilibrium.

The stripe-shaped protrusions at the surface most probably originate from dislocation lines (DLs) similar to the dislocation networks found for other metal heterostructures [14–17]. Indeed, it is expected from strain measurements on Co/W(110), that misfit dislocations reduce the residual strain above a critical coverage of 10 ML [18]. This is consistent with our observation. Furthermore it can be shown, that the spacing of the stripes is consistent with the residual strain measured by LEED [18], if one assumes that each the shallower as well as the higher stripe contain one additional atomic row along the [001] direction [10].

In order to prove that the DLs are located close to the interface and not on the surface, Fig. 3.25 (c) and (e) show atomically resolved constant-current images taken on two different terraces of the Co film from Fig. 3.24 (e). Besides $2 - 3\%$ of adsorbate atoms that are imaged as bright dots, the hexagonal Co lattice is clearly visible. More importantly, the stripe-shaped protrusions are also visible in Fig. 3.25 (c) and (e) and the atomic resolution reveals that there is no shift in the atomic rows within the stripe structure nor any change in atomic distances on the stripes. This can be clearly seen by inspecting the line section of Fig. 3.25 (d) and the corresponding line in Fig. 3.25 (c). We conclude that the DLs are not located within the surface layer. Furthermore, the stripe positions are not affected by the Co step edges of the film as can be seen in Fig. 3.24 (e-g), i.e. the direction and height is not changed from one Co layer to the next higher/lower layer. Only at a few step edges adjacent to the two lowest layers in Fig. 3.24 (e) stripes are disappearing. This means that the DLs are

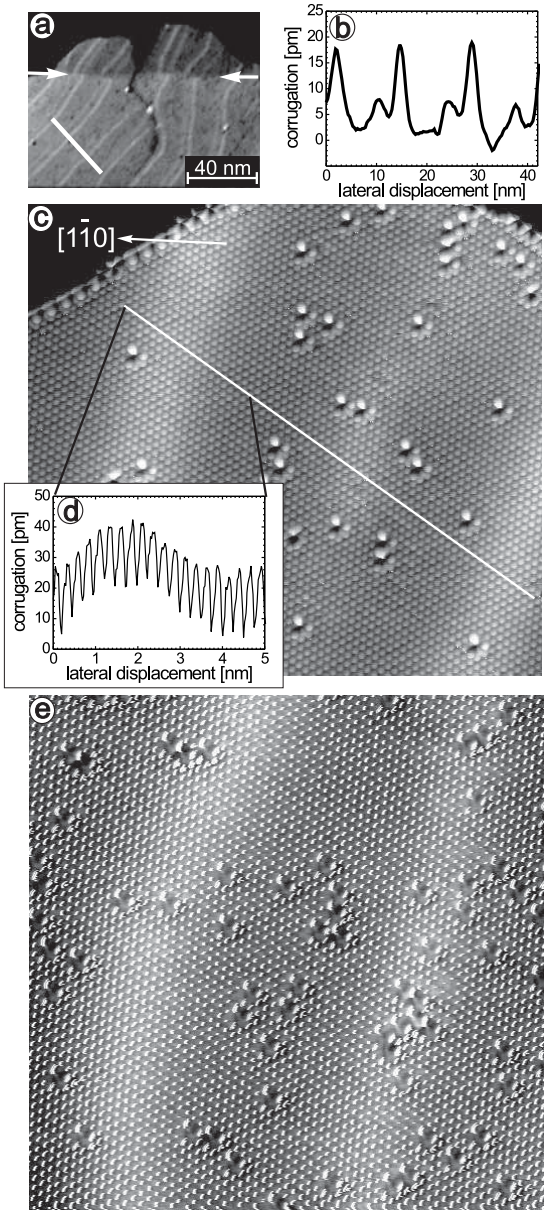

Figure 3.25: (a) Constant-current image of the dislocation network across a W step edge on the 10 ML Co film annealed at 400 K ($I = 0.7$ nA, $V = -0.33$ V; $T = 6$ K). The white arrows indicate the underlying W step edge. (b) Line section along the white line in (a). There are two types of dislocation lines, one appearing as a higher and one as a shallower protrusion. At the underlying W step edge the two types of dislocation lines are interchanged. (c,e) Constant-current images with atomic resolution on different terraces of the 10 ML Co film annealed at 350 K ((c) $I = 5$ nA, $V = 10$ mV; (e) $I = 0.9$ nA, $V = 6$ mV; $T = 6$ K). (d) Line section along the white line in (c).

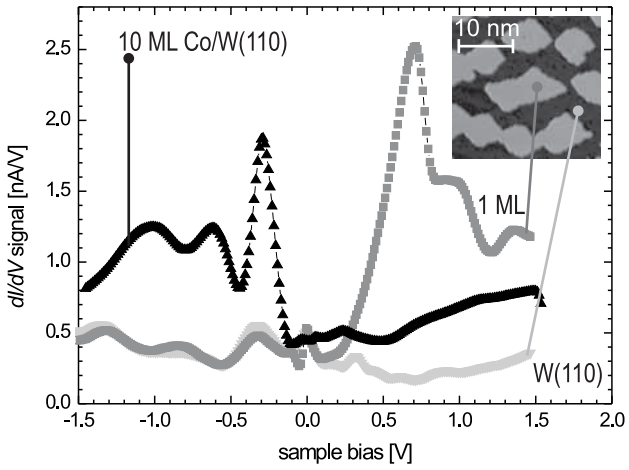

Figure 3.26: Spatially averaged dI/dV-curve on a 10 ML Co film annealed at 450 K (black curve; $I_{stab} = 1$ nA, $V_{stab} = 1.5$ V, $V_{mod} = 10$ mV) compared to dI/dV-curves taken on Co monolayer islands (grey) and on the W(110) substrate (light grey) ($I_{stab} = 0.7$ nA, $V_{stab} = -1.5$ V, $V_{mod} = 10$ mV). Inset: constant-current image of Co monolayer islands prepared by deposition of 0.5 ML Co on W(110) at room temperature ($I = 0.4$ nA, $V = -0.13$ V). Measurement temperature $T = 6$ K.

not located in the open four Co layers, but in the first five layers of the Co film next to the W substrate.

In contrast, the step edges of the underlying W substrate have an obvious effect on the stripe structure. In Fig. 3.25 (a) the step edge of the tungsten substrate is visible as a small height change in the Co film (see arrows). At this step, the higher stripe changes into a shallower one and vice versa, i.e. the stripe character is changed at every step edge of the underlying W substrate. Since only the W step edges have an effect on the stripe structure the most probable position of the DLs is indeed at the Co/W interface in agreement with conventional knowledge on dislocation networks in heterostructures [14–17, 19, 20].

Spectroscopic results

Fig. 3.26 shows three spatially averaged dI/dV-curves. One is taken on the 10 ML Co film of Fig. 3.24 (g). Another one is taken on monolayer high Co islands of a 0.5 ML film shown in the inset. The last one is recorded on the W substrate visible between the Co islands of the inset. The curve of the 10 ML film shows a sharp peak at -0.3 eV below the Fermi energy. Note that this peak has been found on all investigated Co films using different tips (PtIr and W). In measurements at room temperature it exhibits a

full width at half maximum (FWHM) of 0.35 ± 0.05 eV, while at $T = 6$ K a FWHM of 0.2 ± 0.05 eV is observed. Its peak position is at $E - E_F = -0.32 \pm 0.03$ eV averaged over 8 experiments using 3 different macro tips. According to this reproducability the peak is caused by an electronic state of the Co sample. In contrast, the other two peaks below E_F at -0.65 eV and -1 eV are either changing their position from tip to tip or are completely absent, making it difficult to identify them as sample states.

The two remaining dI/dV-curves in Fig. 3.26 were taken on Co ML-islands and on the W(110) substrate surrounding the islands. On the Co monolayer the prominent peak has shifted to 0.8 eV above the Fermi energy. On W(110) a rather structureless dI/dV-curve is found as reported previously [21]. A small peak at -0.3 eV is also present in these dI/dV-curves but with a much smaller intensity. This underlines that the sharp peak at -0.3 eV is indeed characteristic for the thicker Co films. dI/dV-measurements on wedge shaped islands of a three-dimensional film showed, that the peak is allready fully evolved at five monolayers [10]. This means, that regarding the electronic properties, the fifth monolayer is already bulk-like as has previously been found on continuous films by ARUPS [9]. Furthermore we could show that the corresponding state is quenched by the adsorption of oxygen. We thus conclude that the peak at -0.3 eV is either induced by a surface state or by a surface resonance [10].

To find out the spatial distribution of the peak at -0.3 eV we performed dI/dV-maps at the peak position as shown in Fig. 3.27. For both, the islands shown in Figs. 3.27 (a-d) and the continuous film shown in Figs. 3.27 (e,f), a fraction of the dI/dV-maps appears brighter than the surrounding. A histogram of dI/dV-values shown in the inset of Fig. 3.27 (b) reveals that the dI/dV-distribution on the Co islands is bimodal, i.e. there is a large peak that originates from the Co ML between the islands and two smaller peaks which correspond to the dI/dV-intensity on the islands. This implies that there are two spectroscopically distinct island types. One has a larger and the other a smaller dI/dV-signal at -0.3 eV. The same conclusion can be drawn for the continuous film in Fig. 3.27 (f), where a few bright terraces appear among the majority of darker terraces. The less-bright stripe-shaped areas, that are also visible in Fig. 3.27 (h), are caused by the DLs and will be discussed later. Defining a contrast of the dI/dV intensity by

$$C_{a,b} = \frac{(dI/dV)_a - (dI/dV)_b}{[(dI/dV)_a + (dI/dV)_b]/2} \tag{3.8}$$

where a and b denote either dark (d) or bright (b) areas we find a value of $C_{b,d} = 40 \pm 20\%$. This contrast is found for both morphologies, islands and continuous films. It does not depend systematically on the temperature at which spectroscopy is performed. Since $C_{b,d}$ is considerably larger than the thickness-induced contrast mentioned before, the dark and bright areas are not an effect of the film thickness.

Next, we analyse the spatial distribution and the relative frequency of the bright and dark areas. It is obvious that the bright areas appear more often in the island morphology than in the continuous film. Indeed, the continuous film of Fig. 3.27 (h) does not show any bright areas within the image range. A quantitative analysis reveals

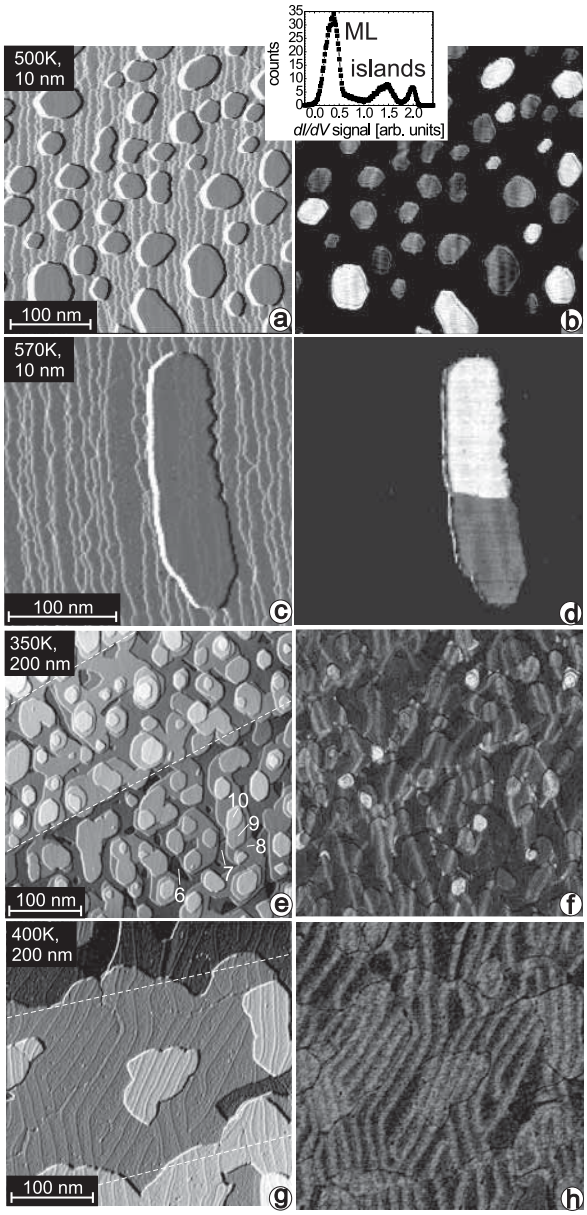

Figure 3.27: Constant-current images (left panels) and corresponding dI/dV-maps (right panels) of the same sample area of different Co films. Terrace width of the W(110) substrate and annealing temperature are indicated in the upper left corners. (a,b) 3 ML Co film ($I_{stab} = 0.3$ nA, $V_{stab} = -0.3$ V, $V_{mod} = 30$ mV, $T = 300$ K). Inset: histogram of dI/dV-values from (b). (c,d) 2 ML Co film. The island is 4 ML thick at the right and 12 ML thick at the left rim and shows a dI/dV-contrast on its atomically flat surface ($I_{stab} = 0.4$ nA, $V_{stab} = -0.3$ V, $V_{mod} = 30$ mV, $T = 300$ K). (e,f) 10 ML Co film. Numbers mark the local Co thickness in ML. (g,h) 10 ML Co film ($I_{stab} = 0.7$ nA, $V_{stab} = -0.33$ V, $V_{mod} = 20$ mV, $T = 6$ K). The dashed white lines in (e) and (g) mark the step edges of the underlying W substrate.

that in the films with island morphology in Fig. 3.27 (b) and Fig. 3.27 (d) the bright areas take $25 \pm 5\%$ of the island surface, while the continuous films in Fig. 3.27 (f) and Fig. 3.27 (h) exhibit only $3 \pm 1\%$ and 0% of bright areas, respectively.

Fig. 3.28 (a) shows local dI/dV-curves taken on the bright and dark areas of Fig. 3.28 (e) as indicated. The spectroscopic difference between bright and dark areas is visible as a different intensity of the peak at -0.3 eV, while the peak position is only slightly changed between the curves. Contrasts in peak intensity ranging from $C_{b,d} = 30\%$ to $C_{b,d} = 70\%$ are found in different measurement sets obtained after preparing different micro tips. The second spectroscopic difference between bright and dark areas is a small but systematic downward shift of the peak position on the bright areas by 55 ± 35 meV. Note finally, that the dI/dV-intensity *above* E_F is basically the same in all three curves in contrast to previous measurements on Co/Cu(111) [1].

The question arises what could be the reason for the spectroscopic difference of bright and dark areas. We can systematically exclude, that the effect is due to different layer thickness, residual gas adsorption, or atomic surface structure of bright and dark terraces [10]. Since it has previously been shown that stacking can be a source of dI/dV-contrast on Co and Gd [1, 2, 22], we check this assumption. A close inspection of Figs. 3.28 (b) and (c) shows indeed that different stacking leads to a contrast change. The figure shows two islands of monolayer height placed on the same Co terrace. Both islands are hexagonal with 3 shorter and 3 longer step edges. However, the short and long step edges are interchanged between the two islands, i.e. the left island reminds of a right pointing triangle, whereas the right island reminds of a left pointing triangle. This indicates different stacking as discussed e.g. by Busse *et al.* [23]. Stackings can be multifold in 10 ML thick films but the upper three layers can only be ABA or ABC corresponding to an hcp- or an fcc-like stacking, respectively. So, we identify the two islands as ABA- and ABC-stacked. Spectroscopically, the right island appears dark in Fig. 3.28 (c), while the left island appears bright with a contrast of $C_{b,d} = 60\%$. This strongly implies that stacking is the origin of the observed bimodal contrast [24]. Since it is moreover known that Co films on W(110) are predominantly hcp stacked [9], it is straightforward to identify the more frequent dark areas with ABA stacking and the less frequent bright areas with ABC stacking.

All found bright areas are consistent with an fcc-like stacking appearing exactly at this layer. We conclude that the peak at -0.3 eV exhibits an intensity change of about $+50\%$ and a peak shift of -55 meV at an fcc-stacking fault. Moreover we conclude, that while hcp stacking is nearly exclusive in continuous films, a significant tendency to fcc stacking appears on Co islands.

Let us come back to the less bright, stripe-shaped areas visible in the dI/dV-maps of Figs. 3.27 (f) and (h). By comparison with the corresponding constant-current images in Figs. 3.27 (e) and (g) it is clear that this contrast is caused by the dislocation lines (DLs) described previously. Note that it is hard to distinguish the shallower and the higher DL in the dI/dV-maps as can be seen in the line sections of Fig. 3.28 (f). The double line consisting of a shallower and a higher DL appears as a broad asymmetric

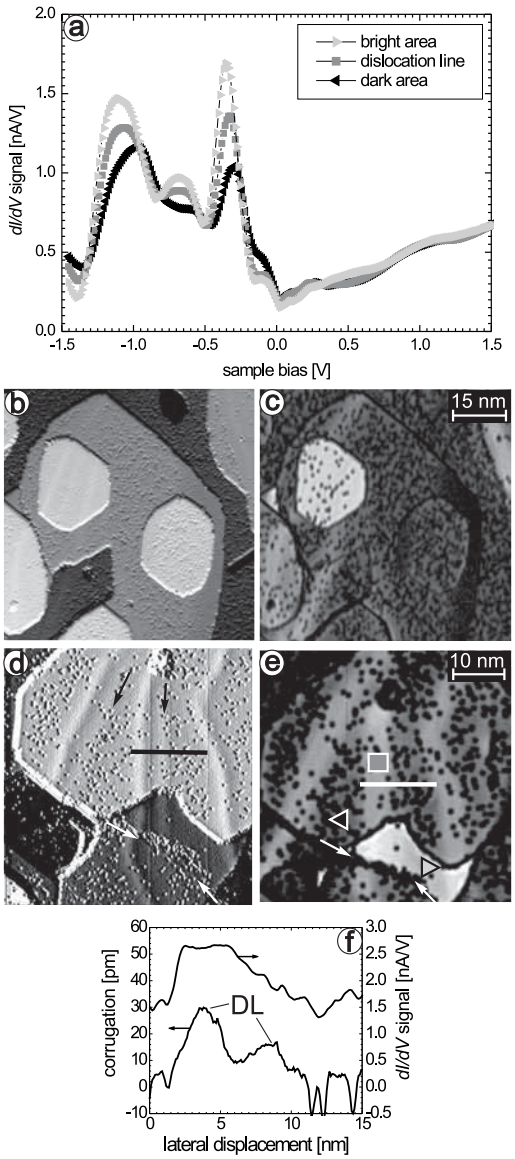

Figure 3.28: (a) Spatially resolved dI/dV-curves taken on bright and dark Co islands and on dislocation lines from a 10 ML Co film annealed at 350 K ($I_{stab} = 0.7$ nA, $V_{stab} = 1.5$ V, $V_{mod} = 10$ mV). The origin of the curves is marked in (e). (b-e) Constant-current images (left panels) and corresponding dI/dV-maps of the same sample area (right panels) of two regions of the Co film ($I_{stab} = 0.7$ nA, $V_{stab} = -0.33$ V, $V_{mod} = 20$ mV). (b,c) shows two adjacent monolayer high fcc- and hcp- stacked islands on the same Co terrace. White arrows in (d) and (e) mark a contrast change in the same atomic layer. Black arrows in (d) mark two shallow dislocation lines. (f) Line sections drawn along the black and white lines in (d) and (e), respectively. Dislocation lines (DL) are marked. Measurement temperature $T = 6$ K.

single stripe in the dI/dV-signal. Local spectroscopy on the double line as shown in Fig. 3.28 (a) reveals that again the intensity of the peak at -0.3 eV is responsible for the contrast. The peak intensity on the double line is by $C_{DL,hcp} = 25 \pm 15\%$ higher than on the surrounding hcp areas and the peak shifts downwards by 40 ± 10 meV. Interestingly the DLs are also brighter than their surrounding on fcc-stacked areas as can be seen on the bright area in Fig. 3.28 (e). Although we currently do not know the origin of the contrast on the DLs, it is likely that the long range strain-field has a strong influence on the peak intensity as will be confirmed in the next section.

Calculations

In order to find the reason for the intensity change of the peak at -0.3 eV on fcc stacking faults, we performed density-functional theory (DFT) calculations [25]. The exchange-correlation functional is formulated within the generalized gradient approximation [26]. The Kohn-Sham equations are solved applying the full-potential linearized plane-wave (FLAPW) method, as realized in the `FLEUR`-code [27, 28]. For simulating the Co(0001) surface we use a film geometry with 12 layers of Co embedded in infinite vacua on both sides of the film. We compare the perfect hcp structure (ABA) with an hcp structure exhibiting an fcc stacking-fault in both surface layers (ABC). Both geometries are optimized by total-energy minimization using the theoretical Co bulk lattice constant, which is determined to 2.509 Å (experimental value: 2.507 Å). Compared with the ideal bulk termination, both surfaces are relaxed inwards. The surface layer of the faulted structure is relaxed by 0.046 Å and that of the unfaulted structure by 0.015 Å, which corresponds to 2.3% and 0.7% of the Co interlayer distance of 2.034 Å, respectively. The workfunctions of the faulted and the unfaulted structure are nearly identical, i.e. 5.143 eV and 5.096 eV, respectively. Thus, the decay constants of the wavefunctions into the vacuum are comparable.

To simulate the spectroscopic measurements we calculated the vacuum DOS for both structures. The energies are given with respect to the Fermi level. The results for majority spin DOS and minority spin DOS as well as the sum of both DOSs are presented in Fig. 3.29 at a distance of 3 Å from the surface layer. We find a dominating peak in the minority-spin DOS at approximately -0.3 eV below E_F exhibiting a FWHM of 0.3 ± 0.05 eV. Since the proportion between different peaks in the vacuum DOS can change with the distance from the surface, we checked the vacuum DOS at distances ranging from 2 Å to 10 Å. For these distances the peak at -0.3 eV remains the dominating feature for both structures. Consequently, this peak corresponds to the one found in STS-measurements.

As visible in Fig. 3.29, the faulted structure (f) exhibits a higher peak intensity than the unfaulted structure (u). According to Eq. 3.8 the contrast amounts to $C_{f,u} = 30\%$ at $2 - 3$ Å distance, but decreases to $C_{f,u} = 5\%$ at 10 Å distance. Moreover, the peak on the faulted structure is at -0.34 eV, while that on the unfaulted structure is at -0.28 eV. This means that the peak on the faulted structure is shifted by 60 meV to

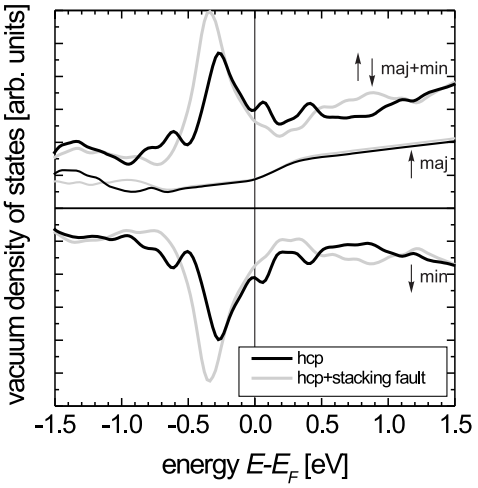

Figure 3.29: Calculated vacuum DOS of the unfaulted structure (black) and of the faulted structure (grey) of a 12 ML Co film at a distance of 3 Å from the surface layer. Maj, min, and $maj + min$ indicate the majority DOS, the minority DOS and the sum of both, respectively. All curves are shown on the same scale.

lower energies. Both is in excellent agreement with the STS results where an intensity change of $(50 \pm 20)\%$ and an energy shift of 55 ± 35 meV are found. Finally, the calculated peak width is in reasonable agreement with the experimental result.

Next we want to understand the mechanism why fcc stacking leads to a higher peak intensity. To answer this question, we first compare the vacuum DOS with the band structures of faulted and unfaulted surfaces. Fig. 3.30 shows band structures of the minority spin for both systems along the high symmetry directions. States, which have more than 10% of their DOS in vacuum, are marked by black dots. The corresponding bands are identified as surface-related bands. One of those bands [29] exists in the energy range corresponding to the peak at -0.3 eV. It has a minimum marked by the circles in Fig. 3.30 at approximately 1/4 of the distance from $\bar{\Gamma}$ to $\bar{K}$ and from $\bar{\Gamma}$ to $\bar{M}$, respectively. This minimum is close to -0.3 eV. We checked that the main contribution to the vacuum DOS comes indeed from this band minimum. A second surface band has a maximum at about -0.5 eV and is located at the $\bar{\Gamma}$-point. The contribution of this band to the peak at -0.3 eV in the vacuum DOS is negligible, since the band maximum occurs at lower energies. In fact, we find that the contribution from $\bar{\Gamma}$ to the peak is a factor of 10 lower than the contribution from the band minimum off from $\bar{\Gamma}$. Consequently the peak at -0.3 eV is caused by the band minimum of the surface band at 1/4 of the 2DBZ. We conclude, that this band minimum is the origin of the peak measured by STS. This is in contrast to conclusions

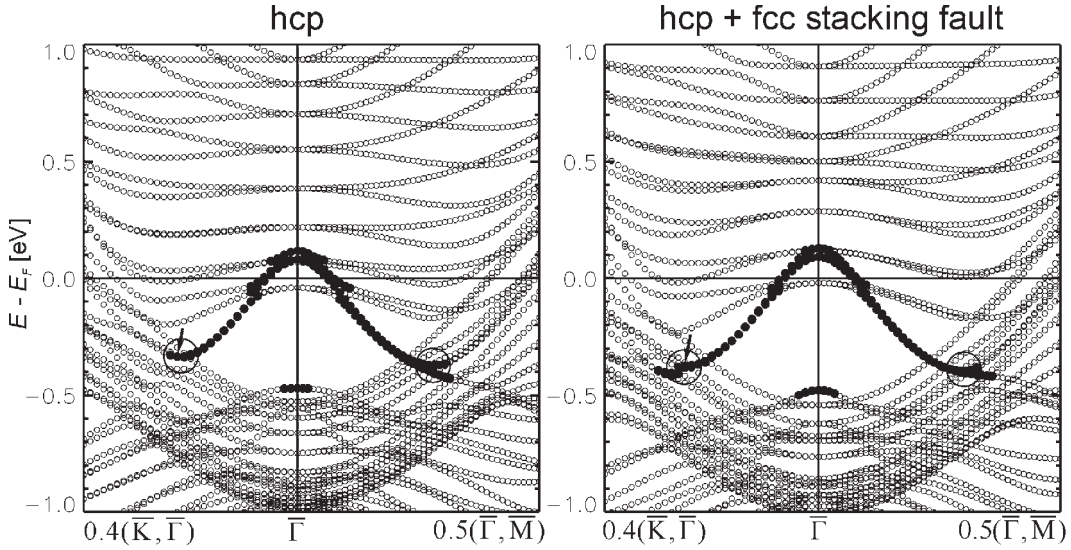

Figure 3.30: Minority-spin band structure of the 12 ML Co film in the unfaulted (left panel) and in the faulted (right panel) structure plotted along the high symmetry directions in the neighborhood of $\bar{\Gamma}$. Black dots mark states that are localized to more than 10% in vacuum. The larger circles mark the band minimum region (see text). The state used for the contour plots in Fig. 3.31 is indicated with an arrow.

given for Co/Cu(111), where a band at $\bar{\Gamma}$ has been proposed to be responsible for the peak [3, 4]. Note, that the band maximum at $\bar{\Gamma}$ is isolated from other bulk bands and is, thus, a surface *state*. In contrast, the band minimum at 1/4 of the 2DBZ crosses other bulk bands and is, thus, probably a surface *resonance*.

Finally, we analyze the charge distribution of the surface bands. The character of the band with the minimum at 1/4 of the 2DBZ changes from the band maximum at $\bar{\Gamma}$, where it has a predominant p-character, to the band minimum, where it has a $d_{3z^2-r^2}$-character with a small contribution of s- and p-states of less than 5%. This is shown in Fig. 3.31, where contour plots of the minority spin-density at the energy and Bloch vector corresponding to the band minimum marked by arrows in Fig. 3.30 are given. For faulted and unfaulted structure the contour plots show a predominant $d_{3z^2-r^2}$-character at the surface layer with a minor superposition of an s-like character. Within the bulk, the LDOS has predominant d_{xz}-character. The contribution of this particular state to the LDOS in each layer and in vacuum is indicated by the numbers next to the contour plots. Obviously, the largest contribution is in the surface layer. Nevertheless, there is a considerable contribution in the subsurface layers. This means that the state at the surface can couple to bulk d-states. That this coupling takes place indeed can be concluded from the hybridization with the bulk d-bands near the band minimum, which is marked in Fig. 3.30. Consequently, the state has to be assigned to a surface *resonance* rather than to a surface *state*. In contrast, the dot marked band

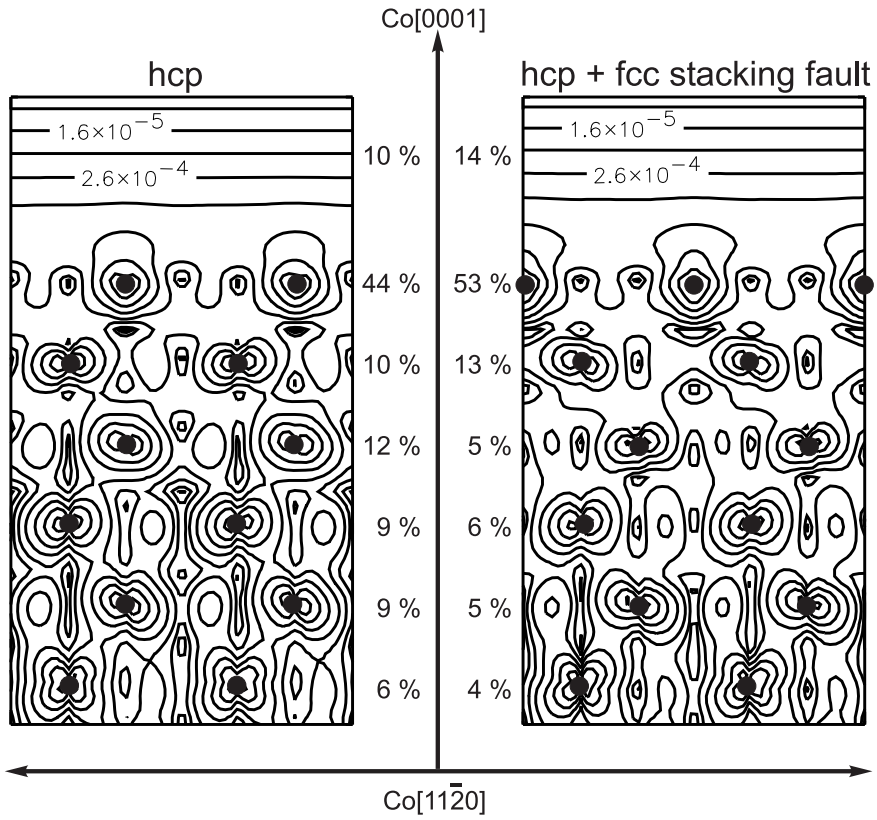

Figure 3.31: Contour plots of the spin-density of the minority electrons for the state marked with an arrow in Fig. 3.30 for the 12 ML Co film in the unfaulted (left panel) and in the faulted (right panel) structure. The numbers marking the contour lines give the corresponding charge density in electrons/au^3. Two successive lines differ by a factor of 4. Crystallographic directions of the Co(0001) lattice are indicated. The black dots mark the positions of the closest atoms projected onto the plane. The numbers beside the contour plots give the contribution of the state to the LDOS in percent for this layer or vacuum, normalized to six layers. They are obtained by integrating over the muffin tins in each layer and over the vacuum, respectively.

with the maximum at -0.5 eV at $\bar{\Gamma}$ is found to be a $d_{3z^2-r^2}$-surface state (not shown) in accordance with the Co/Cu(111)-case [3, 4].
The contour plots in Fig. 3.31 also show that in the case of hcp-stacking the downward oriented lobes of the surface atoms point directly to the atoms in the second subsurface layer. In contrast, in case of the faulted structure, the lobes point into the interstitial region. Accordingly, the surface resonance exhibits a stronger coupling to bulk d-states at pure hcp stacking than at stacking faults. This leads to a weaker localization in the surface layer in the hcp case as can also be seen by comparing the distribution of the LDOS in the different layers (Fig. 3.31). As a consequence, the intensity of the vacuum DOS as measured by STS is lower for the hcp structure. The reason for a different brightness of hcp and fcc areas in dI/dV-maps at -0.3 eV is, thus, a different coupling of the $d_{3z^2-r^2}$-like surface resonance to the underlying bulk. Note that the intensity of the surface resonance in the hcp case is larger in the second subsurface layer than in the first subsurface layer. This stresses that the geometrically induced coupling to the second subsurface layer is indeed the relevant coupling.

Conclusions

In summary, we have investigated the electronic structure of the Co(0001) surface on islands and continuous films grown on W(110) by STS. On both, we found a surface related peak at -0.3 eV below the Fermi energy. By first-principle electronic structure calculations this peak is assigned to a $d_{3z^2-r^2}$-like surface resonance with minority-spin character. It belongs to a band minimum at 1/4 of the two-dimensional Brillouin zone away from $\bar{\Gamma}$. STS reveals that the surface resonance is extremely sensitive to stacking as well as to the strain field of dislocation lines. According to the calculations, fcc stacking at the surface results in an increase of the vacuum density of states by $5-30\%$, depending on the tip-sample distance, while STS experiments find an increase of $(50 \pm 20)\%$. The different intensity is caused by a different coupling strength of the surface resonance to bulk states for fcc and hcp stacking leading to a different localization in the surface layer and, thus, to a different dI/dV-signal. Although a contrast in dI/dV on different stackings has also been found in the Co/Cu(111)-system by Vázques de Parga *et al.* [1], it has been attributed to a peak above E_F, which is at variance with the peak measured on the same system by Pietzsch *et al.* [2], Diekhöner *et al.* [3] and Okuno *et al.* [4]. Since Vázques de Parga *et al.* do not find a feature in the energy range of the surface resonance, one possible explanation for their results could be intermixing or contamination leading to a change in electronic structure. However, since our explanation for the contrast in dI/dV on different stackings is based on the commonly measured peak on both Co systems, we believe that our results are generally correct for clean Co(0001).

Finally, we found that the film morphology is important for the stacking, i.e. fcc stacking appears to be considerably increased in Co islands compared to continuous Co films. This effect should be considered with respect to nanostructuring of magnetic multilayers.

References

[1] A. L. Vázques de Parga *et al.*, Phys. Rev. Lett. **85**, 4365 (2000).

[2] O. Pietzsch *et al.*, Phys. Rev. Lett. **92**, 057202 (2004).

[3] L. Diekhöner *et al.*, Phys. Rev. Lett. **90**, 236801 (2003).

[4] S. N. Okuno *et al.*, Phys. Rev. Lett. **88**, 066803 (2002).

[5] J. de la Figuera *et al.*, Surf. Sci. **307**, 538 (1994).

[6] A. Rabe *et al.*, Phys. Rev. Lett. **73**, 2728 (1994).

[7] F. J. Himpsel, D. E. Eastman; Phys. Rev. B **20**, 3217 (1979).

[8] E. Wetli, T. J. Kreutz, H. Schmid, T. Greber, J. Osterwalder, M. Hochstrasser; Surf. Sci. **402-404**, 551 (1998).

[9] H. Knoppe, E. Bauer; Phys. Rev. B **48**, 1794 (1993).

[10] J. Wiebe, L. Sacharow, A. Wachowiak, G. Bihlmayer, S. Heinze, S. Blügel, M. Morgenstern, R. Wiesendanger; Phys. Rev. B **70**, 35404 (2004).

[11] A. Bauer, A. Mühlig, T. Günther, M. Farle, K. Baberschke, G. Kaindl; Mat. Res. Soc. Symp. Proc. **475**, 27 (1997).

[12] J. Bansmann, L. Lu, V. Senz, A. Bettac, M. Getzlaff, K. W. Meiwes-Broer; Eur. Phys. J. D **9**, 461 (1999).

[13] M. Pratzer, H. Elmers, M. Getzlaff; Phys. Rev. B **67**, 153405 (1998).

[14] J. C. Hamilton, S. M. Foiles; Phys. Rev. Lett. **75**(5), 882 (1995).

[15] J. Malzbender, M. Przybylski, J. Giergel, J. Kirschner; Surf. Sci. **414**, 187 (1998).

[16] M. Stindtmann, M. Farle, T. S. Rahman, L. Benabid, K. Baberschke; Surf. Sci. **381**, 12 (1997).

[17] B. Voigtländer, N. Theuerkauf; Surf. Sci. **461**, L575 (2000).

[18] H. Fritzsche, J. Kohlhepp, U. Gradmann; Phys. Rev. B **51**, 15933 (1995).

[19] J. de la Figuera, A. K. Schmid, N. C. Bartelt, K. Pohl, R. Q. Hwang; Phys. Rev. B **63**, 165431 (2001).

[20] S. Murphy, D. Mac Mathúna, G. Mariotto, I. V. Shvets; Phys. Rev. B **66**, 195417 (2002).

[21] M. Bode, R. Pascal, R. Wiesendanger; J. Vac. Sci. Technol. A **15**, 1285 (1997).

[22] M. Bode, R. Pascal, M. Getzlaff, R. Wiesendanger; Acta Phys. Pol. A **93**, 273 (1998).

[23] C. Busse, C. Polop, M. Müller, K. Albe, U. Linke, T. Michely; Phys. Rev. Lett. **91**, 056103 (2003).

[24] A similar contrast due to stacking of Co on Cu(111) has been found by Pietzsch *et al.* [2].

[25] P. Hohenberg, W. Kohn; Phys. Rev. **136**, 864 (1964).

[26] J. P. Perdew, K. Burke, M. Ernzerhof; Phys. Rev. Lett. **77**, 3865 (1996).

[27] E. Wimmer, H. Krakauer, M. Weinert, A. Freeman; Phys. Rev. B **24**, 864 (1981).

[28] http://www.flapw.de.

[29] More precisely there are two bands being nearly degenerate. Nevertheless, they are due to only one surface band, but for each surface of the film, the upper and the lower. Due to the finite thickness of the film, there remains a small interaction, and the bands are only nearly degenerate.

3.2.6 Imaging ferro- and superparamagnetic nanoislands by SP-STM

O. Pietzsch, A. Kubetzka, and M. Bode, and R. Wiesendanger

Introduction

Most magnets in our everyday life are permanent magnets. In spite of the fact that under ambient conditions they are exposed to thermal fluctuations, permanent magnets have a static magnetization direction that does not change significantly on a typical experimental time scale. The physical origin of this stability is their large anisotropy energy barrier E_{a} which within good approximation is equal to the product of the magnets volume V with the material-specific anisotropy energy density constant K, $E_{\mathrm{a}} = K \cdot V$. Due to the large volume of macroscopic magnets, E_{a} is much larger than the thermal activation energy.

Here we present SPSTM measurements performed on two examples of isolated, epitaxially grown nanoislands. While Co islands on Cu(111) turn out to be perpendicularly magnetized and magnetically stable at the measurement temperature $T = 14\,\mathrm{K}$, small Fe islands on Mo(110) were found to be susceptible to thermal fluctuations which leads to superparamagnetic switching events with a pronounced shape dependence.

Co islands on Cu(111)

The early stages of epitaxial Co growth on Cu(111) have been the subject of intense research during the past decade. Complementary to spatially averaging techniques [1–4], scanning tunneling microscopy (STM) has been applied by several groups. In the sub-monolayer coverage regime, triangular islands were observed protruding to a height of two atomic layers from the Cu surface [5]. In a more recent STM study, Pedersen *et al.* [6] gave evidence that the Co islands are, in fact, three monolayers thick, with the bottom Co layer submerged into the Cu surface. Two distinct island orientations were found, rotated by 180° about the surface normal. It is generally accepted that the orientational variance is due to a stacking fault in one type of the islands, while the other type follows the fcc stacking sequence of the Cu(111) substrate.

In a first set of experiments we have studied the spin-averaged electronic structure of the islands by laterally resolved tunneling spectroscopy using a non-magnetic tungsten tip. In a scan area of $(65\ \mathrm{nm})^2$ a constant current topograph was taken. Simultaneously, we measured an $I(V)$ curve and also the differential conductance $dI/dV(V)$ at every pixel of the image, i.e. 180×180 individual spectra (stabilization parameters: $I = 1.5$ nA, $U = 0.9$ V). Results are shown in Fig. 3.32(a-c). Numerically differentiated $I(V)$ curves are shown in (a), averaged over areas as indicated by boxes in (b). Images (b) and (c) present maps of the $\mathrm{d}I/\mathrm{d}U$ signal, i.e. spectroscopic layers at voltages as indicated. One curve is representative of an fcc island while the other belongs to a faulted island. As a reference, also a spectrum of clean Cu is included,

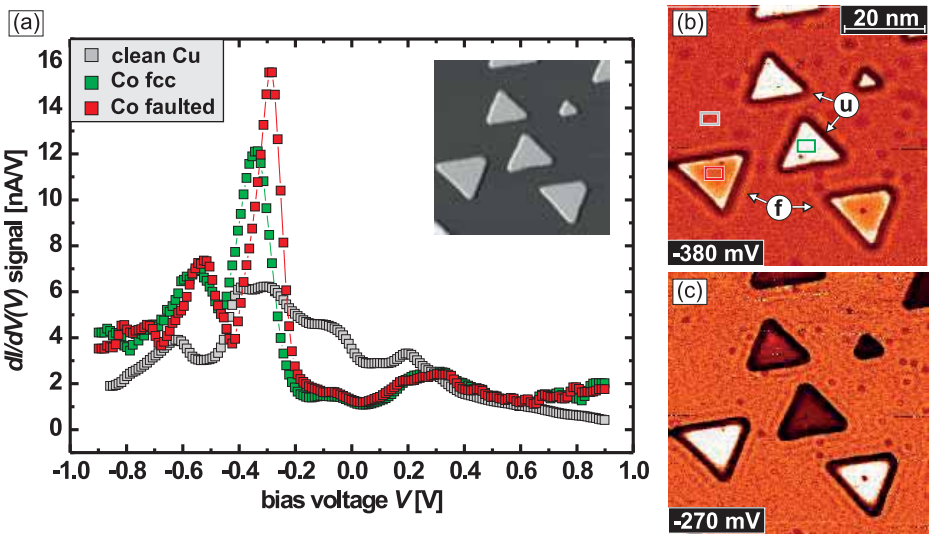

Figure 3.32: (a) Spin-averaged tunneling spectra, (b–c) dI/dU maps at voltages as indicated. The curves were averaged in the boxes in (b), the island types are labeled u (unfaulted) and f (faulted). Spectra of the two island types differ in peak energetic positions and intensities. At the voltages of maps (b–c) the contrasts are maximal. Inset in (a): topographic image.

showing the onset of the well known Cu surface state [7] at −0.46 eV as its main characteristics. In the Co spectra the main features are (i) a strong and sharp occupied peak, similar to the one reported in Ref. [8], and (ii) a second peak about 0.25 eV lower in energy previously not reported in STS experiments.[3]

While the general curve shapes for the two types of islands are quite similar the spectra differ most clearly by a shift in energetic position of the peaks as well as in intensity. On fcc islands the peak is centered at -0.35 eV while it is found at -0.28 eV on faulted islands. Note that the value of -0.31±0.02 eV given in Ref. [8] was obtained by averaging over a large number of spectra on many islands of different size *and orientation*. The electronic differences become even more obvious from inspecting the dI/dU maps (b) and (c). We have chosen the voltages as to maximize the contrasts between the island types. These are found at values slightly off the peak positions. While in (b) the unfaulted islands exhibit a higher LDOS (corresponding to bright areas) than the unfaulted ones, the contrasts are reversed in (c). This finding clearly proves that the electronic structure is inequivalent for the two types of islands. Similar observations of stacking-dependent electronic structure variations were reported for Gd(0001) islands on W(110) [9].

In a second set of experiments we used a Cr coated tip sensitve to the perpendicular component of the sample magnetization. Applying the same procedure as described above for the spin-averaged spectroscopy, we again measured one spectrum at every pixel of the image. The results are displayed in Fig. 3.33. While the spectroscopic

[3]LDOS oscillations similar to those reported in Ref. [8] are also resolved in our dI/dU maps.

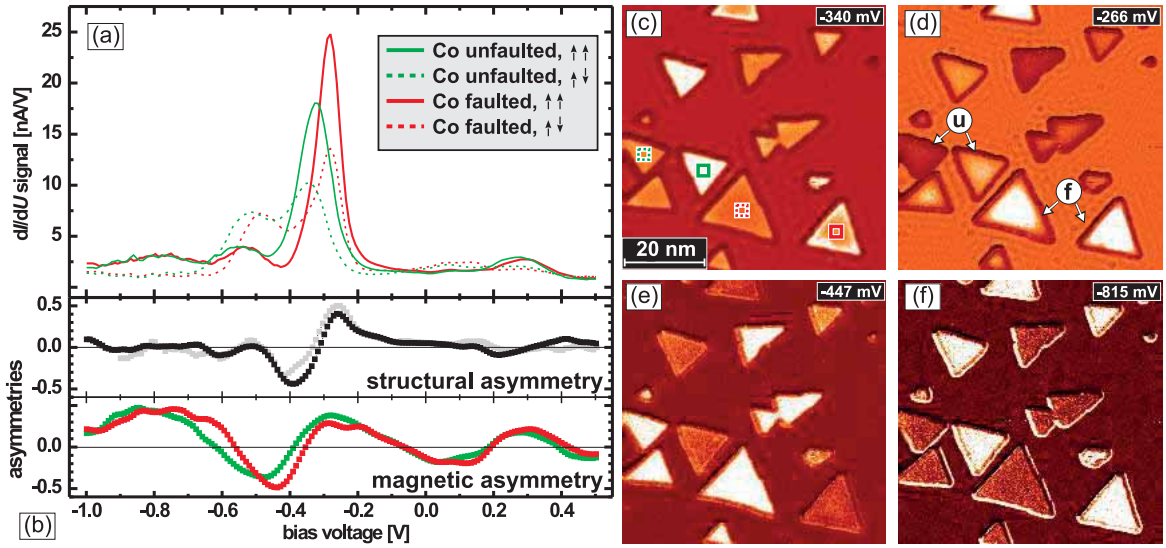

Figure 3.33: (a) Spin-resolved tunneling spectra. Arrows ↑↑ (↓↑) refer to parallel (antiparallel) magnetization alignment of sample and tip. (b) Asymmetries arising from different stacking [upper panel; grey (black) spin-averaged (spin-polarized)], and from opposite magnetization (lower panel). (c–f) $\mathrm{d}I/\mathrm{d}U$ maps at bias voltages as indicated. Maps (c–d) allow a direct comparison to the spin-averaged case in Fig. 3.32(b–c). As exemplified by maps (e–f), the spin-dependent contribution is clearly dominant in most parts of the energy range. Stabilization parameters: $I = 1$ nA, $U = +0.6$ V.

features used to discriminate the differently stacked islands in the spin-averaged measurements are found to be preserved, we now observe two distinct curves for each island type (solid vs. dotted curves). The latter differences are caused by the *magnetic* state of the islands which are magnetized either parallel or antiparallel to the tip magnetization, respectively. This source of contrast was unavailable in the spin-averaged measurements. In Fig. 3.33 (c–f) $\mathrm{d}I/\mathrm{d}U$ maps at selected energies are displayed. Panels (c–d) represent the spin-polarized analogues to Fig. 3.32(b–c), emphasizing contrasts due to different stacking, while the voltages for panels (e–f) are chosen such that the magnetic contrasts are particularly strong. Comparing Figs. 3.32(b–c) and 3.33(c–d) we notice that the stacking dependent contrasts are less clear than in the spin-averaged case. The reason is that, competing with the structural contrast, a spin-dependent LDOS contribution of comparable strength is superimposed. In most parts of the energetic range under study, however, the contrasts are clearly dominated by the magnetic signal. This is exemplified in Fig. 3.33(e–f). We note that the contrasts are reversed in the two images. Thus it is not immediately clear if bright or dark is indicative of a parallel alignment of tip and sample magnetization. SP-STS is sensitive to the spin polarization of the tunneling junction $P_{\mathrm{T,S}}(E)$, which is a convolution of the polarizations of both electrodes involved, i.e. tip and sample. It is well known that Cr (the tip material) is negatively polarized around the Fermi level. Taking the

curves of higher intensities at the Co surface state as indicative of a parallel magnetization alignment (solid curves), we conclude that this sample state is also negatively polarized, in agreement with Ref. [8], thus $P_{\mathrm{T,S}}$ is positive in this energetic region. As indicated by intersections of the solid curves with the dotted ones, a sign reversal happens at -0.38 eV (faulted: -0.35 eV) and again at -0.62 eV (faulted: -0.57 eV), i.e. in the region of the second peak. According to recent spin-density functional calculations this peak has also minority character. Thus, to account for the observed sign reversals of $P_{\mathrm{T,S}}$, the additional assumption is required that the tip polarization is reversed at roughly -0.38 eV.

To get a clearer picture of the relevance of the two major sources of contrasts, i.e. different stacking and opposite magnetization, we have plotted the asymmetries $A = (a - b)/(a + b)$ of the respective curves in Fig. 3.33(b). The upper panel clearly shows the similarity of the structurally caused asymmetries for the spin-averaged (grey) and the spin-polarized (black) case. On the other hand, the magnetic asymmetries as displayed for both island types in the lower panel of (b) follow characteristics being very different from the structural asymmetries. Strong oscillatory behavior is observed over the whole energy range caused by the sign reversal of the spin polarization as discussed above. Guided by these asymmetry curves, any contrasts observed in spin-resolved $\mathrm{d}I/\mathrm{d}U$ maps at various energies can unambiguously be interpreted.

In order to verify the *magnetic* origin of the observed contrasts we recorded $\mathrm{d}I/\mathrm{d}U$ maps in variable magnetic fields applied along the surface normal. In Fig. 3.34 a selection is presented, $(150\ \mathrm{nm})^2$ in size, acquired at $V_{\mathrm{bias}} = -0.18$ V. In the virgin state islands of both orientations are found either dark or bright, corresponding to their magnetization being either parallel or antiparallel to the tip magnetization. A field as strong as 1 T causes only a small fraction of the dark islands, exclusively those of small size, to switch their magnetization so that they are imaged bright (a few of them are marked by circles). A field of 1.5 T is required to switch most islands, still leaving two islands in their initial dark state. Field removal reveals a nearly 100 percent remanence; only two very small islands are switched (see circles), presumably due to stray fields being particularly strong from close-by larger islands. A reversed field of -1.5 T is required to again switch most of the islands into the opposite direction. Even at -1.75 T the sample is not completely saturated as is found in a larger scan [$(350\ \mathrm{nm})^2$, not shown] where still a few islands are observed being magnetized opposite to the applied field.

Fe islands on Mo(110)

With the vast growth of the storage density in magnetic media within the past decades we have witnessed a stunning miniaturization of magnetic grains; the so-called "superparamagnetic limit" is rapidly approached [11]. This term describes the critical size below which small magnetic particles may continually reverse their magnetization direction due to thermal agitation. In early theoretical approaches Néel [12] and Brown [13] calculated the switching probability under the assumption of coherent

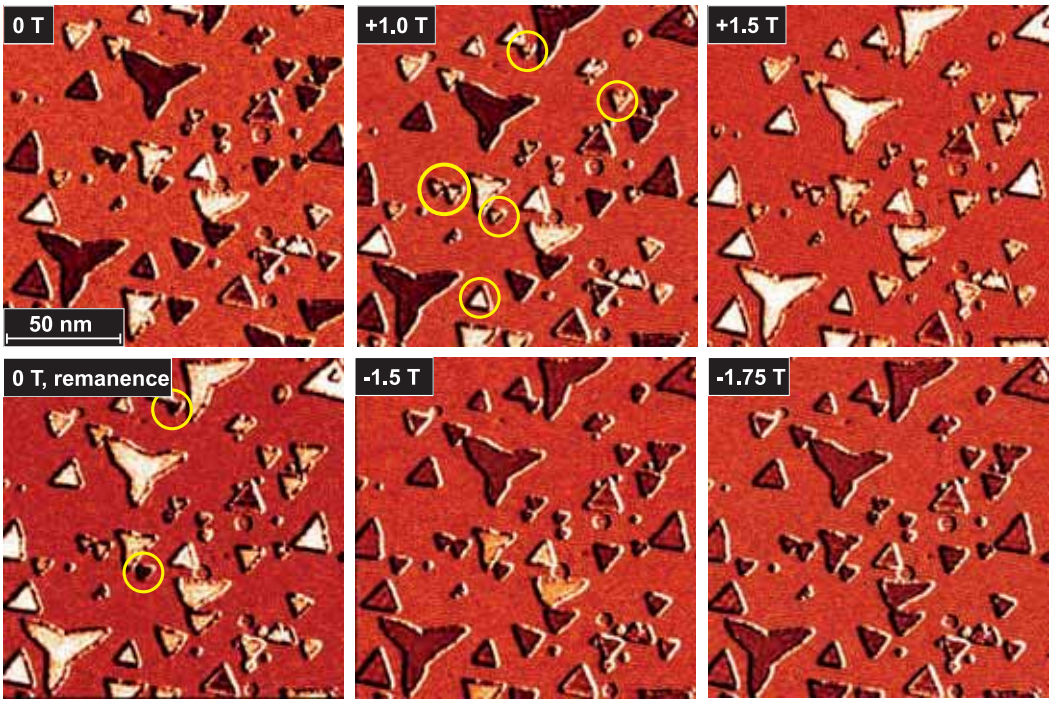

Figure 3.34: Spin-polarized $\mathrm{d}I/\mathrm{d}U$ maps ($U = -0.18$ V) of Co islands in variable perpendicular magnetic fields. At zero field islands of both stacking types are found bright or dark, corresponding to parallel or antiparallel alignment of sample and tip magnetization, respectively. A field of 1 T switches only a few of the smaller islands (circles). 1.5 T is not sufficient to achieve saturation. After field removal, only two small islands reverse their magnetization (circles), indicating a remanence M_r close to saturation M_s.

rotation, i.e., at any time—even during the reversal—the magnetic moments of the entire particle remain magnetized in the same direction, behaving like a single giant spin (superparamagnet). Under these requirements the switching rate is described by the so-called Néel-Brown law

$$\nu = \nu_0 \exp\left(-\frac{E_\mathrm{B}}{k_\mathrm{B}T}\right) \quad , \tag{3.9}$$

with ν_0 the attempt frequency, E_B the energy barrier that separates two degenerate magnetization states (up and down), the Boltzmann constant k_B and the temperature T. Due to sensitivity limitations, early experiments had to be performed on ensembles of supposably identical particles, and effects related to details of the size and the shape of individual particles were concealed by the averaging process. Only recently it became possible to detect the switching behavior of single particles and to relate it to the particle's geometry as measured in a separate scanning electron or magnetic force microscopy investigation [14–18]. Results obtained on single ferromagnetic, ellipsoidal cobalt particles with a diameter of 25 ± 5 nm are in agreement [17], while measurements performed on elongated particles are in disagreement with the Néel-Brown law [16].

Instead, the latter results indicate that the reversal starts in a small fraction of the particle volume. After nucleation of a reversed domain the associated domain walls propagate through the sample [16].

The shape dependence of the thermally activated magnetization reversal rate has been explored theoretically by Braun [19,20,24]. For simple sample geometries Braun found an analytical solution which was recently confirmed by Monte-Carlo simulations [21]. The relevant parameter which allows to predict the reversal mechanism is the critical length l_{crit}. In the case of a sufficiently narrow cylinder-shaped particle l_{crit} is given by $2\pi L$, where L is the magnetic exchange length being defined as $L = \sqrt{A/k_{\mathrm{eff}}}$ with the exchange stiffness A and the effective anisotropy constant k_{eff}. It was found that short particles of length $l \leq l_{\mathrm{crit}}/2$ exclusively reverse their magnetization by coherent rotation. The barrier of this process is the anisotropy energy $E_{\mathrm{a}} = k_{\mathrm{eff}}V$ which is proportional to the particle volume V. The resulting switching rate is consistent with Eq. 3.9. For $l \geq l_{\mathrm{crit}}/2$ the nucleation of a reversed domain at one particle end has to be considered. The energy barrier of this process depends on the energy required to create a single 180° domain wall which then propagates from one particle end to the other, given by $E_{\mathrm{w}} = 4a\sqrt{k_{\mathrm{eff}}A}$ with a being the wall area. Only for $l > l_{\mathrm{crit}}$ the nucleation of a reversed domain in the interior of the sample becomes possible. Braun predicted [19, 20, 24] that the energy barrier related to domain wall creation in an elongated particle with $l \geq l_{\mathrm{crit}}/2$ is lower than the barrier for coherent rotation of a compact particle of the same volume, leading to a crossover between the two reversal mechanisms around $l_{\mathrm{crit}}/2$. Thus the switching rate should depend on the particle shape.

Although a detailed knowledge of the critical length l_{crit} is highly desirable for the future development of ultrahigh-density magnetic recording, Braun's prediction could not yet be verified. We have used the high spatial and magnetic sensitivity of spin-polarized scanning tunneling microscopy (SP-STM) to directly correlate the shape and size of Fe particles with the individually measured switching rates. Indeed, our results reveal that the superparamagnetic limit of out-of-plane magnetized particles is strongly shape dependent, i.e., oblong particles switch much more often than compact, almost circular particles of equal volume.

Figure 3.35(a) shows a constant-current STM image of the topography of 0.25 ML Fe deposited on Mo(110) at room temperature. Within the field of view (110 nm ×110 nm) two atomically flat Mo(110) terraces are visible. They are decorated with Fe islands which are slightly elongated along the [001] direction [22,23]. Our results are in full agreement with previous studies of the morphology of Fe/Mo(110) [22,23]. Simultaneously with the topography we have recorded maps of the differential conductance $\mathrm{d}I/\mathrm{d}U$ using an out-of-plane sensitive Cr coated probe tip [Fig. 3.35(b)]. Although the spin-averaged electronic properties of all Fe islands are identical (not shown here) one can recognize bright and dark islands in Fig. 3.35(b) representing two different values of the local $\mathrm{d}I/\mathrm{d}U$ signal. This variation is caused by spin-polarized vacuum tunneling between the magnetic tip and islands which are magnetized perpen-

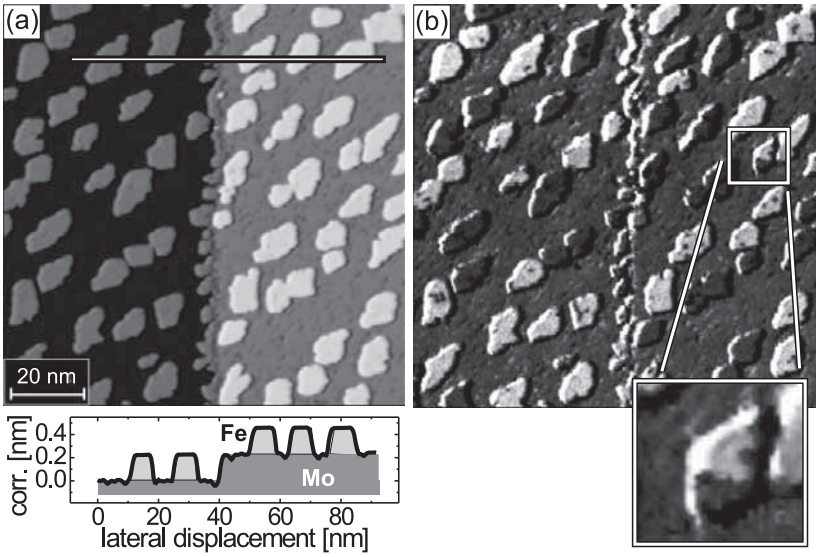

Figure 3.35: (**a**) Topographic STM image and (**b**) the simultaneously measured out-of-plane sensitive magnetic $\mathrm{d}I/\mathrm{d}U$ signal of two Mo(110) terraces decorated with Fe islands (overall coverage 0.25 ML). The line section (lower panel) reveals that the substrate's step edge and the islands are of monatomic height (≈ 2Å). During image recording one island switches from dark to bright (inset). Measurement parameters: $T = 13\,\mathrm{K}$, $U = 90\,\mathrm{mV}$, $I = 1\,\mathrm{nA}$.

dicularly either up or down.

Most of the islands exhibit a surface area $a \geq 40\,\mathrm{nm}^2$ and therefore possess a barrier large enough to inhibit superparamagnetic switching at $T = 13\,\mathrm{K}$. Consequently, their magnetization direction remains constant resulting in the same $\mathrm{d}I/\mathrm{d}U$ signal in successive scans. Few smaller islands, however, are found to be magnetically unstable on the time scale of the experiment, i.e., several minutes. Such an island with $a = 26 \pm 1\,\mathrm{nm}^2$ is highlighted by a box and shown at higher magnification in the inset of Fig. 3.35(b). Here the $\mathrm{d}I/\mathrm{d}U$ signal changes between two subsequent scan lines from a low value (dark) at an early time of the scan (bottom part of the image) to a higher value (bright). This signal variation is caused by superparamagnetic switching.[4]

From Eq. 3.9 it is expected that the switching rate ν exponentially increases with increasing temperature. We checked this by successively scanning along the same line thereby periodically visiting four islands "a"–"d" (inset of Fig. 3.36). Measurements were performed at temperatures $T_1 = 13\,\mathrm{K}$ and $T_2 = 19\,\mathrm{K}$ for 5.5 min with a line repetition frequency of 3 Hz. At every passage the $\mathrm{d}I/\mathrm{d}U$ signal of the islands was recorded [Fig. 3.36]. At $T_1 = 13\,\mathrm{K}$ (left panel) the relatively large islands "a" ($a =$

[4]We would like to emphasize that the image in the inset does not represent a snapshot of the switching island *during* the magnetization reversal. This process occurs on a time scale ($\approx 10^{-12}\,\mathrm{s}$) being much shorter than even the time increment between subsequent pixels ($\approx 10^{-3}\,\mathrm{s}$). Instead, the contrast is caused by the fact that the imaging of the island accidentally coincided with the moment of its magnetization reversal.

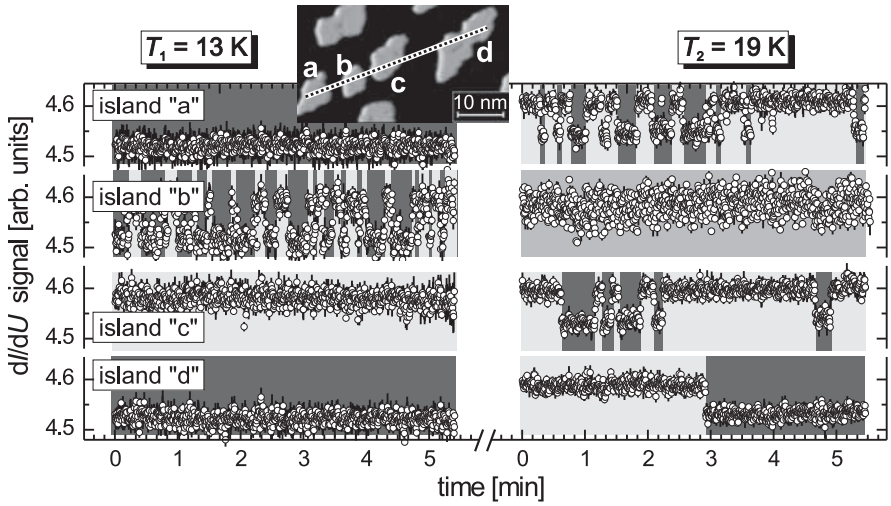

Figure 3.36: Magnetic switching behavior of the Fe islands "a"–"d" (inset) measured at $T = 13 \pm 1\,\mathrm{K}$ (left panel) and $T = 19 \pm 1\,\mathrm{K}$ (right panel). The switching rate increases with increasing temperature thereby proving the thermal nature of the observed effect. At $T = 19 \pm 1\,\mathrm{K}$ the switching rate of island "b" exceeds the line repetition rate resulting in an intermediate and blurred signal.

$30.0\,\mathrm{nm}^2$), "d" ($a = 71.2\,\mathrm{nm}^2$), and "c" ($a = 28.2\,\mathrm{nm}^2$) do not switch. This magnetic stability is a result of their large anisotropy energy that prevents superparamagnetic switching at this temperature. In contrast, island "b" ($a = 17.8\,\mathrm{nm}^2$) with its lower barrier reverses its magnetization direction 31 times within the observation time. In qualitative agreement with Eq. 3.9 the switching rate of any island increases as the temperature is increased to $T_2 = 19\,\mathrm{K}$ (right panel). Islands "a", "c", and "d" reverse their magnetization direction 18, 10, and 1 times, respectively. Since the switching rate of island "b" exceeds the line repetition rate, we cannot resolve single switching events and an intermediate and blurred $\mathrm{d}I/\mathrm{d}U$ signal is measured above "b".

The effective anisotropy constant of individual superparamagnetic particles can be determined by temperature-dependent measurements of the switching rate. Transformation of the Néel-Brown law gives

$$k_{\mathrm{eff}} = \ln \frac{\nu_1}{\nu_2} \cdot \frac{k_{\mathrm{B}}}{V} \cdot \left(\frac{1}{T_2} - \frac{1}{T_1} \right)^{-1} , \tag{3.10}$$

where $\nu_{1,2}$ denote switching rates measured at $T_{1,2}$. We observed two islands with a non-zero and finite switching rate at two temperatures $T_1 = 19\,\mathrm{K}$ and $T_2 = 26\,\mathrm{K}$: the first one has an area of $28.8\,\mathrm{nm}^2$ and switching rates of $\nu_1 = (4.0 \pm 2.0) \times 10^{-4}\,\mathrm{s}^{-1}$ and $\nu_2 = 0.37 \pm 0.11\,\mathrm{s}^{-1}$, while the second island with an area of $33.3\,\mathrm{nm}^2$ switched at rates $\nu_1 = (3.0 \pm 1.7) \times 10^{-4}\,\mathrm{s}^{-1}$ and $\nu_2 = 0.33 \pm 0.1\,\mathrm{s}^{-1}$. Insertion into Eq. 3.10 results in $k_{\mathrm{eff}} = 1.16^{+0.17}_{-0.13} \times 10^6\,\mathrm{J/m}^3$ and $k_{\mathrm{eff}} = 1.04^{+0.16}_{-0.45} \times 10^6\,\mathrm{J/m}^3$ for the two islands, respectively. In the following we will assume an effective anisotropy $k_{\mathrm{eff}} = 1.10^{+0.12}_{-0.24} \times 10^6\,\mathrm{J/m}^3$.

Figure 3.37 shows (a) the topography and (b) a map of the magnetic $\mathrm{d}I/\mathrm{d}U$ signal

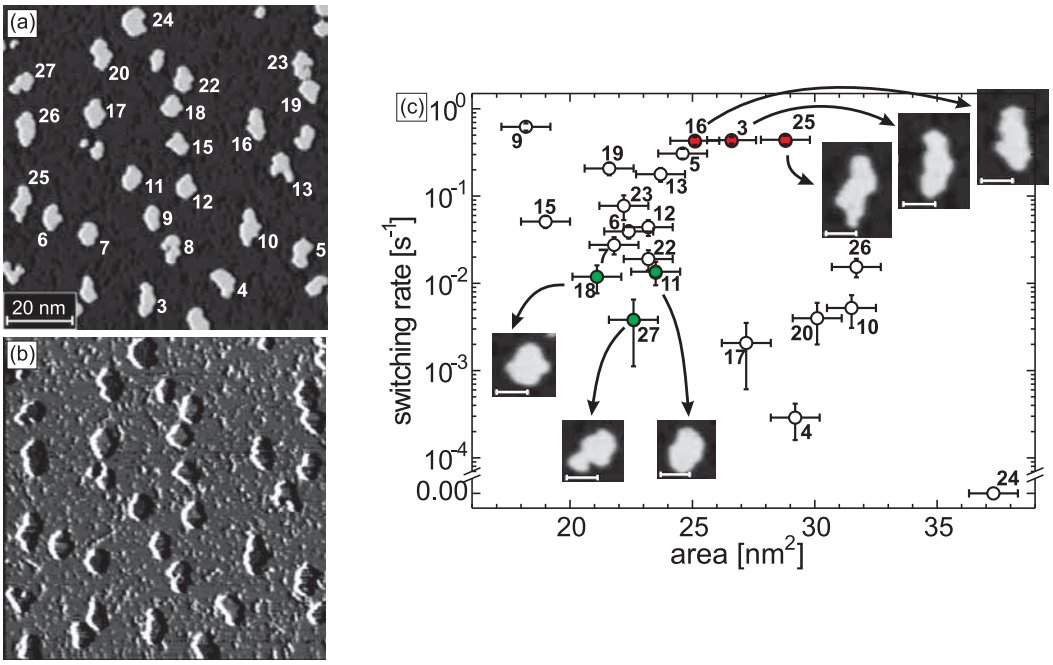

Figure 3.37: (**a**) Topography and (**b**) magnetic dI/dU signal of numbered Fe islands on Mo(110). (**c**) Plot of the switching rate versus the area of individual islands. The scatter of the switching rate points to a shape-dependent crossover from coherent rotation of compact Fe islands towards nucleation and expansion of reversed domains in elongated islands. Insets: topography of selected Fe islands (scale bar: 5 nm).

of 23 numbered islands prepared by room-temperature deposition of 0.08 ± 0.01 ML Fe/Mo(110). Except for islands "19" and "23" the interparticle distance is sufficiently large to exclude any significant dipolar interaction. The complete series consists of 53 images measured over a total time of more than 5 hours. By making use of the three different sampling rates of our experiment, i.e., the increment between successive pixels (≈ 1 ms), succesive scan lines (≈ 1 s), and between successive images (≈ 5 min), we are able to follow the magnetization reversal behavior of individual islands over a wide frequency range. The switching rates are plotted semilogarithmic versus the island area in Fig. 3.37(c). Each data point is labeled with the related island number assigned in Fig. 3.37(a). Although the general trend—small islands switch more often than large islands—can clearly be recognized, the data points scatter strongly around the expected linear relation. which is expected based on the discussion following Eq. 3.9. For example, albeit the area of the islands marked green ("11", "18", and "27") is smaller than the area of the islands marked red ("3", "16", and "25"), the switching rates of the former are one to two orders of magnitude smaller. The topographic images in the insets of Fig. 3.37(c) reveal that this contra-intuitive behavior is associated with the island shape: while the red (rapidly switching) islands are elongated the green (slowly switching) islands are much more compact.

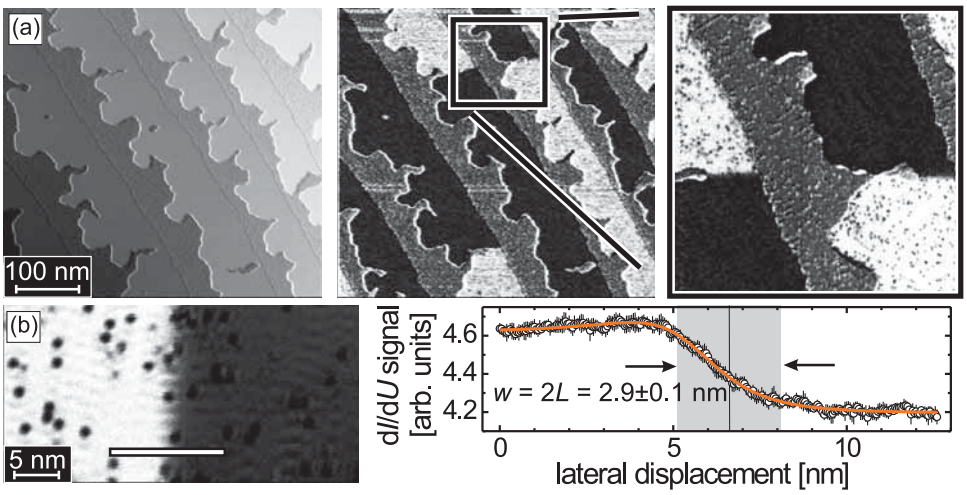

Figure 3.38: (**a**) Overview showing the topography (left panel) and magnetic $\mathrm{d}I/\mathrm{d}U$ signal (middle panel) of Fe nanowires on Mo(110). Four domain walls can be recognized. Right panel: two domain walls at higher magnetification. (**b**) Zoom into the domain wall region (inset, rotated by 90°). The domain wall width is $w = 2.9 \pm 0.1\,\mathrm{nm}$ (orange line).

According to Braun's theory the particular magnetization reversal mechanism of individual islands depends on the ratio between the lateral particle dimensions and the magnetic exchange length L. By making use of the fact that L is also linked to the domain wall width w by $w = 2L = 2(A/k_{\mathrm{eff}})^{1/2}$, we are able to determine L independently [25] by measuring the domain wall width of the Fe monolayer on Mo(110). While we cannot observe domain walls in small islands due to their fast dynamics, static walls can be found in monatomic Fe nanowires grown at the step edges of the Mo(110) substrate (Fig. 3.38). Similar to Fe double-layer nanowires on W(110) [26, 27], the magnetic domain structure of nanowires on Mo is governed by an antiparallel orientation of adjacent nanowires due to dipolar interaction [26]. At structural imperfections occasionally domain walls can be found. The overview of Fig. 3.38(a) shows the topography (left panel) and the magnetic $\mathrm{d}I/\mathrm{d}U$ signal (middle panel) of six nanowires. In four nanowires a domain wall can be recognized. We have zoomed into one domain wall [Fig. 3.38(b)]. From a micromagnetic fit to the measured wall profile [25] we obtain $w = 2.9 \pm 0.1\,\mathrm{nm}$, thus $L = 1.45 \pm 0.05\,\mathrm{nm}$. Using k_{eff} as determined above we find $A = 2.3^{+0.5}_{-0.7} \times 10^{-12}\,\mathrm{J/m}$.

Once L is known we can determine the critical particle length of Fe monolayer islands on Mo(110) to $l_{\mathrm{crit}} = 2\pi L = 9.1 \pm 0.3\,\mathrm{nm}$. Comparing this value with the typical diameter $d \approx 5\,\mathrm{nm}$ of the compact islands marked green in Fig. 3.37(c), we find that d is almost equal to $l_{\mathrm{crit}}/2$. Therefore, we identify coherent rotation as the dominating mechanism of magnetization reversal in the compact particles "11", "18", and "27". Since we know the switching rate of, e.g., particle "11", $\nu_{11} = 0.013 \pm 0.004\,\mathrm{s}^{-1}$ and its volume $V_{11} = (4.7 \pm 0.2) \times 10^{-27}\,\mathrm{m}^3$ we may—using the magnetic material parameters

k_{eff} and A as found above—determine the attempt frequency of that particle to $\nu_0 = 4.08^{+0.14}_{-3.24} \times 10^{10}\,\text{s}^{-1}$ and the energy barrier against coherent rotation which amounts to $E_{\text{B}} = 5.17^{+0.85}_{-1.37} \times 10^{-21}\,\text{J}$.[5]

Island "16" exhibits approximately the same area as island "11". Nevertheless, its switching rate is 31 times higher. This difference is due to a different process of magnetization reversal. In agreement with the analytical solutions of Refs. [19, 20, 24] the elongated shape of island "16" (length $l = 8.65 \pm 0.4\,\text{nm} \approx l_{\text{crit}}$) leads to the fact that the energy of a domain wall E_{w} along the short axis of the island is lower than the barrier against coherent rotation [19, 20, 24]. The same is true for islands "3" and "25". The cross-sectional area of island "16" is $0.6 \pm 0.1\,\text{nm}^2$. With this value we may estimate the domain wall energy $E_{\text{w}} = 3.81^{+1.37}_{-1.46} \times 10^{-21}\,\text{J}$, i.e., for elongated islands the trend is $E_{\text{w}} < E_{\text{B}}$, albeit within a large error margin. This explains qualitatively the higher switching rate compared to that of compact islands of equal volume.

References

[1] M. T. Kief and W. F. Egelhoff, Jr., Phys. Rev. B **47**, 10785 (1993).

[2] A. Rabe *et al.*, Phys. Rev. Lett. **73**, 2728 (1994).

[3] B. P. Tonner, Z.-L. Han, and J. Zhang, Phys. Rev. B **47**, 9723 (1993).

[4] V. Scheuch *et al.*, Surf. Sci. **318**, 115 (1994).

[5] J. de la Figuera *et al.*, Phys. Rev. B **47**, 13043 (1993).

[6] M. Ø. Pedersen *et al.*, Surface Science **387**, 86 (1997).

[7] M. F. Crommie, C. P. Lutz, and D. M. Eigler, Nature **363**, 524 (1993).

[8] L. Diekhöner *et al.*, Phys. Rev. Lett. **90**, 236801 (2003).

[9] M. Bode *et al.*, Acta Phys. Pol. A **93**, 273 (1998).

[10] F. Huang *et al.*, Phys. Rev. B **49**, 3962 (1994).

[11] D. Weller and A. Moser, IEEE Trans. Magn. **35**, 4423 (1999).

[12] M. L. Néel, Ann. Géophys. **5**, 99 (1949).

[13] W. F. Brown, Phys. Rev. **130**, 1677 (1963).

[14] M. Lederman, G. A. Gibson, and S. Schultz, J. Appl. Phys. **73**, 6961 (1993).

[15] M. Lederman, S. Schultz, and M. Ozaki, Phys. Rev. Lett. **73**, 1986 (1994).

[16] W. Wernsdorfer *et al.*, Phys. Rev. Lett. **77**, 1873 (1996).

[17] W. Wernsdorfer *et al.*, Phys. Rev. Lett. **78**, 1791 (1997a).

[18] W. Wernsdorfer *et al.*, Phys. Rev. B **55**, 11552 (1997b).

[19] H.-B. Braun, Phys. Rev. Lett. **71**, 3557 (1993).

[20] H.-B. Braun, J. Appl. Phys. **85**, 16172 (1999).

[5] Since the calculation of the attempt frequency employs several parameters with relatively large error bars, the values obtained for different compact islands strongly scatter between 2×10^{-8} and $5 \times 10^{11}\,\text{s}^{-1}$.

[21] D. Hinzke and U. Nowak, Phys. Rev. B **61**, 6734 (2000).

[22] M. Tikhov and E. Bauer, Surf. Sci. **232**, 73 (1990).

[23] J. Malzbender *et al.*, Surf. Sci. **414**, 187 (1998).

[24] H.-B. Braun, Phys. Rev. B **50**, 16485 (1994).

[25] A. Hubert and R. Schäfer, *Magnetic Domains*, Springer (1998).

[26] H. J. Elmers, J. Hauschild, and U. Gradmann, Phys. Rev. B **59**, 3688 (1999).

[27] O. Pietzsch, A. Kubetzka, M. Bode, and R. Wiesendanger, Phys. Rev. Lett. **84**, 5212 (2000a).

3.2.7 Magnetism of Fe double-layer nanowires on W(110)

A. Kubetzka, M. Bode, K. v. Bergmann, O. Pietzsch, and R. Wiesendanger

Introduction

The sample system consisting of 1–2 ML thin Fe films epitaxially grown on W(110) is an extremely interesting sample system. A local coverage of 1 and 2 ML will be referred to hereafter as ML ("monolayer") and DL ("double layer"), respectively. The typical surface topography and a schematic structure of Fe/W(110) is shown in Fig. 3.39(a) and (b), respectively. The film was grown at a substrate temperature $T \approx 500$ K. This preparation procedure leads to so-called step-flow growth: due to the high mobility

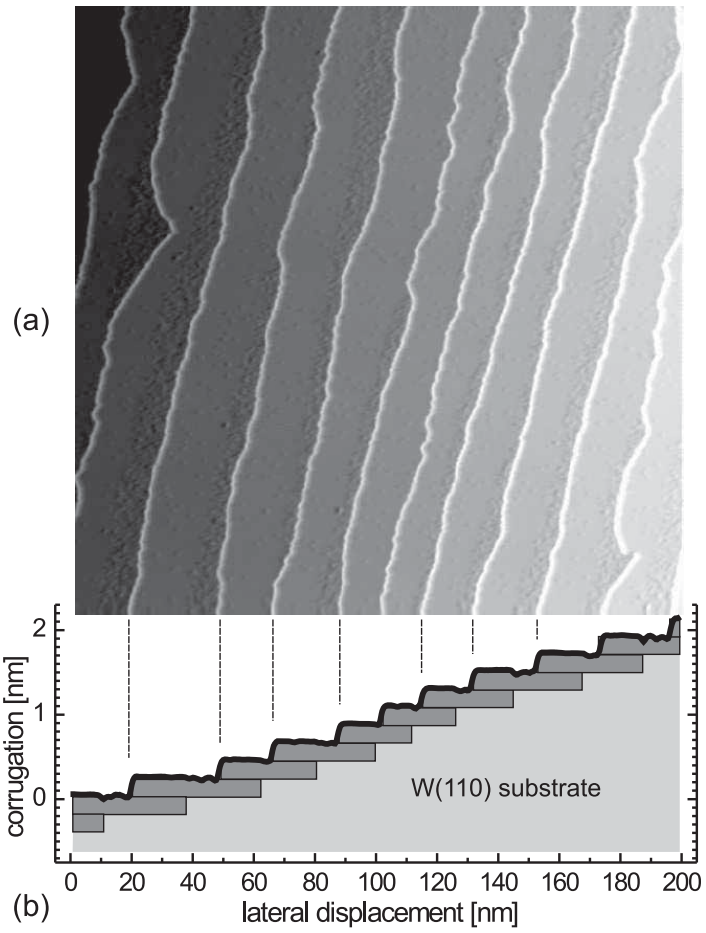

Figure 3.39: **(a)** STM topograph of 1.8 ML Fe epitaxially grown at $T = 500$ K on a W(110) substrate exhibiting an average terrace width of ≈ 20 nm. Step-flow growth leads to the formation of Fe nanowires of alternating ML and DL height along the substrate's step edges. **(b)** Line section drawn at the bottom of the image in (a) and schematic representation of the structure of the sample.

of the Fe adatoms evaporated onto the surface the formation of critical nuclei on the middle of the terrace is avoided. Instead, the adatoms can reach the adsorption site which is energetically most favorable, i.e. at a step edge. Thereby, the one-dimensional step-structure of the substrate is decorated with more or less parallel Fe nanowires. In spite of the large misfit of 9.4% between the lattice constants of W and Fe the first monolayer of Fe grows pseudomorphically on W(110) [1]. Starting with the clean W substrate an increasing Fe coverage leads to Fe nanowires with a local coverage $\Theta_{\mathrm{loc}} = 1\,\mathrm{ML}$ that become broader and broader. Simultaneously, the uncovered fraction of the W(110) substrate decreases. Upon completion of the first Fe layer nanowires with $\Theta_{\mathrm{loc}} = 2\,\mathrm{ML}$ begin to grow. However, the enormous tensile strain is locally relaxed by the formation of non-periodic dislocation lines along the [001] direction which will show up in images presented later.

The magnetic properties of this sample system have been intensively investigated by the research groups around Elmers and Gradmann [1–14]. A parallel and perpendicular easy axis was found for the ML and the DL, respectively. Furthermore, it was found by Kerr-effect measurements [13, 14] and confirmed by SP-STS [15] that for substrates with a terrace width of less than 10 nm adjacent DL nanowires couple antiparallel. This magnetic structure leads to a reduction of the dipolar or stray field energy of the sample. Here, however, we will focus on results which have been obtained using a substrate exhibiting an average terrace width of $\approx 20\,\mathrm{nm}$ caused by a lower miscut angle with respect to the (110) plane. As we will see in the following the reduction of the stray field for this particular sample system is not accomplished by opposite magnetization directions of adjacent DL nanowires but by a periodic reversal within every individual nanowire. The following experiments were performed at low temperature, i.e. $T = 14 \pm 1$ K [16], well below the Curie temperature of the Fe ML of $T_{\mathrm{C}} = 220$ K [10, 11, 17].

Magnetic domain structure of Fe double-layer nanowires

In the first experiment we investigated the sample's initial state with FM tips. Fig. 3.40(a) displays a 3D composite of a constant current image and the simultaneously acquired $\mathrm{d}I/\mathrm{d}U$ map of 2.0 ML Fe/W(110), recorded with a GdFe-coated tip (top view shown in the inset). Since the tip has a magnetization perpendicular to the surface, the $\mathrm{d}I/\mathrm{d}U$ map is an image of the z component of the surface magnetization. We observe stripe domains with a period of 50 ± 5 nm and the domains roughly oriented along $[1\bar{1}0]$. Adjacent terraces are exchange coupled across the step edges. A number of dislocation lines with [001] orientation can be seen which, however, have no detectable influence on the domain structure. The lower panel of Fig. 3.40(a) displays a line section taken as indicated in the inset. It can be fitted by three winding 180° Bloch walls [18], using a standard wall profile, $\sin(\varphi(x)) = \tanh((x - x_0)/(w/2))$ [21], with a wall width of $w = 7$ nm and a distance between wall centers of 23 nm.

To verify that indeed all walls exhibit the same sense of magnetic rotation ("winding" case in Ref. [18]) we employed probe tips with in-plane sensitivity. Fig. 3.40(b)

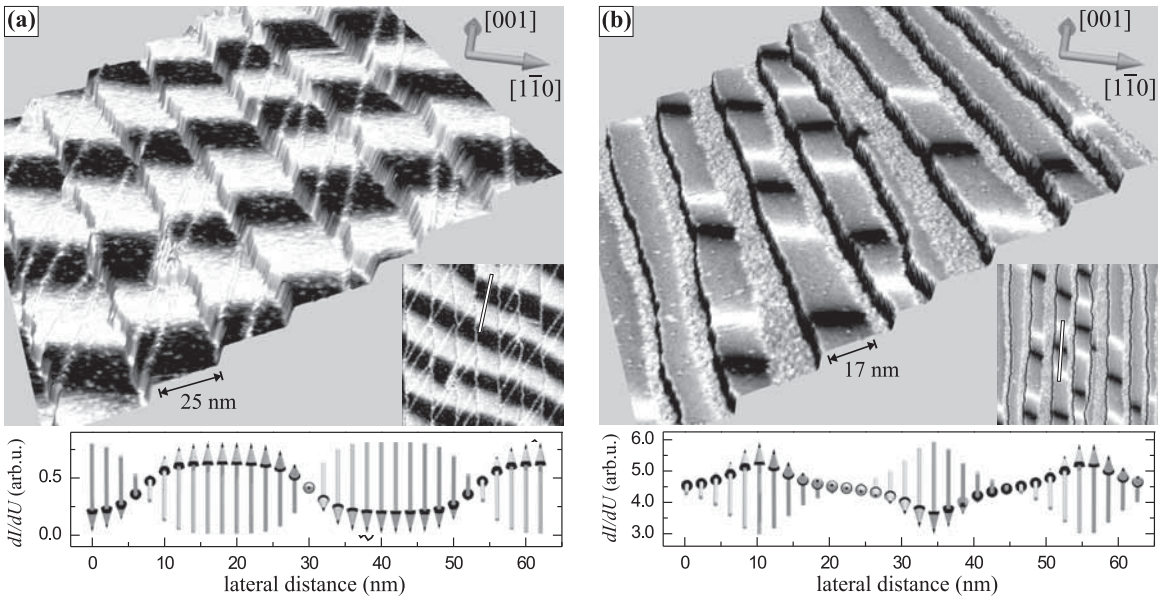

Figure 3.40: **(a)** Constant current topograph of 2.0 ML Fe on W(110) colorized with dI/dU map (I=0.3 nA, U=-0.45 V), recorded with a GdFe tip (out-of-plane contrast) at 14 K. Stripe domains are observed with a magnetic period of 50 ± 5 nm and the domains roughly oriented along [1$\bar{1}$0]. A line section is compared to a proposed magnetic configuration (side view). **(b)** 1.6 ML Fe/W(110) imaged with an Fe tip (in-plane contrast) at I=0.3 nA, U=-0.1 V. Domain walls appear alternately bright and dark. A second line section is compared to the same magnetic configuration (top view).

shows an image of 1.6 ML Fe/W(110) recorded with an Fe tip. In the DL areas the domain walls now appear alternately bright and dark without exception, indicating an opposite magnetization direction within the centers of neighboring walls, in agreement with the assumption made above. This is a general property of the DL domain structure which we also observe on the closed 2.0 ML Fe film (not shown). To further illustrate this point, we took a line section from an area which also contains three domain walls like the section in Fig. 3.40(a). It can be reproduced by the same formula as above if one allows for a rotation of 90° to take the different magnetization direction into account. The two line sections therefore represent one and the same magnetic configuration within our measurement accuracy.

Impact of an external field

Fig. 3.41 shows dI/dU maps of the same surface area in an increasing perpendicular magnetic field of up to 800 mT: Areas magnetized parallel to the field direction grow at the expense of antiparallel ones, and pairs of 180° walls are forced together, which is equivalent to the formation of 360° walls [18]. As expected, their lateral extension decreases with increasing field value.

A closer inspection of these field dependent measurements reveals, that (i) the magnetization rotates along every single nanowire with a defined chirality and that (ii) the rotational sense is the same in each of the 12 wires within the imaged area. Observation (i) is already to be expected for stability reasons: neighboring walls of opposite chirality (unwinding or untwisted walls) attract each other and can easily annihilate, in contrast to winding walls. As a consequence, the cooling process of the sample from above T_C to the measurement temperature of 14 K will result in a defined chirality within every individual wire, since such a structure is more stable against thermal fluctuations. The observed average distance between neighboring walls does therefore not necessarily reflect the magnetic ground state at low temperatures, since it might be a relict from the cooling process which is effectively frozen in a metastable state. Observation (ii) is not yet fully understood. It might be connected to the miscut of the sample and/or the deviation of the axis of the wires from the [001] direction.

With increasing external magnetic field the tip's magnetization is successively rotated from the in-plane towards the perpendicular direction. Also its in-plane direction

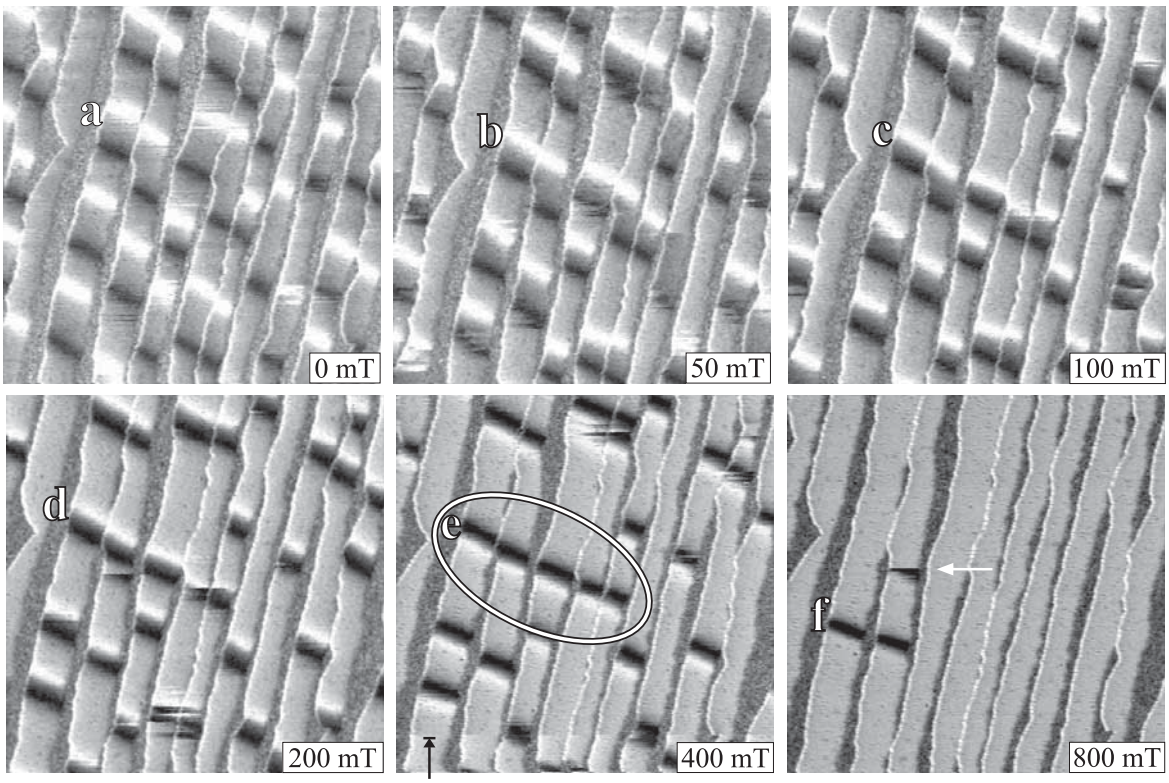

Figure 3.41: $\mathrm{d}I/\mathrm{d}U$ maps of the surface area from Fig. 3.40, imaged in an increasing perpendicular magnetic field. Pairs of 180° domain walls are gradually forced together, which is equivalent to the formation and compression of 360° walls. At 800 mT most of them have vanished [20], i.e., the Fe film is in magnetic saturation. With increasing external magnetic field the tip's magnetization is gradually forced from the in-plane towards the perpendicular direction.

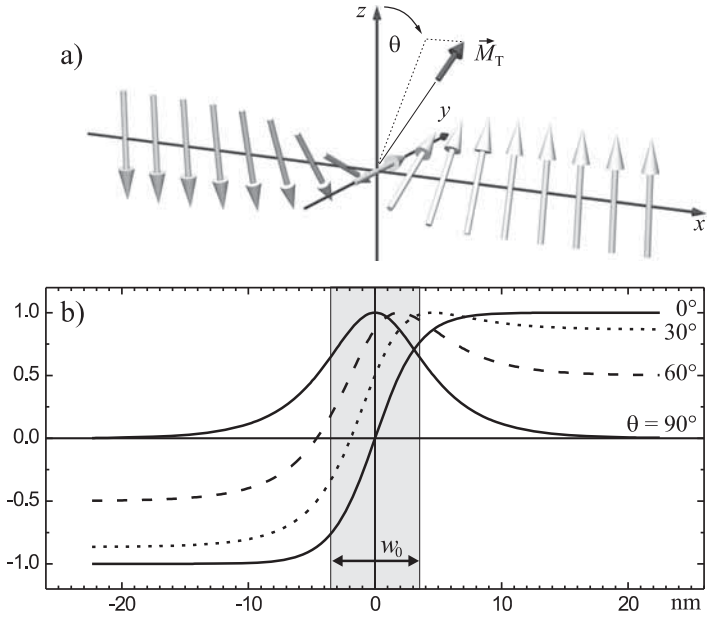

Figure 3.42: (a) Schematic representation of a Bloch wall. (b) Wall profiles strongly depend on the tip's magnetization $\vec{M}_T$. The relevant angle, θ, is the one between the z-direction and the projection of $\vec{M}_T$ onto the yz-plane.

is reversed during data acquisition at 400 mT in Fig. 3.41 (see black arrow), which causes an inverted contrast for the remaining upper part of the image. At this field value a group of five 360° walls has formed a row (see oval), a correlation which might arise from their in-plane stray field. At 800 mT most of the 360° walls within the scanned area have been remagnetized by a rotation via the hard [001] in-plane direction [22,23]. Note, that at 800 mT the tip's magnetization, $\vec{M}_T$, is close to the normal direction, resulting in an almost exclusive perpendicular sensitivity in this $\mathrm{d}I/\mathrm{d}U$ map, in contrast to the previous images. This issue is illustrated in Fig. 3.42 for a single 180° Bloch wall which is described by [21]

$$\varphi_{180}(x) = \arcsin(\tanh(\frac{x}{w_0/2})), \quad w_0 = 2\sqrt{\frac{A}{K_{\mathrm{eff}}}}. \tag{3.11}$$

Since in SP-STM the variation of the $\mathrm{d}I/\mathrm{d}U$ signal is proportional to the projection of the local surface magnetization onto the tip magnetization, measured wall profiles gradually change from pure domain wall contrast at $\theta = 90°$ to pure domain contrast at $\theta = 0°$, where θ is the angle between the easy direction (z) and the projection of $\vec{M}_T$ onto the wall plane (yz).

We will now focus on the internal structure of the 360° walls. Fig. 3.43 displays line sections (grey circles) of the single pair of domain walls which has been marked by the labels a–f in Fig. 3.41. We describe the wall profiles by the sum of two 180°

walls at the positions $\pm c$:

$$\varphi_{360}(x) = \sum_{+,-} \arcsin(\tanh(\frac{x \pm c}{w/2})). \tag{3.12}$$

The values of c and w can then be extracted from the data if the varying tip magnetization is taken into account. Using the function

$$y = y_0 + a \cdot \cos(\varphi_{360}(x) + \theta), \tag{3.13}$$

the fitted curves (black lines) and the resulting fit parameters θ, c, and w are displayed within the figure. The extension of the inner 180° rotation between the two opposite in-plane orientations, which is approximately $2\,c$, has been marked by a shaded area. It successively decreases from 22.2 nm in zero field to 6.7 nm at 800 mT.

This compression of 360° walls observed in Fig. 3.43 can already be reproduced quantitatively within a simple 1D micromagnetic model, which takes into account Zeeman, exchange, and an effective anisotropy energy. The latter includes the crystal anisotropy and the local part of the dipolar energy. Non-local effects are neglected [23]. The total energy per unit area can then be written as:

$$e = \int \underbrace{A \left(\frac{\partial \varphi}{\partial x}\right)^2}_{\text{exchange}} + \underbrace{K_{\text{eff}} \sin^2 \varphi}_{\text{eff. anisotropy}} + \underbrace{M_s B \cos \varphi}_{\text{Zeeman}} \, dx, \tag{3.14}$$

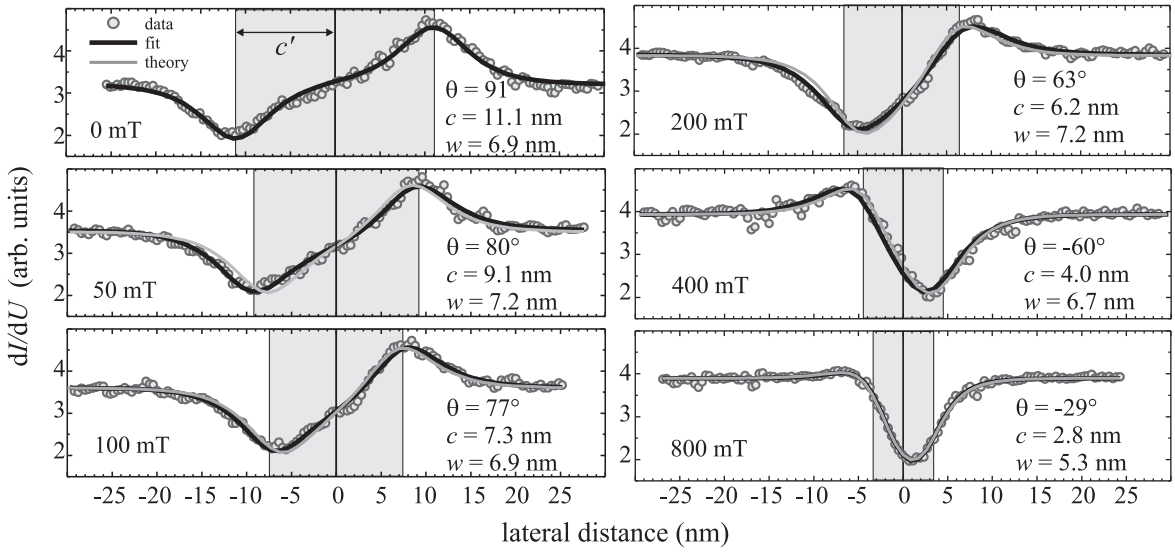

Figure 3.43: Line sections (circles) across a single 360° wall corresponding to the labels a–f in Fig. 3.41, as well as individual fits to the data (black lines) by Eq. 3.13 and expected profiles (white) using Eqs. 3.13 and 3.15. The shaded areas correspond to the walls' inner 180° spin rotation.

where A is the exchange stiffness, K_{eff} the effective anisotropy constant, and M_{s} the saturation magnetization. Energy minimization with appropriate boundary conditions yields a surprisingly simple exact solution [23] which has already been used in the fitting procedure, i.e. Eq. 3.12, where the field dependent values of c and w are now given explicitly by

$$c = \frac{w}{2}\mathrm{arcsinh}(\sqrt{\frac{2K_{\mathrm{eff}}}{M_{\mathrm{s}}B}}), \quad w = 2\sqrt{\frac{A}{K_{\mathrm{eff}} + M_{\mathrm{s}}B/2}}. \tag{3.15}$$

For $B \to 0$ the distance $2\,c$ diverges and the zero field wall width w_0 from Eq. 3.11 is recovered. To compare this model with the measured data we have performed a simultaneous fit to all line sections under the constraint of Eqs. 3.15. Assuming a reasonable value of $M_{\mathrm{s}} = 2.0 \times 10^6$ A/m, the other two magnetic constants are determined to $A = 1.82 \times 10^{-11}$ J/m and $K_{\mathrm{eff}} = 1.25 \times 10^6$ J/m^3 in this procedure. The resulting curves are displayed as white lines in Fig. 3.43 and are in good agreement with the experimental data, even in the low field regime.

Determining the spin-polarization

In principle, SP-STM not only allows the imaging of magnetic domains on the nanometer-scale but also allows the determination of the sample's spin-polarization $P_{\mathrm{S}}(E)$ at the position of the tip, e.g., by comparing the differential conductivities, $dI/dU(U)_{\uparrow\uparrow,\uparrow\downarrow}$, above oppositely magnetized domains or before and after a remagnetization of either tip or sample. An effective spin-polarization of the tunnel junction can be defined as the asymmetry of the $\mathrm{d}I/\mathrm{d}U$ signals:

$$A(U) = \frac{\mathrm{d}I/\mathrm{d}U(U)_{\uparrow\uparrow} - \mathrm{d}I/\mathrm{d}U(U)_{\uparrow\downarrow}}{\mathrm{d}I/\mathrm{d}U(U)_{\uparrow\uparrow} + \mathrm{d}I/\mathrm{d}U(U)_{\uparrow\downarrow}}. \tag{3.16}$$

If the spin-polarization of the tip P_{T} is known and constant within the relevant energy range around the Fermi level E_{F}, the sample's spin-polarization can be estimated by [24, 25]:

$$P_{\mathrm{S}}(U) = A(U)/P_{\mathrm{T}}. \tag{3.17}$$

This equation is, however, only valid if the tunneling distance is the same for the two cases of a parallel ($\uparrow\uparrow$) and antiparallel ($\uparrow\downarrow$) alignment of tip and surface magnetization. In contrast to planar tunnel junctions, where the tunneling distance is determined by the thickness of the insulating barrier, in an STM the width of the vacuum gap is controlled indirectly by the applied bias voltage U_0 and the current feedback set point I_0. As a consequence, the tunneling distance varies with the local magnitude and direction of the surface magnetization, unless U_0 is chosen in such a way that the total current is non–spin-polarized. This magnetization dependent height variation can be exploited for domain imaging [26, 27], but modifies the measured $\mathrm{d}I/\mathrm{d}U$ signal and therefore invalidates Eq. 3.17.

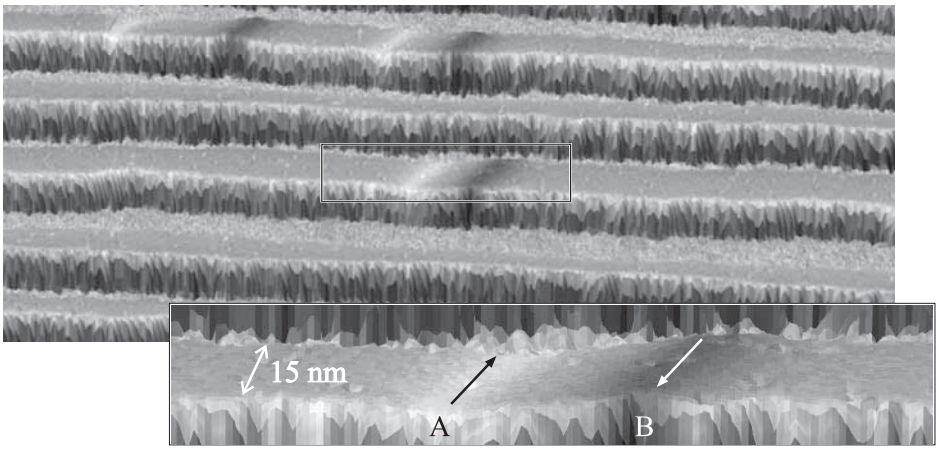

Figure 3.44: Constant current image (I = 0.3 nA) of 1.6 ML Fe/W(110), colorized with dI/dU signal at $U = -100$ V, imaged with an Fe tip (in-plane contrast). 180° domain walls appear as protrusions or depressions as well as a contrast in the dI/dU signal.

We performed two kinds of measurements with both tip and sample held at T = 13 K: (i) Maps of the differential conductance dI/dU were recorded simultaneously to the constant current images (topography) by adding a modulation voltage of U_{mod} = 20 $\mathrm{mV_{rms}}$ to the sample bias U and detecting the dI/dU signal by lock-in technique, in closed feedback circuit configuration. (ii) Full spectroscopy curves were acquired by stabilizing the tip at specific values of U_0 and I_0, ramping the bias voltage U with the feedback circuit open, while recording $I(U)$ directly and the dI/dU signal by lock-in technique. The numerically differentiated $I(U)$ curve can then be used to calibrate the lock-in-signal and correct for the energetic shift of the spectra which results from the lock-in's finite integration time.

Fig. 3.44 shows a perspective view of a constant current image of 1.6 ML Fe/W(110) as measured with an Fe-coated in-plane sensitive probe tip, colorized with the simultaneously acquired dI/dU signal at $U = -100$ mV and I = 0.3 nA. Two types of 180° domain walls can be distinguished by their in-plane magnetization component: They appear as depressions or protrusions in the constant current image as well as areas of enhanced or reduced conductance in the dI/dU map. The magnified pair of walls in Fig. 3.44 is thus equivalent to a full 360° spin rotation. We take a closer look at this pair in Fig. 3.45 by taking line sections at two different voltages, $U = -100$ mV and +700 mV: In both cases the tip approaches the surface at wall A and retracts at wall B, whereas the two dI/dU signals are enhanced at A and reduced at B. Signal amplitudes a and wall widths w can be extracted by a fit with the sum of two standard domain wall profiles (solid lines) [21],

$$y = y_0 + a \cdot \sin\{\sum_{i=1}^{2} \arcsin[\tanh(\frac{x - x_i}{w/2})]\}. \tag{3.18}$$

Values of a and w are given in the figures. The dI/dU signals' asymmetries amount

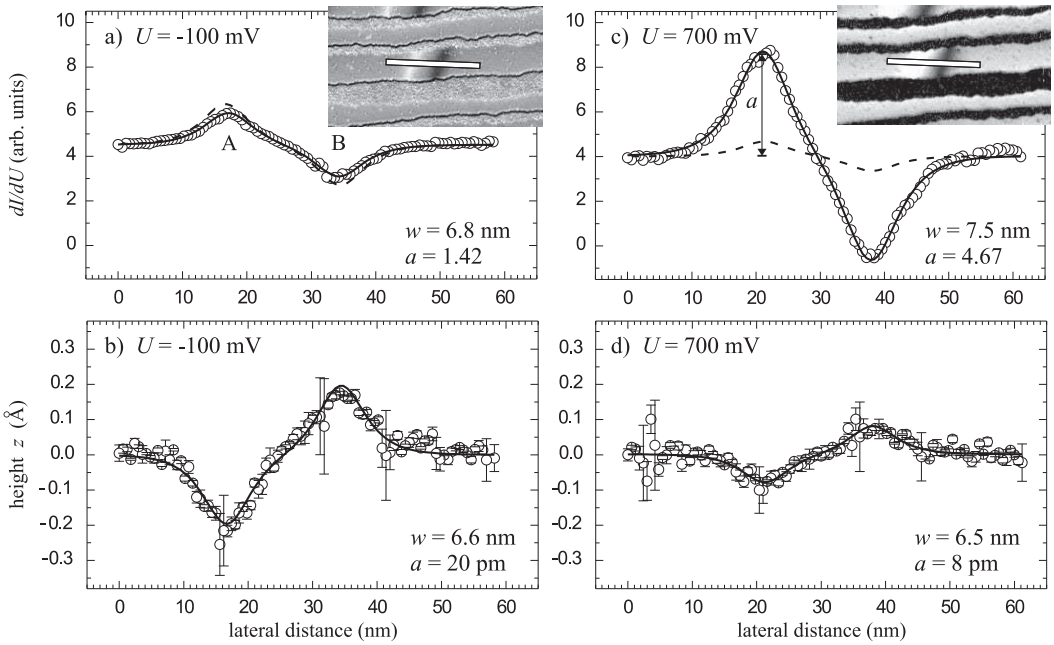

Figure 3.45: Line sections of the domain wall pair from Fig. 3.44: $\mathrm{d}I/\mathrm{d}U$ (a) and z signal (b) at $U = -100$ mV and corresponding sections at $U = 700$ mV (c) and (d). Amplitude a and wall width w are derived by a fit with Eq. 3.18.

to $A(-100\ \mathrm{mV}) = 31\%$ and $A(+700\ \mathrm{mV}) = 116\%$. As has been pointed out, Eq. 3.17 cannot be used to derive P_S at these voltages: At -100 mV the $\mathrm{d}I/\mathrm{d}U$ signal is dominated by the distance variation alone and $P_\mathrm{S}(-100\ \mathrm{mV})$ is presumably close to zero. This can be seen by estimating the $\mathrm{d}I/\mathrm{d}U$ variation which results from the measured height profile alone, by assuming

$$dI/dU \propto \exp(-2\kappa z) \tag{3.19}$$

with a reasonable decay constant

$$\kappa = \sqrt{2m\bar{\phi}}/\hbar, \qquad \bar{\phi} = 4\ \mathrm{eV}. \tag{3.20}$$

The resulting curves are displayed in Fig. 3.45 (dashed lines). At -100 mV it is close to the measured line section, supporting the assumption made above. At 700 mV the z variation is considerably smaller, but nonetheless $A(+700\ \mathrm{mV})$ is enhanced to an (unphysical) value of more than 100%.[6] In principle, Eq. 3.19 can be used to correct

[6]The reason is a negative lock-in signal at domain wall B, which is caused by a crosstalk of the modulation voltage to the tip-sample separation. This measurement artefact can be avoided by choosing a slower response time of the feedback circuit or higher modulation frequencies. The former, however, requires a reduced scanning speed and therefore leads to increased measurement times. Note that this complication is absent when full spectroscopy curves are measured and the feedback circuit is open.

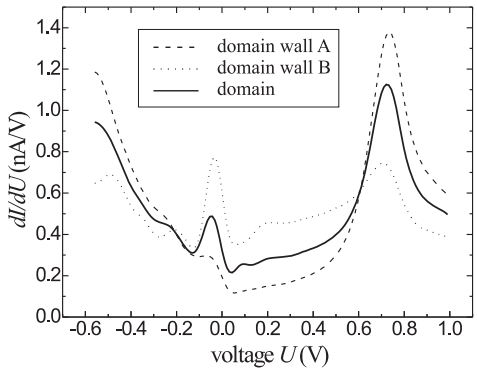

Figure 3.46: $\mathrm{d}I/\mathrm{d}U$ spectra above a domain (solid) and the oppositely magnetized domain walls A and B shown in Figs. 3.44 and 3.45. Stabilization at $I_0 = 0.5$ nA, $U_0 = 990$ mV.

the $\mathrm{d}I/\mathrm{d}U$ signal's z dependence, similar to such procedures in non–spin-polarized STM investigations [28], and $P_\mathrm{S}(U)$ can be calculated if P_T is known and constant. For this purpose κ should be determined accurately by measuring $I(z)$ curves with the same tip used for $\mathrm{d}I/\mathrm{d}U$ mapping. Such an approach is, however, only reasonable if P_S does not significantly depend on z within the relevant distance range.

We like to emphasize that despite these difficulties of determining the sample's spin-polarization, a pure imaging of the magnetic domain structure by $\mathrm{d}I/\mathrm{d}U$ mapping is not significantly affected by its z dependence, as can be seen in Fig. 3.45: In both cases of a high (40 pm) and low (16 pm) height difference all four line sections agree well with domain wall profiles which are expected from micromagnetic theory and assuming the well known $\cos\theta$-law of TMR experiments. The latter was predicted theoretically [29, 30] and confirmed experimentally for planar tunnel junctions [31]. The fact that the wall width w appears 0.7 nm wider at 700 mV than at -100 mV might be connected to different decay lengths of the contributing electronic states.

Full spectroscopy curves, taken above a domain and the domain walls A and B shown previously are displayed in Fig. 3.46. In agreement with the discussion above, the magnetic contrast of the spectra is close to zero at $U = -100$ mV. In this measurement mode all $\mathrm{d}I/\mathrm{d}U$ values of a single curve are taken at the same distance, but the tunneling distance might still depend on the local magnetization direction, hindering a straightforward calculation of $P_\mathrm{S}(U)$. In contrast to $\mathrm{d}I/\mathrm{d}U$ mapping the effect is, however, less pronounced, since higher stabilization voltages U_0 generally lead to a reduced spin-polarization of the total current [30]. Nonetheless, even at $U_0 = 990$ mV the tunneling distance varies with the local magnetization direction, which can be concluded from the fact that the domain spectrum is not identical to the average of the spectra taken at wall A and B, as should be the case in SP-STS at constant separation. This is most apparent at the peak position at $U = 700$ mV.

To capture the essential effects in a simple theoretical approach it is sufficient to

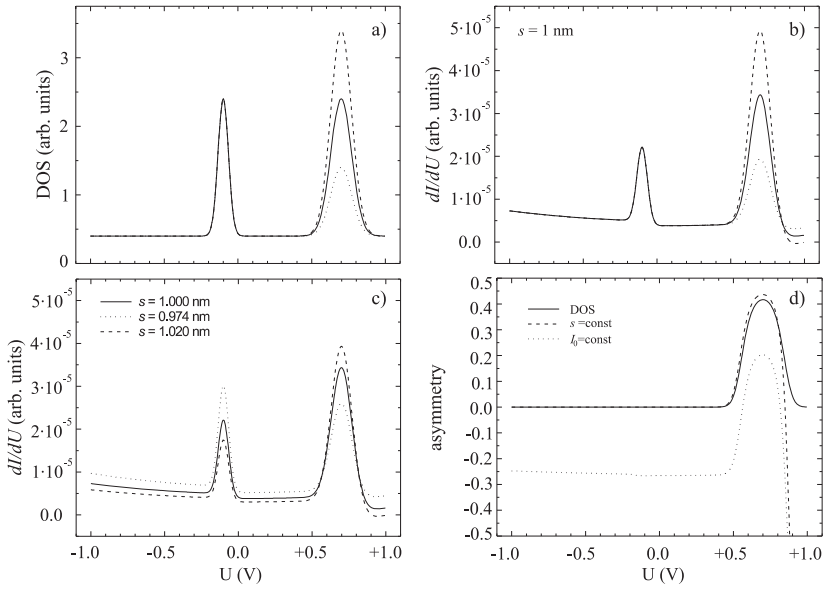

Figure 3.47: a) Input sample DOS ρ_S b) Calculated dI/dU spectra at fixed tip-sample separation $s = 1$ nm. c) dI/dU spectra calculated for constant current I_0 and $U_0 = 1$ V. d) Asymmetry of ρ_S, and the spectra from (b) and (c).

employ a simplified description of the tunneling current following Ref. [32],

$$I \propto \int_0^{eU} \rho_S\left(E_F + \varepsilon\right) \rho_T\left(E_F - eU + \varepsilon\right) T\left(\varepsilon, U, s\right) d\varepsilon, \tag{3.21}$$

where ρ_S and ρ_T denote the density of states (DOS) of surface and tip, respectively, and T is a bias dependent transmission probability for a trapezoidal barrier, derived by the semiclassical WKB approximation:

$$T\left(E, U, s\right) = \exp(-2\,\kappa(E, U)\,s), \tag{3.22}$$

$$\kappa(E, U) = \sqrt{\frac{2m}{\hbar^2}(\bar{\phi} + \frac{eU}{2} - E)}. \tag{3.23}$$

The dependence of T on the electron momentum is neglected in this description. It has been shown in Ref. [33] that tunneling spectra calculated within such a model agree qualitatively to the ones derived by a full calculation using the Bardeen approach [34].

We will now discuss the important difference between spectroscopy at *constant separation* and with *stabilization at constant current* for determining the spin-polarization. Figure 3.47(a) shows three hypothetical ρ_S with a peak height variation at 700 mV equivalent to a spin-polarization of 50%, a non–spin-polarized background and a reference peak at -100 mV. Assuming $\rho_T = \text{const}$ and $\bar{\phi} = 4$ eV the calculated dI/dU spectra for a fixed separation of $s = 1$ nm are displayed in Fig. 3.47(b). They bear a strong resemblance to the input DOS in (a): Though the reference peak at -100 mV appears reduced with respect to the ones at 700 mV due to an enhanced barrier height,

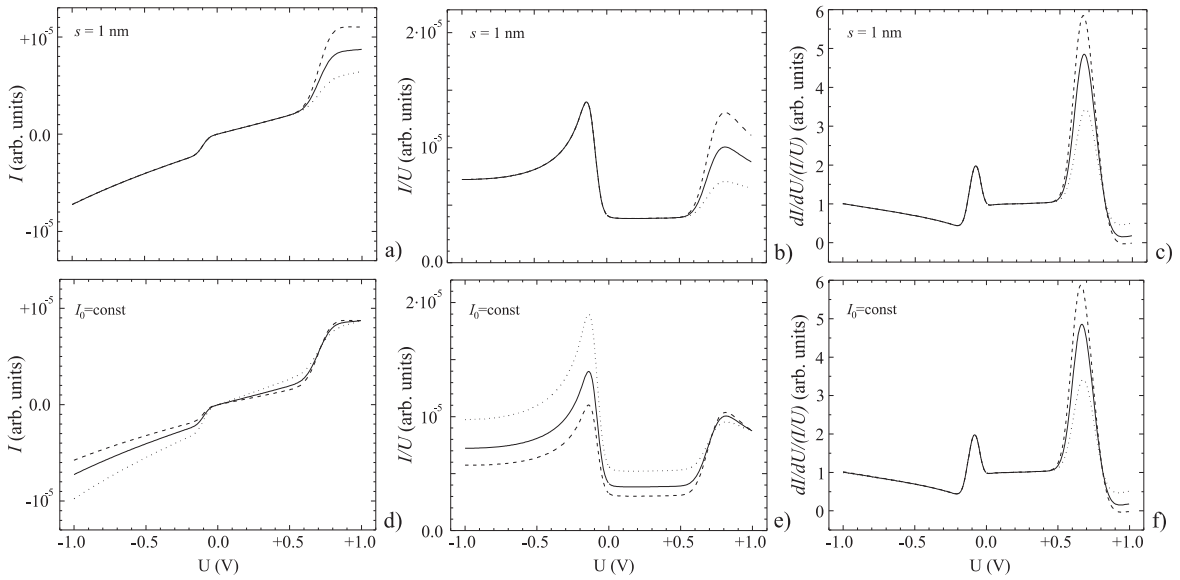

Figure 3.48: Current I (a), total conductivity I/U (b), and spectra normalized by I/U at constant separation $s = 1$ nm. Current I (d), total conductivity I/U (e), and normalized spectra at constant current I_0 and $U_0 = 1$ V.

most importantly, the relative intensities at 700 mV are reproduced correctly, allowing a direct calculation of P_S by Eq. 3.16 and 3.17. The situation is dramatically different if the separation s is determined by a constant current and a stabilization at $U_0 = 1$ V, as can be seen in Fig. 3.47(c). An enhanced DOS between $U = 0$ and U_0 (dashed curve) causes an increased separation s and thereby an overall reduction of the $\mathrm{d}I/\mathrm{d}U$ signal with respect to the dashed curve in (b). The contrary holds for the dotted curve: A reduced DOS between $U = 0$ and U_0 leads to a decreased separation s and to an overall increase of the $\mathrm{d}I/\mathrm{d}U$ signal with respect to the case of constant s in (b). As a result, the relative intensities in Fig. 3.47(c) do not correspond to the ones of the input DOS, and the application of Eq. 3.16 and 3.17 would lead to wrong conclusions about the sample's spin-polarization, as can be seen in Fig. 3.47(d): Whereas the asymmetry $A(U)$ of the spectra from (b) (dashed) is close to the input DOS' asymmetry (solid), at least in the range $U < 0.8$ V, the discrepancy is up to 25% in the case of stabilization at constant current (dotted). The main deviation is a shift of about -25%, which means that in this mode differences of the spin-polarization are measured rather than absolute values. Note, that if $P_S(U)$ is a constant function of U the magnetic information is fully absorbed by the height adjustment and all three spectra in (c) would be identical. This can be seen directly in Eq. 3.21.

Figure 3.48 displays for the two cases—spectroscopy at constant separation and with stabilization at constant current—the tunnel current $I(U)$, the total conductance I/U, and the spectra from Fig. 3.47, normalized by I/U. A comparison of Fig. 3.48(c) and (f) shows that $\mathrm{d}I/\mathrm{d}U$ spectra of one and the same DOS, taken at different separations s, fall onto a universal curve, a fact which has been observed experimentally

a long time ago [35]. However, this does not guarantee that these curves bear a close resemblance to the sample's DOS, or that relative intensities of *different* DOS' are recovered by this normalization procedure. In fact, a plateau is created between the two peaks, which does not correspond to the input DOS in Fig. 3.47(a), and the polarization at 700 mV is still underestimated. Furthermore, since all spectra are normalized to 1 at $U = 0$, the spin-polarization around E_F, which is a characteristic feature of ferromagnets, is completely suppressed. For these reasons a normalization of $\mathrm{d}I/\mathrm{d}U$ spectra by I/U to recover $P_\mathrm{S}(U)$, as has been performed in Ref. [36], seems inadequate.

To extract $P_\mathrm{S}(U)$ from measured SP-STS data it is thus necessary to measure the distance variation as well as the effective decay constant accurately. $P_\mathrm{S}(U)$ can then be estimated within certain model approximations. More elegantly, the problem can be circumvented by measuring at constant separation from the start, i.e. by stabilization at specific voltages U_0, which assure a non–spin-polarized total current. Such an approach requires at least one zero of $P_\mathrm{S}(U)$ between $U = 0$ and U_0. For the calculated example above this could be any voltage $U_0 < 0.5$ V, as can be seen e.g. in Fig. 3.48(a). Experimentally, such an U_0 can be determined by iteratively tuning the bias voltage to values where the signature of domain walls vanishes in the topographic image.

SP-STM using antiferromagnetic probe tips

Despite the fact that the magnetic dipole interaction between the sample and the tip is considerably reduced for FM ultrathin film coatings on a non-magnetic tip in comparison to thicker coatings or even bulk FM tips, a remaining influence cannot be ruled out which might play an important role for magnetically soft or superparamagnetic samples. Pareek and Bruno stated that this interaction "cannot be avoided" [37]. A straightforward and experimentally feasible solution, however, is the use of an AF coated or bulk AF tip. It should exhibit no significant stray field since opposite contributions compensate on an atomic scale. Nevertheless, it is suitable for SP-STM due to a non-vanishing spin-polarization near the Fermi level. Furthermore, the tip is insensitive to external fields, which allows to directly access intrinsic sample properties in field dependent studies.

The influence the tip's dipolar magnetic field may have on the sample's domain structure can be seen in Fig. 3.49(a) which shows a series of $\mathrm{d}I/\mathrm{d}U$ maps of 1.95 ML Fe recorded with a GdFe tip. Panel (i) shows an overview of the initial state. Dislocation lines appear as bright lines along [001], because they locally change the electronic properties. The domain structure is similar to the one in Fig. 3.49(a), except that the exchange coupling across the step edges is significantly reduced. A second image (ii) is taken at higher resolution as indicated by the frame in panel (i). Due to the coverage being slightly below $\theta = 2.0$, narrow ML areas can be seen, appearing bright at the chosen bias voltage. These ML areas efficiently decouple DL regions on adjacent terraces. At 350 mT (iii) the domain distribution is asymmetric: bright domains have grown and dark domains have shrunken which is equivalent to a formation of 360° walls [22]. In some places the magnetic contrast changes abruptly from one horizontal

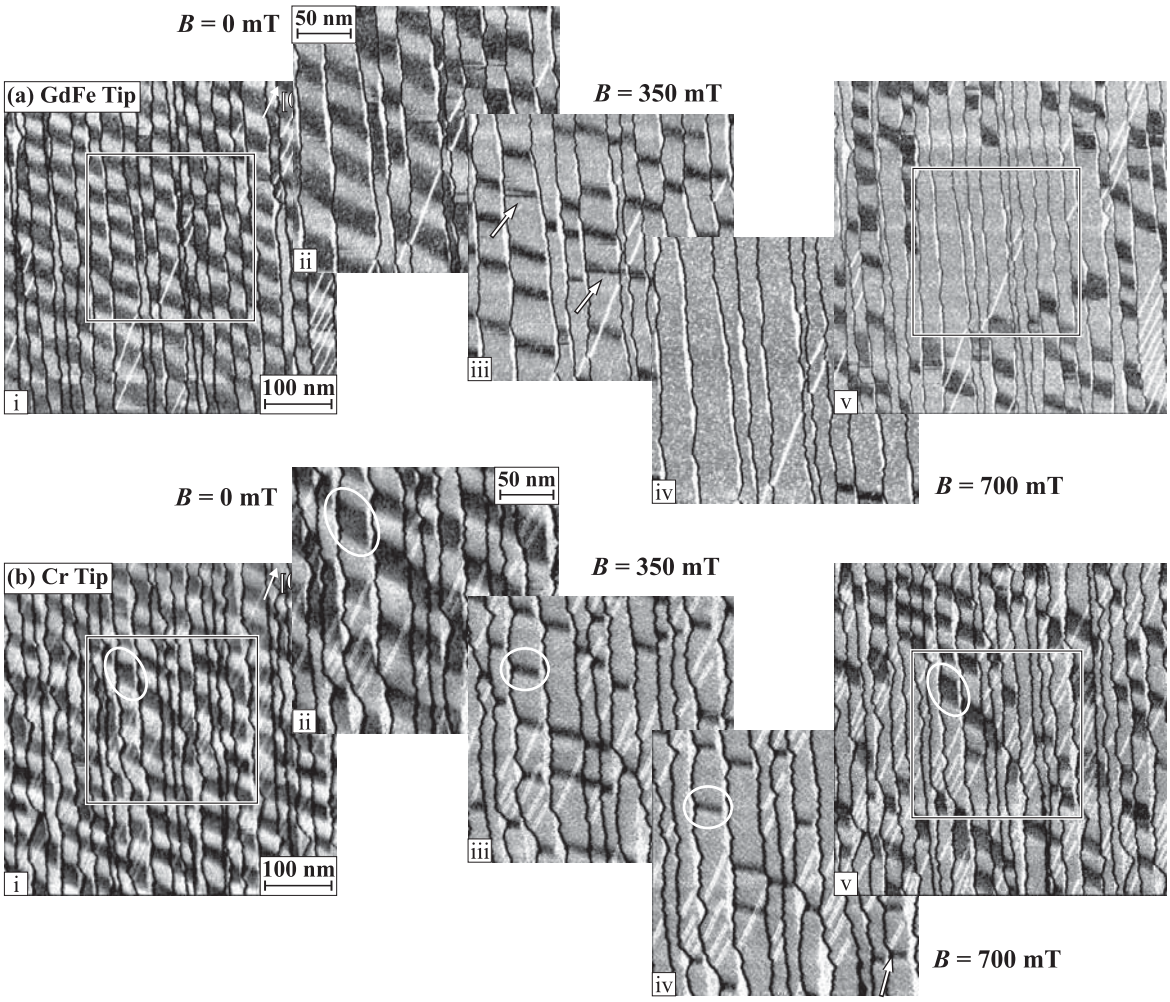

Figure 3.49: **(a)** dI/dU maps of 1.95 ML Fe/W(110) recorded with a GdFe tip (out-of-plane contrast) at I=0.3 nA, U=-0.22 V: **i)** 500 × 500 nm^2 overview of magnetic initial state. **ii)** 250 × 250 nm^2 zoom-in. **iii)** Asymmetry at $B = 350$ mT: Dark domains are compressed and form 360° walls. **iv)** Saturation is observed within the field of view. **v)** The influence of the tip's stray field becomes obvious in the overview recorded at $B = 0$ mT. **(b)** Analogous series of an identically prepared sample, recorded with a Cr-coated tip at I=0.8 nA, U=-0.5 V: **i,ii)** Magnetic initial state. **iv)** A large fraction of walls has survived at 700 mT, in contrast to (a). **v)** The scanned area exhibits no significant difference in comparison to its surrounding.

scan line to the next (see arrows), a result of a rearrangement of the sample's magnetic state during the imaging process. At 700 mT (iv) the sample has reached saturation within the field of view, except for two walls at the lower right. However, it becomes obvious in the overview image, recorded at the same location in zero applied field (v), that this field value does not reflect intrinsic sample properties. A large fraction of dark domains has survived outside the region which was scanned previously at 700 mT. We

conclude that the superposition of the applied field and the additional field emerging from the magnetic coating of the tip is much more efficient in the remagnetization of 360° walls than the applied field alone.

Fig. 3.49(b) shows an analogous series of images of a sample, which was prepared identically, but imaged with an antiferromagnetic Cr-covered tip. It exhibits an out-of-plane sensitivity like the GdFe tips. We have marked a dark domain as an example to be recognized in all five images. The domain structure in the panels (i-iii) displays no significant difference to the corresponding ones in (a). Since a rearrangement of the domain structure during imaging is not observed throughout this series, the occurrence of such events in (a) can be attributed to the GdFe tip's stray field. Alternative explanations like thermally or tunnel current activated wall motion can be excluded by a comparison with (b). As in Fig. 3.49(a)(iii), the dark domains are compressed at 350 mT and rotated away from the $[1\bar{1}0]$ direction, thereby reducing their lengths. These are two processes which proceed at 700 mT. At this field value and in contrast to (a) a large fraction of dark domains has survived. In the overview image (v) taken in zero applied field, the previously scanned area exhibits no significant difference in domain distribution in comparison to its surrounding, a result demonstrating the advantage of a stray field free tip.

To estimate the effect of the GdFe tip's stray field we further increased the field in steps of 50 mT (not shown), in order to reach a magnetic state which is equivalent to Fig. 3.49(a)(iv). At 900 mT only a single dark domain is left, which we marked by an arrow in Fig. 3.49(b)(iv). We conclude that the effect of the GdFe tip's stray field is equivalent to an additional homogeneous perpendicular field of $200 - 300$ mT. Even though this value is considerably below the highest value possible at a Gd surface, $B_{\max} = \mu_0 M_s/2 \approx 1.3$ T, it seems to be inconsistent with the rather weak tip-sample interaction observed in the absence of an applied field. To clarify this issue we calculated the tip's stray field using formulas derived in Ref. [38]. We model the tip by two parts: a smooth thin film on a half sphere, magnetized normal to its surface, and a cone on its apex as a nano-tip being responsible for the tunneling process, magnetized along its axis. Using $M_s = 2.13 \cdot 10^6$ A/m for Gd and a radius of $r = 500$ nm [51] we calculate the field of the thin film to be of the order of 1 mT per nm coating thickness s for $s \ll r$ at a distance of 1 nm from its surface. This contribution is much too weak and too homogeneous to explain the strength and locality of the tip-sample interaction observed in Fig. 3.49(a)(v).[7] We assume the nano-tip to be a triangular pyramid with an aspect ratio of bulk hcp Gd ($h/a = 2.89/3.64$), which we approximate by a point sharp cone of the same height h and the same volume ($h/r \approx 2.14$). Fig. 3.50 displays the perpendicular and in-plane components of the stray field of such a cone at tunneling distance (1 nm) vs. lateral distance x for heights $h = 1 - 3$ nm with the ratio h/r kept constant. These fields are highly localized and their strength increases monotonously with the cone's size. We argue that, for the given sample, such inho-

[7]Note that a radially magnetized sphere or a perpendicularly magnetized and infinitely extended film does not exhibit any external stray field [21]

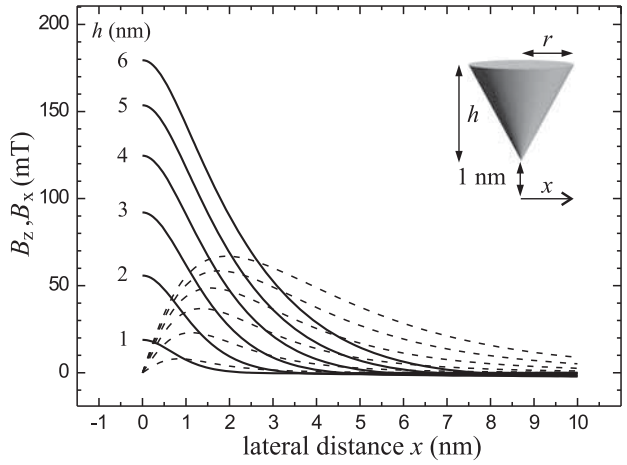

Figure 3.50: Perpendicular stray field component B_z (solid line) and in-plane component B_x (dashed) of a cone vs. lateral distance x from its axis, calculated at $\Delta z = 1$ nm.

mogeneous fields arising from the STM tip's roughness are sufficient to locally trigger remagnetization processes at external fields close to the sample's coercivity, but do not seriously alter the magnetic state in the absence of an external field, due to the small interaction area. The latter might, however, not be the case for magnetically softer substrates or superparamagnetic particles.

To shed some light onto the remagnetization process and to estimate whether the former assumption is quantitatively reasonable we performed micromagnetic calculations for a single 360° wall in an isolated DL section, the details of which will be published elsewhere. In addition to the perpendicular [110] easy axis, we introduced a second uniaxial anisotropy K_h, with the hard axis along [001], which stabilizes these walls in applied perpendicular fields [22, 23]. With increasing field the wall reduces in size until at a critical field B_c a breakdown process occurs, where the uniform state is reached by a rotation via the hard axis. For a given set of reasonable magnetic parameters[8] the experimentally determined critical field $B_c = 900$ mT can be reproduced by choosing $K_h \approx -2.1 \cdot 10^6$ J/m^3. It turns out that at 700 mT a localized field of only 40 mT along the hard direction is sufficient to initiate the remagnetization at the DL boundary. It is thus the in-plane component of the tip's stray field B_x which is most effective in the remagnetization process. Furthermore, since B_c scales down with decreasing K_h, the observed reduced stability of 360° walls in areas with dislocation lines can be explained by a reduced value of K_h. This is plausible, since dislocations locally distort the lattice, thereby lifting the in-plane symmetry of the film.

[8] exchange: A=$1.5 \cdot 10^{-11}$ J/m, magnetization: M_s=$2.0 \cdot 10^6$ A/m, easy axis anisotropy: K_e=$3.5 \cdot 10^6$ J/m^3

Spin-orbit Coupling

Surprisingly, the domain walls in the system of the Fe double layer on W(110) are also visible in data which have been measured with a non-magnetic W tip [39, 40]. This is shown in Fig. 3.51 with the topography in (a) and a corresponding $\mathrm{d}I/\mathrm{d}U$ map at $U = +0.05\,\mathrm{V}$ in (b). Periodically arranged dark lines running along the $[1\bar{1}0]$ direction are observed. The measured periodicity is half the magnetic periodicity, indicating that the contrast is caused by different (spin averaged) electronic properties of domains and domain walls. However, all domain walls exhibit the same $\mathrm{d}I/\mathrm{d}U$ contrast, i.e., at the position of the domain wall the differential conductance is reduced with respect to the domain. As revealed by the $\mathrm{d}I/\mathrm{d}U$ spectra in (c) this contrast is caused by a small difference which is energetically located just above E_F (see inset): while the $\mathrm{d}I/\mathrm{d}U$ spectrum measured with the tip positioned above the domain exhibits a weak peak at $U = +0.07\,\mathrm{V}$, this peak is almost absent in the domain wall spectra. This is further illustrated by the plot of the normalized difference $(\mathrm{d}I/\mathrm{d}U_\mathrm{domain} - \mathrm{d}I/\mathrm{d}U_\mathrm{domain\ wall})/(\mathrm{d}I/\mathrm{d}U_\mathrm{domain} + \mathrm{d}I/\mathrm{d}U_\mathrm{domainwall})$ in the lower panel of

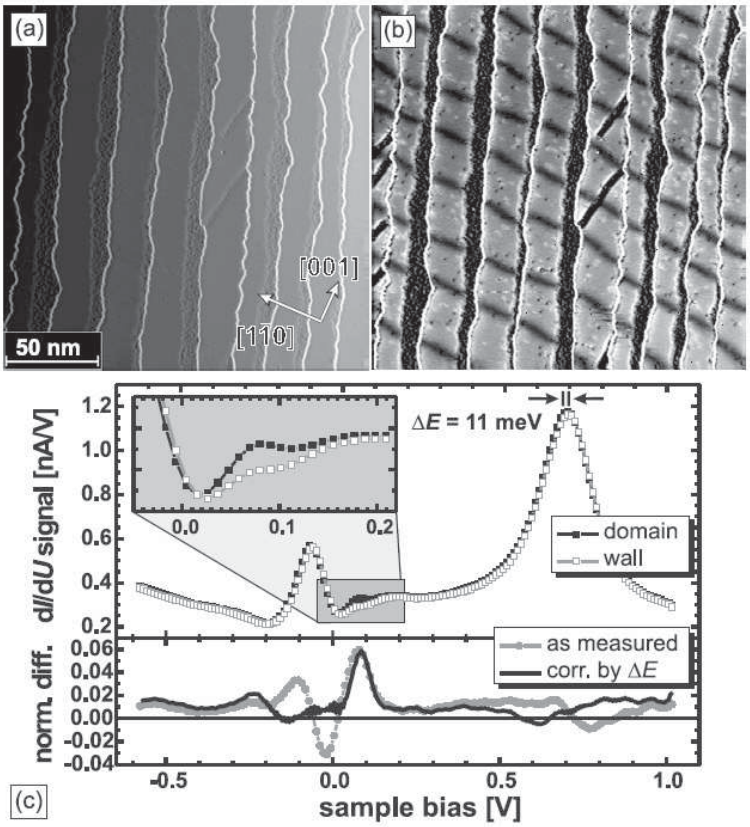

Figure 3.51: (a) Topography of $1.75 \pm 0.1\,\mathrm{ML}$ Fe/W(110) and (b) corresponding $\mathrm{d}I/\mathrm{d}U$ map at $U = +0.05\,\mathrm{V}$; (c) comparison of $\mathrm{d}I/\mathrm{d}U$ spectra measured for domains and domain walls; the normalized difference between both spectra is plotted in the lower panel.

(c). However, if the normalized difference is calculated with the original data (as measured), a pronounced oscillation can be found just below E_F. This oscillation is not caused by any additional or missing spectroscopic features of the dI/dU spectra of domains and walls but by an overall energetic shift $\Delta E = 11$ meV. The physical origin is a difference in the work functions of domains and domain walls and can be corrected by shifting the domain wall spectrum by $-\Delta E$.

In order to understand the reason for the changes in the dI/dU spectra first-principles calculations of the electronic structure of 2 ML Fe/W(110) were performed. From the model of Tersoff and Hamann it is known that the vacuum LDOS should compare directly to the measured differential conductance [41]. Figure 3.52(a) shows the calculated vacuum LDOS, $n(E)$, at a tip–sample distance of about 14 Å for two different magnetization directions of Fe: out-of-plane, representing the magnetization state in the domain (full line), and in-plane along the $[1\bar{1}0]$ direction (dashed line) as a model of the magnetization in the domain wall. For the calculation 3600 $k_\parallel$ points have been used in a square centered at $\overline{\Gamma}$ with an area covering 25% of the Brillouin Zone (BZ). Two d_{z^2}-states from the Fe double layer are found leading to pronounced peaks at -0.18 eV and $+0.85$ eV. These states are located at the $\overline{\Gamma}$-point of the 2D-BZ and therefore they are easily detectable by STS [42]. In fact, they can be assigned to the experimentally observed peaks at -0.08 V and $+0.7$ V (see Fig. 3.51(c)). The distinct shoulder at $+0.35$ eV in the calculated vacuum LDOS decays much more rapidly with increasing distance from the surface than the d_{z^2} states which is probably the reason why it is absent in the experimental data.

A spin analysis reveals that the peaks are caused by electronic states of minority character (neglecting the small spin mixing due to the spin-orbit interaction). A closer look (see inset in Fig. 3.52(a)) reveals a significant enhancement of the LDOS for the

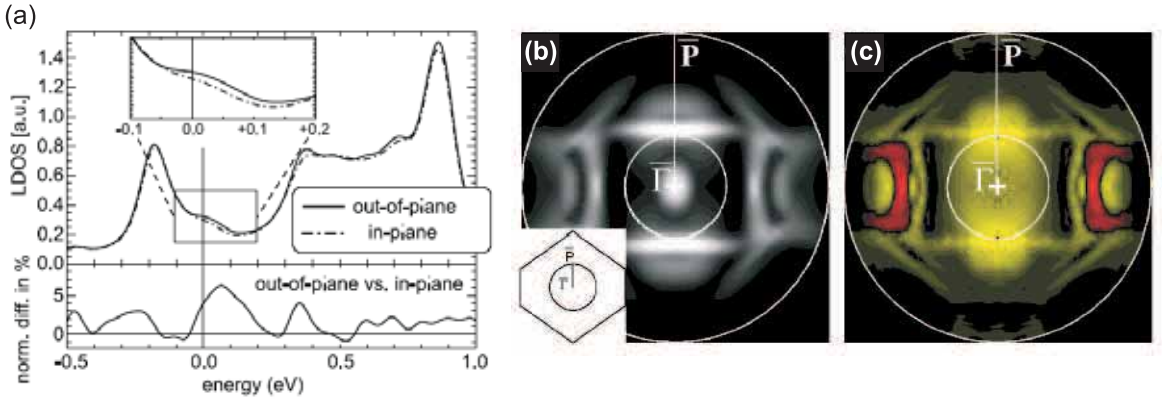

Figure 3.52: (a) Calculated LDOS at about $z = 14$ Å above the surface of 2 ML Fe/W(110), measured from the center of the atom; the lower panel displays the normalized difference; (b),(c) $k_\parallel$-resolved contribution to the minority LDOS for states with an energy of $E_F = +0.05$ eV displayed in the 2D-BZ; (b) the LDOS for the out-of-plane direction, and (c) the difference Δn between the LDOS n for out-of-plane and in-plane magnetization directions.

out-of-plane magnetized film within the energy range $-0.05\,\mathrm{eV} \leq E \leq +0.15\,\mathrm{eV}$. The lower panel of Fig. 3.52(a) shows the normalized difference and three peaks centered at about $-0.3\,\mathrm{eV}$, $+0.06\,\mathrm{eV}$, and $+0.35\,\mathrm{eV}$ can be recognized. The most pronounced peak at $+0.06\,\mathrm{eV}$ in the normalized difference is in good agreement with the experimental data in the lower panel of Fig. 3.51(c). Even the smaller peak at $-0.3\,\mathrm{eV}$ is in accordance with the experimental findings while the peak at $+0.35\,\mathrm{eV}$ is related to the calculated LDOS shoulder and thus absent in the experimental data.

The $k_\parallel$-resolved contribution over the 2D-BZ of the minority projected part of the LDOS at an energy of $E_\mathrm{F} + 0.05\,\mathrm{eV}$ is plotted in Fig. 3.52(b) for the out-of-plane direction. A disk of radius $\overline{\Gamma\mathrm{P}}$ centered around the $\overline{\Gamma}$ point with an area of 20% of the 2D-BZ has been chosen. States with larger $|k_\parallel|$ contribute only insignificantly to the vacuum LDOS. A total of 6000 $k_\parallel$ points have been used to sample the disk. All states have been smeared by a Gaussian of 0.05 eV. A spot at the $\overline{\Gamma}$-point and two stretched spots at the inner circle in the $\overline{\Gamma\mathrm{P}}$ direction can be identified as the origin of the vacuum LDOS at this energy. In the difference plot between the LDOS of out-of-plane and in-plane magnetization presented in Fig. 3.52(c) it is observed that the states at the inner circle cause the changes.

With the additional information from the $k_\parallel$-space resolution it is concluded that the origin of the LDOS change results from an effect in the $\overline{\Gamma\mathrm{P}}$-direction of the band structure (see Fig. 3.55 for a band structure plot along the two high-symmetry directions; the circle indicates the region of interest to the spin-orbit coupling). When the spin-orbit interaction is turned off the majority and minority states diagonalize the Hamilitonian. At the $k_\parallel$ of interest, i.e., at the inner circle in Fig. 3.52(c), three minority state bands cross at the Fermi energy (see also Fig. 3.55, circle). One is rising while two nearly degenerate ones are falling. While the rising band is of d_{z^2} character, the other two consist of states which are linear combinations of d_{xy} and d_{xz} orbitals. Note that states with d_{xy} and d_{xz} orbital character contribute only by a negligible amount to the vacuum LDOS, while d_{z^2}-states often dominate the vacuum LDOS. Since the d_{z^2} band is rather steep when spin-orbit coupling is turned off, it contributes only little to the LDOS above the sample surface. However, depending on the magnetization direction, the spin-orbit coupling can mix the three crossing bands. This is the case for this system and the mixing occurs for the out-of-plane magnetization direction leading to a hybridization gap between one of the d_{xy+xz} bands and the d_{z^2} band (see Fig. 3.55, circle). The introduction of this gap changes the dispersion of the d_{z^2} state (making it even flat at the hybridization gap) upon changing the magnetization direction which explains the detected enhancement of the LDOS in the STS.

There is another interpretation of the effect found experimentally which has not yet been discussed: beside spin-orbit effects the electronic properties might be changed by the canting of adjacent (atomic) spins as well which certainly exists within the domain wall where the magnetization rotates gradually. In order to exclude this possibility measurements at increasing external magnetic fields B were performed. Fig. 3.53 shows the topography (a) of $1.7 \pm 0.1\,\mathrm{ML}$ Fe/W(110) and the corresponding $\mathrm{d}I/\mathrm{d}U$ map (b)

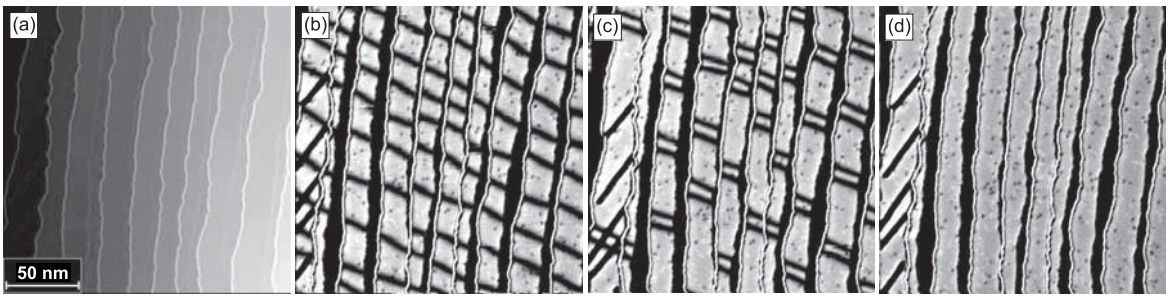

Figure 3.53: (a) Topography of 1.7 ± 0.1 ML Fe/W(110) and $\mathrm{d}I/\mathrm{d}U$ maps at $U = +0.05$ V at (b) $\mu_0 H_{\mathrm{ext}} = 0$ mT, (c) 600 mT and (d) 1000 mT.

at $U = +0.05$ V and $B = 0$ T. Again, a periodic pattern of almost parallel dark lines along the $[1\bar{1}0]$ direction can be recognized on the Fe double layer at zero field. As discussed before the lines represent domain walls of alternating in-plane magnetization. Between the domain walls the Fe double layer shows alternating perpendicularly magnetized domains [43]. Upon application of a perpendicular external field the domains oriented parallel with respect to the field grow on the expense of the domains oriented antiparallel. Fig. 3.53(c) shows that at $\mu_0 H_{\mathrm{ext}} = 600$ mT the antiparallel domains are strongly compressed between the surrounding walls in a way that the magnetization basically performs a continuous 360° wall rotation [18]. If the canting of adjacent spins would be responsible for the observed decrease of the $\mathrm{d}I/\mathrm{d}U$ signal, the whole 360° wall should appear dark at $U = +0.05$ V. This is in contrast to the data in (c) which show two distinct domain walls being about 7 nm apart from each other. A field of 1000 mT is sufficient to saturate the sample completely as shown in Fig. 3.53(d). Consequently, it is concluded that not the canting of adjacent spins causes the domain wall contrast when using non-magnetic tips but instead the spin-orbit coupling induces changes in the LDOS which leads to a different electronic structure for out-of-plane and in-plane magnetized sample areas.

Spin-polarized electron scattering at single oxygen adsorbates

The analysis of electron standing wave patterns [44–47] allows the acquisition of characteristic properties as the symmetry of the wave function, the dispersion relation, or the lifetime of the electronic states. All previous experiments were performed with nonmagnetic tips resulting in spin-averaged data, although scattering processes at magnetic impurities or at nonmagnetic impurities on magnetic surfaces should result in spin-polarized (SP) electron waves. These are of fundamental importance for the understanding of single-particle as well as many-body processes, e.g., the RKKY interaction or the interaction between Kondo impurities.

The iron double layer on W(110) is an ideal model system to study the influence of single adsorbates on the electronic and magnetic structure of surfaces. Since it is known that the exposition of Fe(110) surfaces to oxygen at room temperature leads

to dissociative chemisorption [48], this adsorbate was chosen. The single oxygen adsorbates are distributed randomly and tunneling spectra reveal that for $U \leq +0.8\,\mathrm{V}$ oxygen locally causes an attenuation of the $\mathrm{d}I/\mathrm{d}U$ signal compared to clean Fe spectra.

Figure 3.54 shows a high-resolution topography (a) and corresponding $\mathrm{d}I/\mathrm{d}U$ maps (b),(c) around a single oxygen atom at $U = +0.3\,\mathrm{V}$ and $U = -0.1\,\mathrm{V}$ as indicated with highly anisotropic patterns [49]. The black lines indicate the positions of the line profiles which are plotted in the lower panels. In Fig. 3.54(b) oscillations in the $\mathrm{d}I/\mathrm{d}U$ map along the [001] direction of the substrate are observed with a maximum of the $\mathrm{d}I/\mathrm{d}U$ signal at the center of the oxygen atom (distance $d = 0\,\mathrm{nm}$). The $\mathrm{d}I/\mathrm{d}U$ map in Fig 3.54(c) measured at $U = -0.1\,\mathrm{V}$ shows oscillations along the $[1\bar{1}0]$ direction of the substrate. At this particular voltage a local minimum at $d = 0\,\mathrm{nm}$ is observed. The oscillations of the $\mathrm{d}I/\mathrm{d}U$ signal show a strong attenuation with increasing distance from the center of the oxygen adsorbate.

The oscillations in the differential conductance are interpreted in terms of standing electron waves and will be explained within a single-particle model. In the proximity of impurities electron waves are scattered by the impurity potential. Coherent interference of the incoming with the reflected electron wave results in spatial oscillations of the density of states. The observed real-space oscillations can be analyzed regarding their periodicity and phase. The periodicity contains information about the wave vector component $k_{\parallel}$ of the electron wave.

We have compared the experimental results with first-principles electronic structure

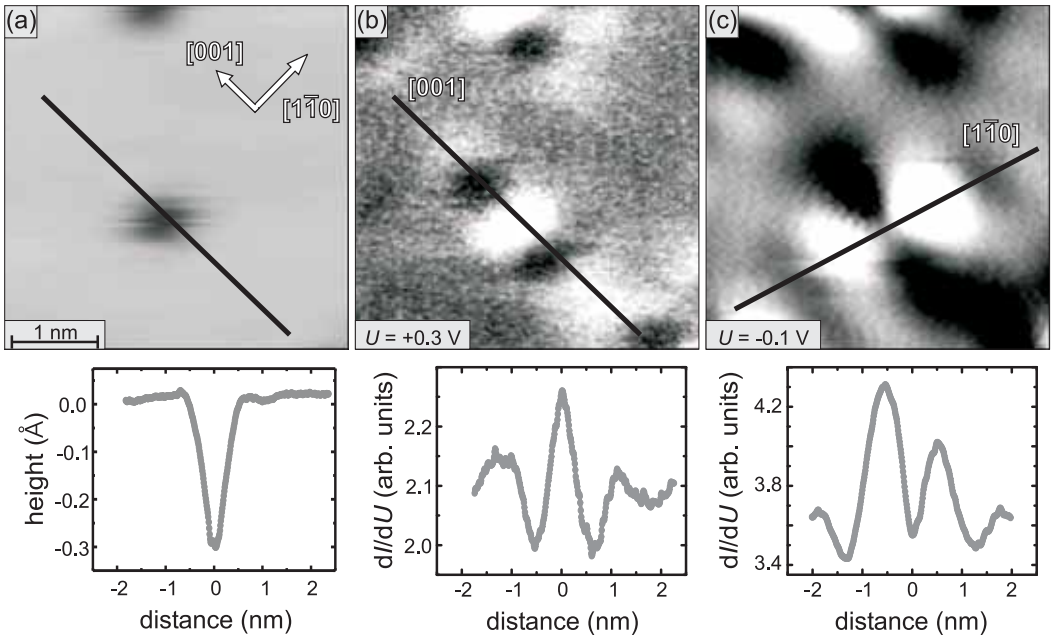

Figure 3.54: Single oxygen adsorbate on Fe on W(110) measured with a W-tip. (a) topography; (b),(c) corresponding $\mathrm{d}I/\mathrm{d}U$ maps, the lines indicate the positions of the profiles shown in the bottom panel.

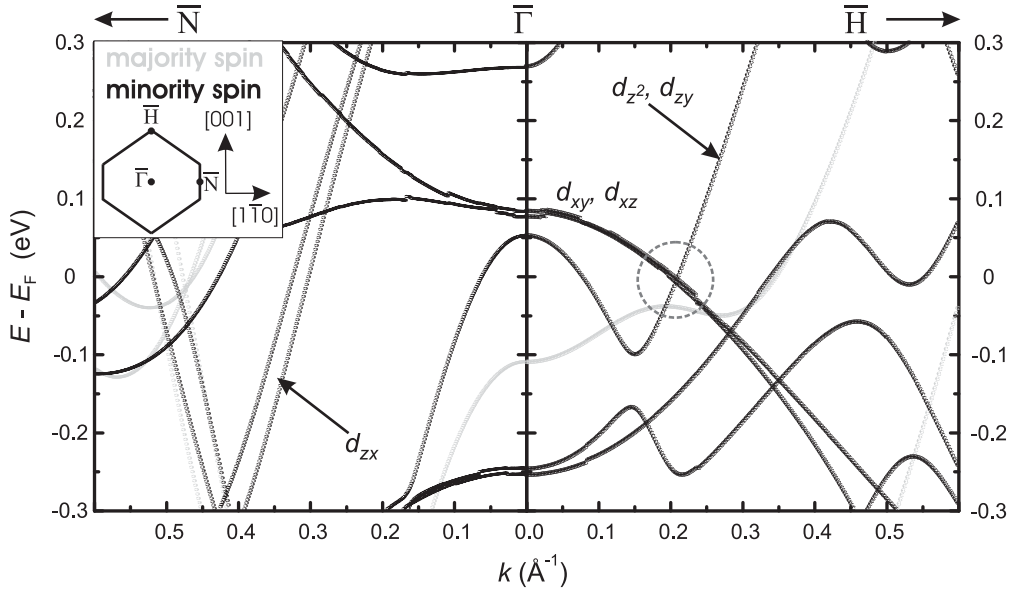

Figure 3.55: Spin-resolved band structure calculation for 2 ML Fe/W(110) [50] (the circle indicates the region of interest of the previously discussed spin-orbit coupling).

calculations based on density functional theory [50]. Figure 3.55 shows the calculated spin-resolved band structure of 2 ML Fe adsorbed pseudomorphically on either side of a 5 layer W(110) slab. From the experimental data we extracted the period of the standing waves at various energies and calculated the k-vectors of the corresponding electron wave functions. This allows the comparison between experimental and theoretical data. The oscillations in [001] can be assigned to a rising minority-spin band in the $\overline{\Gamma\mathrm{H}}$ direction indicated by the arrow in Fig. 3.55. An analysis of the eigenstate reveals that this band consists basically of a superposition of d_{z^2} and d_{zy}-like states in the Fe surface layer. 10% of this state is localized in the vacuum, measured always from a position of 1.2 Å above the surface Fe layer. The oscillations in [1$\bar{1}$0] result from scattering involving one of the two bands which are indicated by the arrow in the $\overline{\Gamma\mathrm{N}}$ direction. Both are of minority-spin character. The band closer to $\overline{\Gamma}$ is a d_{zx}-like state in the Fe surface layer with 8% of its weight localized in the vacuum. The other one is a superposition of d_{z^2}, d_{zx} and $d_{x^2-y^2}$-like states in the Fe surface layer and only 1% is localized in the vacuum. For this reason we assume that the band visible in the scattering process is the one closer to $\overline{\Gamma}$. As we will show below these two bands allow a precise modeling of the observed course of maxima and minima in the dI/dU signal.

If the above mentioned interpretation is correct we expect to see a significant spin-dependence in the electron scattering by spin-polarized STS. In particular, SP-STS measurements on different types of magnetic domains with the same magnetic tip should provide information about the spin characteristics of the electronic states involved in the scattering process. The well-known magnetic structure of 2 ML Fe/W(110) which is characterized by about 20-25 nm wide, perpendicularly magne-

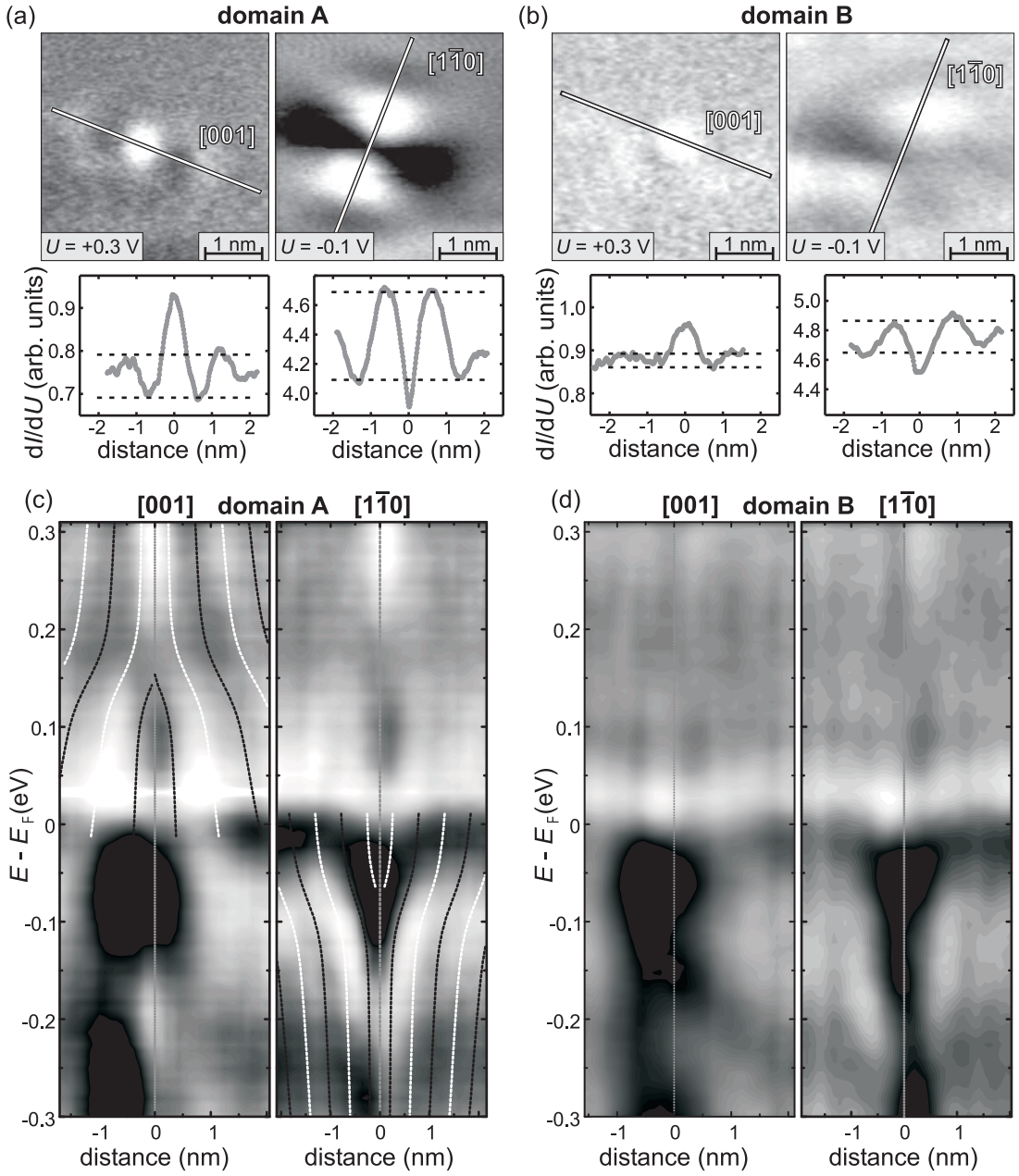

Figure 3.56: Spin-polarized STM measurements (with a Gd/Fe-coated W tip). (a),(b) dI/dU maps showing a single oxygen adsorbates on two different magnetic domains A and B, the lines indicate the positions of the corresponding line profiles shown in the lower panel; (c),(d) data from dI/dU spectroscopy (normalized, logarithmic grey scale) for oppositely magnetized domains A and B along the two crystallographic axes; the black and white lines in (c) indicate the minima and maxima simulated on the basis of the band structure calculation and the experimentally determined phase relation.

tized domains were found to be unchanged by the oxygen adsorbates. Full $\mathrm{d}I/\mathrm{d}U$ spectroscopy was performed around a single oxygen atom adsorbed on one particular type of domain (A). Afterwards, the same measurement was performed around another oxygen atom on the oppositely magnetized domain (B). Eventually, the measurement was repeated on the initial domain (A) to exclude any unwanted tip change.

The experimental data is presented in Fig. 3.56. Indeed, the $\mathrm{d}I/\mathrm{d}U$ maps in (a) and (b) demonstrate that the characteristic patterns in the differential conductance as known from spin-averaged measurements (see Fig. 3.54) can be recognized on domain A, while they are nearly absent on domain B. Lines indicate the position of the corresponding line-profiles shown in the lower panels. Around the oxygen atom on domain A the above mentioned scattering states are enhanced for both high-symmetry directions, whereas on domain B they can hardly be detected.

We have compared the calculated band structure of Fig. 3.55 with the SP-STS measurements by converting the calculated dispersion relation $E(\vec{k})$ of the bands identified to be involved in the scattering process into an energy dependent electron wavelength $\lambda(E) = 2\pi/k(E)$. Then $\lambda/2$ is the periodicity of the LDOS, which is proportional to the STS signal. After correction with the experimentally determined energy-dependent phase the positions of the maxima and minima of the density of states can be simulated as function of energy and of distance from the center of the oxygen atom. The result is shown in Fig. 3.56(c) together with energy-resolved data from $\mathrm{d}I/\mathrm{d}U$ spectroscopy for domain A for both high-symmetry directions. For direct comparison the corresponding experimental data for domain B are shown in (d). Even though the band structure calculation does not account for adsorbate-induced modifications of the electronic structure but only models the oxygen atom as a point scatterer, the simulation is in excellent agreement with the experimental data of domain A. This observation together with the direct comparison between domains A and B proves the strong spin-polarization of the electron waves around the impurity.

References

[1] H. Bethge, D. Heuer, C. Jensen, K. Reshöft, and U. Köhler, Surf. Sci. **331–333**, 878 (1995).

[2] H. J. Elmers and U. Gradmann, Appl. Phys. A **51**, 255 (1990).

[3] H. J. Elmers, T. Furubayashi, M. Albrecht, and U. Gradmann, J. Appl. Phys. **70**, 5764 (1991).

[4] U. Gradmann, J. Korecki, and G. Waller, Appl. Phys. A **39**, 101 (1986).

[5] U. Gradmann and G. Waller, Surf. Sci. **116**, 539 (1982).

[6] M. Przybylski and U. Gradmann, Surf. Sci. **116**, 539 (1987).

[7] U. Gradmann, G. Liu, H. J. Elmers, and M. Przybylski, Hyp. Int. **57**, 1845 (1990).

[8] H. J. Elmers, J. Hauschild, H. Höche, U. Gradmann, H. Bethge, D. Heuer, and U. Köhler, Phys. Rev. Lett. **73**, 898 (1994).

[9] H. J. Elmers, J. Hauschild, H. Fritzsche, G. Liu, U. Gradmann, and U. Köhler, Phys. Rev. Lett. **75**, 2031 (1995).

[10] H. J. Elmers, J. Hauschild, and U. Gradmann, Phys. Rev. B **54**, 15224 (1996).

[11] N. Weber, K. Wagner, H. J. Elmers, J. Hauschild, and U. Gradmann, Phys. Rev. B **55**, 14121 (1997).

[12] H. J. Elmers, J. Magn. Magn. Mater. **185**, 274 (1998).

[13] J. Hauschild, U. Gradmann, and H. J. Elmers, Appl. Phys. Lett. **72**, 3211 (1998).

[14] H. J. Elmers, J. Hauschild, and U. Gradmann, Phys. Rev. B **59**, 3688 (1999).

[15] O. Pietzsch, A. Kubetzka, M. Bode, and R. Wiesendanger, Phys. Rev. Lett. **84**, 5212 (2000a).

[16] O. Pietzsch, A. Kubetzka, D. Haude, M. Bode, and R. Wiesendanger, Rev. Sci. Instr. **71**, 424 (2000b).

[17] H. J. Elmers, Int. J. Mod. Phys. B **9**, 3115 (1995).

[18] O. Pietzsch, A. Kubetzka, M. Bode, and R. Wiesendanger, Science **292**, 2053 (2001).

[19] P. Bödeker, A. Hucht, A. Schreyer, J. Borchers, F. Güthoff, and H. Zabel, Phys. Rev. Lett. **81**, 914 (1998).

[20] A. Kubetzka, M. Bode, O. Pietzsch, and R. Wiesendanger, Phys. Rev. Lett. **88**, 057201 (2002).

[21] A. Hubert and R. Schäfer, *Magnetic Domains*, Springer (1998).

[22] E. Magyari and H. Thomas, Phys. Scripta **T44**, 55 (1992).

[23] H.-B. Braun, Phys. Rev. B **50**, 16485 (1994).

[24] M. Bode, M. Getzlaff, and R. Wiesendanger, Phys. Rev. Lett. **81**, 4256 (1998).

[25] R. Wiesendanger, M. Bode, and M. Getzlaff, Appl. Phys. Lett. **75**, 124 (1999).

[26] R. Wiesendanger, H. J. Güntherodt, G. Güntherodt, R. J. Gambino, and R. Ruf, Phys. Rev. Lett. **65**, 247 (1990).

[27] M. Kleiber, M. Bode, R. Ravlić, and R. Wiesendanger, Phys. Rev. Lett. **85**, 4606 (2000).

[28] Chr. Wittneven, R. Dombrowski, M. Morgenstern, and R. Wiesendanger, Phys. Rev. Lett. **81**, 5616 (1998).

[29] J. C. Slonczewski, Phys. Rev. B **39**, 6995 (1989).

[30] D. Wortmann, S. Heinze, P. Kurz, G. Bihlmayer, and S. Blügel, Phys. Rev. Lett. **86**, 4132 (2001).

[31] M. Kleiber, M. Bode, R. Ravlić, N. Tezuka, and R. Wiesendanger, J. Magn. Magn. Mater. **240**, 64 (2002).

[32] V.A. Ukraintsev, Phys. Rev. B **53**, 11176 (1996).

[33] N.D. Lang, Phys. Rev. B **34** 5947 (1986).

[34] J. Bardeen, Phys. Rev. Lett. **6**, 57 (1961).

[35] R.M. Feenstra, J.A. Stroscio, and A.P. Fein, Surf. Sci. **181** 295-306 (1987).

[36] S.N. Okuno, T. Kishi, and K. Tanaka, Phys. Rev. Lett. **88**, 066803 (2002).

[37] T.P. Pareek and P. Bruno, Phys. Rev. B **63**, 165424 (2001).

[38] A. Wadas and H.J. Hug, J. Appl. Phys. **72**, 203 (1992).

[39] M. Bode, S. Heinze, A. Kubetzka, O. Pietzsch, X. Nie, G. Bihlmayer, S. Blügel, and R. Wiesendanger, Phys. Rev. Lett. **89**, 237205 (2002).

[40] M. Bode, A. Kubetzka, S. Heinze, O. Pietzsch, R. Wiesendanger, M. Heide, X. Nie, G. Bihlmayer, and S. Blügel, J. Phys.: Cond. Matter **15**, S679 (2003).

[41] J. Tersoff, and D. R. Hamann, Phys. Rev. B **31**, 805 (1985).

[42] J. A. Stroscio, D. T. Pierce, A. Davies, R. J. Celotta, and M. Weinert, Phys. Rev. Lett. **75**, 2960 (1995).

[43] M. Bode, A. Kubetzka, O. Pietzsch, and R. Wiesendanger, Appl. Phys. A **72**, S149 (2001).

[44] M. F. Crommie, C. P. Lutz, and D. M. Eigler, Nature **363**, 524 (1993).

[45] J. Li, W.-D. Schneider, R. Berndt, O. R. Bryant, and S. Crampin, Phys. Rev. Lett. **81**, 4464 (1998).

[46] G. A. Fiete, J. S. Hersch, E. J. Heller, H. C. Manoharan, C. P. Lutz, and D. M. Eigler, Phys. Rev. Lett. **86**, 2392 (2001).

[47] M. A. Schneider, L. Vitali, N. Knorr, and K. Kern, Phys. Rev. B **65**, 121406(R) (2002).

[48] W. Erley and H. Ibach, Sol. State Commun. **37**, 937 (1981).

[49] K. von Bergmann, M. Bode, A. Kubetzka, M. Heide, S. Blügel, and R. Wiesendanger, Phys. Rev. Lett. **92**, 046801 (2004).

[50] M. Heide, group of Prof. S. Blügel, Institut für Festkörperforschung, Forschungszentrum Jülich (2003).

[51] M. Bode, O. Pietzsch, A. Kubetzka, and R. Wiesendanger, J. Electr. Spectr. Relat. Phenom. **114-116**, 1055 (2001a).

3.2.8 Theoretical study of the magnetic ordering in nanostructures

E. Y. Vedmedenko, K. von Bergmann, A. Kubetzka, N. Mikuszeit, O. Pietzsch, M. Bode, H. P. Oepen, and R. Wiesendanger

Introduction

Microscopic and macroscopic physical properties of a magnet - hysteresis, magnetotransport and magnetooptical properties, excitation spectrum etc. - in many respects are determined by the configuration of magnetization [1–4]. Therefore, the magnetic ordering on different length scales is one of the central questions of magnetism. The ordering of magnetization is a cooperative effect made possible, below a critical temperature, by the interactions between the magnetic moments of the unpaired electrons throughout a solid. Hence, the understanding of the magnetic structure requires knowledge of the magnetic properties of the individual moments, the interactions between them, and their collective behavior. The magnetization configuration is influenced by many factors, some of the more important of which are spin value and dimensionality, the degree of structural and magnetic disorder, the temperature, and the presence of competing interactions.

A classification of experimentally available magnetic structures may be given in terms of the dimensionality modulation: three-dimensional systems (3D), like bulk materials or thin films; two-dimensional systems (2D), like surfaces, ultrathin films and multilayers; one-dimensional systems (1D), like nanowires; and so-called zero-dimensional materials with all three dimensions on the nanometer scale like small atomic clusters or nanoparticle arrays. With decreasing dimensionality of a magnetic object new factors determining the magnetic ordering come into play. One of the most important factors for the nanomagnetic ordering is the discrete structure of an atomic lattice which is usually neglected in the micromagnetic or mean-field calculations.

During the last years we could reach a considerable progress in the area of application of classical Monte-Carlo (MC) calculations to real magnetic systems [5–7]. A large advantage of the MC approach is that in contrast to the micromagnetic scheme, where a magnetic material is represented by blocks of a continuous medium, a discrete lattice structure of a specific material can be introduced into the calculations. Introduction of lattice symmetry into simulations provides a unique opportunity to account for the effects arising from the discrete nature of matter. Modern micromagnetic and MC computational schemes are able to describe large systems consisting of many tens thousands of atoms [5]. The long-range magnetostatic interactions and temperature can be incorporated into the model Hamiltonian with reasonable efforts. Due to these advantages the MC simulations are successfully applied for many structural phenomena such as magnetization reversal, domain or vortex formation, and spin reorientation transitions [5–7]. Since magnetic ordering is a complicated many-body problem driven by minimization of the total energy this method is extremely powerful

for the description of ground state properties of magnets.

Theoretical Methods

Monte-Carlo Simulations

In the Monte-Carlo approach, magnetization configurations are treated by a model Hamiltonian. The Hamiltonian usually includes magnetic anisotropy energy, spin-spin interaction energies, and the interaction of magnetic moments with an external magnetic field. The calculations with atomistic resolution are very computer power demanding. The computer demand is especially high when the long-range dipolar interaction is considered. For studies of magnetic ordering in objects with reduced dimensionality the dipolar coupling plays a very important role, as it can compete with the exchange interaction due to its long range character. Hence, it must be considered in calculations. This, however, means that large samples can be treated only with periodic boundary conditions, i.e. that one cannot address nanostructures of finite dimension in the conventional MC scheme. Periodic boundaries, in turn, in many cases can introduce artificial periodicity and other unwanted effects in calculated structures. To overcome these difficulties we have developed a scaling approach [8] which enables us to consider very large samples (up to 1 μm) with open boundary conditions which could not be introduced directly in an atomistic numerical computation. In this approach we introduce into the Hamiltonian an effective dimensionless parameter which permits to change the mesh of the calculation in dependence on specific objectives of the system. The developed code has been successfully applied to study the magnetic microstructure of the thickness dependent spin reorientation transition in Co/Au(111). Results of the computer investigation [5] showed an astoundingly good correspondence with the experiment carried out shortly before and led to a microscopic understanding of the spin reorientation transition in the first- and the second-order magnetocrystalline anisotropy approximation [5–7]. In the last years we have applied this technique to the theoretical study of magnetic properties of nanoplatelets [14], ultrathin nanowires [15] and frustrated magnetic ordering in low-dimensional quasicrystals [16].

Phenomenological calculation of the orientation dependent exchange energy loss due to formation of a domain wall

If the exchange interaction is isotropic it cannot affect the global orientation of domain walls in bulk crystals of cubic symmetry as both the spin and the real space are isotropic. Hence, in bulk crystals and ultrathin films the magnetic microstructure is mainly determined by the demagnetizing energy and the anisotropy [11]. On the other hand, in films of a few monolayer thickness the density of nearest neighbor atomic bonds per unit length may differ for different crystallographical directions because of reduced symmetry, i.e. the real space is not isotropic any more. In addition, the demagnetizing energy is highly reduced in the ultrathin film limit [12, 13]. This

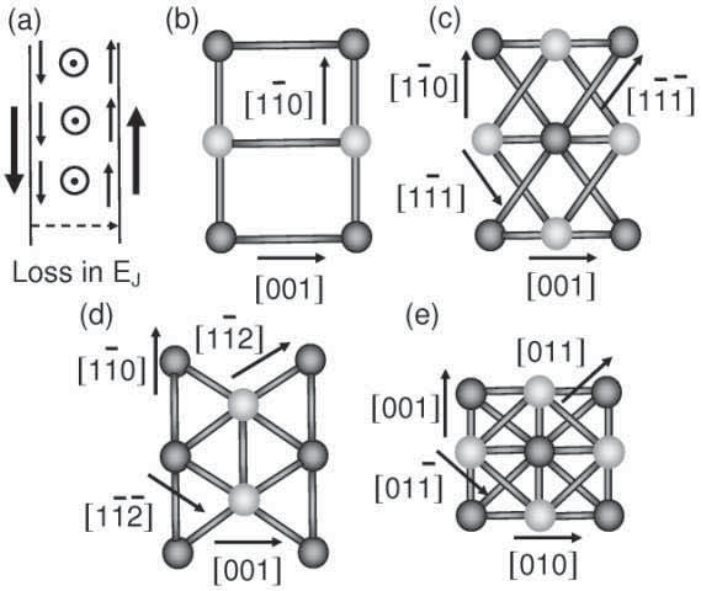

Figure 3.57: Schematic top view of a Bloch wall, the magnetization is represented by arrows **(a)**. Top view of unit cell of 2 ML thick $sc(110)$ **(b)**, $bcc(110)$**(c)**, $fcc(110)$**(d)** and $fcc(100)$**(e)** films. Dark and light balls denote the atoms belonging to the first and the second layer correspondingly. Nearest neighbor bonds are shown as connections between the atoms.

may lead to the orientational dependency of the exchange energy and, hence, to the preference of some crystallographical orientations. We have studied that possibility systematically within a simple analytical approach.

Fig. 3.57 shows a top view of a conventional Bloch wall (a) and unit cells of a double-layer with an $sc(110)$ (b), a $bcc(110)$ (c), a $fcc(110)$ (d) and a $fcc(100)$ (e) crystalline lattice. Atoms are sketched as balls where dark ones belong to the surface and light balls to the subsurface layer. Connections between atoms indicate nearest neighbor bonds. From Fig. 3.57(a) it is clearly visible that the magnetization rotates along an axis perpendicular to the plane of the wall while magnetic moments belonging to planes which are parallel to the plane of the wall are parallel. Since in a ferromagnet neighboring spins hold the lowest energy when they are parallel, the loss in the exchange energy due to the wall formation results from the bonds which have non-zero projection on the direction perpendicular to the course of the wall. For example, if the wall is oriented along the [010] direction of the $fcc(100)$ surface (Fig. 3.57e) the magnetic moments connected by [010] bonds will be parallel while moments connected by [001] bonds will have a maximal possible mutual angle and, consequently, a maximal increase in the exchange energy $\triangle E_J{}^{[001]}$. The moments connected by [011] and $[01\bar{1}]$ bonds will have intermediate mutual angles as they are neither parallel nor perpendicular to the direction of energy loss. It means, that the local increase in the exchange energy due to the magnetization rotation in a domain

Table 3.1: $\triangle E_J^{[xyz]}$ and the projections of nearest-neighbor bonds onto the direction perpendicular to the plane of the domain wall for double layer films with (110) surface orientation.

Stacking	Wall orientation $[xyz]$	$\triangle E_J^{[xyz]}$/ unit cell [a.u.]	$P_{\perp to[xyz]}$[a] of bonds running along		
			[001](4)	$[1\bar{1}0]$ (4)	$[1\bar{1}1]$ (8)
bcc	[001]	8.52	0	$\frac{1}{\sqrt{2}}$	$\frac{1}{\sqrt{2}}$
(110)	$[1\bar{1}0]$	6.00	$\frac{1}{2}$	0	$\frac{1}{2}$
	$[1\bar{1}1]$	6.76	$\frac{1}{\sqrt{6}}$	$\frac{\sqrt{3}}{2}$	$\frac{1}{\sqrt{6}}$
			$[1\bar{1}0](3)$	$[1\bar{1}2](4)$	$[1\bar{1}\bar{2}](4)$
fcc	[001]	7.00	1	$\frac{1}{2}$	$\frac{1}{2}$
(110)	$[1\bar{1}0]$	5.65	0	$\frac{1}{\sqrt{2}}$	$\frac{1}{\sqrt{2}}$
	$[1\bar{1}2]$	5.74	$\sqrt{\frac{2}{3}}$	$\sqrt{\frac{2}{3}}$	$\frac{1}{\sqrt{12}}$
sc			[001](2)	$[1\bar{1}0](2)$	
(110)	[001]	1.41	0	$\frac{1}{\sqrt{2}}$	
	$[1\bar{1}0]$	2.00	1	0	

[a] Number of bonds per unit cell is given in brackets.

wall will be proportional to the projection of an atomic bond on the axis perpendicular to the wall orientation.

To obtain losses in the exchange energy due to formation of a domain wall in this model, in a first step projections of all bonds to the axis perpendicular to the plane of the wall ($P_{\perp to[xyz]}$) were calculated for single and double layers of (100), (111) and (110) surfaces of *bcc*, *fcc* and *sc* crystals. The nearest neighbor bonds have been assumed to be of unit length. The length and the number of projections $P_{\perp to[xyz]}$ for double layers with (110) surface are brought together in Table 3.1. The loss in the exchange energy per unit cell for a wall along one of the $[xyz]$ directions has then been calculated by summing up the exchange coupling constant ($J_{[xyz]} = 1.0$) multiplied by $P_{\perp to[xyz]}$ for all bonds in the unit cell:

$$\triangle E_J^{[xyz]}[a.u./unit\ cell] = \sum_i J_{[xyz]} \cdot P_{\perp to[xyz]}$$

For a wall along $[1\bar{1}2]$ of an $fcc(110)$ lattice, for example, this results in (see also Table 3.1):

$$\triangle E_J^{[1\bar{1}2]} = 3 \cdot \sqrt{\frac{2}{3}} + 4 \cdot \sqrt{\frac{2}{3}} + 4 \cdot \frac{1}{\sqrt{12}} = 5.74\ [a.u.]$$

The exchange energy of a domain wall per unit cell is smallest for the $[1\bar{1}0]$ direction of the $bcc(110)$ and for the [001] direction of the $sc(110)$ surface. In case of an $fcc(110)$ crystal two orientations have similar energy. These are the $[1\bar{1}2]$ direction

with $\triangle {E_J}^{1\bar{1}2} = 5.74$ and $[1\bar{1}0]$ with $\triangle {E_J}^{1\bar{1}0} = 5.65$. Hence, the exchange energy cost in the systems described above is orientation dependent. The preferential orientations of walls derived in the phenomenological model are $[1\bar{1}0]$ for $bcc(110)$ and [001] for $sc(110)$ crystalline films. For $fcc(110)$ the wall orientation is defined by the competition between $[1\bar{1}0]$ and $[1\bar{1}2]$ directions. The cost in the exchange energy $\triangle {E_J}^{xyz}$ for other surfaces is constant and does not depend on the wall orientation. Hence, for [001] and [111] surfaces of a cubic crystal the domain walls are predicted to have no preferential orientation. The results described above give a quantitative measure of the orientation dependent exchange energy loss due to formation of a domain wall.

3.2.9 The anisotropy in the orientation of magnetic domain walls

In the following we describe results of a Monte-Carlo study on the orientation of domain walls in ultrathin films and nanowires and compare the theoretical results with experimental data and the phenomenological approach.

Ultrathin Films

First we simulate the orientation of domain walls in ultrathin films with different atomic symmetries and perpendicular magnetic anisotropy. The system Hamiltonian reads:

$$\begin{aligned} H &= -\sum_{<i,j>} J_{[xyz]} \mathbf{S_i} \cdot \mathbf{S_j} + \mathbf{k_1} \sum_{\mathbf{i}} \sin^{\mathbf{2}} \theta \\ &+ D \sum_{i,j} \left(\frac{\mathbf{S_i} \cdot \mathbf{S_j}}{r_{ij}^3} - 3 \frac{(\mathbf{S_i} \cdot \mathbf{r_{ij}})\,(\mathbf{S_j} \cdot \mathbf{r_{ij}})}{r_{ij}^5} \right), \end{aligned}$$

where $J_{[xyz]}$ denotes the effective nearest neighbor exchange coupling constant, D is the dipolar coupling parameter, θ and φ are the spherical angles and $\mathbf{r_{ij}}$ the vector between sites i and j. The coefficient k_1 is the first-order anisotropy per atom. For the MC computations we consider one or two layers of classical, three-dimensional magnetic moments $\mathbf{S}$ on different surfaces of sc, fcc and bcc lattices of about 20000 effective magnetic sites. The MC procedure is described elsewhere [5]. We use a realistic ratio of the exchange and the dipolar constants $D/J = 10^{-3}$. The exchange constants between all pairs of nearest neighbors are identical. The anisotropy constants have been widely varied in the regime of vertical and in-plane magnetization. The thickness of domain walls decreases with increasing absolute value of k_1. However, the orientation of domain walls is not influenced by k_1 showing that the mechanism of wall orientation described here is distinct from the one observed in bulk material, which is governed by magnetic anisotropy and dipolar energy.

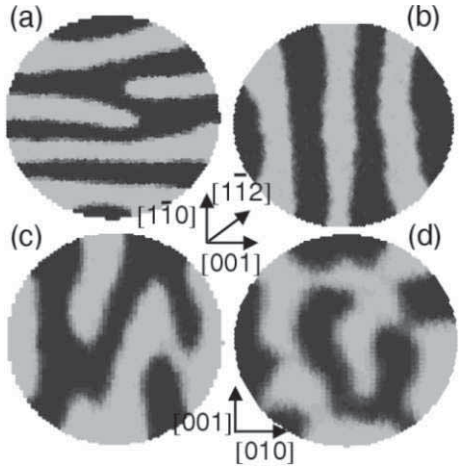

Figure 3.58: Top-view of MC domain configurations in 600 nm large and 2 ML thick samples with: $sc(110)$ **(a)**, $bcc(110)$ **(b)**, $fcc(110)$ **(c)** and $fcc(100)$ **(d)** surfaces. Opposite domains are imaged as dark and light areas. Exchange interactions are isotropic, $kT = 0.05J$, $k_1 = 9 \cdot 10^{-3}J$.

Fig. 3.58 shows typical MC low-temperature domain configurations found for $sc(110)$ (a), $bcc(110)$ (b), $fcc(110)$ (c) and $fcc(100)$ (d) surfaces while Fig. 3.57 gives the structure of the corresponding unit cells. The domain walls in $sc(110)$ films are mainly oriented along [001], while the walls in $bcc(110)$ films are oriented along the [1$\bar{1}$0] direction (Fig. 3.58(a),(b) and Fig. 3.57 (b),(c)). The domain walls of $fcc(110)$ film (Fig. 3.58c and Fig. 3.57d) are more disordered and can run along [1$\bar{1}$0], [1$\bar{1}$2] or intermediate crystallographic directions. However, one never finds a [001] orientation. The domain pattern of an $fcc(100)$ film, shown in Fig. 3.58d, is completely disordered. All possible orientations of domain walls can be found in the magnetization configuration. Similar results have been obtained for all other surfaces of cubic crystals. Thus, for isotropic exchange interactions the orientation of domain walls of (110) surfaces of cubic crystals is highly anisotropic while it is not the case for the (100) and (111) surface orientations. Those results are consistent with experiments where anisotropic wall patterns have been found for Fe/W(110) films [15] while a disordered configuration has been revealed for a Co/Au(111) [17]. In addition, the results of MC simulations are in perfect agreement with those obtained in the framework of the phenomenological model described in Section 3.2.8.

In conclusion, we demonstrate that the orientation of magnetic domain walls in ultrathin single crystalline films of cubic symmetry with (110) surface orientation is highly anisotropic while other surface orientations lead to isotropic wall configurations. The anisotropy is due to the orthorhombic-like symmetry of (110) surfaces of cubic crystals, which leads to an orientation dependent density of the nearest neighbor bonds.

Fe nanowires on W(110)

One experimentally accessible and, for future applications, very perspective geometrical shape is a so-called nanowire - a quasi one-dimensional structure of infinite length and lateral dimensions on the nanometer scale. The nanowire geometry is particularly advantageous for the investigation of the orientation of domain walls as, according

to continuum theory of magnetism, the orientation of a domain wall is governed by a minimization of the total wall length, i.e., the walls should generally be oriented perpendicularly to the sides of a wire.

For many experimental systems, e.g. Fe/Cu(100), the shortest wall-path coincides with one of the crystallographic axes which makes it impossible to distinguish between the role of the lattice for the domain formation and other effects. Only if the shortest distance is different from all principal axes of a lattice the mechanism underlying the orientation of the domain walls can be revealed. A suitable and experimentally well-studied model system are double layer (DL) Fe nanowires on stepped W(110) [18, 19] being characterized by perpendicularly magnetized domains separated by domain walls. Together with *ab-initio* electronic structure calculations [20] this led to a comprehensive understanding of the electronic as well as the magnetic properties. The relationship between the orientation of domain walls and the orientation of the DL Fe stripes, however, has not yet been investigated systematically.

We have analysed the influence of the discrete nature of an atomic lattice on the orientation of domain walls in nanowires experimentally and by means of the Monte-Carlo simulations. Scanning tunneling microscopy on areas with different local miscut orientations reveals that the domain walls are oriented along the $[1\bar{1}0]$ direction, regardless of the orientation of the nanowires. This observation is inconsistent with continuum micromagnetic theory. Employing Monte-Carlo simulations (MCS) we demonstrate that the wall orientation is determined by the underlying crystalline lattice. Accordance with the experiment can be achieved if the film relaxation is taken into account by a reasonable choice of the magnetic exchange constants J_{ij}. The magnetic anisotropy and the magnetostatic energy, which can align walls along certain crystallographic directions in bulk material, do not play any role for the wall orientation. We regard these results to be valid for a large class of low symmetry ultrathin ferromagnetic films.

The experiments have been performed in a commercial variable temperature STM attached to a five-chamber UHV system. The instrument is equipped with an $x - y$ sample positioning facility which allows to access different areas on the same sample. We used etched tungsten tips for the measurements. Fe was deposited onto the W(110) substrate by molecular beam epitaxy at a pressure $p \leq 1 \times 10^{-10}$ mbar. To achieve step flow growth the crystal was held at $T = 500$ K during thin film deposition. Simultaneously to constant current images, maps of the differential conductance $\mathrm{d}I/\mathrm{d}U$ were recorded by means of lock-in technique.

Figure 3.59 shows the topography (a) and maps of differential conductance (b-d) of 1.7 ML Fe/W(110). While the $\mathrm{d}I/\mathrm{d}U$ map of Fig. 3.59(b) has been measured simultaneously with and at the same position as the topographic image, the $\mathrm{d}I/\mathrm{d}U$ maps of Fig. 3.59(c) and (d) show other areas of the same sample which exhibit different local miscut orientations. In any case the Fe DL nanowires can be distinguished from sample locations which are covered by a single Fe layer (SL) due to their different electronic properties resulting in a $\mathrm{d}I/\mathrm{d}U$ signal that is lower for the SL than for the DL. The DL nanowires shown in Fig. 3.59(a,b) extend approximately along [001], the

ones in Fig. 3.59(c) along [1$\bar{1}$0], while in Fig. 3.59(d) the wire direction is intermediate, roughly along [1$\bar{1}$1]. Due to unequal diffusion energies the Fe stripes grow smoothest along [001] and least smooth along [1$\bar{1}$0]. After initial pseudomorphic growth the high tensile strain starts to relax by insertion of dislocation lines in the Fe DL which run along the [001] direction. These are imaged as narrow black lines in the dI/dU maps. The double layer nanowire has a periodic magnetic structure with out-of-plane domains alternatingly magnetized up and down. These domains are separated by 180° in-plane domain walls. The typical distance between adjacent walls is 23 ± 2 nm [18]. Due to spin-orbit coupling we can differentiate between areas with out-of-plane and in-plane magnetization even with non-magnetic tips [19]. Since the bias voltage chosen for the measurements of Fig. 3.59 ($U = 5$ mV) is below the cross-over of domain and domain wall spectra (see Fig. 1(e) in Ref. [19]) the domain walls are imaged as white lines in this experiment. Regardless of the direction of the nanowires the domain walls run along the [1$\bar{1}$0] direction, i.e., perpendicular to the dislocation lines. As a consequence, the domain walls within the nanowires are infinitely long in the case of Fig. 3.59(c) (disregarding interruptions due to structural imperfections), and very short in case of Fig. 3.59(b) where they run perpendicular to the axis of the nanowire. More than that, the predominant [1$\bar{1}$0] direction is not even a principal direction of an ideal bcc-lattice as it does not coincide with the primitive vectors of the bcc-structure.

We have performed calculations following a widely used micromagnetic framework [21], where the nanowires consist of rectangular blocks of continuous material, resulting in a wall direction that is determined by a minimization of the wall length, i.e., perpendicular to the nanowire direction [Fig. 3.60(a)]. This result is not consistent with the experimental observation of Fig. 3.59. It even cannot be corrected by an additional in-plane anisotropy; this only leads to an alignment of the magnetization

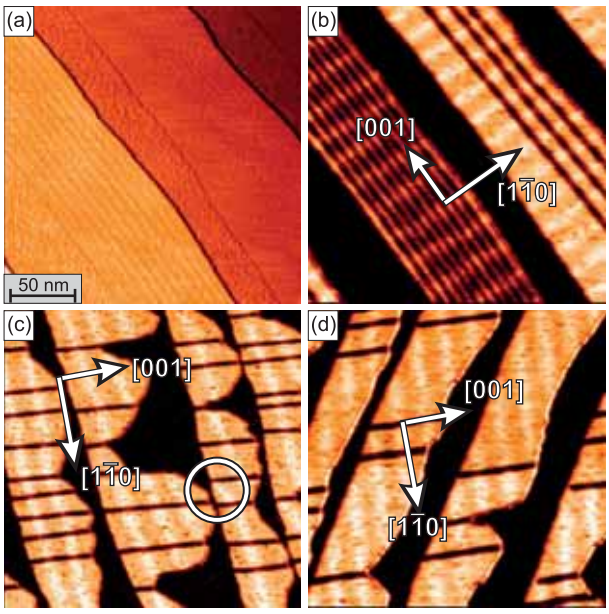

Figure 3.59: **(a)** Topography and **(b)-(d)** dI/dU maps of of 1.7 ML Fe/W(110) at different local miscut orientation. (a) and (b) were recorded simultaneously. The lateral scale is the same in all images. In all cases, domain walls (white lines) are oriented along [1$\bar{1}$0], regardless of the orientation of the nanowires. Parameters: $U = 5$ mV, $I = 0.5$ nA, $T = 75$ K (b, c) and 120 K (d).

within the wall with no consequences for the wall direction. The situation here is distinct from thicker films or bulk material, were walls can couple to certain anisotropy directions due to an energy difference of Bloch and Néel walls, which are energetically almost degenerate in the ultrathin wires.

Since the continuum model is obviously inadequate to describe the experimental results, we performed Monte-Carlo simulations using the system Hamiltonian:

$$\begin{aligned} H &= -\sum_{<i,j>} J_{hkl}\, \mathbf{S_i} \cdot \mathbf{S_j} \\ &+ D \sum_{i,j} \left(\frac{\mathbf{S_i} \cdot \mathbf{S_j}}{r_{ij}^3} - 3 \frac{(\mathbf{S_i} \cdot \mathbf{r_{ij}})\,(\mathbf{S_j} \cdot \mathbf{r_{ij}})}{r_{ij}^5} \right) \\ &+ K_1 \sum_i \sin^2\theta + K_2 \sum_i \sin^4\theta \\ &- K_p \sum_i \sin^2\theta \cos^2(\varphi - \beta)\,, \end{aligned}$$

where J_{hkl} denotes the effective nearest neighbor exchange coupling constant in $[hkl]$ direction, D is the dipolar coupling parameter, θ and φ are the spherical angles and $\mathbf{r_{ij}}$ the vector between sites i and j. The coefficients K_1 and K_2 are the first- and second-order anisotropy constants, respectively. K_p is an in-plane anisotropy constant. The in-plane anisotropy can have any angle β with respect to the x-axis. For the MC computations we consider two layers of classical, three-dimensional magnetic moments $\mathbf{S}$ on a bcc(110) lattice of about 20000 effective magnetic sites. As in the previous case we use a realistic ratio of exchange and dipolar constants $D/J = 10^{-3}$. The anisotropy constants have been widely varied in the regime of the vertical magnetization. The best agreement with the experimental results (domain width of 20–25 nm and wall width of 6–9 nm) give $K_1 = (1.6\text{–}2.0) \cdot K_d$, $K_2 = (0\text{–}0.7) \cdot K_d$, $K_p = (0\text{–}0.6) \cdot K_d$ with $K_d = 2\pi M_s^2$ the shape anisotropy constant. The value of the out-of-plane anisotropy is in good agreement with a recent theoretical result [20] which gives $K_1 = (2\text{–}2.1) \cdot K_d$.

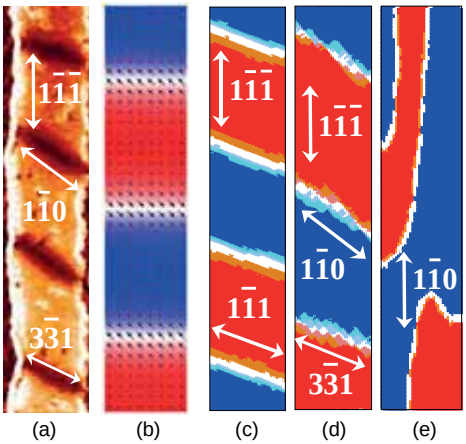

Figure 3.60: Top-view of simulated nanowire sections of 20 nm (a)-(d) and 40 nm width (e): **(a)** continuum theory, isotropic exchange. MCS: **(b)** $J_{1\bar{1}0} : J_{1\bar{1}1} : J_{001} = 0 : 1 : 1$ ('isotropic exchange'). **(c)** $J_{1\bar{1}0} : J_{1\bar{1}1} : J_{001} = 1 : 3 : 6$. **(d)** $J_{1\bar{1}0} : J_{1\bar{1}1} : J_{001} = 4 : 2 : 1$. **(e)** $J_{1\bar{1}0} : J_{1\bar{1}1} : J_{001} = 4 : 2 : 1$.

We have performed calculations for films, single wires and arrays of three wires with periodic boundary conditions along the wires and open boundary conditions in the perpendicular direction.

A typical result for the case of $[1\bar{1}\bar{1}]$ oriented, 20 nm wide nanowires is given in Fig. 3.60(b). We don't find any walls perpendicular to the sides of the wires as expected from the continuum theory. The domain walls are mainly oriented along $[1\bar{1}1]$. That orientation is preferred as the length of a wall in $[1\bar{1}0]$ direction is considerably larger than that in $[1\bar{1}1]$. Thus, the total energy is smallest in case of $[1\bar{1}1]$ walls due to their smallest volume. In case of [001] or $[1\bar{1}0]$ oriented wires (not shown) the domain walls are perpendicular to the wire sides. Those results deviate from the experimental data. In the following we will explain the discrepancy by taking into account the lattice structure of the nanowires which differs from that of a bulk crystal.

Due to pseudomorphic growth the first two Fe layers adopt the lateral lattice constant of tungsten, which is about 10% larger than that of bulk iron. As a consequence, the Fe–Fe interlayer distance relaxes below the Fe bulk value [20]. This leads to a change of the interatomic distances. Namely, the neighbor distance in the $[1\bar{1}0]$ direction, marked red in Fig. 3.61, decreases to a value close to the nearest neighbor distance in bulk iron, and the spacings in $[1\bar{1}1]$ and $[1\bar{1}\bar{1}]$ direction (blue) are increased. Hence, instead of six nearest neighbors as in an ideal, 2 ML thick bcc(110) film, in Fe/W(110) all atoms have eight bonds of similar length. Following Ref. [20], the respective distances in units of the lattice constant of bulk Fe are $d_{001} = 0.95$, $d_{1\bar{1}1} = 1.10$, and $d_{1\bar{1}0} = 1.15$.

In the literature the calculation of J_{ij} as a function of relative position $\mathbf{r_{ij}}$ of the magnetic moments i and j has been performed for several ferromagnetic materials [22, 23]. These calculations show that the strength of the exchange coupling is a function of $\mathbf{r_{ij}}$. Especially interesting is the behavior of $J(\mathbf{r_{ij}})$ in Fe. For Fe a reduction in nearest neighbor spacing d_{NN} with respect to the bulk value drives the exchange towards antiferromagnetism. This effect has been made responsible for the fact that fcc-Fe is antiferromagnetic while bcc-Fe is a ferromagnetic material [24, 25]. This argument is also supported by the position of Fe on the Bethe-Slater curve, which is widely used in the physics of ferromagnetic alloys [25]. Thus, a decrease of the interatomic distance in [001] direction can lead—in contrast to other ferromagnets—to a reduction of the ferromagnetic exchange parameter.

For Fe nanowires on W(110) the situation is even more subtle due to hybridization

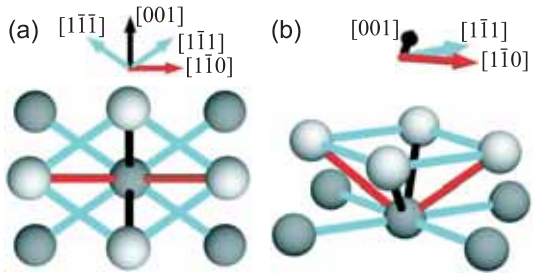

Figure 3.61: Unit cell of 2 ML Fe/W(110) in (a) top and (b) perspective view.

and polarization effects at the Fe/W interface. In recent studies [26, 27], the exchange stiffness of Fe films adsorbed on a W(110) surface has been calculated. The authors find that the exchange stiffness A, which is equal to $2JS^2/a$ for a bcc lattice, depends on the direction along which the spin-wave is excited. For one monolayer Fe/W(110) the exchange stiffness in the $[1\bar{1}0]$ direction is 4 times larger than in the [001] direction [27]. For a 2 ML film the difference is found to be smaller but the tendency remains the same. The physical reason for this anisotropic behavior can lie in changes of interatomic spacing, as discussed above, or in additional indirect spin interactions through the W substrate [27]. In any case, the dependence of the exchange interaction on $\mathbf{r_{ij}}$ must be taken into account in the simulation of the magnetic ordering.

According to this argumentation we introduce 3 different exchange constants J_{hkl} for the 3 nonequivalent pairs of neighboring magnetic moments. We have explored different ratios of $J_{1\bar{1}0} : J_{1\bar{1}1} : J_{001}$ (dark grey, light grey and black bonds in Fig. 3.61, respectively). Generally, the walls tend to be aligned along the axis of the strongest exchange coupling. For example for $J_{1\bar{1}0} : J_{1\bar{1}1} : J_{001} = 1 : 3 : 6$ we find all domain walls oriented in [001] direction, as can be seen in Fig. 3.60(c). The best overall accordance with the experiment is found for $J_{1\bar{1}0} : J_{1\bar{1}1} : J_{001} = 4 : 2 : 1$ [Fig. 3.60(d) and (e)]. For $[1\bar{1}1]$ nanowires [Fig. 3.60(d)] the majority of the walls follow the $[1\bar{1}0]$ axis. However, $[1\bar{1}1]$ walls can also be found. For $[1\bar{1}0]$ nanowires of 40 nm width [Fig. 3.60(e)] we also get $[1\bar{1}0]$ oriented domain walls which cannot be expected from the continuum approximation or for an undistorted lattice. The walls are not perfectly straight but show some irregularities. For example, the wall is forced out of the $[1\bar{1}0]$ direction at the rim of the nanowire. A similar behavior has also been found experimentally [see circle in Fig. 3.59(c)]. We have also explored different orientations and strengths of the in-plane anisotropy K_p. As already mentioned above the only effect of a strong K_p is an alignment of the magnetic moments in the wall along the respective axis and broadening of the walls. The orientation of domain walls is not influenced by K_p, in accordance with the continuum model [Fig. 3.60(a)], showing that the mechanism of wall orientation described here is distinct from the one observed in bulk material, which is governed by magnetic anisotropy and dipolar energy.

In conclusion, we have demonstrated by means of an experimental study and extended Monte-Carlo simulations that in contradiction to the continuum approximation the orientation of magnetic domain walls in ultrathin films is governed by the atomic lattice structure and the set of nearest neighbor moments. Therefore, the direction of the walls in nanostructures can be different from the shortest geometric path between the boundaries of a sample. The magnetic anisotropy and the magnetostatic energy which can govern wall orientations in bulk material, do not play any role in the ultrathin limit.

3.2.10 Noncollinear magnetism in quasicrystals

The last few years have shown a boom in investigations of the spin order in antiferromagnetic films [28, 29] motivated by the dramatic changes in the magnetic properties

of such systems induced by frustration. The magnetic frustration may, for example, lead to formation of unusual noncollinear magnetization configurations. In contrast to the rather well studied spin structure of antiferromagnets on periodic lattices, the antiferromagnetic ordering of quasicrystals is subject of ongoing scientific debate. The highly frustrated quasicrystalline structures are perfect candidates for a noncollinear magnetic ordering. Whereas an experimental finding of long-range antiferromagnetic order in rare-earth icosahedral quasicrystals [30] turned out to be an artefact [31], theoretical models that deal with magnetism in quasicrystals [34] are known to exhibit long-range magnetic order. Recent inelastic neutron scattering experiments on the Zn-Mg-Ho icosahedral quasicrystal [32] revealed a very peculiar diffuse scattering pattern with icosahedral symmetry at temperatures below 6K. Such a pattern, in principle, can originate from a noncollinear spin arrangement first suggested by Lifshitz from pure geometrical considerations [33]. However, real-space magnetic configurations leading to those long wave vector correlations remain obscure despite recent interesting results for quantum spins [34]. Thus, the knowledge about the spin structure on quasiperiodic tilings is of basic importance for experiments as well as for theoretical predictions of new phenomena, which can be expected due to nontrivial frustration effects.

In a recent theoretical study [16] we have derived stable low-temperature magnetization configurations of antiferromagnetic quasicrystals. The results obtained provide an explanation for the origin of the antiferromagnetic modulations observed experimentally in Ref. [32]. While the spin order in antiferromagnets is usually characterized by a periodic modulation described by wave vectors on the order of inverse atomic distances, the spin order in antiferromagnetic quasicrystals admits three-dimensional noncollinear structures consisting of several interpenetrating subtilings with longer wave vectors. Here we report on the details of the low-temperature antiferromagnetic ordering and the map of the local frustration for the octagonal tiling.

We discuss the antiferromagnetic Hamiltonian

$$H = J_{ij} \sum_{\langle i,j \rangle} \mathbf{S}_i \cdot \mathbf{S}_j - K_1 \sum_i (\mathbf{S}_i^z)^2 \tag{3.24}$$

where $\mathbf{S}_i$ is a three- or two-dimensional unit vector in the case of classical vector or xy-spins, and $\mathbf{S}_i^z$ is equal to ± 1 in the case of Ising spins (so $\mathbf{S}_i^x = \mathbf{S}_i^y = 0$); $\langle i,j \rangle$ denotes the nearest neighbor pairs. For an antiferromagnetic system, the exchange

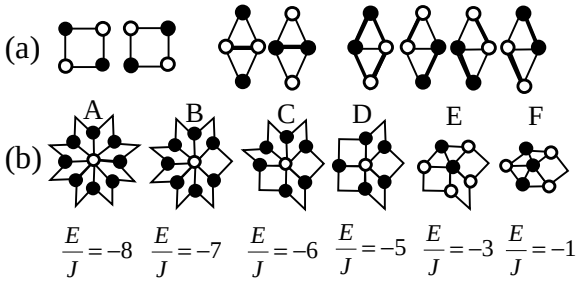

Figure 3.62: Configurations for a frustrated Ising antiferromagnet on (a) elementary tiles and (b) six local environments of the Ammann-Beenker tiling. Bold lines denote the frustrated bonds. The open and filled circles represent different spins.

parameter J_{ij} is positive, and neighboring antiparallel spins contribute a lower energy than parallel neighbors. The coefficient K_1 is the first-order anisotropy constant. Our Monte-Carlo simulations have been carried out on finite Ammann-Beenker tilings with free boundary conditions. The procedure is a simulated annealing method with at least 15 successive temperature steps [16]. At each temperature, the convergence of the relaxation process towards equilibrium has been observed for any initial configuration after a few thousand Monte Carlo steps per spin. Hence, the single-spin-update algorithm is efficient in our case. At the end of the cooling down process, the total energy is just fluctuating around its mean equilibrium value. To reduce boundary effects only the core of a tiling has been analyzed. The samples on the octagonal Ammann-Beenker structure, which we shall concentrate on in what follows, are circular, containing 2193, 11664 and 53018 magnetic moments.

The octagonal tiling consists of two motifs: a square and a rhombus of equal edge lengths a (Fig. 3.62(a)). The diagonal bonds are, usually, neglected in the calculations [34, 35]. We find this disregard physically questionable as the exchange coupling increases exponentially with decreasing interatomic distance. In the present investigation, the short diagonal of the rhombus and the sides of the motifs have been considered as nearest neighbors. We distinguish the two cases $J_d > 2J$ and $J_d < 2J$, where J_d denotes the interaction along the short diagonal and the interaction strength along the sides J is unity. The first case corresponds to a rapid growth of the exchange coupling with decreasing interatomic distance. The two nearest-neighbor bonds form six local environments with coordination numbers varying from 5 to 8 as shown in Fig. 3.62(b). They occur with relative frequencies $\nu_A = 17 - 12\sqrt{2} \approx 2.9\%$, $\nu_B = -41 + 29\sqrt{2} \approx 1.2\%$, $\nu_C = 34 - 24\sqrt{2} \approx 5.9\%$, $\nu_D = -14 + 10\sqrt{2} \approx 14.2\%$, $\nu_E = 6 - 4\sqrt{2} \approx 34.3\%$,

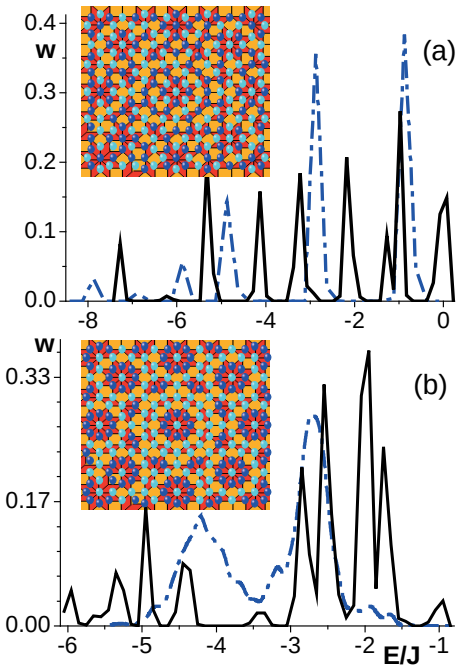

Figure 3.63: The frequency distribution of the energy per spin on the octagonal tiling for (a) Ising and (b) vector spins. Solid lines correspond to the case $J_d < 2J$, dashed lines to $J_d > 2J$. Purely antiferromagnetic interaction at $kT = 0.01J$ is considered. Top-views of portions of Monte-Carlo configurations with underlying tilings are shown as insets. The light and dark circles represent different spins in (a) and different energies in (b), respectively.

and $\nu_F = -1 + \sqrt{2} \approx 41.4\%$. Taking into account the short diagonals of the rhombic tiles increases the average coordination number of the tiling from 4 (the value without diagonals) to $8\nu_A + 7\nu_B + 6\nu_C + 5(\nu_D + \nu_E + \nu_F) = 8 - 2\sqrt{2} \approx 5.17$.

First we discuss the Ising system. The square tile of the octagonal structure is non-frustrated as every pair of the moments can be chosen to be antiparallel (Fig. 3.62(a)). If we had not taken the short diagonals of the rhombic tiles into account, the same would have been true for the entire tiling, and there would be no frustration, because the rhombic tiling is bipartite. Now, we consider spins on short diagonals as nearest neighbors, the rhombic tiles are always frustrated. If the energy of one nearest neighbor pair is minimized by having antiparallel spins, the third and forth spins cannot be chosen to minimize the energy of both of its neighbors (Fig. 3.62(a)). The magnetic moment will necessarily be parallel to one of the neighbors. For $J_d < 2J$ two out of six possible configurations have smaller energy as they possess only one pair of parallel nearest neighbors per rhombus instead of two (Fig. 3.62(a)). In this case spins can have one of six possible energy values corresponding to different local environments (Fig. 3.62(b)). For $J_d > 2J$ the four configurations with two parallel bonds have lowest energy as their weight is smaller than that of the strong diagonal coupling. The second case comprises much more different possibilities of energy distribution. To give a quantitative description of the local frustration we introduce a local parameter f

$$f = \frac{|E_{id}| - |E_i|}{|E_{id}|} \tag{3.25}$$

where E_i is an actual energy of a spin i and E_{id} is a ground state energy of a relevant unfrustrated vertex. With this nomenclature, only the central spins of the vertices F and E are magnetically frustrated $f_F = 0.4$ and $f_E = 0.8$ for $J_d = J < 2J$. The Monte-Carlo simulations confirm our reasoning based on the analysis of frustration. Fig. 3.63a gives the frequency distribution of the exchange energy per atom E for two cases and a top-view of a portion of Ising configuration with $J_d > 2J$. The energy distribution for $J_d < 2J$ simply reproduces the frequency of 6 vertex configurations. The "up" and "down" configurations are perfectly ordered and coincide with the black-and-white model of Niizeki [36]. For large J_d we find 8 possible energy values. The "up" and "down" subtilings, however, are spatially disordered (see inset Fig. 3.62a). We have calculated the magnetic structure factor

$$S^{zz}(\mathbf{k}) = \frac{1}{N} \sum_{\mathbf{r},\mathbf{r}'} e^{i\mathbf{k}\cdot(\mathbf{r}-\mathbf{r}')} \langle S^z_{\mathbf{r}} S^z_{\mathbf{r}'} \rangle \tag{3.26}$$

using the Monte-Carlo data for different samples. Here $\mathbf{k}$ is the wave vector and $S^z_{\mathbf{r}}$ is a vertical component of a magnetic moment at the position $\mathbf{r}$. The diffraction pattern of the Niizeki configuration coincides with that of quantum Monte-Carlo calculations (Fig. 5c,d of Ref. [34]), while the intensity map of the configuration Fig. 3.63a is almost structureless. It means that the Ising solution with $J_d < 2J$ reproduces in essence the antiferromagnetic superstructure, corresponding to a modulation vector

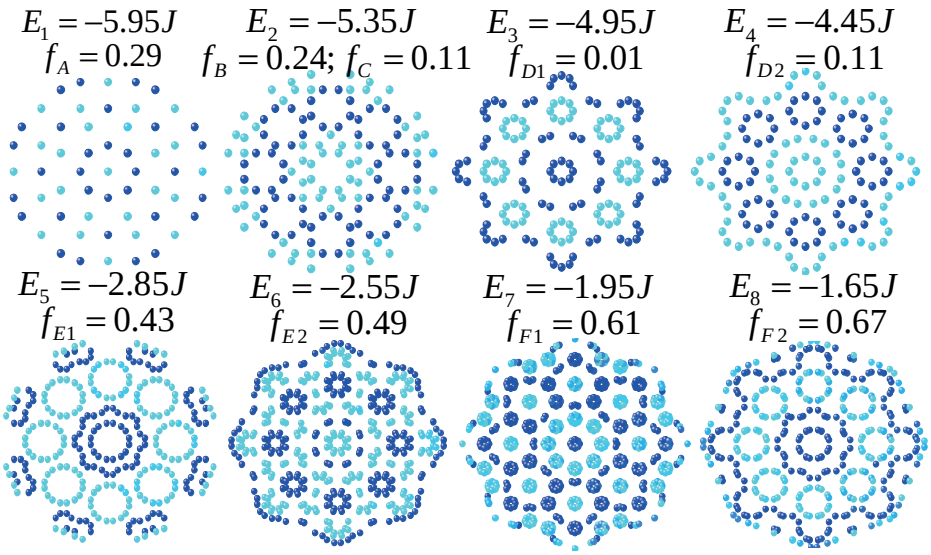

Figure 3.64: Spatial distribution of magnetic moments belonging to eight subtilings of a noncollinear configuration on an octagonal tiling consisting of 2193 spins. $J_d > 2J$. The light and dark circles represent positive and negative x-components of the magnetization. The in-plane components are not given for the sake of simplicity. Average values of the exchange energy E and the local frustration f per spin are indicated.

$\mathbf{q} = (\frac{1}{2}, \frac{1}{2}, \frac{1}{2}, \frac{1}{2})_{a^*}$ [32] in the octagonal tiling, whereas stronger coupling leads to a spin-glass state.

An exciting question is if the further minimization of the total energy and frustration by means of the noncollinear alignment of magnetic moments is possible. At first glance the magnetic structure of the low-temperature pure antiferromagnetic configuration seems to be rather disordered. The analysis of the local energies, however, reveals several characteristic energetic maxima in the frequency distribution shown in Fig. 3.63(b). The simple existence of the peaks means that there are different sorts of magnetic moments having well-defined relative orientation to their nearest neighbors. This orientation, however, is not associated with any absolute direction in space. Therefore, in accordance with the Mermin-Wagner theorem, no long-range order exists in two-dimensions with continuous symmetry, because thermal fluctuations result in a mean-square deviation of the spins from their equilibrium positions which increases logarithmically with the size of the system. The addition of a very weak anisotropy, which often exists in real samples, does not change the distribution of the exchange energy, but permits to anchor the absolute spatial orientation of the magnetization. Nevertheless, at first glance the total structure still looks spin-glass like. In the following, we will show that the antiferromagnetic structure of the octagonal tiling is perfectly ordered, but the order is non-trivial and unusual for periodic crystals. We concentrate on 3D vector spins while similar results for xy-spins have been obtained.

To obtain an absolute symmetry axis, we apply a very weak out-of-plane anisotropy

$K_1 \approx 10^{-3}J$ to the system. The squared vertical component of magnetization $(S^z)^2$ becomes finite. The positions of the energy peaks on the frequency diagram remain unchanged. All maxima are different from those of the Ising model. It means that the angles between the neighboring magnetic moments are not always equal to 180° or 0°, i.e., the magnetic structure is noncollinear. The different number of peaks — eight for $J_d < 2J$ and two for $J_d > 2J$ (Fig. 3.63(b)) — already tells us that, in contrast to the Ising case, the maxima do not coincide with the 6 vertices of the tiling. The minimal possible local energy increases from $-8J$ to approximately $-6J$ for $J_d = J$ or $-5.44J$ for $J_d = 2.2J$. The average energy per spin, however, decreases by more than $0.3J$ and reaches the value of $E \approx -2.85J$ and $E \approx -3.30J$ respectively. Hence, the increase of the entropy permits to minimize the average frustration and the total energy of the system.

Spatial arrangements of the magnetic moments as a function of the exchange energy are given in Fig. 3.64 for $J_d < 2J$ and in the inset to Fig. 3.64(b) for $J_d > 2J$. Each configuration of Fig. 3.64 represents a certain energy range corresponding to one of the eight peaks in the spectrum of Fig. 3.63(b). Colors represent the x-projection of the magnetization. The magnetic moments form 8 subtilings of different energy $(E_1, \ldots, E_8)$ which generally do not coincide with a specific vertex type. The splitting of the energy and frustration levels is described in detail in Fig. 3.64. For example the vertices B and C (Fig. 3.62 belong to the same energy maxima E_2 but have different local frustration $f_B = 0.24$, $f_C = 0.11$ (Fig. 3.64). At the same time the central spin of the vertex D can have either the energy E_3 or E_4 and, therefore, can have two different values of the frustration $f_{D1} = 0.01$ and $f_{D2} = 0.11$ depending on local surroundings. Thus, every configuration of the Fig. 3.64 can enclose either a part of the atomic places belonging to one vertex type or two different vertex types together. Nevertheless all structures have a perfect general spatial ordering. Each subtiling can be separated into the energetically degenerate 'right' and 'left' parts which also have a perfect quasiperiodic arrangement. However, not all 'right' or 'left' moments have identical orientation in space. Fig. 3.65 shows a perspective view of a portion of a typical Monte-Carlo configuration and the corresponding energy map. The central magnetic moment has the lowest energy and belongs to the E_1 subtiling.

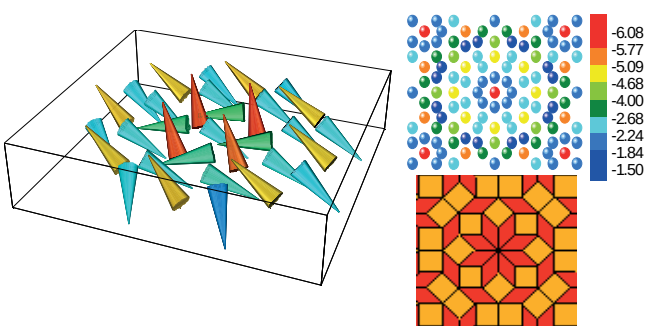

Figure 3.65: Perspective view of a portion of a Monte-Carlo configuration on an octagonal tiling. The top view of the patch and the energy map are shown as insets. Magnetic moments are represented as cones. The cones are colored according to their vertical magnetization. In the energy map inset, the colors encode the energy per moment.

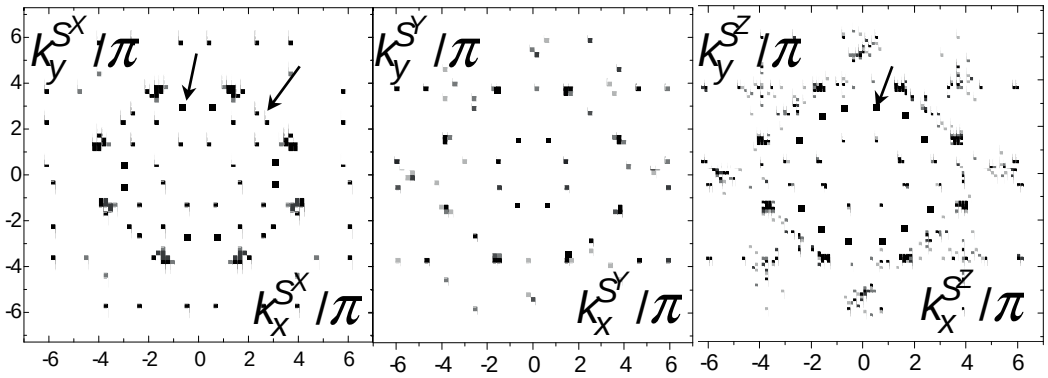

Figure 3.66: The calculated Bragg scattering of S^x, S^y and S^z component of magnetization for the antiferromagnetic superstructure. Reflexes indicated by arrows are new in comparison to previous studies [34].

Its 8 nearest neighbors have identical energies and correspond to the energy E_7 despite having different sets of mutual angles. The moments forming the next ring have energy E_6. The last ring consists of the alternating E_3 and E_6 spins. Fig. 3.65 shows one of the radially symmetric vertices. However, in the octagonal tiling vertices with different surrounding can also be found. The energy distribution is then different. Hence, the magnetic structure for $J_d < 2J$ is noncollinear and consists of eight interpenetrating subtilings. For $J_d > 2J$ we find only two subtilings of different energy.

A frequency distribution of the angle between nearest neighboring moments shows five characteristic angles close to 60°, 80°, 120°, 140° and 180° for small J_d and a single mutual angle of 110° for large J_d. Due to this noncollinearity the energy of the system is decreased. The diffraction pattern of the whole structure is more complex than that of the Ising or the quantum-mechanical [34] model. As the spin structure is noncollinear, not only the structure factor S^{zz}, but also S^{xx} and S^{yy} can be recognized (see Fig. 3.65). The eightfold S^{xx} and S^{zz} patterns contain additional long wave-vector peaks which could not be identified in the previous investigations [34]. In dependence on the anisotropy (or on the initial random configuration for $K_1 = 0$) new peaks also occur in S^{yy}. The Bragg reflexes found in our study select a subset of the wave vectors given in Ref. [33] where $n_1 + n_2 + n_3 + n_4$ is odd. Peaks with $n_1 + n_2 + n_3 + n_4$ even are extinct. The following wave vectors can be identified: $(1,0,0,0)$, $(1,-1,1,0)$, $(3,-2,1,1)$, $(3,-1,-1,2)$, $(1,1,-1,0)$, $(1,0,1,-1)$, $(0,2,-1,0)$, $(0,0,1,-2)$, $(-1,0,1,-3)$, $(0,2,-2,1)$, $(0,1,-2,2)$. Hence, the noncollinearity of the spin structure gives rise to selection rules different from those of collinear models [33, 34]. With increasing sample size the peaks become more diffuse and may correspond to the diffuse scattering signal of Ref. [32].

In conclusion, we demonstrate that the frustrated classical Ising system with antiferromagnetic coupling on a quasiperiodic octagonal tiling is perfectly ordered. All spins can be divided into 6 quasiperiodic (in the 3D physical space) or 6 periodic (in 6D periodic crystal) subtilings of different energy. Each subtiling corresponds to

the one of 6 vertex types of the Ammann-Beenker structure and is degenerated for 'up' and 'down' magnetic moments. Quantitatively, only two out of six subtilings are frustrated with the local coefficients $f_E = 0.4$ and $f_F = 0.8$. The vector spin system admits a three-dimensional noncollinear magnetic structure. For $J_d < 2J$, the whole structure can be decomposed into 8 subtilings of different energy which generally do not coincide with a specific vertex type. All subtilings are frustrated. However, the total degree of frustration and the energy of the system is minimized compared to the noncollinear case. The subtilings are degenerated with respect to the spin direction. The codirectional spins of every subtiling reveal perfect quasiperiodic ordering with a wave vector which is specific for a given subtiling.

References

[1] J. Brooke, T. F. Rosenbaum, G. Aeppli, Nature **413**, 6856 (2001).

[2] C. T. Black, C. B. Murray, R. L. Sandstrom, S. Sand, Science **290**, 5494 (2000).

[3] O. Pietzsch, A. Kubetzka, M. Bode, R. Wiesendanger, Science **292**, 5524 (2001).

[4] J. Fidler,T. Schrefl, W. Scholz, D. Suess, R. Dittrich, M. Kirschner J. Magn. Magn. Mater. **272**, 641 (2004).

[5] E. Y. Vedmedenko, H. P. Oepen, A. Ghazali, J. C. S. Lévy, J. Kirschner, Phys. Rev. Lett. **84**, 5884 (2000).

[6] E. Y. Vedmedenko, H. P. Oepen, J. Kirschner, J. Appl. Phys. **89**, 7145 (2001).

[7] E. Y. Vedmedenko, H. P. Oepen, J. Kirschner, Phys. Rev. B **66**, 214401 (2002).

[8] E. Y. Vedmedenko, A. Ghazali, J. C. S. Lévy, Phys. Rev. B **59**, 3329 (1999).

[9] H. J. G. Draaisma and W. J. M. de Jonge, J. Appl. Phys. **64**, 3610 (1988). bibitemOsb J.A. Osborn, Phys. Rev.**67**, 351 (1945).

[10] E.C. Stoner, Phil. Mag., ser. 7, vol.**36**, 803 (1945).

[11] D. Ha, R. Hertel, and J. Kirschner, Europhys. Lett. **64**, 810 (2003).

[12] E. Y. Vedmedenko, H. P. Oepen, J. Kirschner, J. Magn. Magn. Mater. **256**, 237 (2003).

[13] J. Millev, E. Y. Vedmedenko, H. P. Oepen, J. Phys. D: Appl. Phys. **36**, 2945 (2003).

[14] E. Y. Vedmedenko, K. von Bergmann, H. P. Oepen, R. Wiesendanger, J. Magn. Magn. Mater., in print (2005).

[15] E. Y. Vedmedenko, A. Kubetzka, K. von Bergmann, O. Pietzsch, M. Bode, J. Kirschner, H. P. Oepen, R. Wiesendanger, Phys. Rev. Lett. **92**, 077207 (2004).

[16] E. Y. Vedmedenko, U. G. Grimm, R. Wiesendanger, Phys. Rev. Lett. **93**, 076407 (2004).

[17] M. Speckmann, H. P. Oepen, and H. Ibach, Phys. Rev. Lett. **75**, 2035 (1995).

[18] A. Kubetzka, M. Bode, O. Pietzsch, and R. Wiesendanger, Phys. Rev. Lett. **88**, 057201 (2002).

[19] M. Bode, S. Heinze, A. Kubetzka, O. Pietzsch, X. Nie, G. Bihlmayer, S. Blügel, and R. Wiesendanger, Phys. Rev. Lett. **89**, 237205 (2002).

[20] I. Galanakis, M. Alouani, and H. Dreyssé, Phys. Rev. B **62**, 3923 (2000).

[21] *Object Oriented Micromagnetic Famework (OOMMF)*, http://math.nist.gov/oommf/ (2001).

[22] A. Liechtenstein, M. Katsnelson, V. Antropov, and V. Gubanov, J. Magn. Magn. Mater. **67**, 65 (1987).

[23] S. Frota-Pessôa, R. Muniz, and J. Kudrnovsky, Phys. Rev. B **62**, 5293 (2000).

[24] M. Hatherly, K. Hirakawa, R. Lowde, J. Mallett, M. Stringfellow, and B. Torrie, Proc. Phys. Soc. **84**, 55 (1965).

[25] Q. Pankhurst, L. Barquin, J. Wicks, R. McGreevy, and M. Gibbs, J. Phys.: Condens. Matter **9**, L375 (1997).

[26] R. Muniz and D. Mills, Phys. Rev. B **66**, 174417 (2002).

[27] R. Muniz, A. Costa, and D. Mills, J. Phys.: Condens. Matter **15**, S495 (2003).

[28] Ph. Kurz, B.H. Bihlmayer, K. Hirai, and S. Blügel, Phys. Rev. Lett. **86**, 1106 (2001).

[29] S. Heinze, M. Rode, A. Kubetzka, O. Pietzsch, X. Nie, S. Blugel, R. Wiesendanger, Science **288**, 1805, (2000).

[30] B. Charrier, B. Ouladdiaf, and D. Schmitt, Phys. Rev. Lett. **78**, 4637 (1997).

[31] T. J. Sato, H. Takakura, A. P. Tsai, and K. Shibata, Phys. Rev. Lett. **81**, 2364 (1998).

[32] T.J. Sato, H. Takakura, A.P. Tsai, K. Shibata, K. Ohoyama, and K.H. Andersen, Phys. Rev. B **61**, 476 (2000).

[33] R. Lifshitz, Mater. Sci. Eng. A **294**, 508 (2000).

[34] S. Wessel, A. Jagannathan, and S. Haas, Phys. Rev. Lett. **90**, 177205 (2003).

[35] U. Grimm and M. Baake, Aperiodic Ising Models, in *The Mathematics of Long-Range Aperiodic Order*, edited by R.V. Moody (Kluwer, Dordrecht, 1997) pp. 199.

[36] K. Niizeki, J. Phys. A: Math. Gen.**23**, 5011 (1990).

3.2.11 Magnetic force microscopy (MFM) studies

The following experiments have been performed using magnetic force microscopy (MFM) in ultrahigh vacuum by employing the frequency modulation (FM) technique as described by Albrecht et al. [1]. Details of the instrument and MFM imaging are described in section 3.6.2 (see also Ref. [2]). Basically, a ferromagnetic force sensor is scanned in a certain constant height h above the surface to detect the magnetostatic stray field of the sample, whereby on ferromagnetic samples the domain pattern is obtained (see section 3.2.12 and 3.2.13).

Using this technique, we investigated the magnetization reversal of epitaxially grown disordered ferromagnetic films with a substrate induced out-of-plane anisotropy ($La_{0.7}Sr_{0.3}MnO_3$ and $La_{0.7}Ca_{0.3}MO_3$ on $LaAlO_3$). In particular, we examined individual Barkhausen events and their size distribution with respect to self organized criticality and domain wall propagation through a disordered medium [3]. Moreover, we observed domain nucleation and the influence of structural defects [4] as well as the different zero field domain structures, which depend strongly on the magnetic history of the sample [5].

The same method can be utilized to visualize individual vortices on type II superconductors (see section 3.2.14). On the high T_c superconductor $Bi_2Sr_2CaCu_2O_{8+\delta}$ we studied the pinning behavior of individual vortices within a sample containing artificial columnar defects as well as intrinsic line defects [6–8].

3.2.12 An MFM investigation of the magnetization reversal of $La_{0.7}Sr_{0.3}MnO_3$ on $LaAlO_3$

A. Schwarz, M. Liebmann, U. Kaiser, T. W. Noh, D. W. Kim, and R. Wiesendanger

Introduction

The magnetization reversal of a ferromagnet is a technologically very important process, which is governed by structural as well as magnetic properties of the material. It is characterized by a hysteresis loop, which consists of a series of discrete magnetization jumps, known as Barkhausen effect [9]. It is conventionally observed by slowly changing the external magnetic field and picking up voltage pulses in an induction coil wound around the ferromagnetic sample. While several imaging techniques exist to visualize domain patterns (e.g., Lorentz microscopy, Kerr microscopy, etc.; see Ref. [10], p. 24-77 for the various magnetic microscopies), most investigations of the Barkhausen effect have been carried out by this induction technique, where each voltage pulse represents a process of magnetization reversal. Its time integral of the voltage is proportional to the change of magnetic flux through the coil. A thorough evaluation of these Barkhausen jumps yielded important information with respect to the critical behavior in the presence of an external field [11]. However, only integral information over the whole sample is provided. Furthermore, the method is difficult to apply to magnetic thin films, because of the lower signal level compared to bulk samples. Thus, few direct observations exist [12,13]. On the other hand, MFM enables high resolution observation of domains and surface topography of the same area in external magnetic fields. Thereby, a quantitative analysis of these reversal processes and their location in real space can reveal the interplay between structural and magnetic properties.

In the following, we first investigate the remanent domain strucure and then the magnetization reversal as well as individual Barkhausen events of a ferromagnetic manganese perovskite disordered thin film ($La_{0.7}Sr_{0.3}MnO_3$), which was epitaxially grown on $LaAlO_3$.

Experimental setup

Topography and magnetic force microscopy data are recorded using a home built low-temperature scanning force microscope *(Hamburg Design)* [14] described in section 3.6.2. The microscope is located inside an ultrahigh vacuum (UHV) bath cryostat at a temperature of 5.2 K. All MFM experiments have been performed at this temperature. To apply a perpendicular magnetic field of up to 5 T, the microscope is surrounded by a superconducting split-coil magnet. The stability of our instrument is such that the relative tip-sample position (in particular the distance) does not change significantly within one day and during ramping the magnet to high fields.

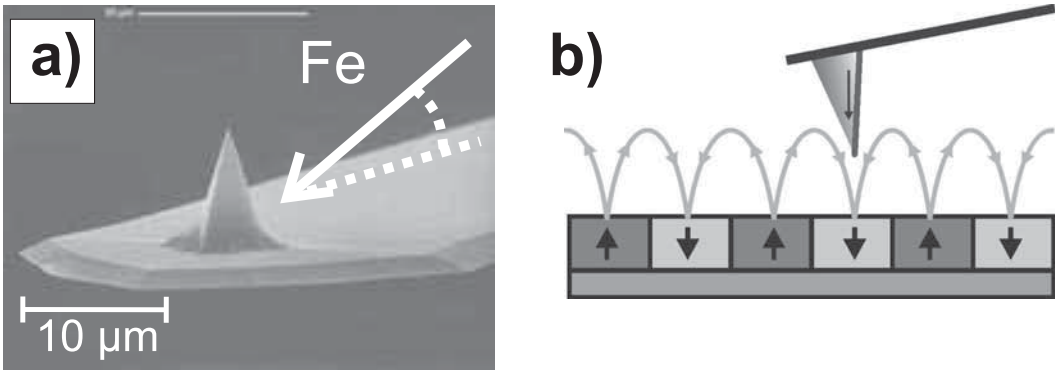

Figure 3.67: (a) Scanning electron microscopy image of a typical silicon cantilever showing the direction of the iron evaporation beam. (b) Geometry of the magnetic film with respect to the sample surface. The magnetization directions are indicated by arrows. This configuration responds nearly exclusively to the out-of-plane component of the sample stray field.

As force sensors, we use commercially available silicon cantilevers with resonance frequencies $f_0 = 183 - 203$ kHz and force constants $c_z = 40 - 57$ N/m. They are prepared *in situ* by argon ion sputtering and evaporation of nominal 5 nm iron on one triangular side face of the tip pyramid as shown in Fig. 3.67(a). The geometry of tip and sample surface is sketched in Fig. 3.67(b).

Micromagnetic simulations [15] indicate that the resulting triangular film develops a strong shape anisotropy, which forces the tip magnetization not only into the film plane but also into the direction of the symmetry axis of the film, pointing towards the tip end. This behavior has been verified by observing the tip magnetization switch in an external field (at typically 30 mT) while imaging a domain structure with a considerably higher coercive field. In this case, the image contrast suddenly inverts, because the magnetization direction of the tip changes by 180° and the formerly attractive interaction becomes repulsive and vice versa. No signs of instability before and after the instantaneous reorientation have been observed. The image contrast on a CoPt multilayer test sample shows that these tips are nearly exclusively sensitive to the out-of-plane component of the sample stray field.

All measurements are performed in the non-contact regime using the frequency modulation (FM) technique: The cantilever is oscillated by self excitation with a constant amplitude, A_0, at its current resonance frequency, f, determined by its eigenfrequency, f_0, and the tip-sample interaction. The measured quantity is the frequency shift, $\Delta f = f - f_0$. For topographic imaging by force microscopy in the dynamic mode (DFM) (see section 3.4), the z-feedback, which controls the tip-sample distance, is active, and a map of constant Δf is acquired. To record topographic images with a ferromagnetic tip, the sample magnetization is fully saturated at 800 mT to eliminate any magnetostatic cross-talk during data acquisition.

For magnetic force microscopy (MFM), we apply the plane subtraction mode, i. e., the tilt between tip and sample is compensated by adding appropriate voltages to

the z electrode of the scanner, dependent on the xy position. The tip is then scanned in a constant height, $h \approx 20...30$ nm, above the sample surface. Since magnetostatic interactions are of long-range nature compared to the oscillation amplitude, the frequency shift is proportional to the force gradient: $\Delta f \approx -(f_0/2c_\mathrm{z})(\partial F_\mathrm{z}/\partial z)$. Using conventional color coding, bright and dark image regions correspond to attractive and repulsive tip-sample interactions, respectively, and therefore reflect the domain configuration. Topographic crosstalk due to the long-range electrostatic force is eliminated by applying a constant bias voltage U_bias, which compensates the average contact potential difference between tip and sample. All images presented in this article show raw data.

Sample

The ferromagnetic thin film studied in this work belongs to the class of manganese perovskites, which recently have attracted a lot of attention because of the large variety of coupled magnetic, electronic, and structural effects [16–19]. Following the composition $\mathrm{RE}_{1-x}\mathrm{AE}_x\mathrm{MnO}_3$, where RE is a rare earth and AE is an alkaline earth element, this class of material exhibits a rich phase diagram with structural, magnetic, and electronic transitions in dependence of composition, x, and temperature. The most prominent property of some of these compounds is the colossal magnetoresistance effect (CMR), a strong decrease of electrical resistance in an external magnetic field. It has been discovered, among others, in thin films of La-Ba-Mn-O [20], La-Ca-Mn-O [21, 22], (cf., section 3.2.13) and in our sample material, La-Sr-Mn-O [23], which is of particular interest, because its Curie temperature lies above room temperature. However, for all materials CMR requires a high magnetic field corresponding to a flux density of several Tesla, which is too large to be useful for applications such as data storage or sensor devices. Therefore, endeavors have been made to explore the low field magnetoresistive behavior (LFMR) of manganites under the influence of extrinsic effects like grain boundaries, strain, spin-polarized transport in tunnelling junctions, and domain-wall magnetoresistance (DWMR) [30]. It has been found that LFMR is enhanced if the film exhibits a stress induced magnetic out-of-plane anisotropy [39] and that grain boundaries could provide a significant contribution due to domain wall pinning [40]. Both effects can be investigated by magnetic imaging, analyzing the magnetic configuration in different fields.

A $\mathrm{La}_{0.7}\mathrm{Sr}_{0.3}\mathrm{MnO}_3$ film (LSMO) of 80 nm thickness was deposited on a LaAlO_3 (001) substrate (LAO) by pulsed laser deposition (PLD) at 750 °C and under 10 mTorr oxygen partial pressure. After deposition, the sample has been annealed for 30 min at 600 °C under 500 Torr oxygen atmosphere. This method has already successfully been applied to the growth of other manganese perovskite thin films [13]. Such films grow epitaxially under a compressively stressed ab plane and an extended c lattice parameter, because the lattice constant of the substrate is 2.4 % smaller than that of the film [41]. In order to relax this stress, misfit dislocations are formed in a rectangular pattern along main crystallographic axes [42]. Above a thickness of around 70 nm, the

film breaks up into rectangular columns of 20-35 nm in size, separated by amorphous grain boundaries [24]. Magnetically, the distortion of the unit cell leads to an easy axis of magnetization perpendicular to the film plane.

For LSMO on LAO, the perpendicular anisotropy was confirmed by magnetic force microscopy showing a characteristic maze type stripe pattern [41]. Other investigations focused on the domain pattern in zero field after different field histories [26, 28, 43, 44], on the surface morphology [45], and the field dependent domain structure in in-plane fields [43].

After preparation, our sample was transferred under ambient conditions and introduced into the ultrahigh vacuum imaging environment via a load lock. Topographic images (see Sec. 3.2.12) reveal a granular morphology with a rms roughness of 0.4 nm and an average grain size of (32 ± 2) nm, which matches the value obtained from transmission electron microscopy (TEM) investigations on similar samples [24], but is a little smaller than reported by Desfeux *et al.*, using force microscopy [45]. However, these values depend on the tip radius, because the real surface structure is geometrically convolved with the tip shape. Besides structural defects, variations of the chemical composition like strontium segregation have been reported [31]. Note that this does not affect the MFM signal, which originates also from regions below the surface.

Temperature dependent magnetization data have been acquired using superconducting quantum interference device (SQUID) magnetometry. The Curie temperature was determined from its point of inflection to be $T_\mathrm{C} = 325$ K. The saturation polarization at 10 K is $I_\mathrm{S} \approx 300$ mT, resulting in a shape anisotropy constant $K_\mathrm{d} \approx I_\mathrm{S}^2/2\mu_0$ of approximately 36000 J/m^3. For a similarly prepared sample on the same substrate and with nominally identical film thickness, Wu *et al.* determined a substrate induced perpendicular anisotropy of $K_\mathrm{u} \approx 20000$ J/m^3 [32]. The exchange stiffness, A_ex, can be estimated from T_C by using the Heisenberg model. Assuming that the magnetic interaction is limited to nearest neighbor Mn sites with the coordination number, $z = 6$, a spin $S = 3/2$, and a lattice parameter, $a = 389$ pm, the molecular field theory yields $J \approx 3k_\mathrm{B}T_\mathrm{C}/2zS(S+1) = 3.0 \times 10^{-22}$ J and $A_\mathrm{ex} \approx JS^2/a = 1.73 \times 10^{-12}$J/m for the exchange integral and the exchange stiffness, respectively.

Zero field domain structures

The domain structure at zero magnetic field was imaged after three different magnetic histories: (i) after thermal demagnetization at $T \approx 370$ K $> T_\mathrm{C}$ (see Fig. 3.68(a)), (ii) after saturation in an in-plane magnetic field of 140 mT (see Fig. 3.68(b) and (c)), and (iii) after saturation in a perpendicular field of 600 mT (see Fig. 3.68(d)). The mean widths of the maze type domain patterns observed in Fig. 3.68 can be defined as the ratio of total image area and domain wall length. This value is estimated using a stereological method by drawing arbitrary cross sections of total length l and counting the number n of intersections with domain walls. Then, $w = 2l/\pi n$ represents the domain width matching the common value for parallel aligned stripes (see p. 331 in Ref. [10]).

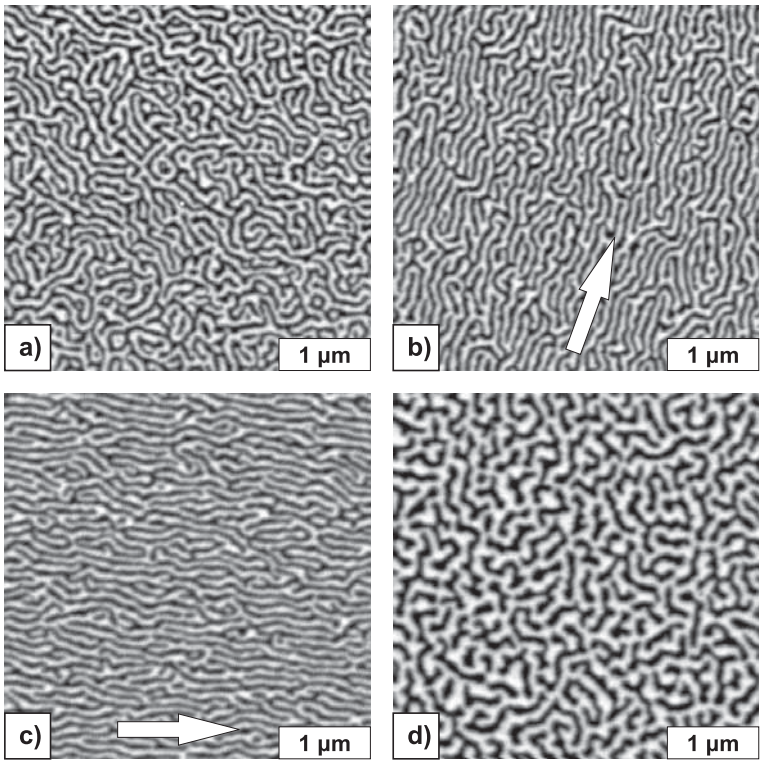

Figure 3.68: FM-MFM images at zero magnetic field (a) after thermal demagnetization, (b), (c) after saturation in an in-plane field, (d) after saturation in a perpendicular field. The arrows in (b) and (c) indicate the direction of the previously applied field. All images have been acquired with the same tip. Parameters: $f_0 = 195$ kHz; $A_0 = \pm 5$ nm; distance h, U_{bias}: (a) 18 nm, -400 mV, (b) 24 nm, -80 mV, (c) 30 nm, +140 mV, (d) 24 nm, -100mV.

In the thermally demagnetized state (Fig. 3.68 a), a maze type domain pattern with no predominant direction and a domain width of $w = (54 \pm 3)$ nm is observed. Per definition, the net magnetization in the demagnetized state is zero, i.e., bright and dark regions are both expected to fill 50% of the total area. However, in Fig. 3.68 (a), bright regions (attractive tip-sample interaction) dominate and occupy 52.6 % of the scan area. This indicates a small disturbance of the sample due to the stray field of the tip which aligns parts of the sample parallel to the tip magnetization. Such an effect has been verified on the same sample during field dependent measurements which included the switching of the tip magnetization direction from parallel to antiparallel with respect to the z direction.

Domain patterns in remanence after saturation in an in-plane field of $\mu_0 H = 140$ mT are presented in Fig. 3.68 (b) and (c). The arrows indicate the direction of the applied field. Domain width ($w = (52 \pm 2)$ nm) and MFM contrast are very similar to those observed after thermal demagnetization, but the stripe patterns are aligned in the direction of the previously applied field.

The domain configuration after saturation in a perpendicular field (Fig. 3.68 d)

has been imaged with the same tip at the same distance as in (b). Again, a maze type domain pattern without preferred direction is observed, but the domain width is increased to $w = (79 \pm 3)$ nm. The fraction of bright contrast amounts to 58.3 % and indicates a remanent perpendicular magnetization. Furthermore, the contrast, i.e., the difference between the average maximum and minimum of frequency shift, increased by 33 %. The formation of this pattern from saturation to remanence could be traced by acquiring MFM images in a continuous manner during ramping the applied field down from 600 mT to zero (Fig. 3.70). The maze type pattern is the result of domain nucleation (a) at high fields near saturation, followed by domain wall motion and strip out (b) to form the observed structure at remanence.

The situation after thermal demagnetization displayed in Fig. 3.68 (a) can be explained in terms of weak stripe domains (see p. 301 in Ref. [10]). The above given values of K_u and K_d result in a reduced anisotropy constant $Q = K_\mathrm{u}/K_\mathrm{d} \approx 0.55$, i.e., the shape anisotropy K_d exceeds the substrate induced uniaxial anisotropy K_u. However, to reduce the anisotropy energy, the magnetization starts to oscillate out-of-plane if the film thickness exceeds a critical value, t_cr. For very low anisotropy films ($Q \ll 1$), this value saturates towards $t_\mathrm{cr} = 2\pi\sqrt{A_\mathrm{ex}/K_\mathrm{u}}$ and equals zero at $Q = 1$. In our case, it amounts to $t_\mathrm{cr} \approx 25$ nm which is well below the film thickness. In consequence, stripe domains with a periodicity in the order of the film thickness evolve. Since the sample should be in its global energy minimum after thermal demagnetization, one can conclude from the isotropic maze type domain pattern that there is no obvious in-plane anisotropy, which would prefer any crystallographic axis of the epitaxially grown film.

An in-plane saturation field aligns all magnetic moments in field direction. Upon reducing the field $\mu_0 H$, the magnetization again starts to oscillate out-of-plane up to a degree $\theta(H)$ preserving the direction of the in-plane component as sketched in Fig. 3.69. The local out-of-plane component, $M_\mathrm{sat} \sin\theta$, gives rise to the imaged domain contrast. In order to estimate the maximum tilting angle θ_0 with respect to the film plane, we calculated the relevant energy terms, magnetostatic, exchange, and anisotropy energy in dependence of domain width w and maximum tilting angle θ_0, using a simple analytical model (see appendix in Ref. [28]). We assumed a magnetization angle $\theta(x)$ which is homogeneous in y and z direction and modulated sinusoidally in x direction: $\theta(x) = \theta_0 \sin(\pi x/w)$. Taylor expansion up to the order θ_0^2 and minimizing the total energy (see pp. 450-453 in Ref. [33]) gives a calculated domain width $w_{th} = 62$ nm which agrees reasonably well with the experimental value, $w = 52$ nm found in Fig. 3.68(b) and (c). If one regards also the 3$^\mathrm{rd}$ and 4$^\mathrm{th}$ order and minimizes the total energy at the domain width w_{th} with respect to θ_0, a maximum tilting angle of $\theta_0 = 63°$ results. The interpretation of a preserved in-plane component is also supported by Hawley *et al.* [43], who performed in-plane field dependent MFM measurements on LSMO/LAO and concluded that there is a parallel in-plane component in aligned stripes. Note that we find nearly identical domain widths after thermal demagnetization and after in-plane saturation. Consequently, the maximum (polar)

tilt angle is also very similar. However, the distribution of the azimuthal angle of the magnetization direction is very different. The regular aligned domains in the latter case indicate an anisotropic distribution in field direction. Without such an aligning field, the stripes are randomly oriented in a maze type pattern, which suggests an isotropic distribution of the azimuthal tilt angle after thermal demagnetization. The fact that the stripe pattern is aligned in field direction further indicates that magnetostriction does not play an energetically important role [34]. Otherwise, one would expect an alignment of stripes perpendicular to the applied field which could more effectively reduce the strain on a length scale larger than the domain width.

The increased contrast in the remanent state after saturation in a perpendicular field suggests an increased out-of-plane tilting of the magnetization compared to the previously discussed cases. To address this question, one has to take into account that the contrast of a periodic structure in a constant height depends on the domain width. From Laplace's equation, it can be seen that the magnetostatic potential σ above the sample surface arising from a stripe domain pattern with constant magnetization of alternating sign decays exponentially (see appendix in Ref. [28]). The decay length $\lambda = w/\pi$ is proportional to the domain width w. This behaviour is known as *spacing loss* in magnetic recording [35] and has been described for MFM earlier [36]. Additionally, one has to regard the oscillation amplitude of the tip with respect to the decay length of the force. These two effects account for a contrast increase of 18 % due to the increased domain width after perpendicular saturation compared to after in-plane saturation. The remaining 13 % can easily be explained by the above mentioned out-of-plane tilting up to $\theta_0 = 90°$ after out-of-plane saturation since the contrast scales with $\sin\theta_0$, and $\sin 90°/\sin 63° = 1.12$. The larger tilting is consistent with an increased domain width, because in this case the magnetization vector has to rotate by a larger angle between bright and dark contrast areas. Moreover, it is consistent with the observation that the MFM contrast of reversed regions is always symmetrical. Assuming that the sample was fully magnetized in z direction before, it is energetically favorable for a nucleated domain to adjust its magnetization direction antiparallel to the surrounding area. This configuration can serve as the initial cause for the out-of-plane tilting of the remanent structure. However, it does not represent the global energy minimum of the film, which is reached in the thermally demagnetized state.

Finally, it is worth to note that the domain widths are always larger than the mean grain size. In fact, we could explain the different observed final states by using only magnetostatic arguments. The role of the grain structure is further discussed below.

Field dependent domain structure

To study the magnetization reversal, we continuously recorded MFM images while ramping a perpendicular field, $\mu_0 H_\perp$, from 0 T to saturation at 600 mT and back to zero field. The stability of our instrument allows this movie-like measurement mode without readjusting any imaging parameter during the 22 h of data acquisition time. Thus, every image of this sequence shows the same sample area. The recording of one

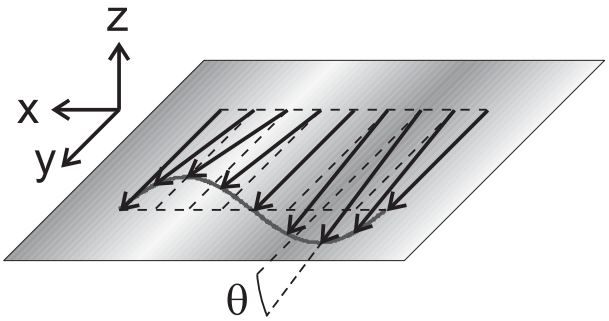

Figure 3.69: One-dimensional model of the magnetization (arrows) and the corresponding MFM contrast (shading) after saturation in an in-plane field in y direction. The magnetization oscillates periodically out-of-plane (θ denotes the polar tilt angle) preserving the direction of the in-plane component.

image took about 8.5 min. Since the ramp rate was varied according to the activity of magnetization reversal processes, each image covers a field range of 5 mT (from 300 up to 500 mT, and 400 down to 200 mT) or 10 mT (others).

Figure 3.70 shows six images of this movie. Starting from a maze type pattern at remanence, the coercive field is passed at about 75 mT (a), where an equal distribution of dark and bright contrast is observed. With increasing field, antiparallel domains shrink, until just before saturation only domains of circular contrast and opposite polarity remain (b). These circular domains are annihilated at a field above 400 mT, until at 600 mT, the magnetic contrast vanishes because the film is homogeneously magnetized (c). The very few remaining features (like the most prominent one marked by an arrow) are of topographic origin. They can be used to track the relative tip-sample position throughout the whole measurement. The lateral drift was less than the distance between two image pixels (below 10 nm). In a decreasing field after saturation, domain formation starts at around 340 mT with the nucleation of few domains which mostly exhibit a circular configuration (d). Below 280 mT, the domains start to become increasingly elongated while new domains still nucleate down to 200 mT. Below this field, only domain growth is observed (e) forming a maze-type domain pattern in remanence (f).

Quantitative analysis of the MFM sequence

The evolution of domains can be clarified by using the concept of difference images: Since there is no significant drift compared to the domain size during the movie, we can directly subtract two consecutive images in order to show the changes of the MFM contrast. In fact, all images of this movie can be subtracted from each other without further corrections, independent of the difference in their acquisition time. In increasing fields the bright areas grow, because they are magnetized parallel to the external field and the tip magnetization, while in decreasing field the fraction of dark regions increases. Therefore, the difference images exhibit bright contrast in increasing,

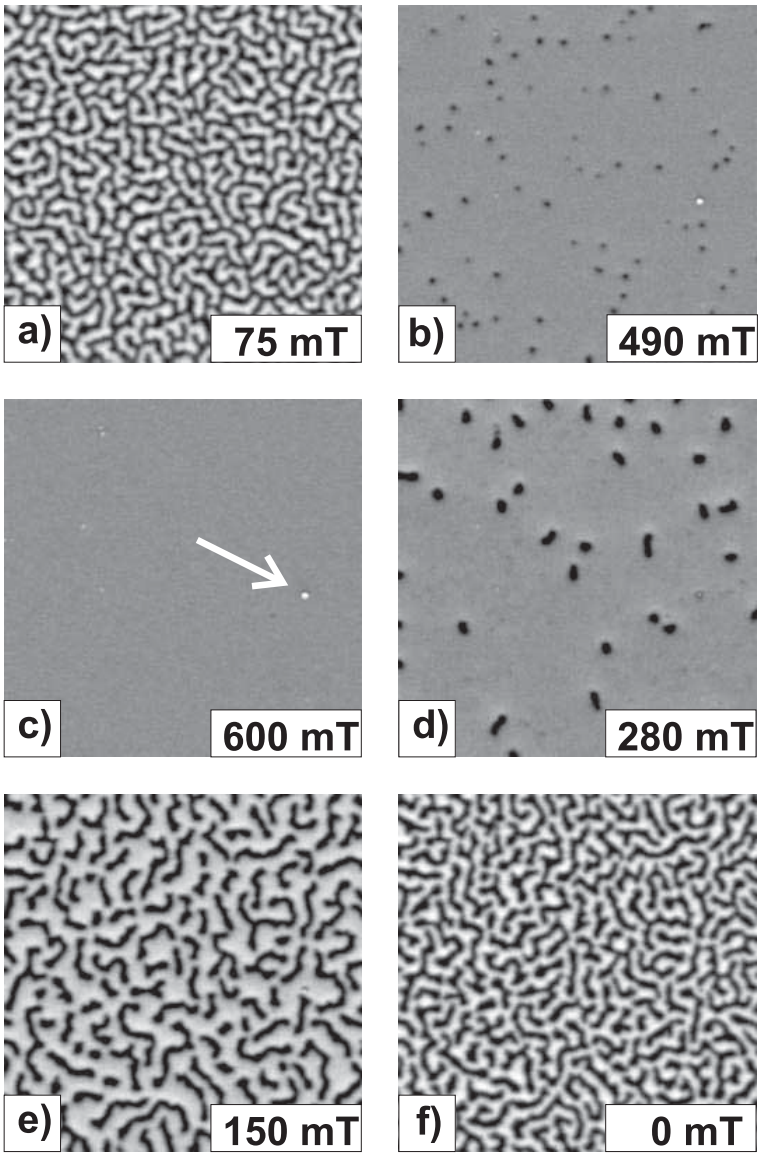

Figure 3.70: Magnetization reversal, visualized by MFM. All images cover the same sample area. Bright contrasts indicates sites where tip and sample magnetization are parallel. (a) and (b) were recorded in increasing, (d) and (e) in decreasing field. (c) In saturation, a topographic feature, marked by an arrow, can be clearly seen and traced through the whole sequence. Parameters: scan area 4×4 μm^2, $h = 24$ nm, $f_0 = 195$ kHz, $A_0 = \pm 5$ nm, $c_z = 51$ N/m, scan speed 8 μm/s, $U_{\text{bias}} = -100$ mV.

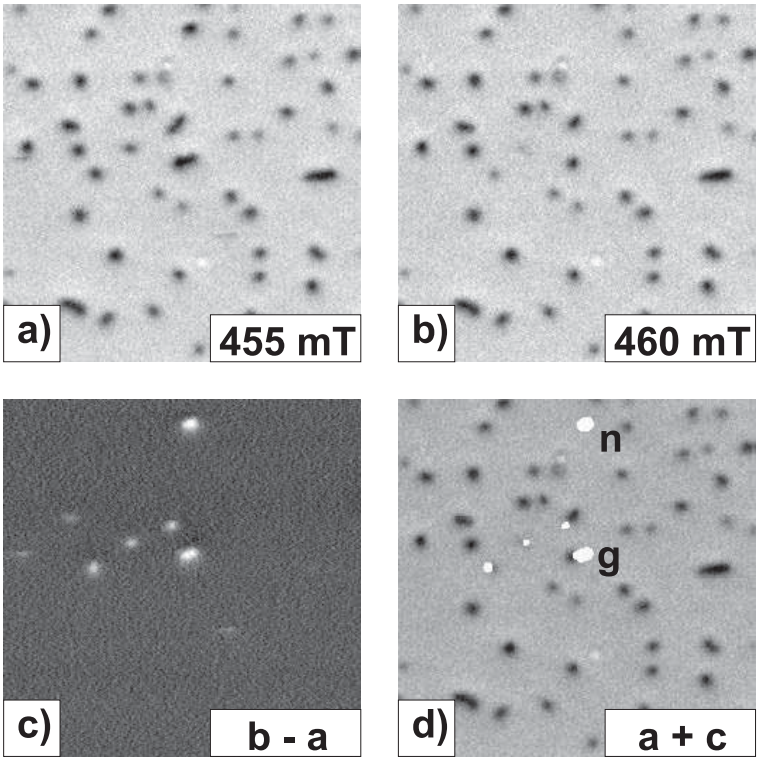

Figure 3.71: Identification of annihilation (n) and growth (g) processes. (a) and (b) show original images in increasing field, (c), the difference image. (d) Changes of the domain structure are highlighted with respect to image (a). For parameters, see Fig. 3.70.

and dark contrast in decreasing fields.

Figure 3.71 (a) and (b) shows an example of two consecutive images obtained at increasing field. The areas of changed magnetization can be found in the difference image (c). In order to distinguish between annihilation and growth, their contours are then plotted into the original image as shown in (d). Contours not connected with dark areas are considered annihilation sites whereas the others are regarded as domain growth due to wall propagation. For decreasing fields domain nucleation and growth processes can be discriminated in the same way as shown in Fig. 3.72.

In almost all parts of the sequence, the difference images display the changes of sample magnetization as an accumulation of well separated units which can be analyzed individually. These difference images are used to identify and characterize individual magnetization reversal processes, in particular the area, contrast, and the position relative to existing domains.

Imaging ferromagnetic thin films that are basically two-dimensional, i.e., the volume is free of magnetic charges, the MFM is sensitive to the magnetic charge density, σ, at the surface [10]:

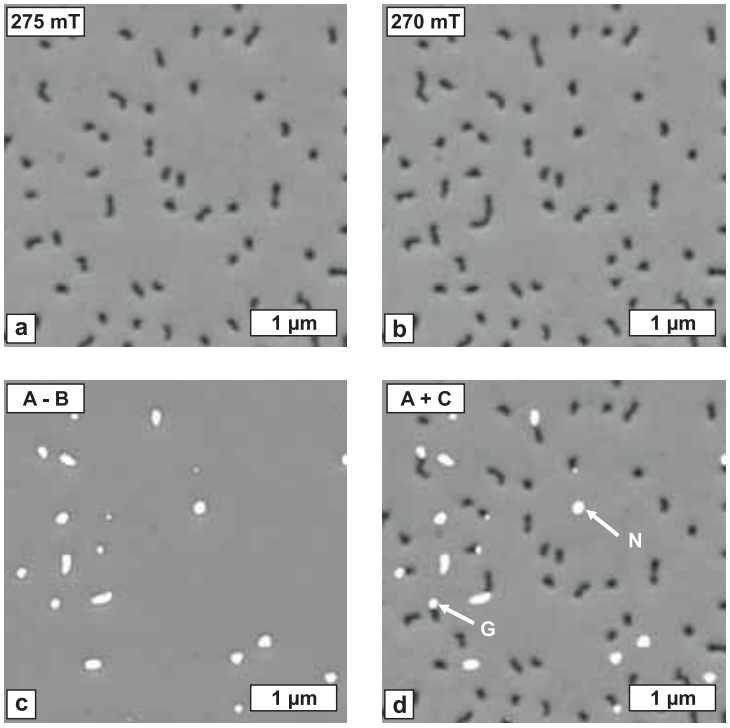

Figure 3.72: Identification of nucleation (n) and growth (g) processes. (a) and (b) show original images in increasing field, (c), the difference image. (d) Changes of the domain structure are highlighted with respect to image (a). For parameters, see Fig. 3.70.

$$\Delta f(x,y) = \frac{f_0}{2c_z} \int_S \sigma(x-x', y-y') \frac{\partial H_z}{\partial z}(x', y')\, dx'\, dy' \,, \tag{3.27}$$

where H_z denotes the tip stray field. However, for the accurate size measurement of individual processes in the difference images as well as those of isolated domains in a homogeneously magnetized surrounding area, the corresponding apparent areas must be corrected due to the extended stray field of the imaging tip. Since our experiments are performed in the dynamic mode with an oscillation amplitude considerably smaller than the decay length of the magnetostatic interaction, the distribution of magnetic surface charges is geometrically convolved with the gradient of the tip stray field. This is equivalent to considering the magnetization of the tip oscillating in the stray field of the sample.

For various scan heights near 25 nm, we have computed the stray field of the magnetic tip coating using micromagnetic simulation [15]. The shape of the corresponding field derivative in z direction can be approximated by evaluating the difference between the stray fields at two scan heights, 20 and 30 nm, corresponding to a cantilever oscillation amplitude of ± 5 nm. We found that this effect is comparable to a smoothing filter of gaussian shape with a diameter (FWHM) of 37 nm. As a result, the total

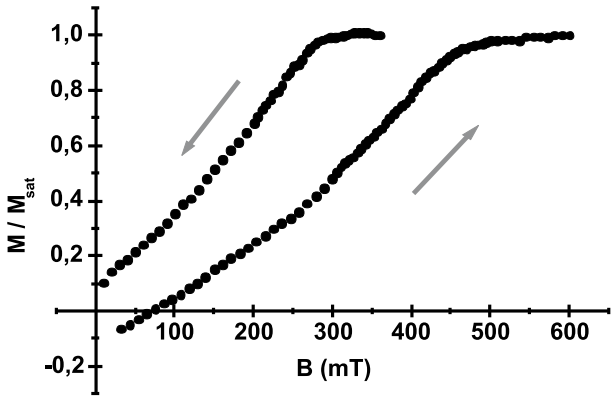

Figure 3.73: Hysteresis from the accumulated magnetization changes, computed from all difference images of the sequence recorded over half a major hysteresis loop.

apparent area of magnetization changes summed over all difference images is 5 times larger than the true reversed area calculated from the coercive field image (which is half of the image area). Since the convolution effect is more severe for smaller areas, it is not sufficient to just divide the apparent areas obtained from difference images like Fig. 3.71(c) by this single correction factor.

To obtain a better estimate of the real reversed area, A_i, of each individual event, we additionally evaluated the integral of the contrast over the apparent area, a_i, of each event: $K_i = \int_{a_i} (\Delta f - f_{\mathrm{med}})\, dx\, dy$, where the median contrast, f_{med}, of the image to be analyzed is taken as zero level, that is, to a very good approximation, the mean level of the undisturbed areas. We defined the apparent area as those image pixels where the contrast exceeds the noise level of the neighborhood. K_i being measured in $\mathrm{Hz} \cdot \mathrm{nm}^2$, is proportional to the underlying magnetic surface charges. The integral of contrast is transformed into a real area using a calibration factor: $A_i = \gamma K_i$, where γ is measured in Hz^{-1}. This factor only depends on the stray field distribution of the tip at the sample surface and can therefore be used for the whole image sequence, for isolated features in difference as well as in original images.

In order to find the value of this calibration factor, the change of integrated contrast in every image is measured, accumulated to form a normalized hysteresis loop (Fig. 3.73), and finally compared to the actually reversed area.

Two calibration points have been used: (a) the saturation magnetization, (b) the average magnetization before and after the reversal of the tip magnetization at 30 mT, computed from original MFM images. At that field, a quasi periodic structure is observed (Fig. 3.70 a, f), and MFM is able to measure domain widths correctly in this case, because the periodicity of a structure is not altered by the effect of smoothing - only the contrast. However, the change in tip magnetization from antiparallel to parallel with respect to the external field causes a jump in the percentage of parallel aligned domains, indicating a tip induced contrast deviation of 3.8%. Taking that into account, the mean percentage of parallel aligned domains at 30 mT is 46.6%, that is

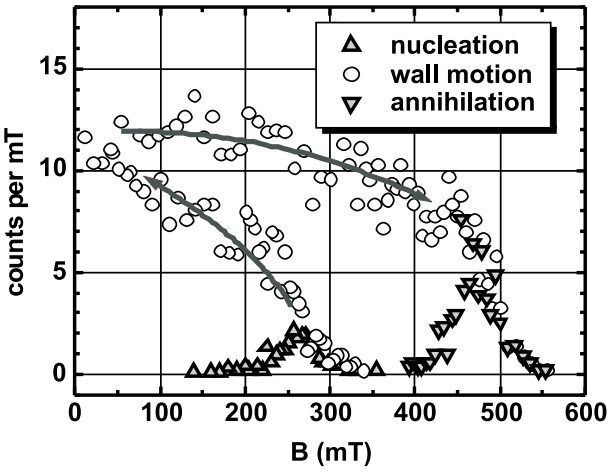

Figure 3.74: Number of magnetization reversal processes in increasing and decreasing external field (see arrows), displayed separately for annihilation, nucleation, and domain wall motion. The latter type dominates the evolution of the domain pattern. Significant contributions from annihilation of a domain or nucleation of new domains occur only near saturation.

an area of 8.544 μm^2 to be reversed before saturation. The resulting local hysteresis loop (measured in an area of 16 μm^2) constructed from the evaluation of individual Barkhausen events is well compatible with those obtained from conventionally measured magnetization data determined from the whole macroscopic sample [37].

Nucleation, annihilation, and growth

By means of the method depicted in Fig. 3.71, more than 5000 wall motion and 400 annihilation events could be distinguished on the increasing branch, and about 2000 wall motion and 100 nucleation processes on the decreasing branch of the hysteresis loop from remanence to saturation and back to remanence. In Fig. 3.74, the number of processes per mT field change is displayed as a function of the external field.

The evolution of the domain pattern is dominated by wall motion. Final annihilation of the shrinking domains is observed between 400-550 mT, and initial nucleation of new domains between 340-200 mT. In either case, they occur only near saturation, and the number of wall motion events is always nearly equal or greater than that of any other process.

Figure 3.75 displays the size distributions of annihilation and nucleation events. In both cases, the distribution can be approximated by a Gaussian profile with a mean diameter of (146$\pm$21) nm for nucleations and (46$\pm$18) nm for annihilations. The average diameter for domain growth by wall propagation of 41 nm (no significant difference is observed for increasing and decreasing fields) is much smaller than the nucleation diameter, but only slightly smaller than the annihilation diameter. Moreover, growth events do not follow a Gaussian distribution.

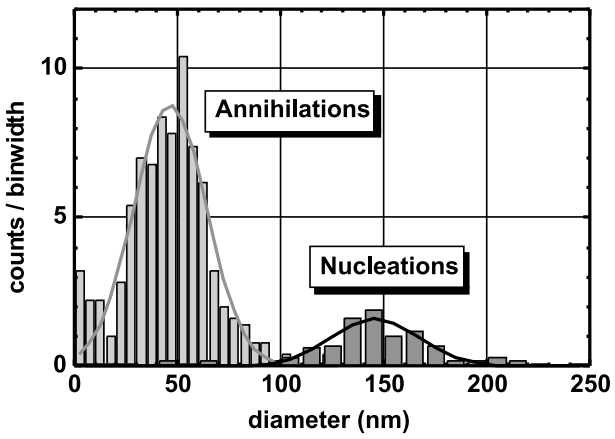

Figure 3.75: Size distribution of reversed magnetization areas for annihilation and nucleation. For both, a Gaussian distribution is observed. Mean diameter: 46 nm for annihilation, 146 nm for nucleation.

Nucleations exhibit a considerably larger diameter than other processes, because they include the formation of a new domain wall which acts as an energy barrier. The creation of a new domain is a thermally activated process which is governed by the presence of surface and volume energy terms. The domain wall energy of a circular domain with radius R is proportional to the wall area: $E_{\mathrm{w}} = 2\pi\gamma Rt$ (with the film thickness t, and the wall energy per unit area $\gamma = 4\sqrt{AK_{\mathrm{u}}}$). The energy E_{ext} of the domain in the external field and the demagnetization energy E_{mag} (for $t \ll R$) are proportional to the magnetic volume: $E_{\mathrm{mag}} = -(2\pi/\mu_0)R^2t|\vec{J}_{\mathrm{s}}|^2$ and $E_{\mathrm{ext}} = (2\pi/\mu_0)R^2t\vec{J}_{\mathrm{s}} \cdot \vec{B}$, where $\vec{J}_{\mathrm{s}}$ denotes the saturation magnetization and $\vec{B}$, the external field.

Whenever such surface and volume energy terms are present, thermodynamics predicts that only those compact fluctuations remain stable, which exceed a certain critical diameter (critical droplet theory) [38]. According to this energy balance, we determined a minimum diameter, $2R_{\mathrm{c}} = \mu_0\gamma/J_{\mathrm{s}}(J_{\mathrm{s}} - B)$, of 104 nm for the typical nucleation field of 270 mT, where we observed the largest number of nucleations [46]. Considering the simplicity of the model, this result is in reasonable agreement with the observed mean value of 146 nm. In an inhomogeneous material (in our case, the film contains structural disorder), exchange stiffness and anisotropy coefficient, and therefore the energy landscape, will vary locally. Consequently, the critical diameter becomes Gaussian broadened.

For annihilation, the energy balance is different. Here, the wall energy is released and does not serve as an energy barrier. Therefore, annihilation processes can be very small. However, since the observation of an annihilation process requires the previous existence of a stable domain, the size of annihilations reflects the size of the smallest stable domains in this material. For a circular domain in a thin film, the different energy contributions E_i can be converted into generalized pressures acting on

the domain wall:

$$p_i = -\frac{1}{2\pi Rt}\frac{\partial E_i}{\partial R}\,, \tag{3.28}$$

where $2\pi Rt$ denotes the domain wall area. The presence of a domain wall therefore provides an inward pressure, p_{w}, comparable to surface tension in a droplet of liquid, being proportional to the curvature of the wall: $p_{\mathrm{w}} \propto 1/R$. The applied external field acts in the same direction, trying to reverse the magnetization into the parallel direction. This pressure does not depend on the domain size or wall curvature but solely on the external field and has the same value for all domains at a given field: $p_{\mathrm{e}} \propto |\vec{B}|$. In order to stabilize the domain wall, these two pressures have to be compensated by the demagnetization effect which tries to minimize the stray field of the magnetic structure by producing equal amounts of parallel and antiparallel magnetized areas and therefore acts as an outward pressure, highly dependent on the domain pattern.

If the external magnetic field rises and the domain radius falls below a certain value (increasing the inward pressure), the domain collapses and is annihilated. Thiele [47] calculated the stability of cylindrical domains in a thin film with uniaxial anisotropy. Given the parameters of our sample (film thickness, saturation magnetization, anisotropy, and exchange stiffness), a minimum diameter of 45 nm can be obtained directly from graphs given by Thiele in Ref. [47], in a very good agreement with the measured mean diameter of (48 ± 16) nm. Note that this calculation does not take into account the pinning of domain walls and local variations of magnetic parameters by structural inhomogeneities, which cause a broadening of the size distribution of annihilation processes, as is observed.

The third type of observed events, domain growth processes, is mainly the result of a simple motion of an existing domain wall. For freshly nucleated circular domains in a decreasing field, this mechanism provides a second cause of instability. Whereas the energy of the domain in an external field and, to some extent, the stray field energy depend on R^2, the wall energy is proportional to R. However, it is possible to decrease the overall energy by forming elongated domains (strip out) which reduces the stray field energy at the slight expense of wall energy. This mechanism leads to the final maze type domain pattern at remanence. The stability of a circular domain against elliptical deformations as described has been calculated by Thiele [47] resulting in a maximum diameter of a circular domain of 121 nm for our sample. The observed average diameter of domains just before strip out has been found to be around (130 ± 24) nm.

For an existing domain wall to move, only a minimal energy is required to depin the wall from its present position which might be determined by small inhomogeneities of the film. Therefore, small processes are much more common in this case. The size distribution for areas a_p which are reversed through domain growth is considerably different from nucleation and annihilation processes (Fig. 3.76). It follows an inverse power law over three decades and then cuts off exponentially, best described by a fit according to $P(a_p) \propto a_p^{-\tau} e^{-a_p/a_0}$ (increasing field: $\tau = 0.50 \pm 0.04$ and $a_0 =$

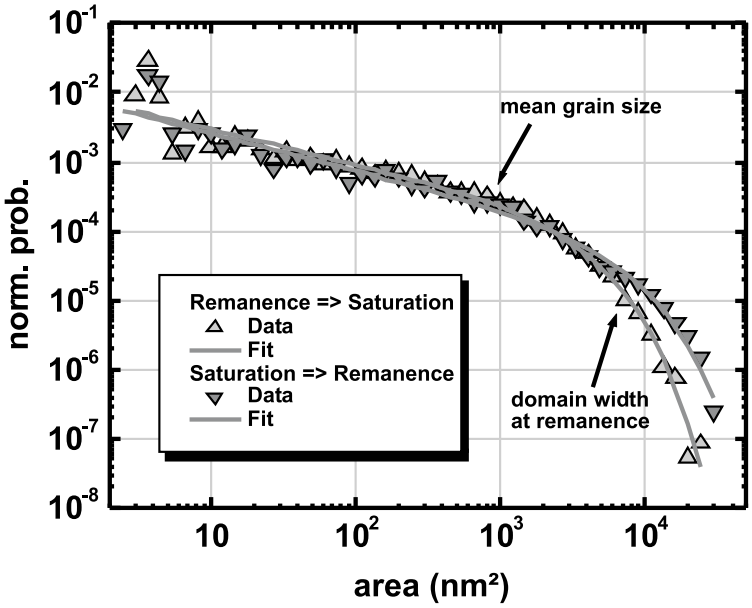

Figure 3.76: Size distribution of reversed magnetization areas due to domain wall motion for increasing and decreasing field. It follows an inverse power law over three orders of magnitude. The area of exponential cut-off is different in both cases, indicating a magnetostatic origin, not a structural one. Note that logarithmic binning was chosen.

(3295 ± 189) nm^2; decreasing field: $\tau = 0.54 \pm 0.03$ and $a_0 = (6624 \pm 551)$ nm^2). A purely thermally activated magnetization reversal would result in a simple exponential size dependence. The observed power law dependence is characteristic for systems at criticality. This issue will be examined more detailed in the following section.

Barkhausen effect and criticality

As can be seen from the difference image in Fig. 3.71, the field dependent magnetization evolves through the reversal of discrete units, which cause a sudden change in the magnetic flux within the sample, according to their volume. These steplike changes of magnetization are known as Barkhausen jumps. Conventionally measured through induction experiments, each voltage pulse corresponds to a switching process within the magnetic material, and its time integral is proportional to the change of magnetic flux. We assume that the magnetization of our film does not change in the direction perpendicular to the film plane so that the surface charge, observed by MFM and calculated by means of the above described integration method for the difference images, is proportional to the reversed magnetic moment. The size distributions extracted from induction experiments are then directly comparable to those given here.

Each reversal event (Barkhausen jump) can be regarded as an avalanche of switching spins, caused by a slowly changing magnetic field. These avalanches keep the system in a critical state near the edge of instability. Such a behavior far from equilibrium

has recently been discussed under the aspect of self organized criticality (SOC) [48] and linked to the Barkhausen effect [11]. It is essential that the critical state is not reached by fine tuning of external parameters (as it would be the case in the proximity of phase transitions in equilibrium thermodynamics) but by self-organization. The avalanches show self-similar structures in space as well as in time. Size distributions follow an inverse power law over many orders of magnitude. In experiments [49] as well as in simulations [50], an exponential cut-off has been observed for large sizes, which has been attributed to a finite size effect, i.e., an avalanche cannot be larger than the investigated system itself. The concept of SOC has been applied to a large variety of phenomena, including earthquakes, growing of sand piles, spin density waves, or flux lines in superconductors [51].

However, it has been argued that SOC is not necessarily needed to obtain such a scaling law [52]. In fact, an inverse power law distribution followed by an exponential cut-off can be found by modulating the speed of domain wall propagation with statistical fluctuations [53], e.g., caused by structural disorder. Increasing the intensity of fluctuations would result in a greater critical exponent τ and cut-off area a_0 and therefore enlarge the tendency of criticality. Recently, the predicted critical exponent of $\tau = 4/3$ for a single domain wall moving in a disordered two-dimensional system [54] has been experimentally confirmed for a thin film with in plane magnetization [56]. However, this model is not applicable to our situation, because interactions between domain walls were neglected. Furthermore, there are some aspects which contradict criticality by self-organization in our case. To consider a system as governed by SOC, one would expect that critical behavior is observed over a wide range of parameters. On the other hand, a theoretical analysis [57] revealed that criticality is only achieved if the typical length scale of structural disorder, ξ, is of the same order of magnitude as the magnetic exchange length $l_{\mathrm{ex}} \approx \sqrt{A_{\mathrm{ex}}/K_{\mathrm{u}}}$. Indeed, this condition is fulfilled for our sample, where we can identify ξ with the mean grain size of 32 nm, which is of the same order of magnitude as $l_{\mathrm{ex}} \approx 10$ nm.

The second aspect deals with the physical origin of the exponential cut-off. As mentioned above, in SOC the finite size of the system limits the avalanche size. Obviously, this is not the reason in our case because even the largest observed avalanches are orders of magnitude smaller than the image area, not to mention the sample size. Basically two mechanisms are capable of slowing down and stopping a moving domain wall: pinning at inhomogeneities [52,57] and long-range dipolar interactions [55]. Pinning sites can be provided by grain boundaries which lower the energy of a passing domain wall. To move from one pinning center to the other, the domain wall has to overcome a certain energy barrier, and the probability to do so at an increasing number of barriers decreases exponentially. In fact, the exponential decay of the observed size distribution starts at the same order of magnitude as the mean grain diameter suggests.

The influence of dipolar interactions can be seen from the decrease of the mean size of the reversed areas as the domain pattern approaches the remanent state (Fig. 3.77).

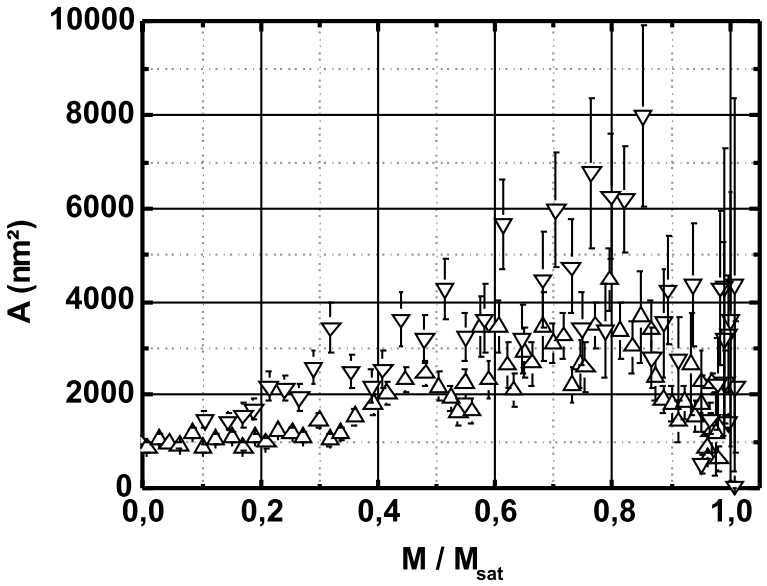

Figure 3.77: Average size of growth processes for each image at increasing ($\triangle$) and decreasing (∇) field. As the magnetic film approaches remanence, the average size decreases and stays small as long as elongated domains are dominating. The large standard deviation (error bars) at high magnetization is due to the smaller number of observed processes.

The reversal of large areas becomes more and more unlikely because the domain width of the thermally demagnetized sample (54 nm), which can be considered as an energy minimum, is just around one third of the mean diameter of nucleated domains. Given that size, it is energetically favorable to reduce the average domain width occurring at high fields by adding small areas of magnetization reversal through growth processes at lower fields. Additionally, the hysteresis curve is nearly linear from the initial nucleation towards remanence indicating that the internal field, $\vec{B} - \vec{J}(\vec{B})$, is almost constant and very small. As a consequence, large processes are suppressed. The same argument is valid for increasing field, where the mean area remains around 1000 nm^2 in the lower field range (Fig. 3.77). As long as elongated domains are the most frequent features, the average size remains small. As the magnetization approaches saturation, the change of the internal field becomes more pronounced, and the mean reversal area increases again. The magnetic structure apparently plays an important role for the size of individual processes.

Another hint towards the influence of dipolar interaction is given by the comparison of the cut-off area in decreasing and increasing field. While the exponent of the inverse power law remains constant within the experimental error, the cut-off area changes by a factor of 2 (see parameters in Sec. 3.2.12), which shows a dependence on the different stages of the magnetic domain evolution. If structural disorder were the origin, both parameters should be unchanged during the whole hysteresis loop. Thus we conclude that the exponential cut-off is most likely determined by dipolar interaction rather

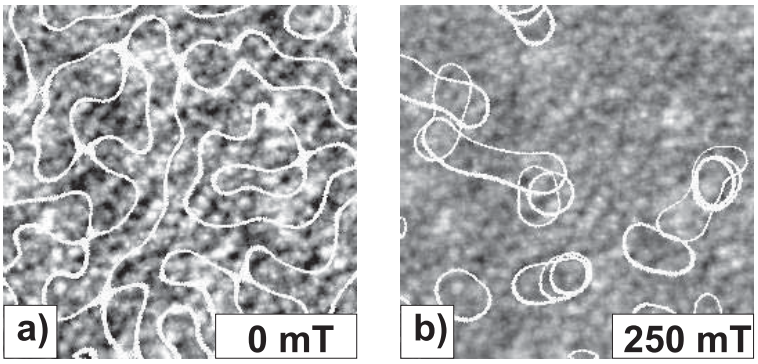

Figure 3.78: Correlation of topography and domain structure. (a) Topography including the contour of the domain pattern. The white contour lines correspond to the boundary, i.e., the mean contrast level, between oppositely polarized domains. No obvious correlation is visible. (b) Initial nucleation sites (white contour lines) of three different hysteresis cycles with respect to topography. Evidently, the first few nucleation events occur at nearly identical locations. Image area 1×1 μm^2.

than structural disorder.

Correlation with topography

Since LSMO thin films exhibit a dislocation network and above 70 nm thickness a columnar structure, the question arises whether there is a correlation between the topography and the domain pattern. To address this issue, we chose a sample area without gross topographic features which is thus representative for most parts of the film. On this area, several topographic images were recorded in saturation, each separated by a hysteresis loop. These cycles took several days, however, the lateral drift during that period was less than 10 nm which is considerably smaller than both, the domain width and the mean grain diameter.

Figure 3.78(a) displays the contours of MFM images in remanence together with the topography of the same area. No correlation with the topography is visible, e.g., the domain width is larger than the grain size and the domain boundaries do neither follow topographical valleys nor ridges. This impression is supported by a numerical cross correlation. As mentioned before, the topography does not necessarily reflect the internal film structure. Thus, volume pinning sites for domain walls cannot be identified. Furthermore, due to the difference in the contrast formation mechanism, there may be a constant lateral shift between the topography and MFM images.

Figure 3.78(b) contains the topography together with the contours of the first few nucleated domains, imaged at 250 mT of three different hysteresis loops in the same scan area. Again, there is no correlation with topography, but four areas were centers of initial nucleation in all three loops. Accordingly, there are internal properties of the film which favor nucleations at special sites, not distinguishable by any topographic

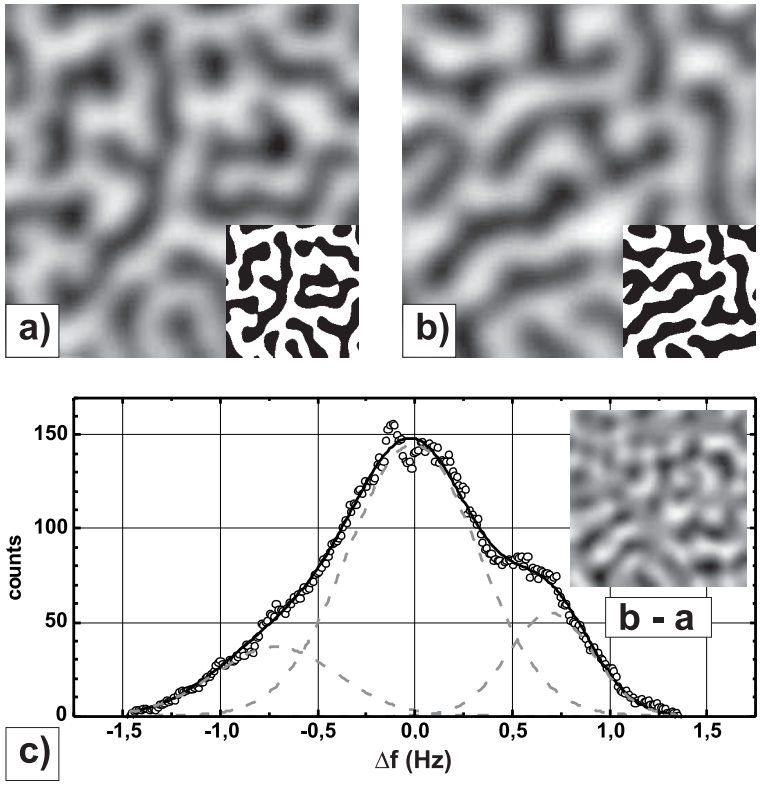

Figure 3.79: (a, b) Remanent domain pattern recorded in the same scan area, with simplified domain patterns as insets. (c) Histogram of the difference image (b-a). The solid line is a three peak Gaussian fit representing three possible changes of contrast. The percentage of the image area which has not changed its polarization is higher than expected from a random distribution.

feature.

Such an influence of subsurface structural inhomogeneities is also supported by a comparison of two zero field images recorded in the same scan area during consecutive hysteresis cycles, as shown in Figure 3.79.

Representing these images in black and white contrast (see insets), the fraction of white image pixels is $p_\mathrm{a} = 0.553$ and $p_\mathrm{b} = 0.544$, respectively. Assuming a purely statistical distribution of black and white regions, the probability that an image pixel did not change its contrast from (a) to (b) is: $p_\mathrm{a}p_\mathrm{b} + (1 - p_\mathrm{a})(1 - p_\mathrm{b}) = 0.505$. The histogram (c) of the difference image (b-a), however, indicates that a considerably higher fraction did not change its contrast. A value of 0.673 was computed from a three peak gaussian fit to the data, representing a change from black to white, white to black, and no change, respectively. As suggested by the existence of preferred nucleation sites, the domain pattern is not completely random but in part determined by internal inhomogeneities of the film.

Conclusions

A detailed magnetic force microscopy study of an epitaxially grown $La_{0.7}Sr_{0.3}MnO_3$ thin film on a $LaAlO_3$ (001) substrate, which exhibits structural disorder and a substrate induced perpendicular anisotropy, is presented. Depending on the magnetic history, in-plane as well as out-of-plane components can be observed. In the thermally demagnetized state and in the remanent state after in-plane saturation the sample exhibits dense stripe domains with similar domain widths, indicating identical mean polar tilt angles. However, the azimuthal tilt angle is isotropically distributed in the former case (maze type domain pattern without preferred direction), but anisotropic in the latter case (domains are aligned in field direction). Estimates of the energetically favorable domain width and maximum tilting angle, $\theta_0 = 63°$, agree well with the experiment. The remanent state after out-of-plane saturation shows an increased domain width and MFM contrast, indicating a full out-of-plane rotation of the magnetization, $\theta_0 = 90°$. This suggests that the tilt angle of the magnetization and the final domain width are not determined by the grain size of the film, but can be explained solely by magnetostatic considerations. This is further supported by the domain structure observed along the major easy axis hysteresis loop. Using the difference image procedure, individual Barkhausen jumps are observed. Nucleation, annihilation, and growth processes could be identified and analyzed in detail. Nucleated and annihilated domains exhibit a Gaussian size distribution whereas growth processes show a critical behavior with an inverse-power law and an exponential cut-off. The distribution of nucleation events can be explained within the critical droplet theory applied to nucleation in an inhomogeneous medium. Calculations concerning the stability of circular domains, i.e., collapse during increasing and elongation during decreasing field, respectively, agree well with the experiment. The distribution of growth processes is discussed in terms of self organized criticality and domain wall movement in a disordered medium. We conclude, that the system cannot be regarded as purely self organized in a strict sense, because the characteristic structural and magnetic length are of similar magnitude. Secondly, the origin of the exponential cut-off is not a finite size effect, but due to the long-range dipolar interaction. A comparison of domain patterns of different hysteresis loops revealed no correlation with topographic features but highlights the existence of preferred nucleation sites in a system that contains structural disorder.

References

[1] T. R. Albrecht, P. Grütter, D. Horne, and D. Rugar, J. Appl. Phys. **69**, 668 (1991).

[2] M. Liebmann, A. Schwarz, S. M. Langkat, and R. Wiesendanger, Rev. Sci. Instrum. **73**, 3508 (2002).

[3] A. Schwarz, M. Liebmann, U. Kaiser, R. Wiesendanger, T. W. Noh, and D. W. Kim, Phys. Rev. Lett. **92**, 077206 (2004).

[4] M. Liebmann, U. Kaiser, A. Schwarz, R. Wiesendanger, T. W. Noh, and D. W. Kim, Phys. Rev. B, in press.

[5] M. Liebmann, U. Kaiser, A. Schwarz, R. Wiesendanger, T. W. Noh, Z. G. Khim, and D. W. Kim, J. Magn. Magn. Mater. **280**, 51 (2004).

[6] U. H. Pi, Z. G. Khim, D. W. Kim, U. Kaiser, M. Liebmann, A. Schwarz, and R. Wiesendanger, J. Low Temp. Phys. **131**, 993 (2003).

[7] U. H. Pi, Z. G. Khim, D. H. Kim, A. Schwarz, M. Liebmann, and R. Wiesendanger, Appl. Phys. Lett. **85**, 5307 (2004).

[8] U. H. Pi, Z. G. Khim, D. H. Kim, A. Schwarz, M. Liebmann, and R. Wiesendanger Phys. Rev B **69**, 094518 (2004).

[9] H. Barkhausen, Z. Phys. **20**, 401 (1919).

[10] A. Hubert and R. Schäfer in *Magnetic domains: The analysis of magnetic microstructures*, Springer-Verlag, Berlin, Germany (1998).

[11] P. J. Cote and L. V. Meisel, Phys. Rev. Lett. **67**, 1334 (1991).

[12] B. Walsh, S. Austvold, and R. Proksch, J. Appl. Phys. **84**, 5709 (1998).

[13] D. W. Kim, T. W. Noh, H. Tanaka, and T. Kawai, Solid State Commun. **125**, 305 (2003).

[14] M. Liebmann, A. Schwarz, S. M. Langkat, and R. Wiesendanger, Rev. Sci. Instrum. **73**, 3508 (2002).

[15] M. Donahue and D. Porter, *Object orientated micromagnetic framework (oommf)*, http://math.nist.gov/oommf/.

[16] A. P. Ramirez, J. Phys. C **9**, 8171 (1997).

[17] J. M. D. Coey, M. Viret, and S. von Moln 'ar, Adv. Ph. **48**, 167 (1999).

[18] Y. Tokura and Y. Tomioka, J. Magn. Magn. Mater. **200**, 1 (1999).

[19] E. Dagotto, T. Hotta, and A. Moreo, Phys. Rep. **344**, 1 (2001).

[20] R. von Helmolt, J. Wecker, B. Holzapfel, L. Schultz, and K. Samwer, Phys. Rev. Lett. **71**, 2331 (1993).

[21] K. Chahara, T. Ohno, M. Kasai, and Y. Kozono, Appl. Phys. Lett. **63**, 1990 (1993).

[22] S. Jin, T. H. Tiefel, M. McCormack, R. A. Fastnacht, R. Ramesh, and L. H. Chen, Science **264**, 413 (1994).

[23] Y. Tokura, A. Urushibara, Y. Moritomo, T. Arima, A. Asamitsu, G. Kido, and N. Furukawa, J. Phys. Soc. Jpn. **63**, 3931 (1994).

[24] J. C. Jiang, E. I. Meletis, and K. I. Gnanasekar, Appl. Phys. Lett. **80**, 4831 (2002).

[25] M. E. Hawley, G. W. Brown, P. C. Yashar, and C. Kwon, J. Cryst. Gr. **211**, 86 (2000).

[26] R. Desfeux, S. Bailleul, A. D. Costa, W. Prellier, and A. M. Haghiri-Gosnet, Appl. Phys. Lett. **78**, 3681 (2001).

[27] J. Dho, Y. N. Kim, Y. S. Hwang, J. C. Kim, and N. H. Hur, Appl. Phys. Lett. **82**, 1434 (2003).

[28] M. Liebmann, U. Kaiser, A. Schwarz, R. Wiesendanger, T. W. Noh, Z. G. Khim, and D. W. Kim, J. Magn. Magn. Mater. **280**, 51 (2004).

[29] R. Desfeux, A. D. Costa, and W. Prellier, Surf. Sci. **497**, 81 (2002).

[30] M. Ziese, Rep. Prog. Phys. **65**, 143 (2002) and Refs. herein.

[31] H. Dulli, P. A. Dowben, S.-H. Liou, and E. W. Plummer, Phys. Rev. B **62**, R14629 (2000).

[32] Y. Wu, Y. Suzuki, U. Rüdiger, J. Yu, A. D. Kent, T. K. Nath, and C. B. Eom, Appl. Phys. Lett. **75**, 2295 (1999).

[33] S. Chikazumi in *Physics of Ferromagnetism*, Clarendon Press, Oxford, U.K. (1997).

[34] R. Schäfer, private communication.

[35] R. L. Wallace, Bell Sys. Tech. J. **30**, 1145 (1951).

[36] X. Che, M. Lederman, G. A. Gibson, H. N. Bertram, and S. Schultz, J. Appl. Phys. **73**, 5805 (1993).

[37] Y. Suzuki, Y. Wu, J. Yu, U. Rüdiger, A. D. Kent, T. K. Nath, and C. B. Eom, J. Appl. Phys. **87**, 6746 (2000).

[38] P. M. Chaikin and T. C. Lubensky in *Principles of condensed matter physics*, Cambridge University Press, Cambridge, UK (1995).

[39] H. S. Wang, Q. Li, K. Liu, and C. L. Chien, Appl. Phys. Lett. **74**, 2212 (1999).

[40] D. J. Garc 'ıa and B. Alascio, Physica B **320**, 7 (2002).

[41] C. Kwon, M. C. Robson, J. Y. Gu, S. E. Lofland, S. M. Bhagat, Z. Trajanovic, M. Rajeswari, T. Venkatesan, A. R. Kratz, R. D. Gomez, J. Magn. Magn. Mater. **172**, 229 (1997).

[42] G. van Tendeloo, O. I. Lebedev, and S. Amelinckx, J. Magn. Magn. Mater. **211**, 73 (2000).

[43] M. E. Hawley, G. W. Brown, P. C. Yashar, and C. Kwon, J. Cryst. Gr. **211**, 86 (2000).

[44] J. Dho, Y. N. Kim, Y. S. Hwang, J. C. Kim, and N. H. Hur, Appl. Phys. Lett. **82**, 1434 (2003).

[45] R. Desfeux, A. D. Costa, and W. Prellier, Surf. Sci. **497**, 81 (2002).

[46] A. Schwarz, M. Liebmann, U. Kaiser, R. Wiesendanger, T. W. Noh, and D. W. Kim, Phys. Rev. Lett. **92**, 077206 (2004).

[47] A. A. Thiele, J. Appl. Phys. **41**, 1139 (1970).

[48] P. Bak, C. Tang, and K. Wiesenfeld, Phys. Rev. Lett. **59**, 381 (1987).

[49] M. R. Freeman and B. C. Choi, Science **294**, 1484 (2001).

[50] L. P. Kadanoff, S. R. Nagel, L. Wu, and S. M. Zhou, Phys. Rev. A **39**, 6524 (1989).

[51] J. P. Sethna, K. A. Dahmen, and C. R. Myers, Nature **410**, 242 (2001).

[52] O. Perkovic, K. Dahmen, and J. P. Sethna, Phys. Rev. Lett. **75**, 4528 (1995).

[53] B. Alessandro, C. Beatrice, G. Bertotti, and A. Montorsi, J. Appl. Phys. **68** 2901 (1990).

[54] S. Zapperi, P. Cizeau, G. Durin, and H. E. Stanley, Phys. Rev. B **58** 6353 (1998).

[55] J. S. Urbach, R. C. Madison, and J. T. Markert Phys. Rev. Lett. **75**, 276 (1995).

[56] D. H. Kim, S. B. Choe, and S. C. Shin, Phys. Rev. Lett. **90**, 087203 (2003).

[57] J. M. Gonz 'alez, O. A. Chubykalo, and J. Gonz 'alez, Phys. Rev. B **55**, 921 (1997).

3.2.13 Domain nucleation and growth of $La_{0.7}Ca_{0.3}MO_3$ on $LaAlO_3$ observed by MFM

M. Liebmann, A. Schwarz, U. Kaiser, T. W. Noh, D. W. Kim, and R. Wiesendanger

Introduction

$La_{0.67}Ca_{0.33}MnO_3$ (LCMO) is, as the previously examined $La_{0.67}Sr_{0.33}MnO_3$ (LSMO, see section 3.2.12) a mixed valence manganite perovskite. The discovery of a colossal magnetoresistance effect (CMR) in LCMO thin films on the (001) surface of a $LaAlO_3$ (LAO) substrate [1] has strongly increased the interest in this class of material. The $La_{1-x}Ca_xMnO_3$ system itself features a rich phase diagram [2]. Furthermore, the investigation of LCMO thin films revealed a strong influence of the substrate. By choosing LAO as substrate, the LCMO film is stressed in its *ab* plane, which causes a tetragonal distortion along the *c* axis (i.e., perpendicular to the sample surface) [3] and induces an out-of-plane anisotropy [4–6].

A qualitative explanation of many electronic and magnetic effects in this material class can be given by the double exchange model [7] based on the exchange of electrons between Mn^{3+} and Mn^{4+} via O^{2-} ions. From this mechanism, it is clear that the complex magnetic and electronic behaviour are closely related and that the oxygen content plays a particularly important role. For example, it has been reported that a lower oxygen content reduces the Curie temperature [8] and magnetoresistance [9].

In spite of the broad interest in LCMO thin films, real space domain observations have only been published by Lu *et al.* on $SrTiO_3$ [10]. However, out-of-plane anisotropy and field dependent domain structure have been previously reported on $La_{0.7}Sr_{0.3}MnO_3$ on a $LaAlO_3$ (001) substrate [11, 12].

Here, we report on external magnetic field, thickness, and particularly oxygen dependent domain structures of epitaxially grown LCMO/LAO thin films studied at 5.2 K by MFM.

Experimental setup

Four $La_{0.7}Ca_{0.3}MnO_{3-\delta}$ films of 50 nm and 100 nm thickness were epitaxially grown on a $LaAlO_3$ (001) substrate by on-axis pulsed laser deposition (PLD) at 750 °C with an oxygen partial pressure of 10 mTorr. Two samples of each film thickness were annealed for 30 min at 600 °C and 500 Torr oxygen atmosphere, and two at 1 Torr oxygen atmosphere, producing films of optimum and reduced oxygen content (denoted by δ), respectively.

Temperature dependent magnetization data were recorded by superconducting quantum interference device (SQUID) magnetometry. Topographic and magnetic force microscopy (MFM) images were acquired with a home-built low-temperature UHV scanning force microscope [13]. Experimental set-up, instrumentation, cantilever

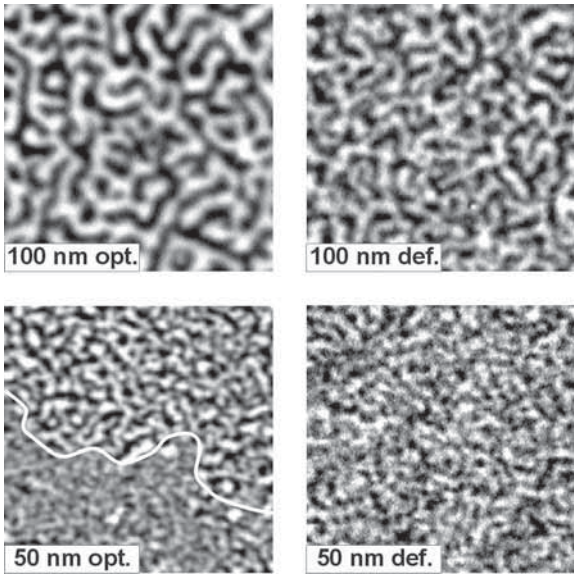

Figure 3.80: 2×2 μm^2 MFM images of the thermally demagnetized samples. Upper row: film thickness 100 nm, lower row: film thickness 50 nm. First column: optimum, second column deficient oxygen content. The 50 nm opt. film is separated into two regions of different constrast, indicated by the white line in the image. Scan heights: 31 nm (100 nm opt.), 33 nm (100 nm def.), 15 nm (50 nm opt. and def.).

preparation, and topographic as well as MFM imaging mode (including the separation of the MFM signal from the topographic and electrostatic tip-sample interaction) are described in section 3.6.2.

All MFM data presented in this article were recorded at 5.2 K by using two commercially available silicon cantilevers both coated with nominally 5 nm iron and with resonance frequencies of 193 kHz (for the 100 nm film with optimum oxygen content) and 192 kHz (for the other samples), respectively, and a force constant of 46 N/m. The oscillation amplitude for all images was $A = \pm5$ nm. Measurement bandwidth and scan rate was 100 Hz and 1 Hz, respectively. Image contrasts vary between 25 mHz and 130 mHz.

Results and discussion

Experimental magnetic parameters of the epitaxially grown $La_{0.7}Ca_{0.3}MnO_{3-\delta}$ films (including the coercive fields and domain widths determined from the MFM data) are summarized in Tab. 3.2. Fig. 3.80 displays the magnetic domain pattern of all four films after thermal demagnetization. As predicted, they exhibit an out-of-plane domain contrast. To evaluate the domain width w of this irregular pattern, a stereological method is used. A sufficiently large number of arbitrarily oriented test lines of total length l are drawn across the MFM image. The number n of intersections between

bright and dark regions, i.e., domain boundaries, are counted. The domain width is then calculated by $w = 2l/\pi n$, giving the ratio between a test area and the total domain wall length in this area (see p. 331 in Ref. [14]). The values obtained by this method in the thermally demagnetized state are noted in the w_{th} column of Table 3.2. The domain width clearly depends on the film thickness t and ranges from 45 nm to 85 nm for the 50 nm and 100 nm optimum oxygen films, respectively. This behaviour can be understood by a simple consideration of domain wall and stray field energy. As the thickness of a perpendicular magnetized film is increased, a given domain wall contains a wall energy per unit length, which is proportional to the film thickness, whereas the stray field of the film remains nearly unchanged. Therefore, the domain width should be slightly increased in order to gain domain wall energy at the expense of stray field energy, which is indeed observed.

The dependence on oxygen content is not so evident. For the 100 nm films, the domain width decreases if the oxygen content is reduced, while the situation is reversed for the 50 nm films. Up to now, the origin of this discrepancy is not clear. In general, one would expect that an increasing oxygen content increases magnetic coupling via the double exchange mechanism and favors a larger domain width. The 50 nm film with optimum oxygen content shows two well separated regions (see the white line in Fig. 3.80), distinguishable by a reduced MFM contrast of 40 % with slightly different domain widths (values for the lower contrast region are given in parentheses in Tab. 3.2). The existence of two regions might indicate a sample inhomogeneity, i.e., a local variation of the oxygen content.

Domain nucleation and growth was observed by ramping a perpendicular magnetic field along one half of a major hysteresis loop from 0 T to 800 mT (600 mT) and back to 0 T for the 100 nm (50 nm) films. Continuous imaging was performed without readjustment of any imaging parameter. Thereby, a field dependent movie of the domain evolution was produced. Every image covers a field range of 5-15 mT according to the applied ramp rate of the magnet, which is small enough to track single image features throughout the whole field range. All four samples behave qualitatively similar. For this reason, we just consider the 100 nm optimum oxygen sample to show the formation of domains during the magnetization process, which is very similar to the LSMO/LAO case described in section 3.2.12.

Fig. 3.81 displays six images of the same sample area as a part of such a movie described above. As the field increases, maze type domains begin to shrink. Right before saturation, only cylindrical domains remain. The image in saturation is shown to demonstrate the contrast due to non-magnetic forces caused by the topography. This image has been used to subtract the topographic contribution from the original data and enhance the magnetic contrast. Note that the grey scale of this image has been readjusted to show the comparably small topographic influence. In a decreasing field after saturation, the domain nucleation starts with the formation of cylindrical regions at 600 mT (400 mT for the 50 nm films). This nucleation mode persists down to a field of 300 mT (150 mT) at which existing domains start to grow in length. This

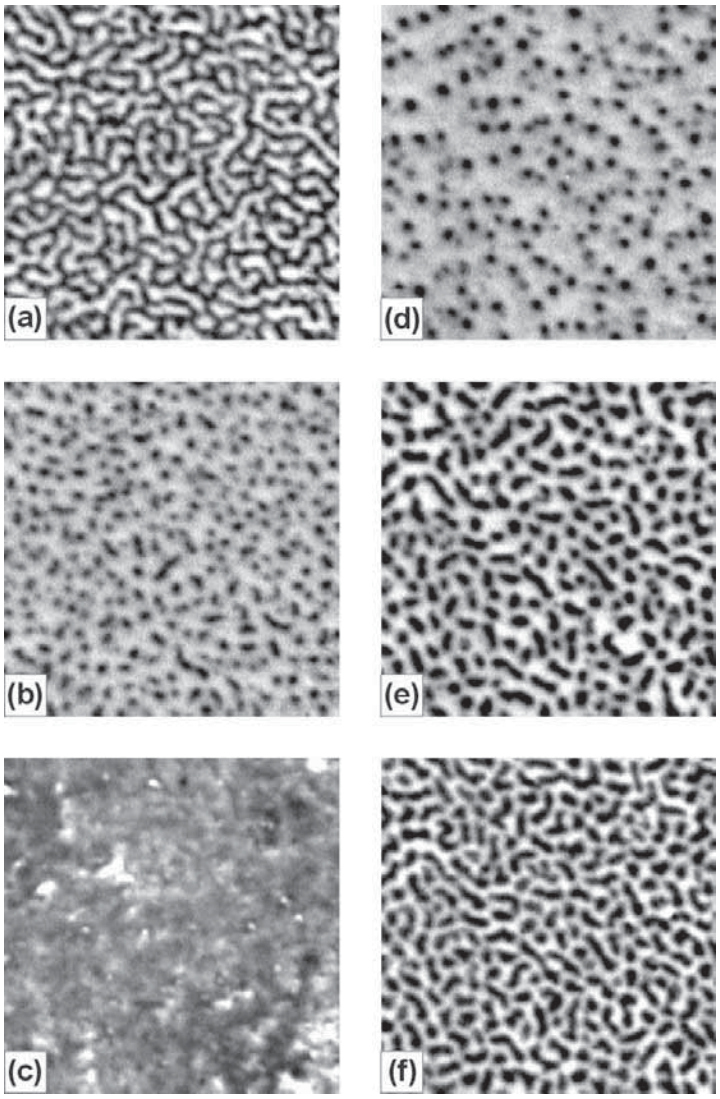

Figure 3.81: Field dependent MFM data of the 100 nm optimum oxygen film. The first column represents the field ramping from zero field to 800 mT, the second column shows images acquired at decreasing field. Image (c) was taken in saturation. The contrast was enhanced in order to show the remaining influence of the topography. This image is subtracted from the originals to obtain images (a,b,d-f) thus enhancing the magnetic contrast. Magnetic field: (a) 205 mT, (b) 400 mT, (c) 800 mT, (d) 360 mT, (e) 200 mT, (f) 0 mT, scan area 4×4 μm^2, scan height 30 nm.

strip-out process gradually increases compared to the nucleation process and dominates the domain evolution down to zero field, where again a maze type domain pattern similar to the thermally demagnetized state is observed. To determine the domain width after saturation in a perpendicular field, the stereological method described

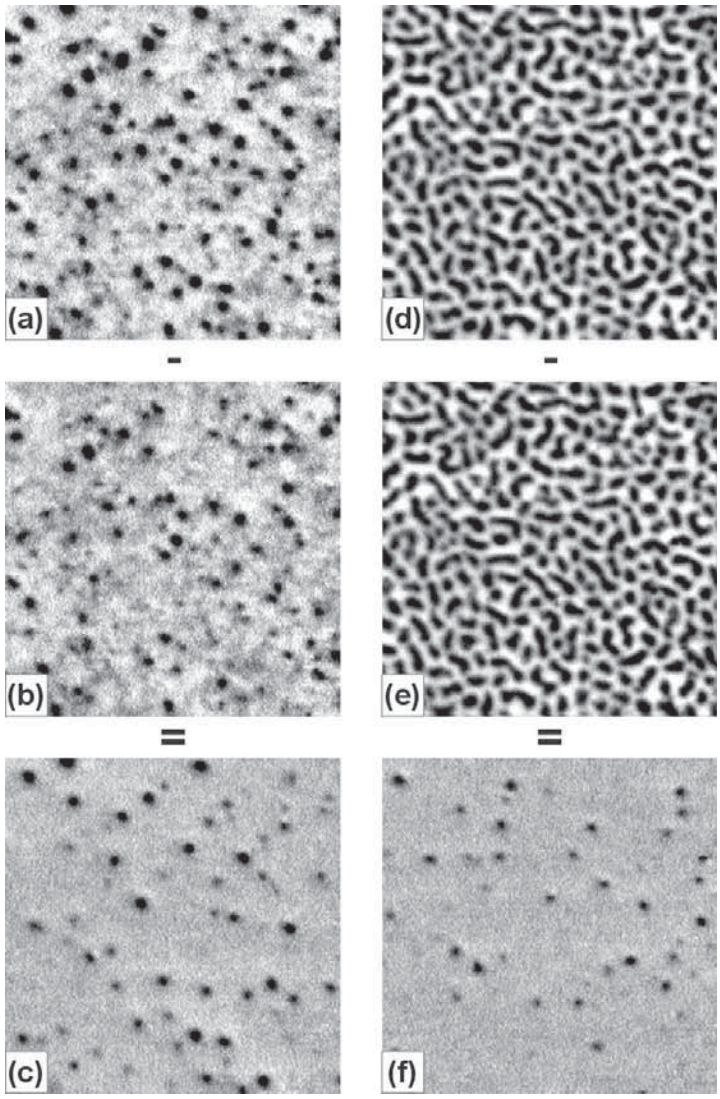

Figure 3.82: Image difference of the 100 nm optimum oxygen film at 400 mT (first column) and 100 mT (second column), acquired at decreasing field. The first two rows show the original images, the last, the image difference (a)-(b) and (d)-(e), respectively. In both cases, the magnetic reorientation takes place in cylindrical units. Magnetic field: (a) 400 mT, (b) 415 mT, (d) 100 mT, (e) 105 mT, scan area 4×4 μm^2, scan height 30 nm.

above has been applied for the image recorded in the coercive field B_C. It can roughly be estimated with an error of several 10 mT from the MFM data set as the field of evenly distributed dark and bright domains. B_C varies from 150 mT (50 nm deficient oxygen) to 250 mT (100 nm optimum oxygen). The values for B_C and the domain width w_c measured at B_C are given in Tab. 3.2.

To further analyse the details of the domain formation process, we make use of

t in nm	oxygen content	T_C in K	M_{sat} in T	B_C in T	w_c in nm	w_{th} in nm
50	deficient	0.170	0.172	0.150	87	63
50	optimal	0.230	0.202	0.200	72 (65)	50 (45)
100	deficient	0.195	0.186	0.230	94	73
100	optimal	0.240	0.285	0.250	109	85

Table 3.2: Samples parameter list. Nominal film thickness t; oxygen content distinguishes between optimum and deficient oxygen concentration; Curie temperature T_C; saturation magnetization M_{sat}; coercive field B_C; domain width in coercive w_c and thermally demagnetized state w_{th}, respectively. The last three rows are extracted from MFM data. Domain widths in parentheses are referred to the area of reduced contrast (see the text).

the negligible lateral drift in our instrument [13]. This stability allows us to directly subtract two consecutive images from each other. As a result, only those areas which reversed their magnetization direction remain visible in the difference image. This is done in Fig. 3.82 for two different fields, around 400 mT (first column) and around 100 mT (second column), respectively. Since the field was reduced during the aquisition of these images, the fraction of dark regions (which are oriented antiparallel to the tip magnetization) increased. Therefore, in the difference image only changes from bright to dark contrast are indicated. We never observed any motion of an existing domain as a whole, which should be displayed as neighboured bright and dark regions in the difference images. In both cases of Fig. 3.82, the changes in the domain pattern appear in circular shape (see images (c) and (f)). Their mean diameter is $\approx$ 110 nm, i.e., of the same order of magnitude as w_c (see Table 3.2). This finding indicates a strong correlation between the final domain width after saturation and the size of the areas which reverse magnetization during domain formation process. However, due to the scan height and the extended stray field of the tip, one cannot make further conclusions concerning the shape of the reversed areas.

Conclusions

We investigated the domain structure of the LCMO/LAO system as a function of film thickness (50 nm and 100 nm) and oxygen content (optimum and reduced). All samples showed an out-of-plane domain contrast. The domain width increased with film thickness while the dependence on oxygen content is not evident. All films behaved qualitatively similar during domain formation. Magnetization reversal during nucleation and growth takes place in units with an apparent diameter comparable to the domain width.

References

[1] S. Jin, T. H. Tiefel, M. McCormack, R. A. Fastnacht, R. Ramesh, and L. H. Chen, Science **264**, 413 (1994).

[2] P. Schiffer, A. P. Ramirez, W. Bao, and S.-W. Cheong, Phys. Rev. Lett. **75**, 3336 (1995).

[3] E. Gommert, H. Cerva, J. Wecker, and K. Samwer, J. Appl. Phys. **85**, 5417 (1999).

[4] T. K. Nath, R. A. Rao, D. Lavric, and C. B. Eom, Appl. Phys. Lett. **74**, 1615 (1999).

[5] M. C. Smoak, P. A. Ryan, F. Tsui, T. K. Nath, R. A. Rao, D. Lavric, and C. B. Eom, J. Appl. Phys. **87**, 6764 (2000).

[6] A. B. Shick, Phys. Rev. B **60**, 6254 (1999).

[7] C. Zener, Phys. Rev. **82**, 403 (1951).

[8] Y. S. Leung and K. H. Wong, Appl. Surf. Sci. **127**, 491 (1998).

[9] B. C. Nam, W. S. Kim, H. S. Choi, J. C. Hur, I. S. Kim, and Y. K. Park, J. Phys. D **34**, 54 (2001).

[10] Q. Lu, C. C. Chen, and A. de Lozanne, Science **276**, 2006 (1997).

[11] C. Kwon, M. C. Robson, J. Y. Gu, S. E. Lofland, S. M. Bhagat, Z. Trajanovic, M. Rajeswari, T. Venkatesan, A. R. Kratz, R. D. Gomez, J. Magn. Magn. Mater. **172**, 229 (1997).

[12] M. E. Hawley, G. W. Brown, P. C. Yashar, and C. Kwon, J. Cryst. Gr. **211**, 86 (2000).

[13] M. Liebmann, A. Schwarz, S. M. Langkat, and R. Wiesendanger, Rev. Sci. Instrum. **73**, 3508 (2002).

[14] A. Hubert and R. Schäfer in *Magnetic domains: The analysis of magnetic microstructures*, Springer-Verlag, Berlin, Germany (1998).

3.2.14 Vortex pinning in $Bi_2SrCa_2Cu_2O_8$ studied by MFM

U. H. Pi, A. Schwarz, M. Liebmann, D. H. Kim, Z. G. Khim, and R. Wiesendanger

Introduction

In the mixed state of type II superconductors normal and superconducting phases coexist. The normal phase is present in the form of individual vortices, containing one quantum flux each in its normal conducting core, which is screened by shielding currents from the superconducting phase. The magnetic properties of type II superconductors are closely related to the field dependent vortex distribution in the mixed state. Vortex pinning at defects in superconductors strongly influence the vortex distribution and thereby the magnetic behaviour of type II superconductors.

Compared to conventional type II superconductors, e.g., niobium, which contain continuous vortex lines (Abrikosov vortices), layered high T_c superconductors like $Bi_2Sr_2CaCu_2O_8$ exhibit so called pancake vortices. Since the coooper pairs are confined into the CuO_2 planes (the coherence length $\zeta \approx 1$ nm is smaller than the distance between the CuO_2 double layers), the individual vortex rings (pancakes) are also located there. However, while vortex rings within the same CuO_2 plane repell each other, those in neighboring planes attract each other via Josephson coupling, thus forming a vortex line.

Several techniques have been utilized to directly observe vortex structures in varying external magnetic fields, e.g., Lorentz microscopy [1], magneto optical microscopy [2], scanning Hall probe microscopy [3] and Bitter decoration method [4]. Lorentz microscopy was very successful for imaging the vortices in a high T_c superconductor. For example, the formation of chain vortices or oscillating vortices were observed in a superconductor subjected to a tilted magnetic field [5]. However, with the above mentioned measurement techniques, it is impossible to observe exact topographic and magnetic profiles of the sample simultaneously. Thereby, it is very difficult to identify any correlation between topographic features and the vortex distribution, and thus the origin of the vortex pinning in the sample.

Compared to the afore-mentioned methods, magnetic force microscopy (MFM) routinely achieves a spatial resolution well below 100 nm [6]. Moreover, topographic images of the sample can be obtained simultaneously using force microscopy in the dynamic mode (DFM) as described in section 3.4. MFM has been successfully used to observe individual vortices [7,8]. Here, we present results of our magnetic field dependent MFM study on vortex distributions in a $Bi_2Sr_2CaCu_2O_8$ single crystal containing artificial columnar defects as well as intrinsic line defects. To clarify the influence of the tip-vortex interaction on the genuine vortex distribution, we also utilized spectroscopy measurements (cf., section 3.5.3 and 3.4.2 to estimate the excerted lateral dragging force.

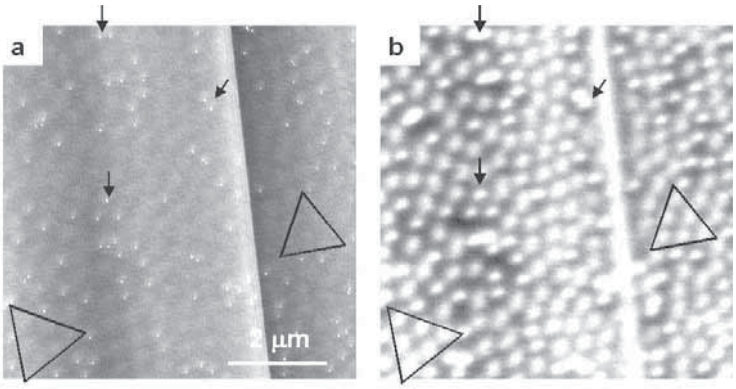

Figure 3.83: Surface topography image (a) and MFM image (b) of the same area of a $Bi_2Sr_2CaCu_2O_8$ single crystal with a low-density of columnar defects. The point like contrast in (a) is the columnar scar due to the uranium ion bombardment. One can notice that every site of the columnar scar is occupied by a vortex. Three positions that are indicated as solid arrow marks show this fact, for example. Free vortices that are not trapped at the columnar defects form a lattice structure distorted by the presence of the randomly distributed columnar defects. In the region enclosed by triangular marks, one can observe a well ordered Abrikosov lattice because there are no columnar defects nearby. There appears a bright line in (b). The corresponding area in the topographic image (a) shows a line step with a 0.36 nm height. Parameters: f_0=204 kHz, c_z=52 N/m, A = 10 nm, Δf = -8 Hz, h = 18 nm, T = 5.2K, image size = $7 \times 7 \mu m^2$.

Sample preparation and experimental setup

The $Bi_2Sr_2CaCu_2O_8$ single crystal was grown by a floating zone method and was irradiated with 1.3 GeV uranium ions to form columnar defects [9]. The uranium ions were irradiated with the ion dose corresponding to a matching magnetic flux density B_m of 2 mT. These artificial columnar defects are aligned parallel to the crystalline c-axis.

The low temperature magnetic force microscope setup, magnetic tip preparation and the MFM plane subtraction mode are described in section 3.6.2 [10]. In the employed dynamic mode, i.e., the frequency modulation technique, the cantilever with eigenfrequency f_0 is oscillated by a self-excitation resonance loop ("self-driven oscillator"). Due to the tip-sample interactions its actual resonance frequency f is shifted by Δf, i.e., $\Delta f = f - f_0$. For attractive interactions Δf is negative. The amplitude A, typically about 10 nm, is kept constant by an additional feedback. For long-range interactions the force gradient can be calculated from the measured frequency shift via $F' = 2c_z \Delta f / f_0$, where c_z is the spring constant of the cantilever.

The sample was cut by approximately 1 mm × 3 mm size, cleaved with an adhesive tape and transferred to the vacuum chamber immediately to reduce surface contaminations. To introduce vortices into the sample by field cooling, the following procedure was applied. First, the sample is held in a wobble-stick at room tempera-

ture. A suitable external magnetic field is adjusted with a superconducting magnet, which has homogeneity of 0.5% at the position of the microscope sample holder. After opening of the shutter the microscope temperature increases to about 30 K. During transfer the crystal is always in contact to room temperature via the wobble stick. Therefore, no vortices can be generated during the transfer through the stray field of the magnet. After reaching the final position in the sample stage, where the magnetic field is very homogeneous, the wobble stick is retracted. Within an hour (after closing the shutter) an equilibrium temperature of 5.2 K is reached.

For topography measurements, the frequency shift Δf was kept constant by a z-feedback, that controls the tip-sample distance via voltages applied to the z-electrode of the piezoelectric scanner. Typically, the tip-sample distance is then below 3 nm. While scanning, we adjusted the x-y plane to match the sample surface plane. After this tilt compensation z-feedback was turned off and the tip was lifted up by a height h of typically about 20 nm. At such a distance the long-range forces, like the magnetostatic force, dominate and MFM data can be acquired. In this way we imaged the magnetic field strength at the surface of $Bi_2Sr_2CaCu_2O_8$ in a mixed state. For parallel tip-magnetization and vortex polarity, the interaction is attractive and the frequency shift is negative (bright in the MFM images) and vice versa for the antiparallel configuration.

To interpret the images it is only important to know that the 20 nm iron coated tip is sensitive to the single magnetic quantum flux associated with each vortex. Therefore, they appear as objects with radii on the order of the London penetration depth $\lambda \simeq 150$ nm for $Bi_2Sr_2CaCu_2O_8$.

Vortex distribution after field cooling in the presence of columar defects

As long as the external magnetic fields $\mu_0 H$ during field cooling is smaller or equal to the matching field, all vortices are pinned at columnar defects. Their arrangement follows the random distribution of the columnar defects characteristic for the vortex glass state. However, if the external magnetic field is larger than the matching field, the additional free vortices form locally an Abrikosov lattices between the strongly pinned vortices.

Figure 3.83(a) and (b) show a topographic and a magnetic images of our sample recorded in the same area for $\mu_0 H \geq B_{\mathrm{m}}$. Each point-like contrast in (a) represents an artificial columnar scar caused by the uranium ion bombardment. The total number of the columnar scars is 106. This value is about 2.3 times larger than the expected number of columnar defects (47) inferred from the irradiation ion dose (matching field of 2 mT) and image area ($7 \times 7 \mu m^2$) and probable due to the fact that the ion irradiation dose was not homogeneous all over the sample. Comparing with the MFM image (b), one can notice that every site of point-like contrast is occupied by a vortex, e.g., the three positions indicated by arrows. Well ordered triangular Abrikosov lattices

as indicated in Fig. 3.83 (b) are present between the randomly distributed columnar defects.

Vortex pinning at intrinsic line defects

In addition to the pinned and free vortices, one can also observe a bright line in Fig. 3.83(b). The corresponding area in Fig. 3.83(a) shows a step. The height of this step obtained from the topographic image Fig. 3.83(a) is 0.36 nm, which is much smaller than a half unit cell of $Bi_2Sr_2CaCu_2O_8$ (1.55 nm). It is well known that the top layer of the cleaved $Bi_2Sr_2CaCu_2O_8$ is the BiO layer because the bonding strength between adjacent BiO layers is the weakest. If the step was formed during the cleavage process, its height should be a multiple of the half unit cell height. Thus, the smaller step height observed in the above image indicates that this step is not a regular cleavage step but an intrinsic crystalline imperfection. It was reported that inserted or missing $Ca + CuO_2$ layer in $Bi_2Sr_2CaCu_2O_8$ results in the size difference of the unit cell about 0.32 nm along the c axis [11]. This value is very close to the height difference observed in our measurement. So we assume that the magnetic contrast in Fig. 3.83(b) originates from magnetic flux due to vortices trapped in a dislocation due to a stacking fault inside the sample.

We investigated the vortex pinning behavior at several topographic steps with different step heights. We found a region that has two different kinds of steps. The topographic image is shown in Fig. 3.84(a). There appear 3 steps and we designate them as A, B and C, respectively from left to right. The shape of step A is different from the others. It has some kinks along the line of the step while others are just straight. It is well known that the topographic step formed during sample cleavage is not completely straight but has some kinks. Thus one can presume that step A was formed during sample cleavage and the other two steps have different origin.

The step height was measured using a histogram of the topographic data (the measured height of each point on the surface). The four peaks in the distribution correspond to a particular terrace and the step height was obtained from the z distances between each pair of the four terraces. The heights of A, B, C steps were 1.71 nm, 0.56 nm, 0.62 nm, respectively. The height of step A is slightly larger than the half unit cell (1.55 nm) while the other two steps are much smaller than that of the half unit cell.

Step A is not parallel with step B and C. So we could find a region where step A meets step B. The topographic image of this region is in Fig. 3.84(b). The topographic height profile at the region marked by solid line in Fig. 3.84(b) is shown in Fig. 3.84(c). As one can see in the height profile, the step B still exists on the left side of step A even when the step A extends to the right side terrace of step B. One can deduce the possible configuration of the step A and B from the height profile. Figure 3.86(d) shows schematically the possible side view configuration of the step A and B after they cross each other. This is a clear evidence that the two steps A and B were not formed simultaneously. Step B was formed prior to step A. Thus, we believe step A

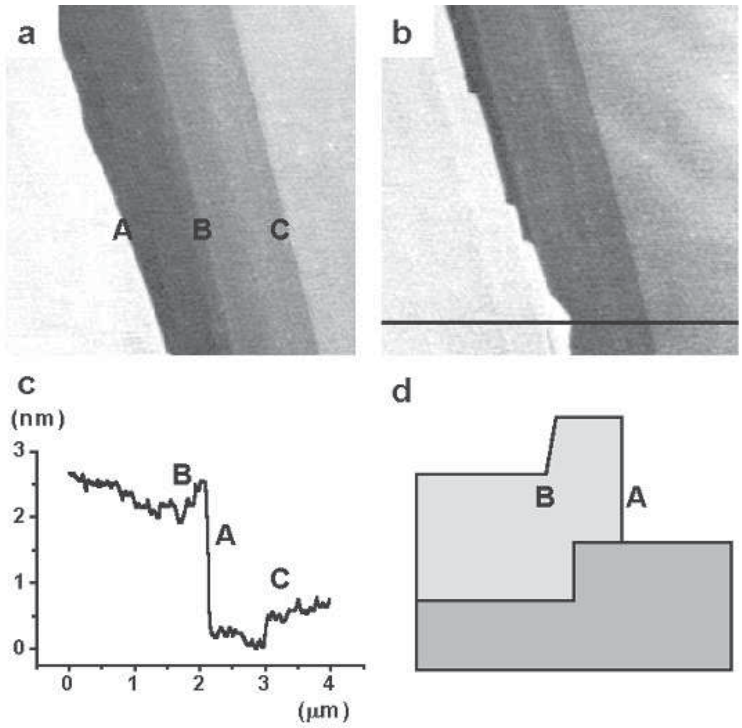

Figure 3.84: Topographic images obtained at 82 K. There are three steps. (a) These steps are named as A, B and C. The heights of these steps are 1.71 nm, 0.56 nm, 0.62 nm, respectively. (b) Step A and B meet because they are not parallel. (c) The height profile at the region marked as a solid line in (b), where step A and B cross. (d) A schematic side view of the possible configuration of the step A and B after they cross each other. Step A and B cannot be formed simultaneously. Parameters: f_0 = 69.7 kHz, c_z = 2.2 N/m, A = 20 nm, Δf = -7 Hz, T = 82 K, image size = $4 \times 4 \mu m^2$.

was formed during cleavage process while step B was formed during crystal growth. The height of step A does not exactly coincide with that of half the unit cell, but the difference is within the uncertainty of the scanner calibration (10%).

Further, we examined the vortex pinning strength behavior at these three different steps. The sample was cooled from 96 K (above T_c of our sample) to 5.2 K without any external magnetic field. Thereafter, images in different external magnetic field (0 mT, 25 mT and 50 mT) at 5.2 K were acquired. Figure 3.85(a) is the topographic image obtained at a frequency shift set value of -7 Hz. Figure 3.85(b), (c) and (d) are magnetic images obtained at 0 mT, 25 mT and 50 mT, respectively.

Unexpectedly, one can observe bright line MFM contrasts in Fig. 3.85(b), implying that vortices are trapped in dislocations even though the sample was cooled without any magnetic field from above its transition temperature. During the cooling process, the magnetic tip was separated from the sample by a few millimeters. So the effect of the stray magnetic field from the tip can be ruled out. However, we did not shield our

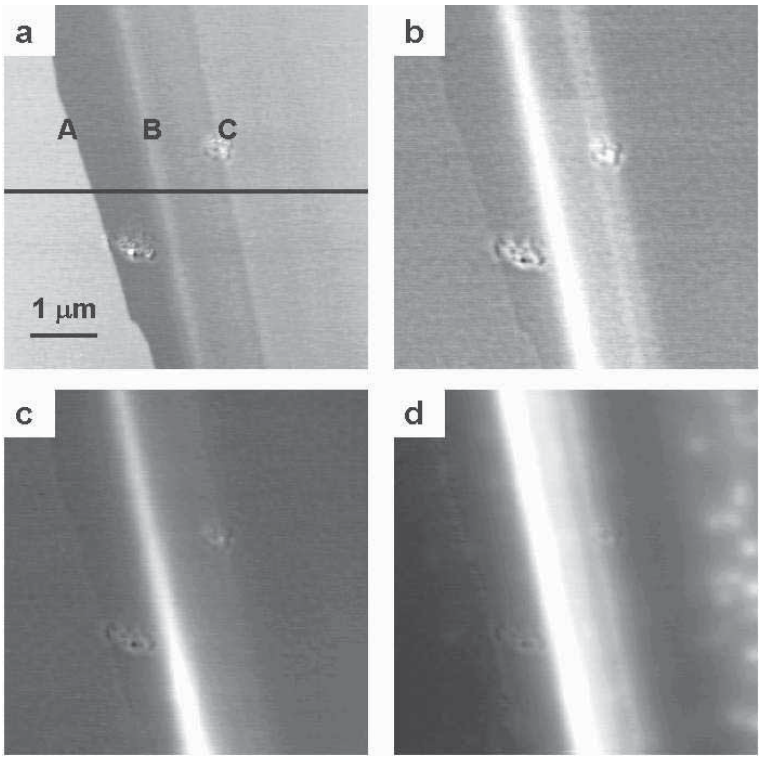

Figure 3.85: Topographic image (a) and MFM image of the same area obtained at 5.2 K under external magnetic field of 0 mT (b), 25 mT (c) and 50 mT (d). Step B and step C are strong vortex pinning centers, while step A has no effect on trapping vortices. The line profiles at the region marked as solid line in (a) will be shown in Fig. 3.86(a). Parameters: f_0 = 69.7 kHz, c_z = 2.2 N/m, A = 20 nm, Δf = -7 Hz, h = 18 nm, T = 5.2 K, image size = $5 \times 5 \mu m^2$.

microscope system magnetically, therefore magnetic fields from the earth or magnetic components near the sample may be present. The magnitude of this magnetic field is less than 0.1 mT in our case, resulting in an expected vortex density of about $0.05/\mu m^2$, i.e., 1.25 vortices in Fig. 3.85(b) considering the image area of $5 \times 5 \mu m^2$. However, the intensity of the line contrast surpasses the expected vortex density here. This is due to the attractive interaction between the magnetic tip and the vortex, whereby vortices are dragged with the scanning tip. The magnitude of the lateral dragging force can be estimated as shown in Fig. 3.89 and will be discussed in detail in the next section.

The bright line surely represents the magnetic field due to the pinned vortices along the dislocation line, because the signal increases for higher external magnetic field and disappears above the transition temperature of $Bi_2Sr_2CaCu_2O_8$. A comparison of the topographic image with the magnetic image as displayed in Fig. 3.86 (a) demonstrates, which step is more effective as a vortex pinning site. The profiles taken from the MFM images in Fig. 3.85 were obtained at several external magnetic fields, i.e., of 0 mT (b), 25 mT (c), and 50 mT (d), respectively. Comparing the MFM profiles with the

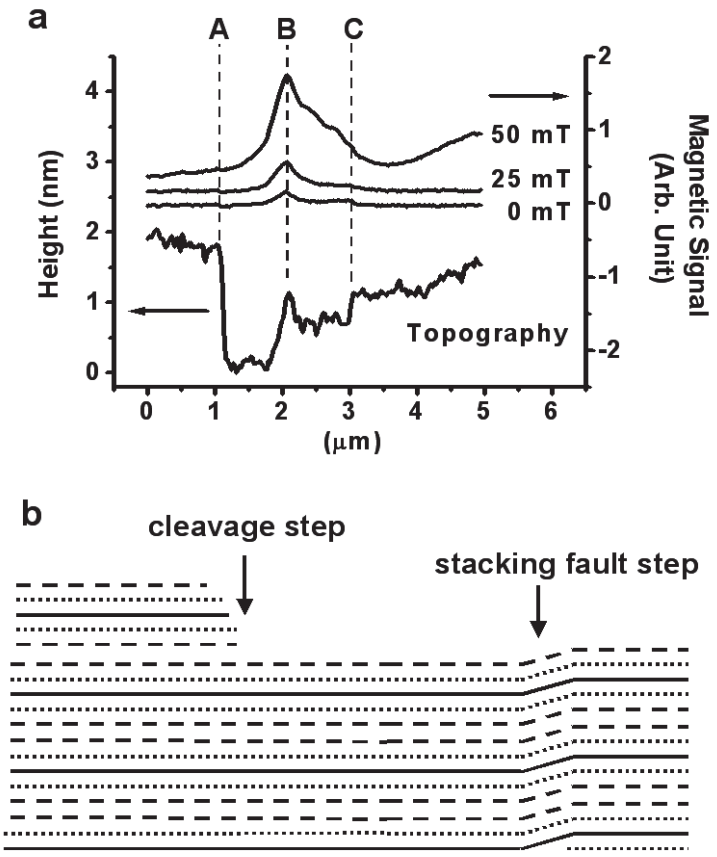

Figure 3.86: (a) Line profiles of Fig. 3.85(a) - (d) along the marked solid line in Fig. 3.85(a). Comparison of the MFM profiles with the topographic profile clearly shows which step is efficient in trapping vortices. Step B is the most efficient in trapping vortices, while step A does not trap any vortices. Each MFM profile is shifted by 0.2 for a better visualization. (b) Schematics of the layer structure between the cleavage step and the stacking fault dislocation. In the stacking fault dislocation, all the layers above the stacking fault are displaced. In the cleavage step, however, all the layers except the exposed top layer remain unchanged.

topography profile, one can find that step B is the most effective in vortex pinning. Step C also traps some vortices, but no vortex is trapped at step A. This implies that the step which occurs from the cleavage process has no effect on vortex pinning while the intrinsic dislocations due to stacking faults act as strong pinning sites.

This fact can be understood simply from the mechanism of the vortex pinning. The schematic diagram of the layer structure in Fig. 3.86(b) shows the difference between the cleavage step and the step due to the stacking fault. Due to the inserted or missing layer, all the layers above the stacking fault are displaced. The connections of the layers may be broken across the stacking fault dislocation, yielding antiphase boundary. Even though they are not broken, their connection involves strain as shown in the schematic layer structure in Fig. 3.86(b). The superconductivity must be weaker in the region

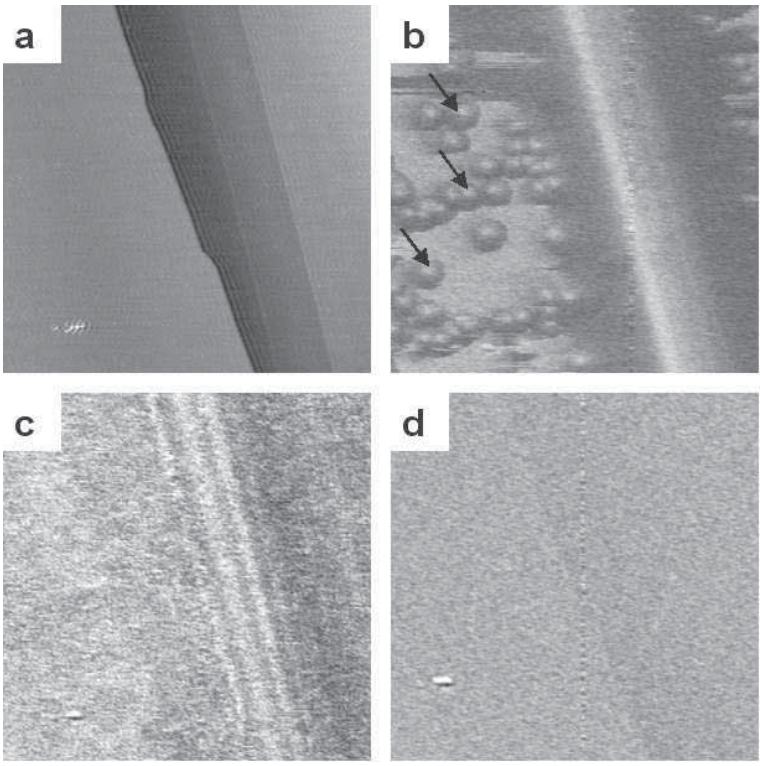

Figure 3.87: Topographic image (a) obtained at 82 K and MFM images obtained at 55 K (b), 82 K (c), 96 K (d) in nearly the same region. At 55 K, vortices are well trapped at both artificial columnar defects and stacking fault dislocations as indicated by arrow marks (b), while vortices are trapped only at stacking fault dislocations at 82 K (c). Above the transition temperature, all vortices are absent (d). Parameters: f_0 = 69.7 kHz, c_z = 2.2 N/m, A = 20 nm, Δf = -8 Hz, h = 18 nm, image size = $7 \times 7 \mu m^2$.

where the layers are broken or strained. The vortices having normal conducting cores are trapped in this weak superconducting region to gain condensation energy. The displacement of the layers due to the stacking fault extends to the top surface of the sample. Thus the weak superconducting region extends along the c axis, rendering the pinning behavior coherently and more effective than at surface steps. Furthermore, there is no energy gain involved at the cleavage step because all the layers except the exposed top layer have the same superconducting property.

It was reported that planar antiphase boundaries in epitaxial YBCO film grown on vicinal $SrTiO_3(001)$ serve as pinning sites [12, 13]. The dislocation found in our sample is the same with the reported antiphase boundary except the fact that it is not due to the vicinal substrate, but due to stacking faults.

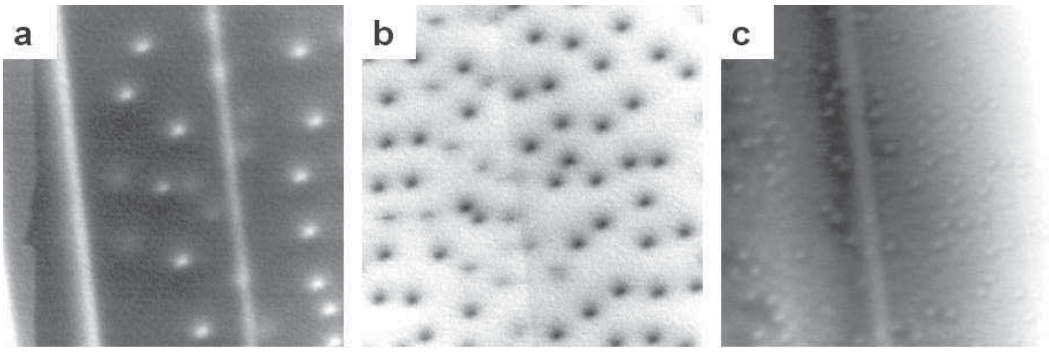

Figure 3.88: MFM images obtained right after field cooling under a magnetic field of 1 mT (a) and -3 mT (b). The total number of vortices is 23 in (a) and 67 in (b). By subtracting this value from the expected value calculated from the applied external magnetic field, we can estimate how many vortices are trapped in the dislocation line. After obtaining MFM image in (b), we increased the external magnetic field up to 50 mT. (c) shows the MFM image obtained at 50 mT. One can observe that many vortices appear from the right side and that the incoming vortices are trapped, forming a line contrast. Parameters: $f_0 = 204$ kHz, $c_z = 52$ N/m, $A = 10$ nm, $\Delta f =$ -8 Hz, $h = 18$ nm, $T = 5.2$ K, image size $= 7 \times 7 \mu m^2$.

Temperature dependence

The pinning behavior of the observed stacking fault dislocation was studied at different temperatures. At 5.2 K, we applied an external magnetic field up to $\mu_0 H = 300$ mT to put large amounts of vortices into the sample. After turning off the magnet the temperature was increased and topographic as well as magnetic images were recorded at several different temperatures. The results are shown in Fig. 3.87. The topographic image obtained at 82 K is displayed in (a), while (b), (c) and (d) are the MFM images obtained at 55 K, 82 K, and 96 K, respectively.

At 55 K (Fig. 3.87(b)), vortices are trapped at the stacking fault dislocation and at artificial columnar defects. Three strongly pinned vortices are marked by arrows in (b). Beside these pinned vortices, much more unpinned and therefore mobile vortices are present. They are dragged due to the attractive tip-vortex interaction with the scanning tip. The dark rings around the strongly pinned vortices are visible, because the mobile vortices are repelled from the location of the fixed vortices. One can also observe a bright contrast spread on the left side of the image. For the same reason no bright contrast exists near the dislocation line, which also contains many vortices.

Note that no vortex appears to be trapped at columnar defects near the stacking fault dislocation. Abrikosov-type vortices, which are oriented parallel to the *c*-axis, tend to be absorbed into nearby planar defects and become a Josephson vortex, which are oriented perpendicular to the *c*-axis, because it is energetically favorable [14]. In fact, near the step dislocation, Abrikosov vortices trapped at columnar defect are just metastable. At higher temperature (55 K) they can hop from a columnar defect to a planar defect and become a Josephson vortex, whereby no Abrikosov vortices remain

near the dislocation line.

Compared to the case at 55 K, the image at 82 K (cf., Fig. 3.87(c)) shows that no vortices are trapped at artificial columnar defects, while a somewhat weaker vortex contrast is still visible near the step dislocation. This may indicate that the pinning strength at the stacking fault dislocation can be stronger than that of artificial pinning sites due to uranium ion irradiation. However, there is a possibility that vortices on the dislocation can be attracted by the magnetic tip, making brighter contrast in the image. This effect will be discussed later with data shown in Fig. 3.88. Furthermore, the Meissner current that repels the magnetic tip is smaller near the stacking fault dislocation, where the superconductivity is weaker, yielding a bright contrast on the dislocation in the image, although no vortex is present.

At 96 K (above the transition temperature of our sample), there is no vortex contrast but just a faint topographic contrast, implying that the bright contrasts are due to the superconducting property of our sample, that is, vortex pinning.

Anisotropic pinning

Regarding the vortex density trapped along the stacking fault dislocation, one can get a quantitative estimate from the MFM image because the image contrast is proportional to the vortex density. This is rather complicated, however, due to the mobility of the vortex along the line of the dislocation. The MFM images obtained right after field cooling under 1 mT and -3 mT are shown in Fig. 3.88(a) and (b) respectively. Here the minus sign implies that the direction of the magnetic field is opposite to the tip magnetization direction. When the magnetized tip and the vortex are magnetically parallel, the interaction is attractive, yielding bright vortex contrast in the MFM image in Fig. 3.88(a). On the other hand, if they are anti-parallel, the interaction is repulsive, yielding dark vortex contrast as shown in Fig. 3.88(b). In Fig. 3.88(a), the total number of the vortices observed inside the image area of $7 \times 7 \mu m^2$ is 23. In this count, we did not include any vortices trapped in the dislocation line. Under an external magnetic field of 1 mT, one can expect the number of vortices to be 23.6, inside of the imaged area of $7 \times 7 \mu m^2$ if there is a single flux quantum of $2.07 \times 10^{-15} \mathrm{T} \cdot \mathrm{m}^2$ for each pinning site. Excluding vortices trapped inside the dislocation line, the experimentally observed vortex number, 23, is nearly equal to the expected value 23.6 Thus the number of vortices in two dislocation lines in Fig. 3.88(a) should be less than 1. However, the MFM image in Fig. 3.88(a) looks as if many vortices are trapped along the dislocation line.

If vortices trapped in the step dislocation move together with the tip along the line due to the attractive tip stray magnetic field, just one vortex could produce a bright contrast along the whole line defect, because it will always appear below the tip. Note, that the motion of the vortex will be confined along the line of dislocation due to the condensation energy cost. If a vortex would leave the dislocation line, the presence of the vortex core inside the perfect superconductor raises the free energy of the superconductor by the condensation energy of the core volume. On the other

hand, the vortex movement along the dislocation line does not cost an additional free energy, because the vortex core stays in the normal or at least weakly superconducting region. Consequently, the movement of the vortex is confined along the step dislocation and impeded across it, hence resulting in an anisotropic pinning behaviour of this type of line defect. This kind of anisotropic pinning behavior at planar defects was already addressed theoretically [14] and experimentally, e.g., epitaxial YBCO film grown on vicinal substrate that includes many planar antiphase boundaries also shows anisotropic pinning behavior [13].

The situation is different, if the vortex-tip interaction is repulsive. In Fig. 3.88(b), the total number of vortices is 67. The expected number of vortices for -3 mT field cool case is 71. About four vortices are missing. There is no clear line contrast in this image, indicating no vortices trapped in the dislocation line. Actually, one can observe a vertical faint line in the middle of the image, but this appears too weak to be considered as vortices trapped in the dislocation, but is likely to be the residual signal from the topography visible in the MFM signal .

Subsequently, an external magnetic field opposite to the direction during field cooling was applied. Figure 3.88(c) shows the MFM image obtained at +50 mT. Many vortices entered the scan area from the right side. The incoming vortices, which now occupy the whole scan area, exhibit a bright contrast, because their magnetization direction is the same with that of the tip. The density of the vortices in Fig. 3.88(c) has a gradient as expected from the Bean model [15].

The important point is that now a bright line contrast is obseved at the same position of the faint line in Fig. 3.88(b). It can be inferred that vortices are trapped, forming a line contrast as described previously for step dislocations. In fact, the faint line contrast in Fig. 3.88(b) exhibits a step height of 0.36 nm in agreement with a stacking fault dislocation.

Why is there no dark line contrast in -3 mT field cool image shown in Fig. 3.88(b)? It seems that the vortex contrast in the dislocation appears in MFM images only when the interaction between the tip and the vortex is attractive. When it is repulsive, the vortex contrast is absent. This is another evidence that supports our assumption: The vortices can move freely along the dislocation line. When the tip is near the dislocation line, it attracts vortices that are moving along the dislocation line, yielding bright vortex contrast. However, if the magnetization direction of the tip is opposite to that of the vortex, the tip repels the vortex away from the tip along the dislocation line, yielding no contrast in the MFM image. The missing four vortices mentioned in Fig. 3.88(b) can also be qualitatively understood. The missing vortices might have been located somewhere in the dislocation. But the tip repels these vortices. One cannot observe these vortices in the MFM image.

Estimation of the lateral dragging force during scanning

For a thorough evaluation of vortex images obtained by MFM it is important to know the lateral dragging force excerted on the vortex during scanning. If the lateral

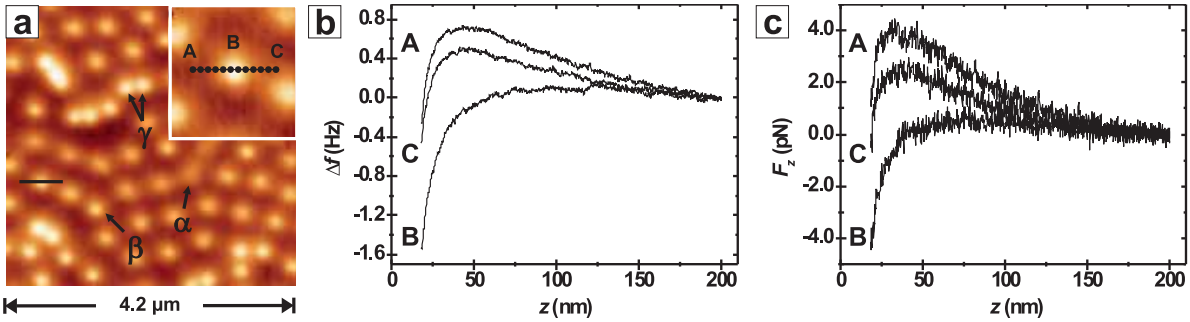

Figure 3.89: (a) A typical MFM image of vortices obtained at 5.2 K. Spectroscopy data were obtained along the solid line across a strongly pinned vortex in the image. In the zoomed image shown in the inset of (a), each spectroscopy site is marked as dot. The site marked as A, B, and C represents the leftmost, central and rightmost position among the spectroscopy points, respectively. (b) $\Delta f(z)$-curves obtained on A, B and C sites. (c) $F_z(z)$-plots converted from $\Delta f(z)$-data shown in (b). Image parameters: f_0 = 69.7 kHz, c_z = 2.2 N/m, A = 20 nm, Δf = -8 Hz, h = 18 nm.

dragging force is larger than the pinning force, it is impossible to visualize the genuine vortex pattern. Obviously, this effect is also important for the appearance of the line defect discussed above. For the same vortex density it appears fully occupied, i.e., as a bright line, if the tip-vortex interaction is attractive or empty, if the tip-vortex interaction is repulsive.

To determine the lateral force, spectroscopy data were recorded and analyzed in the following manner. First, a typical vortex image was obtained at 5.2 K as shown in Fig. 3.89(a). One can notice different levels of vortex intensities in Fig. 3.89(a), although each vortex contains only one quantum flux Φ_0. Several reasons can explain such contrast variations. For a weakly pinned vortex marked as α, thermal fluctuations of the vortex position on a time scale much faster than image acquisition lead to a somewhat blurry and reduced contrast, because the flux is distributed on a larger area. In contrast, a vortex strongly pinned at a columnar defect marked as β shows a stronger contrast. Vortices pinned at closely spaced columnar defects, which is marked as γ, exhibit even more increased contrast due to the overlap of their magnetic flux.

For force spectroscopy measurements, scanning was stopped at spots of interest and the tip was retracted to about 400 nm from the sample and approached again to the original tip-sample separation value h. During retracting and re-approaching the tip, frequency shift data, i.e. $\Delta f(z)$-curves, were recorded and converted into the vertical force $F_z(z)$ by using the formalism introduced by Giessibl [16].

A series of $\Delta f(z)$-curves were obtained across an individual vortex strongly pinned at a columnar defect to determine the positional dependence of the tip-vortex interaction. Note that a weakly pinned vortex is unsuitable, because its position is affected by the stray field from the tip. Thus, the real positional dependence of the interaction cannot be extracted. Such vortices, which are pinned at intrinsic defects or trapped

between strongly pinned vortices due to their mutual repulsion, can be distinguished in Fig. 3.89 from the strongly pinned ones by the reduced contrast.

A data set of twelve $\Delta f(z)$-curves, each with a z-increment of 0.2 nm was captured along the solid line across the vortex as depicted in Fig. 3.89(a). The inset shows a zoomed image around the vortex. The positions of the $\Delta f(z)$-curves along the line across the vortex are marked as dots, each about 55 nm apart. The sites A, B, and C represent the leftmost, central and rightmost positions, respectively.

In Fig. 3.89(b), we plotted three $\Delta f(z)$-curves obtained at both ends (A and C) and directly above the vortex center (B). The other curves are located between these curves and omitted for simplicity. Since the data obtained during retracting and re-approaching the tip were identical, only the retraction data are shown. The curves obtained at A and C are both 300 nm away from the center, which is significantly larger than the London penetration depth of BSCCO of $\lambda \approx 180$ nm. However, they do not coincide due to the difference in the distribution of neighboring vortices. The converted force plots $F_z(z)$ are displayed in Fig. 3.89(c). At a tip-sample separation of 18 nm, the force measured right above the vortex center (B) is more attractive than that measured far away from the vortex (A) by about 5.4 pN.

For tip-sample distances ranging from about 50 nm to 200 nm, the force in all three curves becomes more and more repulsive as the tip-sample separation is reduced. This is due to the Meissner effect, whereby the tip stray field is repelled from the interior of the superconductor by local shielding currents resulting in a repulsive tip-sample interaction. Closer towards the center (B), the attractive force between the tip and the magnetic field of the vortex compensates this repulsive Meissner force, yielding a smaller increase of the force. At small tip-sample distances, the non-magnetic and always attractive van der Waals force plays a role. As a result, the attractive interaction between the tip and the sample is always stronger than the repulsive Meissner force. Therefore, all curves exhibit a steep downward slope for small tip-sample distances, even far away from a vortex.

The tip-sample interaction energy at each spectroscopy point can be obtained by integrating the force data F_z. Since the magnetostatic force between tip and sample is conservative, the interaction energy at any point should be independent of the integration path. Here, we obtain the (x, z)-dependence of the energy by integrating F_z along the z-direction from z to 200 nm. Note that integration up to 200 nm is sufficient in our case, because the interaction becomes negligible and has the same Δf and $F_z(z)$ values for such large tip-sample separations (cf. Fig. 3.89(b) and 1(c)).

A gray scale contour plot of the interaction energy is shown in Fig. 3.90(a). The vertical and horizontal axes represent the tip-sample separation and the lateral tip position across the vortex, respectively. The gradient of the energy to the z direction and to the x direction represents the vertical force and lateral force, respectively. The line profiles of the energy plot obtained at several z values of 18 nm, 68 nm, 118 nm are shown in Fig. 3.90(b). Because the attractive interaction is stronger right above the vortex center, the interaction energy plotted as a function of lateral tip position

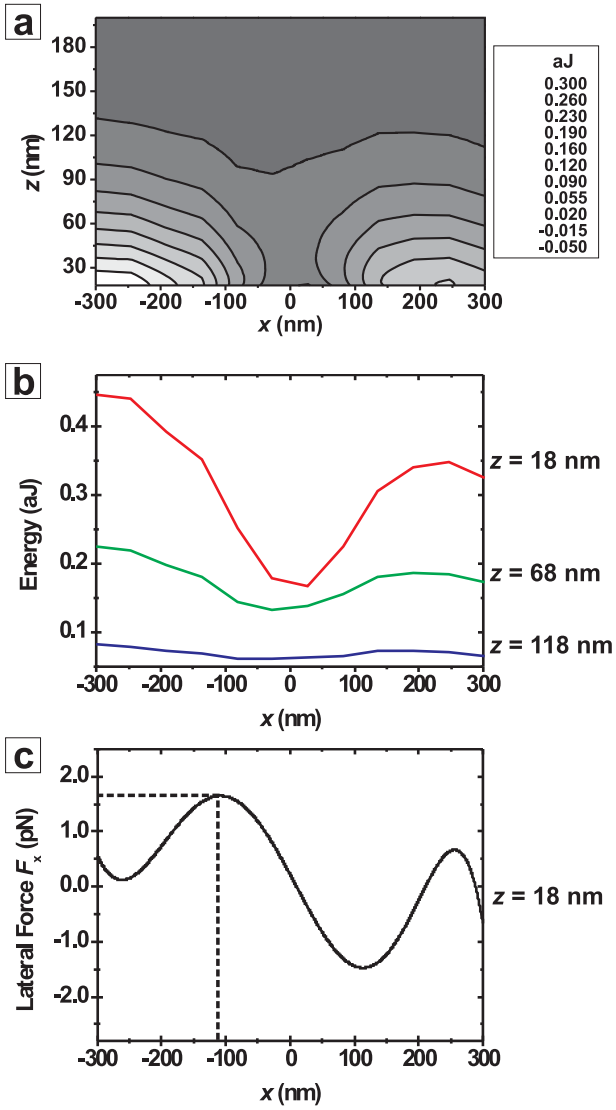

Figure 3.90: (a) Gray scale contour plot of the tip-sample interaction energy. The energy values are plotted as a function of the lateral tip position across the vortex (horizontal axis, x) and with the tip-sample separation (vertical axis, z). Several identical energy values are connected with a solid line to show the contour. (b) Visualization of the potential well due to the attractive interaction between tip and vortex for tip-sample separations z of 118 nm, 68 nm, and 18 nm, respectively. Each potential profile is shifted by 0.05 aJ for a better visualization. (c) Plot of the lateral force $F_x(x)$ at a tip-sample separation z of 18 nm. The lateral force has a maximum value of 1.5 pN at about 110 nm away from the vortex center.

shows a potential well. Due to the different distribution of the neighboring vortices the shape of the potential well is slightly asymmetric (cf., curve A and C in Fig. 3.89(b)). For larger tip-sample separations, the depth of the potential well becomes smaller.

The derivative of the potential with respect to the x-direction represents the lateral force exerted on the vortex due to the presence of the magnetic tip. Since each potential curve contains only twelve data points, it is fitted by a polynomial, which is then differentiated to get a plot of lateral force. In Fig. 3.90(c), the lateral force at a tip-sample separation of 18 nm is plotted with lateral tip position. The lateral force is maximum at about 110 nm away from the vortex center. The maximum lateral dragging force is about 1.5 pN.

According to the model-calculation reported before [17], the lateral force exerted by the tip on a single vortex is about a factor of four smaller than the vertical force. The estimated lateral force of 1.5 pN is about a fourth of the measured vertical force of 5.4 pN. This shows that our procedure to estimate the lateral force from the frequency shift data set works well.

The interaction force between a point magnetic charge and an individual vortex has been exactly calculated before [18]. A magnetic tip can be modelled simply as a point magnetic charge. The vertical force difference measured from the force curves in Fig. 3.90(b) could be compared with the model calculation. The penetration depth was assumed to be in the range from 150 nm to 200 nm, and the value of the magnetic point charge was taken as $5 \times 10^{-10}\mathrm{A} \cdot \mathrm{m}$. These parameters are reasonable for our $Bi_2Sr_2CaCu_2O_8$ sample and typical MFM tips. The calculated force at 18 nm tip-sample separation ranges from 3.6 pN to 6.4 pN. Our value 5.4 pN agrees well with this model calculation.

Conclusion

From the comparison of topographic and MFM images at low temperature, we have shown that columnar defects and line defects act as strong vortex pinning sites in $Bi_2Sr_2CaCu_2O_8$ single crystals. Topography measurements on such line defects revealed steps with heights smaller than that of half unit cell. From this fact, we could confirm that these dislocations were formed by stacking faults. Simple surface steps do not act as pinning sites. Moreover, we found an anisotropic, i.e., direction dependent, pinning behavior of such step dislocations. Vortices move freely along the dislocation line, but their movement across the dislocation line is impeded. Finally, we were able to determine the lateral dragging force excerted by the tip on the vortex during scanning to be a few piconewtons in agreement with theoretical predictions.

References

[1] K. Harada, T. Natsuda, J. Bonevich, M. Igarashi, S. Kondo, G. Pozzi, U. Kawabe, and A. Tonomura, Nature **360**, 51 (1992).

[2] C. Jooss, J. Albrecht, H. Kuhn, S. Leonhardt, and H. Kronmuller, Rep. Prog. Phys. **65**, 651-788 (2002).

[3] A. Oral, J. C. Barnard, S. J. Bending, I. I. Kaya, S. Ooi, T. Tamegai, and M. Henini, Phys. Rev. Lett. **80**, 3610 (1998).

[4] F. Pardo and F. de la Cruz, P. L. Gammel, E. Bucher, C. Ogelsby, and D. J. Bishop, Phys. Rev. Lett. **79**, 1369 (1997).

[5] T. Matsuda, O. Kamimura, H. Kasai, K. Harada, T. Yoshida, T. Akashi, A. Tonomura, Y. Nakayama, J. Shimoyama, K. Kishio, T. Hanaguri, K. Kitazawa, Science **294**, 2136 (2001).

[6] U. Hartmann, Annu. Rev. Mater. Sci. **29**, 53 (1999).

[7] A. Moser, H. J. Hug, I. Parashikov, B. Stiefel, O. Fritz, H. Thomas, A. Baratoff, and H. J. Güntherodt, and P. Chaudhari, Phys. Rev. Lett. **74**, 1847 (1995).

[8] H. J. Hug, B. Stiefel, P. J. A. van Schendel, A. Moser, S. Martin, and H. J. Güntherodt, Rev. Sci. Instr. **70**, 3625 (1999).

[9] T. W. Lee, C. W. Lee, S. Y. Shim, D. H. Ha, D. H. Kim, Progress in Superconductivity **3**, 36 (2001).

[10] M. Liebmann, A. Schwarz, S. M. Langkat, and R. Wiesendanger, Rev. Sci. Instrum. **73**, 3508 (2002).

[11] L. Wu, Y. Zhu, and J. Tafto, Phys. Rev. Lett. **85**, 5126 (2000).

[12] T. Haage, J. Zegenhagen, J. Q. Li, H. -U. Habermeier, M. Cardona, C. Jooss, R. Warthmann, A. Forkl, and H. Kronmuller, Phys. Rev. B, **56**, 8404 (1997).

[13] C. Jooss, R. Warthmann, and H. Kronmuller, Phys. Rev. B, **61**, 12433 (2000).

[14] A. Gurevich and L. D. Cooley, Phys. Rev. B, **50**, 13563 (1994).

[15] U. H. Pi, Z. G. Khim, D. W. Kim, U. Kaiser, M. Liebmann, A. Schwarz, and R. Wiesendanger, J. Low Temp. Phys. **131**, 993 (2003).

[16] F. J. Giessibl, Appl. Phys. Lett. **78**, 123 (2001).

[17] A. Wadas, O. Fritz, H. J. Hug, and H. J. Güntherodt, Z. Phys. B **88**, 317 (1992).

[18] M. W. Coffey, J. Phys. A: Math. Gen. **28**, 4201 (1995).

3.3 Semiconductor quantum structures and hybrid systems

3.3.1 STS on semiconductors

J. Wiebe, J. Klijn, T. Maltezopoulos, F. Meier, Chr. Meyer, L. Sacharow,
A. Wachowiak, K. Hashimoto, M. Janson, M. Morgenstern, and R. Wiesendanger

The unique power of scanning tunneling spectroscopy (STS) is its ability to give direct access to the local density of states (LDOS) of the electron system of solid surfaces, which is measured energetically resolved and with sub-nm spatial resolution. While the high spatial resolution is caused by the principle of operation of the scanning tunneling microscope (STM) itself, a high energy resolution is only possible at low temperatures. However, STS-measurements with high energy resolution are necessary to study effects where the interaction of the electron system plays a major role, because these effects are mostly determined by small energy scales. Since interaction effects often cause a spatial reorganization of the electron system, STS as a local method allows new insight into the physics of interacting electron systems.

As long as a single particle description of the electron system is adequate, the measured LDOS is given by

$$LDOS(E,x,y) = \sum_{\delta E} |\psi_i(E,x,y)|^2 \tag{3.29}$$

with $\psi_i(E,x,y)$ being the single particle wave functions as a function of energy E and position (x,y) and δE being an energy window corresponding to the energy resolution of the experiment. STS usually measures the differential conductivity $dI/dV(E = eV,x,y)$, which is to a good approximation proportional to the LDOS. Thus, STS directly probes a very basic property of the system, that can be compared to the solutions of the Schrödinger equation.

As shown in the previous triannual report we have used the electron system belonging to the conduction band of InAs to study the basic properties of different electron phases in all four dimensions. Cleaving the single crystals in ultra high vacuum results in a nearly defect free InAs(110) surface without Schottky barrier. Thus the three-dimensional electron system (3DES) reaches up to the surface and can be investigated by STS. We find scattering at ionized dopants and, surprisingly, drift states in the extreme quantum limit [1, 2]. Putting low amounts of iron atoms onto the surface results in a disordered two-dimensional electron system (2DES) which resides close to the surface. In this case we were able to image weakly localized electron states in zero magnetic field and the drift states of the 2DES in the Quantum Hall regime [3, 4]. The one-dimensional electron system builds below the charged [112]-step edges. Surprisingly no deviation from the single particle picture was found although electron-electron interaction is stronger than electron-disorder interaction [5]. Finally,

a zero-dimensional electron system (0DES) is formed below the tip due to tip-induced band bending and we get a nice visualization of the non-locality of the exchange interaction [6].

In this triannual research period we extended our investigations to other materials. We were able to induce a strongly disordered 2DES by putting small amounts of cobalt islands onto the InAs(110) surface. This strongly disordered 2DES behaves completely different than the iron-induced 2DES due to a dominating electron-disorder interaction. Interestingly we found a percolation-like transition from quantized states at low energy to delocalized electron states at higher energy [7]. In a nonquantizing magnetic field the strongly disordered 2DES forms local Landau levels. This will be described in Sec. 3.3.3. Besides from that we also looked at the atomic resolution of the InAs(110) surface in STM measurements in more detail and compared to surface electronic structure calculations [8] (Sec. 3.3.4).

In the one- and zero-dimensional case we moved over to materials that are of technological relevance. In Sec. 3.5.1 we show results of the investigation of extended individual single-walled carbon nanotubes in metallic form. We find quantum dots that are induced by scattering at single defects [9]. Finally, we studied strain-induced InAs quantum dots that were grown by molecular beam epitaxy. It will be shown in Sec. 3.3.2 that the sequence of squared wavefunctions of individual quantum dots can be imaged directly and thus compared to theoretical expectations [10].

A further topic, which is of technological interest is the spin-injection of electrons in ferromagnet-semiconductor hybrid systems. In order to get a better understanding of the mechanism we started with density-functional calculations of the Fe-InAs(110) interface. We find that the spin-polarization of Fe at the Fermi-level is much higher than expected from the bulk value. Moreover, the coupling of the As- and In-states to the Fe orbitals leads to a similar high spin polarization of different sign on the InAs side [11] (Sec. 3.3.5).

The report will start with a short description of the basic experimental procedures in the next section.

Experimental procedures

In this chapter we use two different ultra-high vacuum (UHV) low-temperature scanning tunneling microsopes (STMs). One works down to 14 K and has a maximum magnetic field of 2.5 T perpendicular to the sample surface [12]. It is used for the measurements in Sec. 3.5.1. The other STM operates down to 6 K and a maximum field of 6 T can be applied perpendicular to the sample surface [13]. It is used for all other measurements of this chapter. The base pressure of both systems is below 10^{-10} mbar.

The sample preparation is described in each subsection. As STM tips we use either ex-situ mechanically sharpened Pt/Ir tips or electrochemically etched W tips which are afterwards prepared in-situ by field emission or by applying voltage pulses

against a metal single-crystal surface. All topographic STM images are recorded in constant-current mode (CCM) with the voltage V applied to the sample. The differential conductivity $dI/dV(V,x,y)$ is recorded by lock-in technique with a frequency of $f \simeq 1.5$ kHz and a modulation voltage of $V_{\rm mod} \simeq 1-40$ mV$_{rms}$. Therefore, the tip-surface distance is stabilized at each point (x,y) at voltage $V_{\rm stab}$ and current $I_{\rm stab}$. Then, the feedback is switched off and a dI/dV-curve is recorded from $V_{\rm start}$ to $V_{\rm end}$. A sequence of dI/dV-images with different V corresponding to the electron energy with respect to the Fermi level E_F results. These dI/dV-images can be interpreted as maps of the local density of states (LDOS). Some of the dI/dV-images are measured directly in CCM. They are marked by I instead of $I_{\rm stab}$ and $V_{\rm stab}$. It has been checked that the latter images do not show any important difference from the former.

In each experiment, the modulation voltage is chosen small enough to ensure that the spectral resolution $\delta E = \sqrt{(3.3 \cdot kT)^2 + (2.5 \cdot V_{\rm mod})^2}$ is better than the sharpest peaks observed in dI/dV-curves. The influence of the spatially changing tip-surface distances has been checked to be of minor importance in most measurements, and therefore has only been taken into account in Sec. 3.3.4. Several tests have been performed to check that the tip has not changed during a set of measurements.

References

[1] C. Wittneven, R. Dombrowski, M. Morgenstern, R. Wiesendanger: *Scattering States of Ionized Dopants Probed by Low Temperature Scanning Tunneling Spectroscopy.* Phys. Rev. Lett. **81**, 5616 (1998).

[2] D. Haude, M. Morgenstern, I. Meinel, R. Wiesendanger: *Local Density of States of a Three-Dimensional Conductor in the Extreme Quantum Limit.* Phys. Rev. Lett. **86**, 1582 (2001).

[3] M. Morgenstern, J. Klijn, C. Meyer, M. Getzlaff, R. Adelung, R. Römer, K. Rossnagel, L. Kipp, M. Skibowski, R. Wiesendanger: *Direkt Comparison between Potential Landscape and Local Density of States in a Disordered Two-Dimensional Elektron System.* Phys. Rev. Lett. **89**, 136806 (2002).

[4] M. Morgenstern, J. Klijn, C. Meyer, R. Wiesendanger: *Real-Space Observation of Drift States in a Two-Dimensional Electron System at High Magnetic Fields.* Phys. Rev. Lett. **90**, 056804 (2003).

[5] C. Meyer, J. Klijn, M. Morgenstern, R. Wiesendanger: *Direct measurement of the local density of states of a disordered one-dimensional conductor.* Phys. Rev. Lett. **91**, 76803 (2003).

[6] M. Morgenstern, V. Gudmundsson, R. Dombrowski, C. W. R. Wiesendanger: *Nonlocality of the exchange interaction probed by scanning tunneling spectroscopy.* Phys. Rev. B **63**, 201301 (2001).

[7] J. Wiebe, C. Meyer, J. Klijn, M. Morgenstern, R. Wiesendanger: *From quantized states to percolation: Scanning tunneling spectroscopy of a strongly disordered two-dimensional electron system.* Phys. Rev. B **68**, 41402 (2003).

[8] J. Klijn, L. Sacharow, C. Meyer, S. Blügel, M. Morgenstern, R. Wiesendanger: *STM measurements on the InAs(110) surface directly compared with surface electronic structure calculations.* Phys. Rev. B **68**, 205327 (2003).

[9] T. Maltezopoulos, A. Kubetzka, M. Morgenstern, R. Wiesendanger: *Direct observation of confined states in metallic single-walled carbon nanotubes.* Appl. Phys. Lett. **83**, 1011 (2003).

[10] T. Maltezopoulos, A. Bolz, C. Meyer, C. Heyn, W. Hansen, M. Morgenstern, R. Wiesendanger: *Wave-Function Mapping of InAs Quantum Dots by Scanning Tunneling Spectroscopy.* Phys. Rev. Lett. **91**, 196804 (2003).

[11] L. Sacharow, M. Morgenstern, G. Bihlmayer, S. Blügel: *High spin polarization at the interface between a Fe monolayer and InAs(110).* Phys. Rev. B **69**, 85317 (2004).

[12] O. Pietzsch, A. Kubetzka, D. Haude, M. Bode, R. Wiesendanger: *A low-temperature ultrahigh vacuum scanning tunneling microscope with a split-coil magnet and a rotary motion stepper motor for high spatial resolution studies of surface magnetism.* Rev. Sci. Instr. **71**, 424 (1997).

[13] C. Wittneven, R. Dombrowski, S. Pan, R. Wiesendanger: *A low-temperature ultrahigh-vacuum scanning tunneling microscope with rotatable magnetic field.* Rev. Sci. Instr. **68**, 3806 (1997).

3.3.2 Strain induced InAs quantum dots

T. Maltezopoulos, A. Bolz, Chr. Meyer, Chr. Heyn, W. Hansen, M. Morgenstern, and R. Wiesendanger

Strain-induced InAs quantum dots (QDs) belong to the family of artificial atoms [1]. They exhibit confinement on the nm-scale in all three dimensions and atomic-like single-electron states with large energy separations [2–6]. Due to the large energy separation the QDs are interesting for technological applications such as new laser materials [7] or single photon sources [8]. A basic property of the QDs are the wave functions of the confined states. They have previously been probed indirectly by magnetotunneling spectroscopy relying on a transformation of k-space data into real space data [9]. Also cross-sectional scanning tunneling microscopy (STM) images indicate the existence of an s- and a p-state in the conduction band of a single QD, although the corresponding states have not been identified in dI/dV-data [10].

Here, we use low-temperature scanning tunneling spectroscopy (STS) to perform a systematic study of the shape of the squared wave functions $|\Psi_i(x,y)|^2$. We investigate free standing QDs deposited on GaAs(001) and get full access to the geometrical shape of the QDs, their single-particle peaks in the density of states and the spatial distribution of the corresponding $|\Psi_i(x,y)|^2$. Surprisingly, we find that the asymmetric shape of the free standing QDs strongly lifts the degeneracy of the (100) and the (010) state. This partly leads to the appearance of (200)- and (300)-states in the absence of a (010)-state, which should be considered for the interpretation of other physical properties of QDs [11]. The strain-induced InAs-QDs are grown by molecular beam epitaxy (MBE) at a base pressure below 4×10^{-11} mbar. N-doped GaAs(001) ($N_{\mathrm{D}} \simeq 2 \cdot 10^{18}$ cm^{-3}) is first overgrown with an n-doped buffer layer ($N_{\mathrm{D}} \simeq 2 \cdot 10^{18}$ cm^{-3}) of 400 nm thickness at $T = 600^{\circ}$ C followed by an undoped tunneling barrier of 15 nm thickness ($N_{\mathrm{A}} < 10^{15}$ cm^{-3}). Then, 2.0 ML of InAs are deposited at 495°C in order to form the QDs. These growth parameters are found to be suitable to create relatively high QDs with a large number of confined states. The samples are transferred from the MBE system to the STM within 1 h by a mobile UHV transfer system at $p < 10^{-9}$ mbar. Only this in-vacuo transfer allowed us to obtain highly reproducable dI/dV-curves. Figure 3.91(a) shows the sample geometry. The tunnel barrier decouples the states of the QDs from the degenerately doped backgate. The STM tip and the path of the tunneling current (I) are marked. The band profile along the I-path is displayed in Fig. 3.91(b) as estimated with a 1D-Poisson solver neglecting the influence of the 3D confinement [12]. As parameters we use a QD height of $H = 9.4$ nm, a tip work function of 5.3 eV (PtIr) and a conduction band offset between QDs and GaAs of 390 meV according to 40 % Ga content within the QDs [13]. The voltage V_{sample} is adapted to tunnel into a quantized state of the QD. Note the lever arm, i.e. V_{sample} is much larger than the energy of the quantized state with respect to the QD conduction band minimum.

Figure 3.91(c) shows a constant-current image of the QD sample. Besides the

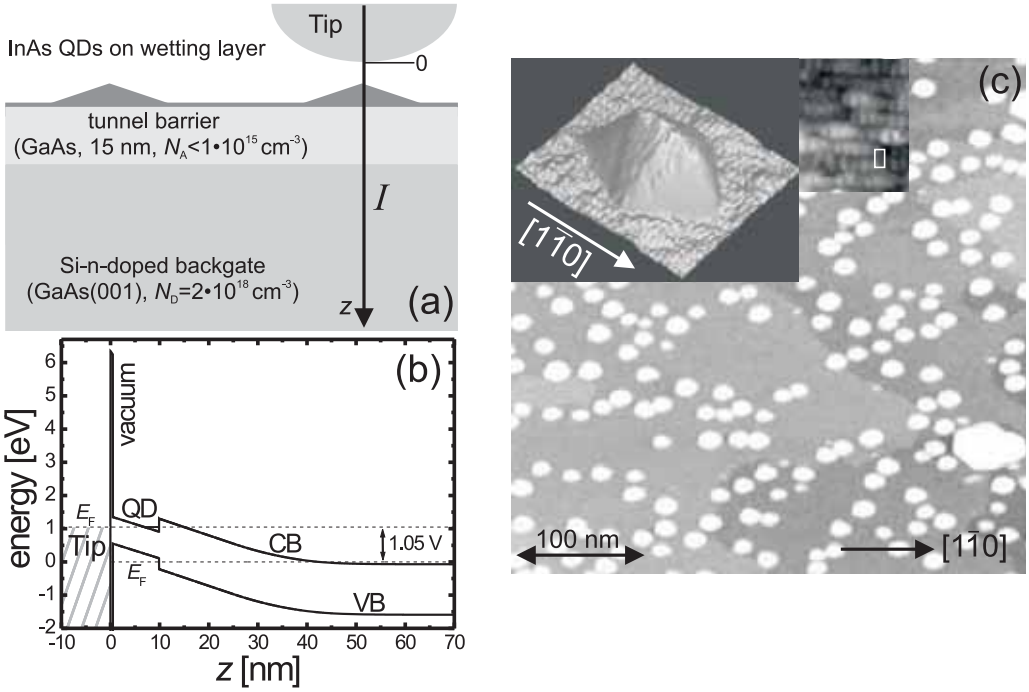

Figure 3.91: (a) Sketch of STS measurement of the sample with free standing InAs-QDs; tunneling path I along z is indicated; (b) band profile along the z-direction marked in (a) as calculated with a 1D-Poisson solver [12], V_{sample} =1.05 V, CB: conduction band, VB: valence band; a confined QD state is marked as a full black line; (c) constant-current image of the InAs-QD sample, V_{sample} =3 V, I =70 pA; left inset: 3D representation of a typical QD with [110]-direction marked; central inset: wetting layer with atomic resolution, (2×4)-unit cell (white rectangle) is marked.

bright QDs, several steps are visible on the wetting layer (WL). Most QDs have a lateral extension of 21 ± 2 nm along [110] and 16 ± 2 nm along [1$\bar{1}$0]. Only one dot in the lower right area is considerably larger (60×40 nm^2). Such dots are regularly found on the sample, but do not show any spectral features in STS. A 3D representation of a typical QD is shown in the left inset being comparable to prevoius STM results [14]. As all QDs, the QD is more extended in [110]-direction, thus, we observe a shape asymmetry. Note the superstructure on the WL shown in the central inset, which is compatible with a disordered (2×4)-reconstruction.

A constant-current image of a single, relatively small QD is shown in Fig. 3.92(a). Fig. 3.92(b) shows the corresponding $I(V)$-curve recorded above the QD (black) in comparison with an $I(V)$-curve recorded on the WL (grey). While only a continuous $I(V)$-increase appears on the WL [15], two current steps are observed on the QD.

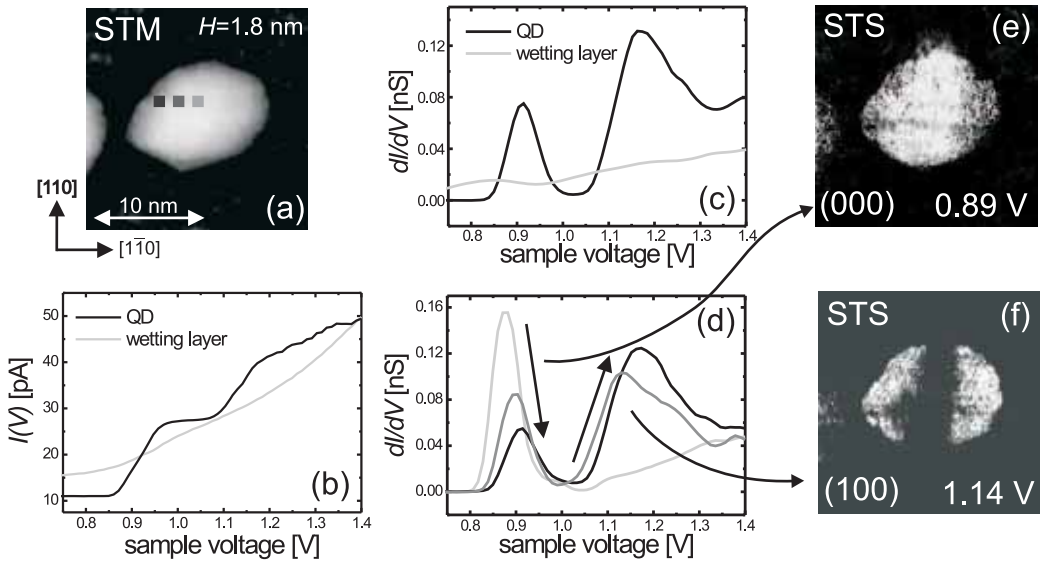

Figure 3.92: Single QD, W-tip: (a) constant-current image, $V_{\text{sample}} = 1.7$ V, $I = 50$ pA, height H and crystallographic directions marked; (b) $I(V)$-curves recorded on the QD (black) and on the wetting layer (grey), V_{stab}=1.6 V, I_{stab}=50 pA; (c) dI/dV-curves recorded simultaneously with (b), V_{mod}=28 mV; (d) dI/dV-curves recorded at different positions above the QD as marked in (a); (e), (f) spatially resolved dI/dV-data at $V_{\text{sample}} = 0.89$ V and $V_{\text{sample}} = 1.14$ V, respectively; all data in Fig. 3.92 are raw data.

In the simultaneously recorded dI/dV-curves (Fig. 3.92(c)), the two steps appear as two peaks with full width at half maximum (FWHM) of 70 meV and 150 meV. The peaks are caused by the two quantized states of the QD. In order to prove that we investigate the peak intensity as a function of position. The dI/dV-curves of Fig. 3.92(d) reveal that the intensity of the first peak decreases with distance from the QD center, while the intensity of the second one increases. In addition, the whole spectrum shifts to higher energies. The latter is probably caused by the increased band bending at smaller distance between tip and degenerately doped GaAs-backgate, if the tip is at the rim of the QD. However, since the resulting peak shifts are small, dI/dV images still largely represent the peak intensity as a function of position. Fig. 3.92(e) shows the dI/dV-image recorded at the first peak of Fig. 3.92(c), while Fig. 3.92(f) shows the dI/dV-image at the second peak. Obviously, the first peak has a circular symmetric intensity distribution as expected for a (000)-state, while the second one has a pronounced node in the center as expected for a (100)-state [3,4]. The measured patterns obviously correspond to the shape of the squared wave functions of individual states.

The width of the peaks in Fig. 3.92(c) requires some discussion. It is basically given by the lifetime of the electrons in the confined states. An upper boundary for

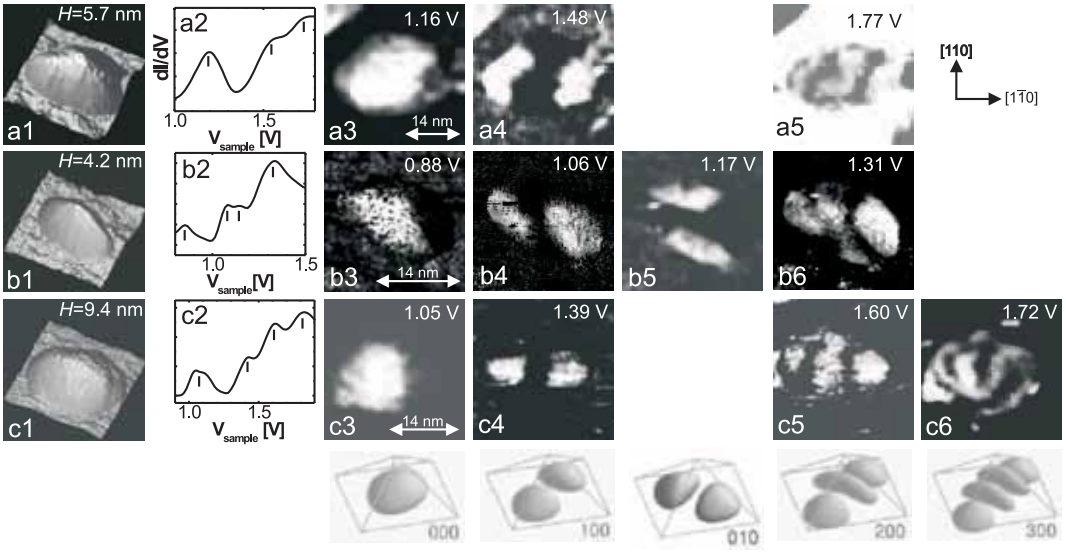

Figure 3.93: STS-data of three different QDs: (a1), (b1), (c1): 3D representation of constant-current images with heights H indicated; (a2), (b2), (c2): $dI/dV(V)$-curves spatially averaged over QD area, peak positions are marked by vertical lines; (a3)−(a5), (b3)−(b6), (c3)−(c6): dI/dV-images recorded at V_{sample} as indicated; data are partly smoothed in order to enhance picture quality; the state in (a5) exhibits an energy close to the onset of the wetting layer, which results in a bright surrounding of the wave function; crystallographic directions are marked; (a1)−(a5): W-tip, V_{stab}=1.85 V, I_{stab}=50 pA, V_{mod}=15 mV; (b1)−(b6): W-tip, V_{stab}=1.6 V, I_{stab}=50 pA, V_{mod}=27 mV; (c1)−(c6): PtIr-tip, V_{stab}=2.4 V, I_{stab}=70 pA, V_{mod}=15 mV; constant-current images at $V_{\mathrm{sample}} = V_{\mathrm{stab}}$ and $I = I_{stab}$; below: calculated squared wave functions taken from [3] and labeled by the number of nodes in different directions.

this lifetime is the tunneling rate r through the undoped GaAs tunnel barrier. It can be estimated according to the method described in [16]. Therefore, the band bending within the sample has to be taken into account. The resulting triangular tunnel barrier is visible in Fig. 3.91(b). Depending on the confinement energy of the state, we find $10^{12}/\mathrm{s} \leq r \leq 3 \cdot 10^{13}/\mathrm{s}$. This is much larger than typical tunneling rates from the tip to the QD ($r \simeq 3 \cdot 10^{8}/\mathrm{s}$). Accordingly, the intrinsic lifetime broadening of the QD states should be up to about 20 meV. Considering the average lever arm factor in our experiment of about 5.5, which is deduced straightforwardly from the 1D-Poisson calculations, we expect single-particle peaks with FWHM up to about 110 meV. As in Fig. 3.92(c), we partly find larger FWHMs by up to a factor of two [17], which we attribute to simplifications within the estimate.

To get statistically relevant information on the state sequences and to prove the reliability of the method, we investigated 25 different QDs deposited on three different samples. The results on three further QDs, all exhibiting more than two states, are shown in Fig. 3.93. Again, the QDs appear elongated in the [110]-direction as shown

in (a1), (b1), and (c1). The dI/dV-curves in (a2), (b2), and (c2) are spatially averaged over the whole QD area. Due to the discussed peak shift as a function of position, the peaks are less well resolved. But since we map the squared wave functions, we can easily attribute the peak-like features to different states. Therefore, we inspect all 64 dI/dV-images for each QD and find only the symmetries presented in Fig. 3.93 which indeed correspond to the peak-like features. The state sequences are (000), (100), and (200) for (a3)−(a5) (upper row), (000), (100), (010), and (200) for (b3)−(b6) (middle row) and (000), (100), (200), and (300) for (c3)−(c6) (lower row). For comparison, calculated squared wave functions labelled accordingly are shown on the bottom of Fig. 3.93 (from [3]).

Table 3.3 summarizes the state sequences found for 25 different QDs with heights between 1.7 nm and 9.4 nm (mean value: 4.5 nm). 40 % of the QDs exhibit only a (000)-state, but up to four states are partly observed. Generally, we find that higher dots exhibit more states. Most surprisingly, (200)- and (300)-states partly appear without the appearance of a (010)-state.

state sequence	number of QDs
(000)	10
(000), (100)	7
(000), (100), (010)	2
(000), (100), (010), (200)	1
(000), (100), (200)	3
(000), (100), (200), (300)	2

Table 3.3: Energetic state sequence for 25 different QDs.

Thus, we find a strong anisotropy in the electronic structure. To emphasize that, we sum up all nodes in [110]- and [1$\bar{1}$0]-direction for the 25 QDs and get 33 and 3 nodes, respectively.

The found electronic anisotropy could be caused by the shape asymmetry of the QDs. An average aspect ratio of $A = 1.3$ is found in the STM image of Fig. 3.91(c). Partly larger aspect ratios appear in Fig. 3.93: $A = 1.6$ for (a1) and (b1) and $A = 1.4$ for (c1). These relatively large aspect ratios lead to a much stronger confinement in [1$\bar{1}$0]- than in [110]-direction. Taking the different base plane lengths of the QDs in Fig. 3.93 as the input parameter for published theoretical calculations of the QD state energies [3, 4], we find that the confinement energy for the (010)-state should be 100 meV higher than the (100)-state. To compare this with experiment, we have to translate the measured peak voltages V_{sample} into energies E by using the 1D-Poisson solver [12]. For the states of Fig. 3(c3)-(c6) at V_{sample} =1.05, 1.39, 1.60, and 1.72 V we find E =139, 212, 254, and 278 meV with respect to the conduction band minimum of the QD. Accordingly, the (010)-state should appear around (212 + 100 = 312) meV, which is indeed above the energy of the (300)-state. Thus, we can explain the state

sequence qualitatively. However, the shape asymmetry cannot explain all details. For example, the shape asymmetry in Fig. 3.93(b1) is larger than in (c1), although the (010)-state is only found in the former case [18]. Thus, detailed calculations taking the shape and the stress fields of the QDs into account are highly desirable.

Note finally that the strong electronic anisotropy found by STS is not found by capacitance measurements [6], far-infrared measurements [5] or magnetotunneling experiments [19], all performed on capped QDs. The magnetotunneling reveals a rather degenerate (010)- and (100)-state, while the other methods imply an energy difference of 2−10 meV between the levels. The difference is tentatively explained by shape asymmetry as well as by exchange effects. Importantly, none of the authors of [5,6,19] find an indication for a (200)-state appearing prior to the (010)-state. The most likely explanation is that the QD shape changes during overgrowth.

In summary, we mapped the squared wave functions of single and free-standing strain-induced InAs QDs grown on GaAs(001). The QDs show one to four single-electron states which are identified as (000)-, (100)-, (010)-, (200)- and (300)-states. The numbers are the number of nodes in [110]-, [1$\bar{1}$0]- and [001]-direction, respectively. Different energy sequences of states are found for different QDs, but states with nodes in [110]-direction appear much more often than states with nodes in [1$\bar{1}$0]-direction. This strong electronic anisotropy is largely attributed to the shape asymmetry of the QDs.

References

[1] D. Bimberg *et al.*, *Quantum Dot Heterostructures*, Wiley, New York, 1999.

[2] H. Jiang *et al.*, Phys. Rev. B **56**, 4696 (1997).

[3] O. Stier *et al.*, Phys. Rev. B **59**, 5688 (1999).

[4] M. Grundmann *et al.*, Phys. Rev. B **52**, 11969 (1995); A. J. Williamson *et al.*, Phys. Rev. B **59**, 15819 (1999); L. C. R. Fonseca *et al.*, Phys. Rev. B **57**, 4017 (1998); C. Pryor, Phys. Rev. B **60**, 2869 (1999).

[5] M. Fricke *et al.*, Europhys. Lett. **36**, 197 (1996).

[6] B. T. Miller *et al.*, Phys. Rev. B **56**, 6764 (1997); R. J. Luyken *et al.*, Appl. Phys. Lett. **74**, 2486 (1999).

[7] Y. Qiu *et al.*, Appl. Phys. Lett. **79**, 3570 (2001).

[8] P. Michler *et al.*, Science **290**, 2282 (2000); Z. Yuan *et al.*, Science **295**, 102 (2002).

[9] E. E. Vdovin *et al.*, Science **290**, 122 (2000); A. Patané *et al.*, Phys. Rev. B **65**, 165308 (2002); M. Narihiro *et al.*, Appl. Phys. Lett. **70**, 105 (1997).

[10] B. Grandidier *et al.*, Phys. Rev. Lett. **85**, 1068 (2000).

[11] see e.g. G. W. Bryant, Appl. Phys. Lett. **72**, 768 (1998); J. Shumway *et al.*, Phys. Rev. B, **63**, 155316 (2001).

[12] G. L. Snider *et al.*, J. of. Appl. Phys. **68**, 2849 (1990), www.nd.edu/~ gsnider.

[13] Grazing incidence x-ray diffraction on an identically grown sample performed according to the method described by I. Kegel *et al.* (Phys. Rev. Lett. **85**, 1694 (2000)) indicate an average Ga content of 33 % increasing towards the bottom of the QD; A. Bolz *et al.*, HASYLAB Ann. Rep. **1**, 733 (2002).

[14] Y. Hasegawa *et al.*, Appl. Phys. Lett. **72**, 2265 (1998); J. Márquez *et al.*, Appl. Phys. Lett. **78**, 2309 (2001); G. Costantini *et al.*, Appl. Phys. Lett. **82**, 3194 (2003).

[15] We interpret the $I(V)$-increase on the WL as due to a direct tunneling of electrons from the tip to the degenerately doped GaAs.

[16] C. M. A. Kapteyn *et al.*, Phys. Rev. B **60**, 14265 (1999).

[17] We checked that the FWHM does not decrease with decreasing V_{mod}.

[18] From previous experiments (Dombrowski *et al.*, Phys. Rev. B **59**, 8043 (1999)), we know that the tip induced electric field typically has a FWHM of about 50 nm, which is significantly larger than the extension of the InAs QDs (20 nm). Thus, we believe that a possible asymmetric electric field from the tip is of minor importance for the electronic anisotropy. Moreover, we found the same anisotropy for about ten individually prepared tips. It is rather unlikely that all these tips have a shape asymmetry along the [110]-direction of the sample.

[19] A. Patané *et al.*, Phys. Rev. B **65**, 165308 (2002); an electronic anisotropy is, however, found for QDs grown on GaAs(113)B.

[20] N. Maslova, S. Oreshkin, V. Panov, S. Savinov, A. Depuydt, C. van Haesendonck: *Scanning tunneling spectroscopy of charge effects on the semiconductor surfaces and atomic clusters.* JEPT Letters **67**, 146 (1998).

[21] A. Depuydt, N. Maslova, V. Panov, V. Rakov, S.V.Savinov, C. van Haesendonck: *Influence of resonant tunneling on the imaging of atomic defects on InAs(110) surfaces by low-temperature scanning tunneling microscopy.* Appl. Phys. A **66**, S171 (1998).

[22] A. Schwarz, W. Allers, U. Schwarz, R. Wiesendanger: *Simultaneous imaging of the In and As sublattice on InAs(110)-(*1×1*) with dynamic scanning force microscopy.* Appl. Surf. Sci. **140**, 293 (1999).

[23] A. Schwarz, W. Allers, U. Schwarz, R. Wiesendanger: *Dynamic-mode scanning force microscopy study of n-InAs(110)-(1x1) at low temperatures.* Phys. Rev. B **61**, 2837 (2000).

3.3.3 Strongly disordered two dimensional electron system

J. Wiebe, Chr. Meyer, J. Klijn, M. Morgenstern, and R. Wiesendanger

The concept of percolation is ubiquitous in solid state physics [1]. Recently, it has been proposed that percolation is responsible for the density-driven transition from metallic to insulating behaviour in two dimensional electron systems (2DESs) [2, 3], that percolation could explain the doping dependence of transition temperatures in high T_c superconductors [4] and that percolation might govern part of the complex phase diagram of the manganites [5]. However, the percolation transition of electron systems has barely been studied on the local scale. Here, we use a specifically prepared 2DES object to a relatively strong disorder potential to investigate the energy dependent transition from localized states to percolation on the nm-scale.

The system is the InAs inversion layer induced by small Co islands on the (110) surface. With angle resolved photoemission spectroscopy (ARUPS) measurements it was shown, that the 2DES resides in a rather strong disorder potential and that one expects electron droplets in the minima of the potential landscape [6]. To prepare the 2DES, we first cleave degenerate p-InAs ($N_{\mathrm{A}} = 4.6 \times 10^{17}/\mathrm{cm}^3$) in-situ at a base pressure of 1×10^{-8} Pa. This results in a clean and mostly defect free InAs(110)-surface. Then, Co is deposited by an e-beam evaporator to induce the inversion layer [6]. The Co coverage is calibrated by measuring the size of epitaxial Co-islands on W(110). Afterwards, the sample is transferred into the low temperature STM.

Fig. 3.94a shows a STM-image of the p-InAs(110) surface covered with $5.5 \cdot 10^{13}$ Co atoms/cm^2. The Co forms islands visible as white bumps [6]. The island density is $3.5 \cdot 10^{12}$ cm^{-2}, i.e. each island contains about 15 atoms. From the previous ARUPS experiments we know that such an island density transfers about $2 \cdot 10^{12}$ electrons/cm^2 to the sample leading to a surface E_F shift of 500 ± 50 meV [6]. Thus, about 50 % of the Co islands are singly and positively charged and a downward band bending on the InAs side results.

Coulomb blockade of the Co clusters

The reason that the Co islands are only singly charged is the Coulomb blockade. It becomes directly visible in dI/dV-curves obtained on a Co cluster. An example is shown in Fig. 3.94c, where two peaks surround a region of zero conductivity. The position of the peaks as well as the width of the gap is different for each cluster. Fig. 3.95 shows for example the dI/dV-curves of two clusters of different size. The larger one marked with (b) has a volume of $V = 1 \pm 0.7\,\mathrm{nm}^3$ and shows a smaller gap of 375 meV. The smaller one marked with (c) has a volume of $V = 0.4 \pm 0.3\,\mathrm{nm}^3$ and shows a larger gap of 950 meV. In principle, two effects could lead to the observed gap in dI/dV-curves: one is Coulomb blockade, the other is the Quantum size effect. To determine, which of the effects is dominant, we estimate on one hand the expected Coulomb blockade E_C and on the other hand the separation of the single particle

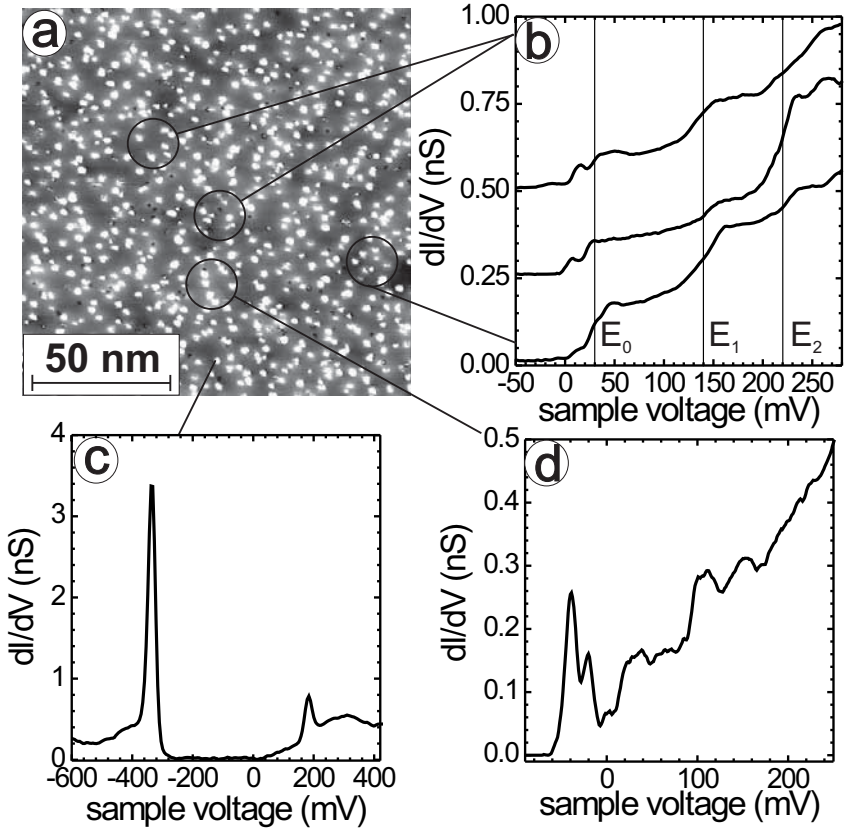

Figure 3.94: (a) STM-image of p-InAs(110) covered with 15 % Co ($V = 500$ mV, $I = 500$ pA); black circles and lines mark positions of spectra shown in (b), (c) and (d). (b), (d) dI/dV-curves averaged over the circle regions marked in (a) ($I_{stab} = 700$ pA, $V_{stab} = 500$ mV, $V_{mod} = 5$ mV). Spectra in (b) are vertically shifted by 0.25 nS steps for clarity. (c) dI/dV-curve taken on a Co cluster ($I_{stab} = 700$ pA, $V_{stab} = 700$ mV, $V_{mod} = 5$ mV).

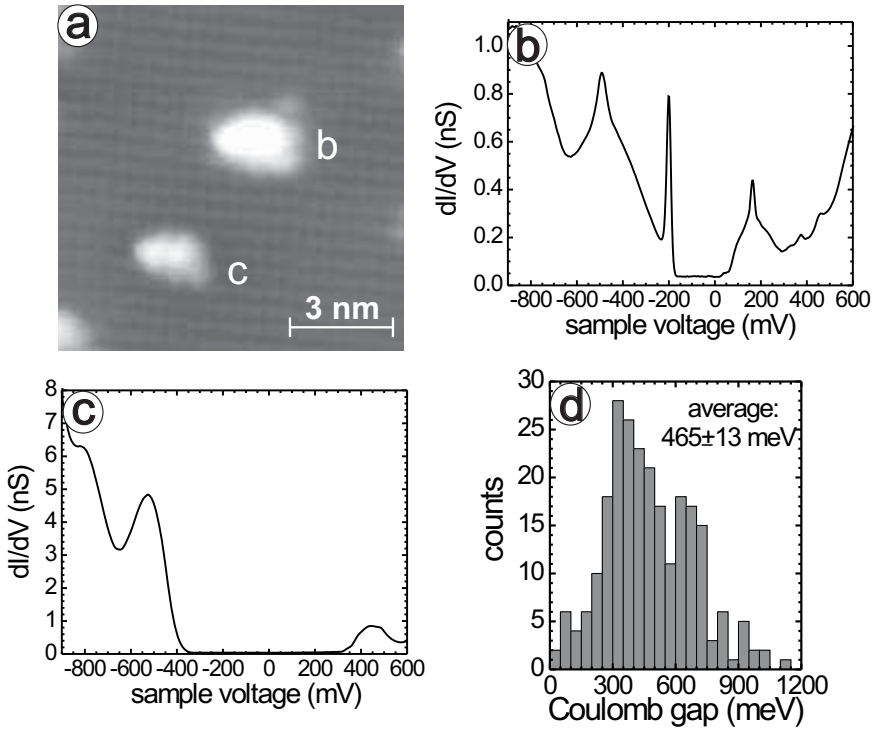

Figure 3.95: (a) STM-image of two Co clusters on InAs(110) ($V = -900$ mV, $I = 300$ pA). (b), (c) dI/dV-curves taken on the larger and the smaller Co cluster marked with (b) and (c) in (a), respectively ($I_{stab} = 500$ pA, $V_{stab} = 700$ mV, $V_{mod} = 5$ mV). (d) Histogram of obtained gaps on different Co clusters with average gap width indicated.

energies E_{SP} of clusters of the measured volume. For the calculation of E_C we take into account the capacity of a spherical metallic cluster placed on the insulating InAs semi-halfspace ($\epsilon = 14.6$) and the STM tip as a metallic half-space with 4 Å distance from the cluster surface. For the calculation of E_{SP} we use $k_F \approx 1.8\,\text{Å}^{-1}$ for cobalt [7]. The result is $E_C = 0.8 \pm 0.2\,\text{eV}$ and $E_{SP} = 40 \pm 30\,\text{meV}$ for the larger and $E_C = 1.1 \pm 0.3\,\text{eV}$ and $E_{SP} = 100 \pm 80\,\text{meV}$ for the smaller cluster. Obviously, the quantum size effect leads to a separation of single particle energies, which is by one order of magnitude too small, to explain the measured gaps. We thus conclude, that for the Co clusters the dominant effect is Coulomb blockade. Admittedly, the calculation results in a Coulomb blockade, that is by a factor of 2 too large. We ascribe this to a leaking of the cluster charge density into the InAs substrate. This is a reasonable assumption, since the clusters can couple to the conduction and valence band of the InAs starting at -100 meV and -500 meV, respectively.

Coulomb gaps as large as 1.1 eV are observed. A histogram of the gap widths is given in Fig. 3.95d revealing an average Coulomb gap of 465 ± 13 meV and a mean square width of the distribution of 420 meV. The average center of the Coulomb gaps is at -140 meV and the width of the distribution is 320 meV. The former represents an average energy of the cluster ensemble, namely the mean of ionization energy and electron affinity. The latter indicates large potential fluctuations on the sample surface. They are caused by the inhomogeneous distribution of charged clusters.

Potential disorder

Since we neither know which clusters are charged nor the position of the compensating acceptors, we cannot calculate the potential landscape exactly. However, a good estimate is obtained. Therefore, we take the 50% clusters with the lower Coulomb gap as charged giving the known 50 % charging probability. To the resulting charge distribution, we add the compensating charged acceptors randomly. Then, we fold the deduced 3D potential with the shape of the first 2DES subband in z-direction [6, 9]. The resulting 2DES potential fluctuates by about 100 meV [8] on a length scale of 40 nm and exhibits valleys which can contain confined states.

Ignoring the potential fluctuations for the moment, we calculate the subband energies E_n of the 2DES. Therefore, we solve the one-dimensional Poisson and Schrödinger equation using the measured surface E_F shift (500 ± 50 meV) as the only input parameter [9, 10]. We find $E_0 - E_F = 20 \pm 20$ meV, $E_1 - E_F = 135 \pm 20$ meV and $E_2 - E_F = 210 \pm 20$ meV, i.e. all subbands are empty. Indeed, if we average dI/dV-curves over certain areas of the sample, we find curves with steps close to the calculated E_n. An example is shown in Fig. 3.94b with steps at 30 mV, 140 mV and 220 mV.

Confined states

Already the photoemission data revealed that part of the 2DES is occupied [6]. This occupied part is also found by scanning tunneling spectroscopy in other areas of the

sample. Fig. 3.94d shows a corresponding dI/dV-curve exhibiting two peaks below E_F.

These peaks represent completely confined states as evidenced in Fig. 3.96. Three dI/dV-curves are displayed in Fig. 3.96a, d and g and LDOS-maps taken close to the peak voltages are shown in Fig. 3.96b, c, e, f and h, i. One recognizes that the lower peaks correspond to a rather symmetric s-like LDOS, while the upper peaks show two lobes as known from p-states of a quantum dot. The Co clusters appear as dark spots due to their vanishing LDOS within the Coulomb gap.

The confinement of the two states is even more obvious in Fig. 3.97 where LDOS-maps of s- and p-like state of the same quantum dot are given in Fig. 3.97b and d, respectively. Fig. 3.97a shows the dependence of the lower peak (marked by 1s) on the distance to the center of the state in a direction perpendicular to the lobes of the p-like state. At a distance of approximately 10 nm, the peak has completely disappeared, as expected from a confined state. Instead, Fig. 3.97c shows the dependence of the lower and the higher peak (marked with 1p) on the distance to the center of the state, but now in a direction parallel to the lobes of the p-like state. The intensity of the 1p-peak is zero in the center of the state and maximum at a distance of approximately 15 nm, while the intensity of the 1s-peak is maximum in the center and again vanishing for larger distances. Both is in perfect agreement with the behaviour of a 1s- and a 1p-state of a quantum dot.

To compare the width and the energetic separation of the quantum dot states with the model of a parabolic potential minimum, we measure the full width at half maximum (FWHM) of the s-like state Δ_s and the distance of the lobes of the p-like state Δ_p as shown in Fig. 3.96j and k. We then calculate the corresponding theoretical values with the measured energetic separation of the states. The result is shown in the following table:

		exp.		theor.	
quantum dot	$\hbar\omega(meV)$	$\Delta_s(nm)$	$\Delta_p(nm)$	$\Delta_s(nm)$	$\Delta_p(nm)$
1	20 ± 5	18 ± 2	32 ± 5	19	23
2	16 ± 2	26 ± 4	25 ± 3	21	25
3	24 ± 2	16 ± 4	23 ± 2	17	20

Obviously, the measured extensions of the wave functions fit reasonably well to the model of a parabolic quantum dot. Instead, the exact shape of the states deviate from that of a perfect parabolic quantum dot, because of a more irregular form of the potential. Since the corresponding valleys are usually asymmetric, we find only one p-state probably elongated in the direction of lowest curvature.

All together, we found 7 valleys with two peaks and, in addition, 50 valleys with only one peak below E_F in a sample region of $(250\ \text{nm})^2$. These peaks correspond to the occupied part of the 2DES already observed in photoemission [6].

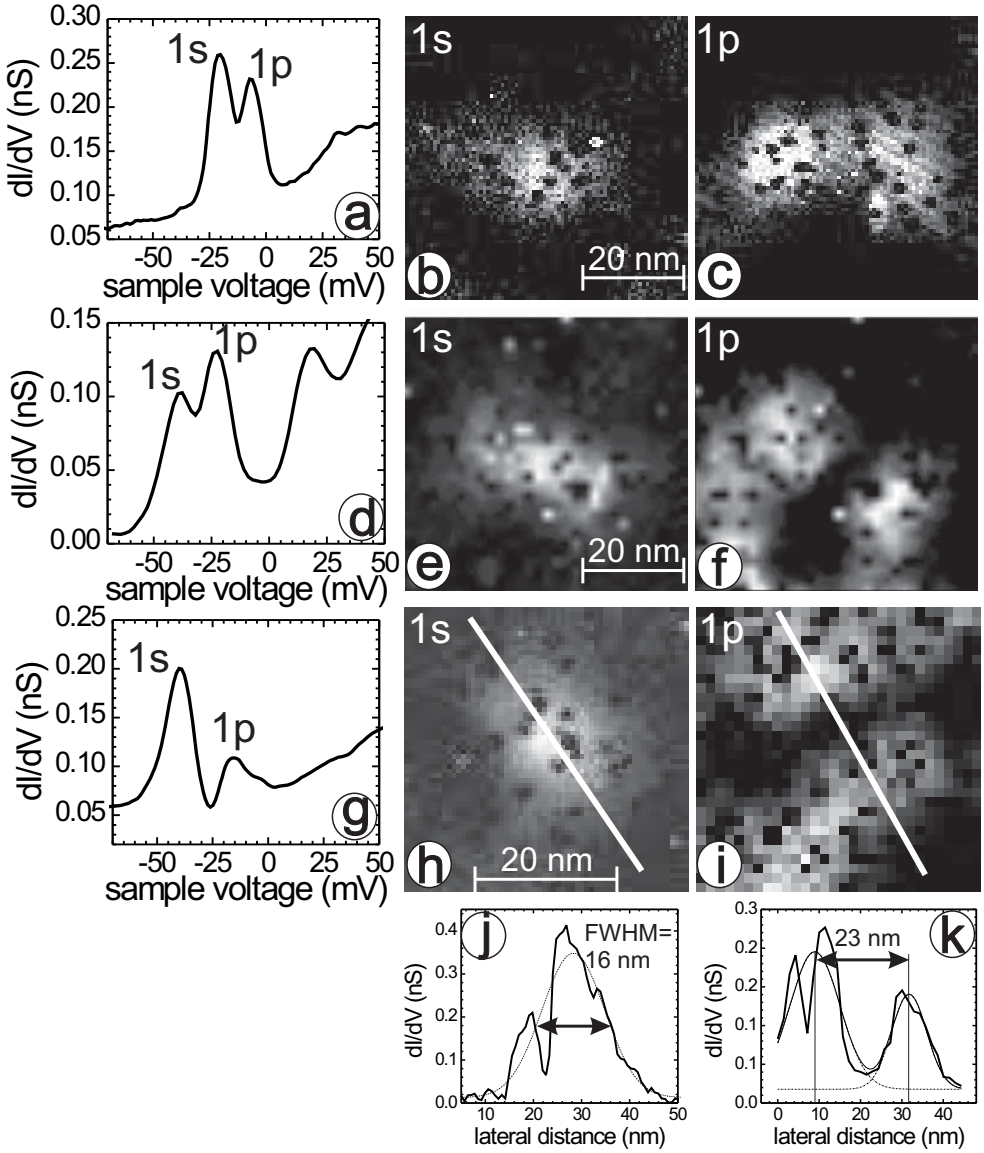

Figure 3.96: (a) dI/dV-curve from a region with two quantum dot states marked by 1s, 1p ($I_{stab} = 700$ pA, $V_{stab} = 500$ mV, $V_{mod} = 5$ mV); (b), (c) dI/dV-images taken in the energy regions of the quantum dot peaks at $V = -25(-16)$ mV ($I_{stab} = 700$ pA, $V_{stab} = 430$ mV, $V_{mod} = 2$ mV). (d) same as (a) but for another region ($I_{stab} = 700$ pA, $V_{stab} = 430$ mV, $V_{mod} = 5$ mV). (e), (f) dI/dV-images taken at peak energies of (d) $V = -40(-24)$ mV ($I_{stab} = 700$ pA, $V_{stab} = 430$ mV, $V_{mod} = 5$ mV). (g) same as (a) but for another region ($I_{stab} = 700$ pA, $V_{stab} = 430$ mV, $V_{mod} = 5$ mV). (h), (i) dI/dV-images taken at peak energies of (g) $V = -40(-16)$ mV ($I_{stab} = 700$ pA, $V_{stab} = 500$ mV, $V_{mod} = 5$ mV). (j), (k) line profiles along the white lines in (h) and (i). Thin lines give fits to gaussian profiles with the full width at half maximum (FWHM) and distance of maxima as indicated.

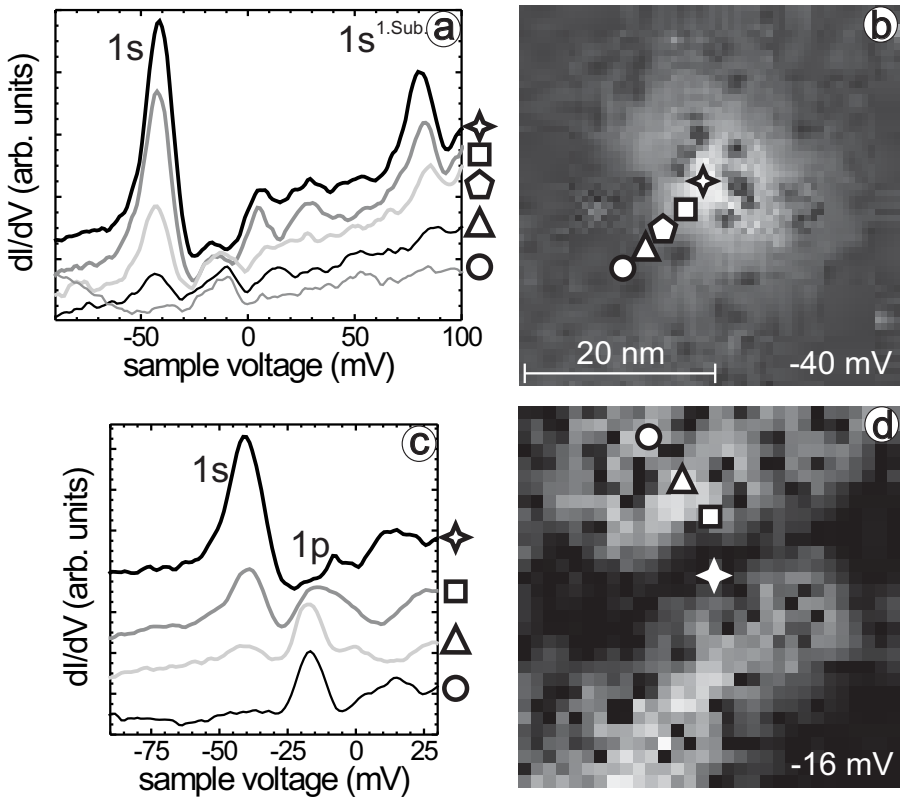

Figure 3.97: (a) dI/dV-curves taken at different positions of an s-like state of a quantum dot shown in (b) ($I_{stab} = 700$ pA, $V_{stab} = 500$ mV, $V_{mod} = 5$ mV). (b) dI/dV-image of the s-like quantum dot state given by the peak in (a) ($I_{stab} = 700$ pA, $V_{stab} = 430$ mV, $V_{mod} = 5$ mV). (c) dI/dV-curves taken at different positions of the same quantum dot at the positions shown in (d) ($I_{stab} = 700$ pA, $V_{stab} = 500$ mV, $V_{mod} = 5$ mV). (d) dI/dV-image of the p-like quantum dot state given by the peak in (c) ($I_{stab} = 700$ pA, $V_{stab} = 500$ mV, $V_{mod} = 5$ mV). Image (b) covers the same area as image (d). The star symbol in (b) is at the same position as in (d).

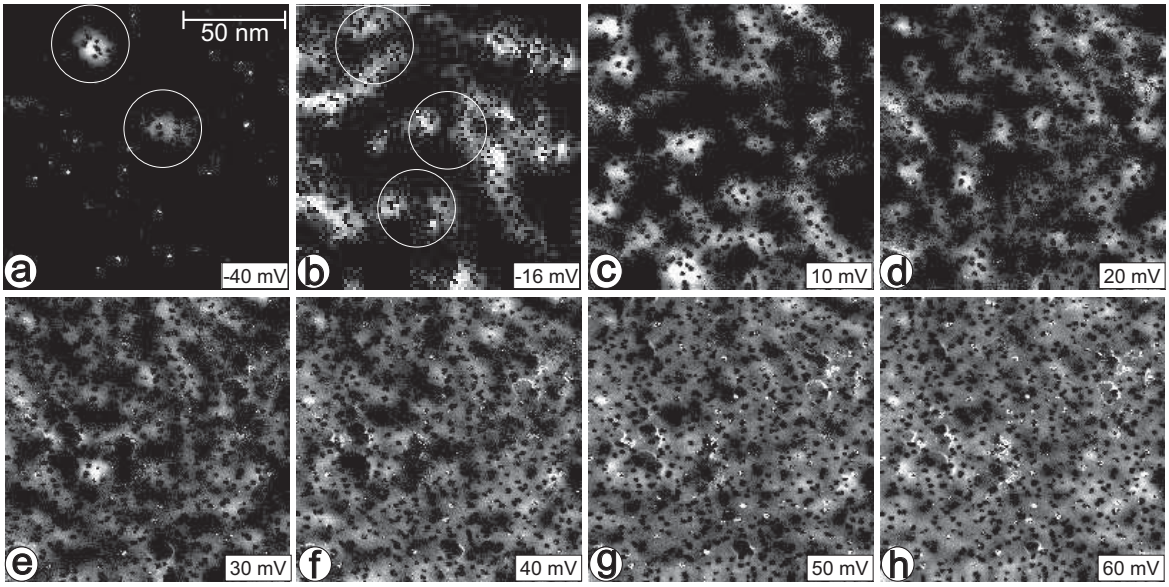

Figure 3.98: (a)−(h) dI/dV-images of a larger 2DES region recorded at different V as indicated, $I_{stab} = 700$ pA, $V_{stab} = 430$ mV, $V_{mod} = 5$ mV; the circles in (b) mark p-states of three quantum dots.

Percolation

A 2DES consisting of separated electron droplets is known to be insulating at low temperature [11]. Ignoring weak localization, one expects a density driven transition to conduction usually described within percolation theory [2]. For symmetric potential landscapes the classical percolation appears at the mean potential value [1], which is identical to the subband energy calculated within the one-dimensional model. Thus, we expect percolation around 20 ± 20 meV. Fig. 3.98 shows larger LDOS-maps obtained at different V. At low V, two s-states are visible in Fig. 3.98a and three p-states are encircled in Fig. 3.98b. While further increasing V, an increasing part of the surface gets covered with LDOS. In a simplified approach, one would identify the percolation with the energy where the bright areas form a percolating path, i.e. at 20 mV. However, since our energy resolution is finite, this apparent percolation could result from overlapping localized states at different energies. Consequently, we cannot determine the percolation threshold by standard analysis [1]. Instead, we found a strong reduction of corrugation close to the expected threshold at 40 mV.

This is demonstrated in Fig. 3.99. Fig. 3.99a shows histograms of the dI/dV-values obtained at different V. Each histogram exhibits two peaks. The origin of these peaks is found by displaying only the spatial areas corresponding to the dI/dV-values within one peak. This reveals that the lower peak corresponds to the Co clusters, where dI/dV is basically zero, and only the upper peak corresponds to the 2DES. For the upper peak, the minimum (min) and the mean dI/dV-value is determined as marked in Fig. 3.99a. A corrugation strength of the corresponding LDOS defined as (mean-

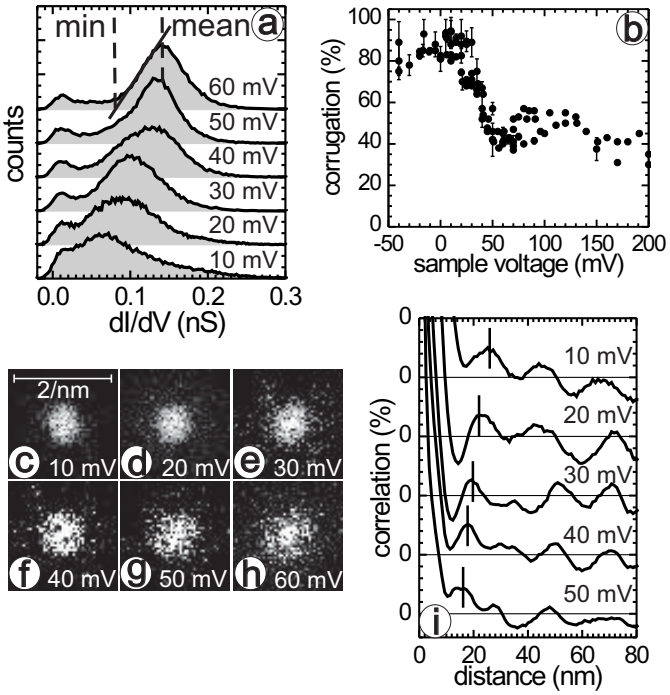

Figure 3.99: (a) histograms of dI/dV-values obtained within the images of Fig. 3.98 (curves offset for clarity); the larger peak in each curve corresponds to the 2DES region; dashed lines on the (60 mV)-curve indicate the minimum and mean value used to determine corrugation (see text); (b) corrugation for different dI/dV-images as a function of V (error bars indicated); (c)-(h) Fourier transforms of dI/dV-images with length bar in units of $k = 2\pi/\lambda$; (i) spatial correlation function of dI/dV-images; curves are offset by the distance of horizontal lines; half wave length as expected from the InAs dispersion is marked by vertical lines.

min)/mean is deduced and plotted as a function of V in Fig. 3.99b. It drops rather sharply around 35 mV. Thus, a drop of LDOS corrugation appears to be indicative for percolation [12].

An interesting question is, whether classical percolation is an adequate model to describe the transition. It assumes that electrons are small enough to fill into the available space given by the potential landscape. Since rearrangements in electron density are typically governed by the Fermi wave length [13], this assumption might be wrong. However, in a strong disorder potential, a significant mixing of electron waves takes place [14–16]. Thus, the Fermi wave length is not a well defined quantity. The mixing becomes evident from Fourier transforms (FTs) representing the k-space distribution of the LDOS and shown in Fig. 3.99c-h. The FT of a clean system would exhibit rings growing in radius with increasing energy as indeed observed for a less disordered 2DES [17]. Here, we find instead a filled circle with a radius barely depending on energy. We conclude that the mixing induced by the strong disorder supresses dominating wave lengths. In other words, the concept of a Fermi wave length breaks down. A small remainder of the dominating wave length is found in the spatial correlation functions of the LDOS shown in Fig. 3.99i. The expected dispersion wave length is indicated and one observes a tiny peak of 1.5 % strength at this distance and further peaks at multiple distances. Obviously, there is a small tendency of the LDOS to prefer next maxima in the distance of the expected wave length. However, we do not think that this small tendency will influence the percolation significantly. We conclude that wavelength effects are of minor importance around percolation implying that a classical description is propably sufficient.

Strongly disordered 2DES in a nonquantizing magnetic field

As shown in the previous section the strong disorder potential results in a strong mixing of electron wavelengths above the percolation threshold. Furthermore, it is interesting to look at the influence of the strong disorder on the Landau levels and the corresponding drift states, which were found in the less disordered 2DES in Fe/InAs(110) in a magnetic field. In that case, the electrons build drift states that have a width according to the magnetic length $l_B = \sqrt{\frac{\hbar}{eB}}$ and run along the equipotential lines of the disorder potential [18].

The condition for the formation of these semi-classical drift states is a disorder potential $V_{dis}(\vec{r})$, that varies less than the Landau level energy spacing on the length scale of the magnetic length, i.e. $\nabla V_{dis} \ll \frac{\hbar\omega_c}{l_B}$. In the case of the strong disordered 2DES investigated here, we found $\nabla V_{dis} \approx 2.5\,\mathrm{meV/nm}$. For the maximum magnetic field of 6 T of our 6 K facility used for these measurements, $\hbar\omega_c/l_B = 2\,\mathrm{meV/nm}$. Thus, we do not expect drift states.

Since the variation of the potential is larger than $\hbar\omega_c$, we also expect a vanishing of the Landau oscillations in the spatially averaged density of states due to overlapping of the Landau levels. Nevertheless, Rudin et al. [19] in this case predict oscillations with

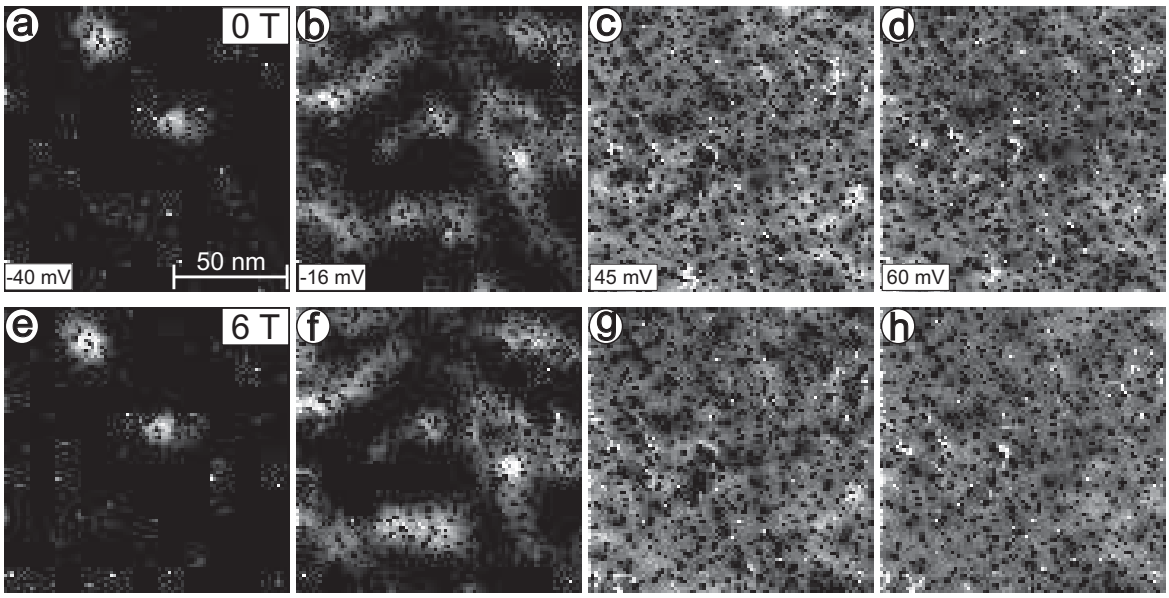

Figure 3.100: (a)-(d) dI/dV-maps without applied magnetic field taken at the indicated voltages. (e)-(h) dI/dV-maps of the same sample area with a magnetic field of 6 T applied perpendicular to the sample surface ($I_{stab} = 700$ pA, $V_{stab} = 500$ mV, $V_{mod} = 5$ mV).

the period $\hbar\omega_c$ in the energetic correlation function of the LDOS. In other words, we expect Landau oscillations in local dI/dV-curves, but, due to shifting in the spatially varying potential, the oscillations are smeared out in the spatially averaged dI/dV-curves.

Figure 3.100 shows dI/dV-maps at different energies below and above the percolation threshold, taken without and with the maximum magnetic field applied perpendicular to the sample surface. Indeed, we do not find any apparent influence of the magnetic field on the LDOS, i.e. for example no condensation into drift states. Also, we do not find Landau oscillations in the spatially averaged dI/dV-curves as shown by Fig. 3.101a. The curve labeled with (mean), which is an average over the whole image area of Fig. 3.101b and c, is only slightly changing, when a magnetic field is applied. Only the dI/dV-curves (1)-(3), that are locally averaged over small areas, show oscillations with a period $\hbar\omega_c \approx 20\,\mathrm{meV}$ according to the Landau level spacing at 6 T. From curve to curve, the positions of the maxima in the oscillation are shifting as caused by the spatial variation of the disorder potential. This causes the vanishing of the Landau oscillations in the totally averaged dI/dV-curve.

These results give an impression, how a strongly disordered 2DES behaves in a non-quantizing magnetic field. Nevertheless, further measurements at intermediate steps of the magnetic field are necessary to draw more definite conclusions.

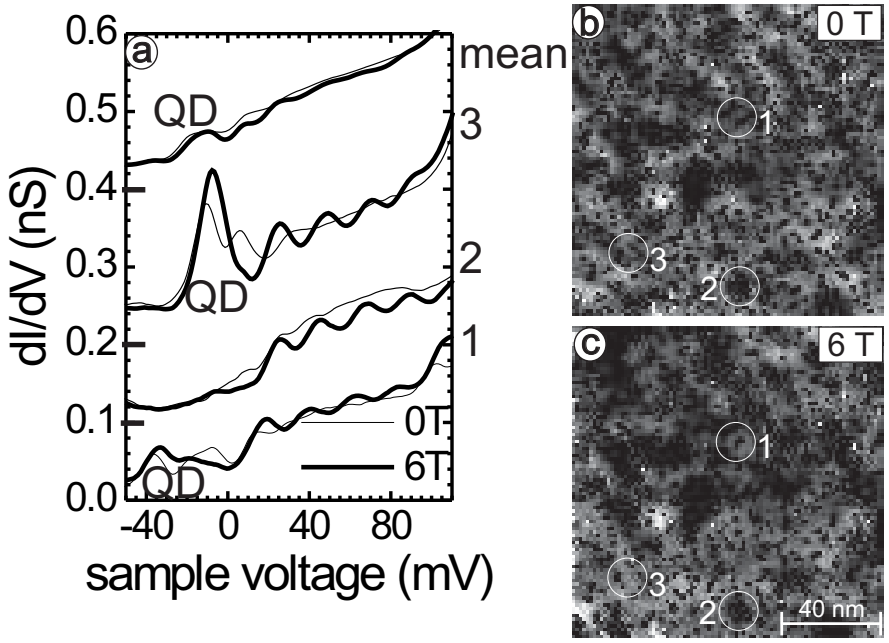

Figure 3.101: (a) dI/dV-curves at 0 T and at 6 T. Curves (1)-(3) are locally averaged over identical areas given by the circles in (b) and (c); curve (mean) is averaged over the total image area. Spectra are shifted vertically for clarity with zero line given by a black dash at the left scale. In curves (mean), (1) and (3) quantum dot states (QD) are visible below the Fermi energy. (b), (c) dI/dV-maps covering the same sample area at 25 mV and at a magnetic field of 0 T and at 6 T, respectively. ($I_{stab} = 700$ pA, $V_{stab} = 500$ mV, $V_{mod} = 5$ mV)

References

[1] D. Stauffer: *Introduction to Pecolation Theory.* Taylor & Francis (1985).

[2] Y. Meir: *Percolation-Type Description of the Metal-Insulator Transition in Two Dimensions.* Phys. Rev. Lett. **83**, 3506 (1999).

[3] S. He, X. C. Xie: *New Liquid Phase and Metal-Insulator Transition in Si MOSFETs.* Phys. Rev. Lett. **80**, 3324 (1998).

[4] K. M. Lang, V. Madhavan, J. E. Hoffman, E. W. Hudson: *Imaging the granular structure of high-T_c superconductivity in underdoped $Bi_2Sr_2CaCu_2O_{8+\delta}$.* Nature **415**, 412 (2002).

[5] M. Fäth, S. Freisem, A. A. Menovsky, Y. Tomioka, J. Aarts, J. A. Mydosh: *Spatially Inhomogeneous Metal-Insulator Transition in Doped Manganites.* Science **285**, 1540 (1999).

[6] M. Morgenstern, J. Wiebe, A. Wachowiak, M. Getzlaff, J. Klijn, L. Plucinski, R. L. Johnson, R. Wiesendanger: *Co/p-InAs(110): An island-induced two-dimensional electron system consisting of electron droplets.* Phys. Rev. B **65**, 155325 (2002).

[7] R. Desmicht, G. Faini, V. Cros, F. Fert, F. Petroff, A. Vaurés: *Point-contact electrodes to probe charging in individual ultrasmall cobalt clusters.* Appl. Phys. Lett. **72**, 386 (1998).

[8] The lower fluctuation with respect to the one deduced from the Coulomb gap centers is a consequence of the distance of the 2DES from the surface.

[9] T. Ando: *Electronic properties of two-dimensional systems.* Rev. Mod. Phys. **54**, 437 (1982).

[10] U. Merkt, S. Oelting: *Simple description of nonparabolic two-dimensional subbands.* Phys. Rev. B **35**, 2460 (1987).

[11] B. I. Shlovskii: *Electronic Properties of Semiconductors.* Springer (1984).

[12] The reason is probably that wave functions significantly overlap only above the percolation threshold which reduces the LDOS corrugation (see also [7]).

[13] J. Friedel, Nuovo Cimento **7**, 287 (1958).

[14] C. Metzner, M. Hofmann, G. H. Döhler: *Intersubband transitions of a quasi-two-dimensional electron gas in the strong disorder regime.* Phys. Rev. B **58**, 7188 (1998).

[15] M. Hofmann, M. Bockstedte, O. Pankratov: *Efficient self-consistent method using basis splines for the investigation of interacting two-dimensional electrons in a random impurity potential.* Phys. Rev. B **64**, 245321 (2001).

[16] J. Shi, X. C. Xie: *Droplet State and the Compressibility Anomaly in Dilute 2D Electron Systems.* Phys. Rev. Lett. **88**, 86401 (2002).

[17] M. Morgenstern, J. Klijn, C. Meyer, M. Getzlaff, R. Adelung, R. Römer, K. Rossnagel, L. Kipp, M. Skibowski, R. Wiesendanger: *Direkt Comparison between Potential Landscape and Local Density of States in a Disordered Two-Dimensional Elektron System.* Phys. Rev. Lett. **89**, 136806 (2002).

[18] M. Morgenstern, J. Klijn, C. Meyer, R. Wiesendanger: *Real-Space Observation of Drift States in a Two-Dimensional Electron System at High Magnetic Fields.* Phys. Rev. Lett. **90**, 056804 (2003).

[19] A. M. Rudin, I. Aleiner, L. I. Glazman: *Density of states of a two-dimensional electron gas in a nonquantizing magnetic field.* Phys. Rev. B **58**, 15698 (1998).

3.3.4 Comparing scanning tunneling microscopy images on InAs(110) with electronic structure calculations

J. Klijn, L. Sacharow, Chr. Meyer, M. Morgenstern, and R. Wiesendanger

There is a continuing interest in the atomic and electronic structure of III-V surfaces, which is related to the technological importance of these materials. In particular, the defect free (110) surface has been investigated intensively. Angular resolved photoemission spectroscopy (ARUPS) and numerical calculations on AlAs, AlSb, GaAs, GaP, GaSb, InAs are reported. However, detailed studies of the electronic structure on the atomic scale are rare. Some scanning tunneling microscopy (STM) and scanning force microscopy (SFM) measurements are available, but only in very few papers theoretical local electronic structure calculations and STM images are directly compared (for publications see [1]).

The latter studies are all focussed on the large band-gap semiconductors GaAs, GaP and InP, which exhibit an important difference to small band gap III-V semiconductors such as InAs and InSb. In the first species, surface states are dominating the STM images at all voltages, while for the second species the density of states (DOS) at small positive and negative energy does not contain any surface state, which allows, e.g., to probe bulk properties by STM.

On the InAs(110) surface, scanning probe microscopy studies with atomic resolution [2, 20–23] exist, but a detailed comparison between STM-results and electronic structure calculations is missing. Here, such a comparison between STM-results and calculations is performed within the local density approximation to the density functional theory. It is found, that the anion (As) is visible not only at negative sample bias as in the large band gap materials, but also at positive bias voltages up to about 1 V, where the indium dangling bond (In-DB) state sets in. The reason is that the LDOS of the parabolic bulk conduction band has a surface appearance very similar to the arsenic dangling bond (As-DB).

In addition, two anomalous types of STM-images on InAs(110) are shown. First, we find atomic resolution at -250 meV in both topography and the simultaneously recorded dI/dV-images, although this voltage corresponds to an energy in the middle of the band gap. The second anomalous imaging occurs with certain tips, if the tunneling current is increased. Sharp subatomic structures are observed in the topography, which are attributed to elastic interactions between the tip and the surface atoms.

Calculations

Electronic structure calculations are performed as described in detail in [1]. We proceed as follows. First, the theoretical lattice constant is calculated in a bulk unit cell to be 6.03 Å in accordance with experimental results [3]. After that, the (110)-surface is introduced using the nine layer slab and relaxed using the energy minimization method.

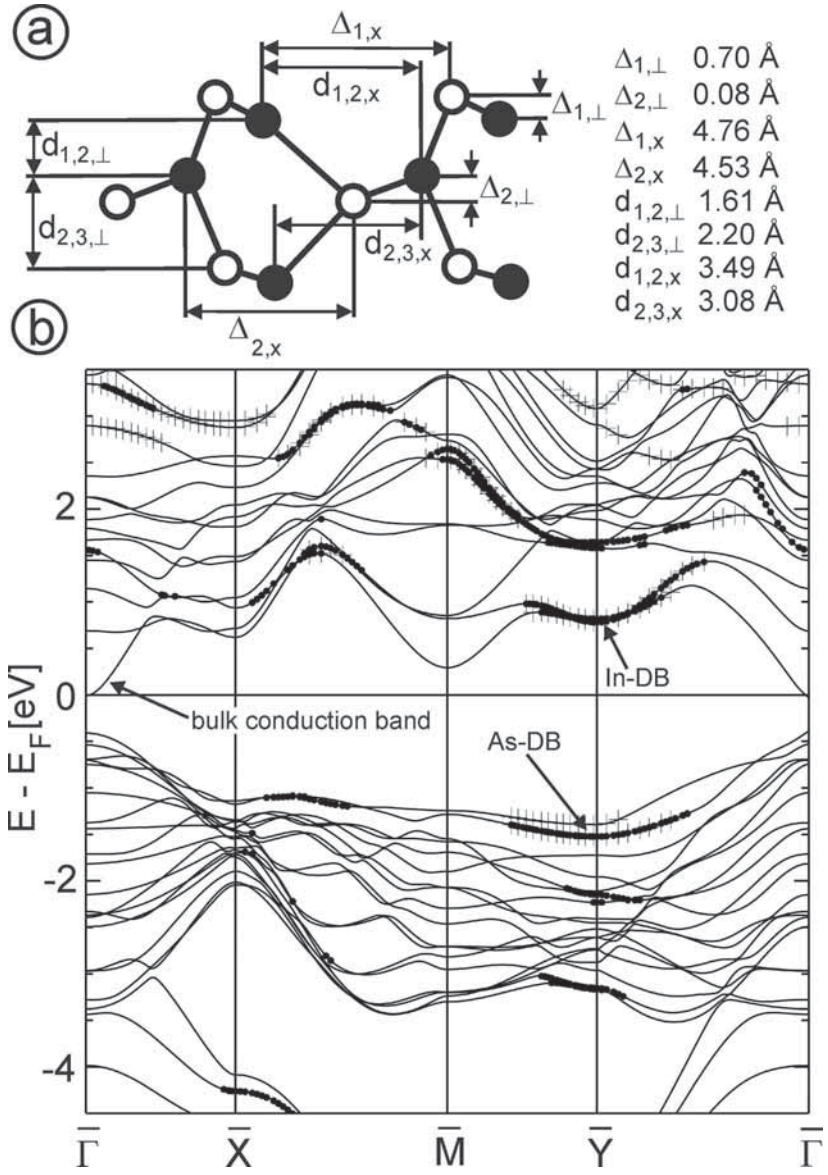

Figure 3.102: **a)** Relaxation of the InAs(110) surface with indicated atomic distances (black dots: In, white dots: As). The calculated values of the relaxed distances are listed on the right. **b)** InAs(110) band structure. Large symbols mark states that lie more than 80% in the upper two layers, crosses (+) mark states with more than 15% probability in the vacuum. The states corresponding to the dangling bonds of the In and As atoms as well as the bulk conduction band at $\overline{\Gamma}$ are marked.

This results in relaxation values as shown in Fig. 3.102(a) which are in agreement with previous calculations [3–5] and with measurements [3, 6].

Finally, the electronic structure of the slab is analysed using the increased number of k-points.

In order to compare the STM constant current mode (CCM) and dI/dV images with theory, we need to simulate these images based on the electronic structure. Within the Tersoff-Hamann model [7, 8], the experimentally determined tunneling current is related to the LDOS of the sample $\rho_s(E, x, y)$ at the lateral position (x, y) of the tip by

$$I_t \propto \int_0^{eV} \rho_t(eV - E)\ \rho_s(E, x, y)\ T(E, V, z)dE \tag{3.30}$$

with ρ_t being the LDOS of the tip, $T(E, V, z) = e^{-2\kappa(E,eV)z}$ the transmission coefficient and $\kappa = \sqrt{2m(V_0 - E)/\hbar^2}$. The dI/dV signal is consequently related to the LDOS by:

$$\begin{aligned}\left(\frac{dI}{dV}\right)_V &\propto e\ \rho_t(0)\ \rho_s(eV, x, y)\ T(eV, V, z) \\ &+ \int_0^{eV} \rho_t(eV - E)\ \rho_s(E, x, y)\ \frac{dT(E, V, z)}{dV}dE \\ &+ \int_0^{eV} \frac{d\rho_t(eV - E)}{dV}\ \rho_s(E, x, y)\ T(E, V, z)dE\end{aligned} \tag{3.31}$$

At low voltages, the second and third term can usually be neglected. Only ρ_s and T have an (x, y)-dependence and $\rho_s(x, y) \cdot T(z(x, y))$ is identical to the LDOS(x, y) of the sample at the position of the tip at height z above the surface. Consequently, to first order the calculated dI/dV images are identical to the LDOS(x, y) at a height z above the surface. In order to increase the signal to noise ratio, the LDOS(x, y) is integrated over an energy interval $\Delta E = 60$ meV at each point (x, y).

Experimental CCM images are compared with LDOS(x, y, z) images integrated over larger energy intervals assuming that ρ_t does not depend on energy (equation 3.30). Partly the integration starts at 0 meV and goes to the energy corresponding to the applied voltage, but partly the integral interval is shifted in energy to take tip-induced band bending into account [9, 10]. We checked that using the more complicated calculation of height profiles corresponding to constant LDOS contours, which would exactly correspond to CCM images, differs only by about 1% from the integrated LDOS images at constant height. Therefore, the more complicated procedure is omitted, and the integrated LDOS images are used for comparison with STM topography.

Experiments

The InAs samples are cleaved in situ at a pressure $\leq 10^{-8}$ Pa and transferred into the cryostat within 5 minutes resulting in a clean (110)-surface with an adsorbate density of about $10^{-7}/^2$. The samples are n-doped ($N_D = 1.1 \cdot 10^{16}$ cm^{-3}), which leads to a Fermi energy about 10 meV above the conduction band minimum (CBM). Scanning tunneling microscopy measurements were performed as described in the introduction

of this chapter.

In order to compare measured dI/dV images with calculated LDOS images, the dI/dV images are normalized according to the method described in [11]. The method transforms dI/dV images recorded in CCM into dI/dV images recorded at constant height. Therefore, one first measures $I(z)$ curves, which are assumed to be proportional to the transmission coefficient $T(z) = e^{-2\kappa z}$ with 2κ being the attenuation coefficient. Then the CCM image $z(x,\ y)$ is used to solve

$$\left[\frac{dI}{dV}(x,y)\right]_{\text{norm}} = \frac{dI/dV(x,\ y)}{e^{-2\kappa z(x,\ y)}} \tag{3.32}$$

which is proportional to the $dI/dV(x,y)$ at constant height.

Theoretical results

The band structure of the relaxed InAs slab projected on the (110)-surface is shown in Fig. 3.102(b). Its general structure is the same as found in earlier calculations [5, 12]. Larger points indicate states lying with more than 80% in the upper two layers of the film, while crosses (+) show states with more than 15% probability in the vacuum, i.e. outside the MT's of the upper layer. These states are basically attributed to surface states. However, crosses at high energies, which are not coincident with larger points, might also be due to the reduced potential barrier height at such energies and might therefore belong to bulk states. Unambiguous surface states are found at different energies around the $\overline{Y}$-point, between the $\overline{X}$ and the $\overline{M}$-point as well as between the $\overline{Y}$ and the $\overline{M}$-point, but not around the $\overline{\Gamma}$-point. Note that our experiments on low dimensional electron systems are all performed in the marked, nearly parabolic band at positive energies around the $\overline{\Gamma}$-point and are, thus, related to electrons within an InAs bulk band [9, 11, 13–16].

The density of states within the MT's corresponding to the different atoms is plotted in Fig. 3.103. In Fig. 3.103(a) the DOS of a surface As-MT is compared with that of a bulk As-MT, while in Fig. 3.103(b) the DOS of a surface and bulk In-MT are compared. At some energies the surface DOS is highly enhanced with respect to the bulk DOS, again indicating the surface states. In Fig. 3.103, however, the surface states can be related to particular atoms. For example, the additional surface DOS at -1.3 eV in the As-MT is assigned to the occupied As-DB, because **(I)** it is concentrated at the As atom as visible in Fig. 3.103(a), **(II)** it has a tilted p_z like structure as can be seen from cuts through the corresponding LDOS [1] and **(III)** it reaches deeply into the vacuum, as visible in Fig. 3.102. Obviously it is centered around the $\overline{Y}$-point as can be seen in Fig. 3.102(b).

The In-DB can be identified in the same way by looking at Fig. 3.103(b) and the corresponding cross sections of the LDOS [1]. It is located at 0.8–1.2 eV above the CBM, has the typical tilted p_z-structure at the In atom and is centered around the $\overline{Y}$-point as well (Fig. 3.102(b)).

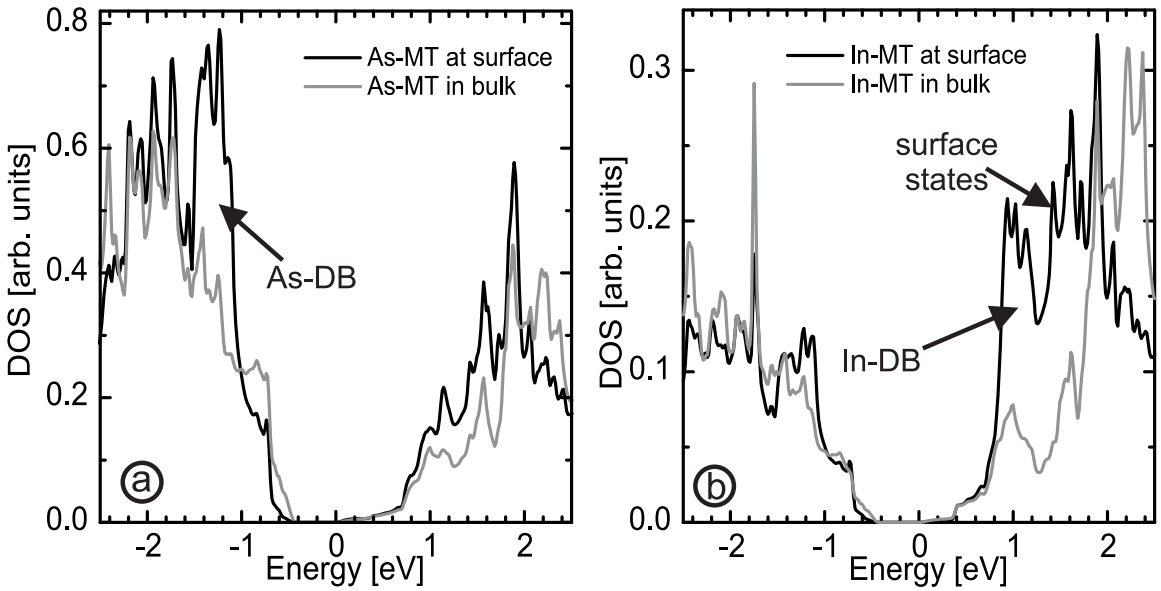

Figure 3.103: Local density of states spatially integrated over MT regions. Black lines correspond to MT's directly at the surface and grey lines to atoms in the middle of the slab. **a)** As-MT's, **b)** In-MT's. The Fermi energy is positioned at the conduction band minimum. Regions corresponding to three different surface states are marked and are discussed in the text.

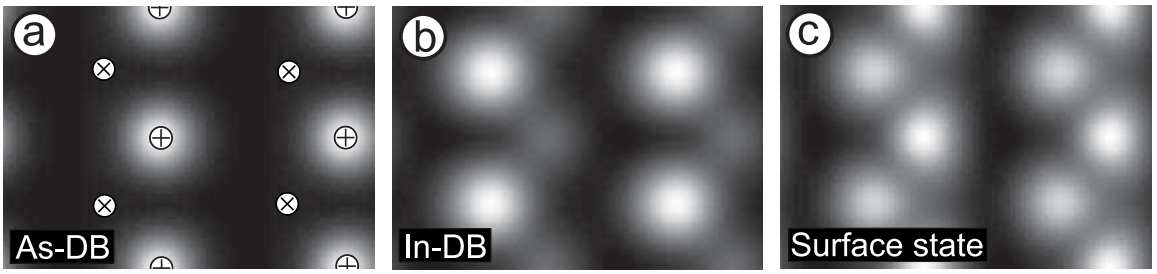

Figure 3.104: LDOS distribution at 2 Å above the surface, with energies with respect to the conduction band minimum. **a)** Integrated LDOS from −1500 to −1100 meV (As-DB). **b)** Integrated LDOS from 870 to 1200 meV (In-DB). **c)** Integrated LDOS from 1450 to 1800 meV (surface state). The positions of the In (⊗) and As (⊕) atoms are marked in a).

LDOS sections at 2 Å above the surface for each of these three surface states are shown in Fig. 3.104. Evidently, only the As atom appears at energies corresponding to the As-DB, the In atom is dominant at the In-DB and both atoms are visible with similar intensity at the third surface state. Note that the As atom is also slightly visible at In-DB energies, which is attributed to an *sp*-like configuration around the As atoms.

The fact that all surface states are well away from the band edges leads to a peculiarity in STM images. The anion As dominates at small positive sample bias, where only the bulk conduction band marked in Fig. 3.102(b) can contribute. This is contrary to large-gap materials, where only the cation (In, Ga) is measured at positive bias [4, 17, 18].

Comparison with STM images

Figure 3.105 shows measured CCM images at small positive voltage in comparison with calculated topography. The measured images are recorded with the same tip, but at different current and voltage. The decreased voltage and increased tunneling current in Fig. 3.105(b) leads to a smaller tip-surface distance than in Fig. 3.105(a). The difference can be estimated from the measured exponential decay of the tunneling current $I = I_0 e^{-2\kappa\Delta z}$ with a measured value of $-2\kappa = -14.5$ nm^{-1} [19]. This tells us that the height difference between the two measurements in Fig. 3.105(a) and (b) is $\Delta z \approx 3$ Å. Consequently, we compare the measured images with calculated topography images at different height, i.e. at 3.5 Å and 1 Å respectively. The distances are much smaller than typical tunneling distances, but this has already been noticed by Engels et al. [18] and has been attributed to influences of higher orbital tip states. The calculated topography images are shown in Fig. 3.105(c) and (d). The LDOS integral is taken over the energy range 100–300 meV, which includes the 100 meV band bending deduced straightforwardly from dI/dV curves exhibiting states of the

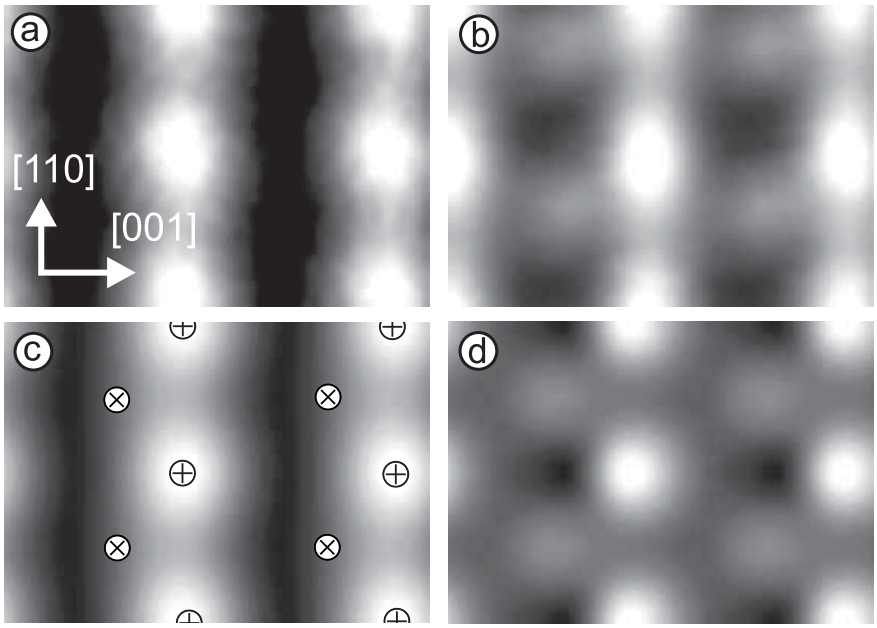

Figure 3.105: Measured CCM images (a, b) and calculated topography (c, d). The tip-induced band bending is determined to be about 100 meV [9]. **a)** $V = 100$ mV, $I = 200$ pA. **b)** $V = 50$ mV, $I = 1.8$ nA. **c)** Integrated LDOS from 100 to 300 meV at 3.5 Å above the surface. **d)** Integrated LDOS from 100 to 300 meV at 1 Å above the surface. The positions of the surface In ($\otimes$) and As ($\oplus$) atoms are marked in c).

tip-induced quantum dot [9]. The agreement between measurement and calculation is excellent. Since the calculated topography at 3.5 Å shows As atoms, while only closer to the surface also In atoms are visible, the intensity in the measured images can be attributed accordingly to the two atoms. So it can be concluded that the As atoms dominate STM images at small positive V. Little change in the atomic appearance in experiment and calculation up to about 650 meV is found. From Fig. 3.102(b) one infers that this energy range is exactly the range of the parabolic conduction band around $\overline{\Gamma}$. Thus, we attribute the As appearance to this band.

Calculated topography images for higher energies taken at 5 Å above the surface are shown in Fig. 3.106. In Fig. 3.106(b) (680 meV), an additional intensity appears at the In atoms, leading to a zig-zag topography. At this energy the In-DB starts to play a role, as visible in Fig. 3.102(b). In Fig. 3.106(c) (1200 meV), only the In atoms are visible showing that the In-DB DOS now dominates with respect to the As DOS from the bulk conduction band at $\overline{\Gamma}$.

The transition to the In-DB regime can be observed more clearly in the calculated LDOS images in Fig. 3.106(d1)–(i1). The LDOS images are compared with measured dI/dV images all recorded with the same tip in Fig. 3.106(d2)–(i2). Again good correspondence between measurements and calculations is found. However, the voltages do not correspond directly to the energies. The apparent difference of about 500 meV, being voltage independent in the whole voltage range above 700 mV, can be attributed to the tip induced band bending [9]. A nearly constant value of 500 meV is reasonable, since this is slightly higher than the band gap of InAs. Then, screening of holes becomes important, giving a band bending rather independent of applied voltage. A detailed discussion of this effect can be found in [10].

Next, we discuss Fig. 3.106(d)-(i) in more detail. In Fig. 3.106(d), the LDOS of the bulk conduction band at $\overline{\Gamma}$ is shown again being concentrated around the As. At an energy of 710 meV, an additional LDOS intensity is seen above the In (Fig. 3.106(e)). A sharp transition into an LDOS completely centered above the In takes place within 50 meV, i.e. between Fig. 3.106(e) and (f). This is exactly at the energy where the In-DB band starts in Fig. 3.102(b). Between 760 meV and 820 meV, the LDOS above the In atoms broadens into the $[00\overline{1}]$ direction. This leads to apparent atomic rows rotated by 90° with respect to the previous images. Above 820 meV, the broadening of the intensity in the $[00\overline{1}]$ direction disappears again (Fig. 3.106(h)) and at 1250 meV, where according to Fig. 3.102(b) and 3.103(b) the In-DB region ends, the main LDOS intensity is rotated back into the [110] direction (Fig. 3.106(i))[9]. Note that Fig. 3.106f and i, both limiting the In-DB regime, are very similar. At even higher energy the third surface state with LDOS located at the In and As atoms comes into play, but STM imaging with atomic resolution at these high voltages was unstable.

In conclusion, the In-DB induces a shift from LDOS intensity from the As to the In atoms and a partial rotation of the LDOS rows from the [110] into the $[00\overline{1}]$ direction.

[9]On large band-gap semiconductors, only the rotation back into the [110] direction has been observed, since the cation dangling bond starts directly at the band edge [17, 18, 20, 21].

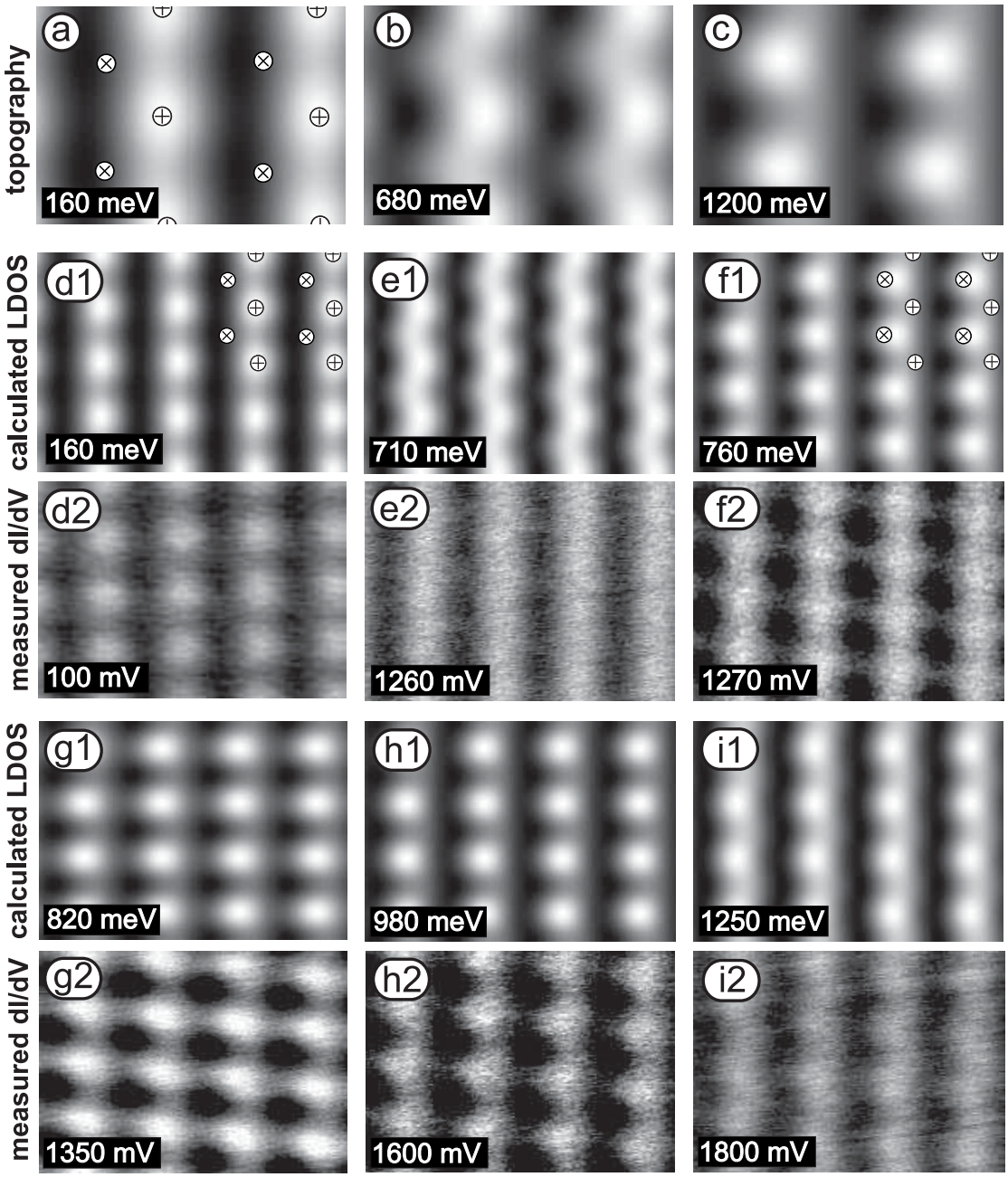

Figure 3.106: **a–c)** Calculated topography images 5 Å above the surface taken at energies as indicated. **d1–i1)** Calculated LDOS at 5 Å above the surface with marked energies given with respect to the conduction band minimum. **d2–i2)** Measured and according to equation 3.32 normalized dI/dV images taken at voltages as indicated, $I = 1500$ pA, $V_{\mathrm{mod}} = 20$–40 mV. The small rotation observed in the measured data is attributed to thermal drift of the sample. All measurements are recorded with the same tip. The $\otimes$ and $\oplus$ mark the positions of In and As atoms, respectively.

The measured dI/dV images can largely be identified with the calculated LDOS within LDA. This confirms that the first term in equation 3.31 is dominating at moderate voltages.

Atomic resolution in the band gap

In the previous section, dI/dV images at small *positive* bias were successfully identified with LDOS images. However, at small *negative* bias, where the energy corresponds to the bulk band gap, this picture has to be modified. A simplified band structure of the n-doped InAs(110) surface below an STM tip is shown in Fig. 3.107(a). It exhibits a Fermi energy at 10 meV above the bulk CBM and a tip-induced band bending downwards by about 300 meV [9]. Two tip-induced quantum dot states are induced by such a band bending and are drawn at -30 and -50 meV. A dI/dV curve within the same energy region is shown in Fig. 3.107(b). A small but non-vanishing dI/dV intensity is found at voltages between 0 mV and -600 mV. The inset in Fig. 3.107(b) shows a close-up of the dI/dV curve, which exhibits two quantum dot states at -52 and -27 mV. Knowing these energies, the band bending can be estimated to be 300 meV according to [9]. This band bending is in agreement with the above interpretation. Note that this excludes any sample states between -60 meV and -400 meV.

STM-CCM images recorded simultaneously at 30 and -250 mV in trace and retrace are shown in Fig. 3.107(c) and (d). Atomic resolution is visible in both images, but this is not surprising, because in both cases the integral of equation 3.30 covers energy regions with states at the surface. Surprisingly, also the dI/dV images in Fig. 3.107(e) and (f) show atomic corrugation at 30 and -250 mV. Note that the rows of the dI/dV image at 30 mV (Fig. 3.107(e)) are one third of an atomic row shifted with respect to the dI/dV image at -250 mV (Fig. 3.107(f)), i.e. only the atomic rows at -250 mV are in phase with the rows of the two CCM images.

The question to discuss is: what causes the atomic corrugation at -250 mV in the dI/dV images, where $\rho_s = 0$? A first reason could be that during the scan, the tip height varies, which can induce an atomic dI/dV corrugation caused by the atomic variation of z and, thus, of $T(z) \propto dI/dV$ (equation 3.31). However, the dI/dV image has maxima at the same position as the corresponding CCM-image, while $T(z)$ varies in anti-phase with z. Thus, this explanation can be excluded.

Another possible reason could be the influence of states made available by the band bending. Such an explanation has been proposed for GaAs(110) by De Raad et al. [22]. However, the two quantum dot states induced by the band bending in the InAs case are measured to be at -52 mV and -27 mV far away from -250 mV. Consequently, such an explanation can be excluded as well.

Finally, our corrugation could be understood by the second and third term of equation 3.31. By a detailed calculation, it can be shown that indeed the observed dI/dV signal in the band gap can be understood within the Tersoff-Hamann model as due to the third term [1]. Thus, $(dI/dV)_{-250}$ basically measures the LDOS(x, y) in the parabolic bulk conduction band, which is represented by the two quantum dot

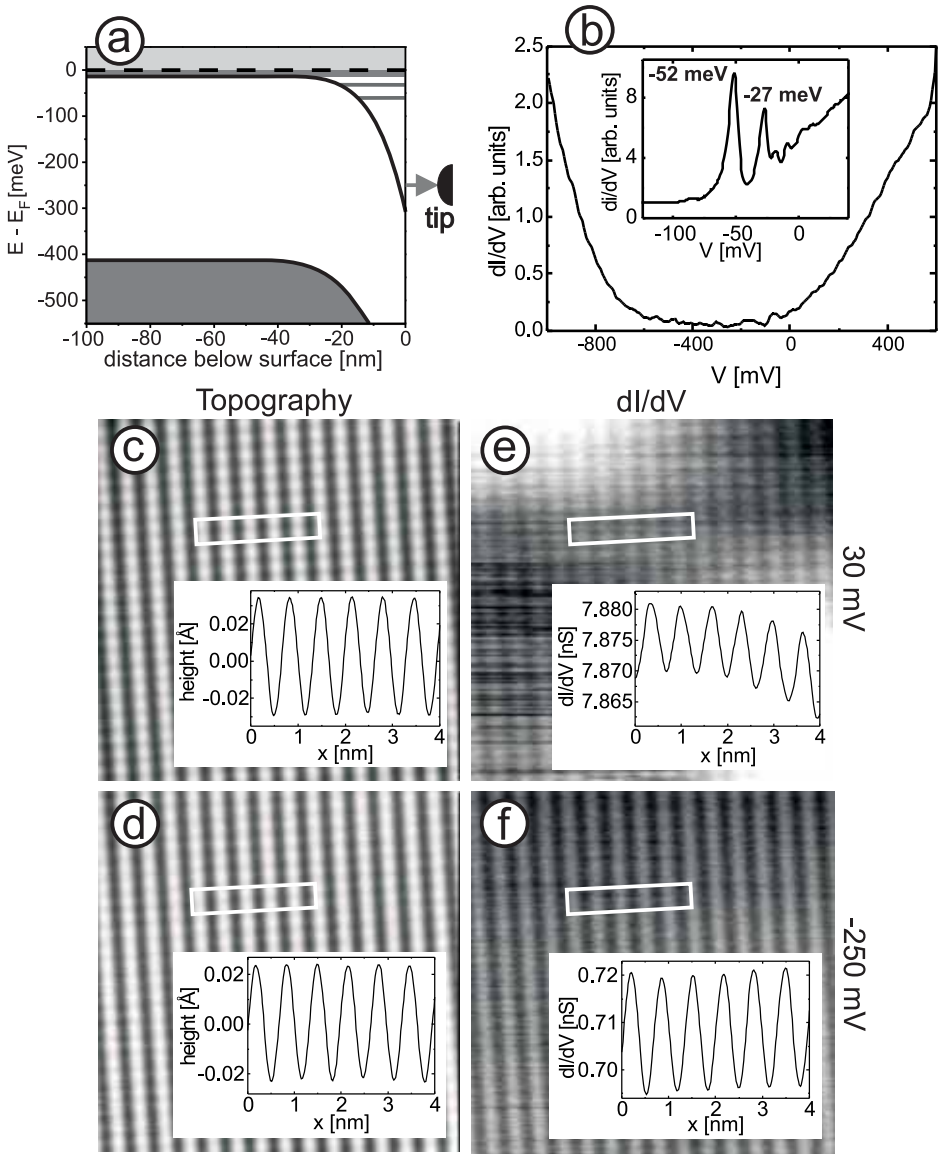

Figure 3.107: **a)** Sketch of the band structure of InAs including tip-induced band bending. The position of the tip indicates $V = -250$ mV. **b)** Spatially averaged $dI/dV(V)$ curve, $V_{\mathrm{stab}} = 600$ mV, $I_{\mathrm{stab}} = 300$ pA, $V_{\mathrm{mod}} = 1$ mV. Inset: higher resolution dI/dV curve exhibiting two quantum dot states as indicated, $V_{\mathrm{stab}} = 70$ mV, $I_{\mathrm{stab}} = 300$ pA, $V_{\mathrm{mod}} = 1$ mV. **c–d)** CCM images, recorded simultaneously at $V = 30$ and $V = -250$ mV in trace and retrace, respectively, $I = 300$ pA. **e–f)** dI/dV images recorded simultaneously to the CCM, $V_{\mathrm{mod}} = 8$ mV. Insets in c–f) show line sections along the rectangles. All measurements in b–f) are recorded simultaneously with the same tip.

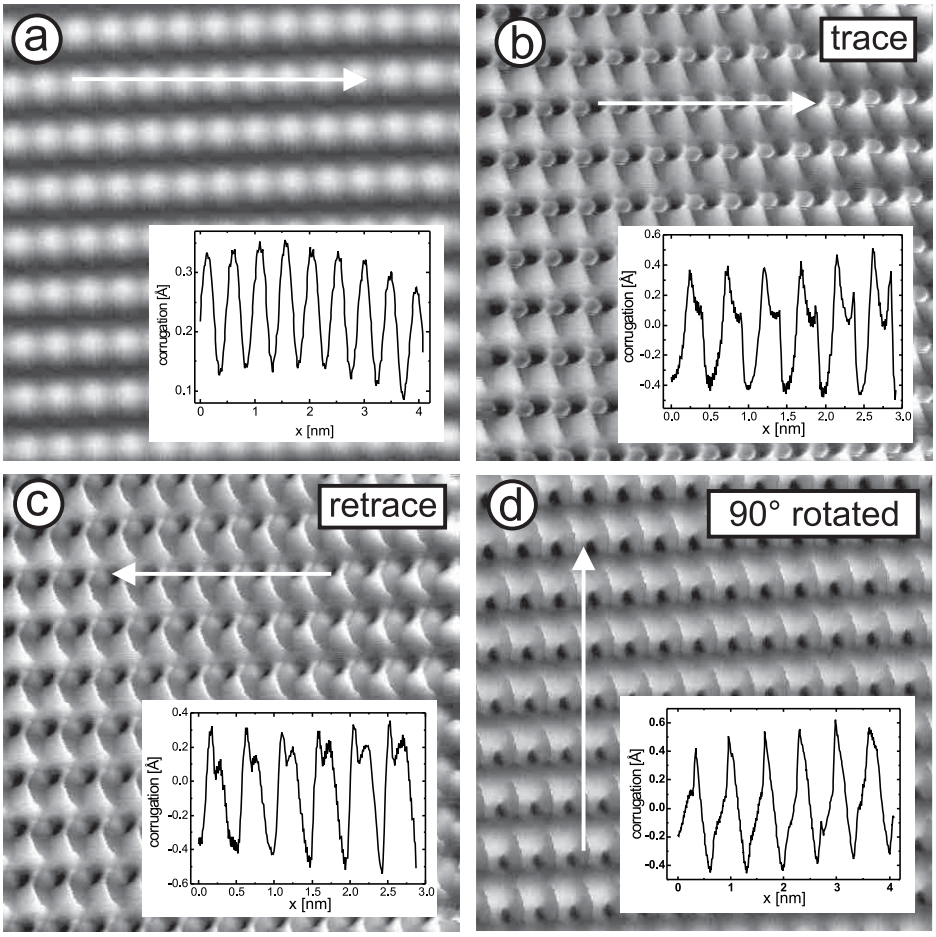

Figure 3.108: CCM images all recorded with the same tip on InAs(110). **a)** Standard atomic resolution. $V = 50$ mV, $I = 450$ pA. **b)** $V = 50$ mV, $I = 710$ pA, scan direction=trace. **c)** Same as in b), but scan direction=retrace. **d)** Same as in b), but scan direction rotated by 90° and $V = 50$ mV, $I = 530$ pA. Insets show line sections along marked arrows. Arrows indicate the scan direction.

states and the DOS in the conduction band below E_F.

In conclusion: atomic resolution in dI/dV images corresponding to band gap voltages is possible, if $\frac{d\rho_t}{dV} \neq 0$ and if there are any states at the surface between E_F and the applied voltage.

Small tip-sample distance imaging

As discussed above, atomic resolution images recorded in CCM at small positive bias usually look like Fig. 3.108(a) (rotated by 90° with respect to Fig. 3.105). They exhibit bumps at the As atoms and are straightforwardly understood in terms of the integrated LDOS. However, with certain tips, the CCM-images change dramatically if

the tunneling current is only slightly increased. An example is shown in Fig. 3.108(b). The effect occurs only with certain tips, but is then reproducible, i.e. one can switch between Fig. 3.108(a) and (b) by repeatingly increasing and decreasing the current. Note that in the measurements shown in Fig. 3.108, the transition takes place between 450 and 530 pA, i.e. it is rather sharp.

Above the transition, subatomic features are visible with an appearance strongly depending on the scan angle. The images in Fig. 3.108(a) and (b) are recorded with the same scan direction (trace), while 3.108c is recorded in opposite scan direction (retrace) and Fig. 3.108(d) is recorded with a scan direction rotated by 90°. Obviously, the features are different in all three images excluding that the unperturbed LDOS is imaged. Probably the image mode is related to a tip-sample interaction. The fact that this interaction depends on scan direction strongly suggests that the interaction shows hysteresis.

Indeed very similar effects and images are found in contact atomic-force microscopy (AFM). There the elastic interaction of a tip in contact with a sample is directly measured [23,24] and the sharp features on the subatomic scale are attributed to a slip-stick motion of the tip with respect to the sample. Hölscher et al. [23, 24] calculated, that the AFM tip while being moved over the surface, sticks in an atomic potential minimum for some time and then jumps suddenly to the next potential minimum, if the lateral force is larger than a certain threshold. Thus, one gets a continuous change of atomic force during the stick and then a sudden jump in force to the next minimum.

This model can be straightforwardly transferred to our case. First, the sharp transition in imaging between 450 pA and 530 pA is the equivalent of the jump-to-contact in AFM. However, our feedback parameter is not force but current, explaining the reversibility of the switching between the two types of imaging. In contact still a resistance of 70 MΩ is measured, which is well above the point contact resistance of 20 kΩ. This requires an insulating region at the tip end. However, the transmittivity of this insulating region depends most likely on elastic deformation. Thus, the sharp features in the CCM images are interpreted as sudden jumps of the atomic contact configuration from one potential minimum to the next one changing the transmittivity. In a sense, the images can be considered as the electric response of a mechanical deformation on the nm-scale. Although Fig. 3.108(d) is similar to non-contact (NC) AFM measurements performed by Schwarz et al. [25], these NC-AFM measurements are similar in all scan-directions, while our measurements are not.

References

[1] J. Klijn, L. Sacharow, C. Meyer, S. Blügel, M. Morgenstern, R. Wiesendanger: *STM measurements on the InAs(110) surface directly compared with surface electronic structure calculations.* Phys. Rev. B **68**, 205327 (2003).

[2] Y. Liang, W. E. Packard, J. D. Dow, H. Ho, G. Lapeyre: *Monatomic steps on the InAs(110) surface.* Phys. Rev. B **48**, 11942 (1993).

[3] C. Mailhiot, C. Duke, D. Chadi: *Calculation of the atomic geometries of the (110) surfaces of III-V compound semiconductors.* Surf. Sci. **149**, 366 (1985).

[4] B. Engels: *Ab initio Berechnung der (110) Oberfläche von III-V Halbleitern: Simulation von Rastertunnelmikroskopie-Aufnahmen.* Dissertation, Reinisch-Westfälische Technische Hochschule, Aachen, Germany (1995).

[5] J. L. Alves, J. Hebenstreit, M. Scheffler: *Calculated atomic structures and electronic properties of GaAs, InP, GaAs, and InAs(110) surfaces.* Phys. Rev. B **44**, 6188 (1991).

[6] C. Duke, A. Paton, A. Kahn, C. Bonapace: *Dynamical analysis of low-energy electron-diffraction intensities from InAs(110).* Phys. Rev. B **27**, 6189 (1983).

[7] J. Tersoff, D. Hamann: *Theory and Application for the Scanning Tunneling Microscope.* Phys. Rev. Lett **50**, 1998 (1983).

[8] J. Tersoff, D. Hamann: *Theory of the scanning tunneling microscope.* Phys. Rev. B **31**, 805 (1985).

[9] R. Dombrowski, C. Steinebach, M. Morgenstern, R. Wiesendanger: *Tip-induced band bending by scanning tunneling spectroscopy of the states of the tip-induced quantum dot on InAs(110).* Phys. Rev. B **59**, 8043 (1999).

[10] R. Feenstra: *Tunneling spectroscopy of the (110) surface of direct-gap III-V semiconductors.* Phys. Rev. B **50**, 4561 (1994).

[11] C. Wittneven, R. Dombrowski, M. Morgenstern, R. Wiesendanger: *Scattering States of Ionized Dopants Probed by Low Temperature Scanning Tunneling Spectrsocopy.* Phys. Rev. Lett **81**, 5616 (1998).

[12] R. P. Beres, R. E. Allen, J. D. Dow: *Surface states and surface resonances in InP, InAs, and InSb.* Phys. Rev. B **26**, 5702 (1982).

[13] M. Morgenstern, D. Haude, V. Gudmundsson, C. Wittneven, R. Dombrowski, R. Wiesendanger: *Origin of Landau oscillations observed in scanning tunneling spectroscopy on n-InAs(110).* Phys. Rev. B **62**, 7257 (2000).

[14] D. Haude, M. Morgenstern, I. Meinel, R. Wiesendanger: *Local Density of States of a Three-Dimensional Conductor in the Extreme Quantum Limit.* Phys. Rev. Lett **86**, 1582 (2001).

[15] M. Morgenstern, J. Klijn, C. Meyer, M. Getzlaff, R. Adelung, R. Römer, K. Rossnagel, L. Kipp, m. Skibowski, R. Wiesendanger: *Direct Comparison between Potential Landscape and Local Density of States in a Disordered Two-Dimensional Electron System.* Phys. Rev. Lett **89**, 136806 (2002).

[16] M. Morgenstern, C. Wittneven, R. Dombrowski, R. Wiesendanger: *Spatial Fluctuations of the Density of States in Magnetic Fields Observed with Scanning Tunneling Spectroscopy.* Phys. Rev. Lett **84**, 5588 (2000).

[17] P. Ebert, B. Engels, P. Richard, K. Schroeder, S. Blügel, C. Domke, M. Heinrich, K. Urban: *contribution of Surface Resonances to Scanning unneling Microscopy Images: (110) Surfaces of III-V Semiconductors.* Phys. Rev. Lett **77**, 2997 (1996).

[18] B. Engels, P. Richard, K. Schroeder, S. Blügel, P. Ebert, K. Urban: *Comparison between ab initio theory and scanning tunneling microscopy for (110) surfaces of III-V semiconductors.* Phys. Rev. B **58**, 7799 (1998).

[19] M. Morgenstern, D. Haude, V. Gudmundsson, C. Wittneven, R. Dombrowski, C. Steinebach, R. Wiesendanger: *Low temperature scanning tunneling spectroscopy on InAs(110).* J. Electr. Spect. Rel. Phen. **109**, 127 (2000).

[20] P. Ebert, G. Cox, U. Poppe, K. Urban: *The electronic structure of the InP(110) surface studied by scanning tunneling microscopy and spectroscopy.* Surf. Sci. **271**, 587 (1992).

[21] G. de Raad, D. Bruls, P. Koenraad, J. Wolter: *Interplay between tip-induced band bending and voltage-dependent surface corrugation on GaAs(110) surfaces.* Phys. Rev. B **66**, 195306 (2002).

[22] G. de Raad, D. Bruls, P. Koenraad, J. Wolter: *STM observations of GaAs(110) showing the top and bottom zig-zag tows of the surface.* Phys. Rev. B **64**, 75314 (2001).

[23] H. Hölscher, U. Schwarz, O. Zwörner, R. Wiesendanger: *Stick-slip movement of a scanned tip on a graphite surface in scanning force microscopy.* Z. Phys. B **104**, 295 (1997).

[24] H. Hölscher, W. Raberg, U. Schwarz, A. Hasbach, K. Wandert, R. Wiesendanger: *Imaging of sub-unit-cell structures in the contact mode of the scanning force microscope.* Phys. Rev. B **59**, 1661 (1999).

[25] A. Schwarz, W. Allers, U. Schwarz, R. Wiesendanger: *Dynamic-mode scanning force microscopy study of n-InAs(110)-(1x1) at low temperatures.* Phys. Rev. B **61**, 2837 (2000).

3.3.5 Density functional calculation of the Fe-InAs(110) interface

L. Sacharow, M. Morgenstern, and R. Wiesendanger

For the fabrication of new electronic devices it is important to understand the interface properties between different materials. Of particular current interest is the interface between ferromagnets and semiconductors. For example, in order to realize the spin transistor proposed by Datta and Das [1], the interface between a ferromagnet and a semiconductor moved into the focus of research. From what is known today, the quality of the interface determines whether the injection of the spin-polarized electrons into the semiconductor is ballistic or diffusive. If it is diffusive, Schmidt [2] and Fert [3] have shown that the spin-polarization of the current injected into the semiconductor is negligibly small. Therefore, a detailed understanding of the ferromagnet/semiconductor interface is very important. An experimental investigation of interfaces consisting of

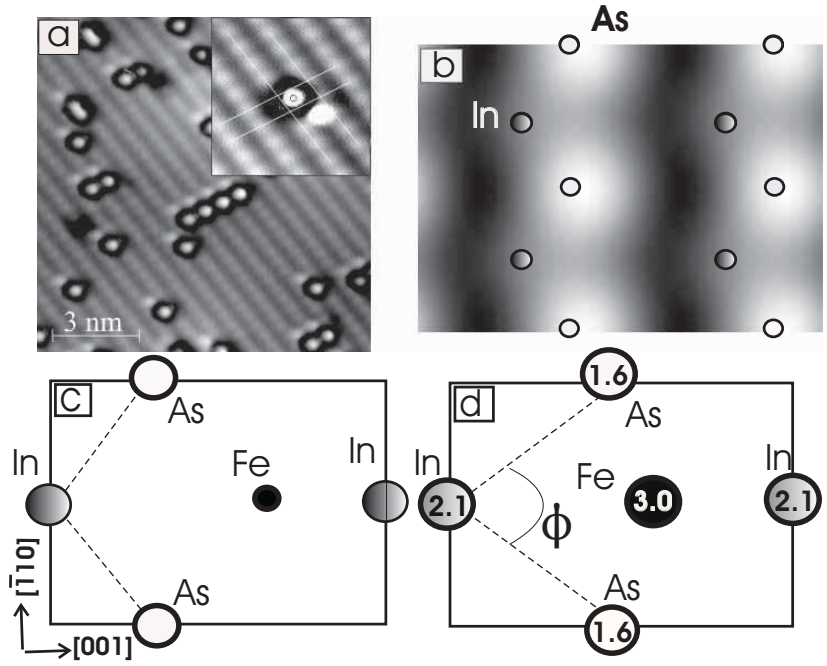

Figure 3.109: (**a**) STM constant-current image of InAs(110) covered with 7.5% Fe, U = 50 mV, I = 200 pA, T = 8 K; [4] (**b**) calculated constant-current image of the relaxed InAs(110) surface, U = 50 mV; the band bending of 300 meV is taken into account; [5] (**c**) from (**a**) and (**b**) deduced position of the Fe-atom in the InAs(110) unit cell; (**d**) calculated position of Fe-atom in the InAs(110) unit cell after relaxation; The numbers on the atoms indicate the vertical relaxation in atomic units from the ideal bulk terminated position of the surface As. The angle ϕ is given in Table 3.5.

thick semiconductor or ferromagnetic films is rather difficult, so it might be appropriate to start with a lower thickness of the ferromagnet. Motivated by recent scanning tunneling microscopy (STM) experiments on Fe atoms and chains on InAs(110) we calculate the atomic configuration, the magnetic properties and the electronic structure of an interface consisting of a monolayer of Fe as a ferromagnetic material and InAs(110) as a semiconductor with large Rashba splitting [4, 6]. Understanding the properties of the monolayer paves also the path to use Fe for preparing nano-structures in order to move into the area of nano-spintronics. We calculated an Fe monolayer on the InAs(110) surface, and relaxed the atom positions to minimize the total energy. The resulting Fe position is in accordance with recent scanning tunneling microscopy (STM) experiments [4]. Finally, the spin-dependent band structure, the local density of states (LDOS) and the spatially integrated density of states (DOS) at the Fe/InAs interface were analyzed. This lead to the conclusion that the Fe spin-polarization at E_F (80%) is much higher than the Fe bulk spin-polarization (40%) [8]. Moreover, the coupling of As p_x- and In sp-states to the Fe d_{xy}- and d_{zy}-orbitals leads to a similar high spin-polarization of different sign on the InAs side.

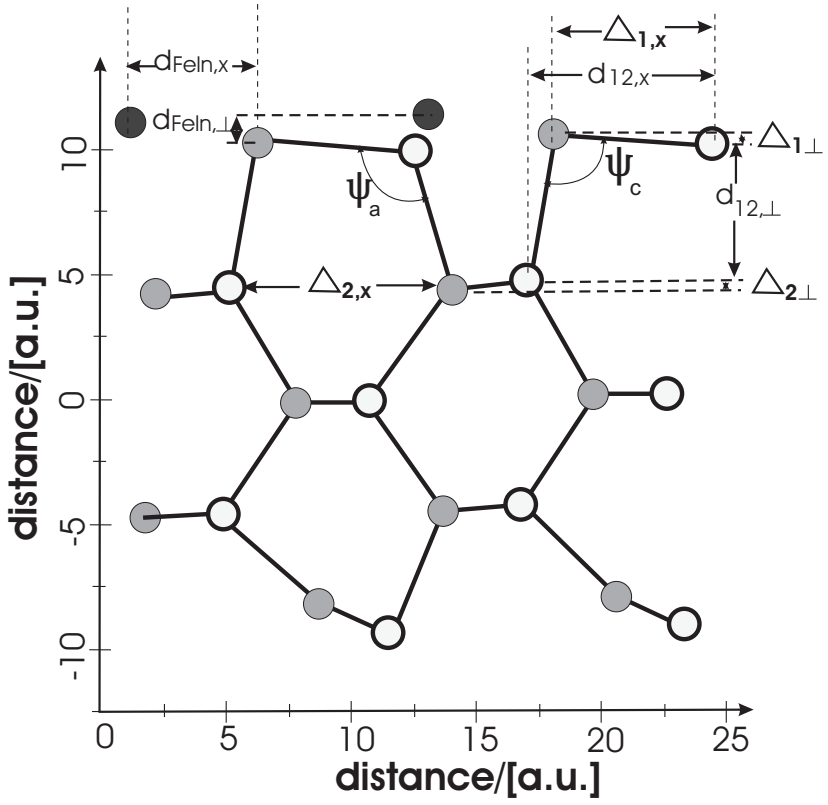

Figure 3.110: Side-view of calculated relaxation positions of InAs(110) surface with Fe-monolayer. Black circles mark the Fe-positions, gray the In- and white the As-positions. Tables 3.4 and 3.5 give the corresponding values of distances, bond lengths and angles.

distance	unit	InAs bulk	InAs(110)	Fe/InAs(110)
a	$[a.u.]$	11.437		
$d_{\mathrm{FeIn},\perp}$	$[\frac{1}{2}a/\sqrt{2}]$			0.079
$d_{\mathrm{FeIn,x}}$	$[a]$			0.429
$\Delta_{1,\perp}$	$[a/\sqrt{2}]$	0.000	-0.164	0.056
$\Delta_{1,x}$	$[\frac{3}{4}a]$	1.000	1.033	0.632
$d_{12,\perp}$	$[\frac{1}{2}a/\sqrt{2}]$	1.000	1.118	1.241
$d_{12,x}$	$[\frac{1}{2}a]$	1.000	1.080	1.266
$\Delta_{2,\perp}$	$[\mathrm{a}/\sqrt{2}]$	0.000	-0.018	0.043
$\Delta_{2,x}$	$[\frac{3}{4}a]$	1.000	0.999	0.996

Table 3.4: Distances between the atoms in the clean relaxed InAs(110) surface and the InAs(110) surface covered with one Fe-atom per unit cell according to the definitions in Fig. 3.110. The distances are expressed in units of the respective InAs bulk distances given in the second column.

System	ϕ [◦]	ψ_a [◦]	ψ_c [◦]	$\delta c_1 a_1$ [%]	$\delta c_2 a_1$ [%]	$\delta c_1 a_2$ [%]
bulk	109.5	109.5	109.5	0.0	0.0	0.0
InAs(110)	110.9	90.1	123.7	-0.7	-0.1	0.5
Fe/InAs(110)	67.7	105.1	96.7	47.9	11.43	13.1

Table 3.5: Comparison of relaxation angles and bond length changes between the InAs(110) surface and Fe/InAs(110) surface. The angles ψ_a and ψ_c are defined in the Fig. 3.110 and ϕ in Fig. 3.109(d). $\delta c_i a_j$ are the changes of the bond lengths between the cation of the i'th layer and the anion of the j'th layer relative to the cation-anion InAs bulk bond length.

The calculations are performed using the density-functional-theory (DFT) as implemented in the FLEUR-code. [9,10]. The calculated system was an InAs slab with an Fe-monolayer, consisting of one Fe atom placed in a InAs(110) unit cell. The starting position for the relaxation of the Fe-atom is deduced from the STM experiment. The measured and calculated image of the clean InAs(110) surface at the same voltage are displayed in Fig. 3.109(a),(b).
From comparison of Fig. 3.109(a) and Fig. 3.109(b) we deduce a lateral position of the Fe atom as displayed in Fig. 3.109(c). The optimization process of this atomic structure led to the structure shown in Fig. 3.109(d).
Fig. 3.110 shows a side-view of the InAs film after relaxation. In contrast to the film without Fe, In and As are nearly at the same height. The In atom is even slightly higher (0.5 a.u.) than the As atom. The bond length between In and As in the uppermost layer as well as the bond length between the uppermost and the next layer

of InAs are increased with respect to the bulk values and with respect to the relaxed InAs film without Fe. Table 3.4 and 3.5 give the corresponding values of distances and bond lengths for the clean relaxed InAs(110) surface and the relaxed InAs(110) surface covered with one Fe atom per unit cell. The results for the clean surface are

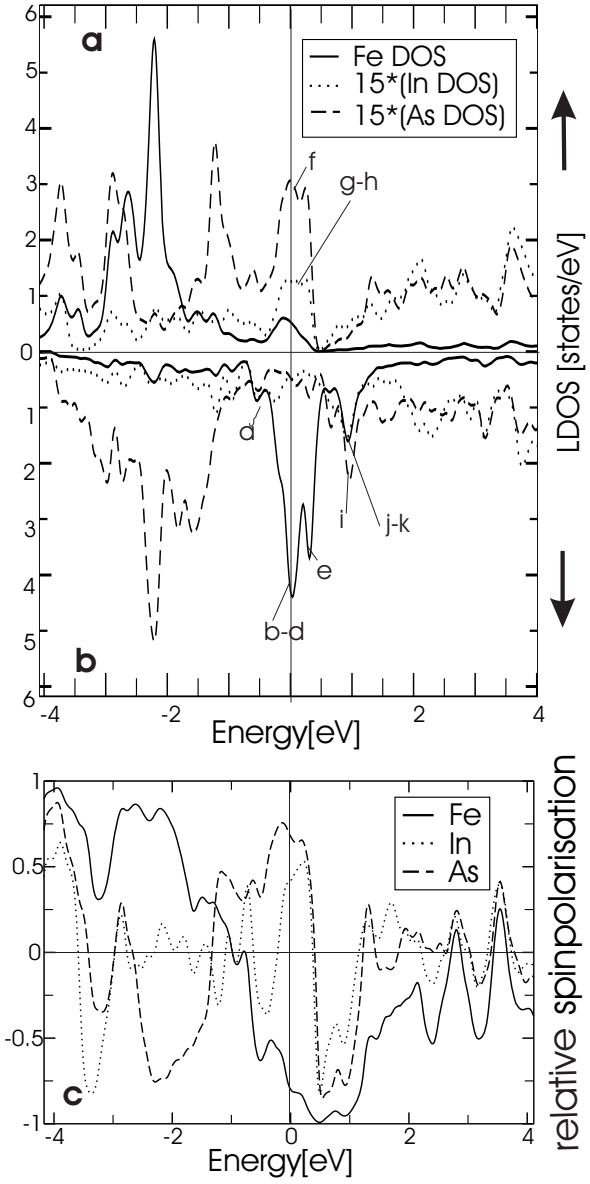

Figure 3.111: (**a**), (**b**) spin-resolved LDOS inside the MT-spheres of Fe (solid line), surface As (dashed line) and surface In (dotted line); LDOS of As and In are multiplied by a factor of 15 to display them on the same scale as the Fe LDOS; (**a**) majority spin (↑); (**b**) minority spin (↓); (**c**) energy dependence of the resulting relative spin-polarization ((n↑ - n↓)/(n↑ + n↓));

in excellent agreement with other theoretical works on III-V semiconductors [11]. A strongly increased In-As bond length in the Fe/InAs(110) case shows that In-As-bonds are weakened in favor of Fe-In and Fe-As bonds [12]. Moreover, the Fe is located nearly equidistant to the adjacent two As and the In atom as visible in Fig. 3.109(d). This indicates that bond formation to both surface species takes place.
Next, we analyze the electronic properties for the optimized atomic configuration. Fig. 3.111 shows the spin-dependent LDOS inside the MTs for the different atoms at the Fe/InAs interface. The LDOS of Fe exhibits one narrow peak in each spin channel, which is caused by the narrow two-dimensional d-bands of different spin. The majority peak is found around -2.4 eV and the minority one around 0.1 eV giving an exchange splitting of about 2.5 eV. The magnetic Fe moment amounts to 2.6 μ_B in the Fe MT-sphere.

In contrast, the magnetic moments of the spheres of the In and As atoms are negligibly small, although both atoms show a strongly energy dependent spin-polarization, which is defined as the difference of the local spin $\uparrow$ and spin $\downarrow$ densities, divided by the spin-integrated LDOS, i.e. (n$\uparrow$ - n$\downarrow$) / (n$\uparrow$ + n$\downarrow$). This can be clearly seen in Fig. 3.111(c), where the spin-polarization of the different atoms is displayed. Both atoms show a polarization up to 75 %, however, partly at different energies. The peaks in Fig. 3.111(a) and (b) can be largely identified with particular atomic orbitals. The details of such identification are published in [13].

Since the spin-polarization at E_F is decisive for spintronic devices, we discuss it more in detail. As visible in Fig. 3.111(c), it is 80 % within the Fe MTs and also large,

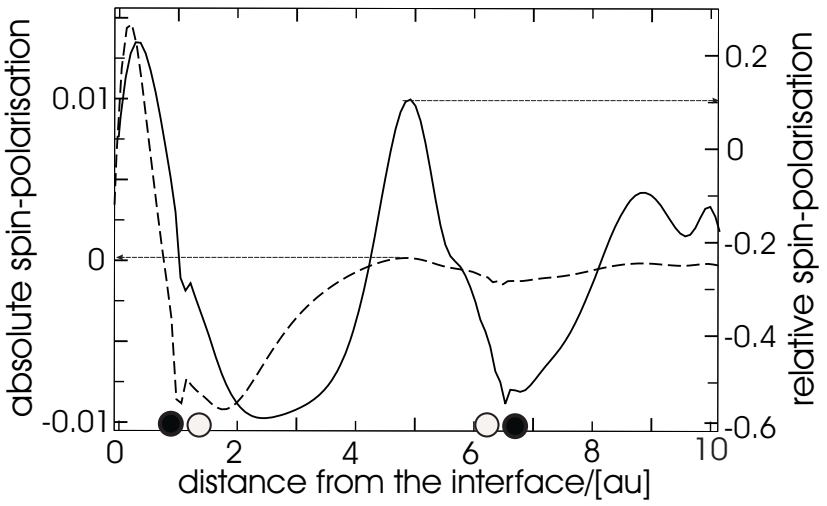

Figure 3.112: Distance dependence of spin-polarization at E_F, integrated over both, the muffin tin and the interstitial region; the circles at the bottom mark the positions of In- (black) and As-atoms (white). The dashed curve represent the absolute spin-polarisation (n$\downarrow$ - n$\uparrow$) and the solid curve the relative spin-polarisation (n$\downarrow$ - n$\uparrow$)/(n$\downarrow$ + n$\uparrow$). Note that the curves display the LDOS of only two calculated states (Kohn-Sham orbitals) near E_F.

but of opposite sign in the In and As MTs at the interface. Fig. 3.112 shows the relative (n↓-n↑)/(n↓+n↑) and the absolute spin-polarization (n↓-n↑) at E_F in the InAs layer as a function of distance from the interface. The energy interval is chosen so that the absolute spin-polarization represents the difference of two Kohn-Sham orbitals. Here, the MTs as well as the interstitial region is considered. The relative spin-polarization exhibits a damped oscillation with atomic periodicity having values as large as 60 %.

In summary, we calculated the electronic and spin properties of a Fe monolayer on InAs(110) using the local density approximation. We find that Fe takes a position equidistant to two As atoms and an In atom and moves all surface atoms outwards with respect to the clean InAs(110) surface. The molecular bonding leads to a large spin-polarization in the Fe layer as well as in the InAs-layer. These results clearly show that details of electronic and magnetic properties of ferromagnet/semiconductor interfaces can be significantly different from the pure materials. Further studies of spin injection properties resulting from such a high spin-polarization would be quite interesting.

References

[1] S. Datta, B. Das: *Electronic analog of the electro-optic modulator.* Appl. Phys. Lett **56**, 665 (1990).

[2] G. Schmidt, D. Ferrand, L. W. Molenkamp, A. T. Flip, B. J. van Wees: *Fundamental obstacle for electical spin injection from a ferromagnetic metal into a diffusive semiconductor.* Phys. Rev. B **62**, R4790 (2000).

[3] A. Fert, H. Jaffrés: *Conditions for efficient spin injection from a ferromagnetic metal into a semiconductor.* Phys. Rev. B **64**, 184420 (2001).

[4] M. Morgenstern, M. Getzlaff, D. Haude, R. L. Johnson, R. Wiesendanger: *Coverage dependence of the Fe-induced Fermi-level shift and the two-dimensional electron gas on InAs(110).* Phys. Rev. B **61**, 13805 (2000).

[5] R. Dombrowski, Chr. Steinebach, Chr. Wittneven, M. Morgenstern, R. Wiesendanger: *Tip-induced band bending by scanning tunneling spectroscopy of the states of the tip-induced quantum dot on InAs(110).* Phys. Rev. B **59**, 8043 (1999).

[6] T. Matsuyama, R. Kürsten, C. Meissner, U. Merkt: Phys. Rev. B **61**, 15588 (2000).

[7] M. Morgenstern, J. Klijn, C. Meyer, M. Getzlaff, R. Adelung, R. Römer, K. Rossnagel, L. Kipp, M. Skibowski, R. Wiesendanger: *Direkt Comparison between Potential Landscape and Local Density of States in a Disordered Two-Dimensional Elektron System.* Phys. Rev. Lett. **89**, 136806 (2002).

[8] B. Sinković, E. Shekel: *Spin-resolved iron surface density of states.* Phys. Rev. B **52**, 8696 (1995).

[9] E. Wimmer, H. Krakauer, M. Weinert, A. Freeman: *Full-potential self-consistent linearized-augmented-plane-wave method for calculating the electronic structure of molecules and surfaces: O_2 molecule.* Phys. Rev. B **24**, 864 (1981).

[10] http://www.flapw.de: .

[11] B. Engels, P. Richard, K. Schröder, S. Blügel, P. Ebert, K. Urban: *Comparison between ab initio theory and scanning tunneling microscopy for (110) surfaces of 3-5 semiconductors.* Phys. Rev. B **58**, 7799 (1998).

[12] S. C. Erwin, S.-H. Lee, M. Scheffler: *First-principles study of nucleation, growth, and interface structure of Fe/GaAs.* Phys. Rev. B **65**, 205422 (2002).

[13] L. Sacharow, M. Morgenstern, G. Bihlmayer, S. Blügel: *High spin polarization at the interface between a Fe monolayer and InAs(110).* Phys. Rev. B **69**, 85317 (2004).

3.4 Insulators

The application of force microscopy in the dynamic mode in ultrahigh vacuum (UHV) is now an established technique to study all kinds of surfaces with high spatial resolution and high force sensitivity [1]. This method is based on the frequency modulation (FM) technique originally introduced by Albrecht *et al.* [2]. Due to its capability to achieve *true* atomic resolution in the attractive non-contact regime of the tip-sample interaction and to distinguish it from the *quasi* atomic resolution observed in static contact mode (many tip apex atoms probe the repulsive regime, whereby individual atomic scale point defects cannot be visualized) this mode of operation has been named non-contact atomic force microscopy (NC-AFM). However, the technique itself is not limited to the attractive non-contact regime and not exclusively used for studies on the atomic scale. Therefore, other names are also common. For example, frequency modulation atomic (or scanning) force microscope (FM-AFM or FM-SFM, respectively), to discriminate it from the amplitude modulation (AM) technique usually employed under ambient conditions and dynamic force microscopy (DFM), which does not refer to a specific modulation method, but points out the difference to the static mode, where the cantilever does not oscillate.

The experimental data in the following sections have been acquired with two instruments. In section 3.4.1 a new low temperature UHV force microscope described in section 3.6.2, where a magnetic field up to $\mu_0 H = 5$ T can be applied [3] was used, while the experiments in sections 3.4.2-3.5.3 have been obtained with our *old* low temperature UHV force microscope [4]. All investigations have been performed using DFM with constant amplitude (CA-mode) and frequency modulation (FM-mode). In this mode of operation the cantilever oscillates with its resonance frequency at an amplitude A, which is kept constant by a regulator, while the frequency shift Δf between the eigenfrequency f_0 and the actual resonance frequency f of the self- oscillating cantilever is the measured quantity. A larger attractive tip-sample interaction results in a larger negative Δf. In the microscopy mode (DFM) this signal is used to adjust the tip-sample distance accordingly, while in the spectroscopy mode (DFS) this signal is directly recorded ($\Delta f(z)$-curves) to obtain the distance dependence of the tip-sample interaction. Using appropriate algorithms [7–9] these curves can be converted into force data ($F(z)$-curves).

In the past three years we studied the antiferromagnetic insulator NiO(001) and single-walled carbon nanotube (SWNT). On both samples we applied force spectroscopy. In particularly, we developed the three dimensional force field spectroscopy (3D-FFS). Thereby, the force-distance relationship and the full interaction potential can be obtained with atomic-site resolution. Using this technique, we were able to detect the difference in chemical reactivity between a iron coated tip and the Ni and O-sites on NiO(001) [10, 11], respectively, and to show that the interatomic van der Waals interaction is sufficient to obtain atomic resolution on the curved surface of an SWNT [12].

3.4.1 Surface and subsurface defects on NiO(001) studied by DFM

U. Kaiser, A. Schwarz, and R. Wiesendanger

Introduction

Transition metal oxides like nickel oxide have already been subject of many studies in recent years [5,6,13–15]. They show interesting properties, which lead to technological applications like catalysis or spin coupled devices. For many of these applications the surface structure of the material plays a major role. Catalytic processes at a NiO surface, for instance, depend strongly on the number of surface defects. In this study, we used a force microscope in the dynamic mode under ultrahigh vacuum (UHV) conditions to analyze the (001) surface of NiO. All measurements have been performed in the attractive non-contact regime, employing the frequency modulation technique while keeping the amplitude of the self oscillating cantilever constant. As a part of the detailed investigation of the surface, we also aim at the direct observation of the magnetic exchange force, which is expected to interact between a ferromagnetic tip atom and the antiferromagnetically aligned Ni atoms at the surface.

Experimantal setup

For this study, we used a home-built low temperature dynamic force microscope, described in [3], which was initially used as a magnetic force microscope (see section 3.6.2). To obtain atomic resolution with this instrument, some modifications of the original design were necessary [16]. In order to decrease the noise level, the microscope was equipped with a smaller sample piezo tube scanner with a scan range of 1.3 μm $\times$ 1.3 μm at 5 K. Moreover, the fiber end was coated with a dielectric material to increase the reflection for the used laser wavelength of 780 nm from slightly less than 4% to $\approx$ 30%. Thereby, the reflectivity from the two mirrors of the interferometer cavity, i.e., the cantilever back side and the fiber end, is about equal. As a result, the cavity is not a simple two beam, but a multiple beam Fabry-Perot type interferometer. With respect to future experiments to measure the exchange force between a magnetic tip and the NiO(001) surface, it is noteworthy that unlike the system used for preceding studies [13, 15], a superconducting magnet in this system can provide a magnetic field $\mu_0 H$ of up to 5 T perpendicular to the sample surface.

NiO itself is an insulating 3d-transition metal oxide with a bandgap of about 4.3 eV, a rocksalt crystal structure and a lattice constant of 417 pm as shown in Fig. 3.113. The (001) easy cleavage surface, which is subject to this study, is bulk-terminated with a small (2%) inward relaxation and shows a rumpling, whereby the Ni atoms are slightly elevated above the oxygen atoms. Below the Néel-temperature of 525 K the Ni atoms in {111}-planes are ferromagnetically coupled, while neighboring {111}-planes exhibit an antiferromagnetic coupling. Ni-spins in the bulk are found pointing

in one of the six possible $\langle 1\bar{2}1\rangle$-directions, but the orientation of the spins at the (001) surface is still under discussion. Stöhr et al. [17] favor an alignment perpendicular to the surface, while Hillebrecht and co-workers [18] found a bulk-like canted orientation in $\langle 1\bar{2}1\rangle$-direction.

For the experiments discussed here, we used NiO single crystal rods supplied by MaTeck [20], which were cleaved *in situ* at room temperature in the load lock chamber of our UHV-system. Afterwards, we directly transferred the samples into the microscope. Low energy electron diffraction (LEED) and Auger electron spectroscopy (AES) data suggest that the surface is well ordered, stochiometric and clean. According to the data displayed in Fig. 3.114 the sample remains clean even weeks after cleavage within the accuracy of the measurement.

As tips we used standard Si-cantilevers as well as supersharp Si-tips, both provided by Nanosensors [21]. To prepare the tips, we removed the native oxide layer by argon ion sputtering and evaporated Fe or Ni for depositing ferromagnetic material to the tip apex.

Results and discussion

Using such freshly prepared tips, we usually obtained images showing cloudy structures without any sharp-edged details. The image quality could be improved drastically by performing controlled tip collisions with the sample, until clear images of monatomic steps (height $\approx$ 220 pm) are observed. Typical terrace widths are a few ten nanometers. The topography of such an image is shown in Fig. 3.115(a). This image was taken about 24 hours after sample cleavage with a sputtered and Ni-coated Si-tip. It shows three terraces of monatomic height with steps along the $\langle 100\rangle$-axes and numerous different defects (overall defect density $\approx 1{\cdot}10^{16}$ m^{-2}). The derivative of the topographic image is shown in Fig. 3.115(b) to clarify the faint contrasts of the defects. Marked with an "A" we can see an asymmetric protrusion with an apparent height of about

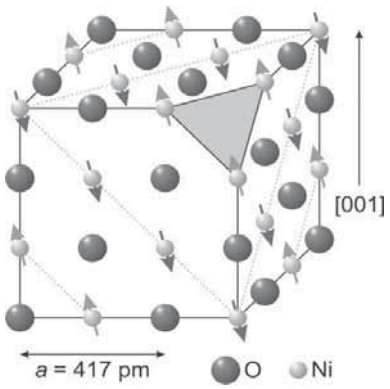

Figure 3.113: Schematic view of a NiO-crystal. The nickel atom spins are ferromagnetically coupled in {111}-planes, indicated by the dotted lines. The (001)-surface consists of nickel atoms with row-wise alternating spin directions.

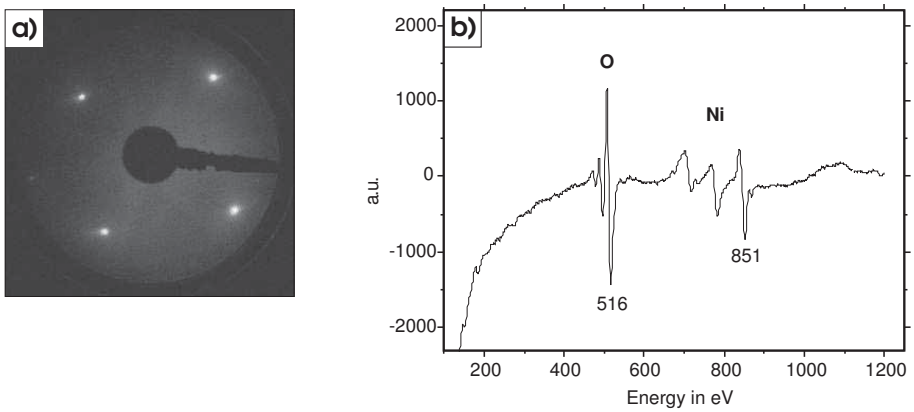

Figure 3.114: (a) Typical LEED pattern of a NiO(001) surface at $E = 62.8$ eV, taken four weeks after cleavage. Clear spots in a fourfold 1×1 symmetry indicate a well-ordered surface. (b) Auger electron spectrum of the same sample. No contaminations are found, indicating a clean surface. The ratio between the heights of the nickel and the oxygen peak is O_{516}:$Ni_{851} = 2.17$ (value given in Ref. [19]: O:Ni = 2.1), which indicates a stochiometric sample surface. Both measurements were performed at a sample temperature of 200°C to avoid charging effects.

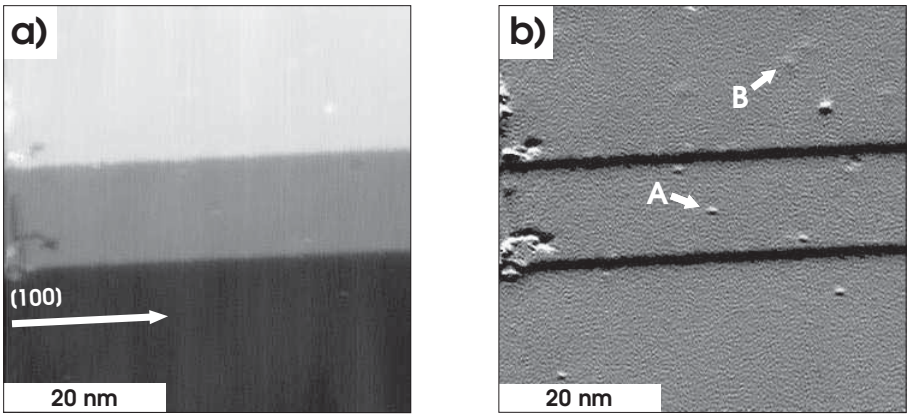

Figure 3.115: (a) Topographic image of the NiO(001) surface. (b) Corresponding derivative image for better contrast on all steps. Various defects can be seen on the monatomic terraces. Arrows highlight very faint objects. The image was obtained on a non-heated NiO sample 24 hours after cleavage, using a sputtered and Ni-coated tip. Parameters: $T = 5$ K, $f_0 = 191$ kHz, Δf = -1.9 Hz, U_{Bias} = -1.3 V, $A = \pm 4$ nm, $c_z \approx 47$ N/m, $\gamma \approx$ -3.3 $\times$ 10^{-16} N$\sqrt{\text{m}}$.

30 pm and a lateral size of approximately 1.1×0.6 nm. Object "B" appears circular, showing a much fainter contrast as we measure a height of circa 16 pm and a diameter of about 1.4 nm. Other images done with the same tip show also larger objects on flat terraces with apparent heights of greater than 100 pm, which accumulate mostly at upper step edges. This indicates, that these are not intrinsic defects, but adsorbates from the residual gas, that are mobile on a flat surface and lose their high mobility

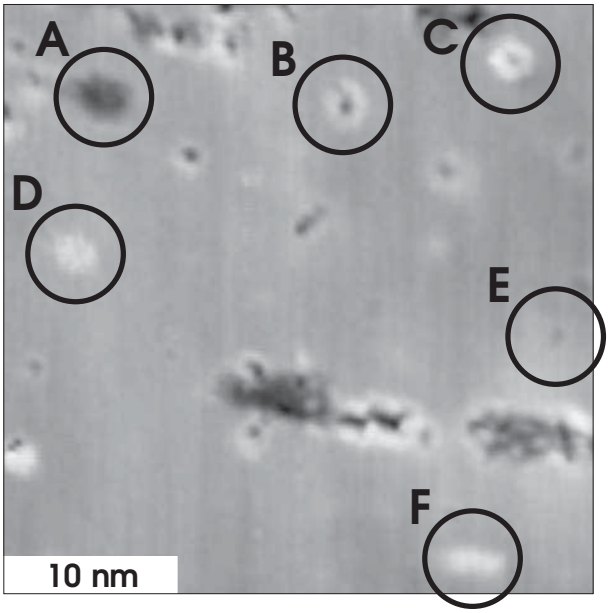

Figure 3.116: DFM-image of various surface defects on a NiO(001)-surface. Sample was heated prior to the imaging for 8 hours at 200°C. The image was taken 24 hours after cleavage with a sputtered, non-metal-coated, supersharp tip. Parameters: $T = 293$ K, $f_0 = 153$ kHz, $\Delta f = -25.4$ Hz, $U_{\mathrm{Bias}} = -0.2$ V, $A = \pm 5$ nm, $c_z \approx 31$ N/m, $\gamma \approx 5.2 \times 10^{-15}\mathrm{N}\sqrt{\mathrm{m}}$, image has been filtered.

when they hit a step edge. The van der Waals radii of contemplable gas molecules, e.g., $r_{vdW}(\mathrm{H_2}) = 110$ pm and $r_{vdW}(\mathrm{C}) = 170$ pm [22] are of the same order of magnitude, which supports this interpretation. Although the origin of the smaller objects is not completely clear, we can conclude that these are probably not adsorbates but defects created during the cleavage process or intrinsic defects, e.g., interstitial atoms or charges near to the surface.

In Fig. 3.116 we present an image recorded on a terrace of a sample, which was prior heated 8 hours at 200°C, showing various surface defects on a flat surface. This image was obtained at room temperature, using a supersharp tip with no metal coating. The defects imaged in this picture show different appearances as we find vacancy-islands without elevated surroundings (marked A and E), vacancy-islands showing a bright circumference (like B and C) and bright diffuse objects having no sharp contours (D and E). As bright contrasts can be caused by charges, this differently looking defects can be interpreted as various charge states of vacancies, as found for example in color centers (see Fig. 3.117). The diffuse objects without vacancy can be explained by sub-surface charges.

On some terraces we also found a large number of vacancy islands of about one monolayer depth with typical lateral sizes of circa 7.5 × 4.5 nm. We studied one of these vacancy islands at different bias voltages U_{Bias}, which is shown in Fig. 3.118. The circumference of the vacancy-island is mapped differently, depending on the bias

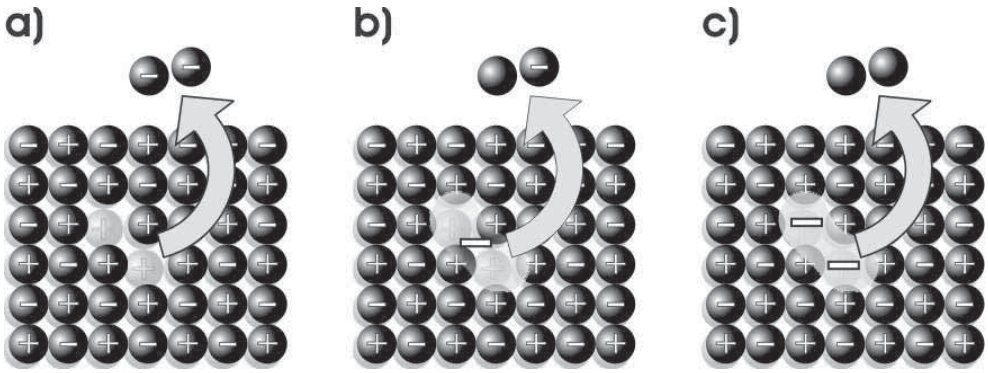

Figure 3.117: Schematics of the creation of differently charged surface defects during the cleavage process of an ionic crystal. The sketch in (a) represents a highly charged defect with a net charge of two positive elementary charges. In (b) one neutral atom and one anion are removed from the surface. One electron remains trapped in the defect, resulting in a defect net charge of one positive elementary charge. Case (c) shows a neutral defect, created by removal of two atoms. Both electrons are localized to the defect, leading to a neutral net charge.

voltage. The arrows highlight two positions, where the contrasts change differently. While at the lower right position the contrast changes from dark to bright, the upper left position acts reciprocal. This behavior can be explained by different localized charges, being situated in the circumference of the vacancy. As the sample is an insulator at 5 K, the mobility there is very low compared to the doped Si-tip. Therefore a change in the bias voltage will primarly lead to a different charge state of the tip, while the localized charge of the insulator remains unchanged. As a result, the imaging characteristics is altered, i.e., the contrast reverses after changing the tip polarity from negative to positive values.

Fig. 3.119 demonstrates the capability of imaging the NiO(001)-surface with true atomic resolution showing a small vacancy-island. This image was taken at room temperature with a sputtered and Fe-coated supersharp tip on a sample which was prior heated a few times at 200°C. As known from earlier studies, only one type of atoms is imaged as a protrusion. The measured corrugation is about 35 pm with a peak-to-peak noise of circa 10 pm along the scanlines and approximately 20 pm along the slow scanning direction, respectively. As this measurement was performed at room temperature, we expect a lower noise level for low temperature measurements. Some of the atoms around the vacancy-islands appear brighter which can be explained by relaxation effects or localized charges. Like in preceding studies we did not find any spin contrast in the atomically resolved images we obtained so far.

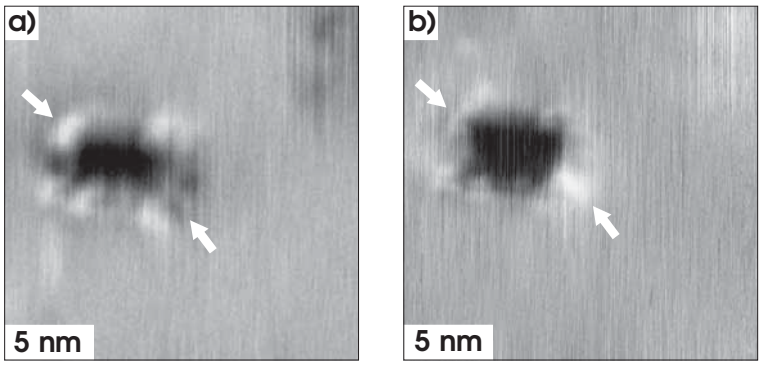

Figure 3.118: Dynamic mode images of a vacancy-island at different bias voltages. Arrows indicate bias-depending contrast changes in the circumference of the vacancy-island. (a) $U_{\mathrm{Bias}} = 0$ V, $A = \pm 8$ nm, $\Delta f = -2.3$ Hz, $\gamma \approx -1.2 \times 10^{-15}$ N$\sqrt{m}$, (b) $U_{\mathrm{Bias}} = 1.5$ V, $\Delta f = -9.24$ Hz, $\gamma \approx -4.9 \times 10^{-15}$ N$\sqrt{\mathrm{m}}$. Parameters: $T = 5$ K, $f_0 = 204$ kHz, $c_z = 53$ N/m, tip sputtered and Nickel-coated, non-heated sample, images have been filtered.

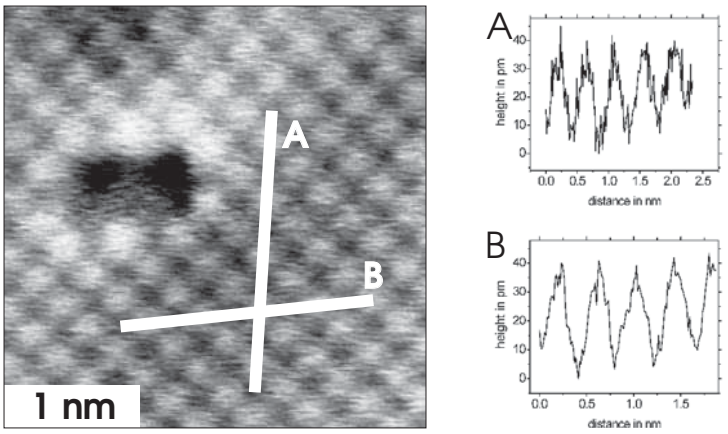

Figure 3.119: True atomic resolution of NiO (001), showing a small vacancy island. The image was acquired at room temperature with a sputtered and iron coated supersharp tip. The corrugation is ≈ 35 pm, with a peak-to-peak noise of about 10 pm along the scanlines and approximately 20 pm perpendicular to the scanlines. Parameters: $T = 293$ K, $f_0 = 161$ kHz, $\Delta f =$ -37.4 Hz, $U_{Bias} = 0$ V, $A = \pm 4$ nm, $c_z \approx 35$ N/m, $\gamma \approx$ -5.8 $\times 10^{-15}$ N$\sqrt{\mathrm{m}}$.

Summary

The results obtained on NiO(001) demonstrate the ability of the modified microscope to achieve true atomic resolution. We presented different types of defects that could be found on the (001) surface of the insulating NiO after cleavage. Vacancy islands with and without a bright contrast around them could be observed. Bias-dependent experiments indicate that the bright circumferential contrast might originate from trapped charges. Sometimes bright contrasts, which could not be identified as adsorbates and without a nearby visible surface defect, could be observed. Subsurface charges, which

might be trapped by a subsurface defect, could be responsible for such a contrast, because an insulator is not able to screen trapped charges.

References

[1] S. Morita, R. Wiesendanger, and E. Meyer (Eds.), Noncontact Atomic Force Microscopy, Springer-Verlag, Berlin, Heidelberg, (2002).

[2] T. R. Albrecht, P. Grütter, D. Horne, and D. Rugar, J. Appl. Phys. **69**, 668 (1991).

[3] M. Liebmann, A. Schwarz, S. Langkat, and R. Wiesendanger, Rev. Sci. Instrum. **73**, 3508 (2002).

[4] W. Allers, A. Schwarz, U.D. Schwarz, and R. Wiesendanger, Rev. Sci. Instrum. **69**, 221 (1998).

[5] M. R. Castell, P. L. Wincott, N. G. Condon, C. Muggelberg, G. Thornton, S. L. Dudarev, A. P. Sutton, and G.

[6] H. Hosoi, K. Sueoka, K. Hayakawa, and K. Musasa, Appl. Surf. Sci. **157**, 218 (2000).

[7] U. Dürig, Appl. Phys. Lett. **75**, 433 (1999).

[8] F. J. Giessibl, Appl. Phys. Lett. **78**, 123 (2001)

[9] J. E. Sader and S. P. Jarvis, Appl. Phys. Lett. **84**, 1801 (2004).

[10] H. Hölscher, S. M. Langkat, A. Schwarz, and R. Wiesendanger, Appl. Phys. Lett. **81**, 4428 (2002).

[11] S. M. Langkat, H. Hölscher, A. Schwarz, and R. Wiesendanger, Surf. Sci. **527**, 12 (2003).

[12] M. Ashino, A. Schwarz, T. Behnke, and R. Wiesendanger, Phys. Rev. Lett. **93**, 136101 (2004).

[13] S. M. Langkat, Dissertation, University of Hamburg, (2002).

[14] R. Hoffmann, M. A. Lantz, H. J. Hug, P. J. A. van Schendel, P. Kappenberger, S. Martin, A. Baratoff, and H. J. Güntherodt, Phys. Rev. B **67** 085402 (2003).

[15] W. Allers, S. Langkat, and R. Wiesendanger, Appl. Phys. A **72** [Suppl.], 27 (2001).

[16] N. Plock , Diploma Thesis, University of Hamburg, Hamburg (2004).

[17] J. Stöhr, A. Scholl, T. J. Regan, S. Anders, J. Lüning, M. R. Scheinfein, H. A. Padmore, and R. L. White, Phys. Rev. Lett. **83**, 1862 (1999).

[18] F. Hillebrecht, H. Ohldag, N. Weber, C. Bethke, and U. Mick, Phys. Rev. Lett. **86**, 3419 (2001).

[19] R. O. Furstenau, G. McDougall, and M. A. Langell, Surf. Sci. **50**, 55 (1985).

[20] Mateck, Im Langenbroich 20, Jülich, www.mateck.de.

[21] Nanosensors, Neuchatel, Switzerland, www.nanosensors.com.

[22] Israelachvili, Intermolecular & Surface Forces, Sec. Ed., Academic Press (1991).

3.4.2 Site specific spectroscopy on NiO(001) using 3D-FFS

S. M. Langkat, H. Hölscher, A. Schwarz, and R. Wiesendanger

Introduction

Force microscopy in the dynamic mode (DFM) using the frequency modulation (FM) technique can be used to examine surfaces with atomic resolution. However, simply scanning the surface does not provide information about the character of the relevant tip-sample forces. An insight into details of the tip-sample interaction is possible with *dynamic force spectroscopy* (DFS) [1,2]. By recording the frequency shift – which is the measured quantity in FM-based DFM – as a function of the resonance amplitude or the cantilever-sample distance, the tip-sample force can be determined by simple semi-analytical formulas. This enables the direct comparison of experiments with specific non-contact and contact force laws [4, 28]. Lantz et. al. [5] measured interactions at specific sites (adatoms and cornerholes) of the Si(111) 7×7 surface.

Here, we report about the measurement of the three-dimensional force field between an atomically sharp iron coated tip and the (001) surface of nickel oxide by applying a systematic recording procedure.

Two aspects of nickel oxide motivated this work. First, transition metal oxides like nickel oxide are well known for their catalytic properties [6]. Since it has been shown that at close tip-sample distances short-range interatomic interactions dominate the DFM contrast [7, 8], our presented experimental technique and data analysis allows us to map the *chemical* reactivity of this surface at the atomic scale. Second, nickel oxide is an antiferromagnetic insulator. Since we used a magnetic tip, which should be sensitive to spin-dependent exchange forces [9–12], we analyze our data with respect to this prediction.

Experimental setup

Measurements shown here were done with a standard doped single crystal silicon cantilever with an eigenfrequency of $f_0 = 195\,\mathrm{kHz}$ and a force constant of $c_z = 48\,\mathrm{Nm}^{-1}$ [13]. After insertion into the vacuum system the tip was first cleaned by argon ion sputtering to remove the silicon oxide layer. Then it was coated with an iron layer of 12.5 nm thickness by thermal evaporation.

The sample was the (001) surface of a nickel oxide single crystal [14]. Its rock salt structure is shown in Fig. 3.113. Both atomic species (Ni and O) are present at the (001) surface. The orientation of the crystal has been determined by low energy electron diffraction (LEED), i.e., the [100]- and [010]-directions are aligned parallel to the x- and y-scan axis, respectively. The top layer is relaxed by $\approx 2\%$ towards the bulk [6]. LEED experiments [15] and theoretical calculations [16] indicate a small rumpling of the surface, i.e., the nickel atoms are located slightly (0-5%) above the

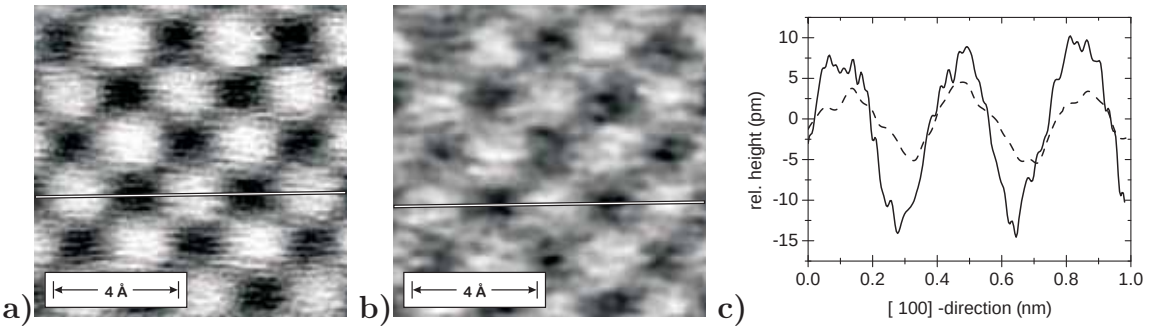

Figure 3.120: NC-AFM data of NiO(001) obtained with an iron-coated tip. Images (a) and (b) were obtained with the same frequency shift, but before (a) and after (b) recording of the spectroscopy field. (c) Two line sections along the [100]-direction as indicated by the line in image (a) and (b). The corrugation height is reduced from $\approx 20\,\mathrm{pm}$ (solid line) before the recording of spectroscopic data to $\approx 7.5\,\mathrm{pm}$ (dashed line) after these measurements. Parameters: $f_0 = 195$ kHz, $\Delta f = -32.2\,\mathrm{Hz}$, $A = 7.3\,\mathrm{nm}$, $c_\mathrm{z} = 48\,\mathrm{Nm}^{-1}$, $T = 14.9$ K.

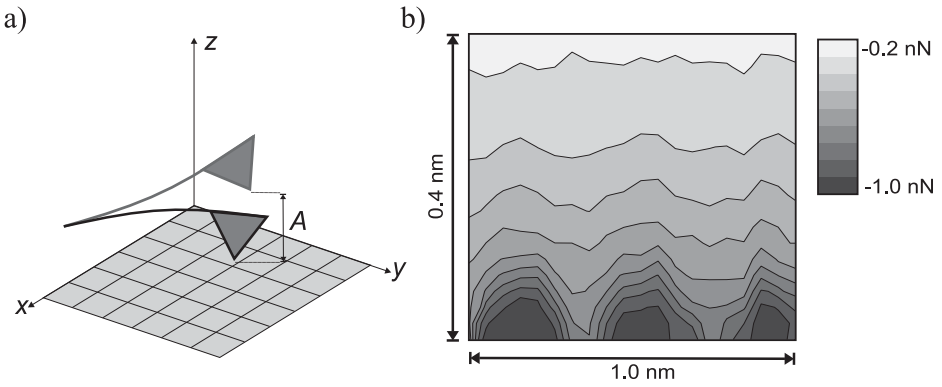

Figure 3.121: (a) Schematic representation of the force field spectroscopy method. The cantilever is oscillated with the amplitude A near the sample surface and scans a box in $x-$, $y-$, and $z-$direction. Parameters used for recording the spectroscopy field: $f_0 = 195$ kHz, stabilization frequency shift = -32.2 Hz, $A = 7.3\,\mathrm{nm}$, $c_\mathrm{z} = 48\,\mathrm{Nm}^{-1}$, $T = 14.9$ K, $32 \times 32 \times 256$ datapoints in $1\,\mathrm{nm} \times 1\,\mathrm{nm} \times 10\,\mathrm{nm}$. (b) Two-dimensional cut along the [100]-direction through the three-dimensional force field. The interaction force has been reconstructed from the $\Delta f(z)$-data and clearly shows atomic resolution close to the sample surface. Note that the scaling in vertical and horizontal direction is different and that the magnitude of the tip sample interaction force is encoded according to the grey scale.

oxygen atoms. Moreover, the nickel atoms exhibit an antiferromagnetic spin structure as indicated by arrows in Fig. 3.113.

The side faces of the cuboid shaped crystal were coated with a gold layer of about 100 nm thickness. These conducting sidewalls were connected to the sample holder. This procedure minimizes surface charging [17]. A clean (001) surface was prepared by cleavage in UHV just before insertion into the microscope. During all experiments cantilever and sample were kept at ground potential.

Spectroscopy of tip-sample force fields

To record a three-dimensional force field with atomic resolution on the lateral scale, we employed the following procedure. First, we adjusted the scanning parameters, particularly the constant frequency shift Δf, to obtain atomic resolution on NiO(001) (see Fig. 3.120(a)). Immediately after scanning this image, we captured two times $32 \times 32 \times 256$ frequency shift values in a box of 1 nm $\times$ 1 nm $\times$ 10 nm above the same scan area (see below for details). The time needed to record this data set was about 80 min. Directly after recording the spectroscopy field, a control image using the same scanning parameters in the constant frequency shift mode was acquired (see Fig. 3.120(b)).

The data acquisition technique for the spectroscopy field is schematically illustrated in Fig. 3.121(a). A grid of 32×32 equidistant points was defined at the scan area of 1 nm $\times$ 1 nm. Using a software routine, the procedure started in the lower left corner and continued line-by-line until the upper right corner was reached. At each grid position the cantilever was first stabilized at a frequency shift of $\Delta f = -32.2\,\mathrm{Hz}$, which had been set to obtain atomic resolution in Fig. 3.120(a). The corresponding absolute $z-$value was recorded in order to define an absolute z-scaling. (As common in digital electronics, the z-values of the $\Delta f(z)$-curves are stored as relative positions.) Then the cantilever was retracted by 9.80 nm from that point, before it was approached by 9.93 nm (trace) and retracted again (retrace). Consequently, the oscillating tip comes nominally 130 pm closer to the sample surface compared with the topography image in Fig. 3.120(a) [18]. On each way (trace and retrace) 256 frequency shift values were recorded. After that, the cantilever was stabilized again and moved to the next scan position, where the recording procedure was repeated. As a result, we obtain two $\Delta f(x, y, z)$-fields with $32 \times 32 \times 256$ frequency shift values. Each $\Delta f(x, y, z)$-field consists of 1024 individual $\Delta f(z)$-curves. Due to the piezo voltage creep, the first data point of all retrace curves is somewhat closer to the sample (about 100 pm) than the last data point of the trace curves.

Using the method introduced by Dürig [2] and our own software code [28] it is straightforward to determine the tip-sample interaction force F_{int} from the $\Delta f(z)$-curves, i.e., the $\Delta f(x, y, z)$-field can be transformed into a $F(x, y, z)$-field. Figure 3.121(b) displays a two-dimensional cut along one scan line of the complete three-dimensional force field $F(x, y, z)$ during retraction. This corresponds nearly to the crystallographic [100]-direction. Since the tip-sample distance is stabilized at the same frequency shift $\Delta f = -32.2\,\mathrm{Hz}$ at every image point, the minimum tip-sample distance between the tip and an imaginary flat plane parallel to the surface is different at every image point. Therefore, the z-scale of all curves within the line were adjusted with the recorded z-position during stabilization at each image point. The lateral distances between the maxima in the force map are identical to those in Fig. 3.120, i.e., atomic resolution has been obtained close to the sample surface. Note, that the corrugation amplitude for the smallest cantilever-sample distance is larger than in Fig. 3.120, because of the above mentioned smaller minimum tip-sample distance.

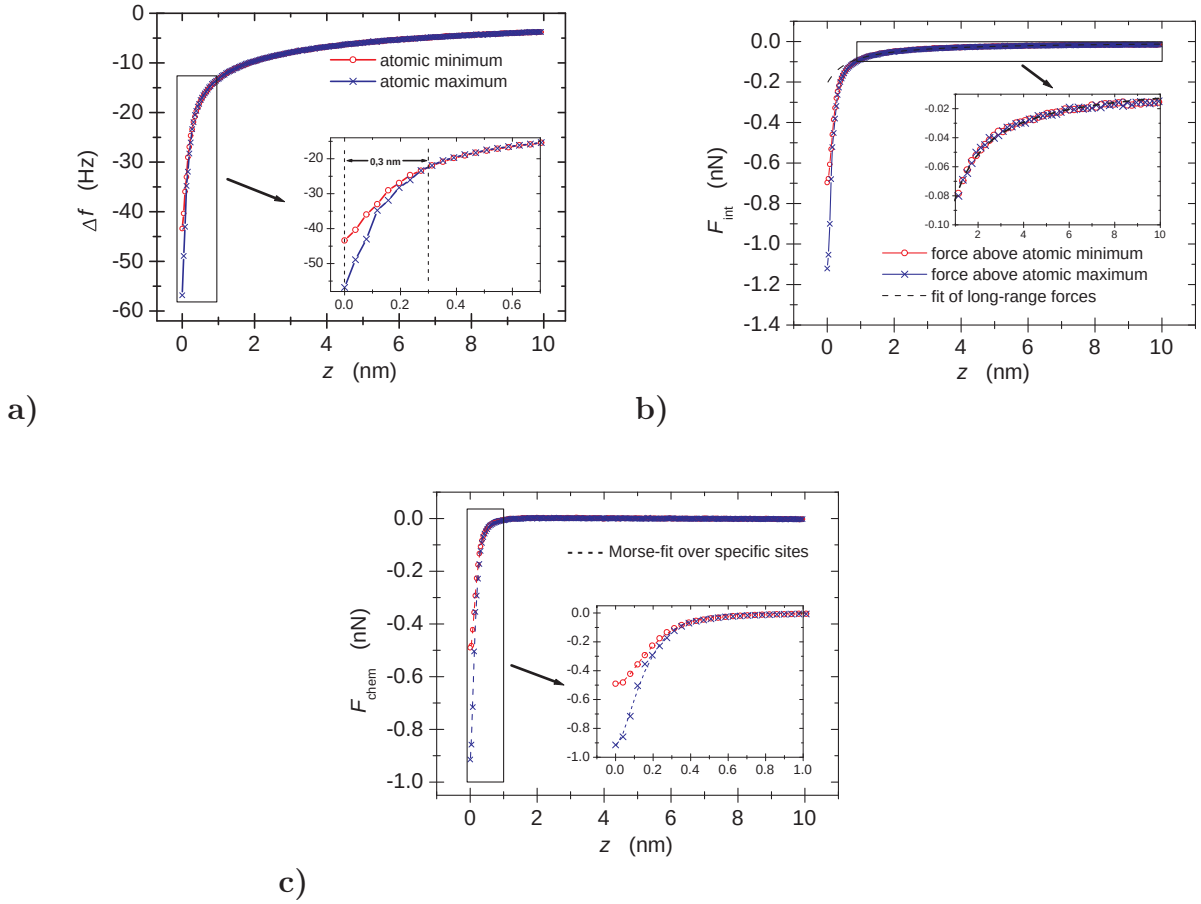

Figure 3.122: Procedure applied to two individual spectroscopy curves to obtain the short-range chemical interaction force (circles = atomic minimum, crosses = atomic maximum). (a) Measured frequency shift as a function of the cantilever sample distance. They differ only for small distances ($< 0.3\,$nm, see inset). (b) The corresponding tip-sample forces $F_{\rm int}$. The long-range forces ($> 1\,$nm) have been fitted to a z^{-1} inverse power law (dashed line). (c) After subtraction of the long-range forces the short-range forces are obtained and fitted with the force of a Morse potential (dashed lines).

The control images displayed in Fig. 3.120 can be used to analyze the amount of drift during the experiment. The lateral displacement between both images in Fig. 3.120 appears to be very small (approximately 0.1 nm). However, a detailed analysis of the spectroscopy field indicates that there was a lateral drift of about one lattice constant in [110]-direction during the entire experiment. This drift rate agrees well with other long term experiments done in the same cryostat system. It can be attributed to a slight temperature increase of ≈ 4 mK/h due to the slowly decreasing helium level in the bath cryostat.

A direct comparison of two scan lines along the [100]-direction before and after

recording the spectroscopy field in Fig. 3.120(c) demonstrates that the second image has a significantly lower corrugation amplitude of ≈ 7.5 pm compared to ≈ 20 pm of the first one. This might be caused by a change of the foremost tip structure. However, a detailed analysis of all $\Delta f(z)$-curves revealed no abrupt frequency shift offsets or any other feature that could indicate a change of the atomic structure at the tip apex between the first and the last frequency shift curve. Instead, we found a continuous drift rate of approximately -1.1 Hz/h by comparing the non-site dependent frequency shift values far away from the sample with each other. (Without any drift, they should have the same value for all 1024 curves.) For constant frequency shift images such a drift results in a larger tip-sample distance, i.e., smaller corrugation amplitudes. Comparing individual frequency shift curves above minima and maxima (cf., inset of Fig. 5a), a total frequency change of about 1.5 Hz around the set-point frequency shift of -32.5 Hz explains the reduced corrugation amplitude from 20 pm down to 7.5 pm quantitatively very well. We found, that the magnitude of the effect cannot be explained by the slight increase of the microscope temperature during the experiment. A quite probable cause is drift in the electronics used to operate the microscope. With respect to the following section, it is important to note that for the analysis of individual $\Delta f(z)$-curves (≈ 2.4 s for each direction) and sets recorded within one scan line (≈ 150 s/line) the amount of drift is negligible.

Analysis of individual spectroscopy curves

In the following we analyze 10 representative examples recorded during retraction from the complete set of spectroscopy curves. We selected 5 curves above 3 different atomic maxima and the other 5 above 2 different atomic minima. All the curves belong to two neighboring rows in the middle of the set, whereby drift effects can be neglected.

An analysis of tip-sample forces above neighboring atomic minima and maxima is shown in Fig. 3.122 for two specific frequency shift curves. Both curves are nearly undistinguishable for larger distances, but they differ within the last 0.3 nm next to the point of closest approach, which we arbitrarily define as the zero point of the z-axes.

Since we are mainly interested in the short-range forces (*chemical forces* F_{chem}), we applied the following procedure to each curve. First, we approximated all long-range forces F_{long} concerning van der Waals and electrostatic forces by a force law of the type

$$F_{\mathrm{long}}(z) = \frac{B}{z - z_{\mathrm{off,long}}}, \tag{3.33}$$

where B and $z_{\mathrm{off,long}}$ are fitting parameters. The constant value B has the unit of an energy. Since we arbitrarily defined the point of closest approach as zero point of the z-axis, the fitting parameter $z_{\mathrm{off,long}}$ is introduced, but does not have any physical significance. This well fitting analytic expression describes either the van der Waals force of a conical or pyramidal tip [19] or the electrostatic force of a spherical tip [20] in front of a flat surface. Both geometries and types of forces are plausible for the used

type of tip. A nonlinear least square fit was applied in the range $z = 1 \ldots 10\,\mathrm{nm}$ from the point of closest approach (see Fig. 3.122(b)). The starting point of 1 nm for the fit was chosen, because both the long-range and the following short-range fit (see next paragraph) match very well. The obtained mean parameters are $z_{\mathrm{off,long}} = -0.62\,\mathrm{nm}$ and $B = -0.85\,\mathrm{eV}$ with a standard deviation below $\pm\,3\,\%$ for both quantities. The value $z_{\mathrm{off,long}}$ can be identified as the negative tip-sample distance at the point of closest approach ($z = 0$) for the macroscopic tip.

For each curve we subtracted the long-range forces from the spectroscopy curves including the short-range regime $z = 0 \ldots 1$ nm. The resulting chemical forces $F_{\mathrm{chem}} = F_{\mathrm{int}} - F_{\mathrm{long}}$ are plotted in Fig. 3.122(c). Chemical forces can be quite often described by a Morse potential of the type

$$U_{\mathrm{chem}}(z) = U_0 \left[\exp\left(-2\frac{z - z_0}{\lambda}\right) - 2\exp\left(-\frac{z - z_0}{\lambda}\right)\right], \tag{3.34}$$

where U_0, λ, and z_0 are the binding energy, the decay length, and the equilibrium position, respectively [21]. We did not try to measure beyond the minimum (because this increases the probability of a tip crash), but include the repulsive part of the Morse potential in the fit. Note, that no additional parameters are introduced by taking the repulsive part into account and that although it has a stronger exponential dependence than the attractive part, it is non-zero before the minimum.

Due to our arbitrary zero point definition the z-scale in our experimental data have an a priori unknown offset $z_{\mathrm{off,chem}}$ compared to the zero point definition of Eq. 3.34. Therefore, we have to replace z_0 by $z_{\mathrm{fit}} = z_0 + z_{\mathrm{off,chem}}$. Fitting the corresponding short-range force $F_{\mathrm{chem}} = -(\partial\, U_{\mathrm{chem}}/\partial z)$ to the experimental data, we end up with the parameters of a Morse potential. The calculated mean parameters of all individually evaluated curves are $U_{0,\mathrm{min}} = 0.99$ eV, $\lambda_{\mathrm{min}} = 147$ pm, $z_{\mathrm{fit,min}} = -73$ pm over an atomic minimum and $U_{0,\mathrm{max}} = 1.37$ eV, $\lambda_{\mathrm{max}} = 116$ pm, $z_{\mathrm{fit,max}} = -49$ pm over an atomic maximum. The standard deviation of the values is $\approx \pm\,10\,\%$ for U_0, $\approx \pm\,5\,\%$ for λ and $\approx \pm\,35\,\%$ for z_{fit}. The differences in the binding energy and the decay length are evident, while the error bars of the z_{fit}-values overlap. Nevertheless, the difference in the z_{fit}-values of 24 pm is on the order of the measured corrugation amplitudes in Fig. 3.120.

It should be mentioned that systematic errors are presumably larger. The largest uncertainty is the force constant c_{z} of the cantilever ($\pm\,8\,\%$), which directly propagates into the calculated force. Probably smaller, but significant are errors in the estimation of the vibration amplitude A and the z-scale of the spectroscopy curve. These uncertainties propagate stronger than linear into the calculated force. Furthermore, the final values for U_0 and λ depend on the distance to which we spread the long-range fit. We also tried larger (up to 1.5 nm) and shorter (down to 0.5 nm) distances. Even though the fitted functions did not match so well, we calculated the U_0, λ and B values. They differ by up to $30\,\%$ for U_0 and λ, while the varitation of B is less than $10\,\%$. Recapitulating, we roughly estimate an error of $\pm\,30\,\%$ for both U_0 and λ and $\pm\,10\,\%$ for B.

The difference between $z_{\mathrm{off,long}}$ and $z_{\mathrm{off,chem}}$ originates from their definition as fit parameters. For the long-range fit, $z - z_{\mathrm{off,long}}$ is the distance between a flat surface and a smooth macroscopic tip shape, no matter how the real end of the tip looks like. On the other hand, $z_{\mathrm{off,chem}}$ is related to the distance beween the center of the foremost tip atom and the center of the surface atom directly below it.

Discussion

Since experimental parameters can only be determined with some error, the uncertainty of the true values for the relevant parameters of the used model potential are relatively large. However, previously such errors have not been given at all for site specific force spectroscopy experiments, because only single curves have been presented [5]. The relatively low statistical mean deviations of the fitting parameters indicate a good reproducibility of our experiment.

Another issue is the concept of using a simple interatomic pair potential. Since atomic resolution is obtained, we can infer that the tip is atomically sharp and that the relevant interaction is short-range. For the sake of simplicity, we assume that the interaction is determined only by the front atom at the tip apex and the atom directly below the tip and that no relaxation takes place. This might be a crude approximation, because simulations performed with specific tips, i.e., a tip with a predefined atomic configuration, suggest that several atoms can be involved in the tip-sample interaction and that tip atoms as well as surface atoms can exhibit a considerable amount of relaxation [22, 23]. If such detailed simulations would become avaiable for the NiO(001)/Fe system, our data might be used to test *ab-initio* calculations with the situation in a real experiment.

The appearance of the images in Fig. 3.120 is similar to previously presented atomically resolved NC-AFM data on NiO(001) [17, 31]. In particular, one type of atom is displayed as a maximum (stronger tip-sample interaction) and the other as a minimum (weaker tip-sample interaction). It is not straightforward to decide, which feature can be identified as nickel or oxygen.

Ciraci et al. [25] pointed out that AFM is sensitive to the total valence charge density for sufficiently small tip induced charge rearrangements. Since the total valence electron charge density at the surface has its maximum above the oxygen ions [26], it is likely that the protrusions represent the positions of the oxygen atoms. Moreover, it has been found that at NiO(001)/Fe interfaces a FeO-layer is formed [27], i.e., the chemical reactivity of iron with oxygen is presumably larger than that between iron and nickel. The value for the binding energy, which represents the strength of the short-range chemical interaction, calculated above the maxima is significantly larger than above the minima. This result indicates, that indeed oxygen is imaged as protrusion and the nickel sites are located in the minima. This interpretation is supported by calculations performed by Kantorovich et al. [23] for a quite similar metal/metal-oxide system. The simulated NC-AFM images for a magnesium terminated tip above MgO(001) revealed that the oxygen sites appear as maxima. Nonetheless, it has to

be mentioned that a contrast inversion, i.e., locations between the real positions of the surface atoms are imaged as protrusions as it has been observed by Hölscher et al. [29] on graphite(0001), cannot be fully ruled out. However, such a scenario is unlikely, because the nearest neighbor distances are larger in NiO(001) compared to graphite(0001).

Concerning the question whether spin-dependent exchange forces play a role in the tip-sample interaction, we compared the parameters of the Morse potential for neighboring minima as well as neighboring maxima sites in [100]-direction. A proof for the detection of exchange forces, i.e., systematic differences according to the alternating spins at the nickel sites, could not be verified. For the resolution of our set-up a detectable effect was predicted for tip-sample distances below 350 pm at the lower turn around point [12]. For the combination Fe/Ni an equilibrium distance of $z_0 \approx 240\,\mathrm{pm}$ has been reported [30]. Using this value for z_0 in Eq. 3.34 the real tip-sample distance at the point of closest approach can be estimated to be $-z_{\mathrm{off,chem}} = z_0 - z_{\mathrm{fit}} \approx 300\,\mathrm{pm}$, which is below the predicted detection limit. However, this estimation and the model used in Ref. [12] might be too simple. Another possible explanation for the non-observation of magnetic exchange forces could also be an unfavorable alignment of the spin of the foremost tip atom with respect to the nickel spins at the surface.

References

[1] H. Hölscher, W. Allers, U. D. Schwarz, A.Schwarz, and R. Wiesendanger, Phys. Rev. Lett. **83**, 4780 (1999).

[2] U. Dürig, Appl. Phys. Lett. **75**, 433 (1999).

[3] H. Hölscher, S. M. Langkat, A. Schwarz, and R. Wiesendanger, Appl. Phys. Lett. **81**, 4428 (2002).

[4] B. Gotsmann and H. Fuchs, Phys. Rev. Lett. **86** (2001) 2597.

[5] M. A. Lantz, H. J. Hug, R. Hoffmann, P. J. A. van Schendel, P. Kappenberger, S. Martin, A. Baratoff, A. Abdurixit, H.-J. Güntherodt, Science **291** 2580, (2001).

[6] V. E. Henrich, P. A. Cox, The surface science of metal oxides, Cambridge University Press (1994).

[7] R. Perez, M. C. Payne, I. Stich, K. Terakura, Phys. Rev. Lett. **78**, 678 (1997).

[8] L. N. Kantorovich, A. S. Foster , A. L. Shluger, A. M. Stoneham, Surf. Sci. **445**, 283 (2000).

[9] R. Wiesendanger, D. Bürgler, G. Tarrach, A. Wadas, D. Brodbeck, H.-J. Güntherodt, G. Güntherodt, R. J. Gambino, R. Ruf, J. Vac. Sci. Technol. B **9**, 519 (1991).

[10] K. Mukasa, H. Hasegawa, Y. Tazuke, K. Sueoka, M. Sasaki, K. Hayakawa, Jpn. J. Appl. Phys. **33**, 2692 (1994).

[11] H. Ness, F. Gautier, Phys. Rev. B **52**, 7352 (1995).

[12] A. S. Foster, and A. L. Shluger, Surf. Sci. **490** 211 (2001).

[13] Nanosensors, Neuchatel, Switzerland, www.nanosensors.com.

[14] Mateck GmbH, Germany.

[15] M. Prutton, J. A. Walker, M. R. Welton-Cook, R. C. Felton, Surf. Sci. **89**, 95 (1979).

[16] P. W. Tasker, D. M. Duffy, Surf. Sci. **137**, 91 (1984).

[17] H. Hosoi, K. Sueoka, K. Hayakawa, and K. Musasa, Appl. Surf. Sci. **157**, 218 (2000).

[18] Due to the piezo creep, the first data point of the retrace curve might be somewhat closer (some tens pm) to the sample than the last data point of the trace curve.

[19] F. J. Giessibl, Phys. Rev. B **56**, 16010 (1997).

[20] L. Olsson, N. Lin, V. Yakimov, R. Erlandsson, J. Appl. Phys. **84**, 4060 (1998).

[21] M. Guggisberg, M. Bammerlin, Ch. Loppacher, O. Pfeiffer, A. Abdurixit, V. Barwich, R. Bennewitz, A. Baratoff, E. Meyer, H.-J. Güntherodt, Phys. Rev. B **61**, 11151 (2000).

[22] S. H. Ke, T. Uda, R. Perez, I. Stich, and K. Terakura, Phys. Rev. B 60, 11631 (1999).

[23] L. N. Kantorovich, A. L. Shluger, A. M. Stoneham, Phys. Rev. B **62**, 184111 (2001).

[24] W. Allers, A. Schwarz, U.D. Schwarz, and R. Wiesendanger, Rev. Sci. Instrum. **69**, 221 (1998).

[25] S. Ciraci, A. Baratoff, I. P. Batra, Phys. Rev. B **41**, 2763 (1990).

[26] M. R. Castell, S. L. Dudarev, G. A. D. Briggs, A.. P. Sutton, Phys. Rev. B **59**, 7342 (1999).

[27] T. J. Regan, H. Ohldag, C. Stamm, F. Nolting, J. Lüning, J. Stöhr, R. L. White, Phys. Rev. B **64**, 214422 (2001).

[28] H. Hölscher, A. Schwarz, W. Allers, U. D.Schwarz, and R. Wiesendanger, Phys. Rev. B **61**, 12678 (2000).

[29] H. Hölscher, W. Allers, U. D. Schwarz, A. Schwarz, R. Wiesendanger, Phys. Rev. B **62**, 6967 (2000).

[30] H. P. Cheng, D. E. Ellis, Phys. Rev. B **39**, 12469 (1989).

[31] W. Allers, S. Langkat, and R. Wiesendanger, Appl. Phys. A **72** [Suppl.], 27 (2001).

3.5 Molecular systems

3.5.1 Single-wall carbon nanotubes

T. Maltezopoulos, A. Kubetzka, M. Morgenstern, and R. Wiesendanger

Single-wall carbon nanotubes (SWCNTs) are considered promising candidates for molecular electronics [1]. It is therefore highly desirable to understand their electronic properties in detail. In particular, the effect of defects on transport properties must be understood and is currently under debate. Early experiments generally assumed ballistic transport in SWCNTs. Indeed, the mean free path in individual as well as in ropes of metallic SWCNTs appeared to be restricted by the contacts [2–4]. Later experiments, however, found evidence for defects in semiconducting SWCNTs by using an AFM-tip to locally change the transport properties of the tube [5]. Theory work explained both results by stating that all defects larger than the lattice constant do not lead to backscattering within metallic tubes, whereas backscattering is present in semiconducting tubes [6, 7]. More recently, low-temperature transport measurements using individual metallic SWCNTs have been interpreted in terms of disorder-induced quantum dots [8, 9]. According to theory a corresponding backscattering could originate from certain arrangements of vacancies [10]. Here, we also found disorder-induced quantum dots in SWCNTs, which are directly probed by low-temperature scanning tunneling spectroscopy (STS).
In order to permit STM and STS on SWCNTs we sonicate the raw SWCNT material in dichloroethane and deposit a droplet of the solution on a freshly evaporated Au/mica surface. This is a common technique for preparing SWCNTs on Au [11]. After checking the surface contamination with atomic force microscopy, the sample was transfered into the STM.

Although the sample preparation is done in air, very reproducible STM images revealing atomic resolution are obtained. The inset of Fig. 3.123 shows an example. Using a technique described in [12] we relate this SWCNT to a (15,6)-type with a chiral angle of 13.9°. According to (n-m)/3=(15-6)/3=3=integer such a tube is metallic.
Metallic SWCNTs can be identified additionally either by their finite dI/dV-magnitude close to E_F or by their relatively large separations between subbands of about 2 V [11]. A spectrum of such a nanotube is shown in Fig. 3.123. As in reference [11] the subband features are not symmetric around 0 V, which has been attributed to a charge transfer from the tube to the Au substrate. Au has a higher workfunction (5.3 eV) than graphite (4.5 eV), suggesting a hole-doping of the SWCNTs.

Surprisingly, there are features close to E_F. Besides a dip at E_F a number of nearly equidistant peaks is found as shown more clearly in Fig. 3.124(b) and (c). The features look like a damped oscillation starting at E_F with a period of about 87 meV in Fig. 3.124(c). At another position of the tube the energy difference between the peaks is different, for example about 38 meV as shown in Fig. 3.124(b). This change in peri-

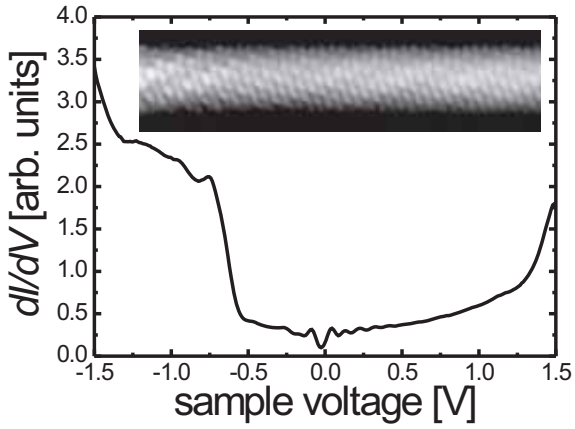

Figure 3.123: dI/dV spectrum of a metallic SWCNT. Subband features as well as oscillations near the Fermi energy are visible. These oscillations are shown in more detail in Fig. 3.124(c) (V_{stab} =1.5 V, I_{stab} =300 pA). Inset: atomically resolved STM-image of a SWCNT (I=1 nA, V_{sample}=-50 mV, 2.3 nm x 9 nm).

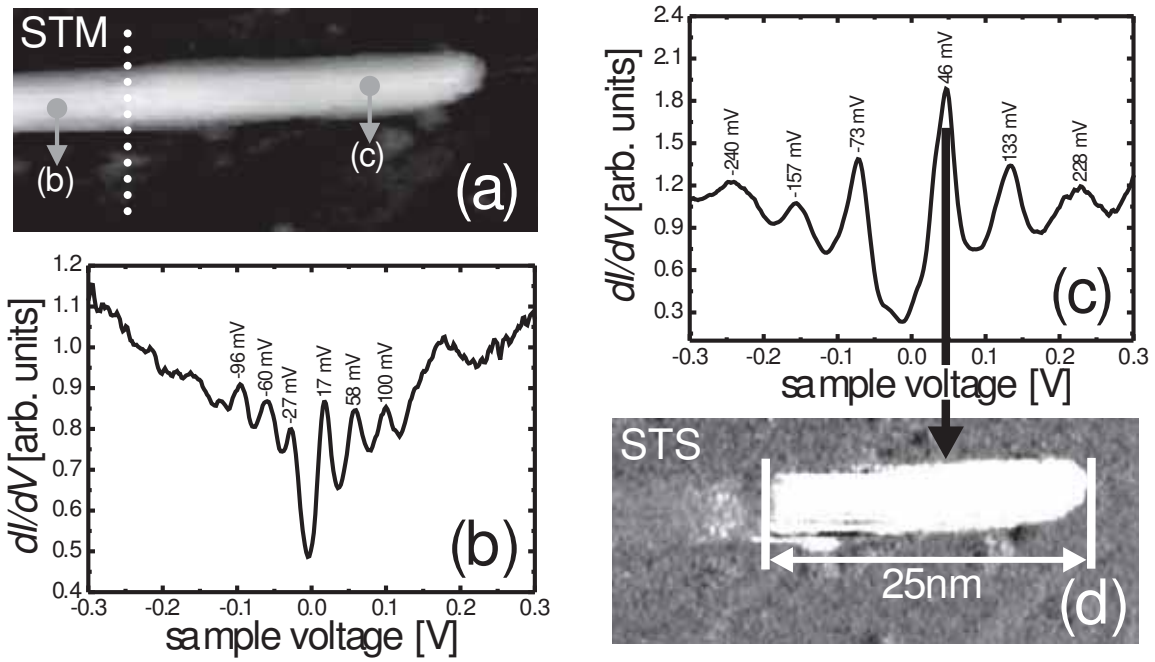

Figure 3.124: (a) STM image of a SWCNT end (I=300 pA, V_{sample}=46 mV, 45 nm x 19 nm). (b) STS-data on the left-hand side of the dotted line in (a). (c) STS-data on the right-hand side of the dotted line in (a) (zoom of the STS-data shown in Fig. 3.123 into the region close to E_{F}). All STS-data in (b) and (c) are taken with V_{stab}=-300 mV, I_{stab}=300 pA and V_{mod}=3 mV. (d) Simultaneously recorded spatially resolved STS image, V_{stab}=46 mV (first peak in Fig. 3.124(c)), I_{stab}=300 pA and V_{mod}=10 mV.

odicity appears quite abruptly at the dotted line in Fig. 3.124(a). To demonstrate this, the spatially resolved dI/dV-signal at the energy of the 46 mV-peak of Fig. 3.124(c) is shown in Fig. 3.124(d). It clearly reveals that the 46 mV-peak is restricted to an area of 25 nm right to the dotted line. The same restriction has been found for the other prominent peaks in Fig. 3.124(c).

Peaks in the LDOS restricted to a certain area are strong indications for confined states. Confined states have previously been found by STS after shortening individual SWCNTs [13, 14]. However they have never been reported on extended tubes with lengths of about 2000 nm as in the present case. In order to verify that the peaks are indeed confined states, we calculate whether the peak separation ΔE is consistent with the size of the confined regions. Therefore we use the approximate formula $\Delta E = hv_{\mathrm{F}}/2L$ with $v_{\mathrm{F}} = 8 * 10^5$ m/sec being the Fermi velocity. For ΔE_1=87 meV and ΔE_2=38 meV we get L_1=19 nm and L_2=44 nm, respectively. L_1 fits approximately with the measured 25 nm restriction length of the 46 mV-peak. Thus, we assign the observed peaks close to E_{F} to confined states within the SWCNT.

Confinement in an extended tube obviously requires scattering. We could not identify the type of scatterer. However, we can rule out a significant bending of the nanotube at the end of the confined region from STM images. Also there is no step edge in the metallic substrate below the tube at this position. Moreover, we can rule out a large contaminant since we observe only a small elevation of 0.7 Å at the scattering point in linescans of STM images. Thus the data suggest that the scatterers are either intrinsic or single adsorbates below, within or above the tube.

Regardless of their exact nature, our data directly show that localized scatterers can lead to significant backscattering. This backscattering has a strong influence on the transport properties of the tube: It modifies the local density of states near the Fermi level and decreases the transmittance of individual modes. The effect of two partly-transmitting barriers on the transport properties of SWCNTs has been measured by Liang et al. [15], and was described in terms of Fabry-Perot-like electron modes in the nanotube. Pursuing this analogy, the energy- and position-dependent LDOS measurements reported here amount to spatial maps of these Fabry-Perot modes, with defect sites playing the role of reflecting barriers. A similarly pronounced modulation of the transmittance can be expected.

This transmission is, of course, related to the LDOS at E_{F}. Since we do not find peaks at E_{F}, the remaining dI/dV-magnitude appears to be related to the widths of the surrounding peaks. These widths are much larger than the estimated energy resolution of the experiment $\delta E = \sqrt{(3.3 \cdot kT)^2 + (2.5 \cdot V_{\mathrm{mod}})^2} = 8.5$ meV. For example, the full width at half maximum of the 46 meV-peak is 47 meV. The width increases with increasing distance from E_{F} suggesting lifetime effects guided by electron-electron interaction. A simple broadening by the escape of the electrons towards the Au substrate would usually not be symmetric around E_{F}. Electron-phonon interaction in SWCNTs is known to be weak [16]. So only electron-electron interaction remains as a possible cause. The same magnitude and energy-dependence of the peak widths is

also observed for shortened SWCNTs [17]. A similar lifetime broadening in SWCNTs can also be deduced from the phase coherence of scattered electron waves observed by STM [18]. In contrast, time-resolved photoemission data of SWCNT bucky papers revealed an electron lifetime close to E_F which corresponds to a broadening of only 4 meV [19]. Since the SWCNTs used in all STM measurements are directly deposited on a Au substrate, which is not the case within the bucky papers used for photoemission, it might be that lifetime effects in SWCNTs depend significantly on the substrate.

In summary, we find quantized states within extended individual metallic SWCNTs confined by defects. They appear as peaks in the dI/dV-curves close to E_F which are restricted to certain areas. Our work, thus, shows that defects can lead to significant backscattering within individual metallic SWCNTs resulting in confined states. Moreover, we found an increase of the peak-widths with increasing voltage.

References

[1] C. Dekker: *Carbon nanotubes as molecular quantum wires.* Physics Today **52**, 22 (1999).

[2] S. J. Tans, M. H. Devoret, H. Dai, A. Thess, R. E. Smalley, L. J. Geerligs, C. Dekker: *Individual single-wall carbon nanotubes as quantum wires.* Nature **386**, 474 (1997).

[3] M. Bockrath, D. H. Cobden, P. L. McEuen, N. G. Chopra, A. Zettl, A. Thess, R. E. Smalley: *Single-electron transport in ropes of carbon nanotubes.* Science **275**, 1922 (1997).

[4] M. Bockrath, D. H. Cobden, J. Lu, A. G. Rinzler, R. E. Smalley, L. Balents, P. L. McEuen: *Luttinger-liquid behaviour in carbon nanotubes.* Nature **397**, 598 (1999).

[5] S. J. Tans, C. Dekker: *Potential modulations along carbon nanotubes.* Nature **404**, 834 (2000).

[6] T. Ando, T. Nakanishi, R. Saito: *Berry's phase and absence of back scattering in carbon nanotubes.* J. Phys. Soc. Japan **67**, 2857 (1998).

[7] P. L. McEuen, M. Bockrath, D. H. Cobden, Y. G. Yoon, S. G. Louie: *Disorder, pseudospins, and backscattering in carbon nanotubes.* Phys. Rev. Lett. **83**, 5098 (1999).

[8] M. Bockrath, W. Liang, D. Bozovic, J. H. Hafner, C. M. Lieber, M. Tinkham, H. Park: *Resonant electron scattering by defects in single-walled carbon nanotubes.* Science **291**, 283 (2001).

[9] M. T. Woodside, P. L. McEuen: *Scanned probe imaging of single-electron charge states in nanotube quantum dots.* Science **296**, 1098 (2002).

[10] T. Ando: *Theory of transport in carbon nanotubes.* Semicond. Sci. Technol. **15**, R13 (2000).

[11] J. W. G. Wildöer, L. C. Venema, C. Dekker, A. G. Rinzler, R. E. Smalley: *Electronic structure of atomically resolved carbon nanotubes.* Nature **391**, 59 (1998).

[12] L. C. Venema, V. Meunier, P. Lambin, C. Dekker: *Atomic structure of carbon nanotubes from scanning tunneling microscopy.* Phys. Rev. B **61**, 2991 (2000).

[13] L. C. Venema, J. W. G. Wildöer, J. W. Janssen, S. J. Tans, H. L. J. T. Tuinstra, L. P. Kouwenhoven, C. Dekker: *Imaging electron wave functions of quantized energy levels in carbon nanotubes.* Science **283**, 52 (1999).

[14] S. G. Lemay, J. W. Janssen, M. v. d. Hout, M. Mooij, M. J. Bronikowski, P. A. Willis, R. E. Smalley, L. P. Kouwenhoven, C. Dekker: *Two-dimensional imaging of electronic wavefunctions in carbon nanotubes.* Nature **412**, 617 (2001).

[15] W. Liang, M. Bockrath, D. Bozovic, J. H. Hafner, M. Tinkham, H. Park: *Fabry-Perot interference in a nanotube electron waveguide.* Nature **411**, 665 (2001).

[16] T. Hertel, R. Fasel, G. Moos: *Charge-carrier dynamics in single-wall carbon nanotube bundles: A time-domain study.* Appl. Phys. A **75**, 449 (2002).

[17] S. G. Lemay: (unpublished) .

[18] M. Ouyang, J. L. Huang, C. M. Lieber: *One-dimensional energy dispersion of single-walled carbon nanotubes by resonant electron scattering.* Phys. Rev. Lett. **88**, 066804 (2002).

[19] T. Hertel, G. Moos: *Influence of excited electron lifetimes on the electronic structure of carbon nanotubes.* Chem. Phys. Lett. **320**, 359 (2000).

3.5.2 Comparison of the atomic scale contrast on SWNT and HOPG obtained with DFM

M. Ashino, A. Schwarz, H. Hölscher, W. Allers, U. D. Schwarz, and R. Wiesendanger

Introduction

A single-walled carbon nanotube (SWNT) consists of a "single" graphene sheet rolled up into a long (up to several hundred micrometer) hollow cylinder with nanometer-scale diameter. Within the graphene sheet, carbon atoms are located at the corners of hexagonal aromatic rings, whose centers are the trigonally arranged hollow sites of the honeycomb structure. The SWNTs tend to form close-packed bundles due to the non-bonding van der Waals interaction [1]. They are not only promising materials for potential applications in developing, for example, nano-electro-mechanical devices because of their unusual mechanical and unique electronic properties, but also model systems to study nanometer-scale molecular systems including biological macromolecules. We report for the first time the achievement of "true" atomic-resolution imaging on curved (cylindrical) surfaces of single-walled carbon nanotubes (SWNTs) using dynamic force microscopy (DFM) and compare these results with previous atomically resolved data obtained on highly oriented graphite (HOPG).

Experimental setup and sample preparation

The experiments were performed with our home-built UHV low-temperature force microscope optimized for atomic-scale studies [2]. Background pressure and temperature were $p < 1 \times 10^{-8}$ Pa and $T = 11$ K, respectively. All results presented here were acquired using silicon cantilevers, which were in situ cleaned by argon ion sputtering. To cancel the electrostatic forces, the average contact potential difference was compensated by applying an appropriate bias voltage $U_{\text{bias}} = -0.31$ V to the cantilever (sample was grounded). The SWNTs with a typical diameter of $d = 1.38$ nm, synthesized as described in Ref. [3], were deposited from a 1,2-dichloroethane dispersion on an air-cleaved graphite surface under ambient conditions. After transfer into the vacuum, the sample was heated at 300°C for 1.5 hours to remove contaminations. The pure HOPG sample was cleaved in situ prior to the measurements.

Atomic scale contrast on SWNT

Under those experimental conditions, atomic resolution has been successfully obtained on the surfaces of individual SWNTs, as shown in a 3D view of Fig. 3.1. On the graphite substrate, the imaged SWNT was found to be in a bundle, which runs parallel to the y-direction in Fig. 3.1. The 3D view actually represents a curved surface corresponding to the individual SWNT, whose diameter would be around 1.38 nm [3]. Figure 3.125

also shows that the atomic-scale contrast is strong in an approximately 0.6 nm-wide region, which corresponds to the top of an individual SWNT. However, the contrast becomes blurry towards the sloping sides as shown in Fig. 3.125. Generally, the atomic-scale contrast can be realized by the short-range forces acting between the foremost tip atom and the sample atom directly below [4]. In the case of imaging the cylindrical surfaces, more atoms can be involved in the short-range forces because of geometrical configurations between the tip apex and the cylindrically sloping sides. Since the image was obtained under feedback control to maintain a constant Δf, which is closely related to the interaction forces, the multiple interatomic forces may let the tip apex away from the close proximity and thereby reduce the atomic-scale contrast.

A close-up image (top view) obtained around the center of Fig. 3.125 is shown in Fig. 3.126(A). Figure 3.126(A) shows that the topographic maxima have six nearest neighbors separated by about 250-pm parallel and 280-pm perpendicular to the tube axis. It should be noted that the lattice constant of carbon nanotubes is 249 pm [1]. Those elongations of separations perpendicular to the tube axis can be geometrically explained by assuming a point-like tip scanning across a curved surface [5]. By taking this into account and from the observed symmetry and the undistorted separation along the tube axis, we infer that the hollow sites of the hexagonal carbon lattice are imaged as topographic maxima.

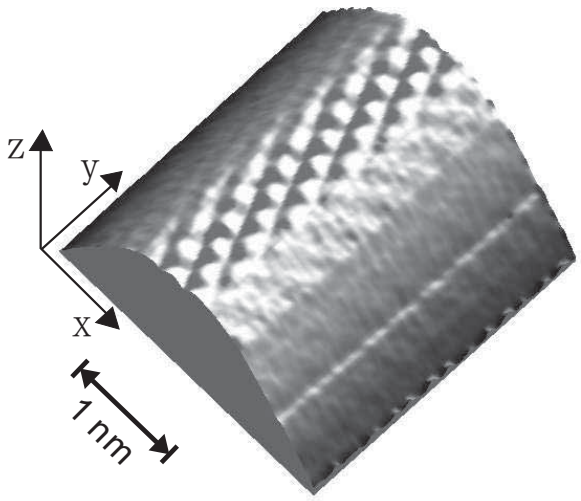

Figure 3.125: A three-dimensional view of a dynamic force microscopy image acquired under constant frequency shift feedback control in the non-contact regime above an individual single-walled carbon nanotube. The atomically-resolved features are clearly observed around the elevated topmost area and are still slightly observed on the sloping sides. The maximum corrugation amplitude is ~ 40 pm. Image parameters: eigenfrequency f_0=159 kHz, frequency shift $\Delta f = -65.3$ Hz, oscillation amplitude $A = 2.4$ nm, spring constant $c_z = 34.3$ N/m, image size 3 nm $\times$ 3 nm.

Comparison with planar graphite

It is interesting to compare the atomic scale contrast on SWNT with those observed in previous experiments on graphite [6]. Both substances consist of the same basic structural unit, i.e., hexagonally arranged carbon rings. However, graphite is planar, while a SWNT is cylindrical. Furthermore, the ABA-stacking of graphene sheets in graphite result in two inequivalent carbon sites, i.e., A- (with carbon atom in the neighboring layer) and B-type (without carbon atom in the neighboring layer) carbon atoms.

It should be noted that the AB stacking of graphene layers results in two inequivalent carbon lattice sites on graphite(0001). The computer simulation reproduced the observed distinguishable features on graphite(0001) (see inset in Fig. 3.126(B)). Obviously, those features can be ruled out for the SWNT, which consists of a single atomic layer. Thereby, the assignment of the maxima to the hollow sites is unambiguous. Furthermore, as shown in the simulation image (bottom left in Fig. 3.126(A)), we expect that the equivalent carbon lattices of the SWNT are imaged as the indistinguishable minima representing hexagonal rings in Fig. 3.126(A).

The maximum tip-sample interaction is observed on graphite as well as on SWNT above the hollow sites and not above the carbon atoms. While on graphite the contrast is different on neighboring carbon atoms, it is indistinguishable on SWNT. Both experimental observations can be explained using a simple Lennard-Jones potential to simulate the data. Figure 3.126 displays the experimental results as well as the calculated image (insets) and profiles along the $[1\bar{1}00]$-direction. The line sections taken in the three equivalent directions on graphite(0001) shown in Fig. 3.126(B) exhibit large maxima and a shallow and a deep minimum separated by a small maximum. On the other hand, the three different profiles across the SWNT in Fig. 3.126(A) show two symmetric contrasts at the carbon sites between the maxima, which represent the hollow sites. However, only in two profiles the carbon positions appear as equally deep minima.

As explained in Ref. [6], the origin of the inverted contrast, i.e., that the carbon atoms appear as minima, is the small intercarbon distance. According to the model, the tip-sample interaction above the hollow site with the six surrounding carbon atom sites is larger than the tip-sample interaction above a carbon atom with its three nearest neighbors. In the simulation for graphite, distinguishable carbon atoms were assumed, as expected for an ABA-stacking of graphene sheets. For the calculation of the SWNT, all carbon atoms were treated indistinguishable as expected for a single graphene sheet. Simulation and the experimental results are in good qualitative agreement with respect to the presence and absence of the carbon site asymmetry on graphite and SWNT, respectively [7]. The different appearance of the experimental profiles along and across the cylindrical axis of the SWNT could be related to the curved surface that was not taken into account for the simulation.

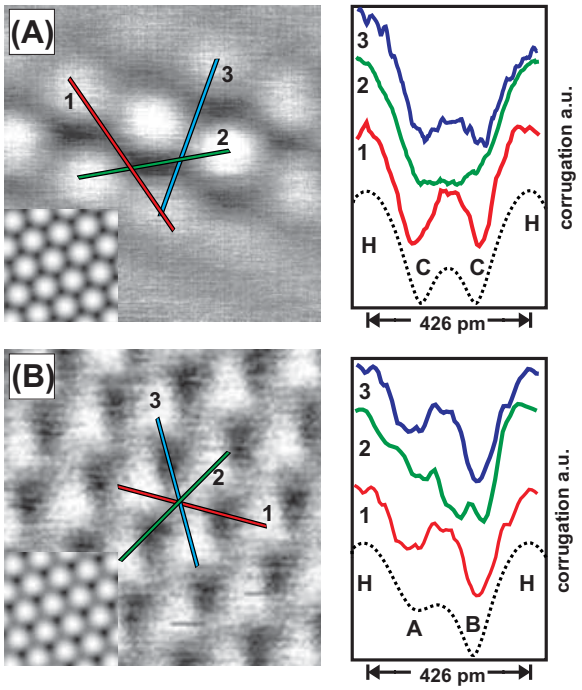

Figure 3.126: Atomic resolution on a SWNT (A) and on graphite (B), obtained in the non-contact regime. The small insets show the simulation images based on a Lennard-Jones potential between a point-like tip and a single planar graphene layer without (A) and with (B) carbon site asymmetry. The line sections displayed on the right sides are taken between second nearest neighbour maxima as indicated by the numbers in the images. The three directions are not equivalent for the cylindrical SWNT, but equivalent for the planar graphite. The dotted lines are taken along the $[1\bar{1}00]$-direction between two H-sites from the simulation. By comparison with the simulations, the experimentally observed atomic-scale features can be related to the SWNT structure as well as to graphite, repectively. Image parameters: (A) $f_0 = 159$ kHz, $\Delta f = -69.6$ Hz, $c_z = 34$ N/m, $A = 2.3$ nm; (B) $f_0 = 160$ kHz, $\Delta f = -63$ Hz, $c_z = 35$ N/m, $A = 8.8$ nm.

Summary

For the first time it could be demonstrated on the cylindrical surface of a SWNT that force microscopy can be used to image a non-planar surface with true atomic resolution. As for the planar graphite, the hollow sites are imaged as maxima. However, since an SWNT consists of a single rolled up graphene layer, i.e., does not exhibit A- and B-type carbon atoms, the contrast does not show a carbon site asymmetry. Using a simple Lennard-Jones potential to model the tip-sample interactions, the experimentally observed atomic scale features observed on graphite and SWNTs could be well reproduced. That the attractive short-range van der Waals interaction is indeed responsible for the atomic scale contrast will be verified in the next section (3.5.3).

References

[1] R. Saito, G. Dresselhaus, and M. S. Dresselhaus, *Physical Properties of Carbon Nanotubes*, Imperial College Press, London, (1998).

[2] W. Allers, A. Schwarz, U.D. Schwarz, and R. Wiesendanger, Rev. Sci. Instrum. **69**, 221 (1998).

[3] A. Thess, *et al.*, Science **273**, 483 (1996).

[4] S. Morita, R. Wiesendanger, and E. Meyer (Eds.), Noncontact Atomic Force Microscopy, Springer-Verlag, Berlin, Heidelberg, (2002).

[5] V. Meunier and P. Lambin, Phys. Rev. Lett. **81**, 5588 (1998).

[6] H. Hölscher, W. Allers, U. D. Schwarz, A. Schwarz, and R. Wiesendanger, Phys. Rev. B **62**, 6967 (2000).

[7] M. Ashino, A. Schwarz, H. Hölscher, U. D. Schwarz, and R. Wiesendanger, submitted to Nanotechnology.

[8] B. Gotsmann and H. Fuchs, Phys. Rev. Lett. **86** (2001) 2597.

[9] M. Guggisberg, M. Bammerlin, Ch. Loppacher, O. Pfeiffer, A. Abdurixit, V. Barwich, R. Bennewitz, A. Baratoff, E. Meyer, H.-J. Güntherodt, Phys. Rev. B **61**, 11151 (2000).

[10] H. Hölscher, W. Allers, U. D. Schwarz, A.Schwarz, and R. Wiesendanger, Phys. Rev. Lett. **83**, 4780 (1999).

[11] F. J. Giessibl, Phys. Rev. B **56**, 16010 (1997).

[12] U. Dürig, Appl. Phys. Lett. **76**, 1203 (2001).

[13] M. A. Lantz, H. J. Hug, R. Hoffmann, P. J. A. van Schendel, P. Kappenberger, S. Martin, A. Baratoff, A. Abdurixit, H.-J. Güntherodt, Science **291** 2580, (2001).

[14] H. Hölscher, S. M. Langkat, A. Schwarz, and R. Wiesendanger, Appl. Phys. Lett. **81**, 4428 (2002).

[15] S. M. Langkat, H. Hölscher, A. Schwarz, and R. Wiesendanger, Surf. Sci. **527**, 12 (2003).

[16] R. Pérez *et al.*, Phys. Rev. B **58**, 10835 (1998).

[17] W. Allers, A. Schwarz, U. D. Schwarz, and R. Wiesendanger, Europhys. Lett. **48**, 276 (1999).

[18] H. Ulbricht, G. Moos, and T. Hertel, Phys. Rev. B **66**, 075404 (2002).

3.5.3 3D-FFS on SWNT with atomic resolution

M. Ashino, T. Behnke, H. Hölscher, A. Schwarz, and R. Wiesendanger

Introduction

The distance dependence of the tip-sample interaction forces $F(z)$ can be determined in dynamic force spectroscopy (DFS) by recording either $\Delta f(z)$- [1–3] or $\Delta f(A)$- [4] curves at a given xy-position and converting them into force data [1, 5, 6]. Recently, DFS was performed on specific atomic lattice sites [7]. Using three-dimensional force field spectroscopy (3D-FFS), $F(x, y, z)$ data were obtained at every image point [8]. Thereby, it has become possible to assign individual curves unambiguously to specific atomic lattice sites as described in section 3.4.2 [9].

Site-specific DFS revealed that the short-range chemical bonding forces between the foremost tip atom and the surface atom underneath are on the order of 1 nN in good agreement with theoretical predictions [10]. In contrast, the interatomic van der Waals (vdW) forces are much weaker. For the atomically-resolved images obtained on the vdW surfaces of graphite(0001) [3] and Xe(111) [11], computer simulations suggested that the short-range vdW forces are relevant. However, experimental site-specific DFS data to support this claim has not been available for these surfaces up to now.

Experimental procedure

Experimental set-up as well as tip and sample preparation has been already described in section 3.5.2. In order to determine the force versus distance relationships $F(z)$ above the specific atomic-lattice sites, we captured a full 3D force field (3D-FFS) similar as in section 3.4.2. After recording an atomically resolved topographic image (Fig. 3.127(A)), $20 \times 20 \times 512$ data points are acquired in a box of 1nm $\times$ 1 nm $\times$ 3 nm in the same area. As in the case of Ref. [8] and [9], the tip was first stabilized at the same Δf, and then approached by 11.5 pm towards the sample during switching off the z-feedback. The $\Delta f(z)$ data was recorded during tip retraction by 3 nm and again during approach by 3 nm. After reestablishing z-regulation, the tip was moved to the next xy-position, and the procedure was repeated. In addition, to characterize the forces in the long-range regime, $\Delta f(z)$ data of 512 points were recorded during retraction and approach by 12 nm at several positions in the same scan area.

Figure 3.127(B) displays variation of the z-values recorded at the stabilization points, which corresponds to the surface topography of the measured area. The obtained image show no significant drift, but nearly perfectly trace the contour of the topographic image obtained before (see Fig. 3.127(A)). Particularly, the atomic structure of the SWNT can be directly identified. Therefore, the assignment of individual spectroscopy curves to specific atomic-lattice sites is unambiguously possible.

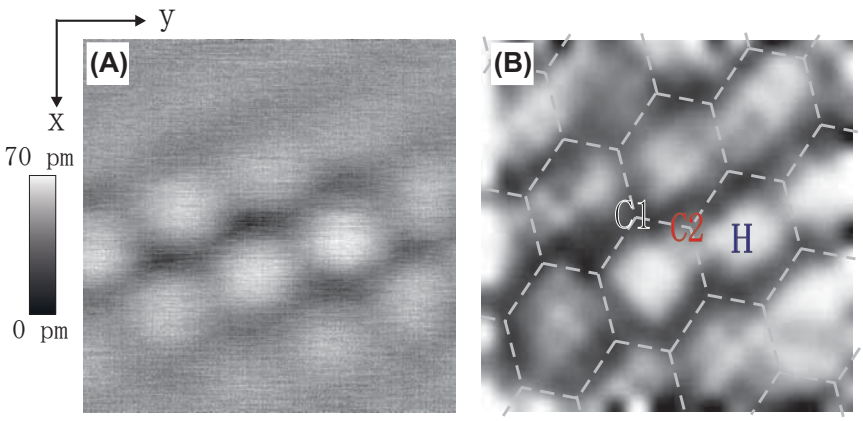

Figure 3.127: (A) Constant frequency shift image with atomic-scale features. (B) Contour plot of the z-values recorded at the stabilizing points during capturing the 3D-FFS. Note that the 20 × 20 data points have been extrapolated to 400 × 400 image points for better visualization. For better visualization of the atomic-scale features, a parabolic curvature has been subtracted from the raw data. The $F(z)$-curves obtained for the positions labeled C1, C2, and H are shown in Fig. 3.128. The slightly distorted corresponding carbon lattice is depicted on the image. Experimental parameters: $f_0 = 159$ kHz, $\Delta f = -69.6$ Hz, $A = 2.3$ nm, $c_z = 34.3$ N/m. Image size: 1 nm × 1 nm (A). Data points: 20 × 20 × 512 in a box of 1 nm × 1 nm × 3 nm (B).

The acquired $\Delta f(x, y, z)$ data sets were converted into force field $F(x, y, z)$ using the equation derived by Dürig [6]:

$$F(S) = \sqrt{2}\frac{c_z A^{3/2}}{f_0}\frac{\partial}{\partial S}\int_S^\infty \frac{\Delta f(z)}{\sqrt{z - S}}dz, \tag{3.35}$$

where S is the closest position during one oscillation. Within the 3D force field $F(x, y, z)$, the interaction forces $F(z)$ for the specific sites C1, C2 and H in Fig. 3.127 are plotted in Fig. 3.128. The attractive forces at their specific sites attain the maximal values $F_{\text{total}}^{\max} \approx -200$ pN, -208 pN, and -216 pN, respectively. On the other hand, the maximal attractive forces of about -6.7 nN [3] and -8.6 nN [4] have been previously reported without any site specifications on the chemically and structurally analogous graphite(0001). Those large differences can be explained by the magnitude of the long-range background forces. The blunter tips ($R_{\text{nominal}} = 10$ nm) in Ref. [3] and [4] generally result in larger long-range attraction. In contrast, the very sharp tip ($R_{\text{nominal}} = 2$ nm) in our experiments would reduce the long-range contribution. Moreover, the long-range vdW forces between the tip and the graphite becomes much smaller when the tip is scanned above a SWNT adsorbed on graphite, and not directly in close proximity to the graphite. Further, the density of carbon atoms in the z-direction is much smaller above SWNTs than above graphite, whereby it is expected that a reduced Hamaker constant for SWNT compared with graphite will indicate a much smaller contribution of the long-range vdW forces.

Extraction and analysis of the short range forces

In the close proximity regime, short-range forces F_{short} become dominant. In order to verify the nature of the short-range force, which is responsible for the atomic-scale contrast, we evaluated the F_{short} using the following procedures. First, we approximated the long-range forces $F_{\text{long}}(z)$ by

$$F_{\text{long}}(z) = \frac{B}{z + z_{\text{l}}}, \tag{3.36}$$

where B and z_{l} are fitting parameters [9]. The constant B has the unit of an energy and indicates the magnitude of the long-range forces. The offset z_{l} is utilized to adjust the z-coordinate since the starting point of each curve was based on the regulating point.

In order to obtain reliable fits for the long-range parts, the data recorded at distances up to 12 nm were examined. By setting $B = -125$ meV, we found good agreement with the experimental data. Successively, by fixing B and changing z_{l}, we found excellent fits with $z_{\text{l}} = -0.020$ nm, -0.020 nm and $+0.020$ nm for the curves C1, C2 and H, respectively. Comparing with $B = -\ 850$ meV in Ref. [8], where a tip with a larger radius ($R_{\text{nominal}} = 10$ nm) was used, the acquired $B = -125$ meV in our experiments indicates a much smaller long-range contribution.

Assuming additivity of the interaction forces, the short-range force is obtained by subtracting the long-range fit from the total force, i.e., $F_{\text{short}}(z) = F_{\text{total}}(z) - F_{\text{long}}(z)$. In the inset of Fig. 3.128, the differences between the F_{short}-curves for the neighboring carbon atoms labeled C1 and C2 is negligibly small compared with the curve for the hollow site of the hexagonal carbon lattice. The attractive short-range forces attain the maximal values $F_{\text{short}}^{\text{max}} = 75.8$ pN, 73.4 pN, and 106 pN (contribution to the maximal total forces $F_{\text{total}}^{\text{max}}$: 37.9%, 35.3%, and 50.0%) for C1, C2, and H, respectively. On the other hand, the short-range chemical bonding forces on NiO(001) are about 0.7 nN and 1.1 nN (contribution to the total force: about 71% and 82%) for the atomic maximum and minimum, respectively [8,9]. Compared to chemical bonding forces, the acquired values of the $F_{\text{short}}^{\text{max}}$ and their contribution to the total forces are very small. Nevertheless, the differences between $F_{\text{short}}^{\text{max}}$ for the H-site and for the C1- and C2-sites are relatively large. These results indicate that indeed interatomic short-range vdW forces were successfully utilized to achieve atomic-scale contrast.

For further analysis of the F_{short}, we fitted the curve to a force derived from the Lennard-Jones potential:

$$F_{L-J}(D) = \frac{12E_0}{z_0}\left[\left(\frac{z_0}{z + z_s}\right)^{13} - \left(\frac{z_0}{z + z_s}\right)^{7}\right], \tag{3.37}$$

where E_0, z_0, and z_s are the adhesion energy, the equilibrium distance and offset to adjust the z-coordinate, respectively. By fixing z_0 to 0.334 nm and taking E_0 and z_s as fitting parameters, we find excellent fits, particularly for the region $z > z^{\text{max}}$

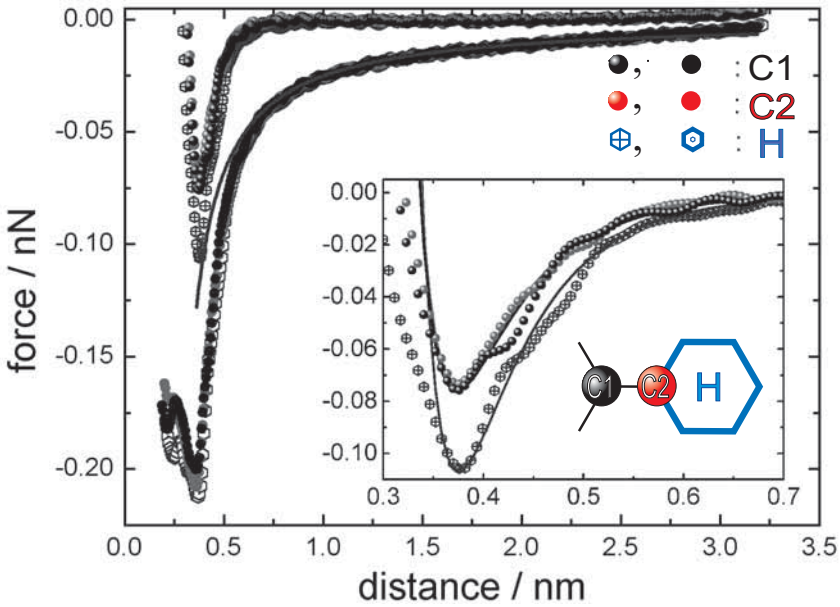

Figure 3.128: Force versus distance curves $F(z)$ at the specific atomic-lattice sites. The labels C1 and C2 (close circle) and label H (open hexagon) correspond to the positions labeled C1, C2, and H in Fig. 3.127(B). The total interaction forces $F_{\mathrm{total}}(z)$ in the lower part have been directly converted from $\Delta f(z)$-curves. The solid line has been fitted to the long-range force data from 3.2 nm to 1 nm using a 1/z force law. The short-range forces F_{short} (upper curves) are obtained by subtracting the long-range fits from the whole total forces. The inset displays the short-range regime (symbols) together with the corresponding Lennard-Jones force fits (lines).

($z^{\max}$: the distance exhibiting $F_{\mathrm{short}}^{\max}$), attaining the value $E_0 = 58.9$ meV, 57.0 meV, and 82.7 meV for the curves C1, C2, and H, respectively. The $F_{\mathrm{short}}(z)$ can be the analogue of the interaction force dominating in molecular physisorption. Indeed, the acquired E_0 values are comparable with the adhesive energy of an oxygen molecule on the SWNT [12]. The deviations of the experimental data from the force fit for the region $z < z^{\max}$ might be related to a deformation of the SWNT, caused by increasing contribution of the repulsive parts. Furthermore, site-specific force curves in the region $z < z^{\max}$ above the SWNTs show characteristic mechanical properties of the SWNT due to its single cylindrical atomic layer. In addition, the 3D force fields of the groove sites, i.e., intermediates between two SWNTs have been successfully achieved. Those results are now under consideration.

Summary

SWNTs can be regarded as model systems of nanometer-scale molecular systems including biological macromolecules. We reported site-specific quantitative force measurements using 3D-FFS with atomic resolution at low temperatures. Thereby, indi-

vidual force curves could be unambiguously assigned to carbon atoms and hollow sites, respectively. A quantitative evaluation of the short and long range forces revealed that the interatomic van der Waals forces are responsible for the atomic resolution. This is in contrast to previous results obtained on more reactive surfaces like silicon [7] and nickel oxide [8, 9], where the chemical bonding forces dominate the atomic scale contrast (cf., section 3.4.2).

References

[1] B. Gotsmann and H. Fuchs, Phys. Rev. Lett. **86** (2001) 2597.

[2] M. Guggisberg, M. Bammerlin, Ch. Loppacher, O. Pfeiffer, A. Abdurixit, V. Barwich, R. Bennewitz, A. Baratoff, E. Meyer, H.-J. Güntherodt, Phys. Rev. B **61**, 11151 (2000).

[3] H. Hölscher, W. Allers, U. D. Schwarz, A. Schwarz, and R. Wiesendanger, Phys. Rev. B **62**, 6967 (2000).

[4] H. Hölscher, W. Allers, U. D. Schwarz, A.Schwarz, and R. Wiesendanger, Phys. Rev. Lett. **83**, 4780 (1999).

[5] F. J. Giessibl, Phys. Rev. B **56**, 16010 (1997).

[6] U. Dürig, Appl. Phys. Lett. **76**, 1203 (2001).

[7] M. A. Lantz, H. J. Hug, R. Hoffmann, P. J. A. van Schendel, P. Kappenberger, S. Martin, A. Baratoff, A. Abdurixit, H.-J. Güntherodt, Science **291** 2580, (2001).

[8] H. Hölscher, S. M. Langkat, A. Schwarz, and R. Wiesendanger, Appl. Phys. Lett. **81**, 4428 (2002).

[9] S. M. Langkat, H. Hölscher, A. Schwarz, and R. Wiesendanger, Surf. Sci. **527**, 12 (2003).

[10] R. Pérez *et al.*, Phys. Rev. B **58**, 10835 (1998).

[11] W. Allers, A. Schwarz, U. D. Schwarz, and R. Wiesendanger, Europhys. Lett. **48**, 276 (1999).

[12] H. Ulbricht, G. Moos, and T. Hertel, Phys. Rev. B **66**, 075404 (2002).

[13] W. Allers, A. Schwarz, U.D. Schwarz, and R. Wiesendanger, Rev. Sci. Instrum. **69**, 221 (1998).

[14] T. R. Albrecht, P. Grütter, D. Horne, and D. Rugar, J. Appl. Phys. **69**, 668 (1991).

3.6 Instrumental developments

3.6.1 The 300 mK scanning tunneling microscope

J. Wiebe, A. Wachowiak, F. Meier, D. Haude, M. Morgenstern, and R. Wiesendanger

In order to increase our energy resolution for spin-polarized scanning tunneling spectroscopy (SP-STS) into the micro-electronvolts range, we built a 300 mK ultra-high vacuum STM with a high magnetic field [1]. STS profits from subkelvin temperatures in two respects. First, many interaction effects of the electron system are determined by small energy scales and demand temperatures below 1 K. Examples are the fractional Quantum Hall effect [2], metal-insulator transitions in two dimensional electron systems [3], superconductivity in heavy fermion compounds [4,5], p-wave superconductivity in systems like Sr_2RuO_4 [6–8], or ferromagnetism of single magnetic atoms on nonmagentic surfaces [9]. Second, even for effects that appear at higher temperature, STS profits from the higher energy resolution achieved in the subkelvin regime. Thus, very small energy scales would be easily resolvable. One example is the Rashba splitting in two dimensional electron systems which is typically of the order of a few meV in InAs inversion layers [10, 11]. Another example is mapping of single wavefunctions in extended systems that are dense in energy on larger length scales [12–16]. Single drift states of the Quantum Hall phase could be mapped with a localization length that is a factor of 5 larger than at 6 K [13]. This allows for experimental investigation of wave function properties which were only theoretically accessible up to now.

We have succeeded in building a ^{3}He refrigerated STM which permits SP-STS measurements with an energy resolution of about 100 μeV [1]. Samples and tips can be exchanged and transferred under true UHV conditions throughout an extensive UHV system equipped with standard surface science methods for sample and tip preparation and characterization. In particular, the *in situ* tip exchange is essential for the preparation of thin film tips to be used for SP-STS measurements.

Instrument design

In order to achieve an energy resolution in STS measurements close to the thermal limit both the mechanical and the electrical noise levels have to be reduced as far as possible. To limit the mechanical noise level, we concentrated on three major points. First, we built an external vibration isolation which decouples the cryostat from the surroundings to reduce noise from outside the experiment. Secondly, we used a ^{3}He-evaporation cryostat with a noiseless ^{3}He sorption pump. Thirdly, the STM head itself is compact and rigid and fairly insusceptible to vibrations. Additional internal vibration isolation is thus not necessary. These major points will be described below.

Fig. 3.129 shows an overview of the facility. The main part is a ^{3}He evaporation refrigerator in a bottom loading cryostat (1) with a superconducting magnet which contains the low temperature STM. The STM can be lowered from the measuring

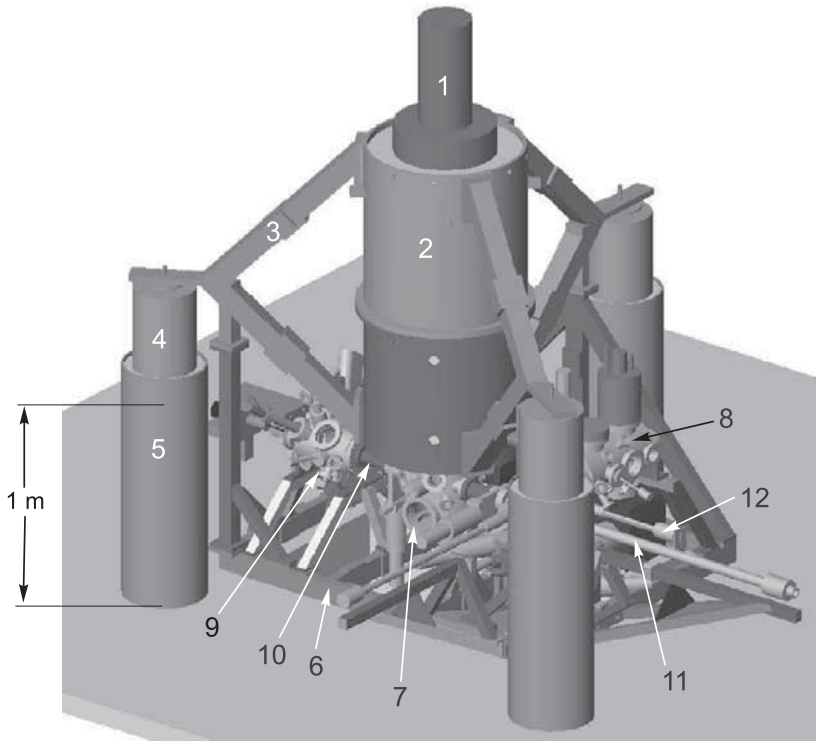

Figure 3.129: Overview of the facility. (1) Bottom loading cryostat containing the ^{3}He refrigerator, the low temperature STM and the superconducting magnet. (2) Sand-filled aluminum barrel, (3) stainless-steel supports filled with sand, (4) air springs, (5) sand-filled supporting legs, (6) sand-filled stainless-steel frame mounted to the supports (3), (7) central UHV chamber for sample- and tip exchange from the low temperature STM, (8) second UHV chamber containing a room temperature STM, molecular beam evaporators and a combined LEED/Auger-system, (9) third UHV chamber containing a variable-temperature MOKE-setup, the tip- and sample heater, molecular beam evaporators and an ion source, (10) edge-welded bellows, (11) magnetic linear and rotary motion drives, (12) load lock.

position inside the cryostat into the central chamber (7) for sample- and tip exchange without leaving UHV. From there, they can be transferred into the two neighboring UHV chambers (8,9) for preparation and characterization.

External vibration isolation

The design of the facility was optimized to reach high mechanical stability of the whole setup. Although the system with its three UHV chambers is relatively extensive, we obtained a compact design by using three support points and an angular arrangement of the chambers. This and the large mass of 2.5 t makes the setup fairly insensitive to vibrations. The facility itself rests on the foundation in the basement of our building.

The cryostat is decoupled from the floor using a three-stage damping system: First, the dewar is embedded in a sand-filled aluminum barrel (2) which screens the walls of the cryostat against sound from the surroundings. Since the cryostat is bottom loading, the sand bed has to be provided with an aperture for the base flange as can be seen in Fig. 3.130. A rubber ring (4) prevents the sand from leaking out. It is at the same time flexible enough to ensure that the base plate of the cryostat rests mainly on sand. Secondly, the three supports (3) (see Fig. 3.129) which carry the barrel rest on air springs (4) with a resonance frequency of about 1 Hz. These absorb the remaining vibrations with a frequency above several Hz. Thirdly, the air springs are supported on a sand layer having a depth of 1 m which is kept within the supporting legs (5). These legs support the frame far above its center of gravity for better stability of the air damping system.

Furthermore, the complete base frame consisting of the supports (3) and the frame (6) is constructed of hollow sections filled with sand to effectively damp sound. Finally, the central UHV chamber (7), which is mounted to the bottom flange of the cryostat, is mechanically decoupled from the two other UHV chambers (8,9), which are fixed to the frame, by the use of edge-welded bellows (10).

Cryogenics, thermometry and magnet

The ^{3}He evaporation refrigerator, which was designed and built by Oxford Instruments Superconductivity [17], is an enhanced version of the cryostat used by Kugler *et al.* [18, 19]. It was designed with the aim of a long base temperature hold time adequate for time-consuming STS measurements, an easy and fast sample exchange during which the STM stays cold, and a refrigeration technique that minimizes vibrations. As opposed to the Kugler system, in our cryostat the entire ^{3}He refrigerator including the STM can be baked out to achieve UHV conditions even with the cryostat at room temperature.

Fig. 3.130 shows a section through the cryostat. It comprises a 77 ℓ liquid ^{4}He- and a 56 ℓ liquid nitrogen dewar (6,5) which is superinsulated in a surrounding isolation vacuum (12). The superconducting solenoid (8) with a 77 mm bore provides a maximum field of 12 T perpendicular to the sample surface at 4.2 K. A lambda fridge (7) can be used to cool the magnet to 2.2 K in order to achieve a field of 14 T. The sample in the STM head is placed in the center of the homogeneous region (0.3% over a 10 mm diameter spherical volume) of the field.

The ^{3}He refrigerator (9) is placed in a UHV tube in the center of the cryostat. This tube extends from the electrical feedthroughs at the top of the cryostat to the bottom flange, where it connects to the central UHV chamber below. The whole tube can be baked out by means of hot nitrogen gas.

The closed single-shot ^{3}He refrigerator consists of a vibrationless charcoal sorption pump connected to the ^{3}He pot via a pumping line that passes through the 1K pot. The residual heat load is shielded by a radiation shield that is thermally coupled to the 1K pot and surrounds the ^{3}He pot and the STM. A patented design allows the

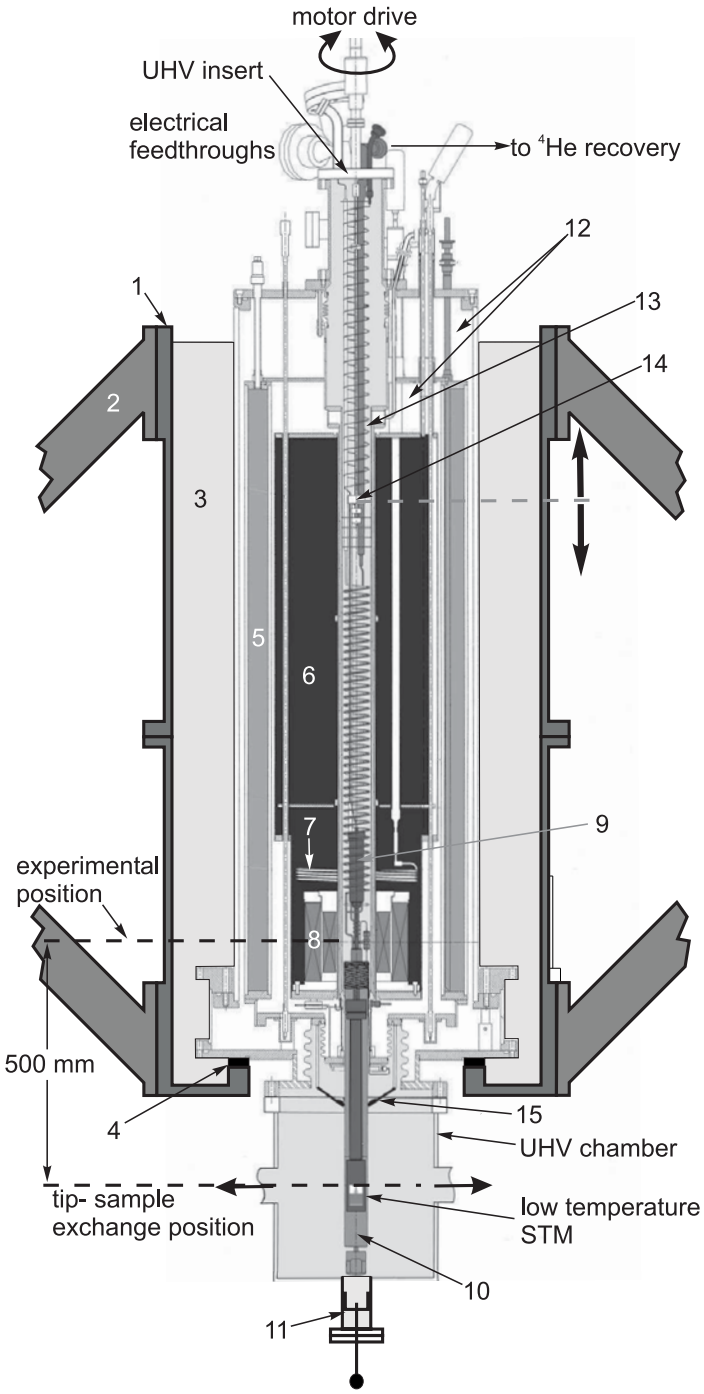

Figure 3.130: The bottom loading cryostat with the ^{3}He refrigerator. The UHV insert is shown in the fully extended position with the STM moved into the UHV chamber for tip- or sample exchange. (1) Aluminum barrel, (2) stainless-steel supports, (3) sand, (4) rubber ring, (5) liquid nitrogen bath, (6) ^{4}He dewar, (7) lambda fridge, (8) 12/14 T magnet, (9) single-shot ^{3}He refrigerator, (10) radiation shield, (11) UHV rotary feedthrough for opening the radiation shield (10), (12) isolation vacuum, (13) threaded leadscrew, (14) aluminum-bronze nut, (15) radiation flaps at 77 K.

whole ^{3}He refrigerator to be moved from the experimental position to the exchange position over a distance of 500 mm as shown in Fig. 3.130 [20, 21]. This is realized by the vertical movement of a nut (14) on a threaded leadscrew (13) that is rotated by a motor drive outside the UHV space via a rotary feedthrough.

The STM itself is mounted to the ^{3}He pot via an OFHC-copper rod with a length of 300 mm. This rod is thermally connected to the ^{3}He pot and to the STM by gold plated pressed contacts. On the STM end, the pressed contact is built as a single plug for all electrical contacts, so that the STM can be easily removed for repair, without removing the ^{3}He refrigerator. All electrical connections to the STM are heat sunk at the ^{4}He exhaust capillary, at the 1K pot, at the ^{3}He pot, at the copper rod, and at the STM.

For temperature measurement we use either a Cernox sensor [22, 23] directly at the STM or a RuO_2 sensor at the ^{3}He pot [17]. At base temperature, the read out of the Cernox and that of the RuO_2 sensor differ by only a few mK, indicating excellent thermal coupling between STM and ^{3}He pot. With a 3.5 ℓ (NTP) ^{3}He-gas charge that condenses into about 5 cc of liquid the STM can be held at a base temperature of 315 ± 5 mK for 30 h. This is achieved without pumping at the 1K pot with the needle valve left fully open. With pumping at the 1K pot the base temperature is reduced to 262 ± 5 mK and the hold time is increased to 130 h. Since this causes additional vibrations and since a time period of 30 h is usually sufficient for high-resolution STS measurements, we achieved all of the following results in the first mode of operation. A complete tip or sample exchange typically takes less than 4 h including recondensation of ^{3}He and cool-down to base temperature. During the whole exchange process the STM temperature stays below 35 K.

An additional feature of the system is the possibility to heat the ^{3}He pot and the sorption pump in order to achieve higher temperatures. Below 4 K the temperature of the STM is regulated by the temperature of the sorption pump. Above 4 K, the heat load is regulated by a resistive heater on the ^{3}He pot. Thereby, a wide temperature range from base temperature up to 100 K is accessible.

STM head and electronics

Fig. 3.131 (a) shows a photo of the home-built STM head. It has been designed to be as small and compact as possible in order to make it less susceptible against vibrations. It measures 26 mm in diameter by 85 mm in length including the connector (13). The compactness is obtained primarily by integration of the tube scanner (5) into the coarse-approach motor as visible in Fig. 3.131 (b). The microscope body (11) is made of phosphorous bronze, a hard, nonmagnetic, and UHV-compatible copper alloy.

The coarse approach motor is of the so-called Walker design [24]. It consists of a sapphire prism (6), which is clamped between 6 thin plates of Al_2O_3 glued on top of shear-piezo stacks (8). The clamping is accomplished by a molybdenum leaf-spring (10) that presses the front two shear-piezo stacks onto the sapphire prism. We drive the motor in stick-slip mode of operation [25] and achieve a step width of 25 nm

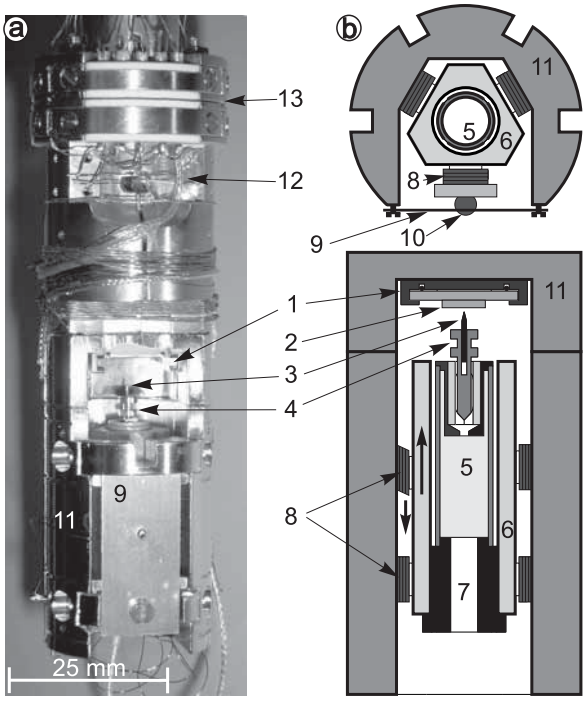

Figure 3.131: (a) Photo of the STM head. (b) Horizontal (top) and vertical (bottom) cross sections. (1) Sample holder, (2) sample, (3) tip, (4) tip holder (molybdenum), (5) tube scanner, (6) sapphire prism, (7) tube scanner holder (macor), (8) shear-piezo stacks, (9) molybdenum leaf-spring, (10) titanium ball, (11) microscope body (phosphorous bronze), (12) Cernox temperature sensor, (13) electrical connector (OFHC copper).

at a voltage of 300 V at base temperature. The coarse motor is very stable and reliable at low temperature.

For scanning, a 1/4 inch *EBL#4* piezo tube scanner (5) with a length of 20 mm is mounted inside a sapphire prism. For the 5 electrodes (4 segments on the outer face, 1 on the inner) we chose copper instead of the often used nickel to avoid magnetic material. The maximum scan range with an applied voltage of ±240 V amounts to 1 μm × 1 μm at base temperature and the z-range is calculated to be 200 nm.

As STM tips (3), we use thin wires of the desired material, which are either mechanically sharpened (Pt/Ir, Nb) or electrochemically etched (W) *ex situ*. The tip wire is then clamped into the tip holder (4), which itself is stuck into the tube scanner. By means of a transporter the tip holder can be safely transferred into the UHV system and inserted into the STM without danger of damage to the tube scanner as described elsewhere [26]. Further *in situ* tip preparation is described below.

The STM is operated by commercial control electronics and software [27] with a home-built preamplifier. Both the sample bias supply and the tunneling current measurement are done fully differentially as outlined by Züger *et al.* [28]. Tip and sample are connected to the preamplifier mounted outside the UHV via shielded twisted-pair cables containing both signal and reference potential line. This circuit combines a low capacitive coupling between tunneling current and bias, which is important for modulation techniques, with an effective shielding against electrical noise. To shield against high frequency noise, all in- and outputs of the preamplifier are filtered through commercial T-filters with a cutoff frequency of about 30 MHz. The preamplifier with cables has a total gain of 1 V/1 nA at a bandwidth of approx. 5 kHz, and an input current noise of 3 $\mathrm{pA_{rms}}$.

UHV system

Fig. 3.129 shows a survey of the UHV system composed of three chambers that are separated by UHV valves. Each chamber is pumped by a 150 ℓ/sec ion getter pump including a titanium sublimation pump, connected to the chambers via a 100 mm ID flange. After baking the system including the UHV tube of the cryostat for about one week, we reach a base pressure of $p < 1 \cdot 10^{-10}$ mbar in each chamber, even with the cryostat at room temperature.

In the central UHV chamber (7), STM tips and samples can be transferred into and out of the STM. From there, they are transported between the chambers by means of magnetic drives (11) and wobblesticks. The second UHV chamber (8) contains several molecular beam evaporators, a room-temperature STM [29] including a resistive heater ($T_{\max} = 700$ K) for easy and fast sample characterization and a combined LEED/Auger-electron spectroscopy unit [30]. The third UHV chamber (9) contains an ion source for sputtering, a gas inlet for gas dosage, several metal beam evaporators, a quadrupole mass spectrometer [31], and a home-built electron bombardment heater for tips and samples with $T_{\max} > 2400$ K assembled on a commercial x,y,z-manipulator. By a load lock (12) tips and samples are easily transferred into the system with-

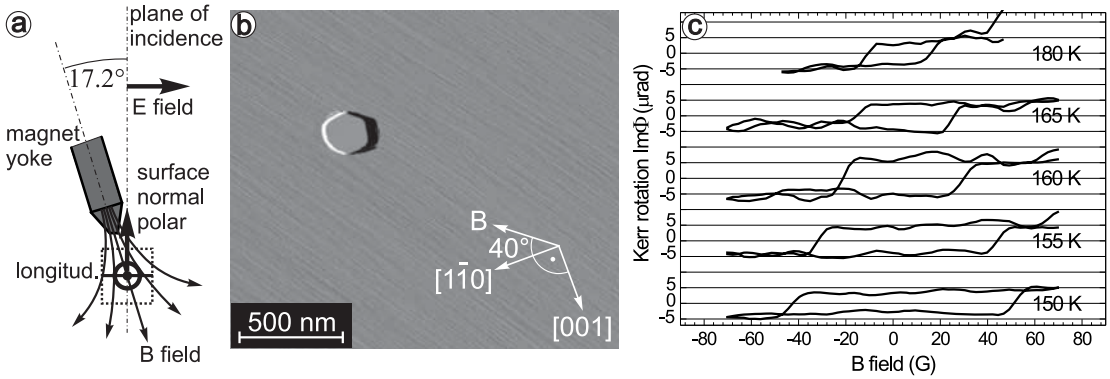

Figure 3.132: (a) Geometry of the MOKE setup. The sample surface in polar geometry is represented by the black line with the surface normal pointing upwards. In longitudinal geometry the sample surface is represented by the dotted square with the surface normal perpendicular to the sheet plane. (b) Constant-current image of 1 ML Fe/W(110) annealed at 800 ± 100 K ($I = 0.04$ nA, $V = -0.8$ V). The Fe material in excess of 1 ML forms large islands on the closed Fe monolayer. (c) Hysteresis curves in longitudinal geometry of the sample in (b) measured by MOKE at temperatures close to T_C. The magnetic field B is applied along the arrow shown in (b). The x-axis corresponds to the component parallel to [1$\bar{1}$0].

out breaking UHV in the main chambers. The x,y,z-manipulator in the third UHV chamber additionally contains a stage that allows *in situ* magneto-optical Kerr-effect (MOKE) measurements at variable temperatures. The home-built MOKE setup uses a conventional laser/detector setup mounted on two viewports outside the UHV chamber. It includes a 670 nm constant-current stabilized laser diode, a polarizer, a $\lambda/4$ phase shifter, an analyser, a colour filter and a photodiode detector. The magnetic field is generated by a single yoke electromagnet with the coil mounted outside the UHV chamber. The soft-magnetic yoke is mounted inside the UHV chamber and can be moved close to the sample surface.

The geometry of the setup is shown in Fig. 3.132 (a). The sample surface can be moved in polar as well as in longitudinal geometry in order to be sensitive to the out-of-plane and to the in-plane components of the sample magnetization, respectively. The imaginary part of the Kerr angle ImΦ(B) is measured by ramping the magnetic field and recording the output of the detector [32, 33]. We achieve a maximum magnetic field of 35 mT at the sample position. Due to the restricted geometry of the UHV chamber, the axis of the yoke has an angle of 17.2° to the plane of incidence of the laser

light. Consequently, the magnetic field has a small component (30%) perpendicular to the plane of incidence. Since this component is parallel to the electric field direction, the corresponding magnetization component does not enter into the measured Kerr angle.

For the purpose of variable temperatures, the sample holder includes a resistive heater and is coupled to a ^{4}He continuous-flow cryostat [34] via flexible copper braids. The temperature is measured with a Si diode attached to the sample holder [35]. We achieve temperatures between 30 K and 450 K.

To test the sensitivity of the MOKE setup, we prepared a 1 ML Fe film on W(110). The W(110) substrate was cleaned by repeated cycles of heating at 1500 K in an oxygen atmosphere of $5 \cdot 10^{-7}$ mbar and subsequent flashing to 2300 K [36]. The Fe film was deposited at room temperature with an e-beam evaporator at a rate of 0.5 ML/min and was subsequently thermally annealed for 10 min at 800 ± 100 K. During preparation the pressure remained below $2 \cdot 10^{-10}$ mbar. The topography of the sample is shown in Fig. 3.132 (b). The Fe material in excess of 1 ML forms a few large islands with a height of about 35 ML which cover only 1% of the surface. On the remaining major part of the surface the substrate is covered with a closed Fe monolayer [37].

The Kerr loops measured in longitudinal geometry with the B-field direction close to $[1\bar{1}0]$ are shown in Fig. 3.132 (c). They are measured on the identical sample of (b) at different temperatures. We find squarelike hysteresis curves indicating an easy axis in the film plane. The coercivity field clearly decreases with increasing temperature. At higher temperatures, the hysteretic behaviour vanishes (not shown). It is known that the Fe monolayer is ferromagnetic with a Curie temperature T_C well below room temperature. It has an easy axis pointing in $[1\bar{1}0]$ direction. T_C can be estimated to be 210 K given the terrace width of 10 nm [38]. On the other hand, Fe islands of the height found here are known to show a magnetic vortex structure with a T_C above room temperature [39, 40]. This indicates that the hysteretic signal in Fig. 3.132 (c) originates from the Fe monolayer and not from the few islands. From the signal strength, we thus determine that the MOKE setup can easily resolve a coverage below 1 ML. Moreover, the experiment shows that the ferromagnetism of low dimensional structures, usually exhibiting a high coercivity field, can be measured with this setup by heating the sample to about T_C.

Tip preparation for spin-polarized measurements

For spin-polarized STS measurements, the tungsten STM tips are prepared *in situ* similarly to previous experiments [39, 41]. We typically flash to about 2300 K, then coat with several monolayers of magnetic material and afterwards anneal for 5 min at about 500 K. A convenient sample system to test the magnetic sensitivity of our tips is the vortex domain configuration of Fe islands which are prepared as described above [39, 40]. As an example, we show the domain configuration as measured with an in-plane sensitive tip obtained by coating with $5 - 6$ ML of Fe. Fig. 3.133 (a) shows the topography of the sample and Fig. 3.133 (b) the simultaneously recorded,

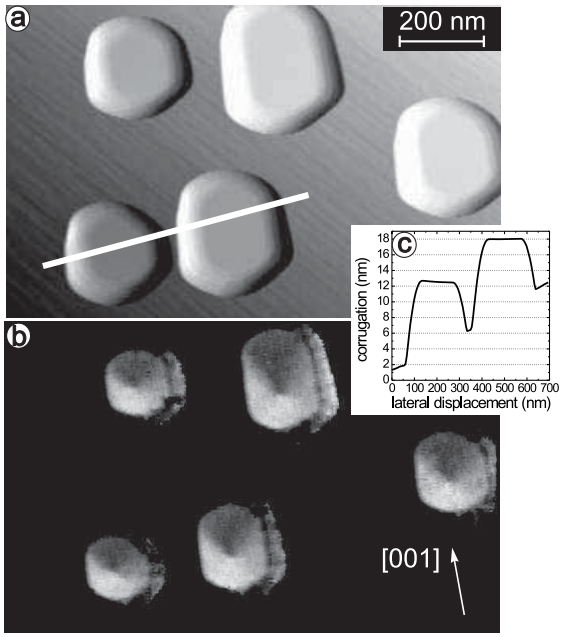

Figure 3.133: (a) Constant-current image of Fe islands on W(110) measured with an Fe coated tip. (b) Simultaneously recorded, spin-resolved dI/dV map showing magnetic vortex states of the Fe islands at room temperature ($I_{\mathrm{stab}} = 0.3$ nA, $V_{\mathrm{stab}} = -0.3$ V, $V_{\mathrm{mod}} = 30$ $\mathrm{mV_{rms}}$). (c) Line section taken along the white line in (a).

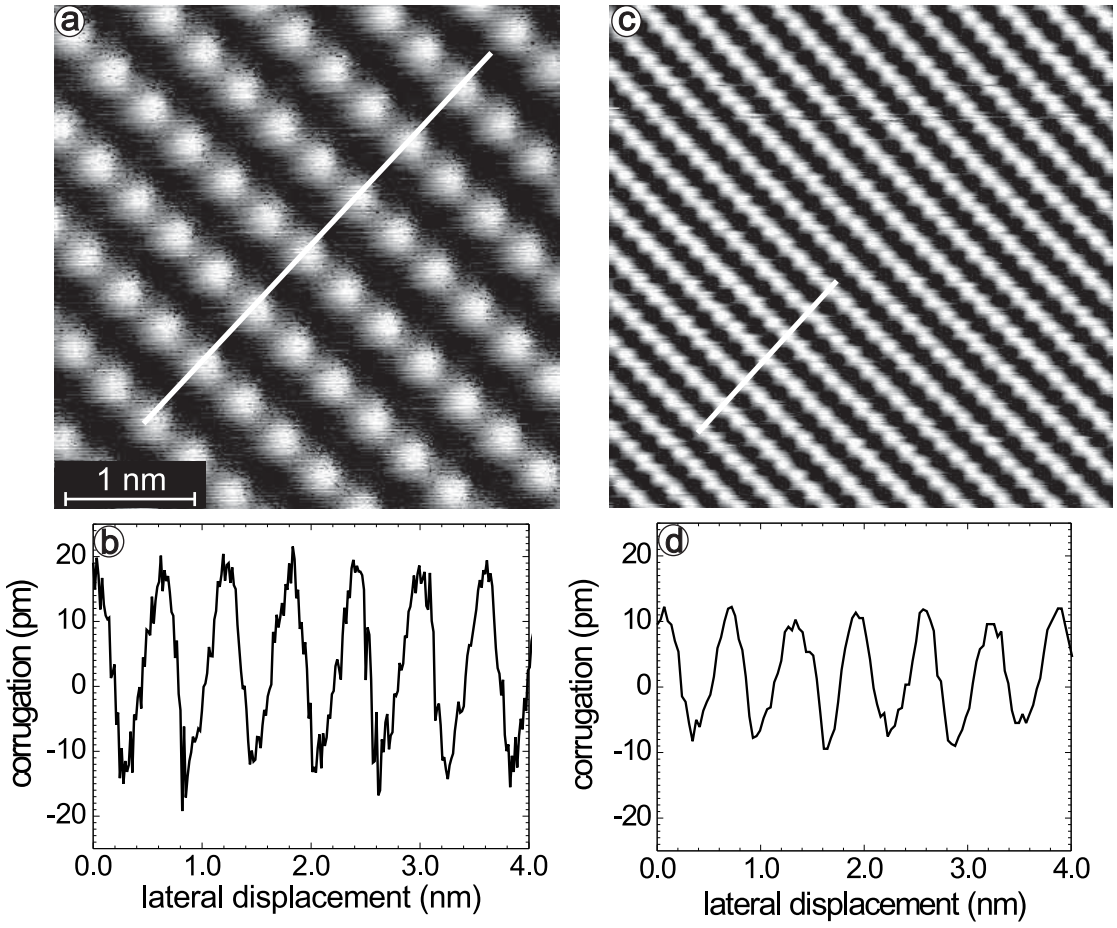

Figure 3.134: (a) Constant-current image taken at 315 mK showing atomic resolution on InAs(110) (unfiltered data, $I = 0.8$ nA, $V = -0.9$ V). (b) The line section along the white line in (a) shows a noise level of 5 $\mathrm{pm_{pp}}$. (c),(d) Same as (a),(b) but in a magnetic field of 4 T (unfiltered data, $I = 1.5$ nA, $V = -1$ V). Note that the atomic corrugation is reduced due to a different micro-tip. The noise level is still below 5 $\mathrm{pm_{pp}}$.

spin-resolved dI/dV map of the same area. These data were recorded at room temperature. We clearly observe the in-plane domains of the magnetic vortex configuration as found at 14 K [39], proving that the tip is sensitive to the in-plane component of the magnetization.

Experimental results at base temperature

The principal tests of our facility concern the stability of the STM, the spin resolution and the energy resolution in the STS mode at base temperature.

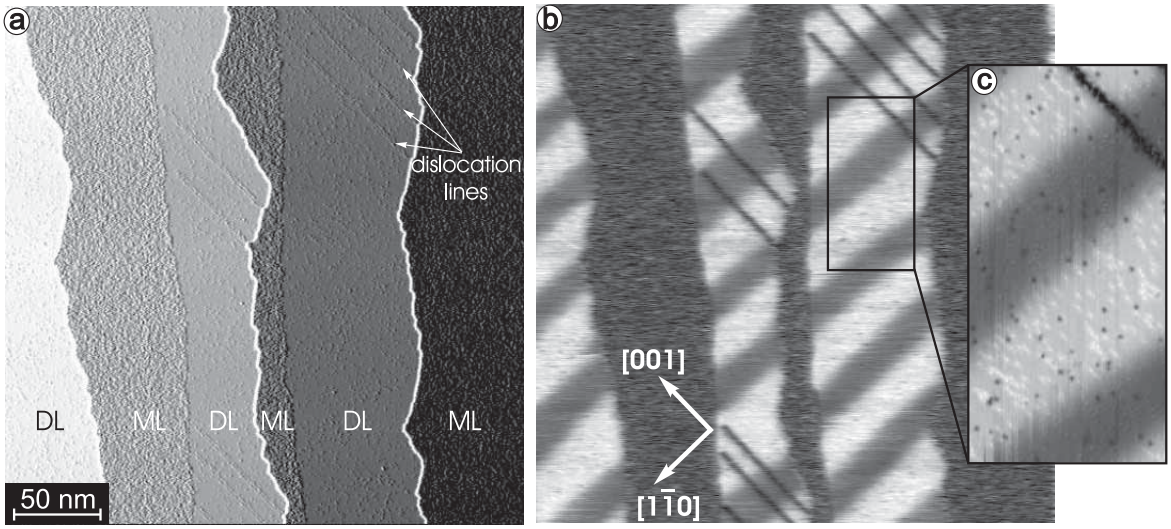

Figure 3.135: Constant-current image (a) and simultaneously recorded, spin-resolved dI/dV map (b) of 1.5 ML Fe/W(110) measured with an out-of-plane sensitive tip (I_{stab} = 1 nA, V_{stab} = 0.7 V, V_{mod} = 20 $\mathrm{mV_{rms}}$, T = 315 mK). The Fe overlayer forms alternating monolayer (ML) and double-layer (DL) stripes running parallel to the step edges of the W(110) substrate. The dI/dV map clearly shows the domain contrast of the DL stripes with the domain walls oriented roughly along [1$\bar{1}$0] perpendicular to the dislocation lines marked in (a). (c) dI/dV map with higher spatial resolution of the area marked in (b).

Z-Stability

First tests of the STM were performed on *in situ* cleaved InAs single crystals. This procedure yields an atomically flat and largely defect free InAs(110) surface [42]. The z-calibration was performed on step edges that occasionally appear on the surface [15]. The constant-current image on a small length scale is shown in Fig. 3.134 (a). The dangling bonds of the As atoms are clearly resolved [43]. A line section taken perpendicular to the atomic rows in Fig. 3.134 (b) reveals an atomic corrugation of about 30 pm with a z-noise level of 5 $\mathrm{pm_{pp}}$. In order to demonstrate the performance in a magnetic field we imaged the same surface at 4 T as shown in Fig. 3.134 (c) and (d). The z-noise level is still below 5 $\mathrm{pm_{pp}}$.

Note, that these results were obtained at an early stage with a non-optimized setup. Up to that time, there was no sand in the aluminum barrel, no acoustic shielding and only partial electrical filtering of the STM cables. The z-noise could further be reduced by optimizing the setup.

Spin resolution

To demonstrate our ability to perform spin-polarized measurements at 300 mK we imaged the stripe-domain structure of Fe double-layer (DL) nanowires on W(110) [41,44].

The nanowires are prepared by deposition of 1.5 ML Fe at a rate of 0.5 ML/min and at a temperature of approx. 500 K. As seen in Fig. 3.135 (a) this procedure results in a grating of alternating Fe monolayer (ML) and Fe double-layer (DL) stripes running parallel to the step edges of the W(110) substrate. In this particular measurement, we succeeded in preparing a spin-sensitive tip by gently touching the Fe surface with a tungsten tip. Fig. 3.135 (b) shows the resulting spin-resolved dI/dV map recorded simultaneously with the topography in (a). A higher resolution dI/dV map is shown in Fig. 3.135 (c). We clearly observe the out-of-plane stripe-domains of the Fe DL nanowires which are oriented roughly parallel to the $[1\bar{1}0]$ direction and perpendicular to the dislocation lines, as found at 14 K [41]. Obviously, our tip creates a strong out-of-plane contrast of about 30%. Fitting the domain-wall profiles as described by Kubetzka *et al.* [44] reveals a tip-magnetization angle of $10° \pm 10°$ relative to the surface normal. The fit results in a domain-wall width of 7 ± 1 nm which is consistent with the value found at 14 K [44]. We want to point out, that similar to voltage pulses [45], the particular tip preparation used here is responsible for the out-of-plane sensitivity in contrast to the usual in-plane sensitivity achieved by coating with several monolayers of Fe as described in Sec. 3.6.1.

To our knowledge, these measurements show for the first time spin-polarized contrast in STS measurements at subkelvin temperatures. They demonstrate that the preparation of spin-sensitive tips could be quite easy at very low temperatures.

Energy resolution

To demonstrate the high energy resolution of our STM we performed STS measurements on $NbSe_2$, a well studied layered material that has a superconducting phase transition at approx. 7.2 K [46]. A dI/dV map of the cleaved surface taken at a magnetic field of 0.5 T is shown in Fig. 3.136 (a). The Abrikosov flux lattice of the type II superconductor is well resolved. Fig. 3.136 (b) shows dI/dV curves measured by lock-in technique at variable temperatures in zero magnetic field. The temperature dependence of the superconducting energy gap can clearly be observed. We see a difference between the curve measured at 700 mK and the curve measured at 310 mK, i.e. an earlier onset of nonzero conductance within the gap. This indicates that our electronic tip temperature is at least below 700 mK.

Since the superconducting gap of $NbSe_2$ is anisotropic, a fit to conventional BCS theory is not possible. Therefore we also measured dI/dV curves on the normal metal W(110) using a superconducting niobium tip. A similar experiment using the Au(111) surface is known to yield dI/dV curves that fit well to BCS theory [47]. We used mechanically sharpened, polycrystalline Nb wires with a diameter of 0.8 mm. The W(110) surface is prepared as described before. After inserting the tip into the STM, we applied voltage pulses on the W(110) surface to remove the oxide from the tip. The dI/dV curves are then measured on a clean sample area. Fig. 3.137 shows a dI/dV curve measured at base temperature. The superconducting energy gap is clearly resolved. To determine the electronic temperature of the sample, we use the standard

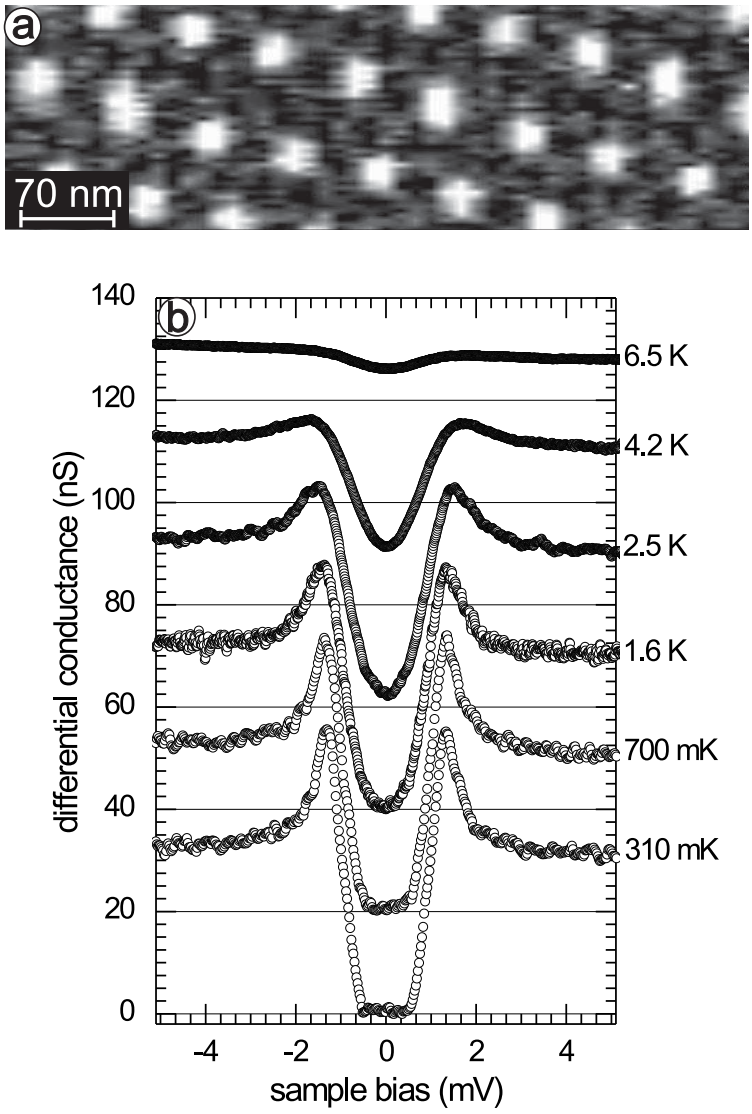

Figure 3.136: (a) dI/dV map of the cleaved $NbSe_2$ surface showing the Abrikosov flux lattice at a magnetic field of 0.5 T and at a sample bias of 0 mV ($I_{\mathrm{stab}} = 0.2$ nA, $V_{\mathrm{stab}} = -6.8$ mV, $V_{\mathrm{mod}} = 80$ μV_{rms}, $T = 310$ mK). (b) dI/dV curves measured by lock-in technique on $NbSe_2$ at $B = 0$ T using a tungsten tip. The measurement temperature is given beside each curve. The curves are averages from several single curves taken on the same sample area; 300 mK-1.6 K: average of 2×2 curves; 2.5 K: 3×3; 4.2 K-6.5 K: 10×10. The curves are offset by 20 nS steps for clarity ($I_{\mathrm{stab}} = 0.2$ nA, $V_{\mathrm{stab}} = 6$ mV, $V_{\mathrm{mod}} = 24$ μV_{rms}).

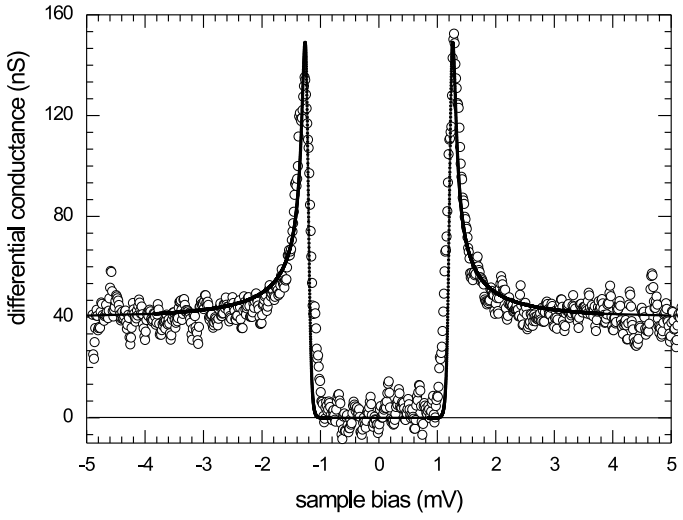

Figure 3.137: Open circles: dI/dV curve measured by lock-in technique with a Nb tip on a W(110) sample ($I_{\mathrm{stab}} = 0.2$ nA, $V_{\mathrm{stab}} = -5$ mV, $V_{\mathrm{mod}} = 20\ \mu\mathrm{V_{rms}}$, $T = 315\,\mathrm{mK}$). Solid line: fit to the experimental data revealing a superconducting energy gap of $\Delta = 1.23\,\mathrm{meV}$ and a fit temperature of $T_{\mathrm{fit}} = 315\,\mathrm{mK}$.

relation for STM $I(V)$ spectra [48–50]

$$I(V) \propto \int_{-\infty}^{\infty} \rho_s(\epsilon + eV) \cdot \rho_t(\epsilon) \cdot [f_s(\epsilon + eV) - f_t(\epsilon)] d\epsilon \tag{3.38}$$

with the sample and the tip density of states ρ_s and ρ_t and the corresponding Fermi functions f_s and f_t. We assume that ρ_s is approximately constant in the small energy range around E_F [51] and use the standard BCS density of states for the tip

$$\rho_t(\epsilon) \propto \begin{cases} \frac{|\epsilon|}{\sqrt{\epsilon^2 - \Delta^2}} & : \quad |\epsilon| > \Delta \\ 0 & : \quad |\epsilon| < \Delta \end{cases} \tag{3.39}$$

with the superconducting energy gap Δ [52]. The detection of the differential conductivity via lock-in amplifier with a modulation voltage of $V_\mathrm{mod} = 20\ \mu\mathrm{V_{rms}}$ is then taken into acount by numerically integrating

$$\frac{dI}{dV}(V) \propto \int_{-\pi/2}^{\pi/2} sin\alpha \cdot I\left(V + \sqrt{2} \cdot V_\mathrm{mod} \cdot sin\alpha\right) d\alpha \tag{3.40}$$

The resulting curve is fitted to our data by adjusting the energy gap Δ and the temperature T_fit of the Fermi function. The measured energy gap Δ depends on the micro-tip, i.e. it can change after field emission, as already described by Pan *et al.* [47]. We find that this effect results in a variation of the gap by approximately $\pm 10\%$. The fit result is shown in Fig. 3.137 as a solid line revealing a fit temperature of $T_\mathrm{fit} = 315\,\mathrm{mK}$ and an energy gap of $\Delta = 1.23\,\mathrm{meV}$. The same procedure was carried out for several different measurements using different micro-tips and different stabilization currents resulting in an average sample temperature of $T_\mathrm{fit} = 350 \pm 35\,\mathrm{mK}$. This is only slightly higher than the sample temperature read from the Cernox sensor on the STM head indicating that our energy resolution is close to the thermal limit of $3.3kT = 85\,\mu\mathrm{eV}$.

References

[1] J. Wiebe, A. Wachowiak, F. Meier, D. Haude, T. Foster, M. Morgenstern, R. Wiesendanger; Rev. Sci. Instrum. **75**, 4871 (2004).

[2] D. C. Tsui, H. L. Stormer, A. C. Gossard; Phys. Rev. Lett. **48**, 1559 (1982).

[3] E. Abrahams, S. V. Kravchenko, M. Sarachik; Rev. Mod. Phys. **73**, 251 (2001).

[4] Z. Fisk, D. W. Hess, C. J. Pethick, D. Pines, J. L. Smith, J. D. Thompson, J. O. Willi; Science **239**, 33 (1988).

[5] M. Jourdan, M. Huth, H. Adrian; Nature **398**, 47 (1999).

[6] T. M. Risemann, P. G. Kealey, E. M. Forgan, A. P. Mackenzie, L. M. Galvin, A. W. Tyler, S. L. Lee, C. Ager, D. McK. Paul, C. M. Aegerter, R. Cubitt, Z. Q. Mao, T. Akima, Y. Maeno; Nature **396**, 242 (1998).

[7] K. Ishida, H. Mukuda, Y. Kitaoka, K. Asayama, Z. Q. Mao, Y. Mori, Y. Maeno; Nature **396**, 658 (1998).

[8] B. I. Barker, S. K. Dutta, C. Lupien, P. L. McEuen, N. Kikuagawa, Y. Maeno, J. C. Davis; Physica B **329**, 1334 (2003).

[9] P. Gambardella, S. Rusponi, M. Veronese, S. S. Dhesi, C. Grazioli, A. Dallmeyer, I. Cabria, R. Zeller, P. H. Dederichs, K. Kern, C. Carbone, H. P. Brune; Science **300**, 1130 (2003).

[10] D. Grundler; Phys. Rev. Lett. **84**, 6074 (2000).

[11] T. Matsuyama, R. Kürsten, C. Meißner, U. Merkt; Phys. Rev. B **61**, 15588 (2000).

[12] M. Morgenstern, J. Klijn, Chr. Meyer, M. Getzlaff, R. A. Adelung, R. Römer, K. Rossnagel, L. Kipp, M. Skibowski, R. Wiesendanger; Phys. Rev. Lett. **89**, 136806 (2002).

[13] M. Morgenstern, J. Klijn, Chr. Meyer, R. Wiesendanger; Phys. Rev. Lett. **90**, 056804 (2003).

[14] J. Wiebe, Chr. Meyer, J. Klijn, M. Morgenstern, R. Wiesendanger: Phys. Rev. B **68**, 041402 (2003).

[15] Chr. Meyer, J. Klijn, M. Morgenstern, R. Wiesendanger: Phys. Rev. Lett. **91**, 076803 (2003).

[16] K. Kanisawa, M. J. Butcher, Y. Tokura, H. Yamaguchi, Y. Hirayama: Phys. Rev. Lett. **87**, 196804 (2001).

[17] Oxford Instruments Superconductivity, Research Instruments, Tubney Woods, Oxon OX13 5QX, United Kingdom.

[18] M. Kugler, Ch. Renner, Ø. Fischer, V. Mikheev, G. Batey; Rev. Sci. Instrum. **71**, 1475 (2000).

[19] M. Kugler, Ch. Renner, V. Mikheev, G. Batey, Ø. Fischer; Physica B **280**, 551 (2000).

[20] V. Mikheev, United States Patent No. 5829270, Nov 3, 1998.

[21] G. Batey, V. Mikheev; J. Low Temp. Phys. **113**, 933 (1998).

[22] Cernox-1030-SD-HT. Lake Shore Cryotronics (www.lakeshore.com), Westerville, Ohio, USA.

[23] Cryophysics GmbH. D-64293 Darmstadt, Germany.

[24] S. H. Pan, International Patent Publication No. WO 93/19494 (International Bureau, World Intellectual Property Organization), Sep 30, 1993.

[25] G. Mariotto, M. D. Angelo, I. V. Shvets; Rev. Sci. Instrum. **70**, 3651 (1999).

[26] O. Pietzsch, A. Kubetzka, D. Haude, M. Bode, R. Wiesendanger; Rev. Sci. Instrum. **71**, 424 (2000).

[27] Scala SPM control unit. Omicron NanoTechnology GmbH, Limburger Strasse 75, D-65232 Taunusstein, Germany.

[28] O. Züger, H. P. Ott, U. Dürig: Rev. Sci. Instrum. **63**, 5634 (1992).

[29] Ch. Witt, U. Mick, M. Bode, R. Wiesendanger: Rev. Sci. Instrum. **68**, 1455 (1997).

[30] Spectaleed optic. Omicron NanoTechnology GmbH, Limburger Strasse 75, D-65232 Taunusstein, Germany.

[31] Transpector C100M. Inficon, Two Technology Place, East Syracuse, New York 13057-9714, USA.

[32] F. Meier: Diplomarbeit, Institut of Applied Physics, University of Hamburg, Germany (2002).

[33] J. Wiebe: Dissertation, Institute of Applied Physics, University of Hamburg, Germany (2003).

[34] Konti cryostat. CryoVac GmbH & Co KG, Heuserweg 14, D-53842 Troisdorf, Germany.

[35] DT 670C-SD. Lake Shore Cryotronics (www.lakeshore.com), Westerville, Ohio, USA.

[36] M. Bode, R. Pascal, R. Wiesendanger: Surf. Sci. **344**, 185 (1995).

[37] U. Gradmann, G. Liu, H. J. Elmers, M. Przybylski: Hyperfine Interactions **57**, 1845 (1990).

[38] H.-J. Elmers: *Magnetismus dünner Filme.* In: *Magnetische Schichtsysteme ,* Kapitel B1. Ferienkurse Forschungszentrum Jülich (1999).

[39] A. Wachowiak, J. Wiebe, M. Bode, O. Pietzsch, M. Morgenstern, R. Wiesendanger; Science **298**, 577 (2002).

[40] M. Bode, A. Wachowiak, J. Wiebe, A. Kubetzka, M. Morgenstern, R. Wiesendanger; Appl. Phys. Lett. **84**, 948 (2004).

[41] A. Kubetzka, M. Bode, O. Pietzsch, R. Wiesendanger; Phys. Rev. Lett. **88**, 057201 (2002).

[42] M. Morgenstern, D. Haude, V. Gudmundsson, Chr. Wittneven, R. Dombrowski, Chr. Steinebach, R. Wiesendanger; J. Electron. Spectrosc. Relat. Phenom. **109**, 127 (2000).

[43] J. Klijn, L. Sacharow, C. Meyer, S. Blügel, M. Morgenstern, R. Wiesendanger; Phys. Rev. B **68**, 205327 (2003).

[44] A. Kubetzka, O. Pietzsch, M. Bode, R. Wiesendanger; Phys. Rev. B **67**, 020401 (2003).

[45] T. K. Yamada, M. M. J. Bischoff, T. Mizoguchi, H. van Kempen; Appl. Phys. Lett. **82**, 1437 (2003).

[46] H. F. Hess, R. B. Robinson, R. C. Dynes, J. J. M. Valles, J. V. Waszczak; Phys. Rev. Lett. **62**, 214 (1989).

[47] S. H. Pan, E. W. Hudson, J. C. Davis; Appl. Phys. Lett. **73**, 2992 (1998).

[48] J. Bardeen; Phys. Rev. Lett. **6**, 57 (1961).

[49] J. Tersoff, D. R. Hamann; Phys. Rev. Lett. **50**, 1998 (1983).

[50] J. Tersoff, D. R. Hamann; Phys. Rev. B **31**, 805 (1985).

[51] M. Bode, R. Pascal, R. Wiesendanger; J. Vac. Sci. Technol. A **15**, 1285 (1997).

[52] D. R. Tilley, J. Tilley: *Superfluidity and Superconductivity.* Institute of Physics Publishing Ltd London (1990).

3.6.2 A low temperature force microscope with a 5 T split-coil magnet

M. Liebmann, U. Kaiser, N. Plock, A. Schwarz, and R. Wiesendanger

Introduction

Since its invention, force microscopy has been applied under different conditions. From the viewpoint of surface science and investigation of basic processes in solid state physics, it is promising to extend this powerful tool of real space imaging to low temperatures in conjunction with high magnetic fields and to combine it with preparation and analysis techniques in an ultrahigh vacuum (UHV) environment. In particular, such an instrument allows to study the large variety of magnetic phenomena by using magnetic force microscopy (MFM). Previously, we successfully set up an instrument with high force sensitivity and capable of atomic resolution in UHV at low temperatures, but without a magnetic field [1]. The combination of bakability, low vapor pressure, and matching of thermal contraction coefficients strongly limits the choice of materials under UHV and low temperature conditions. So far, it has only been realized by very few groups [1–4] and only one UHV-compatible cryostat has been equipped with a superconducting magnet [3].

Here, we present a force microscope based on the original Hamburg design as described in Ref. [1]. In the past years this design has been modified and now incorporates an xy-stage and a more modular design, which allows to replace the complete sample stage rather easily [5]. The microscope is placed in an UHV compatible bath cryostat with a superconducting magnet, which is located in the transfer level of the UHV system. Easy access is provided by using a split-coil magnet and two shutters in front of a cutaway through the liquid helium tank. Thereby, in contrast to the first instrument set up in Hamburg [34], the microscope itself remains fixed to its thermal anchoring during in situ tip or sample exchange, which allows a fast, safe, and reliable operation.

UHV-system

To study clean surfaces with well defined tips, the opportunity of in situ preparation like cleavage, heating, sputtering, and evaporation is essential. Therefore, the cryostat is part of a standard UHV system [6] consisting also of a preparation chamber (electron beam heating, argon ion sputter gun, evaporation cells, and a resistive or direct current heating) and an analysis chamber (low energy electron diffraction, Auger electron spectroscopy, room temperature combined force and tunnelling microscope). To introduce cantilevers and samples into the UHV system, a load lock is connected to the preparation chamber. Access to the different chambers is provided by magnetic linear and rotary motion drives with perpendicular handing over. Sample holders in

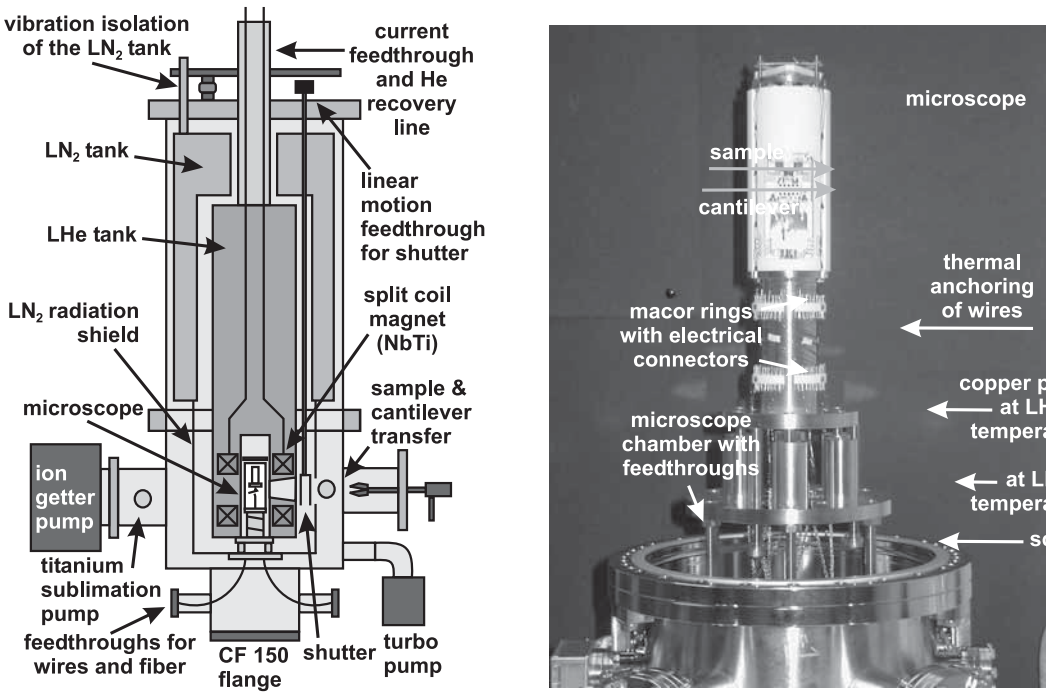

Figure 3.138: Left panel: Cross section of the magnet. The microscope is inserted from below together with the microscope chamber containing the electrical and fiber-optical feedthroughs. Right panel: Thermal anchoring of the microscope. During insertion, the copper parts are connected via screws to the microscope chamber, but disconnected afterwards.

the preparation and analysis chamber can be positioned by xyz-manipulators. In particular, the orientation of the tip towards the sputter gun and the iron evaporator can be adjusted precisely. To achieve pressures better than 10^{-8} Pa, the UHV system is baked at 120°C for three days, while the temperature of the superconducting magnet has to be kept below 100°C. In order to realize a sufficient vibration isolation of the microscope from external noise sources, the UHV system is mounted on pneumatic damping legs which in turn stands on a separate foundation. Due to the rigid microscope design, no additional internal damping stage for the microscope inside the cryostat is needed.

Magnet cryostat

The design of the magnet cryostat is guided by the demand for a strong magnetic field, combined with easy and fast access to the microscope and reliable operation. This is best attained, if the microscope in the center of the magnet is located in the transfer level of the UHV system. A cross section of the cryostat chamber is shown in Fig. 3.138. The magnet cryostat [7] fits into a DN 450 COF flange on top of the cryostat chamber [8]. A separate microscope chamber with all necessary

feedthroughs for the operation of the microscope is connected via a DN 250 flange at the bottom. Viewports offer optical access to the microscope under various angles, when the shutters are opened, thus facilitating coarse approach and exchange of tip and sample with a wobble stick. The cryostat consists of two tanks for cooling liquids. The outer tank serves as a radiation shield and is filled with up to 35.5 l of liquid nitrogen. It is mechanically decoupled from the vacuum chamber by viton stacks and edge welded bellows. A pump line can be added for solidifying the nitrogen in order to minimize perturbations due to the boiling refrigerant. Below the LN_2 tank, a gold coated copper radiation shield is mounted, which encloses the lower part of the LHe tank. The inner tank includes the magnet and is filled with up to 33.5 l of LHe which yields a hold time of 48 h. The current feedthroughs for the magnet, which are capable of 100 A, run through the tank and the exhaust dome and are thus directly cooled by the evaporating cryogen. Additionally, they may be disconnected inside the tank and retracted during persistent operation of the magnet. Two 50 W resistive heaters with PT100 temperature sensors are mounted on the bottom of the LHe tank. They are used to evaporate any remaining cryogen after the magnet has been precooled with liquid nitrogen, and to assist the bakeout procedure. Moreover, it enables variable temperature measurements up to a certain degree by heating the large thermal mass of the magnet. Two additional PT100 temperature sensors are fixed to the side face of the magnet to measure the magnet temperature during bakeout and cooling. The magnet [9] has a split-coil geometry with a central bore of 60 mm in diameter, which hosts the microscope. With its superconducting NbTi coils, it produces a maximum field of $\mu_0 H = 5$ T vertical, which is perpendicular to the sample surface. The homogeneity is specified to be better than 10^{-3} within a 10 mm diameter at the sample location.

In order to exchange tip and sample without moving the microscope, there has to be an access from the side through the radiation shield and the LHe tank to the microscope in the center of the magnet. This is provided by an 80° cutaway with a height of at least 40 mm between the two magnet coils. The cutaway can be closed by two copper shutters, which are moved simultaneously by a linear motion feedthrough operated from the top of the cryostat. They are thermally connected with stranded copper wires to the LHe and LN_2 tank, respectively, and gold coated to reduce thermal radiation.

Thermal anchoring, electrical and optical connections

To reach a low final temperature and a short cooling time, the thermal conductivity from the microscope to the cryogen has to be maximized, and the thermal load from room temperature has to be minimized. Heat transfer through the electrical connections and pressed contacts has to be considered as well as thermal radiation [10]. Figure 3.138 shows a photo of the microscope and its thermal anchoring on the left side. In the lower part, the microscope chamber is visible, which contains the side flanges for all feedthroughs of the electrical connections and the fiber. The copper parts with the

microscope body on top are connected to the LN_2 radiation shield and the LHe tank. Up to now, no UHV compatible detachable fiber connections are available. Therefore, the whole setup has to be mounted from below into the bore of the cryostat. During insertion, the microscope chamber is held by a cardanic suspension, which allows to adjust the microscope position very carefully with respect to the central bore of the magnet. This procedure is needed, because the diameter of the microscope (58 mm) is only 2 mm less than that of the magnet bore. After insertion, the screws, which connect the copper parts to the microscope chamber, are removed through a CF 150 flange at the bottom (see left panel of Fig. 3.138). The microscope is screwed to an oxygen-free high conductivity copper cylinder with a cylindrical ground plate, which in turn is screwed to the bottom of the LHe tank. Another copper plate is screwed to the bottom of the LN_2 radiation shield. To enhance the reliability of the connections and to achieve higher contact pressures, heli coils are used in all copper threads of the LHe tank and the LN_2 radiation shield. To improve the thermal conductivity through the pressed contacts, the copper parts are gold coated [11, 12]. Moreover, the gold coating prevents oxidation of the copper parts and reduces thermal radiation. The copper cylinder serves as a thermal anchoring of the electrical wires as well, which are glued to it over a length of 10 mm. Below and above these glue points, there are two rings of electrical connectors. Thus it is possible to detach the microscope from the copper base without destroying the thermal anchoring of the wires. Further anchoring is not useful due to the small distance between LN_2 and LHe temperature parts. All electrical connections between room temperature and LHe temperature are made out of manganin wires (0.1 mm diameter) because of their reduced thermal conductivity compared to copper. Corresponding wires such as tip-sample bias are twisted. For electrical shielding and protection, they are guided through the two cylindrical copper plates in copper beryllium meshes towards the feedthrough flanges at the microscope chamber. The optical fiber for the detection of cantilever displacement is directed through the center of the microscope and the copper base. It ends outside the chamber after passing a small bore in which it is glued with UHV compatible epoxy resin. With LHe cooling and closed shutters, a temperature of 5.2 K is routinely achieved. Main heat sources are the nearly 50 wires needed to operate the microscope, and thermal radiation from the shutters, which do not have exactly the same temperature as the refrigerant. With opened shutters during tip or sample exchange, the temperature usually stays below 25 K and returns to thermal equilibrium within 1 h. Initial cooling from room temperature to 78 K takes 12 h, and 4 h from 78 K down to 5.2 K, due to the large thermal mass of the magnet. In the microscope body, only copper wires (0.127 mm diameter) are used. All metallic parts are grounded. Permanent electrical connections are glued with silver epoxy or soldered. Removable connections use gold coated integrated circuit (IC) pins. The temperature is monitored by a Cernox temperature sensor [14] attached to the microscope body next to the sample position. Magnetic fields change the temperature reading of this sensor type by less than 0.2%.

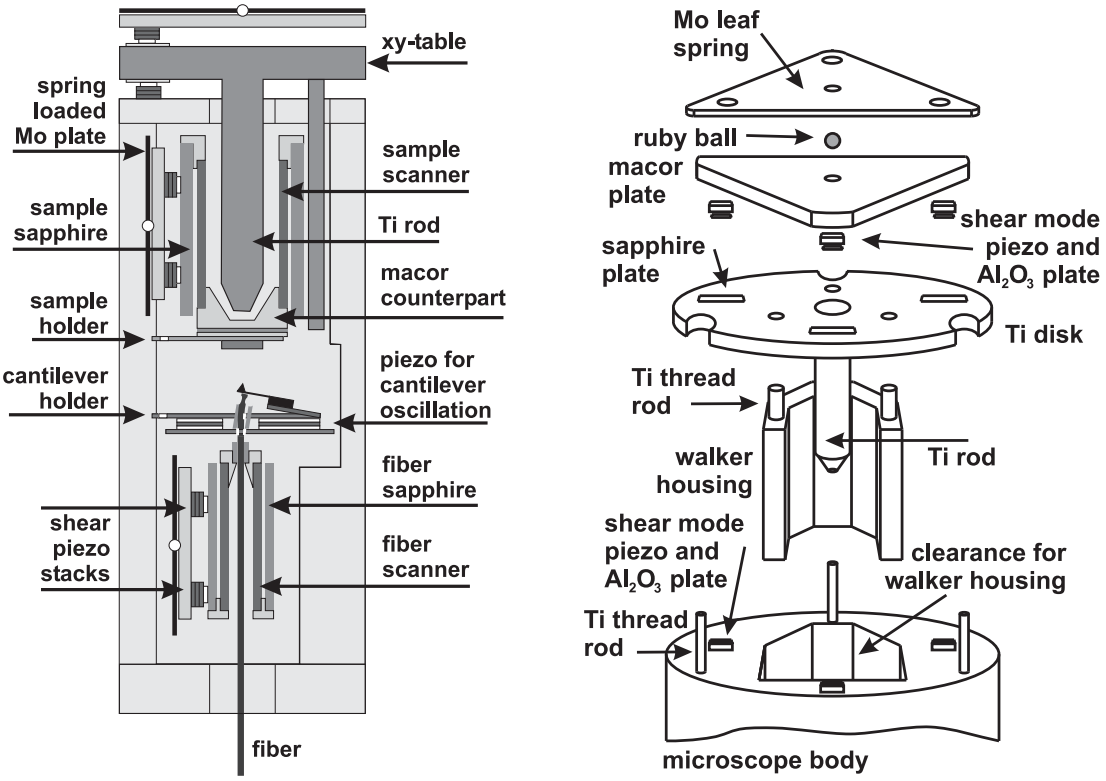

Figure 3.139: Left panel: Cross section along the mirror plane of the microscope. The exchangable sample stage with the xy-table is on top, the cantilever stage in the middle and the fiber on the bottom. Right panel: Schematic view of the xy-table. The walker housing is screwed to the titanium disk. The molybdenum leaf spring is held by screw-nuts on the thread rods and determines the load on the titanium disk via the macor plate and the ruby ball. The xy-table with the walker housing can easiliy be removed in order to change the scanner.

Microscope design

The operation of a microscope in UHV, at low temperatures, and in strong magnetic fields requires careful consideration of the possible materials. For UHV compatibility, a low vapor pressure and bake-out temperatures up to 150°C are necessary. For low temperature applications, one has to regard the matching of thermal contraction coefficients of different materials to avoid mechanical stress during cool down. In particular, strong magnetic fields and MFM experiments require nonmagnetic components. These properties are almost perfectly fulfilled by the used combination of the piezoelectric material lead zirconate titanate (PZT), macor, and titanium [15]. A schematic cross section of the microscope is given on the left panel in Fig. 3.139. To keep the microscope as rigid as possible, the main body is made out of one piece of macor. It has a cylindrical shape of 125 mm in length and 58 mm in diameter. The fixed cantilever

stage is located in the middle of the macor body. The upper part hosts the approach mechanism for the sample. The lower part of the microscope contains the mechanism for the detection of cantilever deflections. We chose a fiber optic interferometer based on the setup given in Ref. [16], because it allows a very compact and rigid design and is, at the same time, a very sensitive method. Light emitted by a laser diode is guided through an optical single mode fiber and is reflected into the fiber from the backside of the cantilever. This allows to keep the laser diode, the photodetector, and the amplification circuit at room temperature and outside of the vacuum chamber. In the present stage, the fiber end is coated with a dielectric material to match the reflectivity of the cantilever back side, i.e., about 30 % for Si at a wavelength of 780 nm. As a result, the interferometer resembles more a Fabry-Perot than the original simple two beam set up. Since the deflection signal is transported by light to the photodetector, it is not affected by any electromagnetic noise sources like stray fields from the electrical signals used to operate the microscope. As the wavelength of the laser light is known, one has a direct calibration of the cantilever deflection, which is necessary for quantitative measurements. The well matched thermal expansion coefficient of the used microscope materials and the symmetry of the microscope along the cantilever axis avoid a lateral misalignment between fiber and cantilever during the cool down process. Therefore, only the separation between cantilever and fiber has to be readjusted. Coarse positioning is provided by a walker step motor as described below. Fine adjustment to the most sensitive point of the interferometer is realized by means of a piezoelectric scanner that holds the very end of the fiber and allows a vertical displacement of $\pm$400 nm at low temperatures. The fiber scanner also allows for a small lateral adjustment, but due to our reliable ex situ cantilever positioning and the symmetric microscope design, this facility is usually not needed. Cantilevers are glued on commercially available cantilever holders [6] and are inserted into a fixed pick-up stage. This stage is mounted on top of a wobble piezo providing the oscillation of the cantilever in the dynamic force microscopy mode. The above mentioned ex situ cantilever positioning mechanism is realized as follows: Before inserting the microscope into the cryostat, a cantilever is directly glued onto and aligned on a cantilever holder, which is already inserted into the pick-up stage in the microscope. This well aligned cantilever is used as a master in a second identical stage. From this master cantilever, an alignment mask is made, and other cantilevers can be glued ex situ by means of an optical microscope. Samples are mounted on a small titanium plate, which can be inserted into the sample holder using a wobble stick. It is held on the sample scanner by two springs. A grounded layer of conducting glue prevents crosstalk between the scan voltage and the tip-sample bias. The sample scanner as well as the fiber scanner has gold electrodes and is made of EBL 4 piezoelectric material [17]. This type is reported to have small hysteresis and creep effects. The dimensions of the sample scanner are 6.35 mm in diameter and 58 mm in length. Its lowest resonance frequency is about 700 Hz, which approximately matches the predicted value calculated from Ref. [18]. Coarse approach of sample and fiber towards the cantilever is realized by

two single-axis piezoelectric step motors based on the walker principle [19, 20]. Fiber and sample scanner are glued into the bore of a sapphire prism each, which is held by six stacks of piezo plates. For sample exchange, the sample walker is fully retracted. At the end position, the conical end of a titanium rod fits precisely into a counterpart at the backside of the sample holder, thus absorbing the force applied to the scanner during sample exchange. For lateral coarse positioning of the sample relative to the tip, an xy-table is implemented in the microscope (right panel of Fig. 3.139). The walker housing with the sample coarse approach mechanism is mounted on a titanium disk, which can be moved by six piezo stacks. Three stacks are glued on a triangular macor plate, while the other three are glued on the top of the main microscope body. Each piezo stack consists of four shear piezos: two for the x and two for the y direction. For the two axis lateral movement of the titanium disk, the walker principle is used, analogous to the single axis movement described above. The load on the disk, and thereby the step width of the walker, can be adjusted by a molybdenum leaf spring, which presses onto the triangular macor plate via a ruby ball and is held by three screws on thread rods sticking out of the main body. Due to the high maximum pressures allowed by this design without preventing an xy motion, the microscope keeps its overall stability. The xy-table can be moved within a 4×4 mm^2 area. Lateral calibration of the scanner was accomplished by means of a silicon test grid and yields scan ranges of 18×25 μm^2 at room temperature, $15.5 \times 18 \mu m^2$ at 78 K, and 7.5×7.5 μm^2 at 5.2 K with a voltage of ± 130 V applied to the piezo electrodes. Additionally, a compact disk, the fiber optic interferometer, and monoatomic steps on a NiO surface are used for z calibration.

Resolution and noise

Both atomic and magnetic force microscopy mode benefit from the enhanced sensitivity of cantilever frequency detection due to their much higher quality factor in vacuum. All images presented in this section show raw data and are recorded in the dynamic mode with the frequency modulation (FM) technique described in Ref. [35]. The thermal limit of the detectable frequency shift Δf is given by

$$\langle (\delta f)^2 \rangle = \frac{f_0 k_B T B}{\pi k_L Q A^2}, \tag{3.41}$$

where f_0 denotes the resonance frequency of the free cantilever, c_z the spring constant, Q the mechanical quality factor, k_B the Boltzmann constant, T the temperature, B the measurement bandwidth, and A the oscillation amplitude. At room temperature, we typically achieve a frequency resolution of 40 mHz$_{rms}$ ($A = 5$ nm, bandwidth $B = 100$ Hz) matching the thermodynamical limit. At 5.2 K, the rms noise δf amounts to 30 mHz$_{rms}$, which exceeds the thermodynamical limit by a factor of 5.8. In both cases, we find that δf is proportional to $1/A$ as expected. The main contribution to the noise at low temperatures is given by the preamplifier electronics (e.g., shot noise in the photodiode) and scales with the square root of optical power hitting the photodiode.

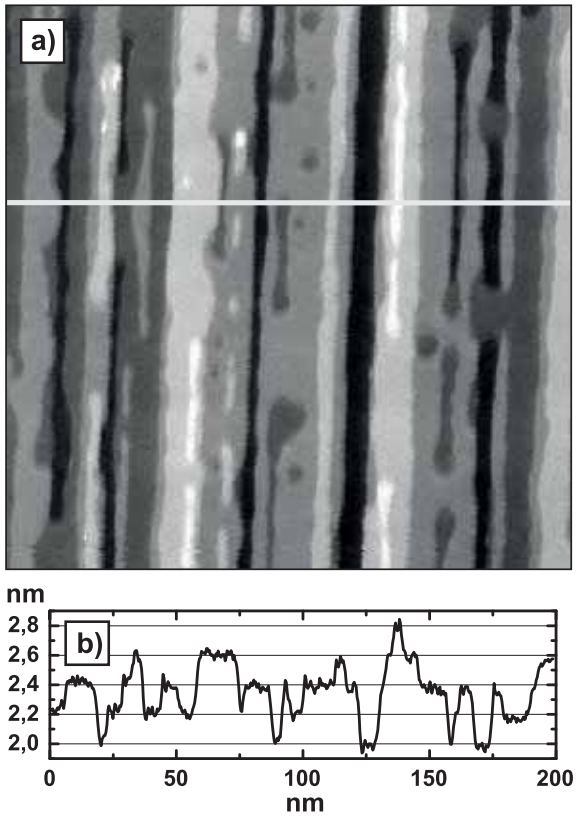

Figure 3.140: (a) Topographic image of the (001) surface of an *in-situ* cleaved and annealed NiO single crystal. Data aquisition has been performed after solidifying the LN_2 in the radiation shield. Monoatomic steps (208 pm) are clearly resolved. (b) Display of a single scan line of image (a). Parameters: Scan area 200×200 nm^2, T = 5.5 K, f_0 = 192 kHz, $\Delta f = -10$ Hz, $A = \pm 5$ nm, $U_{bias} = 1.1$ V, scan speed 222 nm/s, bandwidth 300 Hz.

Therefore, an increase of the oscillation amplitude, laser power, or backreflection from fiber and cantilever would improve the signal-to-noise ratio.

For imaging, commercially available silicon cantilevers with resonance frequencies of 183-203 kHz and force constants of 40-57 N/m are used. To remove the native oxide layer, they have been sputtered with argon ions. During measurements, the amplitude of the self-oscillating cantilever is kept constant by means of an amplitude regulator. The z-resolution of the instrument is demonstrated by imaging the (001) surface of an in situ cleaved NiO single crystal. The image displayed in Fig. 3.140 has been acquired at 5.2 K while pumping on the LN_2 tank, which effectively removes stochastic noise due to bubbling nitrogen. The measured step heights correspond to the half of the lattice constant $a = 417$ pm. Within each terrace, we observed a z-noise of 22 pm$_{rms}$. Using a smaller scanner, atomic resolution including the observation of defects is possible on the flat terraces.

Magnetic imaging is performed by coating that side of the tip pyramid, which

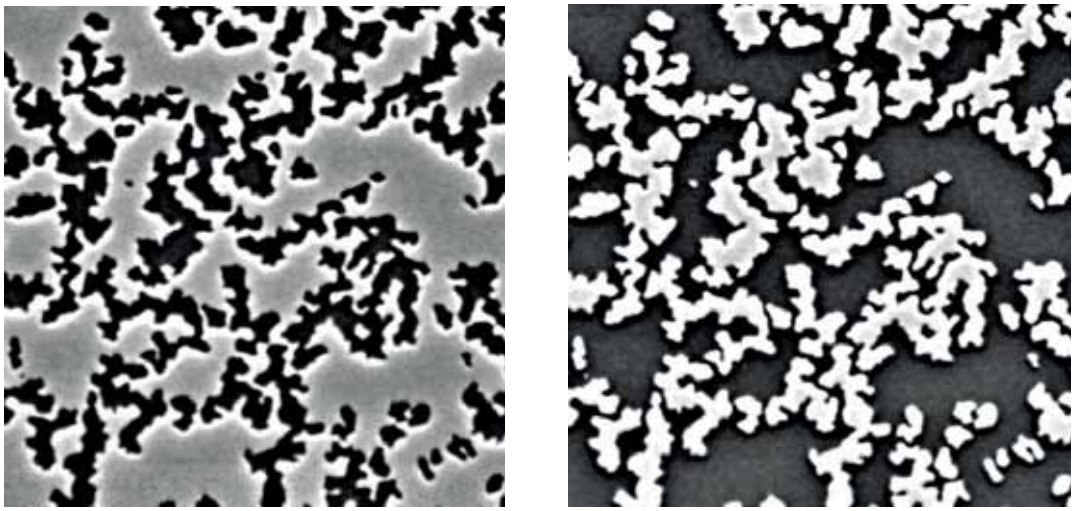

Figure 3.141: MFM image of a CoPt multilayer sample. Both images are aquired at zero field and at the same location. The image on the right is recorded after applying 50 mT in order to reverse the tip magnetization. The domain structure remains unchanged, but the contrast is inverted. Parameters: Scan area 7×7 μm^2, $T = 5.5$ K, $f_0 = 201$ kHz, $A = \pm 5$ nm, $h = 30$ nm, $U_{bias} = 20$ mV, grey scale 400 mHz, scan speed 5 μm/s, bandwidth 100 Hz, $\delta f_{noise} = 42$ mHz$_{rms}$.

faces the cantilever substrate, with a ferromagnetic material like iron. This results in a thin film of prolonged triangular shape with a magnetization along its symmetry axis. We found that such tips are nearly exclusively sensitive to the out-of-plane component of the sample stray field and exhibit a vanishing small in-plane component. The appropriate thickness of the iron film depends on the magnetic characteristics of the sample and should be a compromise between signal strength and minimized disturbance of the sample magnetization. For MFM measurements, we apply the plane-subtraction mode: In the topographic mode (feedback on), the sample slope is compensated by adding appropriate voltages to the z-electrode of the sample scanner. Thereafter, the feedback is switched off, and the tip is retracted from the sample surface to a scanning height h of typically 20-30 nm. A MFM image is obtained by scanning in this plane and recording the frequency shift, which is in this case dominated by long range forces of electrostatic or magnetostatic nature. The electrostatic contribution can be minimized by applying a bias voltage to compensate for the contact potential difference.

An MFM image of a CoPt multilayer sample with a strong perpendicular anisotropy is shown in Fig. 3.141. Both images are taken at the same tip-sample separation, with a bias voltage of 20 mV, and at zero magnetic field. The tip was coated with 5 nm iron on the side face towards the cantilever and 2.4 nm on the two outer sides of the tip pyramid. The CoPt sample has a much higher coercive field than the iron film on the

tip. So it was possible to reverse the magnetization of the tip by applying a vertical magnetic field of 50 mT without changing the domain structure of the sample. This causes an inversion of contrast in the MFM image. The stability of the instrument and the use of nonmagnetic materials allows ramping the magnetic field and imaging simultaneously for more than 20 h at LHe temperature without readjustment of the tip-sample or fiber-cantilever distance. Thus it is possible to record the domain evolution in a movielike manner [21]. Several examples of MFM studies performed in external fields on ferromagnetic thin films and high temperature superconductors are described in sections 3.2.12-3.2.14.

References

[1] W. Allers, A. Schwarz, U. D. Schwarz, and R. Wiesendanger, Rev. Sci. Instrum. **69**, 221 (1998).

[2] F. J. Giessibl, C. Gerber, and G. Binnig, J. Vac. Sci. Technol. B **9**, 984 (1991).

[3] H. J. Hug, B. Stiefel, P. J. A. van Schendel, A. Moser, S. Martin, and H. J. Güntherodt, Rev. Sci. Instrum. **70**, 3625 (1999).

[4] N. Suehira, Y. Tomiyoshi, Y. Sugawara, and S. Morita, Rev. Sci. Instrum. **72**, 2971 (2001).

[5] A. Schwarz, U. D. Schwarz, S. Langkat, H. Hölscher, W. Allers, and R. Wiesendanger, Appl. Surf. Sci. **188**, 245 (2002).

[6] Omicron NanoTechnology GmbH, Taunusstein, Germany.

[7] CryoVac, Troisdorf, Germany.

[8] Vacuum Generators, Hastings, UK.

[9] American Magnetics, Inc., Oak Ridge, TN.

[10] G. K. White, Experimental Techniques in Low-Temperature Physics (Oxford University Press, Oxford, 1979).

[11] R. Berman, J. Appl. Phys. **27**, 318 (1956).

[12] R. Berman and C. F. Mate, Nature **182**, 1661 (1958).

[13] T. R. Albrecht, P. Grütter, D. Horne, and D. Rugar, J. Appl. Phys. **69**, 668 (1991).

[14] Lake Shore Cryotronics, Inc., Westerville, Ohio, USA.

[15] G. Nunes, Jr. and D. Williams, J. Vac. Sci. Technol. B **13**, 1063 (1995).

[16] D. Rugar, H. J. Mamin, and P. Güthner, Appl. Phys. Lett. **55**, 2588 (1989).

[17] Staveley Sensors Inc., East Hartford, CT. EBL 4 denotes industry type PZT-8.

[18] M. E. Taylor, Rev. Sci. Instrum. **64**, 154 (1993).

[19] S. H. Pan, S. Behler, M. Bernasconi, and H. J. Güntherodt, Bull. Am. Phys. Soc. **37**, 167 (1992).

[20] C. Wittneven, R. Dombrowski, S. H. Pan, and R. Wiesendanger, Rev. Sci. Instrum. **68**, 3806 (1997).

[21] A. Schwarz, M. Liebmann, U. Kaiser, R. Wiesendanger, T. W. Noh, and D. W. Kim, Phys. Rev. Lett. **92**, 077206 (2004).

[22] C. B. Prater, M. R. Wilson, J. Garnaes, J. Massie, V. B. Elings, and P. K. Hansma, J. Vac. Sci. Technol. B **9**, 989 (1991).

[23] K. Nakamoto, C. B. Mooney, and M. Iwatsuki, Rev. Sci. Instrum. **72**, 1445 (2001).

[24] Q. Dai, R. Vollmer, R. W. Carpick, D. F. Ogletree, and M. Salmeron, Rev.Sci. Instrum. **66**, 5266 (1995).

[25] K. Suzuki, M. Iwatsuki, S. Kitamura, and C. B. Mooney, Jpn. J. Appl. Phys., Part 1 **39**, 3750 (2000).

[26] M. D. Kirk, T. R. Albrecht, and C. F. Quate, Rev. Sci. Instrum. **59**, 833 (1988).

[27] T. R. Albrecht, P. Grütter, D. Rugar, and D. P. E. Smith, Ultramicroscopy **42-44**, 1638 (1992).

[28] H. J. Hug, A. Moser, T. Jung, O. Fritz, A. Wadas, I. Parashikov, and H. J. Güntherodt, Rev. Sci. Instrum. **64**, 2920 (1993).

[29] C. W. Yuan, E. Batalla, M. Zacher, A. L. de Lozanne, M. D. Kirk, and M. Tortonese, Appl. Phys. Lett. **65**, 1308 (1994).

[30] R. Euler, U. Memmert, and U. Hartmann, Rev. Sci. Instrum. **68**, 1776 (1997).

[31] D. V. Pelekhov, J. B. Becker, and G. Nunes, Jr., Rev. Sci. Instrum. **70**, 114 (1999).

[32] R. E. Thomson, Rev. Sci. Instrum. **70**, 3369 (1999).

[33] J. Rychen, T. Ihn, P. Studerus, A. Herrmann, and K. Ensslin, Rev. Sci. Instrum. **70**, 2765 (1999).

[34] W. Allers, A. Schwarz, U.D. Schwarz, and R. Wiesendanger, Rev. Sci. Instrum. **69**, 221 (1998).

[35] T. R. Albrecht, P. Grütter, D. Horne, and D. Rugar, J. Appl. Phys. **69**, 668 (1991).

Chapter 4

Collaborations

4.1 Research Partners

- Institute of Applied Physics and MARCH, University of Hamburg:
  Prof. Dr. W. Hansen, Jr.-Prof. Dr. S. Heinze, Prof. Dr. D.Heitmann,
  Prof. Dr. J. Kötzler, Prof. Dr. U. Merkt, Prof. Dr. H.P. Oepen

- I. Institute of Theoretical Physics, University of Hamburg:
  Prof. Dr. A. Lichtenstein, Prof. Dr. D. Pfannkuche

- Institute of Experimental Physics, University of Hamburg:
  Prof. Dr. R. L. Johnson

- HASYLAB / DESY, Hamburg:
  Prof. Dr. G. Materlik

- Institute for Physical Chemistry, University of Hamburg:
  Prof. H. Weller

- Institute of Mineralogy, University of Hamburg:
  Prof. Dr. U. Bismayer

- Department of Computer Science, University of Hamburg:
  Prof. Dr. H. S. Stiehl, Prof. Dr. J. Zhang

- HGF-Forschungszentrum GKSS:
  Prof. Dr. A. Schreyer

- University of Kiel:
  Prof. Dr. L. Kipp, Prof. Dr. W. Schattke, Prof. Dr. M. Skibowski

- University of Münster:
  Prof. Dr. H. Fuchs

- HGF-Forschungszentrum Jülich:
  Prof. Dr. S. Blügel
- IFW Dresden:
  Prof. Dr. M. Richter
- TU Delft, The Netherlands:
  Prof. Dr. C. Dekker
- Radboud University Nijmegen, The Netherlands:
  Prof. Dr. S. Speller
- IEMN / ISEN, Lille, France:
  Prof. Dr. Ch. Delerue
- IMEC, Leuven, Belgium:
  Prof. Dr. W. Vandervorst
- University of Reijkjavik, Iceland:
  Prof. Dr. V. Gudmundsson
- Seoul National University, South Korea:
  Prof. Dr. Z. G. Khim, Prof. Dr. D. H. Kim, Prof. Dr. T. W. Noh, Dr. U. H. Pi

4.2 Industrial Partners

- Beiersdorf, Hamburg
- Omicron Nanotechnology GmbH, Taunusstein, Germany
- Oxford Instruments, Cambridge, U.K.

Chapter 5

Theses

5.1 Diploma Theses

1. Lilli Sacharow (2002):
   Berechnung der elektronischen Struktur der reinen InAs(110)- und der Fe/InAs(110)-Oberfläche

2. Focko Meier (2002)::
   Aufbau eines temperaturvariablen MOKE-Systems zur Charakterisierung ultradünner Schichten im Ultrahochvakuum

3. Martin von Sprekelsen (2002):
   Implementierung eines Hochgeschwindigkeitsmodus für die Rasterkapazitätsspektroskopie

4. Uwe Kaiser (2002):
   Magnetkraftmikroskopie im Ultrahochvakuum, bei tiefen Temperaturen und im Magnetfeld

5. Luis Berbil-Bautista (2002):
   Structure and electronic properties of thin metallic films: STM and STS investigations on 5f systems

6. Stefan Krause (2003):
   Untersuchung der temperaturabhängigen Magnetisierungsstruktur an der Cr(001)-Oberfläche mittels spinpolarisierter Rastertunnelspektroskopie

7. Stefan Kuck (2004):
   Aufbau eines Rastertunnelmikroskops im Ultrahochvakuum bei variablen Temperaturen

8. Timo Behnke (2004):
   Rasterkraftmikroskopie an einwandigen Kohlenstoff-Nanoröhren

9. Nico Plock (2004):
   Optimierung eines Tieftemperatur-Rasterkraftmikroskops zur Messung magnetischer Austauschkräfte auf der NiO(001)-Oberfläche

10. Torge Mashoff (2004):
    Aufbau eines UHV-Rastertunnelmikroskops mit X-Y-Verschiebetisch für den Einsatz bei tiefen Temperaturen und im Magnetfeld

11. Oliver Lemcke (2004):
    Simulation von Temperatureffekten in magnetischen Nanostrukturen

12. Felix Marczinowski (2004):
    Untersuchung des Wachstums und der elektronischen Struktur ultradünner Chromschichten auf Iridium(111)

5.2 Ph. D. Theses

1. André Kubetzka (2002):
   Spinpolarisierte Rastertunnelmikroskopie an magnetischen Nanostrukturen: Fe/W(110)

2. Shenja Mirko Langkat (2002):
   Tieftemperatur-Rasterkraftmikroskopie auf antiferromagnetischen Übergangsmetalloxiden

3. Marcus Liebmann (2003):
   Tieftemperatur-Magnetkraftmikroskopie an dünnen Manganperowskit-Filmen und Hochtemperatursupraleiter-Einkristallen

4. Jens Wiebe (2003):
   Aufbau einer 300mK-Ultrahochvakuum-Rastertunnelmikroskopie-Anlage mit 14T-Magnet und Untersuchung eines stark ungeordneten zweidimensionalen Elektronensystems

5. André Wachowiak (2003):
   Aufbau einer 300mK-Ultrahochvakuum-Rastertunnelmikroskopie-Anlage mit 14 Tesla Magnet und spinpolarisierte Rastertunnelspektroskopie an ferromagnetischen Fe-Inseln

6. Jan Klijn (2003):
   Local density of states of the adsorbate-induced two-dimensional electron system studied at zero and strong magnetic fields

7. Robert Ravlić (2003):
   Magnetische Studien der Cr(001)-Oberfläche und des Fe/Cr(001)-Systems mittels spinpolarisierter Rastertunnelspektroskopie

8. Jörg-Christian Wolfgang Meyer (2003):
Tieftemperatur-Rastertunnelspektroskopie an niederdimensionalen Halbleiter-Elektronensystemen

9. Theophilos Maltezopoulos (2004):
Wave-Function mapping of electronic states in nanostructures by scanning tunneling spectroscopy

10. Kirsten von Bergmann (2004):
Iron nanostructures studied by spin-polarised scanning tunneling microscopy

11. Tobias Richter (2004):
In Vitro-Hydratationsdynamik der menschlichen Hautbarriere: Eine Tieftemperatur-REM und TEM Studie von Wassereffekten im Stratum Corneum

5.3 Habilitation Theses

1. Markus Morgenstern (2002):
Probing the Local Density of States of Dilute Electron Systems in Different Dimensions

2. Matthias Bode (2002):
Spin-polarized scanning tunneling microscopy

Chapter 6

Scientific Publications

6.1 Books

1. S. Morita, R. Wiesendanger, and E. Meyer (eds.), Springer Berlin, Heidelberg 2002: *Non-Contact Atomic Force Microscopy.*

2. H. Bienlein and R. Wiesendanger, Teubner, Stuttgart 2003: *Einführung in die Struktur der Materie.*

3. R. Wiesendanger (ed.), Springer, Berlin 2003: *Proc. Workshop on Highlights of Research in Nano-Scale Analysis in Germany.*

4. H. Oechsner, J. Kirschner, and R. Wiesendanger (eds.), Springer, Berlin 2003: *Proc. 1st DVG-Symposium.*

5. A Benninghoven, J.-J. Pireaux, R. Wiesendanger, and K. Jousten Elsevier 2004: *Proc. 8th European Vacuum Congress, Applied Surface Science Vol. 235 (1-2).*

6.2 Book Contributions and Review Articles

1. W. Allers, A. Schwarz, U. D. Schwarz, in Noncontact Atomic Force Microscopy, eds. S. Morita, R. Wiesendanger, and E. Meyer, Springer-Verlag, Berlin Heidelberg New York (2002), 233: *Low-Temperature Measurements: Principles, Instrumentation, and Application.*

2. M. Bode, Rep. Prog. Phys. **66**, 523 (2003), *Spin-polarized scanning tunneling microscopy.*

3. M. Bode and R. Wiesendanger, in: Magnetic Microscopy of Nanostructures (eds. H. Hopster and H. P. Oepen), Springer Berlin, Heidelberg (2004): *Spin-Polarized Scanning Tunneling Spectroscopy.*

4. E. Y. Vedmedenko, K. H. J. Buschow, R. W. Cahn, M. C. Flemings, B. Ilschner, E. J. Kramer, S. Mahajan, and P. Veyssière (Eds.) (2004): *Quasicrystals: Magnetism in Encyclopedia of Materials.*

5. M. Morgenstern, A. Schwarz, and U. D. Schwarz, Springer Nanotechnology Handbook (ed. B. Bushan), Springer Verlag (2004): *Low Temperature Scanning Probe Microscopy.*

6. M. Morgenstern, Physik Journal (8/2004) S. 83: *Der direkte Blick auf Elektronensysteme.*

6.3 Original Articles

1. H. Hölscher, B. Gotsmann, W. Allers, U. D. Schwarz, H. Fuchs, and R. Wiesendanger, Phys. Rev. Lett. **88**, 019601 (2002): *Comment on "Damping mechanism in dynamic force microscopy".*

2. A. Kubetzka, M. Bode, O. Pietzsch, and R. Wiesendanger, Phys. Rev. Lett. **88**, 057201 (2002): *Spin-Polarized Scanning Tunneling Microscopy with Antiferromagnetic Probe Tips.*

3. M. Kleiber, M. Bode, R. Ravlić, N. Tezuka, and R. Wiesendanger, J. Magn. Magn. Mater. **240**, 64 (2002): *Magnetic properties of the Cr(001) surface studied by spin-polarized scanning tunneling spectroscopy.*

4. A. Schwarz, U. D. Schwarz, S. Langkat, H. Hölscher, W. Allers, and R. Wiesendanger, Appl. Surf. Sci. **188**, 245 (2002): *Dynamic force microscopy with atomic resolution at low temperatures.*

5. M. Morgenstern, J. Wiebe, A. Wachowiak, M. Getzlaff, J. Klijn, L. Plucinks, R. L. Johnson, and R. Wiesendanger, Phys. Rev. B **65**, 155325 (2002): *Co on p-InAs(110): An island induced two-dimensional electron system consisting of electron droplets.*

6. M. Bode, A. Kubetzka, O. Pietzsch, and R. Wiesendanger, Surf. Sci. **514**, 135 (2002): *Spin-resolved spectro-microscopy of magnetic nanowire arrays.*

7. R. Wiesendanger, Vacuum **65**, 235 (2002): *Nano-scale studies of quantum phenomena by scanning probe spectroscopy.*

8. M. Bode, S. Heinze, A. Kubetzka, O. Pietzsch, M. Hennefarth, M. Getzlaff, R. Wiesendanger, X. Nie, G. Bihlmayer, and S. Blügel, Phys. Rev. B **66**, 014425 (2002): *Structural, electronic, and magnetic properties of a Mn monolayer on W(110).*

9. M. Morgenstern, J. Klijn, Chr. Meyer, M. Getzlaff, R. Adelung, K. Roßnagel, L. Kipp, M. Skibowski, and R. Wiesendanger, Phys. Rev. Lett. **89**, 136806 (2002): *Direct comparison of potential landscape and resulting local density of states of a disordered two-dimensional electron system.*

10. A. Wachowiak, J. Wiebe, M. Bode, O. Pietzsch, M. Morgenstern, and R. Wiesendanger, Science **298**, 577 (2002): *Direct Observation of Internal Spin-Structure of Magnetic Vortex Cores.*

11. M. Liebmann, A. Schwarz, S. M. Langkat, and R. Wiesendanger, Rev. Sci. Instrum. **73**, 3508 (2002): *A low-temperature ultrahigh vacuum scanning force microscope with a split-coil magnet.*

12. M. Morgenstern, V. Gudmundsson, Chr. Wittneven, R. Dombrowski, and R. Wiesendanger, J. Vac. Sci. & Technol. A **20**, 2032 (2002): *The influence of potential fluctuations on Landau quantization and spin splitting studied by Low Temperature Scanning Tunneling Spectroscopy on InAs(110).*

13. M. Bode, S. Heinze, A. Kubetzka, O. Pietzsch, X. Nie, G. Bihlmayer, S. Blügel, and R. Wiesendanger, Phys. Rev. Lett. **89**, 237205 (2002): *Magnetization-direction dependent local electronic structure probed by scanning tunneling spectroscopy.*

14. M. Morgenstern, D. Haude, J. Klijn, and R. Wiesendanger, Phys. Rev. B **66**, 121102 (2002): *Coulomb pseudogap caused by partial localization of a three dimensional electron system in the extreme quantum limit.*

15. H. Hölscher, S. M. Langkat, A. Schwarz, and R. Wiesendanger, Appl. Phys. Lett. **81**, 4428 (2002): *Measurement of three-dimensional force fields with atomic resolution using dynamic force spectroscopy.*

16. G. Kuri, Th. Schmidt, V. Hagen, G. Materlik, R. Wiesendanger, and J. Falta, J. Vac. Sci. & Technol. A **20**, 1997 (2002): *Subsurface interstitials as promoters of three-dimensional growth on Ti on Si(111): An X-ray standing wave, X-ray photoelectron spectroscopy, and atomic force microscopy investigation.*

17. A. Kubetzka, O. Pietzsch, M. Bode, and R. Wiesendanger, Phys. Rev. B **67**, 020401 (2003): *Spin-polarized scanning tunneling microscopy study of 360° walls in an external magnetic field.*

18. M. Morgenstern, D. Haude, J. Klijn, Chr. Meyer, L. Sacharow, S. Heinze, S. Blügel, and R. Wiesendanger, Physica E **16**, 121 (2003): *Comparing the local density of states of three- and two-dimensional electron systems by low-temperature scanning tunneling spectroscopy.*

19. M. Bode, A. Kubetzka, S. Heinze, O. Pietzsch, R. Wiesendanger, M. Heide, X. Nie, G. Bihlmayer, and S. Blügel, J. Phys.: Condens. Matter **15**, S679 (2003): *Spin-orbit induced local band structure variations revealed by scanning tunneling spectroscopy.*

20. M. Bartels, V. Hagen, M. Burianek, M. Getzlaff, U. Bismayer, and R. Wiesendanger, J. Phys.: Condens. Matter **15**, 957 (2003): *Impurity-induced resistivity of ferroelastic domain walls in doped lead phosphate.*

21. M. Morgenstern, J. Klijn, Chr. Meyer, and R. Wiesendanger, Phys. Rev. Lett. **90**, 056804 (2003): *Real-space observation of drift states in a two-dimensional electron system at high magnetic fields.*

22. S. M. Langkat, H. Hölscher, A. Schwarz, and R. Wiesendanger, Surf. Sci. **527**, 12 (2003): *Determination of site specific interatomic forces between an iron coated tip and the NiO(001) surface by force field spectroscopy.*

23. A. Kubetzka, O. Pietzsch, M. Bode, and R. Wiesendanger, Appl. Phys. A **76**, 873 (2003): *Determining the spin-polarization of surfaces by spin-polarized scanning tunneling spectroscopy.*

24. J. H. Müller, U. D. Schwarz, R. Wepf, and R. Wiesendanger, Appl. Phys. A **76**, 893 (2003): *A cryogenic scanning force microscope for the characterization of frozen biological samples.*

25. R. Ravlić, M. Bode, A. Kubetzka, and R. Wiesendanger, Phys. Rev. B **67**, 174411 (2003): *Correlation of dislocation and domain structure of Cr(001) investigated by spin-polarized scanning tunneling microscopy.*

26. M. Liebmann, U. Kaiser, A. Schwarz, R. Wiesendanger, U. H. Pi, T. W. Noh, Z. G. Khim and D.-W. Kim, J. Appl. Phys. **93**, 8319 (2003): *Domain nucleation and growth of $La_{0.7}Ca_{0.3}Mn_{O3-\delta}/LaAlO_3$ films studied by low temperature MFM.*

27. Th. Maltezopoulos, A. Kubetzka, M. Morgenstern, R. Wiesendanger, S. G. Lemay, and C. Dekker, Appl. Phys. Lett. **83**, 1011 (2003): *Direct observation of confined states in individual metallic single wall carbon nanotubes.*

28. R. Ravlić, M. Bode, and R. Wiesendanger, J. Phys.: Condens. Matter **15**, S 2513 (2003): *Correlation of structural, local electronic and magnetic properties of Fe on Cr(001) studied by spin-polarized scanning tunneling spectroscopy.*

29. G. Kuri, G. Materlik, V. Hagen, and R. Wiesendanger, J. Vac. Sci. & Technol. B **21**, 1134 (2003): *Comparative study of MeV C^+ and C^{++} ions implantation in GaAs(100): surface roughness and evaluation of lattice strain.*

30. Chr. Meyer, J. Klijn, M. Morgenstern, and R. Wiesendanger, Phys. Rev. Lett. **91**, 076803 (2003): *Direct measurement of the local density of states of a disordered one-dimensional conductor.*

31. J. Wiebe, Chr. Meyer, J. Klijn, M. Morgenstern, and R. Wiesendanger, Phys. Rev. B **68**, 041402 (2003): *From quantized states to percolation: Scanning tunneling spectroscopy of a strongly disordered two-dimensional electron system.*

32. U. H. Pi, D. H. Kim, Z. G. Khim, U. Kaiser, M. Liebmann, A. Schwarz, and R. Wiesendanger, Proc. Int. Conf. Physics and Chemistry of Molecular and Oxide Superconductors, J. Low Temp. Phys. **131**, 993 (2003): *Vortex dynamics in $Bi_2Sr_2CaCu_2O_8$ single crystals with low density columnar defects studied by magnetic force microscopy.*

33. M. Morgenstern, J. Klijn, Chr. Meyer, M. Getzlaff, R. L. Johnson, R. Adelung, L. Kipp, R. A. Römer, and R. Wiesendanger, Jpn. J. Appl. Phys. **42**, 4809 (2003): *Low density two-dimensional electron systems studied by scanning tunneling spectroscopy.*

34. A. Kubetzka, O. Pietzsch, M. Bode, R. Ravlic, and R. Wiesendanger, Acta Phys. Pol. A **104**, 259 (2003): *Spin-polarized STM investigation of magnetic domain walls.*

35. M. Getzlaff, M. Bode, and R. Wiesendanger, Acta Phys. Pol. A **104**, 327 (2003): *Surface electronic properties of Fe nanoparticles on c(2x2)-N/Cu(001).*

36. Th. Maltezopoulos, A. Bolz, Chr. Meyer, Ch. Heyn, W. Hansen, M. Morgenstern, and R. Wiesendanger, Phys. Rev. Lett. **91**, 196804 (2003): *Wave function mapping of InAs quantum dots by scanning tunneling spectroscopy.*

37. M. Morgenstern, J. Klijn, Chr. Meyer, D. Haude, and R. Wiesendanger, Proc. STM'03 Conference, Eindhoven, NL (eds. P. M. Koenraad and M. Kemerink), AIP Conf. Proc., Vol. **696**, p. 11 (2003): *Visualizing the influence of interactions on the nanoscale: simple electron systems.*

38. A. Schwarz, H. Hölscher, S. M. Langkat, and R. Wiesendanger, Proc. STM'03 Conference, Eindhoven, NL (eds. P. M. Koenraad and M. Kemerink), AIP Conf. Proc., Vol. **696**, p. 68 (2003): *Three-dimensional force field spectroscopy.*

39. T. Richter, M. Sattler, R. Wiesendanger, K.-P. Wittern, and R. Wepf, Microscopy and Microanalysis **9** (Suppl. 2), p. 1546 (2003): *Frozen hydrated bloc-face investigation of tissue for Cryo-SEM.*

40. L. Sacharow, G. Bihlmayer, S. Blügel, and M. Morgenstern, Phys. Rev. B (R) **69**, 085317 (2004): *High spin polarization at the Fe/InAs(110) interface.*

41. M. Bode, Science **306**, 423 (2004): *The Environment Matters—Even on the Atomic Scale.*

42. E. Y. Vedmedenko, Ferroelectrics **305**, 129-132 (2004): *Quasiperiodic magnetic Order and geometrical Frustration on the Penrose Tiling.*

43. K. von Bergmann, M. Bode, A. Kubetzka, M. Heide, S. Blügel, and R. Wiesendanger, Phys. Rev. Lett. **92**, 046801 (2004): *Spin-polarized electron scattering at single oxygen adsorbates on a magnetic surface.*

44. O. Pietzsch, A. Kubetzka, M. Bode, and R. Wiesendanger, Phys. Rev. Lett. **92**, 057202 (2004): *Spin-polarized scanning tunneling spectroscopy of nano-scale cobalt islands on Cu(111).*

45. M. Bode, O. Pietzsch, A. Kubetzka, and R. Wiesendanger, Phys. Rev. Lett. **92**, 067201 (2004): *Shape dependent Thermal Switching Behavior of Superparamagnetic Nanoislands.*

46. M. Bode, A. Wachowiak, J. Wiebe, A. Kubetzka, M. Morgenstern, and R. Wiesendanger, Appl. Phys. Lett. **84**, 948 (2004): *Thickness dependent magnetization states of Fe islands on W(110): From single domain to vortex and diamond patterns.*

47. A. Schwarz, M. Liebmann, U. Kaiser, R. Wiesendanger, T. W. Noh, and D. W. Kim, Phys. Rev. Lett. **92**, 077206 (2004): *Visualization of the Barkhausen Effect by Magnetic Force Microscopy.*

48. E. Y. Vedmedenko, A. Kubetzka, K. von Bergmann, O. Pietzsch, M. Bode, J. Kirschner, H. P. Oepen, and R. Wiesendanger, Phys. Rev. Lett. **92**, 077207 (2004): *Domain Wall Orientation in Magnetic Nanowires.*

49. N. Duhayon, P. Eyben, M. Fouchier, T. Clarysse, W. Vandervorst, D. Alvarez, S. Schoemann, M. Ciappa, M. Stangoni, W. Fichtner, P. Formanek, M. Kittler, V. Raineri, F. Giannazzo, D. Goghero, Y. Rosenwaks, R. Shikler, S. Saraf, S. Sadewasser, N. Barreau, T. Glatzel, M. Verheijen, S. A. M. Mentink, M. von Sprekelsen, T. Maltezopoulos, R. Wiesendanger, and L. Hellemans, J. Vac. Sci. Technol. B **22**, 385 (2004): *Assessing the performance of two dimensional dopant profiling techniques.*

50. O. Pietzsch, A. Kubetzka, M. Bode, and R. Wiesendanger, Appl. Phys. A **78**, 781 (2004): *Recent Advances in Spin-Polarized Scanning Tunneling Microscopy.*

51. J. Klijn, L. Sacharow, Chr. Meyer, S. Blügel, M. Morgenstern, and R. Wiesendanger, Phys. Rev. B **68**, 205327 (2004): *STM measurements on the InAs(110) surface directly compared with surface electronic structure calculations.*

52. U. H. Pi, Z. G. Khim, D. H. Kim, A. Schwarz, M. Liebmann, and R. Wiesendanger, Phys. Rev. B **69**, 094518 (2004): *Direct observation of the vortices trapped in stacking fault dislocations of $Bi_2Sr_2CaCu_2O_8$ by a low-temperature magnetic force microscope.*

53. R. Wiesendanger, M. Bode, A. Kubetzka, O. Pietzsch, M. Morgenstern, A. Wachowiak, and J. Wiebe, J. Magn. Magn. Mater. **272 - 276**, 2115 (2004): *Fundamental studies of magnetism down to the atomic scale: present status and future perspectives of spin-polarized scanning tunneling microscopy.*

54. M. Liebmann, U. Kaiser, A. Schwarz, R. Wiesendanger, U. H. Pi, T. W. Noh, Z. G. Khim, and D.-W. Kim, J. Magn. Magn. Mater. **280/1**, 51 (2004): *Tilted magnetization of a $La_{0.7}Sr_{0.3}MnO_3/LaAlO_3(001)$ thin film.*

55. J. Wiebe, L. Sacharow, A. Wachowiak, G. Bihlmayer, S. Heinze, S. Blügel, M. Morgenstern, and R. Wiesendanger, Phys. Rev. B **70**, 035404 (2004): *Scanning tunneling spectroscopy on cobalt(0001): spectroscopic signature of stacking faults and dislocation lines.*

56. M. Morgenstern, T. Strasser, R. Adelung, M. Getzlaff, L. Kipp, W. Schattke, M. Skibowski, and R. Wiesendanger, Phys. Rev. B **70**, 081305 (2004): *Contributions of escape depth to photoelectron intensity of a well defined initial state.*

57. E. Y. Vedmedenko. U. Grimm, and R. Wiesendanger, Phys. Rev. Lett. **93**, 076407 (2004): *Noncollinear magnetic order in quasicrystals.*

58. M. Ashino, A. Schwarz, T. Behnke, and R. Wiesendanger, Phys. Rev. Lett. **93**, 136101 (2004): *Atomic-resolution dynamic force microscopy and spectroscopy of a single walled carbon nanotube: characterization of interatomic van der Waals forces.*

59. T. Richter, C. Peuckert, M. Sattler, K. König, I. Riemann, U. Hintze, K.-P. Wittern, R. Wiesendanger, and R. Wepf, Skin pharmacology and physiology **17**, 246 (2004): *Dead but highly dynamic - the stratum corneum is divided into three hydration zones.*

60. J. Wiebe, A. Wachowiak, F. Meier, D. Haude, T. Foster, M. Morgenstern, and R. Wiesendanger, Rev. Sci. Instrum. **75**, 4871 (2004): *A 300 mK ultra-high vacuum scanning tunneling microscope facility for spin-resolved spectroscopy.*

61. L. Berbil-Bautista, T. Hänke, M. Getzlaff, R. Wiesendanger, I. Opahle, K. Koepernitz, and M. Richter, Phys. Rev. B **70**, 113401 (2004): *Observation of 5f-states on U/W(110) films by means of scanning tunneling spectroscopy.*

62. K. von Bergmann, M. Bode, and R. Wiesendanger, Phys. Rev. B **70**, 174455 (2004): *Magnetism of iron on tungsten(001) studied by spin-resolved scanning tunneling microscopy and spectroscopy.*

63. M. Getzlaff, R. Pascal, and R. Wiesendanger, Surf. Sci. **566**, 236 (2004): *Controlled preparation of a magnetic thin film alloy: $GdFe_2$ and $GdFe_3$.*

64. U. H. Pi, Z. G. Khim, D. H. Kim, A. Schwarz, M. Liebmann, and R. Wiesendanger, Appl. Phys. Lett. **85**, 5307 (2004): *Dynamic force spectroscopy across an individual strongly pinned Vortex in a $Bi_2Sr_2CaCu_2O_{8+\delta}$ single crystal.*

Chapter 7

Talks

7.1 Invited Talks

08.01.02: M. Bode, A. Kubetzka, O. Pietzsch, M. Kleiber, R. Ravlić, and R. Wiesendanger, 190. WE–Heraeus-Seminar on Magnetism on the Sub-Micrometer Scale: Interactions and Microscopy, Bad Honnef (Germany): *Magnetism under the spin-polarized scanning tunneling microscope.*

14.02.02: R. Wiesendanger, DFG-Rundgespräch: Schichtsysteme, Bad Honnef (Germany): *Mikroskopische Aspekte magnetischer Schichtsysteme.*

15.02.02: R. Wiesendanger, ESRF–Workshop on Surfaces and Interfaces on the Atomic- and Nano-Scale: Semiconductors, Magnetic Materials and Oxides, Grenoble (France): *Nano- and Atomic-Scale Magnetism: Novel Insight by Spin-Polarized Scanning Tunneling Spectroscopy.*

26.02.02: R. Wiesendanger, 12^{th} International Winterschool on New Developments in Solid State Physics: Low-Dimensional Systems: From 2D to Molecules, Mauterndorf (Austria): *Tunneling Spectroscopy on Low-Dimensional Semiconductor and Magnetic Systems.*

20.03.02: R. Wiesendanger, APS March Meeting, Indianapolis (USA): *Novel Insight into Nano- and Atomic-Scale Magnetism by Spin-Polarized STM.*

01.05.02: M. Bode, A. Kubetzka, O. Pietzsch, M. Kleiber, R. Ravlić, and R. Wiesendanger, Intermag Europe 2002, Amsterdam, (The Netherlands): *Imaging magnetic domains with sub-nanometer resolution using spin-polarized STM.*

06.05.02: M. Bode, A. Kubetzka, O. Pietzsch, and R. Wiesendanger, Magneto-Optical Recording International Symposium (MORIS), Benodet (France): *Imaging magnetic domains with sub-nanometer resolution.*

13.05.02: R. Wiesendanger, Materialforum Rhein-Main, RWE Solar GmbH, Alzenau (Germany): *Reise in den Mikrokosmos mit Hilfe neuer mikroskopischer Methoden.*

14.05.02: M. Bode, A. Kubetzka, O. Pietzsch, A. Wachowiak, J. Wiebe, and R. Wiesendanger, Gordon Research Conference on Magnetic Nanostructures, Il Ciocco (Italy): *Frontiers of nanomagnetism explored by spin-polarized STM.*

29.05.02: A. Schwarz, The 4^{th} Nordic Baltic SPM Workshop, Tartu (Estonia): *Advances in Low Temperature Force Microscopy.*

12.06.02: M. Bode, S. Heinze, A. Kubetzka, O. Pietzsch, X. Nie, G. Bihlmayer, S. Blügel, and R. Wiesendanger, 281. WE–Heraeus-Seminar on Spin-Orbit Interactions and Local Structure in Magnetic Systems with Reduced Dimensions, Wandlitz (Germany): *Spin-orbit effects on Fe/W(110) revealed by scanning tunneling spectroscopy.*

20.06.02: R. Wiesendanger, E-MRS Spring Meeting, Strasbourg (France): *Nano-Scale Electronic and Magnetic Properties of Ultrathin Films Probed by Spin-Polarized Scanning Tunneling Spectroscopy.*

24.06.02: M. Bode, O. Pietzsch, A. Kubetzka, R. Ravlić, A. Wachowiak, J. Wiebe, M. Morgenstern, and R. Wiesendanger, Joint 7^{th} International Conference on Nanometer-Scale Science and Technology and 21st European Conference on Surface Science, Malmö (Sweden): *Spin-polarized scanning tunneling microscopy.*

28.06.02: M. Morgenstern, Werner-Brandt Workshop 22, Namur (Belgium): *Scanning Tunneling Spectroscopy on Quantum Systems.*

06.07.02: M. Bode, A. Kubetzka, O. Pietzsch, and R. Wiesendanger, Symposium Latsis on Spin Injection Induced Magnetization Reversal, Lausanne (Switzerland): *Spin-polarized STM.*

16.07.02: R. Wiesendanger, Euroconference on Quantum Phases at the Nanoscale, Erice (Italy): *Nano-Scale Studies of Low-Dimensional Electron Systems by Low-Temperature Scanning Tunneling Spectroscopy (STS).*

12.08.02: R. Wiesendanger, Special Public Lecture at Asia SPM 4 & Taipei Symposium on Nanotechnology, Taipei (Taiwan): *Novel Insight into Nano- and Atomic-Scale Magnetism.*

20.08.02: R. Wiesendanger, Int. Conf. on Science and Technology of Spin Transport in Nanostructures, Trieste (Italy): *Novel Insight into Nano- and Atomic-Scale Magnetism by Spin-Polarized Scanning Tunneling Spectroscopy.*

25.08.02: R. Wiesendanger, 23rd Int. Conf. on Low-Temperature Physics, LT-23, Hiroshima (Japan): *Novel Insight into Nano- and Atomic-Scale Magnetism.*

10.09.02: M. Bode, A. Kubetzka, O. Pietzsch, and R. Wiesendanger, Discussion Meeting on Magnetism at the Spatial Limit of the Max-Planck-Gesellschaft, Schloss Ringberg (Germany): *Spin-polarized STM: Imaging of magnetic nanostructures with sub-nanometer resolution.*

27.09.02: M. Bode, O. Pietzsch, A. Kubetzka, R. Ravlić, A. Wachowiak, J. Wiebe, M. Morgenstern, and R. Wiesendanger, III. Congreso Español de Microscopía de Fuerzas y Efecto Túnel, Zamora (Spain): *Imaging surface magnetic structures by spin-polarized STM.*

04.10.02: M. Morgenstern, NATO ASI Workshop Scanning Probe Microscopy, Albufeira (Portugal): *Nano-Scale Studies of Quantum Phenomena in Electron Systems of Different Dimension.*

07.10.02: M. Morgenstern, NATO ASI Workshop Scanning Probe Microscopy, Albufeira (Portugal): *Novel Insight into Nanoscale Magnetism by Spin Polarized Scanning Tunneling Spectroscopy.*

11.10.02: M. Getzlaff, Workshop "Functionalized Materials", Wandlitz (Berlin): *Magnetism on macroscopic and microscopic scales.*

14.10.02: R. Wiesendanger, Workshop über Materialwissenschaften in Hamburg 2002, Hamburg (Germany): *Beiträge der Rastersondenmikroskopie und -spektroskopie in der Materialforschung.*

14.10.02: M. Morgenstern, International Conference on Solid States Crystals, Krakau (Poland): *Probing the internal spin structure of a magnetic vortex core.*

24.10.02: R. Wiesendanger, Int. Conf. on Nano-Science and Technology in celebration of the 50^{th} anniversary of the Korean Physical Society, Seoul (South Korea): *Novel Insight into Nano- and Atomic-Scale Magnetism.*

30.10.02: M. Bode, O. Pietzsch, A. Kubetzka, R. Ravlić, A. Wachowiak, J. Wiebe, M. Morgenstern, and R. Wiesendanger, Satellite Workshop on Properties of Magnetic Nanostructures, Trieste (Italy): *Imaging Magnetic Nanostructures by Spin Polarized STM.*

01.11.02: M. Morgenstern, The 10^{th} International Colloquium on Scanning Probe Microscopy, Hawaii (USA): *Nano-Scale Studies of Quantum Phenomena in Electron Systems of Different Dimension.*

15.11.02: R. Wiesendanger, 47^{th} Conf. on Magnetism & Magnetic Materials, Tampa (USA): *Novel Insight into Nano- and Atomic-Scale Magnetism.*

29.11.02: R. Wiesendanger, Fachkongress Nanotechnologie, Handelskammer Hamburg (Germany): *Von der Nanowissenschaft zur Nanotechnologie: Beiträge der Rastersondenmethoden.*

03.12.02: M. Bode, A. Kubetzka, O. Pietzsch, and R. Wiesendanger, Fall Meeting of the Material Research Society, Boston (USA): *Frontiers of Nanomagnetism explored by Spin-Polarized STM.*

06.02.03: R. Wiesendanger, Winterschool on Scanning Probe Microscopy and Spectroscopy, Hanse-Wissenschaftskolleg Delmenhorst (Germany): *Spin-resolved Spectro-Microscopy.*

11.03.03: M. Morgenstern, International Symposium on Carrier Interactions and Spintronics in Nanostructures, Tokyo (Japan): *Towards spin polarized imaging of ferromagnet-semiconductor interfaces.*

25.03.03: O. Pietzsch, M. Bode, A. Kubetzka, K. v. Bergmann, A. Wachowiak, J. Wiebe, M. Morgenstern, and R. Wiesendanger, Früjahrstagung der Deutschen Physikalischen Gesellschaft, Dresden (Germany): *Neuere Entwicklung in der spin-polarisierten Rastertunnel-Mikroskopie.*

17.06.03: R. Wiesendanger, 14^{th} Interdisciplinary Surface Science Conference, Liverpool (U.K.): *Novel Insight into Nano- and Atomic-Scale Magnetism.*

28.06.03: M. Morgenstern, 3^{rd} Celdis Workshop on Diluted Magnetic and Hybrid Low Dimensional Structures, Warschau (Poland): *Towards spin polarized imaging of ferromagnet-semiconductor interfaces.*

09.07.03: M. Bode, SFB 513 Workshop 2003 & Krupp-Symposium, Konstanz (Germany): *Spin-polarized STM: New Insight in the Magnetism of Nanostructures.*

17.07.03: R. Wiesendanger, 3^{rd} International Symposium on Scanning Probe Spectroscopy, Poznan (Poland): *Spin-Polarized Scanning Tunneling Spectroscopy.*

17.07.03: A. Schwarz, 3^{rd} International Symposium on Scanning Probe Spectroscopy and Related Methods, Poznan (Poland): *Low temperature magnetic force microscopy in high magnetic fields.*

21.07.03: M. Morgenstern, 12^{th} International Conference on Scanning Tunneling Microscopy and Related Techniques, Eindhoven (The Netherlands): *Visualizing the influence of interactions on the nanoscale: simple electron systems.*

24.07.03: A. Schwarz, H. Hölscher, S. M. Langkat, and R. Wiesendanger, 12^{th} International Conference on Scanning Tunneling Microscopy/Spectroscopy and Related Techniques, Eindhoven (The Netherlands): *3D-force field spectroscopy with atomic resolution on NiO(001).*

24.07.03: R. Wiesendanger, 12^{th} International Conference on Scanning Tunneling Microscopy/Spectroscopy and Related Techniques, Eindhoven (The Netherlands): *Internal spin structure of magnetic vortex cores studied by spin-polarized scanning tunneling spectroscopy.*

28.07.03: R. Wiesendanger, International Conference on Magnetism, Rome (Italy): *Fundamental studies of magnetism down to the atomic scale: present status and future perspectives of spin-polarized scanning tunneling microscopy.*

26.08.03: M. Bode, The Applied Statistical Physics: Molecular Engineering Conference, Puerto Vallarta (Mexico): *Imaging Surface Magnetic Structures by Spin-Polarized STM.*

03.09.03: A. Schwarz, M. Liebmann, R. Wiesendanger, U. H. Pi, Z. G. Khim, and D. H. Kim, 6^{th} International Conference on Noncontact Atomic Force Microscopy, Dingle (Ireland): *Vortex phase transitions observed by magnetic force microscopy.*

05.09.03: M. Bode, Leopoldina Symposium: From Nanoscience to Nanotechnology, Karlsruhe (Germany): *Exploring the Frontiers of Nanomagnetism by Spin-Polarized STM.*

12.09.03: R. Wiesendanger, 24^{th} Int. Symposium on Materials Science: Superconductivity and Magnetism, Roskilde (Denmark): *Novel insight into nanomagnetism by spin-polarized scanning tunneling microscopy.*

16.09.03: R. Wiesendanger, Summer School on New Magnetics, Bedlewo (Poland): *Frontiers of nanomagnetism investigated by spin-polarized scanning tunneling spectroscopy.*

23.09.03: R. Wiesendanger, 3^{rd} European Conference on Vortex Matter in Superconductors, Crete (Greece) : *Visualization of vortex states in superconductors and mesoscopic magnets by scanning probe methods.*

01.10.03: R. Wiesendanger, 53^{rd} Annual ÖPG-Meeting, Salzburg (Austria) : *Magnetismus auf atomarer Skala: Neue Einblicke in ein altbekanntes Phänomen.*

08.10.03: M. Bode, 4^{th} International Symposium on Atomic Level Characterizations for New Materials and Devices, Lihue/Hawaii (USA): *Imaging magnetic nanostructures by spin-polarized STM.*

10.10.03: R. Wiesendanger, 1^{st} iNANO-School, arhus (Denmark) : *Scanning Tunneling Microscopy in Nanoscience.*

13.10.03: E. Y. Vedmedenko, Elementary excitations in Quasicrystals, Chemnitz (Germany): *Order by Frustration in Quasicrystals.*

22.10.03: M. Bode, International Workshop on Microspectroscopy of Quantum, Magnetic and Biological Nanostructures, Osaka (Japan): *Imaging of Nanoscale Magnetic Structures with Spin-Resolved STM.*

23.10.03: M. Morgenstern, International Workshop on Microspectroscopy of Quantum, Magnetic and Biological Nanostructures, Osaka (Japan): *Scanning Tunneling Spectroscopy: Interacting electron systems in different dimensions.*

31.10.03: R. Wiesendanger, Joachim Jungius-Gesellschaft der Wissenschaften, Hamburg (Germany): *Nanotechnologie - Aufbruch in neue Welten.*

04.11.03: R. Wiesendanger, Public Lecture, Hamburg (Germany): *Nanotechnologie - Aufbruch in neue Welten.*

13.11.03: R. Wiesendanger, 1^{st} International Symposium on Active Nano-Characterization and Technology, Tsukuba (Japan): *Quantum Phenomena of Nanostructures studied by Scanning Probe Spectroscopy at Low Temperatures and High Magnetic Fields.*

14.11.03: R. Wiesendanger, International Symposium on Functional Semiconductor Nanosystems, Atsugi (Japan): *Nano-Scale Studies of Low-Dimensional Systems by Low-Temperature Scanning Tunneling Spectroscopy.*

17.11.03: R. Wiesendanger, 7^{th} International Conference on Atomically Controlled Surfaces, Interfaces and Nanostructures, Nara (Japan): *Orbital Symmetry and Spin Character of Electronic States revealed by Spin-Polarized Scanning Tunneling Spectroscopy.*

19.11.03: R. Wiesendanger, Asia Pacific Nanotechnology Forum, Cairns (Australia): *The German Center of Competence in Nano-Scale Analysis: From basic research to industrial applications.*

20.11.03: R. Wiesendanger, Asia Pacific Nanotechnology Forum, Cairns (Australia): *Nano-Scale Studies of Magnetic Materials by Spin-Polarized Scanning Tunneling Spectroscopy.*

02.12.03: R. Wiesendanger, MRS Fall Meeting, Boston (USA): *Spin-Polarized Scanning Tunneling Microscopy as an Ultimate Tool for Future Magnetic Data Storage Technology.*

11.12.03: R. Wiesendanger, EuroNanoForum 2003, Triest (Italy): *Scanning Probe Methods: The Eyes for the Nano-World.*

11.02.04: R. Wiesendanger, 191. PTB-Seminar: Magnetische Speichermedien der Zukunft, PTB Braunschweig (Germany): *Magnetische Datenspeicherung auf dem Weg von Gigabits zu Terabits.*

27.02.04: R. Wiesendanger, 19^{th} Workshop on Novel Materials and Superconductivity, Donnersbach (Austria) : *Magnetism at the Atomic Scale: Novel Insight by Spin-Polarized STM.*

08.03.04: R. Wiesendanger, 18th Int. Winterschool on Electronic Properties of Novel Materials: Molecular Nanostructures, Kirchberg i.T. (Austria) : *Local electronic and mechanical properties of carbon nanotubes studied by low-temperature scanning probe spectroscopy.*

08.03.04: M. Bode, 68^{th} Spring Conference, Deutsche Physikalische Gesellschaft, Regensburg (Germany): *Spin-Polarized Scanning Tunneling Microscopy: From Nanomagnetism to the Spin-Resolved Bandstructure.*

10.03.04: M. Morgenstern, 68^{th} Spring Conference, Deutsche Physikalische Gesellschaft, Regensburg (Germany): *Nanoscale Study of Quantum Phenomena: Influence of Dimension, Magnetic Field and Disorder on Simple Electron Systems.*

27.04.04: R. Wiesendanger, Vortragssitzung der Akademie Leopoldina, Halle (Germany): *Nanotechnologie - Aufbruch in neue Welten.*

07.05.04: R. Wiesendanger, Leybold Vacuum GmbH, Schloß Bensberg, Bergisch-Gladbach (Germany): *Vacuum-based Science and Technology at the Nano-scale: Present Status and Future Perspectives.*

12.05.04: R. Wiesendanger, Research Conference on: "Advancing Frontiers of Optical and Quantum Effects in Condensed Matter", Trieste (Italy): *Quantum Phenomena of Nanostructures studied by Scanning Probe Spectroscopy at Low Temperatures and High Magnetic Fields.*

28.05.04: M. Bode, 3rd International Workshop on Surface, Interface and Thin Film Physics, Shanghai (China): *Spin-Polarized Scanning Tunneling Microscopy: From Nanomagnetism to the Spin-Resolved Bandstructure.*

04.06.04: R. Wiesendanger, International CeNTech Workshop, Münster (Germany): *Nanomagnetics: Current Status and Future Perspectives.*

09.06.04: R. Wiesendanger, CNR-INFM National Conference on the Physics of Matter, Genova (Italy): *Quantum Phenomena of Nanostructures studied by Scanning Probe Spectroscopy at Low Temperatures and High Magnetic Fields.*

10.06.04: M. Morgenstern, Workshop on Cooperative Phenomena in Optics and Transport in Nanostructures, Dresden (Germany): *"Local density of states of interacting electron systems in different dimensions.*

20.06.04: M. Morgenstern, Summer School Nanospectra 2004: Fabrication, Manipulation and Spectroscopy of Nanostructures, Porquerolles (France): *Scanning Tunneling Spectroscopy on Semiconductors: From Quantum Dots to More Complex Systems.*

22.06.04: O. Pietzsch, A. Kubetzka, M. Bode, S. Heinze, and R. Wiesendanger, 7^{th} International Conference on Nanostructured Materials and NanoDE, Nanoscience Award 2004 Lecture, Wiesbaden (Germany): *Imaging Magnetic Nanostructures: Spin-Polarized Scanning Tunneling Microscopy of Co/Cu(111).*

22.06.04: R. Wiesendanger, 7^{th} Int. Conference on Nanostructured Materials NANO 2004, Wiesbaden (Germany): *Nano-Scale Analysis of Nanostructured Materials by Scanning Probe Methods.*

23.06.04: R. Wiesendanger, Laserion-Workshop 2004: "Microfabrication, nanostructured materials and biotechnology", Schloß Ringberg, Tegernsee (Germany): *Frontiers of Nanomagnetism explored by Spin-Polarized Scanning Tunneling Spectroscopy.*

25.06.04: R. Wiesendanger, Summer School on Fabrication, Manipulation and Spectroscopy of Nanostructures, Porquerolles (France): *Spin-Sensitive Scanning Tunneling Microscopy and Spectroscopy.*

03.07.04: R. Wiesendanger, International Symposium on Nanobiomedicine: Moving Nanotechnology from Bench to Bedside, Hamburg (Germany): *Cryogenic scanning force microscopy with true atomic resolution: Current status and challenges for the future.*

02.08.04: M. Bode, Microscopy and Microanalysis 2004, Savanah (USA): *Recent Progress in Spin-Polarized Scanning Tunneling Microscopy.*

23.08.04: R. Wiesendanger, Gordon Research Conference on Magnetic Nanostructures, Big Sky Resort, Montana (USA): *Frontiers of Nanomagnetism studied by Spin-Polarized Scanning Tunneling Microscopy.*

06.09.04: R. Wiesendanger, Joint European Magnetic Symposium JEMS'04, Dresden (Germany): *Nano-Scale Studies of Magnetic Materials by Spin-Polarized Scanning Tunneling Spectroscopy.*

13.09.04: R. Wiesendanger, 11^{th} International Summer School Nicol*ás* Cabrera: Frontiers in Science and Technology-Magnetic Nanostructures, Madrid (Spain): *Spin-Resolved Spectroscopy and Magnetic Imaging at the Nano-scale.*

14.09.04: R. Wiesendanger, 11^{th} International Summer School Nicol*ás* Cabrera: Frontiers in Science and Technology-Magnetic Nanostructures, Madrid (Spain): *Perspectives of Magnetic-Sensitive Imaging and Recording Using Scanning Probes.*

23.09.04: M. Morgenstern, International Symposium on Quantum Hall Systems and Quantum Materials, Hamburg (Germany): *Scanning Tunneling Spectroscopy of Quantum Systems in Semiconductors.*

28.09.04: R. Wiesendanger, IRC Workshop on Nanoscale Characterisation and Biological Nanoscience, Bristol (U.K.): *Frontiers of Nanomagnetism Studied by Spin-Polarized Scanning Tunneling Spectroscopy.*

08.10.04: R. Wiesendanger, Colloquium on Nanoscience and Atomic Processes in Materials, University of Stuttgart (Germany): *Neue Einblicke in die Nanowelt mittels Rastersondenspektroskopie.*

14.10.04: M. Bode, International Symposium: "Atom Manipulation, Single Spins and Atomic Forces: Novel Perspectives in the Nanoscience Era", Hamburg (Germany): *Spin-polarized STM: Achievements and Perspectives.*

15.10.04: A. Schwarz, International Symposium: "Atom Manipulation, Single Spins and Atomic Forces: Novel Perspectives in the Nanoscience Era", Hamburg (Germany): *High Resolution Force Microscopy and Spectroscopy at Low Temperatures.*

27.10.04: R. Wiesendanger, Public Lecture, Hamburg (Germany): *Nanotechnologie - Chancen und Perspektiven.*

29.10.04: R. Wiesendanger, Symposium on Magnetic Nanostructures, Heverlee (Belgium): *Novel Insight into Magnetic Nanostructures by Spin-Polarized Scanning Tunneling Microscopy and Spectroscopy.*

10.11.04: M. Bode, 49^{th} Conference on Magnetism and Magnetic Materials, Jacksonville (USA): *Thermal Switching Behavior of Superparamagnetic Nanoislands: Imaging and Manipulation by SP-STM.*

15.11.04: M. Bode, 51^{st} Intl. Symposium of the American Vacuum Society , Anaheim (USA): *Spin-Polarized Scanning Tunneling Microscopy: Achievements and Perspectives.*

18.11.04: R. Wiesendanger, Todai International Symposium 2004 on Quantum Condensed Systems ISSP-9, Kashiwa, Chiba (Japan): *Spin-Polarized Electron Physics with the STM.*

23.11.04: R. Wiesendanger, International Symposium on Nanostructures and Physicochemical Properties of Polyoxometalate Superclusters and Related Colloid Particles, Shonan Village Center, Kanagawa (Japan): *Low-Temperature Scanning Probe Spectroscopy of Molecular Systems and Quantum Dots.*

30.11.04: R. Wiesendanger, (International Symposium on New Horizons in Condensed-Matter Physics, University of Tokyo (Japan): *New Horizons in Magnetism by Atomic-Scale Magnetic Probing.*

06.12.04: M. Bode, Sanken International Symposium on Scientific and Industrial Nanotechnology 2004 (SISSIN-2004), Osaka (Japan): *Imaging the Magnetic Nanoworld by Spin-Polarized Scanning Tunneling Microscopy.*

7.2 Conference Contributions and Talks at Other Institutes

7.2.1 Talks

17.01.02: M. Morgenstern, Ringvorlesung des Instituts für Angewandte Physik, Hamburg (Germany): *Messung der lokalen Zustandsdichte verdünnter Elektronensysteme in verschiedenen Dimensionen.*

21.01.02: M. Bode, O. Pietzsch, A. Kubetzka, S. Heinze, X. Nie, G. Bihlmayer, S. Blügel, and R. Wiesendanger, University College London, London (UK): *Imaging magnetic nanostructures by spin-polarized scanning tunneling microscopy.*

23.01.02: M. Bode, O. Pietzsch, A. Kubetzka, R. Ravlić, M. Kleiber, S. Heinze, X. Nie, S. Blügel, and R. Wiesendanger, Cavendish Laboratory, Cambridge (UK): *Imaging magnetic nanostructures by spin-polarized scanning tunneling microscopy.*

29.01.02: R. Wiesendanger, Colloquium, University of Kiel (Germany): *Quantenphänomene auf der Nanometerskala: Neue Einblicke mittels Rastertunnelspektroskopie.*

01.02.02: M. Bode, O. Pietzsch, A. Kubetzka, R. Ravlić, M. Kleiber, S. Heinze, X. Nie, S. Blügel, and R. Wiesendanger, Fritz-Haber-Institut der Max-Planck-Gesellschaft, Berlin (Germany): *Imaging magnetic nanostructures by spin-polarized scanning tunneling microscopy.*

04.02.02: R. Wiesendanger, cNM Seminar, TU Eindhoven (The Netherlands): *Nanoscale studies of quantum phenomena by scanning probe spectroscopy.*

28.02.02: M. Bode, Institut für Festkörper– und Werkstoffforschung (IFW), Dresden (Germany): *Höchstauflösende Abbildung magnetischer Domänen mittels spinpolarisierter Rastertunnelmikroskopie.*

11.03.02: Chr. Meyer, J. Klijn, M. Morgenstern, and R. Wiesendanger, DPG-Frühjahrstagung AK Festkörperphysik, Regensburg (Germany): *Die lokale Zustandsdichte eines eindimensionalen Elektronensystems unterhalb einer geladenen Stufenkante.*

11.03.02: M. v. Sprekelsen, J. Isenbart, R. Wiesendanger, Frühjahrstagung der Deutschen Physikalischen Gesellschaft, Regensburg (Germany): *Hochgeschwindigkeit-Rasterkapazitätsspektroskopie an Halbleitermikrostrukturen.*

11.03.02. M. Bode, A. Kubetzka, O. Pietzsch, and R. Wiesendanger, 66. Frühjahrstagung der Deutschen Physikalischen Gesellschaft, Regensburg (Germany): *Spin–polarisierte Rastertunnelmikroskopie mit antiferromagetischen Sondenspitzen.*

11.03.02: M. Bode, S. Heinze, A. Kubetzka, O. Pietzsch, X. Nie, G. Bihlmayer, S. Blügel, and R. Wiesendanger, 66. Frühjahrstagung der Deutschen Physikalischen Gesellschaft, Regensburg (Germany): *Direkte Beobachtung von Spin-Bahn–Kopplung mittels Rastertunnelspektroskopie.*

13.03.02: K. v. Bergmann, M. Bode, M. Getzlaff, A. Kubetzka, O. Pietzsch, and R. Wiesendanger, Frühjahrstagung der Deutschen Physikalischen Gesellschaft, Regensburg (Germany): *Temperaturabhängigkeit der magnetischen Struktur von 2 ML Fe auf W(110).*

13.03.02: R. Ravlić, Frühjahrstagung der Deutschen Physikalischen Gesellschaft, Regensburg (Germany): *SP-STS/STM Untersuchung von Sub-Monolagen Fe-Filmen auf Cr(001).*

14.03.02: M. Liebmann, A. Schwarz, U. H. Pi, Z. G. Khim, and R. Wiesendanger, Frühjahrstagung der Deutschen Physikalischen Gesellschaft, Regensburg (Germany): *Magnetische Domänenstruktur von $La_{07}Sr_{03}MnO_3$-Schichten.*

14.03.02: A. Schwarz, M. Liebmann, U. Kaiser, U. H. Pi, Z. G. Khim, and R. Wiesendanger, Frühjahrstagung der Deutschen Physikalischen Gesellschaft, Regensburg (Germany): *Domänennukleation in $La_{0.7}Ca_{0.3}MnO_3$-Schichten.*

14.03.02: M. Bode, A. Kubetzka, O. Pietzsch, and R. Wiesendanger, 66. Frühjahrstagung der Deutschen Physikalischen Gesellschaft, Regensburg (Germany): *Direkte Beobachtung des Schaltverhaltens superparamagnetischer Fe–Cluster auf Mo(110).*

14.03.02: M. Getzlaff, A. Kubetzka, O. Pietzsch, M. Bode, and R. Wiesendanger, Frühjahrstagung der Deutschen Physikalischen Gesellschaft, Regensburg (Germany): *Selbstanordnung von Fe-Nanopartikeln auf vorstrukturierten Unterlagen.*

15.03.02: A. Schwarz, S. M. Langkat, and R. Wiesendanger, Frühjahrstagung der Deutschen Physikalischen Gesellschaft, Regensburg (Germany): *Dissipative Wechselwirkung auf Atomarer Skala im Dynamischen Modus der Rasterkraftmikroskopie.*

15.03.02: O. Pietzsch, A. Kubetzka, M. Bode, and R. Wiesendanger, Spring Conference, Deutsche Physikalische Gesellschaft, Regensburg (Germany): *Rastertunnelmikroskopie und -spektroskopie an Co-Inseln auf der Cu(111) Oberfläche.*

09.04.02: R. Wiesendanger, Handelskammer-Forum "Wirtschaft trifft Wissenschaft", University of Hamburg (Germany): *Nano-Biotechnologie: Innovationen an der Schnittstelle der Disziplinen.*

14.05.02: R. Wiesendanger, Hamburger Tag der Physik für Lehrer, University of Hamburg (Germany): *Nanotechnologie - Aufbruch in neue Welten.*

17.05.02: M. Getzlaff, Kolloquium des Hahn-Meitner-Instituts, Berlin (Germany): *Niederdimensionale Systeme: Korrelation struktureller, elektronischer und magnetischer Eigenschaften.*

24.05.02: R. Wiesendanger, Seminar, University of Lund (Sweden): *Nano-Scale Studies of Low-Dimensional Electron Systems by Low-Temperature Scanning Tunneling Spectroscopy.*

03.06.02: M. Bode, O. Pietzsch, A. Kubetzka, A. Wachowiak, J. Wiebe, and R. Wiesendanger, Physikalisches Kolloquium, Universität Regensburg (Germany): *Spinpolarisierte Tunnelmikroskopie: magnetische Abbildung mit atomarer Auflösung.*

11.06.02: M. Bode, Institut für Theoretische und Angewandte Physik, University of Stuttgart (Germany): *Frontiers of nanomagnetism explored by spin-polarized STM.*

20.06.02: M. v. Sprekelsen, J. Isenbart, and R. Wiesendanger, Jahrestagung der Deutschen Vakuum Gesellschaft, Magdeburg (Germany): *Hochgeschwindigkeits-Rasterkapazitätsspektroskopie an Halbleitermikrostrukturen.*

24.06.02: M. Getzlaff, T. Hänke, L. J. Berbil-Bautista, and R. Wiesendanger, ECOSS-21 (2002), Malmö, (Sweden), *Uranium thin films: structural and electronic properties.*

25.06.02: M. v. Sprekelsen, J. Isenbart, and R. Wiesendanger, NANO-7/ECOSS-21, Malmö (Sweden): *High speed-Scanning Capacitance Spectroscopy on semiconductor microstructures.*

27.06.02: R. Wiesendanger, ECOSS-21/NANO-7, Malmö (Sweden): *Nano-Scale Studies of Quantum Phenomena in Low-Dimensional Electron Systems.*

27.06.02: T. Richter, S. S. Biel, M. Sattler, R. Wiesendanger, K. P. Wittern, and R. Wepf, Joint Microscopy Meeting Lille (France): *Frozen hydrated bloc-face investigation of tissue for Cryo SEM.*

28.06.02: O. Pietzsch, A. Kubetzka, K. v. Bergmann, M. Bode, and R. Wiesendanger, 21st European Conference on Surface Science and 7^{th} International Conference on Nanometer-Scale Science and Technology, Malmö (Sweden): *The Many Faces of Magnetism in Ultrathin Fe/W(110) Films.*

03.07.02: F. Meier, Graduiertenkolleg "Nanostrukturierter Festkörper", Hamburg (Germany): *Aufbau eines temperaturvariablen MOKE-Systems für die Charakterisierung ultradünner, magnetischer Schichten im UHV.*

04.07.02: M. Morgenstern, Kolloquium der Universität Hamburg (Germany): *Probing the local density of states of electron system in different dimensions.*

11.07.02: M. Morgenstern, Festkörperkolloquium, RWTH Aachen (Germany): *Probing the Local Density of States of Dilute Electron Systems in different Dimensions.*

30.07.02: M. v. Sprekelsen, M. Langer, J. Isenbart, and R. Wiesendanger, BMBF-Projekt-Abschlusstreffen, Düsseldorf (Germany): *Hochgeschwindigkeits-Rasterkapazitätsspektroskopie an Halbleitermikrostrukturen.*

01.08.02: M. Morgenstern, Int. Conf. of the Physics of Semiconductors, Edinburgh (UK): *Comparison of the local density of states in dilute two-dimensional and three-dimensional electron systems.*

12.08.02: A. Schwarz, U. H. Pi, M. Liebmann, U. Kaiser, Z. G. Khim, and R. Wiesendanger, NC-AFM 2002, Montreal (Canada): *Direct Observation of Vortex-Antivortex Annihilation.*

14.08.02: S. M. Langkat, A. Schwarz, H. Hölscher, and R. Wiesendanger, NC-AFM 2002, Montreal (Canada): *Determination of the Three Dimensional Force Field Between an Iron Coated Tip and NiO(001) with Atomic Resolution.*

25.09.02: Chr. Meyer, J. Klijn, M. Morgenstern, and R. Wiesendanger, GrK Workshop Nanostrukturierter Festkörper, Wismar (Germany): *Scanning tunneling spectroscopy on low dimensional electron systems.*

02.10.02: M. v. Sprekelsen, Th. Maltezopoulos, J. Isenbart, M. Langer, and R. Wiesendanger, HERCULAS-meeting at STMicroelectronics (Catania): *High speed-Scanning Capacitance Spectroscopy on semiconductor microstructures.*

08.10.02: A. Wachowiak, J. Wiebe, M. Morgenstern, M. Bode, and R. Wiesendanger, SFB-Workshop on "Quantum Materials", SFB-508, Haus Rissen, Hamburg (Germany): *Nano-Scale Study of a Ferromagnetic Vortex Structure.*

11.10.02: Th. Maltezopoulos, Workshop des Graduiertenkollegs Design and Characterisation of Functional Materials, Wandlitz (Germany): *Scanning Tunneling Spectroscopy Applied to Nanostructures.*

17.10.02: J. Klijn, Chr. Meyer, M. Morgenstern, R. Wiesendanger, GrK Workshop "Spektroskopie an lokalisierten atomaren Systemen", Lüneburg (Germany): *Rastertunnelspektroskopie an niederdimensionalen Elektronensystemen bei bekannten Potentiallandschaft.*

21.10.02: M. Morgenstern, Seminar der AG Mertens, University of Bayreuth (Germany): *Spinpolarasierte Rastertunnelspektroskopie einer magnetischen Vortexstruktur.*

07.11.02: M. Bode, S. Heinze, A. Kubetzka, O. Pietzsch, X. Nie, G. Bihlmayer, S. Blügel, and R. Wiesendanger, 49^{th} Intl. Symposium of the American Vacuum Society, Denver (USA): *Spin-Orbit Effects on Fe/W(110) Revealed by Scanning Tunneling Spectroscopy.*

15.11.02: M. Liebmann, A. Schwarz, U. Kaiser, R. Wiesendanger, U. H. Pi, and Z. G. Khim, 47^{th} Conference on Magnetism and Magnetic, Tampa, Florida (USA): *Domain nucleation and growth of $La_{0.7}Ca_{0.3}MnO_{3-\delta}/LaAlO_3$ films studied by MFM.*

15.11.02: A. Schwarz, U. H. Pi, M. Liebmann, U. Kaiser, D. H. Kim, Z. G. Khim, and R. Wiesendanger, MMM 2002, Tampa, Florida (USA): *Real Space Observation of Vortex-Antivortex Annihilation on a HTc-Superconductor by MFM.*

03.12.02: R. Wiesendanger, Colloquium, University of Mainz (Germany): *Magnetismus auf atomarer Skala: Neue Einblicke in ein altbekanntes Phänomen.*

07.12.02: J. Bansmann, A. Kleibert, R. Methling, V. Senz, M. Getzlaff, and K. H. Meiwes-Broer, XMRS 2002, Dresden (Germany): *Mass-filtered iron clusters in contact with ferromagnetic surfaces.*

10.12.02: M. Morgenstern, Colloquium Universiteit Nijmegen (The Netherlands): *Nano-Scale Studies of Quantum Phenomena in Electron Systems of Different Dimension.*

10.12.02: M. Bode, A. Kubetzka, O. Pietzsch, R. Ravlić, and R. Wiesendanger, Oak Ridge National Laboratory, Seminar of the Condensed Matter Sciences Division: *Recent Progress in Magnetic Imaging by Spin-Polarized STM.*

06.01.03: Th. Maltezopoulos, Seminar über Nahfeldgrenzflächenphysik und Nanotechnologie, Hamburg (Germany): *Rastertunnelspektroskopie an verspannungsinduzierten InAs-Quantenpunkten.*

10.01.03: M. Morgenstern, DFG-Kolloquium Quanten-Hall-Systeme, Bad Honnef (Germany): *Scanning tunneling spectroscopy of two-dimensional electron systems.*

17.01.03: M. Morgenstern, Kolloquium der FU Berlin (Germany): *Rastertunnelspektroskopie an verdünnten Elektronensystemen verschiedener Dimension.*

20.01.03: R. Wiesendanger, Colloquium, University of Leuven (Belgium): *Novel Insight into Nano- and Atomic-Scale Magnetism by Spin-Polarized Scanning Tunneling Spectroscopy.*

03.02.03: R. Wiesendanger, Colloquium, University of Bochum (Germany): *Novel Insight into Nano- and Atomic-Scale Magnetism by Spin-Polarized Scanning Tunneling Spectroscopy.*

13.02.03: Th. Maltezopoulos, A. Bolz, Chr. Meyer, M. v. Sprekelsen, Chr. Heyn, M. Morgenstern and R. Wiesendanger, HERCULAS project meeting, Berlin (Germany): *Scanning capacitance microscopy and scanning tunneling spectroscopy applied to strain-induced InAs quantum dots.*

13.02.03: M. v. Sprekelsen , T. Maltezopoulos, and R. Wiesendanger, HERCULAS meeting at HMI, Berlin (Germany): *High speed - Scanning Capacitance Spectroscopy on semiconductor microstructures.*

19.02.03: M. Morgenstern, Kolloquium der RWTH Aachen (Germany): *Nanoskalige Untersuchung von Quanten- und Spinphänomenen in wechselwirkenden Elektronensystemen.*

25.02.03: M. Bode, Max-Planck-Institut für Mikrostrukturforschung, Halle (Germany): *Magnetic imaging of films and clusters by spin-polarized STM.*

24.03.03: L. Sacharow, M. Morgenstern, G. Bihlmayer, S. Blügel, and R. Wiesendanger, Frühjahrstagung der Deutschen Physikalischen Gesellschaft, Dresden (Germany): *Hohe Spinpolarisation an der Fe/InAs(110) Grenzfläche.*

24.03.03: Th. Maltezopoulos, A. Kubetzka, M. Morgenstern, S. G. Lemay, C. Dekker and R. Wiesendanger, Frühjahrstagung der Deutschen Physikalischen Gesellschaft, Dresden (Germany): *Rastertunnelspektroskopie an defektinduzierten Quantenpunktzuständen in single-walled Carbon Nanotubes.*

24.03.03: M. Morgenstern, J. Wiebe, Chr. Meyer, J. Klijn, and R. Wiesendanger, Frühjahrstagung der Deutschen Physikalischen Gesellschaft, Dresden (Germany): *Rastertunnelspektroskopie eines stark ungeordneten zweidimensionalen Elektronensystems: Von quanisierten Zuständen zur Perkolation.*

24.03.03: L. Berbil-Bautista, T. Hänke, M. Getzlaff, I. Opahle, M. Richter, and R. Wiesendanger, Frühjahrstagung der Deutschen Physikalischen Gesellschaft, Dresden (Germany): *Observation of 5f-states on U/W(110) films by means of STS.*

25.03.03: M. Morgenstern, J. Klijn, Chr. Meyer, and R. Wiesendanger, Frühjahrstagung der Deutschen Physikalischen Gesellschaft, Dresden (Germany): *Realraumabbildung von Driftzuständen eines zweidimensionalen Elektronensystems.*

25.03.03 U. Kaiser, A. Schwarz, U. H. Pi, M. Liebmann, Z. G. Khim, T. W. Noh, D. W. Kim, and R. Wiesendanger, Spring Conference, Deutsche Physikalische Gesellschaft, Dresden (Germany): *Visualisierung der Barkhausen-Volumen einer ferromagnetischen Schicht mittels Magnetkraftmikroskopie.*

25.03.03: M. Getzlaff, T. Hänke, L. Berbil-Bautista, and R. Wiesendanger, Frühjahrstagung der Deutschen Physikalischen Gesellschaft, Dresden (Germany): *Uranium thin films: structural and electronic properties.*

26.03.03: R. Ravlić, S. Kuck, M. Bode, and R. Wiesendanger, Frühjahrstagung der Deutschen Physikalischen Gesellschaft, Dresden (Germany): *STM/STS Untersuchungen der morphologischen und elektronischen Eigenschaften von dünnen Fe-Filmen auf Cr(001).*

26.03.03: M. Bode, A. Wachowiak, J. Wiebe, O. Pietzsch, M. Morgenstern, and R. Wiesendanger, Frühjahrstagung der Deutschen Physikalischen Gesellschaft, Dresden (Germany): *Direct Observation of Internal Spin-Structure of Magnetic Vortex Cores.*

27.03.03: A. Kubetzka, O. Pietzsch, M. Bode, S. Krause, and R. Wiesendanger, Frühjahrstagung der Deutschen Physikalischen Gesellschaft, Dresden (Germany): *SP-STM study of 360 ° domain walls in an external magnetic field.*

27.03.03: R. Ravlić, M. Bode, and R. Wiesendanger, Frühjahrstagung der Deutschen Physikalischen Gesellschaft, Dresden (Germany): *Korrelation von morphologischen und magnetischen Eigenschaften von Fe/Cr(001): Untersuchung mittels SP-STS/STM.*

28.03.03 A. Schwarz, U. H. Pi, M. Liebmann, U. Kaiser, Z. G. Khim, D. H. Kim und R. Wiesendanger, Spring Conference, Deutsche Physikalische Gesellschaft, Dresden (Germany): *Beobachtung der Vortex-Antivortex-Vernichtung auf BSCCO-(2212) im Realraum mittels Magnetkraftmikroskopie.*

28.03.03 A. Schwarz, S. M. Langkat, H. Hölscher, and R. Wiesendanger, Spring Conference, Deutsche Physikalische Gesellschaft,Dresden (Germany): *3-Dimensionale Kraftfeldspektroskopie mit atomarer Auflösung.*

28.03.03: K. v. Bergmann, M. Bode, A. Kubetzka, O. Pietzsch, and R. Wiesendanger, Frühjahrstagung der Deutschen Physikalischen Gesellschaft, Dresden (Germany): *Influence of isolated oxygen adsorbates on the local electronic structure of 2 ML Fe/W (110).*

12.05.03: M. Bode, I. Physikalisches Institut, Universität Göttingen (Germany): *Spinpolarisierte Rastertunnelmikroskopie: Methodik und Möglichkeiten.*

14.05.03: R. Wiesendanger, Rotary Club HH-Blankenese, Hamburg (Germany): *Vorstoß in den Mikrokosmos.*

14.05.03: F. Meier, Graduiertenkolleg "Nanostrukturierter Festkörper", Hamburg, Germany: *Erste Rastertunnelmikroskopie-Messungen bei T = 300 mK.*

22.05.03: M. Morgenstern, Kolloquium der Universität Regensburg (Germany): *Abbildung von Spinverteilung und lokaler Zustandsdichte in Elektronensystemen verschiedener Dimension.*

13.06.03: R. Wiesendanger, Colloquium, University of Basel (Switzerland): *Novel Insight into Nano- and Atomic-Scale Magnetism.*

18.06.03: K. v. Bergmann, Graduiertenkolleg-Seminar (Design and Characterisation of functional materials), Hamburg (Germany): *Influence of isolated oxygen adsorbates on the local electronic structure of 2 ML Fe/W (110).*

23.06.03: M. Morgenstern, Kolloquium der Universität Hamburg (Germany): *Die lokale Zustandsdichte in wechselwirkenden Elektronensystemen verschiedener Dimension.*

03.07.03: G. Hoffmann, Seminar Talk, Informatikanwendungen in Nanotechnologien, Universität Hamburg (Germany): *Nanomanipulation.*

21.07.03: K. v. Bergmann, M. Bode, A. Kubetzka, O. Pietzsch, and R. Wiesendanger, 12^{th} International conference on STM, Eindhoven, (The Netherlands): *Spin-polarised Friedel oscillations on 2 ML Fe on W(110).*

21.07.03: R. Ravlić, M. Bode, T. Hänke, and R. Wiesendanger, 12^{th} International conference on STM, Eindhoven, (The Netherlands): *Correlation of the electronic and magnetic structure of Fe on Cr(001) by Spin-Polarized Scanning Tunneling Microscopy.*

21.07.03: M. Bode, S. Heinze, A. Kubetzka, O. Pietzsch, K. v. Bergmann, X. Nie, G. Bihlmayer, S. Blügel, and R. Wiesendanger, 12^{th} International conference on STM, Eindhoven, (The Netherlands): *Magnetization direction dependent electronic structure variations revealed by scanning tunneling spectroscopy.*

22.07.03: L. Berbil-Bautista, T. Hänke, M. Getzlaff, I. Opahle, M. Richter, and R. Wiesendanger, 12^{th} International conference on STM, Eindhoven, (The Netherlands): *Observation of 5f-states on U/W(110) films by means of STS.*

22.07.03: M. Bode, O. Pietzsch, A. Kubetzka, and R. Wiesendanger, XVIII. International Colloquium on Magnetic Films and Surfaces (ICMFS), Madrid (Spain): *Direct Imaging of Exchange Coupled and Isolated Nanoislands: Magnetism at the Thermal Stability Limit.*

23.07.03: O. Pietzsch, A. Kubetzka, M. Bode, and R. Wiesendanger, 12^{th} International conference on STM, Eindhoven, (The Netherlands): *Structural, electronic, and magnetic properties of Co islands on Cu(111).*

23.07.03: F. Meier, J. Wiebe, A. Wachowiak, D. Haude, M. Morgenstern, and R. Wiesendanger, 12^{th} International Conference on Scanning Tunneling Micrsiscopy/Spectroscopy and Related Techniques (2003), Eindhoven (The Netherlands): *A Ultra High Vacuum (UHV)-Scanning Tunneling Microscope (STM) system operating at 300 mK and 14 T.*

23.07.03: J. Wiebe, Chr. Meyer, J. Klijn, M. Morgenstern, and R. Wiesendanger, 12^{th} International conference on scanning tunneling microoscopy/spectroscopy and related techniques, Eindhoven (The Netherlands): *From Quantized States to Percolation: Scanning tunneling spectroscopy of a strongy disordered two-dimensional electron system.*

24.07.03: R. Ravlić, M. Bode, T. Hänke, and R. Wiesendanger, 12^{th} International conference on STM, Eindhoven, (The Netherlands): *Spin-polarized Scanning Tunneling Microscopy study of dislocations and the resulting domain structure on a Cr(001) surface.*

24.07.03: Th. Maltezopoulos, A. Bolz, Chr. Meyer, Chr. Heyn, W. Hansen, M. Morgenstern and R. Wiesendanger, 12^{th} International conference on scanning tunneling microscopy/spectroscopy and related techniques, Eindhoven (The Netherlands): *Wave-function mapping of strain-induced InAs quantum dots.*

25.07.03: M. Ashino, Th. Maltezopoulos, A. Schwarz, S. G. Lemay, C. Dekker, and R. Wiesendanger, 12^{th} International Conference on Scanning Tunneling Microscopy/Spectroscopy and Related Techniques, Eindhoven (The Netherlands): *Scanning dynamic force microscopy/spectroscopy of single wall carbon nanotubes including defects.*

09.09.03: E. Y. Vedmedenko, H. P. Oepen, and J. Kirschner, Aperidodic 2003, Belo Horizonte (Brazil): *Quasiperidodic magnetic Order and geometrical Frustration on the Penrose Tiling.*

16.09.03: J. Klijn, Van der Waals-Zeeman Colloquium, Van der Waals-Zeeman Institute, University of Amsterdam, Amsterdam, (The Netherlands): *Local density of states of the adsorbate-induced two-dimensional electron system studied at zero and strong magnetic fields.*

13.10.03: M. v. Sprekelsen , T. Maltezopoulos, and R. Wiesendanger, HERCULAS-meeting at KTH, Kysta (Sweden): *High speed - Scanning Capacitance Spectroscopy on semiconductor microstructures.*

14.10.03: M. Bode, IBM Research, Almaden (USA): *Recent Progress in Spin-Polarized STM.*

17.10.03: Th. Maltezopoulos, A. Kubetzka, A. Bolz, Chr. Meyer, Chr. Heyn, W. Hansen, M. Morgenstern, R. Wiesendanger, S. G. Lemay, C. Dekker, D. Talapin and H. Weller, Workshop des Graduiertenkollegs "Design and Characterisation of Functional Materials", Leck (Germany): *Electronic states in nanostructures studied by scanning tunneling spectroscopy.*

04.11.03: M. Bode, O. Pietzsch, A. Kubetzka, and R. Wiesendanger, 50^{th} Intl. Symposium of the American Vacuum Society , Baltimore (USA): *Imaging of Magnetic Nanoislands at the Thermal Stability Limit.*

10.11.03: Th. Maltezopoulos, A. Bolz, Chr. Meyer, Chr. Heyn, W. Hansen, M. Morgenstern and R. Wiesendanger, Seminar über ausgewählte Kapitel der Festkörperphysik, -technologie und Photonik, Berlin (Germany): *Wave-function mapping of InAs quantum dots by scanning tunneling spectroscopy.*

11.11.03: E. Y. Vedmedenko, Kolloquium des Instituts für Mathematik und Informatik, Greifswald (Germany): *Angeordnete Unordnung in Quasikristallen.*

12.11.03: M. Morgenstern, Seminar, MPI für Festkörperforschung, Stuttgart (Germany): *Abbildung von Spinverteilung und lokaler Zustandsdichte in Elektronensystemen verschiedener Dimension.*

20.11.03: M. Morgenstern, Kolloquium der Universität Linz (Austria): *Local Density of States of III-V Semiconductors: Two-Dimensional Electron Systems and Quantum Dots.*

10.12.03: G. Hoffmann, Graduiertenkolleg "Physik der Nanostrukturen", Universität Hamburg (Germany): *Local Physical Properties of Magnetic Molecules.*

16.12.03: G. Hoffmann, Seminar University of Florenz (Italy): *Magnetic Spectroscopy with a Scanning Tunneling Microscope at an Atomic Scale.*

07.01.04: M. Janson, T. Maltezopoulos, M. Morgenstern, and R. Wiesendanger NANOSPECTRA network meeting in Nottingham (UK): *Wave Function Mapping of Quantum Dots using Scanning Tunneling Spectroscopy.*

13.01.04: E. Y. Vedmedenko, Seminar "Physik amorpher und flüssiger Legierungen", Chemnitz University, Chemnitz (Germany): *Simulation magnetische Eigenschaften aperiodische Parketierungen.*

15.01.04: M. von Sprekelsen, T. Maltezopoulos, and R. Wiesendanger, HERCULAS-meeting at HMI in Berlin (Germany): *High speed - Scanning Capacitance Spectroscopy on semiconductor microstructures.*

02.02.04: R. Wiesendanger, Colloquium, University of Erlangen (Germany): *Magnetismus auf atomarer Skala: Neue Einblicke in ein alt bekanntes Phänomen.*

13.02.04: R. Wiesendanger, Rotary Club HH-Blankenese, Hamburg (Germany): *Nanotechnologie - Aufbruch in neue Welten.*

08.03.04: O. Pietzsch, S. Heinze, A. Kubetzka, M. Bode, and R. Wiesendanger, 68. Spring Conference, Deutsche Physikalische Gesellschaft, Regensburg (Germany): *Spin-polarized scanning tunneling spectroscopy of Co islands on Cu(111).*

08.03.04: K. von Bergmann, M. Bode, and R. Wiesendanger, 68. Spring Conference, Deutsche Physikalische Gesellschaft, Regensburg (Germany): *Magnetism of Fe on W(001).*

08.03.04: M. Ashino, T. Behnke, A. Schwarz, K. A. Williams, C. Dekker, and R. Wiesendanger, 68. Spring Conference, Deutsche Physikalische Gesellschaft, Regensburg (Germany): *Three-dimensional force fields of single wall carbon nanotubes by scanning dynamic force spectroscopy*

08.03.04: O. Lemcke, A. Kubetzka, and R. Wiesendanger, 68. Spring Conference, Deutsche Physikalische Gesellschaft, Regensburg (Germany): *Simulation von Temperatureffekten im mikromagnetischen Modell.*

08.03.04: O. Pietzsch, S. Heinze, A. Kubetzka, M. Bode, and R. Wiesendanger, 68. Spring Conference, Deutsche Physikalische Gesellschaft, Regensburg (Germany): *Spin-Polarized Scanning Tunneling Spectroscopy of Co islands on Cu(111).*

08.03.04: L. Sacharow, S. Heinze, G. Bihlmayer, S. Blügel, J. Wiebe, M. Morgenstern, and R. Wiesendanger, 68. Spring Conference, Deutsche Physikalische Gesellschaft, Regensburg (Germany): *Vergleich der* ab-initio *berechneten elektronischen Struktur verschiedener Stapelfolgen von Co(0001).*

09.03.04: F. Meier, J. Wiebe, A. Wachowiak, D. Haude, T. Foster, M. Morgenstern, and R. Wiesendanger, 68. Spring Conference, Deutsche Physikalische Gesellschaft, Regensburg (Germany): *An Ultra High Vacuum Scanning Tunneling Microscope system operating at 300 mK and 14 T.*

09.03.04: T. Hänke,S. Krause, R. Ravlić, M. Bode, and R. Wiesendanger, 68. Spring Conference, Deutsche Physikalische Gesellschaft, Regensburg (Germany): *Temperaturabhängige Untersuchungen des Cr(001)-Oberflächenzustandes mittels SP-STM/STS.*

10.03.04: S. Krause, T. Hänke, M. Bode, and R. Wiesendanger, 68. Spring Conference, Deutsche Physikalische Gesellschaft, Regensburg (Germany): *Spinpolarisierte Rastertunnelmikroskopie der Cr(001)-Oberfläche bei variabler Temperatur.*

10.03.04: T. Behnke, M. Ashino, A. Schwarz, R. Wiesendanger, K. A. Williams, and C. Dekker, 68. Spring Conference, Deutsche Physikalische Gesellschaft,

Regensburg (Germany): *Dynamic Mode Force Microscopy Studies of Individual Single Wall Nanotubes on HOPG.*

11.03.04: T. Maltezopoulos, A. Bolz, C. Meyer, C. Heyn, W. Hansen, M. Morgenstern, and R. Wiesendanger, 68. Spring Conference, Deutsche Physikalische Gesellschaft, Regensburg (Germany): *Wave-function mapping of InAs quantum dots by scanning tunneling spectroscopy*

11.03.04: A. Kubetzka, E. Vedmendenko, K. von Bergmann, O. Pietzsch, M. Bode, and R. Wiesendanger, 68. Spring Conference, Deutsche Physikalische Gesellschaft, Regensburg (Germany): *Domain wall orientation in magnetic nanowires: Anisotropy of the exchange interaction*

11.03.04: J. Wiebe, L. Sacharow, A. Wachowiak, M. Morgenstern, and R. Wiesendanger, 68. Spring Conference, Deutsche Physikalische Gesellschaft, Regensburg (Germany): *Spectroscopic Signature of Stacking Faults and Dislocation Lines on Co(0001).*

12.03.04 A. Schwarz, M. Liebmann, and R. Wiesendanger, 68. Spring Conference, Deutsche Physikalische Gesellschaft, Regensburg (Germany): *Observation of Abrikosov lattice melting in real space by magnetic force microscopy.*

15.03.04: C. Meyer, and R. Wiesendanger, EU-ASPRINT kickoff meeting at the Studiecentrum Soeterbeeck in Ravenstein (Netherlands): *Atomic manipulation and characterization of artificial nanostructures by a spin-polarized scanning tunneling microscope.*

24.03.04: M. von Sprekelsen, T. Maltezopoulos, and R. Wiesendanger, HERCULAS-meeting at IMEC in Leuven (Belgium): *High speed - Scanning Capacitance Spectroscopy on semiconductor microstructures.*

08.04.04: M. Morgenstern, Colloquium at Fritz-Haber-Institut, Berlin (Germany): *Scanning Tunneling Spectroscopy of Quantum Systems in Semiconductors.*

13.04.04: R. Wiesendanger, Rotary Club HH-Steintor, Hamburg (Germany): *Nanotechnologie - Aufbruch in neue Welten.*

14.04.04: R. Wiesendanger, Rotary Club HH-Haake, Hamburg (Germany): *Nanotechnologie - Aufbruch in neue Welten.*

26.04.04: C. J. Chen, Seminar Talk, University of Hamburg (Germany): *Blueprints of Six New Experiments in SP-STM and NC-AFM.*

30.04.04: R. Wiesendanger, Workshop "Nanotechnologie: Vom Studium zum eigenen Unternehmen", Hamburg (Germany): *Nanotechnologie an der Universität Hamburg.*

18.05.04: R. Wiesendanger, Spring School on "Interdisciplinary Nanoscience: From Basic Research to Applications, Hamburg (Germany): *Scanning Probe Methods: Novel Insight into the Nanoworld.*

24.05.04: M. Bode, Hong Kong University of Science & Technology, Hong Kong (China): *Spin-Polarized Scanning Tunneling Microscopy: Achievements and Perspectives.*

28.05.04: R. Wiesendanger, unaxis Seminar, Balzers (Liechtenstein): *Magnetische Lesetechnik auf der Sub-Nanometerskala: Basis einer neuen magnetischen Speichertechnologie?*

14./15.06.04: C. J. Chen, Lecture Series at the Summer School, University of Hamburg (Germany): *STM, NC-AFM, and Atom Manipulation: From Personal Art to Exact Science.*

17.06.04: O. Pietzsch, A. Kubetzka, M. Bode, K. von Bergmann, S. Heinze, E. Y. Vedmedenko, and R. Wiesendanger, Seminar, Max-Planck-Institut für Chemische Physik fester Stoffe, Dresden (Germany): *Imaging Magnetic Nanostructures: Spin-Polarized Scanning Tunneling Microscopy of Fe/W(110) and Co/Cu(111).*

22.06.04: A. Schwarz, U. Kaiser, M. Liebmann, and R. Wiesendanger, 7^{th} International Conference on Nanostructured Materials (Nano '04), Wiesbaden (Germany): *Real space observation of individual Barkhausen jumps by magnetic force microscopy.*

30.06.04: M. Morgenstern, Kolloquium des SFB 513, Universität Konstanz (Germany): *Scanning Tunneling Spectroscopy of Semiconductors in Different Dimensions.*

20.07.04: M. Morgenstern, Seminar National Nanotechnology Lab, University of Lecce (Italy): *Scanning Tunneling Spectroscopy: Interacting Electron Systems in Different Dimensions.*

05.09.04: E. Y. Vedmedenko, N. Mikuszeit, H. P. Oepen, and R. Wiesendanger, Joint European Magnetic Symposium JEMS'04, Dresden (Germany): *Anisotropic domain wall orientation for isotropic exchange interactions.*

12.09.04: M. Ashino, T. Maltezopoulos, T. Benke, A. Schwarz, and R. Wiesendanger, 7^{th} International Conference on non-contact Atomic Force Microscopy, Seattle, Washington (USA): *Three-dimensional force field spectroscopy of a single-walled carbon nanotube.*

12.09.04: M. Ashino, A. Schwarz, H. Hölscher, U. D. Schwarz, W. Allers, and R. Wiesendanger, 7^{th} International Conference on non-contact Atomic Force

Microscopy, Seattle, Washington (USA): *Contrast Formation on Surfaces Composed of Hexagonally Aranged Carbon Atoms.*

13.09.04: M. Liebmann, A. Schwarz, U. Kaiser, R. Wiesendanger, T. W. Noh, and D. W. Kim, 7^{th} International Conference on Noncontact Atomic Force Microscopy (NCAFM '04), Seattle, Washington (USA): *Visualization of the Barkhausen Effect by Magnetic Force Microscopy.*

15.09.04: U. Kaiser, N. Plock, A. Schwarz, and R. Wiesendanger, Seventh International Conference on non-contact Atomic Force Microscopy, Seattle (USA): *Charged and non-charged surface defects on NiO(001) investigated by dynamic mode SFM*

22.09.04: C. J. Chen, O. Pietzsch, and D. Haude, Seminar Talk, University of Hamburg (Germany): *A Simple and Rigid Rotational Stepper, for Scanning Probe Microscopes.*

11.10.04: C. J. Chen, Seminar Talk, University of Hamburg (Germany): *Self-Actuating Self-Measuring Optimized Cantilever for FM-AFM.*

14.10.04: M. Morgenstern, Ornstein-Colloquium at Utrecht University (Netherlands): *Scanning Tunneling Spectroscopy of Semiconductors: From Quantum Dots to More Complex Systems.*

22.10.04: R. Wiesendanger, Nanoscience Seminar, University of Cambridge (U.K.): *Frontiers of Nanomagnetism Studied by Spin-Polarized Scanning Tunneling Spectroscopy.*

05.11.04: C. J. Chen, Colloquium at Free University of Berlin (Germany): *Recent Advances in Fundamental Physics of STM and AFM.*

07.11.04: E. Y. Vedmedenko, N. Mikuszeit, H. P. Oepen, and R. Wiesendanger, 49^{th} Annual Conference on Magnetism and Magnetic Materials MMM 2004, Jacksonville, Florida (USA): *Multipole moments and interactions between magnetic nanoparticles.*

24.11.04: K. von Bergmann, Seminar, Surface Science Research Center, University of Liverpool (UK): *Iron nanostructures studied by spin-polarised scanning tunneling microscopy.*

12.11.04: M. Bode, Colloquium of the Physics Department at Ohio University, Athens (USA): *Exploring the Frontiers of Nanomagnetism by Spin-Polarized STM.*

7.2.2 Posters

26.02.02: J. Klijn, Chr. Meyer, M. Morgenstern, and R. Wiesendanger, 12^{th} International Winterschool on New Developments in Solid State Physics/Low-Dimensional Systems: From 2D to Molecules, Mauterndorf (Austria): *Scanning Tunneling Spectroscopy of an Adsorbate Induced Two Dimensinal System on InAs(110).*

27.02.02: M. Morgenstern, 12^{th} Int. Winterschool, Low Dimensional Systems, Mauterndorf (Austria): *Two-Dimensional Properties of a Three-Dimensional Electron System in the Extreme Quantum Limit.*

27.02.02: Chr. Meyer, J. Klijn, M. Morgenstern, and R. Wiesendanger, 12^{th} Int. Winterschool, Low Dimensional Systems, Mauterndorf (Austria): *Local Density of states of a one dimensional conductor confined below a charged step edge.*

11.03.02: J. Wiebe, M. Morgenstern, A. Wachowiak, M. Getzlaff, J. Klijn, L. Plucinski, R. L. Johnson, and R. Wiesendanger, DPG-Frühjahrstagung AK Festkörperphysik, Regensburg (Germany): *Co-p-InAs(110): Ein durch Co-Inseln induziertes zweidimensionales Elektronensystem bestehend aus Elektronenpfützen.*

11.03.02: J. Klijn, Chr. Meyer, M. Morgenstern, and R. Wiesendanger, Frühjahrstagung der Deutschen Physikalischen Gesellschaft, Regensburg (Germany): *Rastertunnelspektroskopie am adsorbadinduzierten 2DES in Magnetfeldern bis zu 6T.*

11.03.02: L. Sacharow, Chr. Meyer, J. Klijn, M. Morgenstern, S. Heinze, G. Bihlmayer, S. Blügel and R. Wiesendanger, Frühjahrstagung der Deutschen Physikalischen Gesellschaft, Regensburg (Germany): *Ab initio Berechnung von Fe- und Nb-Monolagen auf InAs(110).*

12.03.02: F. Meier, Frühjahrstagung des AK Festkörperphysik bei der DPG, Regensburg (Germany): *Aufbau eines temperaturvariablen MOKE-Systems für die Charakterisierung ultradünner, magnetischer Schichten im UHV.*

13.03.02: S. M. Langkat, and R. Wiesendanger, Frühjahrstagung der Deutschen Physikalischen Gesellschaft, Regensburg (Germany): *Experimentelle Voraussetzungen zur Abbildung magnetischer Austauchkräfte mit einem Rasterkraftmikroskop.*

13.03.02: V. Hagen, M. Getzlaff, M. Bode, and R. Wiesendanger, Frühjahrstagung der Deutschen Physikalischen Gesellschaft, Regensburg (Germany): *Kontrolle der strukturellen, elektrischen und magnetischen Eigenschaften oxidbedeckter Co-Schichten mit dem Rasterkraftmikroskop.*

13.03.02: Th. Maltezopoulos, A. Bolz, J. Klijn, Chr. Meyer, Chr. Heyn , D. Talapin, A. Rogach, M. Morgenstern, and R. Wiesendanger, Frühjahrstagung der Deutschen Physikalischen Gesellschaft, Regensburg (Germany): *Rastertunnelmikroskopie und -Spektroskopie an Halbeiter-Quantenpunkten.*

06.05.02: M. Bode, M. Getzlaff, O. Pietzsch, A. Kubetzka, R. Ravlić, and R. Wiesendanger, NanoDE Innovation durch Nanotechnologie, BMBF, Bonn (Germany): *Hochauflösende Abbildung magnetischer Oberflächen.*

06.05.02: M. Bode, M. Hennefarth, M. Getzlaff, D. Haude, and R. Wiesendanger, NanoDE Innovation durch Nanotechnologie, BMBF, Bonn (Germany): *Wachstum und elektronische Struktur ultradünner Manganfilme auf W(110).*

07.05.02: M. v. Sprekelsen, J. Isenbart, M. Langer, and R. Wiesendanger, Kongress NanoDE Innovation durch Nanotechnologie, Bonn (Germany): *Rasterkapazitätsmikroskopie und -spektroskopie an Halbleitermikrostrukturen.*

01.06.02: Th. Maltezopoulos, A. Bolz, J. Klijn, Chr. Meyer, V. Hagen, M. Tews, D. Talapin, A. Rogach, Chr. Heyn, M. Morgenstern, and R. Wiesendanger, Euresco Conference Cluster-Surface Interactions, Granada (Spain): *Scanning Probe Microscopy and Spectroscopy on Semiconductor Quantum Dots.*

09.09.02: K. v. Bergmann, M. Bode, M. Getzlaff, A. Kubetzka, O. Pietzsch, and R. Wiesendanger, 3rd International Conference on Inorganic Materials, Konstanz (Germany): *Investigation of Magnetism by Scanning Tunneling Microscopy on the System Fe/W(110).*

05.12.02: J. Bansmann, A. Kleibert, M. Getzlaff, R. P. Methling, V. Senz, and K. H. Meiwes-Broer, BESSY-Nutzertreffen, Berlin (Germany): *Magnetic properties of large mass-filtered metal clusters on surfaces studied with soft X-rays.*

07.01.03: M. Bode, S. Heinze, A. Kubetzka, O. Pietzsch, X. Nie, G. Bihlmayer, S. Blügel, and R. Wiesendanger, 294. WE-Heraeus-Seminar on Frontiers in Nanomagnetism, Bad Honnef (Germany): *Magnetization-Axis Dependent Local Electronic Structure Probed by Scanning Tunneling Spectroscopy.*

07.01.03: M. Bode, A. Wachowiak, J. Wiebe, O. Pietzsch, M. Morgenstern, and R. Wiesendanger, 294. WE-Heraeus-Seminar on Frontiers in Nanomagnetism, Bad Honnef (Germany): *Direct Observation of Internal Spin-Structure of Magnetic Vortex Cores.*

12.03.03: M. Ashino, Th. Maltezopoulos, A. Schwarz, S. G. Lemay, C. Dekker, and R. Wiesendanger, Deutsche Physikalische Gesellschaft, Spring Meeting, Dresden (Germany): *Scanning force microscopy/spectroscopy studies of single wall carbon nanotubes including defects.*

24.03.03: F. Meier, A. Wachowiak, J. Wiebe, D. Haude, M. Morgenstern, and R. Wiesendanger, Frühjahrstagung des AK Festkörperphysik bei der DPG, Regensburg, (Germany): *Eine UHV-Rastertunnelmikroskopieanlage für Messungen bei 300 mK und 14 T.*

24.03.03: T. Hänke, S. Krause, M. Bode, and R. Wiesendanger, Frühjahrstagung des AK Festkörperphysik bei der DPG, Regensburg, (Germany): *Aufbau eines UHV-SPSTM für Untersuchungen bei variablen Temperaturen.*

24.03.03: M. v. Sprekelsen, J. Isenbart, and R. Wiesendanger, Frühjahrstagung der Deutschen Physikalischen Gesellschaft, Dresden (Germany): *Hochgeschwindigkeits-Rasterkapazitätsspektroskopie an Halbleitermikrostrukturen - Lokalisierung von pn-Übergängen.*

27.06.03: J. Wiebe, Chr. Meyer, J. Klijn, M. Morgenstern, and R. Wiesendanger, Center of Excellence for Low Dimensional Structures, Warswaw, (Poland): *From Quantized States to Percolation: Scanning tunneling spectroscopy of a strongly disordered two-dimensional electron system.*

03.07.03: M. Morgenstern, J. Klijn, Chr. Meyer, J. Wiebe, and R. Wiesendanger, International Workshop "Quantum Hall Effect: Past, Present and Future", Stuttgart (Germany): *Scanning Tunneling Spectroscopy of Two-Dimensional Electron Systems in Magnetic Field.*

22.07.03: U. Kaiser, M. Liebmann, A. Schwarz, U. H. Pi, Z. G. Khim, T. W. Noh, D. W. Kim, and R. Wiesendanger, 12^{th} International Conference on Scanning Tunneling Microscopy/Spectroscopy and Related Techniques, Eindhoven (The Netherlands): *Domain nucleation and growth of ferromagnetic $La_{0.7}Sr_{0.3}MnO_3/LaAlO_3$ films at variable magnetic fields studied with low-temperature MFM.*

05.08.03: M. Morgenstern, A. Wachowiak, J. Wiebe, J. Klijn, Chr. Meyer, M. Bode, and R. Wiesendanger, 2nd International Conference on Semiconductor Spintronics and Quantum Information Technology, Brügge (Germany): *Towards spin polarized imaging of ferromagnet-semiconductor interfaces.*

02.09.03: M. Liebmann, U. Kaiser, A. Schwarz, R. Wiesendanger, U. H. Pi, T. W. Noh, D. W. Kim, and Z. G. Khim, 6^{th} International Conference on Noncontact Atomic Force Microscopy, Dingle (Ireland): *Domain nucleation and growth of $La_{0.7}Ca_{0.3}MnO_{3-\delta}/LaAlO_3$ films studied by low-temperature magnetic force microscopy.*

16.02.04: J. Wiebe, Chr. Meyer, J. Klijn, M. Morgenstern, and R. Wiesendanger, 13^{th} International Winterschool on New Developments in Solid State Physics, Mauterndorf (Austria): *From Quantized States to Percolation: Scanning Tunneling Spectroscopy of a Strongly Disordered Two-dimensional Electron System.*

16.02.04: F. Meier, J. Wiebe, A. Wachowiak, D. Haude, M. Morgenstern, and R. Wiesendanger, 13^{th} International Winterschool on New Developments in Solid State Physics, Mauterndorf (Austria): *An Ultra High Vacuum Scanning Tunneling Microscope system operating at 300 mK and 14 T.*

08.03.04: T. Mashoff, D. Haude, M. Morgenstern, and R. Wiesendanger, Spring Conference, Deutsche Physikalische Gesellschaft, Regensburg (Germany): *Aufbau eines Tieftemperatur-Hochmagnetfeld-Rastertunnelmikroskops mit X-Y-Verschiebetisch und Spitzenwechsel.*

08.03.04: S. Kuck, G. Hoffmann, and R. Wiesendanger, Spring Conference, Deutsche Physikalische Gesellschaft, Regensburg (Germany): *Design of a scanning tunneling microscope for variable temperatures in an ultra-high-vacuum environment.*

08.03.04: M. von Sprekelsen, V. Hagen, T. Maltezopoulos, R. Wiesendanger, Spring Conference, Deutsche Physikalische Gesellschaft, Regensburg (Germany): *Hochauflösende Rasterkapazitätsspektroskopie an Halbleitermikrostrukturen.*

08.03.04: N. Plock, U. Kaiser, A. Schwarz and R. Wiesendanger, Spring Conference, Deutsche Physikalische Gesellschaft, Regensburg (Germany): *Untersuchung von Punkt- und Liniendefekten auf der NiO(001)-Spaltfläche mittels Rasterkraftmikroskopie.*

09.03.04: U. Kaiser, M. Liebmann, A. Schwarz, R. Wiesendanger, U. H. Pi, Z. G. Khim, T. W. Noh and D. W. Kim, Spring Conference, Deutsche Physikalische Gesellschaft, Regensburg (Germany): *Magnetkraftmikroskopische Untersuchungen ferromagnetischer* $La_{0.7}Ca_{0.3}MnO_{3-\delta}/LaAlO_3$*-Filme in variablen Magnetfeldern.*

10.03.04: T. Behnke, M. Ashino, A. Schwarz, R. Wiesendanger, K. A. Williams, and C. Dekker, Spring Conference, Deutsche Physikalische Gesellschaft, Regensburg (Germany): *Dynamic Mode Force Microscopy Studies of Individual Single Wall Nanotubes on HOPG.*

20.06.04: M. Janson, T. Maltezopoulos, A. Bolz, C. Meyer, C. Heyn, W. Hansen, M. Morgenstern, and R. Wiesendanger, NANOSPECTRA Summer School at Porquerolles (France): *Wave-function mapping of single-electron states in semiconducting quantum dots by scanning tunneling spectroscopy.*

12.09.04: C. J. Chen, The Seventh International Conference of NC-AFM, Seattle (USA): *A Universal Relation in NC-AFM, STM, and Atom Manipulation.*

15.09.04: U. Kaiser, N. Plock, A. Schwarz, R. Wiesendanger, T. W. Noh, and D. W. Kim, 7^{th} International Conference on Noncontact Atomic Force Microscopy (NCAFM '04), Seattle, Washington (USA): *Charged and non-charged surface defects on NiO (001) investigated by dynamic mode SFM.*

23.09.04: J. Wiebe, Chr. Meyer, J. Klijn, M. Morgenstern, and R. Wiesendanger, International Symposium on "Quantum Hall Systems and Quantum Materials", Hamburg (Germany): *The transition from quantized states to percolation in a strongly disordered two-dimensional electron system investigated by scanning tunneling spectroscopy.*

23.09.04: T. Maltezopoulos, A. Bolz, C. Meyer, M. Janson, D. Haude, C. Heyn, W. Hansen, M. Morgenstern, and R. Wiesendanger, International Symposium on Quantum Hall Systems and Quantum Materials, Hamburg (Germany): *Wavefunction mapping of single-electron states in strain-induced InAs quantum dots by scanning tunneling spectroscopy.*

23.09.04: F. Meier, J. Wiebe, A. Wachowiak, D. Haude, M. Morgenstern, and R. Wiesendanger, International Symposium on "Quantum Hall Systems and Quantum Materials", Hamburg (Germany): *An Ultra High Vacuum Scanning Tunneling Microscope system operating at 300 mK and high magnetic fields.*

13.10.04: M. Ashino, T. Behnke, A. Schwarz, and R. Wiesendanger, Seeing at the Nanoscale II International Conference, Grenoble (France): *Atomic resolution three-dimensional force field spectroscopy of single walled carbon nanotubes.*

13.10.04: C. J. Chen, O. Pietzsch, D. Haude, and R. Wiesendanger, Seeing at the Nanometer Scale Conference, Grenoble (France): *Subnanometer Physics Explored by STM and NC-AFM having Tip-Characterization and Tip-Rotation Capabilities.*

Chapter 8

Talks Given by Guests

21.01.2002: Dipl.-Phys. E. Ahlswede (MPI Stuttgart): *Potential Distribution of the Quantum Hall Effect measured by Scanning Force Microscopy.*

22.01.2002: Prof. Dr. G. Schönhense (Univ. Mainz): *Time-resolved PEEM.*

28.01.2002: Prof. Dr. M. Richter (IFW Dresden): *Electronic structure of 4f- and 5f-systems.*

15.02.2002: Dr. H. Tokumoto (JRCAT, Tsukuba, Japan): *How have carbon nanotubes revolutionalized scanning probe microscopy?*

19.02.2002: Dr. M. Takeuchi (JRCAT, Tsukuba, Japan): *Structural Analysis of Two-Dimensional Crystals of Intercalated DNA by Scanning Probe Microscopy.*

22.02.2002: Dr. Z. Lu (Univ. of Plymouth, U. K.): *Spin-engineered spin valves.*

03.04.2002: Dr. D. Orgassa (Caltech, USA): *Spinpolarisation in Leitern: Gleichgewicht, Nicht-Gleichgewicht und Meßmethoden.*

04.04.2002: Dr. S. Heinze (IBM Yorktown Heights, USA): *Verständnis von Materialien für die Magneto- und Nanoelektronik auf der Grundlage ihrer elektronischen Struktur.*

05.04.2002: Dr. P. Rottländer (CNRS, Nancy, France): *Barrieren von ferromagnetischen Tunnelkontakten - Aspekte der Herstellung und der Transporteigenschaften.*

08.04.2002: Dipl.-Phys. J. Dumont (Univ. of Namur, Belgium): *Investigation of the workfunction of metallic superlattices in order to improve the properties of contacts of metals with wide-band gap semiconductors.*

15.04.2002: Dr. M. Bischoff (Univ. of Nijmegen, Netherlands): *Surface States on Transition Metal Surfaces studied by Scanning Tunneling Spectroscopy.*

25.04.2002: Dr. S. Parkin (IBM San Jose, USA): *Instant access memory: tunneling into the future with MRAM.*

08.05.2002: Dr. W. Hübner (MPI Halle): *Dünne magnetische Filme: Nichtlineare Optik und Kurzzeitdynamik.*

27.05.2002: Dr. S. Demokritov (Univ. Kaiserslautern): *Spinwellendynamik lateral strukturierter magnetischer Systeme.*

03.06.2002: Dr. V. Stepanyuk (MPI Halle): *Magnetism and Structure on the Atomic Scale.*

10.06.2002: Dr. E. Konenkova (Ioffe Institute, St. Petersburg, Russia): *Modification of GaAs surfaces by treatment in sulfide alcoholic solutions.*

05.08.2002: Prof. Dr. I. Schuller (Univ. of San Diego, CA, USA): *Nanostructures and the Proximity Effect.*

29.08.2002: Dr. O. Hellwig (IBM Almaden, USA): *Magnetic structure and reversal of exchange-coupled thin films with perpendicular anisotropy.*

30.08.2002: Dipl.-Phys. U. Keyser (Univ. Hannover): *Nanostrukturierung mit dem Rasterkraftmikroskop: Kondoeffekt in kleinen Quantenringen.*

02.09.2002: Dr. J. Dumont (Univ. of Namur, Belgium): *Growth and electronic properties of Ag/Pd multilayers.*

05.09.2002: Dr. Ch. Idriss (Univ. of Strasbourg, France): *Study of the growth and the magnetic properties of Co, Co-Au and Rh dots and ultra-thin films on the Au(111) surface.*

13.09.2002: Prof. Dr. S. Abeygunaratne (Univ. of Akron, Ohio, USA): *Liquid Crystal Display Technology and Banana Shaped Liquid Crystals.*

23.09.2002: Dr. A. Heinrich (IBM Almaden, USA): *Molecular Dominos.*

02.12.2002: Dr. J. Wecker (Siemens AG, Erlangen): *Magnetische Tunnelstrukturen und ihre Anwendungen.*

16.12.2002: Prof. Dr. Ch. Gerber (IBM Rüschlikon): *Nanomechanics the Link to Chemistry and Biology.*

13.01.2003: Prof. Dr. R. Schäfer (IFW Dresden): *Kerr-Mikroskopie an magnetischen Vielfachschichten.*

14.01.2003: Prof. Dr. B.-G. Liu (Chinese Academy of Sciences, Beijing, China): *Theoretical study of high-spin-polarized materials.*

20.01.2003: Dr. P. Koenraad (Univ. Eindhoven, Netherlands): *Analysis of III-V semiconductor nanostructures with cross-sectional scanning tunneling microscopy.*

28.01.2003: Dr. Jordan (Charité Berlin): *Magnetic Fluid Hyperthermia - eine neue Option in der kombinierten Krebstherapie mit Nanopartikeln.*

02.04.2003: Prof. Dr. A. Engel (M. E. Müller-Institute for Structural Biology, Biocenter, Univ. Basel, Switzerland): *Nanomachines of the Biological Membrane: Surface Structure and Dynamics Assessed by AFM.*

07.04.2003: Dr. M. Zeyer (Univ. Jena): *Untersuchungen zur Netzwerkstruktur phosphathaltiger Gläser mittels Festkörper-Kernresonanzspektroskopie.*

28.04.2003: Dr. M. Janson (RIT, Stockholm, Sweden): *Hydrogen diffusion and interaction with acceptors in the wide bandgap semiconductor silicon carbide.*

02.05.2003: Prof. Dr. T. Fukuda (Präsident des IEEE Nanotechnology Council): *Nano-Robotic Manipulation for Carbon Nanotubes.*

05.05.2003: Dr. M. Rost (Univ. Leiden, Netherlands): *Energetics of the Au(110)-surface: one reason for many structures.*

12.05.2003: Dr. G. Costantini (MPI Stuttgart): *Growth and overgrowth of semiconductor quantum dots studied by in-situ STM.*

16.06.2003: Dr. K. Sauthoff (Univ. Göttingen): *Einzelne Donatoren und Donatorkomplexe nahe der GaAs(110)-Oberfläche bei 8K.*

24.06.2003: Prof. Dr. W. Heckl (LMU München): *Rastersondenmethoden in den Lebenswissenschaften.*

18.06.2003: Dr. H.-B. Braun (ETH Zürich, Switzerland): *Magnetism in nanostructures from superparamagnetism to mesoscopic quantum effects.*

15.07.2003: Dr. F. Silly (Univ. Lausanne, Switzerland): *Superlattices of Magnetic Adatoms in a Two-Dimensional Electron Sea.*

15.07.2003: Prof. Dr. U. Schwarz (Yale University, USA): *Ein analytisches Modell für den Kugel-Ebenen-Kontakt und seine Anwendung in der Rastersondenmikroskopie.*

16.09.2003: Dr. P. Ferriani (Univ. Modena, Italy): *Angle resolved resonant inelastic X-Ray Scattering: Intensity and dichroism from 3d transition metals in special geometries.*

16.09.2003: Prof. Dr. R. W. Saalfrank (Univ. Erlangen-Nürnberg): *Aktuelle Beiträge zum Synergieeffekt von Zufallsentdeckung und rationalem Design in der Supramolekularen Koordinationschemie: Unkonventionelle Wege zu neuen Materialien.*

23.10.2003: Prof. Dr. D. Bimberg (TU Berlin): *Quantum Dots for Lasers, Amplifiers and Computers.*

13.11.2003: Prof. Dr. G. Bauer (Univ. Linz, Austria): *Strukturelle Charakterisierung von Halbleiternanostrukturen.*

27.10.2003: Prof. Dr. A. Maziewski (Univ. Bialystok, Poland): *Magnetic ordering in ultrathin cobalt films.*

10.11.2003: Prof. Dr. P. D. Esquinazi (Univ. Leipzig): *Transport properties of graphite: an overview of the experimental evidence.*

17.11.2003: Dr. A. Schirmeisen (Univ. Münster): *Quantitative Interpretation of Forces during Single Atom Manipulation and Imaging of Organic Molecules in Dynamic AFM.*

08.01.2004: Prof. Dr. V. V. Moshchalkov (KU Leuven, Belgium): *Nanostructured Superconductors.*

12.01.2004: Dr. J. Halbritter (FZ Karlsruhe): *Direct and intermediate state tunneling and scanning tunnel microscopies and spectroscopies.*

19.01.2004: Dr. J. Honolka (MPI Stuttgart): *Domain wall dynamics and magnetotransport in (Ga,Mn)As at low temperatures.*

01.03.2004: Dr. T. Matsui (Univ. of Tokyo, Japan): *Tieftemperatur-Hochmagnetfeld-Rastertunnelspektroskopie an Landauzuständen von Graphit.*

29.03.2004: Dr. S. Lanyi (Inst. of Physics, Bratislava, Slovakia): *SCM - Analyse der Möglichkeiten und Grenzen.*

05.05.2004: Dr. S. Roth (MPI Stuttgart): *Carbon Nanotubes and Nano-Peapods: Physics and Applications.*

10.05.2004: O. Douheret (KTH, Kista, Sweden): *Nanoscale electrical characterization of semiconductor materials and devices using scanning probe microscopy.*

17.05.2004: Dr. R. Hoffmann (FZ Karlsruhe): *Forces and molecules on insulating surfaces.*

07.06.2004: Dr. M. Kläui (Univ. Konstanz): *Magnetic Rings - Intriguing Intrinsic Properties: a Playground to Study Domain Walls.*

15.06.2004: Dr. P. Johansson (Univ. of Örebro/Sweden): *Applications of surface electrodynamics to STM-induced light emission from metallic quantum well systems.*

01.07.2004: Dr. A. Schliwa (TU Berlin): *Modellierung elektronischer Zustände in InGaAs-Quantenpunkten.*

03.07.2004: Prof. Dr. U. Aebi (M. E. Müller Institute, Biocenter, University of Basel, Switzerland): *Nanomedicine: Moving nanotechnology from bench to the patient.*

03.07.2004: Prof. Dr. R. M. Taylor (Department of Computer Science, Physics and Astronomy, University of North Carolina, USA): *Direct Nanomanipulation: Its impact on the scientific method in biomedicine*

03.07.2004: Prof. Dr. D. Müller (Biotechnological Center, TU Dresden): *Observing structure, function and folding of single proteins.*

03.07.2004: Prof. Dr. M. Grunze (Inst. of Appl. Physical Chemistry, Univ. Heidelberg): *Surface Properties of thin organic films in biotechnology and medical applications.*

15.07.2004: Dr. A. Wachowiak (UC Berkeley, USA): *Doping of C60 molecules and dimers.*

29.07.2004: Prof. Dr. K. Mibu (Kyoto University, Japan): *Magnetic structures and magnetization process of magnetic vortices induced in circular, rectangular, and elliptical dots.*

19.08.2004: Dr. C. Hess (Univ. of Geneva, Switzerland): *The Vasa - A new low temperature STM.*

30.08.2004: Dr. Neng-Ping Wang (Intern. Univ. Bremen): *Time Development of Electronic Excitations of CO on MgO(001).*

22.09.2004: Dr. G. Maruccio (National Nanotechnology Laboratory, Lecce, Italy): *Biomolecular devices at the nanoscale.*

14.10.2004: Dr. A. Heinrich (IBM Almaden, USA): *Inelastic Tunneling Spectroscopy on the Atomic Scale.*

14.10.2004: Dr. J. Stroscio (NIST Gaithersburg, USA): *Listening to Atoms in Atom Manipulation and Autonomous Atom Assembly.*

14.10.2004: Prof. Dr. K.-H. Rieder (FU Berlin): *STM-Manipulation of Atoms and Molecules: Principles and Applications.*

14.10.2004: Dr. G. Meyer (IBM Rüschlikon, Switzerland): *STM Investigations of Ultrathin Insulating Films: Interface States and Atomic Manipulation.*

14.10.2004: Prof. Dr. R. Berndt, (Univ. Kiel): *Inelastic Tunneling Spectroscopy and Photon Emission.*

14.10.2004: Prof. Dr. S. Pan (Univ. of Houston, USA): *Scanning Tunneling Spectroscopy of High-Tc Superconductors.*

15.10.2004: Dr. F. Giessibl (Univ. Augsburg): *Atomic force microscopy - entering the picometer resolution range.*

08.11.2004: Dr. C. Höberger (LMU München): *Laser cooling of a microlever.*

15.11.2004: Prof. Dr. W. Brenig (TU München): *Reaktionen von Wasserstoff-Molekülen auf Silizium-Oberflächen: Zwei Puzzles - Zwei Mechanismen.*

22.11.2004: Dr. P. Mavropoulos (FZ Jülich): *Magnetic Clusters on Surfaces (DFT calculations with the KKR method).*

02.12.2004: Dr. V. Derycke (CEA/DSM Saclay, France): *Chemical and optical control of self-assembled nanotube transistors.*

13.12.2004: Dr. A. Schneider (MPI Stuttgart): *Atomic Scale Spectroscopy of magnetic and vibrational properties of atoms and molecules at surfaces.*

15.12.2004: Dipl.-Phys. Y. Mokrousov (FZ Jülich): *First-principle calculations of 1D systems: metallic nanowires and carbon nanotubes.*

Chapter 9

Lectures and Courses at the University of Hamburg

Einführung in die Struktur der Materie

Einführung in die Nanowissenschaft und Nanotechnologie

Einführung in die Rastersondenmikroskopie und -spektroskopie

Ringvorlesung Physik der Mikro- und Nanostrukturen

Seminar über Nahfeldgrenzflächenphysik und Nanotechnologie

Seminar über aktuelle Probleme der Rastersensorphysik

Proseminar über Theorie und Praxis der Rastersensormethoden

Proseminar über Oberflächenphysik und Magnetismus

Übungen zur Einführung in die Struktur der Materie

Übungen zur Einführung in die Rastersondenmikroskopie und -spektroskopie

Physikalisches Praktikum für Fortgeschrittene

TU - Praktikum

Schwerpunktpraktikum Grenzflächen- und Tieftemperaturphysik

Diplompraktikum Grenzflächen- und Tieftemperaturphysik

Studienarbeiten zur Rastersondenmikroskopie

Chapter 10

Contributions to International Organizations

- Member of the Program Committee of the "SPM-2002 International Workshop" (Nizhny Novgorod, Russia, 2002)
- Organizer of the Workshop "Highlights der Nanoanalytik-Forschung in Deutschland" (Hamburg 2002)
- Member of the Program Committee of the NanoDE-Meeting (Bonn 2002)
- Member of the Program Committee of the "1st DVG-Symposium" (Magdeburg 2002)
- Co-Chair of the NANO-7 International Advisory Board (Malmö, Sweden 2002)
- Member of the International Program Committee NANO-7 / ECOSS-21 (Malmö, Sweden 2002)
- Member of the Intl. Steering Committee of the "5th International Conference on Noncontact Atomic Force Microscopy" (Montreal, Canada 2002)
- Co-Organizer of the DPG-Symposium "Magnetismus an Oberflächen und Grenzflächen" (Dresden 2003)
- Member of the Program Committee of the "8th European Vacuum Conference and DVG-Meeting" (Berlin 2003)
- Chairman of the "3rd International Symposium on Scanning Probe Spectroscopy SPS'03" (Poznan, Poland 2003)
- Member of the Program Committee of the "12th International Conference on Scanning Tunneling Microscopy STM'03" (Eindhoven, The Netherlands 2003)
- Member of the Intl. Steering Committee of the "6th International Conference on Noncontact Atomic Force Microscopy" (Dingle, Ireland 2003)

- Co-Organizer of the Leopoldina-Symposium "From Nanoscience to Nanotechnology" (Karlsruhe 2003)
- Member of the International Advisory Board of the Workshop "Microspectroscopy of Quantum, Magnetic and Biological Nanostructures" (Osaka, Japan 2003)
- Member of the International Advisory Board and Executive Organizing Committee of the "Asia Pacific Nanotechnology Conference OzNano03" (Cairns, Australia 2003)
- Organizer of the Workshop "Nanotechnologie: Vom Studium zum eigenen Unternehmen" (Hamburg 2004)
- Member of the Program Committee of the "SPM-2004 International Workshop" (Nizhny Novgorod, Russia 2004)
- Organizer of the "Spring School on Interdisciplinary Nanoscience" (Hamburg 2004)
- Member of the Program Committee of the "7^{th} International Conference on Nanostructured Materials: Nano 2004" (Wiesbaden 2004)
- Member of the International Scientific Committee of the "Spring School on Fabrication, Manipulation and Spectroscopy of Nanostructures" (Porquerolles Island, France 2004)
- Member of the International Program Committee NANO-8 / IVC-16 (Venice, Italy 2004)
- Member of the Scientific Advisory Board of the International Symposium "Nanobiomedicine: Moving Nanotechnology from Bench to Bedside" (Hamburg 2004)
- Member of the Intl. Steering Committee of the "7^{th} International Conference on Noncontact Atomic Force Microscopy" (Seattle, USA 2004)
- Organizer of the International Symposium "Atom Manipulation, Single Spins and Atomic Forces: Novel Perspectives in the Nanoscience Era" (Hamburg 2004)

Chapter 11

How to reach us

... by mail	write to University of Hamburg, Microstructure Advanced Research Center and Institute of Applied Physics, Jungiusstraße 11, D-20355 Hamburg, Germany.
... by phone	call (++49) 40 42838 5244.
... by fax	send to (++49) 40 42838 6188.
... by e-mail	send to `wiesendanger@physnet.uni-hamburg.de`
... within the WWW	`www.nanoscience.de`
... personally